



HAL
open science

Machine learning assisted probabilistic prediction of long-term fatigue damage and vibration reduction of wind turbine tower using active damping system

Hao Bai

► **To cite this version:**

Hao Bai. Machine learning assisted probabilistic prediction of long-term fatigue damage and vibration reduction of wind turbine tower using active damping system. Mechanical engineering [physics.class-ph]. Normandie Université, 2021. English. NNT : 2021NORMIR01 . tel-03219841

HAL Id: tel-03219841

<https://theses.hal.science/tel-03219841v1>

Submitted on 6 May 2021

HAL is a multi-disciplinary open access archive for the deposit and dissemination of scientific research documents, whether they are published or not. The documents may come from teaching and research institutions in France or abroad, or from public or private research centers.

L'archive ouverte pluridisciplinaire **HAL**, est destinée au dépôt et à la diffusion de documents scientifiques de niveau recherche, publiés ou non, émanant des établissements d'enseignement et de recherche français ou étrangers, des laboratoires publics ou privés.



Normandie Université

THESE

Pour obtenir le diplôme de doctorat

Spécialité Génie Mécanique

Préparée au sein de l'Institut National des Sciences Appliquées de Rouen Normandie

Machine learning assisted probabilistic prediction of long-term fatigue damage and vibration reduction of wind turbine tower using active damping system

Présentée et soutenue par
Hao BAI

Thèse soutenue publiquement le 18 février 2021
devant le jury composé de

M. Uwe Starossek	Professeur, Technische Universität Hamburg	Président du jury
M. Yue Li	Professeur, Case Western Reserve University	Rapporteur
M. Edgar Emilio Bastidas-Arteaga	Professeur, La Rochelle Université	Rapporteur
Mme Anne Pantet	Professeure, Université Le Havre Normandie	Examinatrice
M. Le Corre Vincent	Docteur, IFP Energies nouvelles	Examinateur
M. Jean-Marc Cherfils	Docteur, INSA Rouen Normandie	Examinateur
M. Younes Aoues	Maître de conférences, INSA Rouen Normandie	Examinateur
M. Didier Lemosse	Habilitation à diriger des recherches, INSA Rouen Normandie	Directeur de thèse

Thèse dirigée par M. Didier LEMOSSE,
Laboratoire de Mécanique de Normandie - LMN (EA 3828)



MACHINE LEARNING
ASSISTED
PROBABILISTIC
PREDICTION OF
LONG-TERM FATIGUE
DAMAGE AND
VIBRATION
REDUCTION OF WIND
TURBINE TOWER
USING ACTIVE
DAMPING SYSTEM

Hao Bai

*Laboratory of Mechanics of Normandy
INSA Rouen Normandy, France*

Cover photo: “Wind turbine in Fécamp”, by Hao Bai, licensed under CC BY-SA 4.0



In memory of Hua Hua (2008-2019):

*Thank you for this wonderful adventure. It's
time for you to have a new one.*

Acknowledgments

It's clear that I can't achieve my Ph.D. degree without the guidance of my mentor, Assoc. Prof. Didier Lemosse. In fact, he had great influence on my life. We met each other when I was an engineering student. As a numerical analyst, he showed me all fundamentals in computational mechanics which turned out to be my research interest. After I obtained my engineer's degree, I had a chance to work with him on project EOLIFT. As a colleague, he showed me his passion for challenging difficulties in researches. As my tutor, he gave me many advice and instructions during my preparation. It is really my fortune to meet him as my advisor and mentor.

Asst. Prof. Younes Aoues is another guide in my research life since the beginning. He has impressed me with his sense of humor as well as the professional attitude. I'm really thankful to him that I could study with him as a student, work with him as a colleague and do the search with him as a Ph.D. candidate.

Prof. Elie Rivoalen is the best talent scout that I have ever met. I fully appreciate that he had introduced Assoc. Prof. Lemosse and Asst. Prof. Aoues to me when I was in the department of civil engineering. Without him, certainly, I would never reach my achievement today.

Dr. Jean-Marc Cherfils is another great colleague that I, fortunately, met since the EOLIFT project. His talent, his humor and his life experience showed me an entirely new way of living that I could not imagine. There are many other colleagues that I would like to thank for their kindness. Mrs. Elisabeth Lesage, the secretary of the laboratory and my witness to the wedding, helped me a lot in my professional life and personal life. Asst. Prof. Changwu Huang, a predecessor in our research team, gave me much counsel during my Ph.D. study. Asst. Prof. Yujun Cao, an experienced lecturer, kindly shared his teaching skills with me. Prof. Yong Liao, a thoughtful compatriot, shared his life experience with me. Prof. Denis Lebrun, director of Ph.D. school PSIME, offered me a chance to represent all the Ph.D. students in Rouen. Prof. Luc Vervisch, a professor in fluid mechanics, showed me his rigor in teaching. Dr. Hongbo Zhang and Dr. Wilson Javier Veloz Parra are brilliant scientists who collaborated with me on many research. M.Sc. Lujie Shi and M.Sc. Zhanyong Cao helped me a lot in my Ph.D. dissertation.

Rome wasn't built in a day. The present work would not be accomplished without all these people's care and help. Having them in my life is definitely my treasure.

H.B.

Contents

Acknowledgments	i
List of Figures	ix
List of Tables	xv
List of Algorithms	xvii
General Introduction	xxiii

Part I

Chapter 1 Scope of this thesis

1.1	Cost of wind power	4
1.2	Modern wind turbine design	6
1.2.1	Wind turbine components	6
1.2.2	Wind turbine control	13
1.2.3	Fatigue loading	15
1.3	Vibration and associated problems	17
1.3.1	Single degree of freedom system	17
1.3.2	Wind turbine damping systems	20
1.3.3	Methods of damping wind tower vibrations	21
1.4	Conclusions	23

Chapter 2 Methodology of design for wind turbine tower

2.1	Wind loads and tower loads	26
2.1.1	Source of loads	26
2.1.2	Major types of load for wind turbine	27
2.1.3	Major types of load for wind tower	28
2.2	Design process	29
2.2.1	Design standards	30
2.2.2	Wind turbine classification	32
2.2.3	Design wind conditions	33
2.2.4	Design load cases (DLC)	36

2.3	Computational mechanics for wind turbine	38
2.3.1	Modeling methods	39
2.3.2	Mathematical models for load analysis	39
2.3.3	Numerical approaches	42
2.4	Conclusions	42

Part II

Chapter 3 **Dynamic analysis of wind tower under grid loss**

3.1	Reference wind turbine	48
3.1.1	Key features	48
3.1.2	Modeling assumptions	50
3.1.3	Dynamic analysis using FAST	51
3.2	Validation of reference wind turbine for power production	52
3.2.1	Design load case of uniform steady wind (DLC0.1)	53
3.2.2	Design load case of uniform steady wind with operational maneuvers (DLC0.2)	58
3.3	Scenario U: ultimate loads analysis	65
3.3.1	Design load case of power production with grid loss (DLC2.3)	65
3.3.2	Design situation	65
3.3.3	Extreme wind and grid loss	66
3.3.4	Results and discussions	67
3.4	Conclusions	72

Chapter 4 **Probabilistic fatigue life prediction using deep neural network**

4.1	Deterministic fatigue analysis	74
4.1.1	Load-stress relation	75
4.1.2	Stress-life relation	77
4.1.3	Rainflow counting	80
4.1.4	Summary	80
4.2	Probabilistic fatigue analysis	83
4.2.1	Monte Carlo simulation	83
4.2.2	Statistical analysis	83
4.2.3	Novel framework for assessing fatigue life of wind turbine tower	86
4.2.4	Summary	91
4.3	Scenario F: fatigue loads analysis	93

4.3.1	Design load case of power production with normal turbulence model (DLC1.2)	93
4.3.2	Design situation	93
4.3.3	Process of analysis	95
4.3.4	Results and discussions	97
4.3.5	Summary	101
4.4	Empirical study	102
4.4.1	Dominant probability distribution of fatigue damage	102
4.4.2	Silhouette of the distribution of fatigue damage	104
4.4.3	Spatial distribution of fatigue damage along the tower	107
4.4.4	Summary	110
4.5	Machine learning for probabilistic fatigue estimation	110
4.5.1	Machine learning and deep neural network	111
4.5.2	Introduction to neural network	112
4.5.3	Building a deep neural network for probabilistic fatigue analysis	119
4.5.4	Results and discussions	123
4.5.5	Summary	128
4.6	Application: long-term fatigue life estimation of wind turbine tower in Caen	129
4.6.1	Prediction of fatigue life using numerical simulations	130
4.6.2	Prediction of fatigue life using neural network	132
4.6.3	Summary	134
4.7	Conclusions	134

Part III

Chapter 5 Design of an active damping system for wind turbine

5.1	Twin rotor damper (TRD)	138
5.1.1	Design of TRD	138
5.1.2	Operating modes	139
5.1.3	TRD in single degree of freedom oscillator	140
5.1.4	Summary	143
5.2	Integration of TRD into wind turbine	144
5.2.1	Structural design	144
5.2.2	Controller design	145
5.2.3	Digital implementation and numerical simulation	148
5.3	Evaluation of TRD performance	149
5.3.1	DLC2.3 with TRD	149

5.3.2	DLC1.2 with TRD	152
5.4	Optimization of the design parameters of TRD for wind turbine	155
5.4.1	Optimization problem set-up	155
5.4.2	Results and discussions	156
5.5	Conclusions	157

Chapter 6 Automatic parameter tuning optimization algorithm

6.1	Evolutionary algorithm	160
6.1.1	Differential evolution algorithm	162
6.1.2	Review of adaptive differential evolution algorithms	164
6.1.3	Summary	169
6.2	Proposed adaptive DE algorithm	169
6.2.1	Adaptive algorithm configuration for differential evolution (AAC-DE)	170
6.2.2	Measurement of exploration and exploitation	170
6.2.3	Generation Strategy Selection	172
6.2.4	Control Parameter (F and CR) Adaptation	174
6.2.5	Adaptive equilibrium between exploration and exploitation	175
6.2.6	Discussions	175
6.3	Experimental Study	176
6.3.1	Comparison with five state-of-the-art adaptive DE	177
6.3.2	Summary	181
6.4	Conclusions	182

Chapter 7 Conclusions and perspective work

Appendix

A	Basic notions	189
A.1	Levelized cost of electricity generation	189
A.2	Capacity factor	190
A.3	Betz's limit	191
A.4	Power coefficient	194
A.5	Free damped vibration	197
B	IEC normal wind conditions	199
C	IEC extreme wind conditions	203

D NREL 5MW reference wind turbine	205
<hr/>	
E Coordinate system	213
<hr/>	
E.1 Cartesian coordinate system	213
E.2 Cylindrical coordinate system	213
F Statistical methods	217
<hr/>	
F.1 Maximum likelihood estimation	217
F.2 Kolmogorov-Smirnov test	218
G Deterministic fatigue analysis	221
<hr/>	
G.1 Mean stress effect	221
G.2 Palmgren-Miner's rule	223
G.3 Rainflow counting	224
H Methods for determining tower frequencies	229
<hr/>	
H.1 Uniform tower	229
H.2 Non-uniform tower	229
H.3 Guyed tower	230
I Supplementary figures	233

French Abstract

R Résumé en français	257
<hr/>	
R.1 Introduction générale	257
R.2 Chapitre 1 : Objectives	259
R.3 Chapitre 2 : Méthodologie de dimensionnement du mât d'éolienne	260
R.4 Chapitre 3 : Analyse dynamique du mât d'éolienne en cas de perte du réseau	261
R.5 Chapitre 4 : Prévission probabiliste de la durée de vie en fatigue à l'aide d'un réseau neuronal profond	266
R.6 Chapitre 5 : Développement d'un système d'amortissement actif pour les éoliennes	282
R.7 Chapitre 6 : Optimisation du TRD à l'aide d'un algorithme évolutif adaptatif	291

R.8 Chapitre 7 : Conclusions et perspectives 298

Bibliography

A	303
B	304
C	306
D	307
E	308
F	309
G	310
H	311
I	313
J	314
K	315
L	316
M	318
N	320
O	321
P	321
Q	323
R	323
S	324
T	325
U	326
V	327
W	327
X	327
Y	328
Z	328

List of Figures

1.1	Global installed wind capacity and electricity generation by wind	5
1.2	Levelized cost of energy (LCOE) of wind turbine	6
1.3	Principal subsystems of a typical horizontal-axis wind turbine (HAWT) .	7
1.4	Main turbine components in nacelle	9
1.5	Offshore wind turbine foundations designs	12
1.6	Rotor thrust of pitch- and stall- regulated designs	16
1.7	Frequency response of the spring-mass system with damping under some harmonic force	19
1.8	Possible dampers for wind turbine	22
2.1	Types of wind turbine tower according to the blade passing frequencies .	29
2.2	Normal turbulence model (NTM) extracted from IEC 61400-1 standard .	34
2.3	Flowchart for evaluating loads and designing the wind turbine and its subsystems	40
2.4	Overview of FAST/OpenFAST and its sub-modules	43
2.5	Design process for an active damping system	44
3.1	Tower-base coordinate system for upwind turbine: (a) a sketch; (b) an example of land-based wind turbine	50
3.2	Dynamic analysis for wind turbine using FAST codes	52
3.3	Tower gage 9 deflection at rated wind speed $V_{rate}=11.4$ m/s	54
3.4	Tower gage 1 local force at rated wind speed $V_{rate}= 11.4$ m/s	55
3.5	Tower gage 1 local moment at rated wind speed $V_{rate}= 11.4$ m/s	56
3.6	Representative value of tower fore-after deflection, fore-after force and pitching moment for all wind speeds in the operational range	57
3.7	Electrical generator power and torque in normal production	58
3.8	Overall integrated control system of NREL 5MW reference wind turbine	59
3.9	Deflections on tower gage 9 during the first minute in (a) DLC0.1 and (b) DLC0.2	61
3.10	DLC0.2 rotor reactions	63
3.11	DLC0.2 tower reactions	64
3.12	Longitudinal wind velocity of extreme operating gust (EOG) at hub height	67

3.13	Grid loss timing in the range of operating wind speed regarding tower deflection	69
3.14	DLC2.3 tower reactions at V_{rate} with grid loss at 14.6s	70
3.15	DLC2.3 rotor reactions at V_{rate} with grid loss at 14.6s	71
4.1	Fatigue life estimation process	75
4.2	Top view of cross section and illustration of spot point	76
4.3	An example of S-N curve	78
4.4	Workflow for assessing cumulative fatigue damage D on tower gage i and local spot j	82
4.5	An example of distribution fitting using the maximum likelihood estimation (MLE)	84
4.6	An example of the K-S statistic	85
4.7	An example of probabilistic fatigue analysis on tower gage 1 local spot 1 during a period of 10 min	87
4.8	An example of probabilistic profile of fatigue life on tower gage 1 and local spot 1 during a period of 10 min	90
4.9	An example of overall probability profile of fatigue life on tower gage 1	92
4.10	An example of normal turbulence model (NTM) at mean wind speed of 11 m/s	94
4.11	Workflow for probabilistic fatigue analysis on DLC1.2	96
4.12	DLC1.2 wind speed, tower reactions and tower stress state on tower gage 1 local spot 1 during 10-min simulated time	98
4.13	DLC1.2 distribution of 10-min cumulative fatigue damage on tower gage 1 (a) local spot 1, (b) local spot 10, (c) local spot 19 and (d) local spot 28	99
4.14	DLC1.2 distribution of 10-min cumulative fatigue damage on tower gage 1	100
4.15	DLC1.2 distribution of 10-min cumulative fatigue damage on tower gage 1 re-graphed in (a) contour map (Cartesian coordinate system) and (b) radar map (cylindrical coordinate system)	101
4.16	Estimated distributions on tower gage 1 with reference to all mean wind speed and all local spots	103
4.17	Number of estimated distributions on tower gage 1 grouped by types	104
4.18	Distribution of 10-min cumulative fatigue damage on tower gage 1 under different mean wind speed	106
4.19	Distribution of 10-min cumulative fatigue damage at the different height of tower at mean wind speed of 12.0 m/s	109
4.20	Illustration of a perceptron	113
4.21	Illustration of a fully connected multilayer perceptron	115
4.22	Illustration of residual network (ResNet)	116
4.23	Scatter plot matrix of input data and labels	121

4.24	Architecture of the residual multilayer perceptrons (ResMLP)	122
4.25	Loss history of the proposed neural network	124
4.26	Semi-log plot of moving average of loss history	124
4.27	Comparison between the predicted values and the simulated values for 10-min cumulative fatigue damage at mean wind speed of 3.5 m/s, 11.5 m/s and 24.5 m/s in: (a, c, e) correlation plot and (b, d, f) histogram	126
4.28	Comparison between the predicted values and the simulated values for 10-min cumulative fatigue damage in 10 000 cases of stochastic mean wind speed between V_{in} (3.0 m/s) and V_{out} (25.0 m/s) in (a) correlation plot and (b) histogram	127
4.29	Illustration of the predicted values and the simulated values for 10-min cumulative fatigue damage in 10 000 cases of stochastic mean wind speed between V_{in} (3.0 m/s) and V_{out} (25.0 m/s)	128
4.30	Wind rose plot of wind conditions in Caen (France) during 1 year	130
4.31	Prediction of cumulative fatigue damage for all directions at the end of 20 years	131
4.32	Prediction of cumulative fatigue damage for all directions at the end of 20 years using FAST numerical simulator and ResMLP surrogate model	133
5.1	Layout of twin rotor damper (TRD)	138
5.2	twin rotor damper (TRD) for single degree of freedom (SDOF)	140
5.3	Design of TRD for wind turbine	144
5.4	Integration of on-off control of TRD to the NREL 5MW reference wind turbine	146
5.5	Example of computer codes for TRD modeling in FAST codes	148
5.6	Tower gage 9 fore-after deflection in DLC2.3 at cut-out wind speed ($V_{out}=25.0$ m/s) with TRD	150
5.7	Status of TRD in DLC2.3 at V_{out}	150
5.8	Tower gage 1 fore-after force in DLC1.2 at cut-out wind speed ($V_{mean}=V_{out}$) with TRD	153
5.9	Status of TRD in DLC1.2 at V_{out}	154
5.10	Fore-after deflection on tower gage 9 considering the TRD with optimized configurations for wind turbine tower under DLC2.3	157
6.1	The average and standard deviation of the rankings of the compared DE algorithms on the test functions.	181
6.2	Box plots of the ranks of the compared DE algorithms on the test functions.	182
A.1	Disk actuator model	192
A.2	Power coefficient of wind turbine in different designs	195
D.1	Blade layout	207

D.2	Torque-versus-speed response of the variable-speed controller	210
E.1	Tower-base coordinate system for upwind turbine: (a) a sketch; (b) an example of land-based wind turbine ¹	214
F.1	An example of distribution fitting using the MLE	218
F.2	An example of the K-S statistic	220
G.1	Mean stress effects on S-N curve	222
G.2	A demonstration of Goodman-Haigh diagram	222
G.3	Hysteresis filtering of signal	225
G.4	Peak-Valley filtering of signal	226
G.5	Discretization	226
G.6	Extraction of cycle	227
I.1	Grid loss timing in the range of operating wind speed regarding tower force	233
I.2	Grid loss timing in the range of operating wind speed regarding tower moment	234
I.3	DLC2.3 rotor and tower reactions at V_{rate-2}	235
I.4	DLC2.3 rotor and tower reactions at V_{rate+2}	236
I.5	DLC2.3 rotor and tower reactions at V_{out}	237
I.9	Distribution of 10-min cumulative fatigue damage at the different height of tower at mean wind speed of 3.0 m/s	238
I.6	Visualization of all simulated fatigue damage highlighted by minimal values, mean values and maximal values	239
I.7	Distribution of 10-min cumulative fatigue damage on tower gage 1 under different mean wind speed represented by box-and-whisker diagram	240
I.8	Distribution of 10-min cumulative fatigue damage on tower gage 1 under different mean wind speed represented by bar chart	241
I.10	Distribution of 10-min cumulative fatigue damage at the different height of tower at mean wind speed of 25.0 m/s	242
I.11	Comparison between the predicted values and the simulated values for 10-min cumulative fatigue damage at mean wind speed of 3.5 m/s, 4.5 m/s, 5.5 m/s and 6.5 m/s	243
I.12	Comparison between the predicted values and the simulated values for 10-min cumulative fatigue damage at mean wind speed of 7.5 m/s, 8.5 m/s, 9.5 m/s and 10.5 m/s	244
I.13	Comparison between the predicted values and the simulated values for 10-min cumulative fatigue damage at mean wind speed of 11.5 m/s, 12.5 m/s, 13.5 m/s and 14.5 m/s	245

I.14	Comparison between the predicted values and the simulated values for 10-min cumulative fatigue damage at mean wind speed of 15.5 m/s, 16.5 m/s, 17.5 m/s and 18.5 m/s	246
I.15	Comparison between the predicted values and the simulated values for 10-min cumulative fatigue damage at mean wind speed of 19.5 m/s, 20.5 m/s, 21.5 m/s and 22.5 m/s	247
I.16	Comparison between the predicted values and the simulated values for 10-min cumulative fatigue damage at mean wind speed of 23.5 m/s and 24.5 m/s	248
I.17	Tower-top fore-after deflection and status of TRD in DLC2.3 at V_{rate+2}	248
I.18	Tower-top fore-after deflection and status of TRD in DLC2.3 at V_{rate}	249
I.19	Tower-top fore-after deflection and status of TRD in DLC2.3 at V_{rate-2}	249
R.1	Dimensionnement d'un système d'amortissement actif pour les éoliennes	261
R.2	Vitesse longitudinale du vent de EOG à la hauteur du moyeu	263
R.3	Moment de la perte de réseau dans la plage de la vitesse du vent de fonctionnement en ce qui concerne la déviation du mât	265
R.4	Fonctionnement pour l'évaluation des dommages cumulés dus à la fatigue D sur le gage du mât i et le spot local j	268
R.5	Exemple de profil probabiliste de la durée de vie en fatigue sur la jauge 1 du mât et le spot local 1 pendant une période de 10 min	271
R.6	Un exemple de NTM à la vitesse moyenne du vent de 11 m/s	273
R.7	DLC1.2 distribution des dommages de fatigue cumulés sur 10 minutes sur le gage 1 du mât montrée dans (a) diagramme en isoligne (système de coordonnées cartésiennes) et (b) diagramme en radar (système de coordonnées cylindriques)	274
R.8	Architecture des perceptrons multicouches résiduels (ResMLP)	276
R.9	Comparison between the predicted values and the simulated values for 10-min cumulative fatigue damage in 10 000 cases of stochastic mean wind speed between V_{in} (3.0 m/s) et V_{out} (25.0 m/s) in (a) correlation plot and (b) histogram	278
R.10	Graphique des conditions de vent à Caen (France) pendant 1 an	279
R.11	Prévision des dommages de fatigue cumulés pour toutes les directions au bout de 20 ans	280
R.12	Prévision des dommages cumulés dus à la fatigue dans toutes les directions au bout de 20 ans à l'aide du simulateur numérique FAST et du modèle de substitution ResMLP	281
R.13	Conception de TRD pour l'éolienne	283
R.14	Intégration de la commande ON-OFF de TRD à la NREL 5MW reference wind turbine	285
R.15	Déflexion avant-après au gage 9 sous DLC2.3 à la vitesse du vent V_{out} (25.0 m/s) avec TRD activé	287

R.16 Etat de TRD dans DLC2.3 à V_{out} 288

R.17 Tour gage 1 force avant-après dans DLC1.2 à la vitesse du vent cut-out ($V_{mean}=V_{out}$)
avec TRD 290

R.18 La moyenne et l'écart-type des classements des algorithmes d'ED comparés sur
les fonctions de test. 295

R.19 Box plots of the ranks of the compared DE algorithms on the test functions. 295

R.20 Déflexion avant-après sur la tour gage 9 en considérant le TRD avec des confi-
gurations optimisées pour la tour d'éolienne sous DLC2.3 298

List of Tables

1.1	Global weighted cost of electricity by renewable energy source in 2019 . . .	4
2.1	IEC standards for wind energy generation systems	31
2.2	IEC 61400-1 wind turbine classes	32
2.3	Some other environmental conditions in IEC 61400-1 standard	32
2.4	Types of design load cases (DLCs)	38
3.1	Overview of NREL 5MW baseline wind turbine	49
3.2	Tower nodes on beam element model used for post-processing	51
3.3	Representative value of tower fore-aft deflection, fore-aft force and pitching moment at V_{in} , V_{rate} and V_{out}	57
3.4	Summary of uniform steady wind with operational maneuvers (DLC0.2)	62
3.5	Summary of extreme operating gust with electrical fault (DLC2.3)	66
3.6	Grid loss timing to achieve the worst loading on wind turbine	68
4.1	Summary of DLC1.2	94
4.2	Hyperparameters for multilayer perceptrons using residual learning . . .	123
5.1	Mechanical properties of TRD for NREL 5MW reference wind turbine . .	145
5.2	Dynamic properties of TRD for NREL 5MW reference wind turbine . . .	148
6.1	Various mutation operators for DE.	163
6.2	Comparison between the proposed method AAC-DE and some DE variants given in Section 6.1.2	176
6.3	Experimental Results of seven algorithms on 30D test functions of CEC2017.	178
6.4	Experimental Results of seven algorithms on 50D test functions of CEC2017.	179
6.5	The average and standard deviation of ranks of all compared DE algorithms on 30D test functions	180
6.6	The average and standard deviation of ranks of all compared DE algorithms on 50D test functions	180
D.1	Gross properties of NREL 5MW reference wind turbine	206

D.2	Blade structural properties	206
D.3	Distributed blade aerodynamic properties	207
D.4	Nacelle and hub properties	208
D.5	Drivetrain properties	209
D.6	Distributed tower properties	209
D.7	Sensitivity of aerodynamic power P to blade pitch angle θ in Region 3 .	211
D.8	Full-System Natural Frequencies	212
R.1	Propriétés mécaniques de TRD pour l'éolienne NREL 5MW	284
R.2	La moyenne et l'écart-type des rangs de tous les algorithmes DE comparés sur les fonctions de test 30D	294
R.3	La moyenne et l'écart-type des rangs de tous les algorithmes DE comparés sur les fonctions de test 50D	294

List of Algorithms

4.1	Deterministic fatigue assessment on wind turbine tower	81
4.2	Probabilistic fatigue assessment on wind turbine tower	88
4.3	Probabilistic fatigue life estimation of wind turbine tower	90
5.1	On-Off control of TRD for deflection of wind turbine tower	146
6.1	Fundamental framework of differential evolution (DE)	162
6.2	Exponential crossover operator: selection of L integer	164
6.3	AAC-DE algorithm	171
6.4	Adaptive exploration-exploitation control (AEEC)	176
R.1	Évaluation déterministe de la fatigue sur une tour d'éolienne	267
R.2	Evaluation probabiliste de la durée de vie en fatigue d'une tour d'éolienne	270
R.3	AAC-DE algorithme	293

Glossaries

V_{in} cut-in speed of wind turbine refers to the lowest wind speed at hub height at which the wind turbine starts to produce power in the case of steady wind without turbulence (m/s)

V_{mean} mean wind speed refers to statistical mean of the instantaneous value of the wind speed averaged over a given time period which can vary from a few seconds to many years (m/s)

V_{out} cut-out speed of wind turbine refers to the highest wind speed at hub height at which the wind turbine is designed to produce power in the case of steady wind without turbulence (m/s)

V_{rate} rated speed of wind turbine refers to the minimum wind speed at hub height at which a wind turbine's rated power is achieved in the case of steady wind without turbulence (m/s)

\vec{v} wind velocity, a vector value (wind speed with wind direction) (m/s)

v wind speed, a scalar value (m/s)

design load case combination of external conditions with wind turbine operational modes and other design situations

downwind in the direction of the main wind vector

electrical power network particular installations, substations, lines or cables for the transmission and distribution of electricity

emergency shutdown rapid shutdown of the wind turbine triggered by turbine control system or by manual intervention

external condition factors affecting operation of a wind turbine, including the environmental conditions (temperature, snow, ice, etc.) and the electrical network conditions

Friedman test a non-parametric test that measures the differences in observations across multiple test attempts

gage nodes from beam element model used for post-processing

grid loss (a.k.a. network loss) loss of electrical power network for period exceeding any ride through provision in the turbine control system

gust temporary change in the wind speed which may be characterized by its rise-time, its magnitude and its duration

hub height height of the center of the swept area of the wind turbine rotor above the terrain surface (m)

hub fixture for attaching the blades or blade assembly to the rotor shaft

Kolmogorov-Smirnov test a non-parametric test that assesses the equality between a sample and a reference distribution or compares two samples

Mann-Whitney U test (a.k.a. Wilcoxon rank-sum test) a non-parametric statistic hypothesis test that is used to analyze or compare the difference between two independent samples

Maximum likelihood estimation a statistical method of estimating the parameters of a probability distribution by maximizing a likelihood function

nacelle housing which contains the drive-train and other elements on top of a horizontal axis wind turbine tower

Nemenyi post-hoc test a post-hoc test that makes pair-wise tests of performance

peak-to-peak amplitude change between peak (highest amplitude value) and trough (lowest amplitude value)

power output (a.k.a. power production) electric power delivered by a wind turbine

rated power maximum continuous electrical power output which a wind turbine is designed to achieve under normal operating and external conditions

rotor speed rotational speed of a wind turbine rotor about its axis

spot fictive nodes on cross section used for post-processing

swept area projected area perpendicular to the wind direction that a rotor will describe during one complete rotation

upwind in the direction opposite to the main wind vector

wind shear variation of wind speed across a plane perpendicular to the wind direction (m/s)

wind turbine generator system converts kinetic energy in the wind into electrical energy

yawing (only for horizontal axis wind turbines) rotation of the rotor axis about the vertically central axis of wind tower

Abbreviations

a.k.a. also known as

AANN Auto-Associative Neural Network

ANN Artificial Neural Network

CDF Cumulative Distribution Function

cf. confer

CNN Convolutional Neural Network

DE Differential Evolution

DL Deep Learning

DLC Design Load Case

DNN Deep Neural Network

DOWEC Dutch Offshore Wind Energy Converter Project

e.g. exempli gratia

EA Evolutionary Algorithm

ECDF Empirical Distribution Function

EOG Extreme Operating Gust

FAST Fatigue, Aerodynamic, Structure and Turbulence code

FEM Finite Element Model

GWEC Global Wind Energy Council

HAWT Horizontal-Axis Wind Turbine

HH Hub Height

HSS rotor High-Speed Shaft brake system

i.e. id est

i.i.d. independent and identically distributed

IEA International Energy Agency

IRENA International Renewable Energy Agency

K-S test	Kolmogorov-Smirnov test
LCOE	Levelized Cost Of Energy
LSTM	Long Short-Term Memory network
LTI	Linear Time-Invariant
MAE	Mean Absolute Error
MAPE	Mean Absolute Percentage Error
MaxFES	Maximum number of Function Evaluations
MDN	Mixture Density Network
ML	Machine Learning
MLE	Maximum Likelihood Estimation
MLP	Multilayer Perceptron
MRBM	Multilayer Restricted Boltzmann Machine
MSE	Mean Squared Error
MSLE	Mean Squared Logarithmic Error
NREL	National Renewable Energy Laboratory
NTM	Normal Turbulence Model
PCE	Polynomial Chaos Expansion
PDF	Probability Density Function
PTF	blade Pitch-To-Feather maneuver
RBDO	Reliability-Based Design Optimization
ReLU	Rectified Linear Unit
ResMLP	Residual Multilayer Perceptron
ResNet	Residual Network
RMSE	Root Mean Square Error
RNN	Recurrent Neural Network
SDOF	Single Degree Of Freedom
SHM	Structural Health Monitoring
SVM	Support Vector Machine
TRD	Twin Rotor Damper
VAWT	Vertical-Axis Wind Turbine

General Introduction

With the fast-growing wind energy industry, the requirement for a reliable wind turbine tower is critical in terms of the safety of the structure and the power production. Since the wind resource is more stable (i.e., less wind turbulence) and more sustainable (i.e., more convertible wind resource) in high altitude (generally speaking, higher than 100 m), the wind turbines are growing taller to extract more energy. However, just like all the other technologies in this world, there is always a trade-off — The quest for higher and larger turbines comes with its fair share of engineering challenges.

To give an illustration, taller wind turbine tower suffers to highly intensive loads directly from airflow and indirectly from the nacelle. The latter are subjected to the wind blade loads which can often create vibrations, or impose an ultimate change in the magnitude of loads, or even charge these two loadings simultaneously. The vibrations and ultimate loads transferred to the tower reduce the life of tower and involve many other problems such as fissures (or cracks) due to the fatigue damage. To overcome this engineering challenge, an embedded damping system inside the wind turbine offers an appropriate solution, especially, an active damping system that can anticipate the vibration directions and reduce the vibrations with feedback control.

In this dissertation, a damping system using an active damper is developed to control the vibrations on the wind turbine tower. This thesis details the design process covering the motivation to develop an active damping system for wind turbines, an initial design for integrating twin rotor damper (TRD) into the wind turbine tower, the numerical verification of the design, and the optimization of the design of TRD using modified differential evolution (DE) algorithm.

The outline of this work is organized as follows:

Chapter 1 a brief review of the wind energy industry takes place demonstrating the motivation to develop an active damping system for wind turbine.

Chapter 2 a design process for the active damping system is proposed regarding both the scientific consideration and the engineering requirement.

Chapter 3 a reference wind turbine, NREL 5MW, is introduced and simulated under gusty wind with technical fault. The numerical result obtained in this chapter offers a baseline for evaluating the performance of the proposed damping system.

Chapter 4 a novel neural network-assisted probabilistic framework of fatigue analysis is proposed. The proposed framework is applied to the reference wind turbine

to investigate the probability distributions of long-term cumulative fatigue damage along the wind turbine tower under turbulent wind condition. Likewise, the result achieved through numerical simulation will be used as the reference in evaluating the performance of the proposed damping system in future study.

Chapter 5 an active damping device known as twin rotor damper (TRD) is introduced. A damping system for the reference wind turbine is subsequently developed by integrating the TRD into the wind turbine tower. The damping performance of such system is estimated for two different design load cases (DLCs) and compared to the baseline data that have been studied previously in Chapter 3 and Chapter 4.

Chapter 6 a novel adaptive algorithm configuration is proposed for differential evolution algorithms (a branch of evolutionary algorithm family). The proposed algorithm, namely *adaptive algorithm configuration for differential evolution* (AAC-DE), is compared to other six state-of-the-art derivative DE algorithms and validated by performing an experimental study on the benchmark test problems. An application of the proposed algorithm is carried out for searching the optimal design of TRD for the reference wind turbine.

This dissertation finally ends in a general conclusion with perspective work.

To enable an identical visual-data interpretation to both those with red-green colorblindness and those without a color vision deficiency (CVD), a CVD-optimized colormap named *cividis* [NAR18] is practiced in this work.



Part I



Chapter 1

Scope of this thesis

There is no doubt that renewable energies become more and more important in today's energy market. At the time of writing, International Energy Agency (IEA) states that 13.5% of the world total energy supply in 2018 was produced from renewable energy sources [Int20a] of which 66.4% was produced from biofuels and waste, 18.8% was produced from hydro, 5.7% was produced from wind, 4.8% was produced from geothermal and 4.4% was produced from solar and tidal [Int20b].

The presence of renewable energies has joined in all sectors of our daily life especially in power generation sector where 25.6% of world electricity generation was produced from renewables in 2018 [Int20b]. The growth of renewable energies in power generation sector is significant. In 2018, a total of 181 GW of renewable energy was installed [REN19]. It is around 64% of net additions of power generating capacity in 2018, marking the fourth consecutive year that the net additions from renewable energy outpaced the net additions from conventional energy. Overall, 33% of worldwide electricity demand in 2018 was met by renewable energies.

The essential motivation behind this impressive growth in renewables relies upon their competitiveness in cost compared to conventional energies that is detailed in the first section of the present chapter. The cost of wind power is considerably attractive in comparison with other renewable sources and, accordingly, a brief introduction about the design of wind turbine is given in the second section. The last section reveals the design of wind turbine damping system in terms of vibration reduction.

1.1. Cost of wind power

As the cost of electricity generated from renewable energy keeps going down in recent years, more electricity is generated from renewable energy than in the previous year. According to a cost analysis from International Renewable Energy Agency (IRENA), the average cost of electricity has fallen into the current cost range of power from fossil fuels, which ranges from 0.05\$ to 0.17\$ per kWh (Table 1.1). The analysis highlights the significant decline in cost of electricity from solar photovoltaic (PV) and wind over the last decade. Since 2010, onshore wind price has dropped by about 25%, with the cost of solar PV dropping by 73% at the same time [REN19]. Onshore wind and solar PV are expected to be the less costly sources of electricity by 2021 than the cheapest fossil fuel fired power generation, without any financial support.

Table 1.1: Global weighted cost of electricity by renewable energy source in 2019

Energy resource	Average electricity cost (\$/kWh)	5 th and 95 th percentiles of electricity cost (\$/kWh)	Capacity factor (%)
Hydropower	0.047	0.030-0.136	47
Onshore wind	0.056	0.044-0.100	34
Bioenergy	0.062	0.048-0.243	78
Geothermal	0.072	0.060-0.143	84
Solar photovoltaic	0.085	0.058-0.219	18
Offshore wind	0.127	0.102-0.198	43
Concentrating solar power	0.185	0.109-2.272	45

Source: *International Renewable Energy Agency (IRENA) [Int19b]*

In 2019, the global weighted-average cost of electricity of onshore wind projects was at 0.056\$/kWh, which was 13% lower than in 2017 and 35% lower than in 2010. Costs of electricity from onshore wind are now at the lower bound of the cost range of electricity from fossil fuel. The onshore wind price continues to dropping as a result of the continued reductions in total installed costs and the improvements in the average capacity factor¹. According to the IRENA database, the total installed costs of onshore wind projects was 1497M\$ in 2019, which was 22% lower than in 2010. In the case of the capacity factor, it has increased from 27% in 2010 to 34% in 2019.

On the other hand, the global installed capacity of wind power projects keeps growing since the beginning of this century as illustrated in Figure 1.1. As mentioned earlier, with 51 GW newly added in 2019, the global cumulative installed capacity of wind power was boosted about 9% to 591 GW.

To characterize these economic trends related to renewable energy, many institutes

¹. Capacity factor is a non-dimensional factor that measures the actual usage of a power plant. More information is detailed in Section A.2

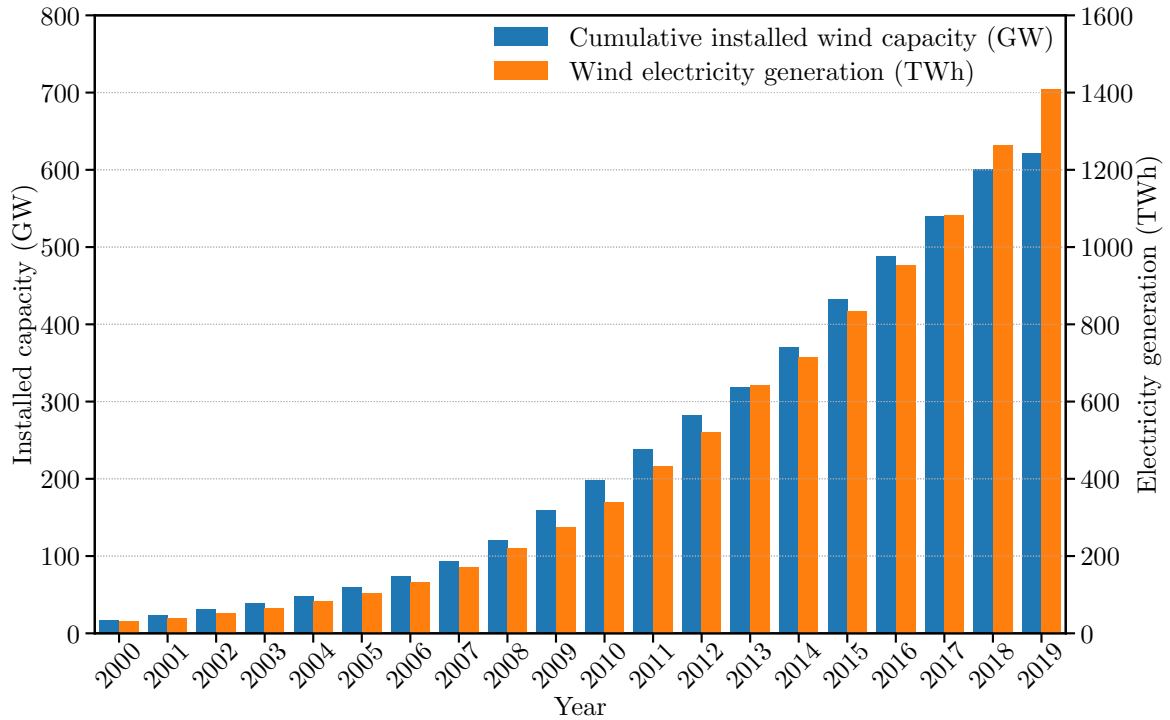


Figure 1.1: Global installed wind capacity and electricity generation by wind

Source: International Renewable Energy Agency (IRENA) [Int20c], Global Wind Energy Council (GWEC) [Glo20]

and researchers use the levelized cost of energy (LCOE) to compare the cost of different methods of power generation on a consistent basis. This factor represents the present value of the total cost of building and operating an electricity generation plant over its financial life, converted to equal annual payments and amortized over expected annual generation from an assumed duty cycle. The key factors contributing to levelized costs include the cost of constructing the plant, the time required to construct the plant, the non-fuel costs of operating the plant, the fuel costs, the cost of financing, and the utilization of the plant. The availability of various policies including state or regional tax credits can impact these costs as well².

In the case of wind energy, the onshore turbine has clearly a striking advantage in cost comparing to offshore turbine (Figure 1.2). The average LCOE of onshore projects is around one-third of offshore projects. The key factors driving this trend include technically continued improvements in wind turbine design and manufacturing as well as economically more competitive global supply chains.

2. The mathematical definition of levelized cost of energy (LCOE) can be found in Section A.1

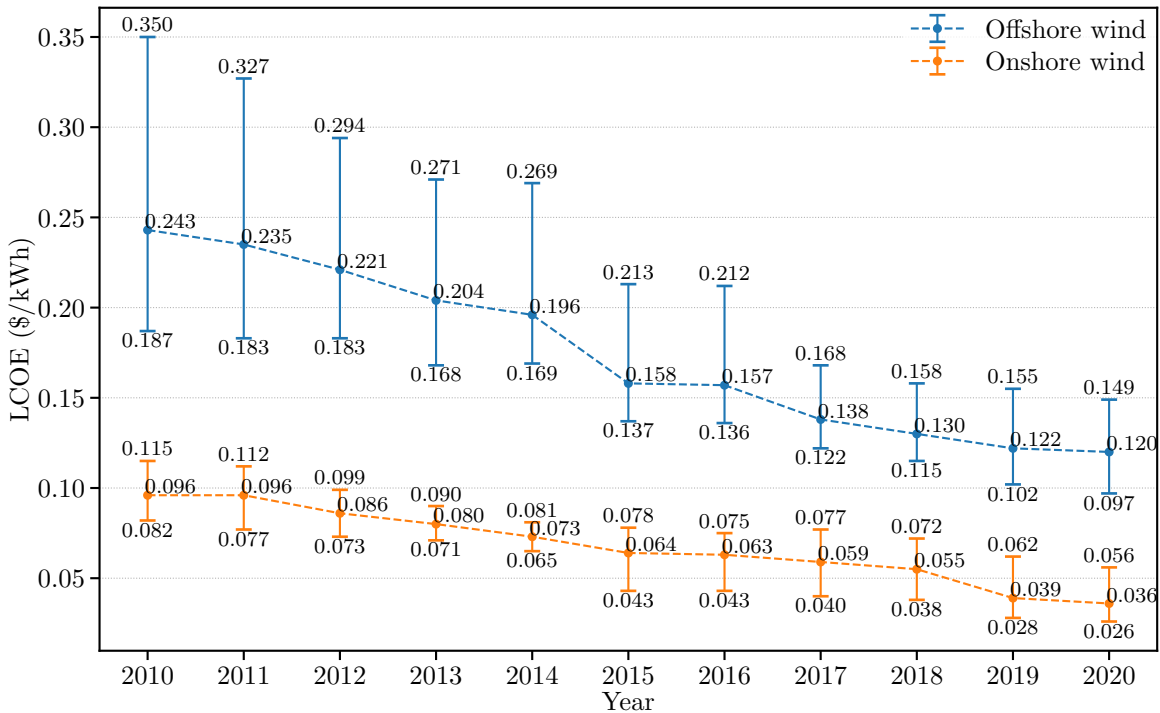


Figure 1.2: Levelized cost of energy (LCOE) of wind turbine

Source: U.S. Energy Information Administration [U.S11; U.S12; U.S13; U.S14; U.S15; U.S16; U.S17; U.S18; U.S19; U.S20; U.S21]

1.2. Modern wind turbine design

Form the technical side, the trend towards higher wind turbine hub heights, larger swept areas (longer wind turbine blades) and higher nameplate capacities is observed in all major onshore wind markets [Int16]. These improvements allow harvesting more electricity from the same wind resource. Higher hub heights allow more steady wind speeds to be accessed. Larger swept areas permit increasing output across the range of operating wind speeds. Higher nameplate capacities outputs more power at the same wind speed. A slightly higher costs are involved for longer blades and taller towers, but an overall reduction in LCOE can be achieved with the right optimization.

1.2.1. Wind turbine components

Nowadays, the most commercialized design for wind turbine is the three-bladed horizontal-axis wind turbine (HAWT) because of its efficiency and balance in economic, technology and manufacturing aspects. With aerodynamic energy loss of 50-60% at the rotor, mechanical loss of 5% at the drive-train and electromechanical loss of 5% at the generator, the modern three-bladed HAWT offers usually an overall effi-

ciency around 40-50%³ [REN20]. This is much higher than other turbine designs like two-bladed HAWT or vertical-axis wind turbine (VAWT).

The HAWT can be commonly classified by the rotor type (upwind/downwind), the site characteristic (onshore/offshore), the number of blades (three blades, two blades or single blade), the type of drive-train (direct-drive/gearbox), the generator type (fixed speed/variable speed) and the grid connectivity (connected/stand-alone). A sketch of onshore HAWT design is illustrated in Figure 1.3.

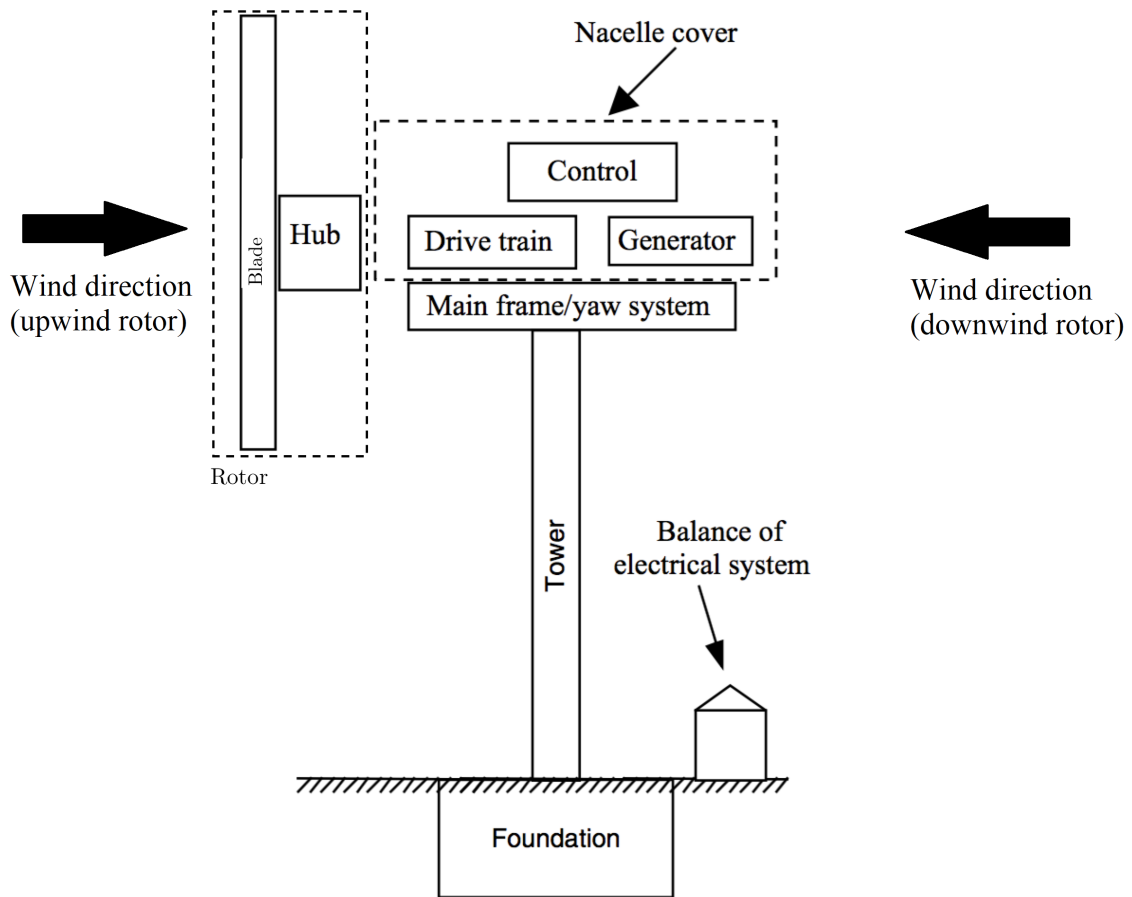


Figure 1.3: Principal subsystems of a typical horizontal-axis wind turbine (HAWT) [MMR09]

Rotor

The rotor consists of the blades of the wind turbine and the supporting hub. It is often considered as the most important components from both the performance and the cost point of view. Most modern turbines typically have three-bladed upwind rotors, although there are other possible configurations with 2 blades or with downwind

3. This overall efficiency, called power coefficient, is usually used to evaluate the overall performance of wind turbine design (more information in Section A.4).

rotors.

Blades

Typically, turbine blades are made of composites due to their ease of fabrication into the desired aerodynamic shape as well as their high strength and high stiffness to weight ratio. These characteristics are the essential needs for fabricating larger blades with additionally other advantages such as resistant to corrosion, resistant to environmental degradation, etc. The most common composite are fiberglass or carbon fiber reinforced plastics (GRP or CFRP). The blades can also be made from polyester, epoxy resin or laminated wood [Pra19; Mis17]. New materials, for instance, multi walled carbon nano tubes (MWCNT), are being introduced to satisfy the requirements for developing longer rotor blades [Arb05].

Hub

Wind turbine blades are attached to the hub via the blade root which is the end of the blade closest to the hub. Depending on turbine size and design (constant or variable speed), the turbine rotor and hub assembly rotates at a rate of 10 to 25 revolutions per minute (rpm) [Mor11]. A low-speed shaft connected to the turbine gearbox is usually attached to the hub. If the blade-pitch-control system is invoked, the pitch angle of the blade is adjusted by the rotation of the bearing at the blade root. This allows us to keep the rotation speed of the rotor in the optimal design range and generate electricity steadily. In high wind conditions, this control system allows the blades to be feathered by triggering the brake.

Nacelle

This is the main structure of the turbine where locates the principal turbine components like generator, drive-train and brake. The nacelle housing protects the main turbine components from the undesirable weather such as rain, ice or snow. It also provides a mounting point for the yaw bearing that is bolted to the tower top.

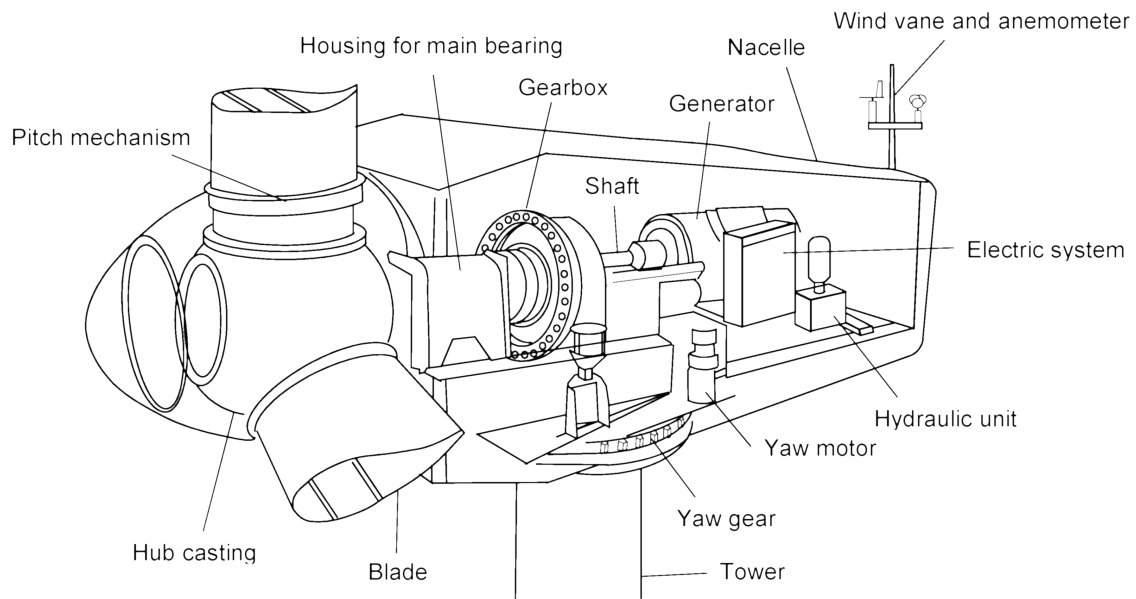


Figure 1.4: Main turbine components in nacelle [Jia17]

Like the blades, the nacelle is usually made from a lightweight material, for example, fiberglass. For large wind turbines, the nacelle is designed to be large enough for personnel to check or repair the wind turbine components inside the nacelle.

Drive-train

The drive-train includes the rotating parts namely shafts, bearings, brakes and commonly a gearbox. That last component distinguishes between the direct-drive model and the gearbox model.

The direct-drive turbine, just like its name, drives directly the generator by the rotor making it less complex than gearbox model and leading to easier operations and maintenance. This model yields several benefits including quiet operation, lower cost in maintenance and long-term reliability. But it requires a large and expensive low-speed generator.

On the opposite side, the gearbox turbine converts the low-speed, high-torque rotation of the rotor to the high-speed, low-torque rotation of the generator through multiple wheels and bearings in a gearbox. In this model, the gearbox is usually one of the heaviest and most complicated components. So, there is a trade-off between the reliability of gearbox and the cost of low-speed generator.

Generator

The generator is located in the nacelle and transforms mechanical energy into electrical energy. It can be categorized by fixed speed model or variable speed model.

The fixed speed generator has a constant or nearly constant rotational speed so that it can be directly connected to a utility power network. This resulted in the

rotor likewise running at only one wind speed at which the rotor is operating at its optimum efficiency. Both synchronous generator and asynchronous generator (also known as induction generator) are commonly used in fixed speed wind turbine.

The variable speed generator is able to run at varying speeds since the generator is in conjunction with power electronic converters. There are some noteworthy advantages of variable speed turbine:

1. The rotor is able to operate at varying speed with respect to wind speed. So the tip speed ratio can be kept constant, and hence, the wind turbine rotor can extract the most energy.
2. The fluctuating loads on the drive-train are reduced due to variable speed operation. The cumulative fatigue damage over the drive-train is consequently reduced.
3. If the blade is equipped with pitch control system, which is the case for most large wind turbines, the variable speed operation also minimizes the adjustment of pitch angle. Because there is no need for keeping the rotation speed of rotor to be constant.

However, these advantages have to be balanced by the additional cost of the indispensable power electronic converters and the extra complication in generating alternating current (AC) electricity.

Detailed discussion of these electrical machines is beyond the scope of this dissertation and is not necessary to understand the operation of a generator for the purposes of interest here. Most electrical machinery books have a full development of the theory and the application of both synchronous and asynchronous machine [BH85; NU83].

Yaw system

Nearly all HAWTs are equipped with a yaw orientation system so that they are able to orient themselves in line with the wind direction. To ensure the wind turbine is continuously facing the wind, a large bearing is planted at the tower top attaching the nacelle to the tower. Basically, there are two types of yaw system: active yaw system and free yaw system.

The first one is typically embedded in an upwind turbine. An active yaw system requires one or more yaw motors, each of which drives a pinion gear against a bull gear connected to the yaw bearing. This mechanism is controlled by an automated yaw control system with its wind direction sensor normally mounted on the cover of wind turbine nacelle.

The free yaw system is usually used in downwind turbine. It is dependent on the rotor's aerodynamics to align the turbine with the wind. Nevertheless, as wind turbine gets larger, the active yaw system for downwind turbine is likely be considered as well.

Tower

Wind turbine tower is the structure supporting the nacelle and the rotor in the air. In the current design of tower, the principal types are free-standing truss, tubular tower as well as guyed tower. Compared to the other two options, the tubular tower is commonly used in large wind turbine since it has some notable advantages. The tubular tower, unlike truss towers, doesn't rely on many bolted connections that need to be periodically checked. This makes it to be a more reliable structure. Ladders, or elevators, can be installed inside the tower allowing protected access to the nacelle for service staff.

Steel is the most popular material used in wind turbine tower. Reinforced concrete trends to be another noticeable solution because of its cost and easy erection. Some technologies, that have been proved effective in civil engineering, are introduced in wind turbine tower to improve its reliability of structure or performance-to-cost ratio. For instance, EOLIFT project [BCL17] developed by Freyssinet had applied the pre-stressed concrete in manufacturing turbine tower and proposed a craneless solution for tower erection.

The tower height is typically 1–1.5 times the diameter of the rotor, but it is at least 20 m because of the slow and turbulent wind near the ground level. The choice of tower is strongly dependent on the characteristics of the site. But, as mentioned before, a trend of taller tower is observed in all newly established wind power site because of the more steady and less turbulent wind resource at high level.

Foundation

A wind turbine's foundation must have adequate capacity to keep the wind turbine stable and upright even for the extreme load conditions. In the case of onshore wind turbine, the foundation is constructed as a reinforced concrete pad. Like the wind turbine tower, the foundation is very site-specific as well. The type and dimension of the foundation depends on the weather conditions, expected turbine loading, tower design and soil characteristics.

In the case of offshore wind turbine, the structure of foundation is more complex and involves greater technical challenges. In addition to the design requirements for onshore wind turbine foundation, the offshore foundation should endure both the impact of surging waves and the bleak weather conditions. Some of today's offshore foundations are summarized in Figure 1.5. The choice of foundation type depends highly on the seabed conditions, water depth and estimated costs. In addition, the floating foundations have great development in recent years allowing to access the wind resource in deep water (farshore).

Transformer

The power transformer is an electromagnetic machine that adapts the voltage of AC generated by the wind turbine to the connected electrical network or to the voltage required by the other auxiliary equipment at the local site, for example, lighting system, control system, etc. It works based on Faraday's Law of Induction and has losses related to the current. The transformer is usually housed inside the wind turbine tower at ground level.

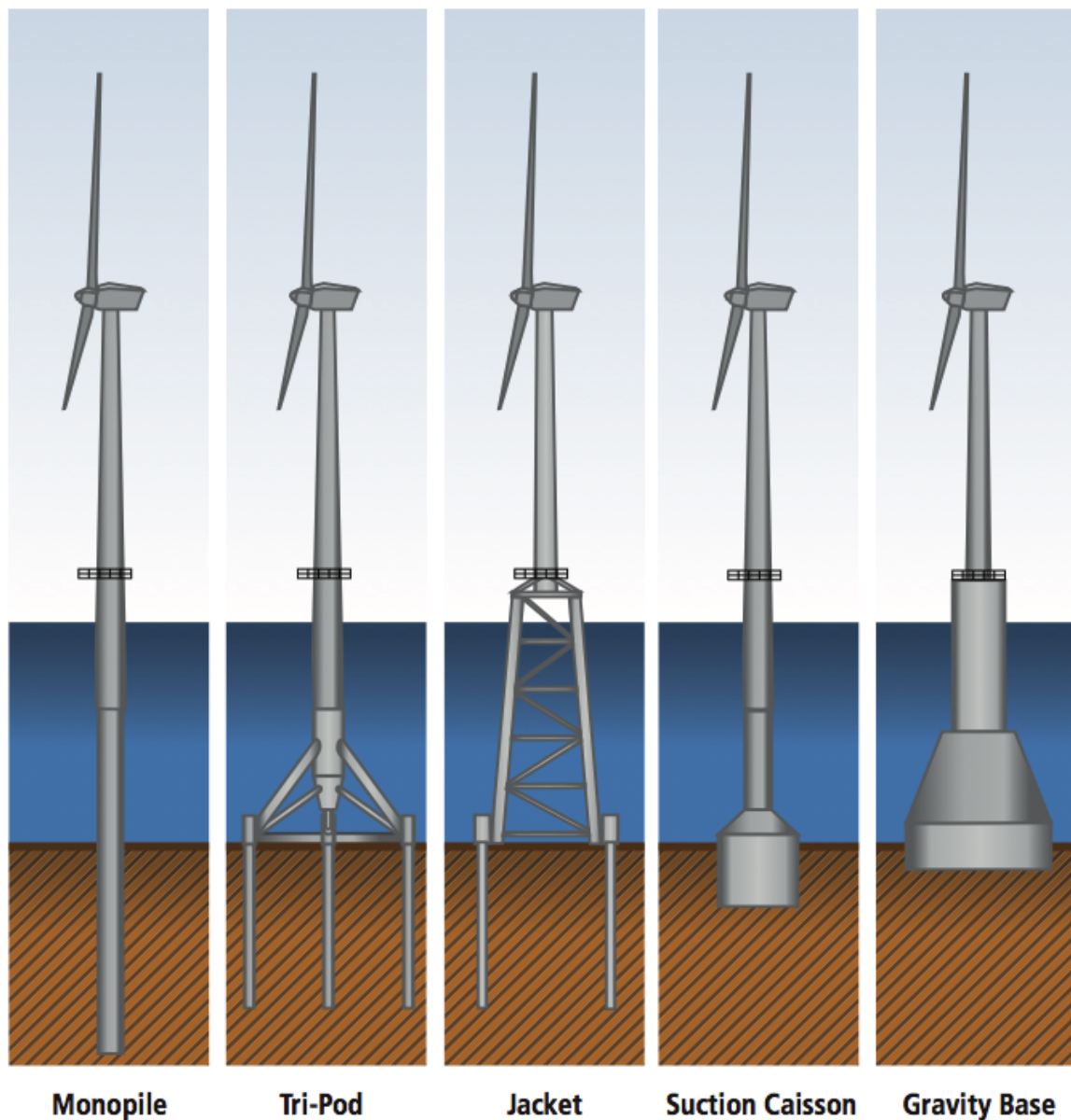


Figure 1.5: Offshore wind turbine foundations designs [Ede11]

1.2.2. Wind turbine control

A control system for wind turbine is important in terms of both machine operation and power production. It monitors the safety of operations, controls the turbine and collects the operational data. It is carried out by implementing various sensors (e.g. anemometer, wind vane, thermometer, etc.), controllers (e.g. mechanical mechanisms, electrical circuits, hydraulic units, etc.), electrical amplifiers (e.g. breakers, converters, switches, power amplifiers, etc.), actuators (e.g. yaw motors, pitch motors, shaft brakes, etc.) and computers.

Good implementation of control system can have a significant improvement on the turbine's power output and service life. It strikes a balance between several aspects especially as:

1. Maximizing the power output.
2. Maximizing the service life of wind turbine in consideration of the uncertain wind (including turbulence, gust and changes of wind direction) as well as the fluctuating and cyclic loads (resulting in cumulative fatigue damage on many components).
3. Setting admissible limits on components for purpose of safety power production.

The design of control system is deeply interactive with the design of other systems such as rotor aerodynamics, structural dynamics and drive-train dynamics. Security is the priority in operating wind turbine and it is hence an aim of design to provide an electrically and mechanically fail-safe system in the event of any predictable faults. All modern wind turbines are driven by a computer-based active control system to manage the production of electricity by making decisions on startup, shutdown, yaw braking, pitch angle tuning and other procedures. The prevalent design among three-bladed wind turbines is pitch-regulated-variable-speed wind turbine. This control system changes the pitch angle of the blades and also regulates the reaction torque of the generator. It works on the basis of pitch angle feedback, rotor speed, and measurement of generator torque. The main objective of such system may be to rectify the power output to a predefined value or to maximize power by tracking a recommended torque-speed curve.

1.2.2.1. Passive stall control system

Most wind turbine designs were regulated by stall control system for several years back in 1990s [Sne93]. The stall-controlled wind turbine operates at almost constant speed in high wind speeds as well as at variable speed since 2000s [MB96; MPM98; LC00]. This control system eliminates many difficulties associated with the sensitivities of peak power, whereas, on the other hand, it does not produce excessive power. Maintaining approximately constant rotor speed is critical and depends on the con-

nection of the asynchronous electrical generator to the grid. The grid acts like a large flywheel in this way, keeping the turbine's speed nearly independent to changes in wind speed. When the wind speed increases, so long as the rotor speed is kept steady, the angles of inflow and angles of attack often increase over the blade. To achieve this object, the blade sections become more and more stalled limiting the power to reasonable levels without any active control system.

Stall control system has an important advantage over pitch control or other active aerodynamic control system. It sets an automatic limit on loads over the blades and rotor, whereas the pitch control system is at risk of having excessive high loads in turbulent wind if the blades would be in some improper positions incurring an irrelevant attack angle of airflow. Yet there are also downsides to the stall control such as the delay effect [DS98; HHD06; Bre08] and the conjunction with variable speed generator [Eke94; MHJ97]. Since it can only regulate power output to an approximately satisfactory point and not to a specific point in the way that pitch control system can. In a stall-controlled wind turbine, avoiding excessive power typically means sacrificing the power curve below the rated power level and implies some related loss in energy capture. It also increases acoustic noise and leads to further reduction of power output. In the event of wind with gust, the generator must provide reaction torque to keep constant speed and this implies that the drive-train torque rating may need to be comparatively greater than that in a pitch-controlled turbine.

1.2.2.2. Pitch control system (pitch-to-feather)

Pitch control system is another predominant design in wind turbine. This is an active control procedure which rotates the blades of the wind turbine around its longitudinal axis to control the power produced by the rotor. Unlike the stall-controlled turbine, the geometry of a pitch-controlled rotor needs to be essentially changed in order to detect the blade position, measure the power extracted by the rotor and regulate the appropriate pitch angle of blade. This allows the possibility of regulating the power output to a precise set point as opposite to the stall control system which approaches to the set point approximately.

The pitch control system was firstly introduced into the market in combination with the constant speed turbine [LLR92]. But the pitch-controlled turbine had many problems while operating at high wind speed. In order to prevent superfluous loads, the pitch-controlled fixed-speed wind turbine had to reduce the set points for power output or shut down the turbine at wind speeds far below the 25m/s mean wind speed. This operating issue cuts down the electric production and thus discounts the advantages of pitch control system comparing to the stall control system. To address these industrial problems, many manufacturers have developed different technologies based on slip rings allowing about 10% to 20% slip above the rated power so that

the rotor could capture energy in gust wind event and reduce the maneuver of blade pitch in such situation. As the result, the power control on full load is more reliable and stable than the precedent one. However, these systems only took place in high speed operation. It did not benefit from the advantages of variable speed in low speed operation. When wind speeds are below the rated speed, the wind turbine always works at constant speed and, in consequence, the emission of noise and the capacity of capturing energy remains as stall-controlled fixed speed turbine.

Finally, with the choice of variable-speed turbine in combination with pitch control system is commonly applied on modern wind turbine systems, the problems of combining fixed-speed turbine with pitch control were settled [Per99; MB01; HK01; BMC04]. Generally speaking, the generator reaction torque can be managed to respond immediately to rapid changes in aerodynamic loading. The rotor's high rotational inertia ensures that rotor speed is changed by piecemeal. The pitch control system can work relatively slowly to the changes in aerodynamic input torque and restrict exorbitant changes in blade tip speed.

1.2.2.3. Active stall control system (pitch-to-stall)

Basically, this is a combined control system of pitch- and stall-regulated system. Like the pitch controlled system, this control strategy regulates the pitch angle of blades to obtain optimum power production. Unlike the pitch-to-feather, which increases the pitch angle as wind speed rises, it reduces the pitch angle as wind speed rises. So the incidence angle is increased and the stall is actively induced above rated speed. Comparing to the passive stall control system, this method offers a better regulation features thanks to control flexibility. And it also requires less control effort than pitch-to-feather to regulate power generation. However, just like other strategies based on stall, the drawback of this strategy is that the rotor thrust increases exceedingly large when the turbine goes into stall (Figure 1.6).

1.2.3. Fatigue loading

No matter the turbine is stall- or pitch-controlled, the fatigue loading over the whole structure is always a crucial part in design [RV00]. The overall accumulated fatigue damage can be qualitatively interpreted by examining rotor thrust characteristics as a function of mean wind speed [FSH10].

In the case of stall control system, the rotor thrust loading rises progressively with mild gradient above rated wind speed. Therefore, rapid changes in wind speeds do not bring out significant changes in load level on the turbine which involves fatigue loads on the structure. However, the inherent nature of the stall is unstable in reality. It is a phenomenon in fluid mechanics involving unsteady aerodynamic effects. It means that

wind turbine cannot always work in steady-state in high wind speeds and the changes in the load level are much greater than that can be presumed from the steady-state characteristic.

In the case of pitch control system, the thrust loading decreases expeditiously above rated wind speed. In consequence, both lift loading and thrust loading are remarkably reduced and can even be negative if large rapid pitch occurs. This maneuver is applied as emergency braking procedure by pitching blades rapidly into attached flow. The precipitous change of slope of rotor thrust around rated speed entails great changes in load level and is thus a cause of fatigue loads.

In conclusion, when wind speeds are above rated speed, the stall control system has a mild slope in the changes of rotor thrust loading (or out-of-plane blade bending), whereas, the unsteady effects of stall contribute to large fatigue variations; the pitch control system has an advantage of avoiding the unsteady-state but the rapid change in the gradient of load characteristic involves fatigue loading on both the blades and the rotor. The combat between these two control systems in respect of fatigue damage remains unclear [Ban07; Pol07; Ken18].

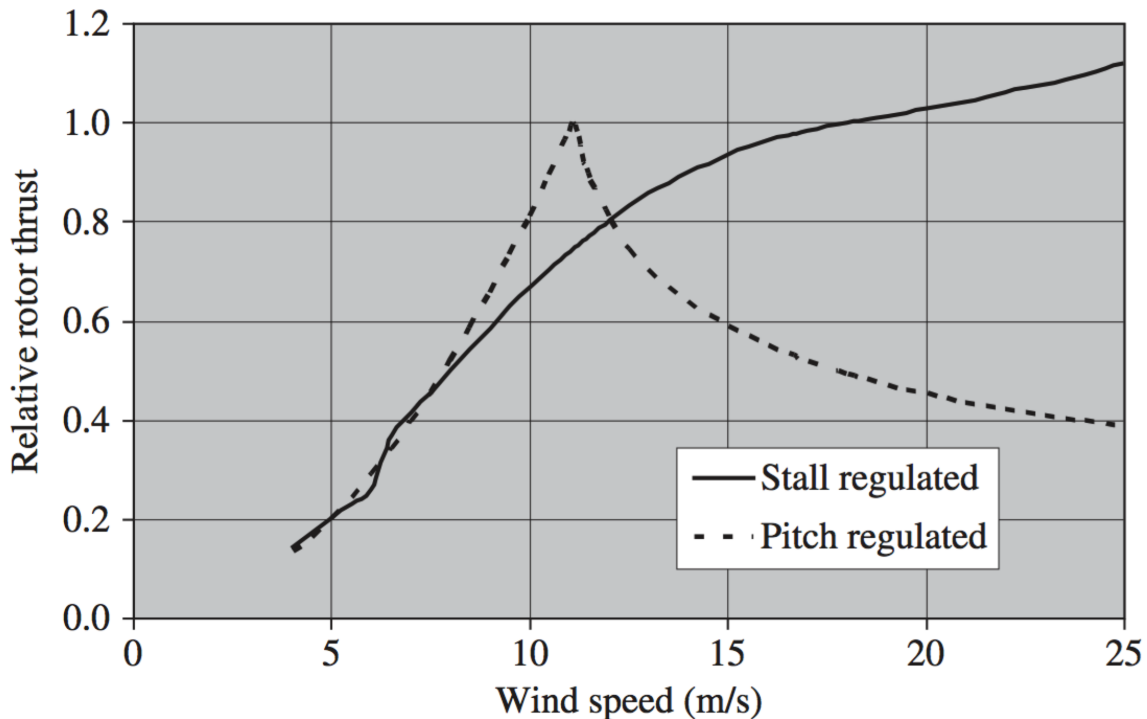


Figure 1.6: Rotor thrust of pitch- and stall- regulated designs [Jam17]

1.3. Vibration and associated problems

Although the choice between stall- and pitch-controlled design is still unclear with respect to fatigue damage, the pitch control system is implemented in most large wind turbines because of its possibility of extracting excessive power. No matter which control system is dominant, the source of fatigue loading is always a topic that need to be optimized.

Since the stiffness of the tower is an important factor in wind turbine system dynamics due to the possibility of coupled vibrations between the tower and rotor. The vibrations are important not only because they are relevant to the structural loads, they can also be used to describe many behaviors of the wind turbine rotor. One significant aspect among those behaviors is the fatigue load. It occurs in the entire wind turbine structure (e.g. blades, tower, components in nacelle) and affects how turbine components are supposed to withstand constantly changing loads over their lifetime.

Cyclic loads are time-varying loads which change in a periodic manner. The term arises as a result of the rotation of the rotor. It can also be connected to the vibration of the turbine, the vibration of the blades or the yaw motion.

The principles of the mechanics of wind turbines are in fact the same as those of other similar structures. An overview of the vibration will be pursued here in detail, the other fundamentals of mechanics can be easily found in many engineering books [JBE09; Mer04; MK12; BNH17].

In mechanics, the “vibration” refers to the reciprocating movement of an object in an elastic system. The movement pass in an equilibrium position on either side. Vibration is important in wind turbines because the latter are partly elastic system operating in an unstable environment which tends to produce a vibrating response. The presence of vibrations can lead to the ultimate deflections which have to be taken into account in the design of the turbine and may also lead to a failure due to the material’s fatigue.

1.3.1. Single degree of freedom system

1.3.1.1. Free undamped vibration

Considering a spring-mass system in which a mass m is attached to a massless spring with spring constant k . The spring is fixed to a rigid support on the other side. When the mass displace a distance x and is released to freely move, the mass will vibrate back and forth. The Newton’s Second Law gives the relation:

$$m\ddot{x} + kx = 0 \tag{1.1}$$

Imposing an initial condition that the mass is at the position x_0 at time $t = 0$, the solution of Equation 1.1 is:

$$x = x_0 \cos(\omega_n t) \quad (1.2)$$

where,

$$\omega_n = 2\pi f_n = \sqrt{\frac{k}{m}} \quad (1.3)$$

f_n is called the undamped natural frequency and ω_n is called the undamped angular frequency.

If the mass is positioned at x_0 and moving at the velocity v_0 at time $t = 0$, the solution of Equation 1.1 becomes:

$$x = x_0 \cos(\omega_n t) + \frac{v_0}{\omega_n} \sin(\omega_n t) = C \sin(\omega_n t + \phi) \quad (1.4)$$

where:

$$C = \sqrt{x_0^2 + \left(\frac{v_0}{\omega_n}\right)^2} \quad (1.5)$$

$$\phi = \tan^{-1} \left(\frac{x_0 \omega_n}{v_0} \right) \quad (1.6)$$

1.3.1.2. Free damped vibration

In real vibrations, the motion described in the last section will diminish due to many reasons, for instance, the force of friction between the system and the environment (air). This effect can be modeled by adding a viscous damping term in Equation 1.1. The force generated by the damping effect is usually assumed to be proportional to the velocity and in the opposite direction of the motion. So the new equation of motion is:

$$m\ddot{x} + c\dot{x} + kx = 0 \quad (1.7)$$

where, c = damping constant (actual amount of damping)

The solution of Equation 1.7 depends on the amount of damping that can be characterized by the damping ratio between the actual damping constant c and the critical damping constant c_c given by:

$$c_c = 2\sqrt{km} \quad (1.8)$$

In convention, the damping ratio is expressed by ξ :

$$\xi = \frac{c}{c_c} = \frac{c}{2\sqrt{km}} = \frac{c}{2m\omega_n} \quad (1.9)$$

This ratio describes whether the motion is underdamped (i.e., $0 < \xi < 1$), critically damped (i.e., $\xi = 1$) or overdamped ($\xi > 1$). The equations of motion for these three

types of damping motion are detailed in Appendix A.5.

In general, as for wind turbine, the structural damping ratio is really small around 1% [Pel11; Dev13; BH14]. For this reason, integrating a supplementary damping system in wind turbine is a worthwhile work. More information about wind turbine dampers will be discussed in Section 1.3.2.

1.3.1.3. Forced damping vibration

Supposing that the spring-mass system discussed above is driven by a harmonic force of magnitude F_0 and frequency ω , the equation of motion in this case is:

$$m\ddot{x} + c\dot{x} + kx = F_0 \sin(\omega t) \quad (1.10)$$

And the steady state solution of this problem is:

$$x = C \sin(\omega t + \phi) \quad (1.11)$$

where:

$$C = \frac{F_0}{k} \frac{1}{(1 - r^2)^2 + (2\xi r)^2} \quad (1.12)$$

$$\phi = \tan^{-1} \left(\frac{-2\xi r}{1 - r^2} \right) \quad (1.13)$$

r is the ratio of the harmonic force frequency f over the undamped natural frequency f_n of the spring-mass system:

$$r = \frac{f}{f_n} = \frac{\omega}{\omega_n} \quad (1.14)$$

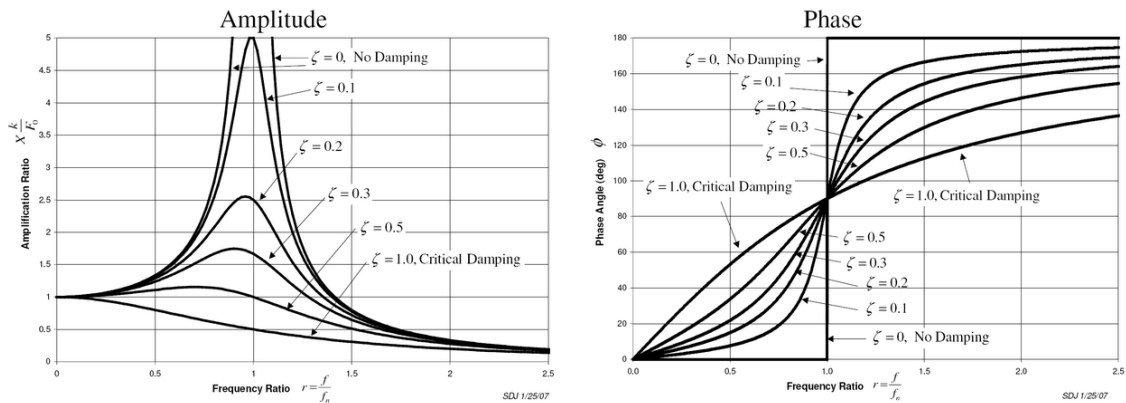


Figure 1.7: Frequency response of the spring-mass system with damping under some harmonic force [Lzy07]

When the ratio of frequency r is close to 1 (i.e. the exciting force frequency f nears

the natural frequency f_n) in a lightly damping system (i.e. $\xi \approx 0$), the amplitude of the vibration goes extremely high. This is the so-called “resonance” phenomenon which is deeply adverse to the structure’s safety. Hereby, one of the main reasons for the vibration analysis is to predict when the resonance will occur and then to decide what steps to take to prevent it from occurring. As Figure 1.7 shows, there are two possible solutions:

- If the frequency of the system and the exciting force cannot be changed, adding a damper to the system can dramatically reduce the amplitude of the vibration in the resonance. This approach gives a way to cut down the damage due to the resonance. It can be applied to the case in which the design of the wind turbine is fixed and the nominal rotation speed of the rotor is also fixed.
- If the damping capacity of the system cannot be enhanced, the amplitude of the vibration can be weakened by shifting the natural frequency of the system away from the forcing frequency through modifying the stiffness or mass of the system. Otherwise, if the system is not allowed to change, shifting the force frequency may be a possible solution. This approach offers a method to avoid the occurrence of resonance.

1.3.2. Wind turbine damping systems

With potentially harmful effects, wind turbines are subject to dynamic events. Furthermore, wind turbines have very low damping properties compared to other structures. The wind turbine’s overall damping ratio resulting from structural and aerodynamic damping is generally less than 2% [Cha06; Shi13]. This situation can be enhanced by using ancillary dampers. Currently, several types of devices can be used as dampers in the design of wind turbine:

Fluid couplings are often used in the drive-train, which refers to the component between the gearbox and the generator, to reduce torque vibrations. They are most often used in combination with synchronous generators which are mechanically rigid (unless the variable ratio gear box embeds a hydraulic system). Such a system requires both compliance and damping in the drive-train to avoid unacceptable torsional fluctuations. The solution to this problem is the use of a constant volume fluid coupling. This type of damper costs typically about 1% slip and, therefore, thermal losses at full load. But, in the contrast, it has negligible losses at low part loads.

Hydraulic pumping loops consist of a hydraulic pump and a closed hydraulic circuit with inner orifices. They can be used in yaw damping system especially when a wind turbine is in free yaw. This kind of wind turbine may have extremely rapid yaw motions that introduce undesirable gyroscopic loads into the

wind blades and thus requires a strong yaw damping system.

Fluid dampers are basically hydraulic cylinders with internal orifices. Such system may be used as teeter dampers. It consists of a tube embedded in the blade and containing an accurately calibrated volume of temperature-resistant fluid. This fluid absorbs the vibration's energy in order to reduce it.

Tuned mass damper is a passive control device to mitigate the amplitude of mechanical vibrations to an acceptable level whenever a strong lateral force occurs (such as an earthquake, the high winds and the strong waves). It is widely used in buildings, automobiles and power transmission lines. It consists of an auxiliary mass, which is attached via spring and dashpot to the main structure. This damper is named "tuned" because the key concept of such system is to match the inherent frequency of the damper with the structure itself. This allows the auxiliary mass to oscillate with a phase shift with respect to the displacement of the structure, resulting in the damping forces on the structure.

1.3.3. Methods of damping wind tower vibrations

One of the major structural problems in the wind energy industry is the vibrations in wind turbine tower which not only limits power generation efficiency but also causes fatigue issues with high maintenance costs. In addition to static loading from tower top structure (mainly blades, hub and nacelle), the wind turbine tower should also resist to the dynamic loadings from airflow such as wind-induced loading in fore-aft direction and vortex-induced loading in side-to-side direction. Moreover, in regions at high risk of earthquake, the onshore wind turbine suffers potentially seismic loading. As for offshore wind turbine, the wave-induced loading and the interaction between different sources of dynamic loading must be taken into account. Such complex loading environment jeopardizes structural safety and lifetime of wind turbine. Because the dynamic loadings can cause cyclic loads and transient loads resulting in cumulative fatigue damage on tower and other parts of wind turbine. The fatigue damage accumulates slowly and leads eventually to a halt or a complete collapse of wind turbine. These undesired vibrations induced by dynamic loadings also introduce a factor of uncertainty to predict the effects of loads on wind turbine.

The dynamic characteristics of wind turbine tower depend on the construction material and structural properties, in particular stiffness and mass which are important to the resonance behavior of wind turbines as they define the natural frequencies of the tower. Hence, the damping properties must be considered in addition to material and structural strength.

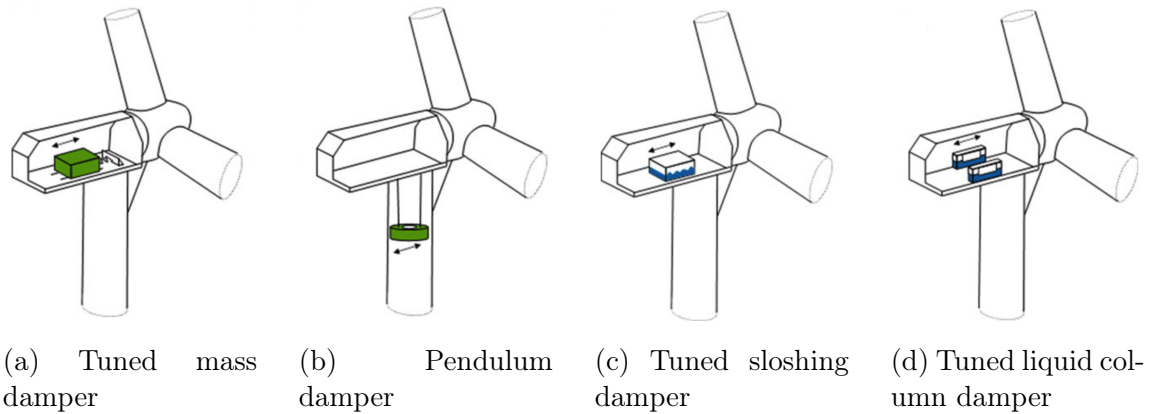


Figure 1.8: Possible dampers for wind turbine [Alt14]: (a) tuned mass damper, (b) pendulum damper, (c) tuned sloshing damper and (d) tuned liquid column damper

1.3.3.1. Passive damping system

The most universally used passive damper in wind turbines and other slender structures is tuned mass damper (TMD) mentioned in Section 1.3.2. Due to its success in eliminating periodic vibrations, TMD has many variants such as tuned liquid column damper, tuned sloshing damper, pendulum damper and semi-active tuned mass damper. The latter is usually combined with a semi-active structural control system to monitor and adapt the dynamic behavior of damper based on the real-time condition of structure and environment. Nonetheless, the basic concept of all these dampers remains unchanged, that is an auxiliary mass attached to the structure by means of spring and dashpot elements.

A difficulty of applying TMD in wind turbine relates to the low natural frequency of structure. Generally speaking, the fundamental frequency of the wind turbine system is under 0.4Hz [Hu14]. It is hard to find an applicable spring element which can be tuned to such low frequency in reality. So, TMD is mainly applied to reduce the vibrations in higher modes of wind tower.

Another possible inconvenient of TMD comes from its basic concept: the mass. In order to have an effective reduction of vibrations, the mass ratio of TMD to the entire mass of the assembly equals at least 1% that means more than 1 tonne equipment need to be hanged or attached at the top of wind turbine tower [Mur08]. This additional mass penalizes the static loads on the tower and likewise the narrow space in nacelle or below yaw bearing.

1.3.3.2. Active damping system

As discussed in Section 1.2.2.2, the pitch control system can prevent excessive loading over the rotor and maintain steady power output. To brake aerodynamically the rotor, the control system need to pitch the blades to the feathered position. By

means of these maneuvers, wind turbines can avoid high vibrations in high wind speeds but have to suffer a violent change of load level at rated speed inducing extreme loading and fatigue loading on blades and rotor.

Many patents can be found in this domain [HPK84; KPH83; Wil10]. And there are also many researches developing appropriate control strategies to optimize the aerodynamic damping gained from pitch controller [GN18]. The major downsides of pitch control system include the extra cost for complex equipment required by pitch mechanism (i.e. rotor blade bearings, blade pitch drive, actuator elements, ...), and the wind power excursions during high-wind stochastic conditions (i.e. strong wind gust). Sudden changes in wind speed would result in an increase in attack angle of blades, wind loads and electricity production. Power fluctuations can surpass the rated power levels twice before the pitch control system can compensate for increase of wind speed caused by the gust [BDM07].

1.4. Conclusions

In this chapter, the renewable energies show the dramatic growth in the cost of power generation. In the ongoing trend towards lower cost than the least-cost fossil fuel fired power generation, onshore wind and solar PV stand out. Wind energy acts now as one of the most preminent technologies in the development of renewables and plays a growing role in the market share of power generation. One of the major factors that drives the dropping of LCOE of onshore wind is the continued advancement of wind turbine design including higher wind turbine hug height, larger swept areas and higher nameplate capacity. With the increasing hub heights, the mechanic vibration over the wind turbine tower is consequently enlarged by excitation forces induced from wind, wave and potential earthquake. The vibrations induce mainly the fatigue damage over the tower and reduce the design lifetime of plant. To counterbalance this inconvenience from vibration, various methods can be used to minimize vibrations in the tower and enhance structural dynamics of wind turbine. An embedded damping system in wind tower is one of the attractive solutions. Two major control systems are implemented in wind power industry: stall control system and pitch control system. Both of them have some disadvantages either in mechanical aspect or in aerodynamic aspect which limit the application of these methods in modern large wind turbines.

In this dissertation, an innovating active damper named twin rotor damper (TRD) is introduced and expected to surmount the difficulties in the vibration of onshore wind turbine tower. Before studying the damping system, a new approach of evaluating the fatigue damage is proposed to better understand the fatigue damage induced by the vibration in a probabilistic way.

Chapter 2

Methodology of design for wind turbine tower

To design a wind turbine, three fundamental requirements should be taken into consideration by the designer: the effectiveness in power production, the structural safety of wind turbine, and the return of investment in finance. This implies that the wind turbine must resist not only the loads during its lifetime but also produce enough energy to compensate its cost.

This chapter aims at reviewing the mechanical framework under which the wind turbine needs to meet. This invokes the necessary of further analysis (like fatigue analysis, resonance analysis etc.) to better understand the turbine's behavior under various internal and external conditions.

2.1. Wind loads and tower loads

2.1.1. Source of loads

When talking about “loads” in wind turbine design, it refers to forces or moments acting upon the structure. The loads come from different sources in nature or from maneuver during operation like gravity, aerodynamics, dynamic interactions and mechanical control.

Gravity

Gravity is a significant source of loads on utility-scale wind turbine blades. As today’s largest wind blade has already reached 100m, the effects of gravity is no doubt an important issue in wind turbine design [Kel19]. Beyond its importance in blade, the tower top weight is another decisive component while designing wind tower, foundation and the installation method.

Aerodynamics

Based on the basic notion of converting energy in wind turbine, the aerodynamics is a primary source of loads related to many aspects in design. In structural design, the aerodynamic loads that occur in high wind speeds and that cause the fatigue damage are particularly important and will be accordingly discussed in this dissertation.

Dynamic interactions

The interactions between the two previous sources of loads, gravity and aerodynamics, induce loads at other parts of the turbine. For instance, on a yaw-free turbine, if yaw motion happens while the rotor is operating, the gyroscopic forces will be consequently induced.

Mechanical control

The last source of loads comes from the eventual controls of wind turbine. For example, applying brakes from a shutdown procedure or rotating the pitch angle of blades in high winds can lead to substantial loads throughout the whole turbine.

The loads induced from these numerous sources can be summarized into four categories: steady loads, transient loads (including impulsive loads), cyclic loads (including resonance-induced loads) and stochastic loads.

2.1.2. Major types of load for wind turbine

2.1.2.1. Steady loads

Steady loads are either static or rotating loads that do not vary over a long time period. Static loads are non time varying loads on a structure not in motion, while rotating loads are that on moving structure. For instance, a steady wind blowing on a wind turbine induces steady static loads, meanwhile a steady wind blowing on an idle or operating turbine induces steady rotating loads on rotor.

2.1.2.2. Transient loads

Transient loads are time-varying loads that occur in response to a temporary external event. Some oscillations may be associated with the transient loads, but they will decay sooner or later. For example, the response of tower after a Mexican-hat wind gust results in a decaying deflection at tower-top.

When the duration of transient loads is rather short but may result in peak magnitudes, these loads are impulsive loads.

2.1.2.3. Cyclic loads

Cyclic loads are another type of time-varying loads which vary periodically. They are often associated with the vibration of the structure and the fatigue damage over some components of wind turbine. For instance, rotor thrust is a cyclic load related to the rotation of the blades. By convention, a load varies in relation to a complete revolution of rotor is called 'per-revolution' load (noted as 'P'). Hereby, a blade rotating in wind will lead to a one-per-revolution load (1P). Depending on the number of blades, the loads on two-bladed wind turbine will suffer a two-per-revolution load (2P) and a three-per-revolution load (3P) on three-bladed turbine.

When the cyclic loads are induced from dynamic interactions between different components of wind turbine and result in a high magnitude, these loads are resonance-induced loads. The term applies especially when the wind turbine is excited at one of its natural frequencies. As an instance of this, the rotational frequency of rotor is mostly very close to the fore-aft natural frequency of the tower. In order to prevent the eventually resonant vibration, the fundamental frequencies of tower need to be chosen carefully based on the rotor blade revolution frequencies. Like notation on cyclic loads, the rotational frequency of rotor is named one-per-revolution frequency (1P) which is also equivalent to the one blade passing frequency. Two-per-revolution frequency (2P) and three-per-revolution frequency (3P) are used to specify the blade passing frequency of two-bladed and three-bladed wind turbine.

2.1.2.4. Stochastic loads

Stochastic loads are the last type of time-varying loads that change almost randomly. In some cases, the mean value of stochastic loads may remain constant, but a serious variation in time domain may be observed. For instance, the drag force on blade under turbulent wind condition is stochastic load.

2.1.3. Major types of load for wind tower

As noted in Chapter 1, the main interest of this dissertation focus on the reliability of wind tower safety. Thus, it is necessary to summarize the loads exciting on tower and the relevant requirements in design process. Since the wind tower is the structure supposed to raise the wind turbine up in the air and maintain safety of turbine both in operating state and stationary state, the tower is designed to stand all kinds of loads primarily from two categories: steady loads and time-varying loads (dynamic loads). Generally speaking, these loads come from aerodynamic loads on the tower, the weight of blades, rotor, nacelle and tower, and lastly from all forces on the turbine itself like resonance-induced loads.

2.1.3.1. Steady loads

The leading steady tower loads are loads like the weight of the tower-top structure (blades, rotor, nacelle and yaw system), rotor thrust and rotor torque. A uniformly constant wind speed air flow and the centrifugal forces produce time-independent steady-state loads as long as the rotor is working at fixed speed. For an investigation of structural stresses, IEC standards recommend that at least two conditions of steady loads must be evaluated:

1. operating state at rated wind speed (see Section 2.2.4)
2. stationary state at extreme wind speed

2.1.3.2. Dynamic loads

Dynamic loads on the tower come from the dynamic response of the wind turbine itself. Apart from the blade moments (flap-wise, edgewise and torsion), the resonant response is another main source of dynamic tower loads. Depending on the relationship between tower natural frequencies and rotor revolution frequencies, wind turbine towers can be categorized into soft-soft, soft and stiff types as shown in Figure 2.1:

Stiff tower has a natural frequency higher than the blade revolution frequencies (3P)

Soft tower has a natural frequency between the rotational frequency of rotor (1P) and the blade passing frequencies (3P)

Soft-soft tower has a natural frequency lower than the rotor frequency (1P)

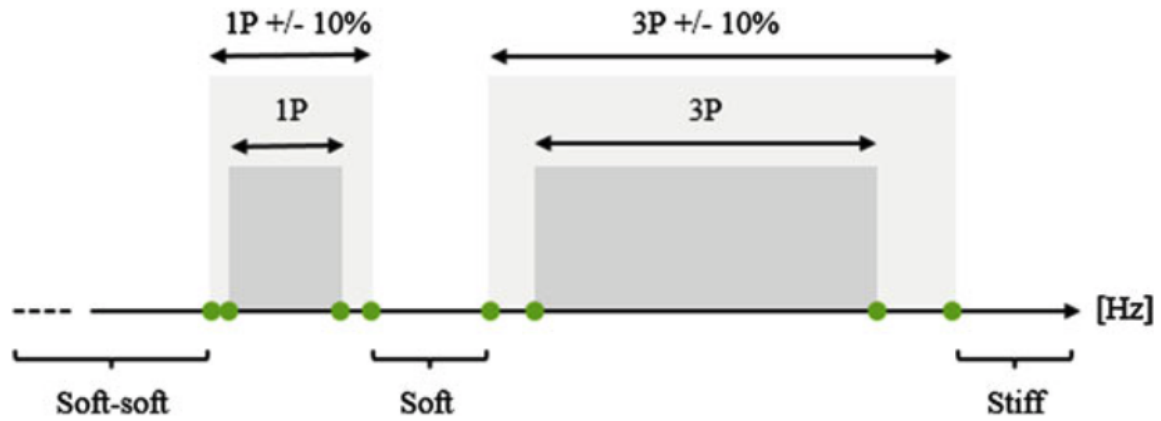


Figure 2.1: Types of wind turbine tower according to the blade passing frequencies [LVA14]

The regions of rotor frequency (1P) and blade passing frequency (3P) are defined by the cut-in speed V_{in} and rated speed V_{rate} of wind turbine. A tower should be designed so that its natural frequencies do not stay in the range of excitation frequencies (1P and 3P). A factor of safety of 10% is usually required by certification documents in order to prevent the eventual resonance. On soft or soft–soft towers, dynamic effects can be a significant source of loads. For instance, a soft–soft tower can be excited resonantly both in start-up phase and shutdown phase. The effect of fatigue loading generated during these phases depends on the duration of resonant event.

2.2. Design process

The load level over the wind turbine depends not only on the exciting loads but also on the design of the structure. It is impossible to determine in advance which loads will be dominant. To ensure the safety of wind turbine within its service lifetime, the machine must resist two kinds of load: ultimate loads and fatigue loads. Ultimate loads stand for the maximum load multiplied by the safety factor. Fatigue loads stand for the ability of the component to endure an expected number of cycles of changing magnitude.

It is not possible to evaluate the performance of wind turbine under every realistic condition during its lifetime. In design process, a wind turbine is therefore designed for a set of operating conditions in such a way that, if the environment meets that condition in reality, the wind turbine should perform the desired performance at least. To adequately cover the realistic conditions, design conditions are generally categorized into normal condition, where most of the power should be generated safely and extreme condition, where the turbine should withstand without significant damage. Among all the design conditions, the crucial considerations are (1) the expected event

during normal operation, (2) the extreme event and (3) the fatigue load cases [Bak13].

A range of standards related to the design, testing and operation of wind turbines are, therefore, being prepared to describe adequately enough conditions in which the turbine must withstand. The next section provides a summary of these standards and a notable standard IEC 61400-1 as it applies to the design process.

2.2.1. Design standards

The first attempt at definition of wind turbines had been undertaken in 1980s in connection with a German certification organization Germanischer Lloyd (GL) [FTP82; HH86]. Standards and technical specifications had been established by country or by organization like International Electrotechnical Commission (IEC), Det Norske Veritas (DNV) or GL. Since 1988, the IEC took over this mission and issued a series of international standard for wind turbine. In the last decade, the IEC began to enlarge these standards to all wind energy generation systems. The most recent IEC standards that are in active till today are listed in Table 2.1.

An important thing to note is that most of the IEC standards are still in process of updating and revision. The decisive basis of the IEC standards is IEC 61400-1 which suggests specifically design requirements with regard to the load assumptions. It is designed for modern large onshore wind turbines, but it applies to offshore wind turbines and small wind turbines as well. The information stated in this standard gives a target for design propose, so it must be considered early in the design process. An extract of the standard relevant to load cases is provided in the following section.

Beyond the IEC standards, which are mainly considered as a global basis for wind turbine design and certification nowadays, there are many other standards or norms that are likewise pertinent to the design of wind turbines. The majority of these standards concern the national implementation of wind turbines or some specific design for the component of turbine. For instance, GB/T 13981-92 is a Chinese standard dealing with the general design requirements for wind turbines in China; DNVGL-RP-C203 [DNV16] is a technical specification for fatigue design of sea-based wind turbines issued by DNV. The latest version of the DNVGL-RP-C203 is published in 2016 with numerous complementary information and items required by the wind industry, for instance, residual stresses in tubular sections made from cold forming [LFR16]. This standard has been widely applied in both academic research and industrial application for assessing fatigue damage over various components of wind turbine [Mou20; Has20; Les19; KFR19]. Accordingly, the DNVGL-RP-C203 standard is applied in this dissertation for fatigue damage assessment in order to conform to the mainstream studies and ensure that the present work is totally valuable from the industrial point of view.

Table 2.1: IEC standards for wind energy generation systems

Number and edition	Normative title
IEC 61400-1:2019	Part 1: Design requirements
IEC 61400-2:2019	Part 2: Small wind turbines
IEC 61400-3:2009	Part 3: Design requirements for offshore wind turbines
IEC 61400-3-1:2019	Part 3-1: Design requirements for fixed offshore wind turbines
IEC TS 61400-3-2:2019	Part 3-2: Design requirements for floating offshore wind turbines
IEC 61400-4:2012	Part 4: Design requirements for wind turbine gearboxes
IEC 61400-5:2020	Part 5: Wind turbine blades
IEC 61400-6:2020	Part 6: Tower and foundation design requirements
IEC 61400-11:2019	Part 11: Acoustic noise measurement techniques
IEC 61400-12-1:2020	Part 12-1: Power performance measurements of electricity producing wind turbines
IEC 61400-12-2:2016	Part 12-2: Power performance of electricity producing wind turbines based on nacelle anemometry
IEC 61400-13:2015	Part 13: Measurement of mechanical loads
IEC 61400-14:2005	Part 14: Declaration of apparent sound power level and tonality values
IEC 61400-21-1:2019	Part 21-1: Measurement and assessment of electrical characteristics – Wind turbines
IEC TR 61400-21-3:2019	Part 21-3: Measurement and assessment of electrical characteristics – Wind turbine harmonic model and its application
IEC 61400-22:2010	Part 22: Conformity testing and certification
IEC 61400-23:2014	Part 23: Full-scale structural testing of rotor blades
IEC 61400-24:2019	Part 24: Lightning protection
IEC 61400-25-1:2017	Part 25-1: Communications for monitoring and control of wind power plants – Overall description of principles and models
IEC 61400-25-2:2015	Part 25-2: Communications for monitoring and control of wind power plants – Information models
IEC 61400-25-3:2015	Part 25-3: Communications for monitoring and control of wind power plants - Information exchange models
IEC 61400-25-4:2016	Part 25-4: Communications for monitoring and control of wind power plants - Mapping to communication profile
IEC 61400-25-5:2017	Part 25-5: Communications for monitoring and control of wind power plants – Compliance testing
IEC 61400-25-6:2016	Part 25-6: Communications for monitoring and control of wind power plants – Logical node classes and data classes for condition monitoring
IEC TS 61400-25-71:2019	Part 25-71: Communications for monitoring and control of wind power plants – Configuration description language
IEC 61400-26-1:2019	Part 26-1: Availability for wind energy generation systems
IEC 61400-27-1:2015	Part 27-1: Electrical simulation models – Wind turbines

2.2.2. Wind turbine classification

First and foremost, IEC 61400-1 categorizes wind turbine in accordance with the on-site wind conditions. To quantitatively identify wind conditions, IEC 61400-1 uses the referenced wind speed V_{ref} to characterize wind turbine in three classes, namely I, II and III, and uses the turbulence intensity I_{ref} to characterize turbulent wind condition in three classes, namely A, B and C. The V_{ref} is a 10-min measured mean wind speed at turbine hub height. It is a maximum wind speed that can be exceeded only once in 50 years. In other words, the turbine is expected to operate under the extreme 10-min mean wind speed with a recurrence period of 50 years that is equal to or lower than V_{ref} . As for I_{ref} , it is the expected ratio of wind speed standard deviation at hub height to 10-min mean wind speed of 15 m/s.

It should be noted that the planned lifetime for all wind turbine classes is at least 20 years. Another important thing to note is that a special class, denoted S, is reserved for special on-site conditions where the specific values are defined by the designer. The values to be used in this class must be agreed with the local authorities.

Table 2.2: IEC 61400-1 wind turbine classes

Wind turbine class	I	II	III	S
V_{ref} (m/s)	50	42.5	37.5	
A I_{ref} (-)		0.16		Values to be specified by designer
B I_{ref} (-)		0.14		
C I_{ref} (-)		0.12		

Apart from the above characteristics listed in Table 2.2, some other climatic conditions (i.e., ice accretion, earthquakes, etc.) and external conditions (i.e., salinity, lightning, electrical power network conditions, etc.) can also influence the loads acting on a wind turbine. Table 2.3 summarizes further crucial factors.

Table 2.3: Some other environmental conditions in IEC 61400-1 standard

Factor	Normal condition	Extreme condition
Ambient temperature range (°C)	-10 to +40	-20 to +50
Relative humidity (-)	up to 95%	
Solar radiation intensity (W/m ²)	1000	
Air density (kg/m ³)	1.225	

It should be pointed out that the extreme environmental conditions must be associ-

ated with normal wind conditions except that a correlation between them is observed. Here, the normal wind conditions mean the frequency of wind speed distribution is assumed to be a Rayleigh distribution. The definition of normal wind conditions and extreme wind conditions are detailed in the following sections.

2.2.3. Design wind conditions

2.2.3.1. Normal wind conditions

Mean wind speed

The most essential parameter for characterizing the wind conditions is the mean wind speed. It is the mean value of wind speeds measured at hub height over a time period of 10 minutes during several years. The annual mean wind speed at hub height V_{avg} is imperative in identifying normal conditions as well as in extreme conditions.

Wind speed distribution

The wind speed distribution is a probability distribution function describing the wind speed at hub height. For the normal wind conditions, it is assumed to follow a Rayleigh distribution, that is to say, a Weibull distribution with a shape factor of 2. Equation 2.1 gives the cumulative probability function for this condition.

$$F(V < V_{hub}) = 1 - \exp \left[-\pi \left(\frac{V_{hub}}{2V_{avg}} \right)^2 \right] \quad (2.1)$$

where, V_{hub} = wind speed at hub height (m/s)

$V_{avg} = 0.2V_{ref}$ for wind turbine classes demonstrated in Table 2.2 (m/s)

The wind speed distribution determines the occurrence of individual load condition over wind turbine.

Normal wind profile (NWP)

The wind profile (or vertical wind shear) describes the mean wind speed as a function of height z above the ground. For standard wind turbine classes Table 2.2, the wind profile is assumed to follow Hellmann power law model with an exponent of 0.2, i.e.:

$$V(z) = V_{hub} \left(\frac{z}{z_{hub}} \right)^{0.2} \quad (2.2)$$

where, z = height above ground level (m)

z_{hub} = wind turbine hub height (m)

Equation 2.2 is known as Normal Wind Profile (NWP).

NTM

Wind turbulence is a decisive factor for the fatigue strength and power output [FT99; RB99; EDC03]. For the purpose of the IEC 61400-1 requirements, the standard deviation of turbulence in longitudinal direction σ_1 is assumed to be:

$$\sigma_1 = I_{ref}(0.75V_{hub} + 5.6) \quad (2.3)$$

This is a representative value that should be given by the 90% quantile for the given hub height wind speed. The values of σ_1 and the turbulence intensity $\frac{\sigma_1}{V_{hub}}$ are illustrated in Figure 2.2a and Figure 2.2b), respectively.

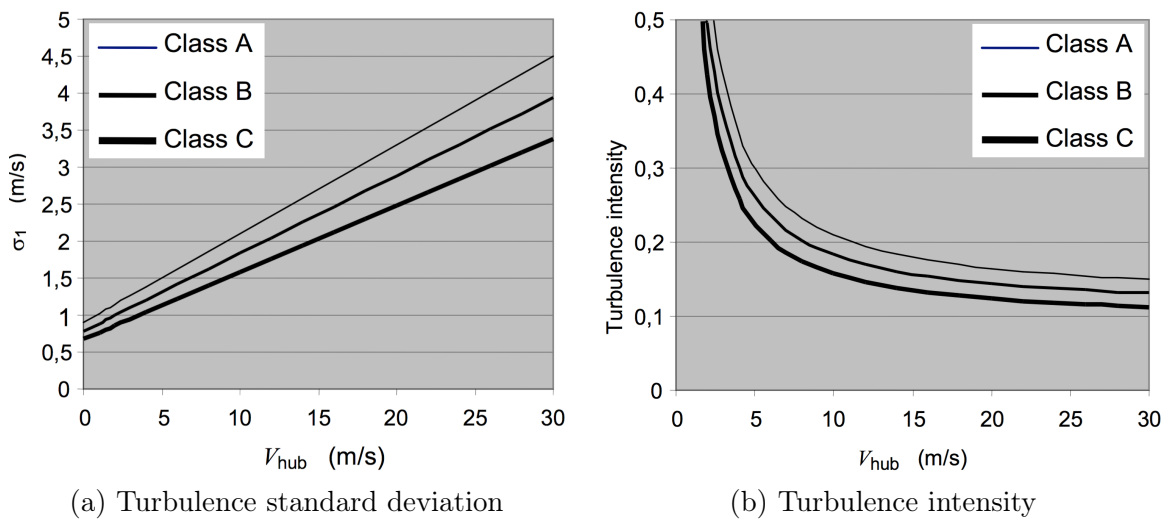


Figure 2.2: Normal turbulence model (NTM) extracted from IEC 61400-1 standard [Int05]

The continuous nature of the wind speed have variations not only in the direction of the mean wind speed (i.e., longitudinal direction) but also in lateral direction. Mathematical analysis of a two-dimensional turbulence model is a arduous task and usually not required when dealing with wind turbines. In fact, the spatial distribution of turbulence in longitudinal direction over the blade-swept area is more important in regard to analyzing loading on the wind turbine. Commonly used turbulence spectral model is the Kaimal spectrum or Mann spectrum (a variant of the Von Kármán spectrum) [For85]. Appendix B gives more information about the IEC Kaimal spectral model that will be employed in this dissertation.

2.2.3.2. Extreme wind conditions

In order to study the ultimate loads on wind turbine, the extreme wind conditions must be designated. Six scenarios are contained in IEC 61400-1 specifications:

- Extreme wind speed model (EWM)

- EOG
- Extreme turbulence model (ETM)
- Extreme direction change (EDC)
- Extreme coherent gust with direction change (ECD)
- Extreme wind shear (EWS)

The last three extreme conditions are beyond the scope of this dissertation. Their definition are explicitly explained in Appendix C.

Extreme wind speed model (EWM)

The extreme wind speed (EWM) model is an elementary model often referred in other extreme conditions. It is defined either in a steady way or a turbulent way.

For the steady extreme model, the extreme wind speed V_{e50} , with a recurrence period of 50 years, is expressed as a function of height z . And the annual extreme wind speed V_{e1} is computed as in Equation 2.4. The constant yaw misalignment is assumed to be in the interval $[-15^\circ, 15^\circ]$.

$$\begin{aligned} V_{e50}(z) &= 1.4V_{ref} \left(\frac{z}{z_{hub}} \right)^{0.11} \\ V_{e1}(z) &= 0.8V_{e50}(z) \end{aligned} \quad (2.4)$$

where, V_{ref} = reference wind speed given in Table 2.2 (m/s)

z = height above ground level (m)

z_{hub} = wind turbine hub height (m)

For the turbulent extreme model, the 10-min mean wind speed with a recurrence period of 50 years V_{50} and that with a recurrence period of 1 year V_1 are defined in Equation 2.5. The standard deviation of wind speed longitudinal component is fixed as $\sigma_1 = 0.11V_{hub}$.

$$\begin{aligned} V_{50}(z) &= V_{ref} \left(\frac{z}{z_{hub}} \right)^{0.11} \\ V_1(z) &= 0.8V_{50}(z) \end{aligned} \quad (2.5)$$

Extreme operating gust (EOG)

A gust is a rapid change in the wind speed. It needs to be characterized by its rise-time, its magnitude and its duration. An extreme operating gust (EOG) is a gust appearing in a short period of time T_{gust} when the turbine is operating at the same time. The magnitude of EOG at hub height V_{gust} depends on the turbulence standard deviation σ_1 , the scale of the turbulence Λ_1 , and the rotor diameter of the turbine D .

$$V_{gust} = \min \left\{ 1.35(V_{e1} - V_{hub}), \quad 3.3 \left(\frac{\sigma_1}{1 + 0.1 \left(\frac{D}{\Lambda_1} \right)} \right) \right\} \quad (2.6)$$

where, V_{e1} = annual extreme wind speed given by Equation 2.4 for the EWM (m/s)

V_{hub} = wind speed at hub height (m/s)

σ_1 = standard deviation of wind speed given by Equation 2.3 for the NTM

D = diameter of the rotor (m)

Λ_1 = longitudinal turbulence scale parameter (m)

The longitudinal turbulence scale parameter Λ_1 is defined as the wavelength where the non-dimensional, longitudinal power spectral density is equal to 0.05, i.e.:

$$\Lambda_1 = \frac{V_{hub}}{f} \quad \text{where} \quad \frac{f S_1(f)}{\sigma_1^2} = 0.05 \quad (2.7)$$

where, $S_1(f)$ = power spectral density function for the longitudinal wind velocity

At hub height z , the value of Equation 2.7 is given by:

$$\Lambda_1 = \begin{cases} 0.7z & \text{if } z \leq 60 \text{ m} \\ 42 & \text{otherwise} \end{cases} \quad (2.8)$$

The wind speed of gust is, therefore, given by its magnitude V_{gust} and its duration T_{gust} :

$$V(z, t) = \begin{cases} V(z) - 0.37V_{gust} \sin\left(\frac{3\pi t}{T_{gust}}\right) \left(1 - \cos\left(\frac{2\pi t}{T_{gust}}\right)\right) & \text{for } 0 \leq t \leq T_{gust} \\ V(z) & \text{otherwise} \end{cases} \quad (2.9)$$

The standard sets the duration of gust T_{gust} to 10.5s. More information about the probability of occurrence, the period and the spatial distribution of the gust can be found in [FLT78].

Extreme turbulence model (ETM)

Extreme turbulence model (ETM) is defined in an analogous way to NTM except that the standard deviation of turbulence in the direction of the mean wind speed σ_1 is assumed to be:

$$\sigma_1 = 2I_{ref} \left(0.072 \left(\frac{V_{avg}}{2} + 3 \right) \left(\frac{V_{hub}}{2} - 4 \right) + 10 \right) \quad (2.10)$$

2.2.4. Design load cases (DLC)

A load case refers to a specific situation in which loads occur. By the definition, the design load case (DLC) should cover all operating conditions and other critical states of wind turbine. The latter can be predicted with a certain probability during wind turbine's design life. To achieve this goal, all conceivable combinations between the turbine states and the wind conditions must be considered in defining a DLC. Take

DLC2.3 as an example, it claims a design situation that the wind turbine is acting an emergent shutdown while the presence of gust is occurring in the same time.

2.2.4.1. Turbine states

The status of wind turbine are grouped by two major categories: normal operation and fault condition. The first concerns the normal operation conditions of wind turbine including power production, start-up, shutdown, parked or idle state of turbine, etc. The last deals with technical faults or defects including emergency stop, malfunctions of turbine, improper maneuver and so on.

Normal operation

This category covers the operational status occurring most of the time in wind turbine's life. It contains all the phases and operations related to the power production. Due to the high load cycles of bending moments and forces resulting from the cyclic rotation of rotor and blades, the loads comprised in this category are mainly related to wind turbine's fatigue life. Moreover, the continuous wind turbulence and the asymmetric aerodynamic forces alternating periodically through the rotation of the rotor contribute to increase the fatigue loads on the turbine. Forasmuch as this reason, the load cases in this category are mostly linked to fatigue strength assessment of the wind turbine.

Faults and defects

This part of turbine state comprises some undesired operations (i.e., human faults in manipulation), some malfunction (i.e., protecting system faults) and some unpredictable situations (i.e., loss of electrical network connection). Most of these faults and defects result in an emergency shutdown so that the wind turbine is protected and will not suffer any terrific loads. But some events can still harm the structure before the protecting system is turned on or before the turbine is completely stopped. Hence, the analysis of ultimate loads is indispensable for all loads cases in this category.

2.2.4.2. Design situations

Combining the wind conditions described in Section 2.2.3 and turbine stats mentioned in Section 2.2.4.1, twenty-two DLCs are designated by the IEC 61400-1 standard which are categorized in eight design situations. Each situation is defined by the internal mechanic states, on the one hand, and the external environment conditions on the other hand.

1. power production: DLC1.1 to DLC1.5
2. power production with occurrence of fault: DLC2.1 to DLC2.4
3. start-up: DLC3.1 to DLC3.3
4. normal shutdown: DLC4.1 to DLC4.2

5. emergency shutdown: DLC5.1
6. parked (standing still or idling): DLC6.1 to DLC6.4
7. parked with occurrence of fault: DLC7.1
8. transport, assembly, maintenance and repair: DLC8.1

Table 2.4 summarizes comprehensively the combinations of all these design situations. Be aware that each DLC is assigned to an analysis of fatigue loads or an analysis of ultimate loads. The former analysis refers to the assessment of fatigue strength of turbine while the latter refers to the ultimate load level with respect to blade tip deflection, material strength and structural stability.

Table 2.4: Types of design load cases (DLCs)

		Wind conditions	
		Normal	Extreme
Turbine states	Normal operation	DLC1.1 ¹ , DLC1.2 ²	DLC1.3 ¹ , DLC1.4 ¹ , DLC1.5 ¹
		DLC3.1 ²	DLC3.2 ¹ , DLC3.3 ¹
		DLC4.1 ²	DLC4.2 ¹
		DLC6.4 ²	DLC6.1 ¹
		DLC8.1 ¹	DLC8.2 ¹
	Faults and defects	DLC2.1 ¹ , DLC2.2 ¹ , DLC2.4 ²	DLC2.3 ¹
		DLC5.1 ¹	DLC6.2 ¹ , DLC6.3 ¹
			DLC7.1 ¹

¹ Ultimate loads analysis

² Fatigue loads analysis

2.3. Computational mechanics for wind turbine

Once the design process is determined, an appropriate analytical approach needs to be specified. For structures as complex as wind turbines, different aspects of their response, such as stress within the structure, deflections, natural frequencies, fatigue strength, etc., are frequently required to accomplish a complete design. Until now, there is not a single mathematical model or method that can deal with all of these aspects. But there are many methods which can investigate certain subsystems of wind turbine in a linear or nonlinear way. A collection of common used methods in the structural analysis of wind turbines are exhibited in the next section.

2.3.1. Modeling methods

Finite element method

This is the most commonly used method in computational mechanics. Many textbooks have explained its basis and application in engineering science [ZM71; BC97; ZTZ05; Hug12]. The finite element model (FEM) divides a structure into a range of relatively tiny elements formed by a number of nodes and segments. Each element is affected by a set of parameters representing different characteristics and properties, like density, thickness, stiffness, Young's modulus, coefficient of thermal expansion and so on. All elements are connected side-by-side through nodes and segments. But they interact with each other only through nodes at the boundary. Nowadays, this method is largely implemented in computer codes.

Multibody simulation

Multibody simulation (MBS) is a useful tool to investigate the dynamic behavior of interconnected structures. A multibody system consists of rigid or flexible bodies. Each body represents an individual component of the entire structure and can experience individually large translational and rotational displacements. All bodies are linked together under some constraint conditions so that individual movement can be performed by a single body with respect to each other. This method involves a variety of computation algorithms to solve equations of motion. Like FEM, this method is often implemented in a computer-aided way to achieve a motion analysis. An example of these digital computer codes is introduced in Section 2.3.3.1. More details on MBS are given in many textbooks on the subject [WAWW07; DB12; Sch13].

Modal analysis

The object of modal analysis is to determine the dynamic properties of the structure namely the natural frequencies and the corresponding mode shapes. This method converts the coupled equations of motion into uncoupled equations that can be solved separately by FEM or lumped-element method. By assuming that the overall system is linear, a number of solutions obtained from uncoupled equations are then superimposed together to get the overall natural frequencies and mode shapes. More details on modal analysis can be found in [HLS97; FH01]. An example of modal analysis studying the dynamic properties of the guyed tower is given in Section H.3.

2.3.2. Mathematical models for load analysis

A complete load analysis requires several modeling methods, even all of them, to solve the structural dynamic problem in wind generation system. This entails a variety of mathematical models representing different components of wind turbine. For any

type of load analysis mentioned in Section 2.2.4.2, a typical load assessment procedure for dimensioning wind turbine and its components is illustrated in Figure 2.3.

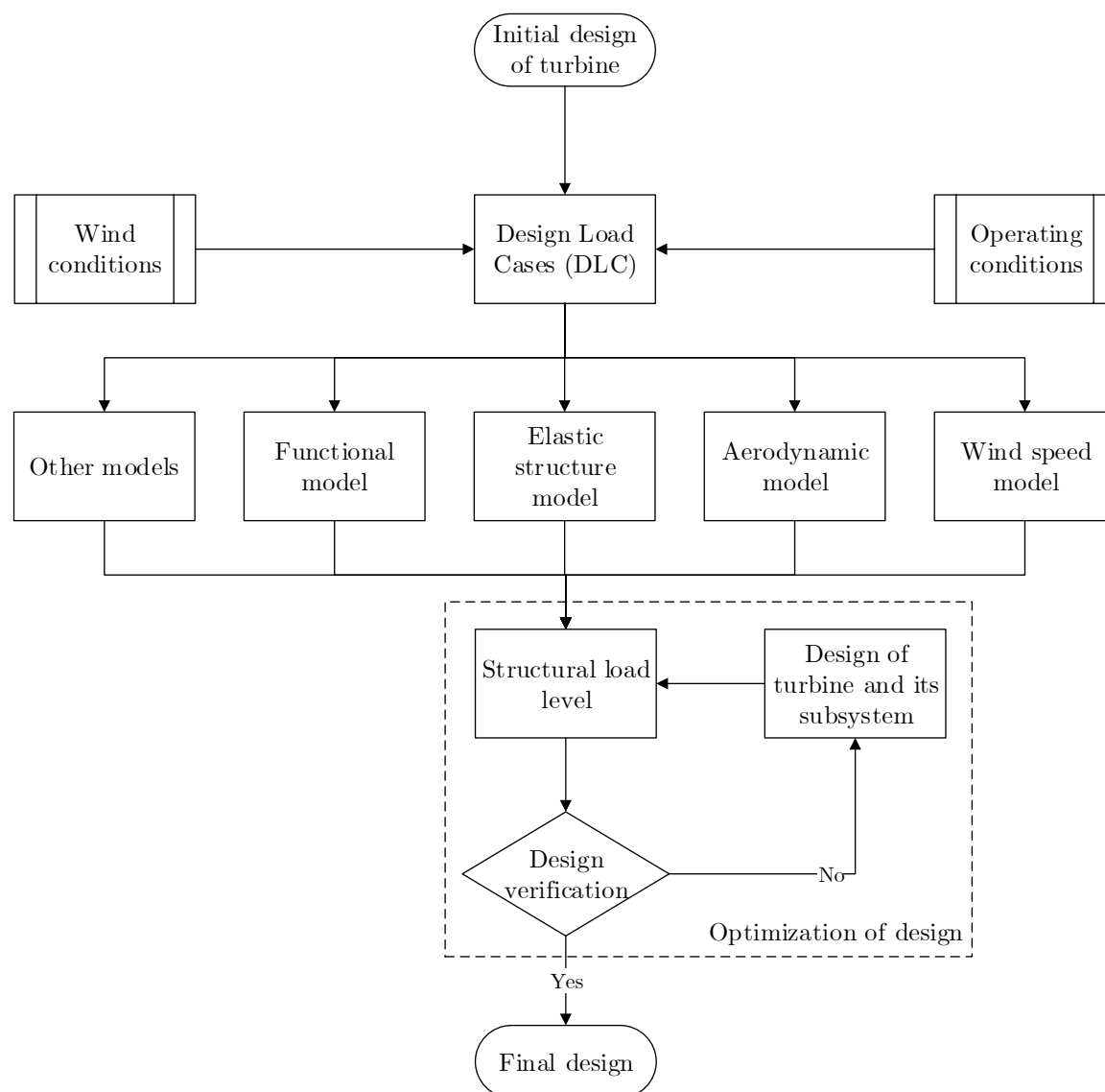


Figure 2.3: Flowchart for evaluating loads and designing the wind turbine and its subsystems

As discussed earlier, an initial design of wind turbine and the load cases of interest should be predefined by the designer. These preliminary conditions are used to generate other environmental conditions or to evaluate loading in each subsystem.

Wind speed model

As explained in Section 2.2.3, various wind speed models are developed to the nature of wind. Both steady state flow and unsteady state flow must be considered. Each type of flow should include at least a normal condition for investigating the dynamic response of turbine during normal operations, and an extreme condition in

which the turbine must withstand.

Aerodynamic model

An aerodynamic model is indispensable to estimate aerodynamic loading under the steady state and the unsteady state wind flow. Blade element momentum theory (BEMT) and its variant are widely applied for calculating aerodynamic loading [BT02; Ing11; Pon16; Sun16] while other theories are also relevant to the subject [BS02; Wan14; Li20].

Elastic structure model

The elastic structure model for wind turbine system is generally based on FEM [Bot06; HJB10; OPL11]. This model allows the estimation of the dynamic properties (natural frequencies and mode shapes) of the whole wind turbine. Once the dynamic properties are figured out, the dynamic response of the structure (deformation, acceleration, stress) resulting from the external forces can be calculated.

Functional model

Whether the wind turbine is equipped with a blade pitch control and/or a variable-speed rotor, a functional model is vital for evaluating the loading resulting from functional behaviors such like blade rotation, shaft break, etc. A simplified linear model is often used to evaluate the influence of the control characteristics [Nov95; Kas12].

Other models

Some extra models may be required with regard to the specific problem. For instance, a hydrodynamic model must be included when dimensioning an offshore wind turbine. The methods used in these models depend on the nature of the problem and the related external conditions.

Design verification and optimization

After assessing the load level through the above models, the structural stress, deformation and other relevant dynamic responses should meet the requirements specified in design standards or the limits from material properties. If one or several constraint conditions are not satisfied, a modification on design parameters of wind turbine and a reassessment of structural loading are unavoidable. This procedure forms an optimization design of the wind turbine and its components. Both deterministic and stochastic optimization approaches are often invoked at this step to seek an optimal design of machine regarding a group of constraints. As an example, an optimization of wind tower thickness is given in Chapter 6.

2.3.3. Numerical approaches

Nowadays, with the availability of rising computing resources, numerical simulation codes for structural analysis are commonly in use. A brief introduction of digital computer codes that will be used afterward is presented in the following sections. All computer codes involved in the present dissertation are open source and distributed under free software licenses [Lic89]. This guarantees the maximum possibility to modify the source codes and integrate new codes in accordance with necessary. More details on numerical simulators in computational mechanics can be found in [JT99; Poz02; Liu12; Ber15] and more numerical simulators relevant to wind turbine design can be found in [LH07; BC16].

2.3.3.1. FAST

FAST, or OpenFAST, is a cross-platform numeral simulator for two- and three-bladed HAWTs. The name comes from the acronyms of *Fatigue, Aerodynamic, Structure and Turbulence* [JB05]. It is a multibody based aero-hydro-servo-elastic simulation tool composed by a variety of sub-modules Figure 2.4.

The code models the entire wind turbine as a combination of flexible and rigid bodies. It is developed and supported by National Renewable Energy Laboratory (NREL). The code is licensed under the open-source Apache License, Version 2.0 [Apa04] and distributed on GitHub now [NRE].

2.4. Conclusions

As previously mentioned, the IEC 61400-1 standard can be used as an elementary wind turbine design norm. It outlines minimum design requirements for wind turbines and it is not intended for detailed assessment or complete design specification. As such, it does not include all the details required to manufacture a wind turbine, so there are things that need to be addressed beyond the scope of this standard.

According to the IEC 61400-1 specifications, the process of evaluating loads comprise the following steps:

1. define the class of wind turbine that meets the design target
2. determine design load cases of interest which consists of both normal operating conditions and extreme wind conditions
3. assess the load level on the turbine under the chosen load cases
4. substantiate that the stresses due to the loads are acceptable

FAST / OpenFAST	Wind speed model	
	InflowWind	
		Wind-inflow
	Aerodynamic model	
	AeroDyn	
		Aerodynamics
	Elastic structure model	
	ElastoDyn	
		Platform dynamics
		Tower dynamics
		Nacelle dynamics
		Rotor dynamics
		Drivetrain dynamics
	BeamDyn	
		Finite element blade
		Structural dynamics
	Functional model	
	ServoDyn	
		Power generation
		Control system & Actuators
	Other models	
	SubDyn	
		Multimember substructural dynamics
	HydroDyn	
		Hydrodynamics
		Waves & Currents
	Mooring dynamics	
		MAP++ (Mooring statics)
	MoorDyn (Lumped mass mooring dynamics)	
	FEAMooring (Finite element mooring dynamics)	
	OrcaFlexInterface (Mooring and hydrodynamics from Orcina)	
Ice dynamics		
	IceFloe (Ice dynamics from DNV-GL)	
	IceDyn (Ice dynamics from UMich)	

Figure 2.4: Overview of FAST/OpenFAST and its sub-modules

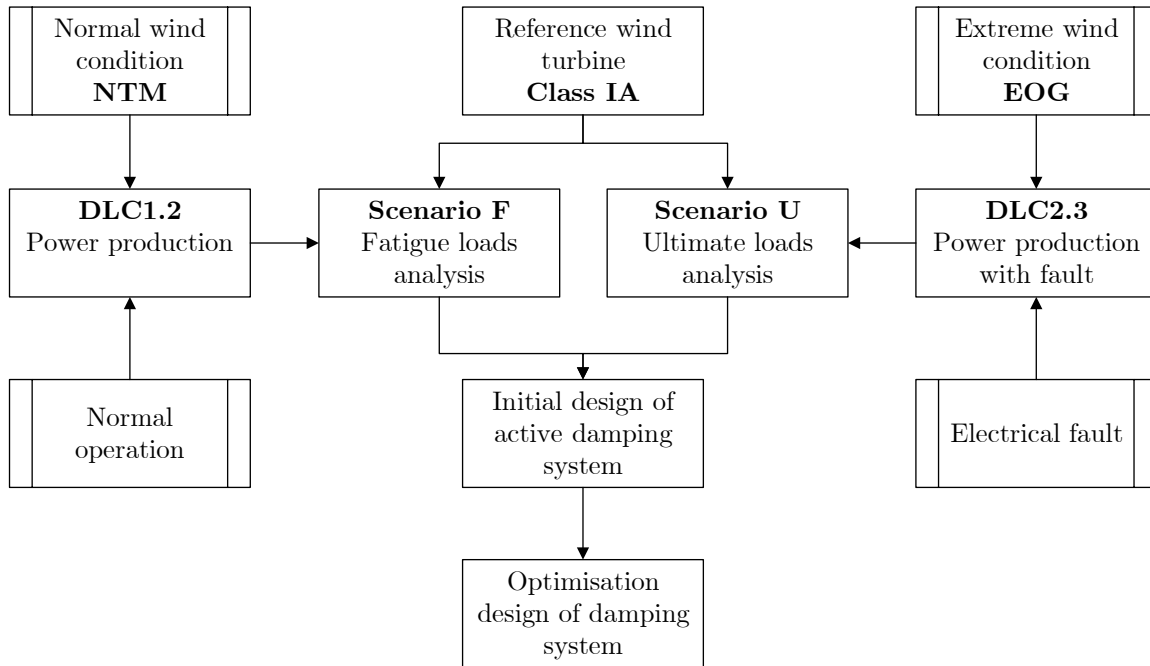


Figure 2.5: Design process for an active damping system

In order to develop an active damping system that can be widely applied in most wind turbines, a wind turbine of class IA is preferred. A load case with normal conditions, DLC2.3, and a load case with extreme conditions, DLC1.1, are selected to accomplish ultimate loads analysis and fatigue loads analysis, respectively.

Both types of analysis are firstly carried out on a reference wind turbine in order to quantify the demand for active damping system. A scenario U, denoting analysis of ultimate loads on reference wind turbine, and a scenario F, denoting analysis of fatigue on reference wind turbine, are worked out to initialize a primary design for active damper. Further, these scenarios are served as the baseline in the optimization of control parameters of active damper.

A brief introduction of a reference wind turbine is given in the next chapter along with the implementation of numerical modeling methods. The scenario U and the scenario F are individually presented in Chapter 3 and Chapter 4. An initial design of active damping system is established in Chapter 5 while the optimization of this damping system's characteristics is embedded in Chapter 6.



Part II



Chapter 3

Dynamic analysis of wind tower under grid loss

This chapter provides a summary of reference wind turbine and how it is applied through design process. The first section provides some details on the key characteristics of baseline wind turbine. The second section provides a validation of this turbine under steady-state wind flow. It is followed by another section investigating the response of turbine under both extreme wind condition and grid loss. The latter implies that a wind turbine is disconnected from the power network by unpredictable fault. The last section highlights the improvements or new proposals mentioned in the current chapter.

The results obtained in this chapter are prerequisite for designing a structural damper and will be subsequently served as a scenario for evaluating the performance of the damping system.

3.1. Reference wind turbine

3.1.1. Key features

Two reference wind turbines are commonly used in the field of numerical simulations: 1) NREL offshore 5MW baseline wind turbine [Jon09]; 2) DTU 10-MW reference wind turbine [Bak13]. Both are initially designed for offshore scenario. But NREL 5MW reference wind turbine also provides possibility to simulate the land-standing use in its own simulation tool FAST. Despite that there is no real-world implementation or application of NREL 5MW turbine, it is still a meaningful reference wind turbine that has been widely studied in academic researches and often used as a benchmark in developing or investigating wind turbine technologies [Di 21; Arc21; LK20; CHW19; EM17; LPO13; CV12]. For this reason, this baseline wind turbine is modeled in FAST and served as an initial design for onshore wind turbine in this dissertation.

The key characteristics of NREL 5MW reference wind turbine are mainly based on the specification of the REpower 5M wind turbine and the Dutch Offshore Wind Energy Converter Project (DOWEC) project [Koo03]. Table 3.1 summarizes some important properties.

The NREL 5MW reference wind turbine is a three-bladed HAWT with a hub height (HH) of 90 m. All blades are prebend with an upwind precone of 2.5° and, by this means, the tower clearance is increased without a large rotor overhang. The diameter of rotor is 125.88 m sweeping an area of 12 445.24 m². The cut-in rotor speed 6.9 rpm and the rated rotor speed 12.1 rpm agree with the cut-in wind speed $V_{in} = 3$ m/s and the rated wind speed $V_r = 11.4$ m/s, correspondingly. With the rated electric power of 5 MW and an efficiency of 94.4% on generator, the rated mechanical power is 5.297 MW.

The upper structure (nacelle, rotor and blades) has a total mass of 240 t on the top of the tower (87.60 m). A metallic adapter of 2.4 m high is installed to ensure the connection between the wind tower and the nacelle. The typical material properties of steel is used for the tower except the density which is scaled to 8500 kg/m³ taking account of paint, bolts, welds, and flanges.

The outer diameter and thickness of the tower are assumed to be linearly tapered from the tower base 0.0 m to tower top 87.6 m. The tower base diameter and the tower top diameter is the same as the one in DOWEC [Koo03], i.e., 6.00 m and 3.87 m, respectively. Due to the region of rotor frequency (1P) and the region of blade passing frequency (3P) discussed in Section 2.1.3.2, the thickness of tower is increased 30% to ensure that the 1st fore-aft frequency and the 1st side-to-side frequency are not placed in the range of 1P and 3P. This leads to a thickness of 0.0351 m on the tower base

Table 3.1: Overview of NREL 5MW baseline wind turbine

Component	Property	Value
Blade	Variable-speed collective pitch control	-
	Number of blades	3
	Length (with respect to root along preconed axis)	61.5 m
	Precone	2.5 °
	Mass	17.74 t
	1 st mass moment of inertia (w.r.t. blade root)	363 231 kg m
	2 nd mass moment of inertia (w.r.t. blade root)	11 776 047 kg m ²
	Nominal radial center of mass location	20.475 m
Rotor	Structural damping ratio under all modes	0.477465%
	Rated electric power	5 MW
	Electrical generator efficiency	94.4%
	Rotor orientation	Upwind
	Rotor diameter	125.88 m
	Cut-in rotor speed	6.9 rpm
	Rated rotor speed	12.1 rpm
	Rotor mass	110 t
	Cut-in wind speed V_{in}	3.0 m/s
	Rated wind speed V_{rate}	11.4 m/s
Hub and nacelle	Cut-out wind speed V_{out}	25.0 m/s
	Hub diameter	3 m
	Hub mass	56.78 t
	Hub height (HH)	90.00 m
	Elevation of yaw bearing above ground (or MSL) ¹	87.60 m
Drivetrain	Nacelle mass	240 t
	High-speed multiple-stage gearbox	
	Gearbox ratio	97:1
	Rated generator speed	1173.7 rpm
Tower	High-speed shaft brake time	0.6 s
	Mass	347.46 t
	Density	8500 kg/m ³
	Young's modulus	210 GPa
	Shear modulus	80.8 GPa
	Poisson's ratio	0.3
	1 st tower fore-after	0.324
	1 st tower side-to-side	0.312
Structural damping ratio under all modes	1.00%	

¹ Mean sea level (MSL) = Hub height (HH) – Vertical distance from the tower top to the HH

and a thickness of 0.0247 m on the tower top. More details about the NREL 5MW reference wind turbine are carried out in Appendix D.

3.1.2. Modeling assumptions

The entire characteristics of the reference tower are introduced in FAST using the tower-base coordinate system (Figure 3.1). The tower is characterized by its distributed properties (see Table D.6 in Appendix D), and it is modeled by a beam model of FEM with 22 nodes including 1 node for tower-top, 1 node for tower-base and 20 nodes for the tower body. All the nodes of beam model are defined in the Cartesian coordinate system (Figure 3.1a) where the origin point O is fixed on the level of tower base connection to the support platform.

It should be noticed that, in real life, the wind tower base is always fixed on the top of support platform by bolts (as photographed in Figure 3.1b¹), reinforced concrete or other embedding techniques. These techniques ensure that the boundary conditions on the tower-base node ($z = 0.00$ m) can be considered as fixed support. As for the interaction between the support platform and the soil, it is beyond the scope of this dissertation and can be found in other essays [PDK19; ZBH18; FB16; PEL10].



Figure 3.1: Tower-base coordinate system for upwind turbine: (a) a sketch; (b) an example of land-based wind turbine

Undoubtedly, it is arduous and worthless to export the results over all tower nodes of the mesh. Table 3.2 exhibits the nodes used for post-processing (i.e., local force, stress, displacement, etc.) in this work. These nodes reserved for output are named as “gage”.

The gage 1 ($z = 2.19$ m) is the closest node to the tower-base. For many onshore wind turbines, this elevation is very close to door openings [Tra13] and as such, it

1. “Wind turbine stairs”, by Patrick Finnegan, licensed under CC BY 2.0 / Add lines and texts

Table 3.2: Tower nodes on beam element model used for post-processing

Tower gage n°	Tower node n°	Coordinate	Remark
Tower-top	-	(0.00, 0.00, 87.60)	Tower-top or yaw bearing
Gage 9	20	(0.00, 0.00, 85.41)	
Gage 8	19	(0.00, 0.00, 81.03)	
Gage 7	15	(0.00, 0.00, 63.51)	
Gage 6	11	(0.00, 0.00, 45.99)	
Gage 5	10	(0.00, 0.00, 41.61)	
Gage 4	7	(0.00, 0.00, 28.47)	
Gage 3	3	(0.00, 0.00, 10.95)	
Gage 2	2	(0.00, 0.00, 6.57)	
Gage 1	1	(0.00, 0.00, 2.19)	
Tower-base	-	(0.00, 0.00, 0.00)	Tower-base

is quite worthwhile for assessing the cumulative fatigue damages as well as many other dynamic responses on this gage. The tower-top node ($z = 87.60$ m) and the gage 9 ($z = 85.41$ m) are the two highest nodes on the beam element model that are important for assessing the tower deflection and displacement resulting from air-tower interaction and nacelle-tower interaction.

In next chapter, Chapter 4, a cylindrical coordinate system is involved to investigate the stress-history on the cross-section of wind tower. The definition of this coordinate system and the conversion between the system and the Cartesian coordinate system is detailed in Appendix E.

3.1.3. Dynamic analysis using FAST

As mentioned in Chapter 1 Section 1.3.1.3, the essential problem that needs to be solved by dynamic analysis in the context of wind turbine tower is to figure out the solution for the equation of motion:

$$m\ddot{x} + c\dot{x} + kx = \mathcal{F}(t) \quad (3.1)$$

where, $\mathcal{F}(t)$ is a temporal signal representing the loadings over the structure. It depends on all kinds of wind loads, the interaction between solid (wind blade, wind tower etc.) and fluid (air flow, waves etc.), the control loads and the steady loads that are already discussed in Chapter 2 Section 2.1.

The numerical simulator FAST (Section 2.3.3.1) is practiced in this dissertation to offer a numerical solution for dynamic analysis. Firstly, the wind condition (i.e., a time series of wind speed in spatial domain) is generated by using its InflowWind

sub-module (Figure 2.4). The mathematical definitions behind this numerical generation process is given in Appendix B and Appendix C. The dynamic analysis is then carried out by calling its AeroDyn, ElastoDyn, BeamDyn and ServoDyn sub-modules. Finally, the resulting deflections, forces and moments of wind turbine tower is outputted by FAST and will be used in the following analysis. Each of these reactions (i.e., deflections, forces or moments) has three components projected to the principal axes of Cartesian coordinate system defined in Appendix E.1.

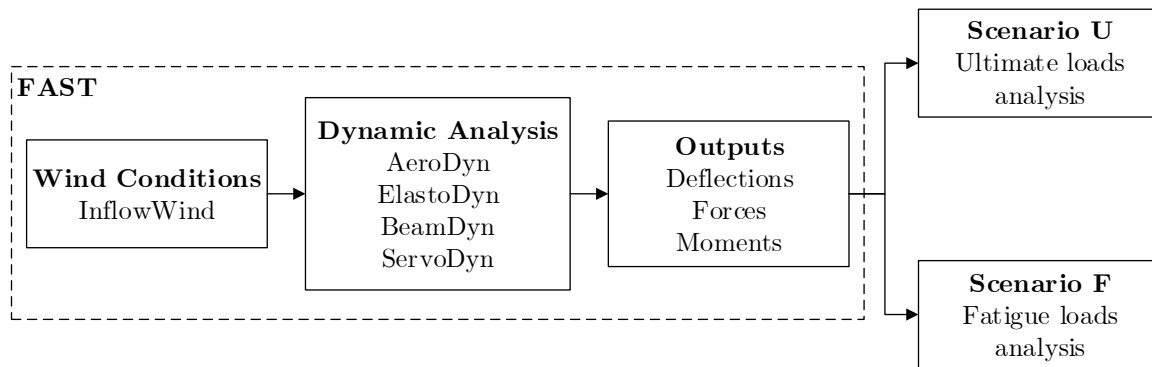


Figure 3.2: Dynamic analysis for wind turbine using FAST codes

Figure 3.2 illustrates the major steps of modeling a wind turbine in FAST where a successive ultimate loads analysis (Scenario U) and a fatigue loads analysis (Scenario F) will be discussed in Section 3.3.1 and Chapter 4, respectively.

3.2. Validation of reference wind turbine for power production

To understand the behavior of the NREL 5MW reference wind turbine, especially the response of its actual control system, a baseline investigation is thus proposed. This inquiry is not made on a theoretical underpinning, but it allows a thorough survey on the reference wind turbine and the simulation code.

3.2.1. Design load case of uniform steady wind (DLC0.1)

Remark

Please be aware that the DLC0.1 is defined by the author for convenient use. It doesn't exist in IEC 61400-1 standard.

3.2.1.1. Design situation

Inspired by the IEC standards, a steady-state uniform wind condition in the range of V_{in} and V_{out} is created for this personalized design load case. More specifically, it means that the mean wind speed V_{mean} changes between $V_{in}= 3.0$ m/s and $V_{out}= 25.0$ m/s at step of 0.1 m/s. By this means, it requires a total of 221 runs in FAST.

As for the operational condition, the turbine is supposed to be in the normal operating state. This decision is made considering two main reasons:

1. the state of turbine at the end of each run will be reused as the initial state in the scenario F (see Section 4.3.1) for saving computing time in those simulations under turbulent wind conditions;
2. the behavior of wind turbine obtained in this DLC0.1 is a basis for evaluating the performance of turbine without any extreme conditions and for estimating the gain from the control system when an additional event occurs.

In order to export final state of wind turbine, an ultimate loads analysis is performed. Not only the state of rotor (including blades) but also the state of tower and other components are all exported and will be reused as initial conditions in scenario F.

The simulated duration is settled to 10 min corresponding to the simulated time required by the IEC 61400-1 standard for DLCs with turbulent wind (Section 2.2.3).

3.2.1.2. Results and discussions

Deflection and force

To have a first impression about the deflection level, the tower deflection on gage 9, when mean wind speed equals to the rated wind speed (i.e., $V_{mean}=V_{rate}= 11.4$ m/s), is exported. All results are expressed with respect to the node's original position in tower-base coordinate system, i.e.:

fore-after direction aligned with \vec{x}_t -axis

side-to-side direction aligned with \vec{y}_t -axis

axial direction aligned with \vec{z}_t -axis

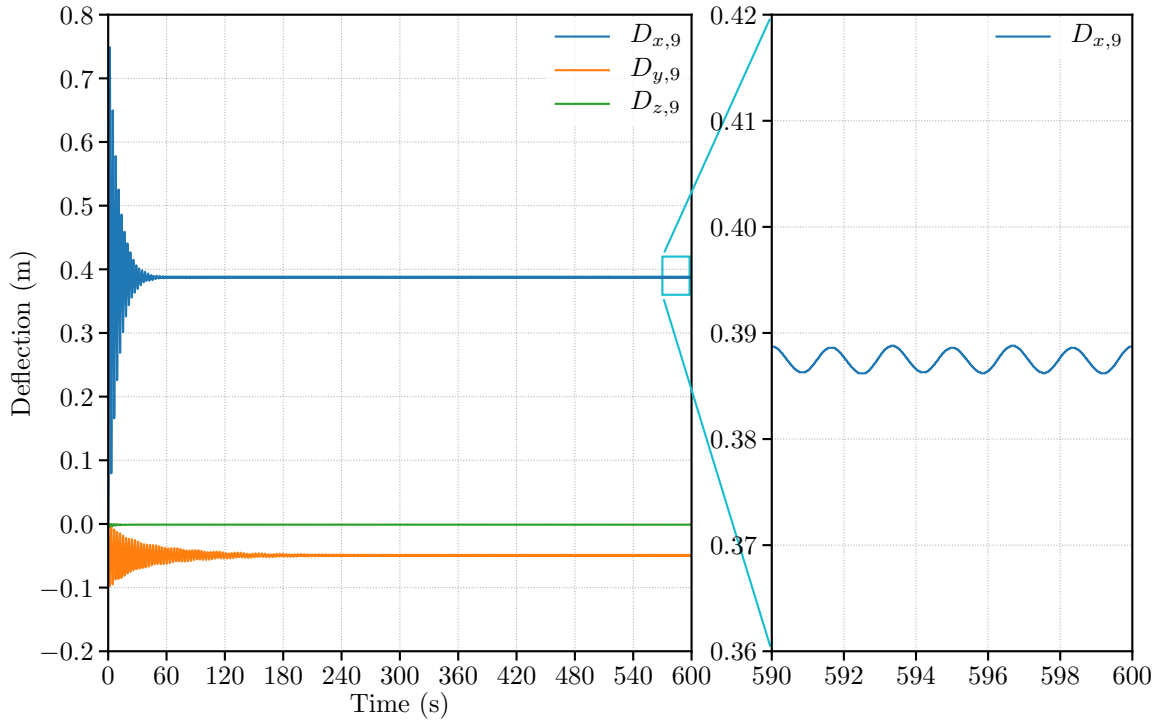


Figure 3.3: Tower gage 9 deflection (relative to the undeflected position) at rated wind speed $V_{rate}=11.4$ m/s

Due to the neglect of the start-up phase of wind turbine in numerical simulation, the tower is stricken by the wind at the beginning (Figure 3.3 left). Thus, a significant vibration is observed during the first minute in horizontal direction and lateral direction (i.e., \vec{x}_t -axis and \vec{y}_t -axis, respectively). After that, the tower tends to stabilize at a constant deflection level till the end. Actually, the tower is still in vibration if we zoom in the last 10 s of the simulation (Figure 3.3 right). Nonetheless, the changes in the deflection is relatively low. For instance, the amplitude of fore-aft deflection D_x is between 0.385 m and 0.389 m which gives a variation about 1%. For the side-to-side deflection D_y , it stabilizes around -0.05 m at the end of 10 min, and the axial deflection D_z is negligible ($D_z \leq 0.001$ m).

The local force on gage 1 is plotted in Figure 3.4. Like the deflection, the local force in fore-aft direction F_x fluctuates violently between 0 kN and 1500 kN at the beginning and, later, between 710 kN and 730 kN (a change of 2.8%) during the last 10 s. The side-to-side force F_y stabilizes between 0 kN and 12 kN at the end. An amplitude of 10 kN is also observed for the axial force F_z . It should be noted that the axial force F_z is opposite to the axial direction because it accumulates the weight from the tower, nacelle and rotor. The mean value of axial force F_z is approximately 6798 kN.

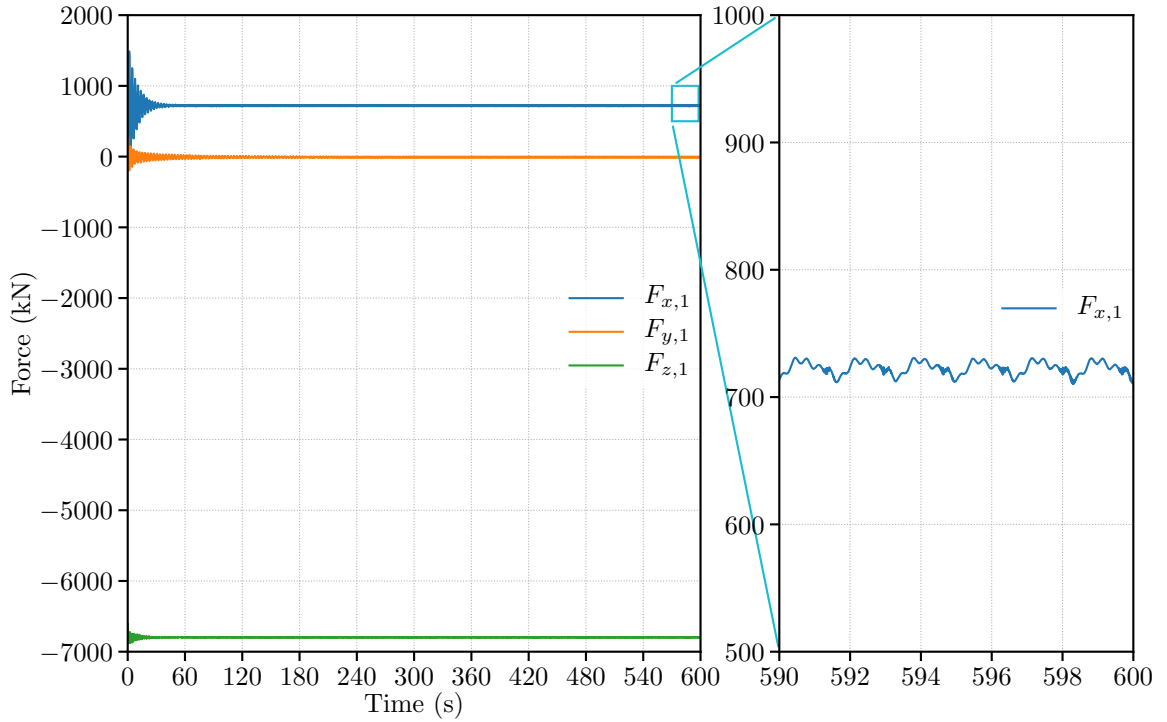


Figure 3.4: Tower gage 1 local force at rated wind speed $V_{rate} = 11.4$ m/s

Moment

The local tower moments are also expressed in the tower-base coordinate system where:

roll moment is in the \vec{x}_t direction (also named side-to-side moment because the movement excited by this moment aligns in side-to-side direction)

pitching moment is in the \vec{y}_t direction (also named fore-aft moment because the movement excited by this moment aligns in fore-aft direction)

yaw moment is in the \vec{z}_t direction (also named torsional moment)

Figure 3.5 gives the local tower moment on tower gage 1. It is clear that the pitching moment M_y has a leading role comparing to moments in other directions. It stabilizes in the range of $64.50 \text{ MN}\cdot\text{m}$ and $65.00 \text{ MN}\cdot\text{m}$, in other words, a variation of 0.8%. The roll moment M_x ends at $4.985 \pm 0.24 \text{ MN}\cdot\text{m}$ and the yaw moment M_z ends at $0.430 \pm 0.28 \text{ MN}\cdot\text{m}$.

Summary

To conclude, Figure 3.3, Figure 3.4 and Figure 3.5 have proven that the mechanic responses obtained from the simulation codes FAST always end in tiny fluctuations. Despite the existence of the fluctuations the influence of which are negligible considering its magnitude and period. To get rid of this influence, the average value of every mechanic response (i.e., deflection, force or moment) during the last 10 s is named as *representative value*.

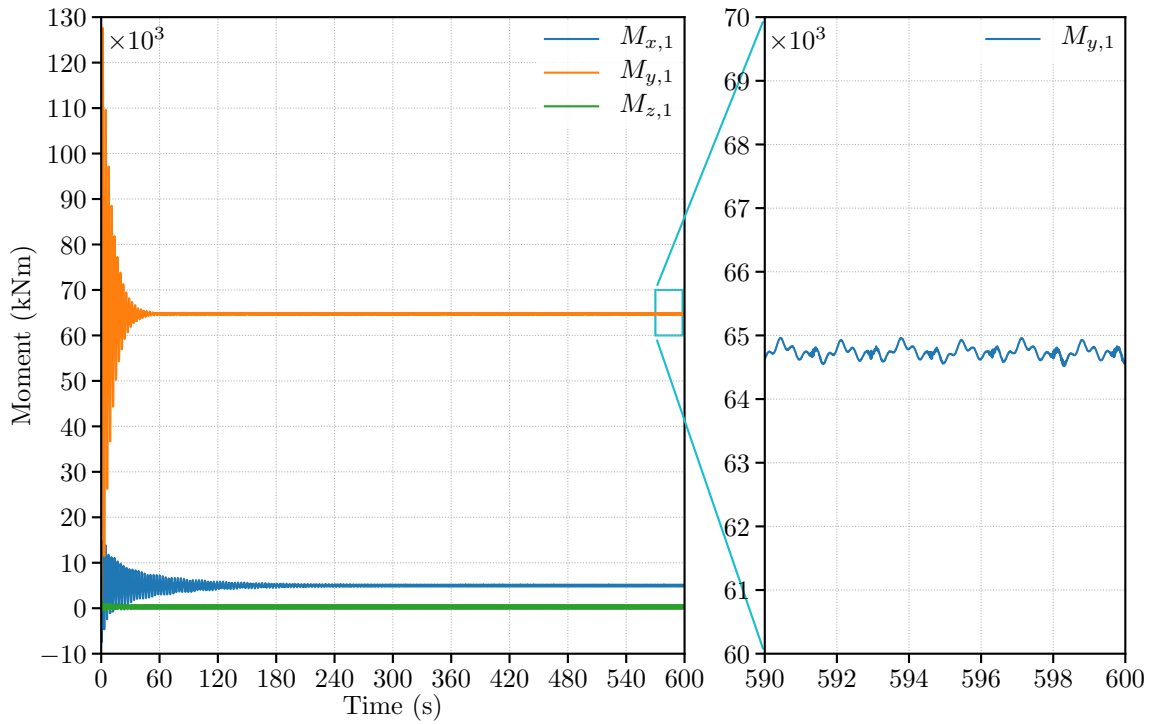


Figure 3.5: Tower gage 1 local moment at rated wind speed $V_{rate} = 11.4$ m/s

The representative value describes the loads level on the wind tower when the whole structure is stabilized at a given mean wind speed. To eliminate the negligible vibrations at the end of numerical simulation, a $\pm 2\%$ deviation from the representative value is considered as acceptable in this dissertation. In other words, if the changes in the amplitude is less or equal to 4% at the end of simulation, the structure is considered as stable.

Figure 3.6 summarizes the representative value of major deflection, force and moment (i.e., D_x, F_x, M_y , respectively) on tower gage 1 and gage 9 for wind speed in the range of $[V_{in}, V_{out}]$ (i.e., $[3$ m/s, 25 m/s]). Take the tower gage 9 fore-aft deflection $D_{x,9}$ for example, the response during the last 10s of 10-min simulation (as shown in Figure 3.3) is used to calculate its representative value. Each 10-min simulation subjects to a uniformly constant wind flow characterized by mean wind speed V_{mean} . The numerical results of $D_{x,9}$ are plotted by the blue dashed line in Figure 3.6. The deflection on tower gage 1 as well as other types of response are proceeded in the same and shown in sub-charts of Figure 3.6.

It is obvious that all types of response have reached its maximum magnitude at the rated wind speed V_{rate} . More clearly, the fore-aft deflection on gage 9, $D_{x,9}$, the fore-aft force on gage 1, $F_{x,1}$, and the pitching moment on gage 1, $M_{y,1}$, are the most predominant components comparing to other types of response along different directions. The representative value of these three components at V_{in} , V_{rate} and V_{out} are listed in Table 3.3 and will be mainly discussed in the following chapters.

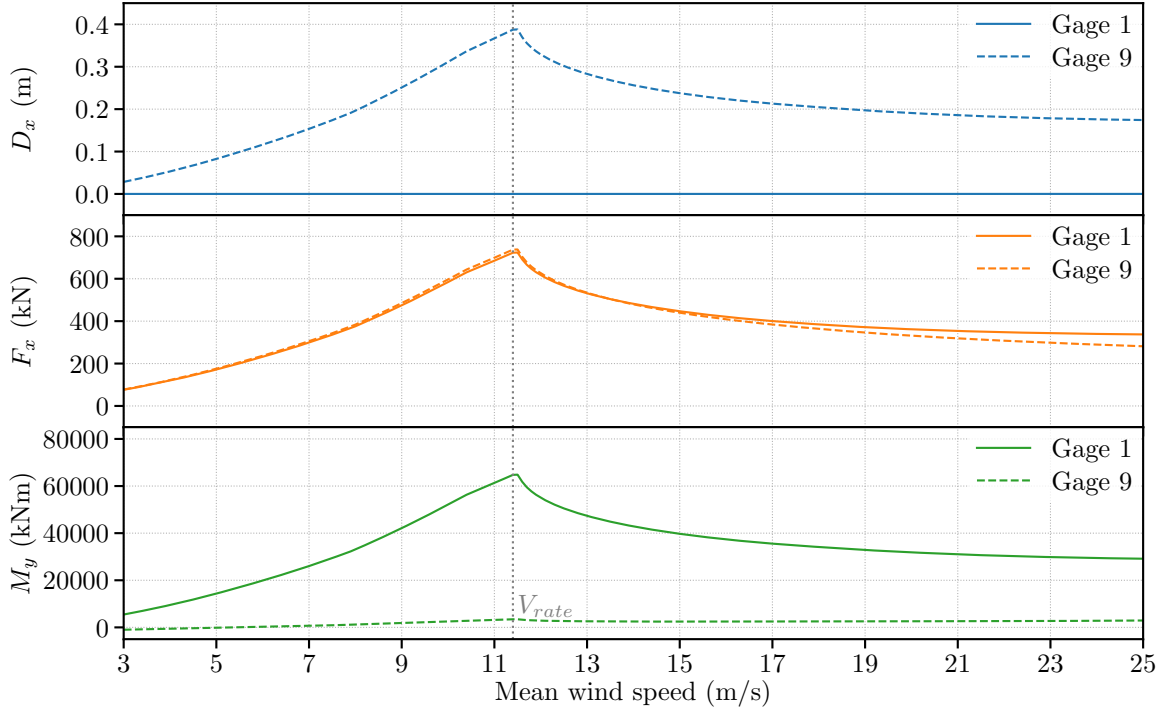


Figure 3.6: Representative value of tower fore-aft deflection, fore-aft force and pitching moment for all wind speeds in the operational range

Table 3.3: Representative value of tower fore-aft deflection, fore-aft force and pitching moment at V_{in} , V_{rate} and V_{out}

Mean wind speed (value)	$D_{x,9}$ (m)	$F_{x,1}$ (kN)	$M_{y,1}$ (kN·m)	Remark
V_{in} (3.0 m/s)	0.028	76.361	5459.244	cut-in speed
V_{rate} (11.4 m/s)	0.387	722.726	64 739.850	rated speed
V_{out} (25.0 m/s)	0.174	337.443	29 152.550	cut-out speed

Since the DLC0.1 is a DLC in normal production, the production curve under all operating speeds is plotted in Figure 3.7. The energy extracted from the wind increases progressively from V_{in} to V_{rate} , then reaches the nominal level (i.e., 5 MW) at the rated wind speed V_{rate} and maintains this production for all wind speeds between V_{rate} and V_{out} .

The generator power production, as well as generator torque, is controlled by a conventional variable-speed controller and a variable blade pitch-to-feather (PTF) controller. The former is designed to maximize power capture in the range of $[V_{in}, V_{rate}]$ while the latter is designed to regulate generator speed in the range of $[V_{rate}, V_{out}]$. These two controllers are discussed in the next section with a detailed study concerning shutdown procedure.

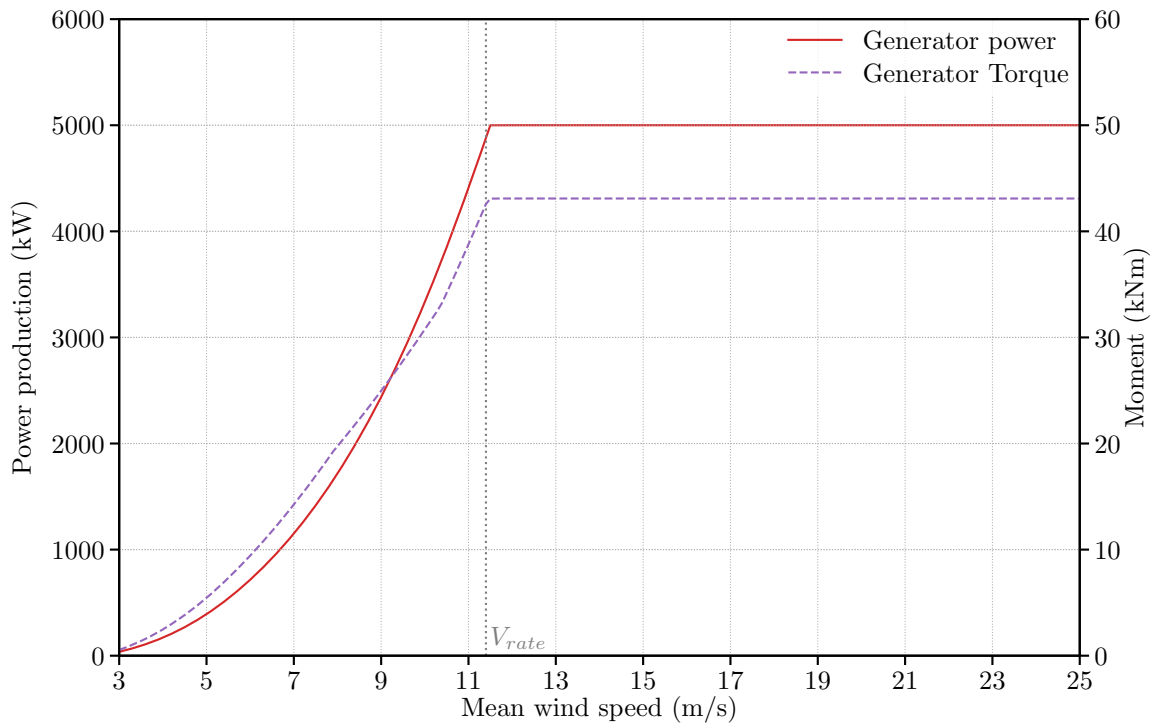


Figure 3.7: Electrical generator power and torque in normal production

3.2.2. Design load case of uniform steady wind with operational maneuvers (DLC0.2)

Remark

Please be aware that the DLC0.2 is defined by the author for convenient use. It doesn't exist in IEC 61400-1 standard.

3.2.2.1. Design situation

On the investigation subsequent to DLC0.1, a further inquiry into the control system of the reference wind turbine is designed. The present DLC focus on examining the sequences of emergency shutdown and the corresponding influence from this maneuver.

3.2.2.2. Control system

The overall integrated control system of NREL 5MW reference wind turbine is established on the conventional design approach for controlling power-production operation (Figure 3.8). It depends on a generator-torque controller and a rotor-collective blade-pitch controller. However, this control system is designed to take control of wind

turbine only in power production phase. Other operations like normal start-up procedure, normal shutdown procedure and protection functions are not included in the control system. Nor is the nacelle yaw controller included because its response is slow enough that it does not usually contribute to significant extreme loads or fatigue damage [Jon09]. More details about the design of variable-speed generator-torque controller and full-span rotor-collective blade-pitch-angle controller are described in Appendix D.

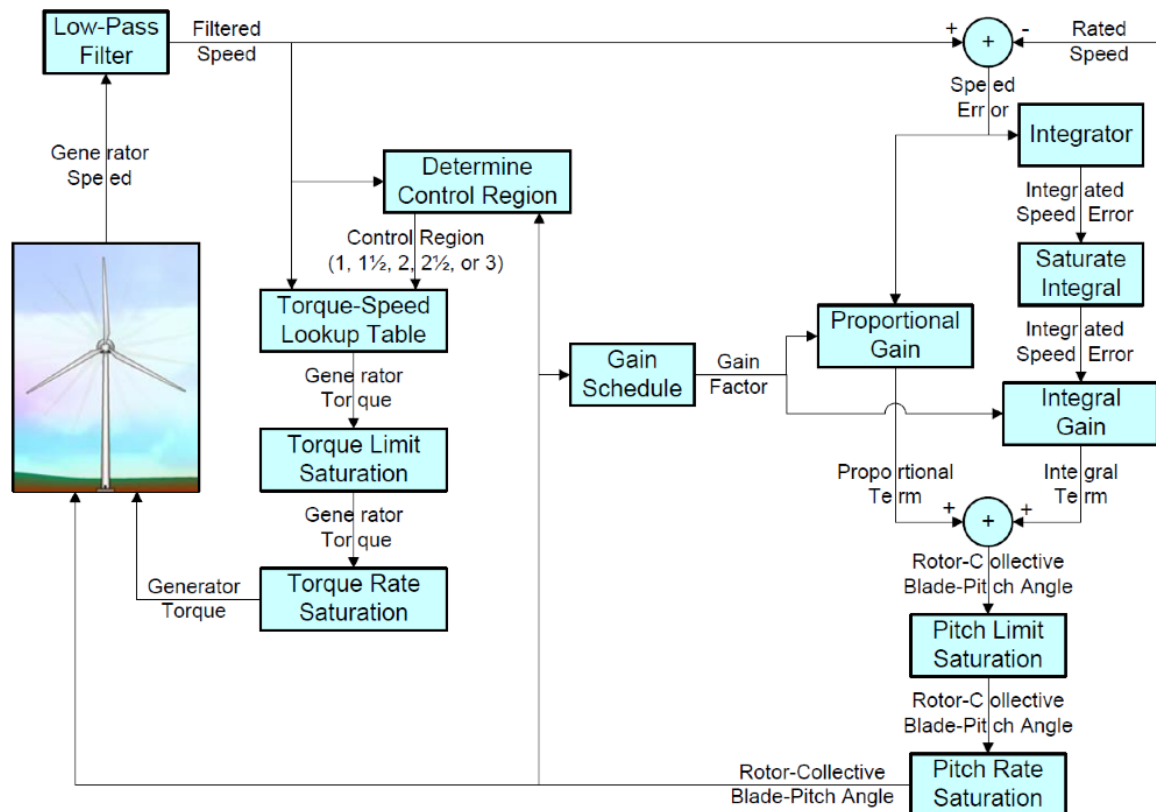


Figure 3.8: Overall integrated control system of NREL 5MW reference wind turbine [Jon09]

3.2.2.3. Protection system

In order to analyze the behavior of turbine in the face of abnormal conditions (e.g., control system failure, extremely climatic condition), a protection system must be firstly designed. Protection system shall be activated as a result of a malfunction of the control system or as a result of an internal or external harmful incident. To design a basic protection system including an emergency shutdown procedure with respect to the overall control system, two types of shutdown system are available in FAST codes: pitch-to-feather (PTF) operation and high-speed shaft (HSS) brake.

The PTF operation is one of the most common maneuvers in normal shutdown

procedure through controlling the pitch angle of blades. Since the active blade controller of NREL 5MW reference wind turbine is collective, the pitch angle of all three blades is changed simultaneously. The fundamental idea of PTF is turning the blade pitch angle into the feathered position (i.e., pitch angle = 90°) so that the rotor is aligned with the wind direction. This action reduces gradually the rotor speed to zero, and consequently, the generator is shut down due to the loss of the aerodynamic torque.

The HSS brake is an operation which deploys a brake at the high speed end of shaft to stop the rotor. It can be used in both normal and emergency shutdown procedure. It cooperates commonly with other control sequences to stop the rotor. For instance, a generator brake, which uses the electrical generator as a dynamic brake, can be deployed firstly to slow down the rotor until the speed is slow enough that the HSS brake can stop the rotor. The numerical implementation of HSS in FAST starts the brake at a time specified by user with a brake torque of 0. Then it increases the brake torque linearly from 0 to a fixed value over a short period. Once the brake is fully deployed, the magnitude of the torque is maintained constantly as long as the shaft speed is nonzero.

To develop an emergency shutdown procedure that serves in the case of fault or extreme conditions, a combination of PTF maneuver and HSS brake is developed. The first phase of this emergency control system is to deploy the normal PTF shutdown sequences at a fixed angular speed of blade pitch angle. This will reduce the rotation speed of blade azimuth and, consequently, reduce the rotor speed and the aerodynamic torque. As soon as all the blades are feathered, the control system launches the second phase in which the HSS brake is initiated in order to disengage the electrical generator. The brake torque will be increased linearly from zero to a constant over a short period and keep this level till the entire system is shut down or the end of simulation. The numerical implementation and the load analysis of this emergency shutdown procedure is described in the next section. An application of such procedure in a special event combining the extreme wind condition and the loss of electrical network is given in Section 3.3.1.

3.2.2.4. Results and discussions

Initial conditions

For the purpose of saving the simulation time for the current DLC and ensuring the wind turbine is already stabilized before the deployment of controlling operations, the turbine is initialized by using the state at the last second in DLC0.1 (i.e., the turbine state at the 600th s in DLC0.1). This simulation technique reduces undoubtedly the time required by the initialization stage at the beginning of simulation. Take the tower deflection as an example (Figure 3.9), the fore-aft deflection $D_{x,9}$ oscillates fiercely

at the beginning of simulation in DLC0.1 whereas it fluctuates slightly in DLC0.2. The side-to-side deflection $D_{y,9}$ remains fluctuating till 60s in DLC0.1 whereas it retains smooth in the other. The time required for stabilizing the wind turbine (i.e., initialization stage) in DLC0.2 is much less than that in DLC0.1.

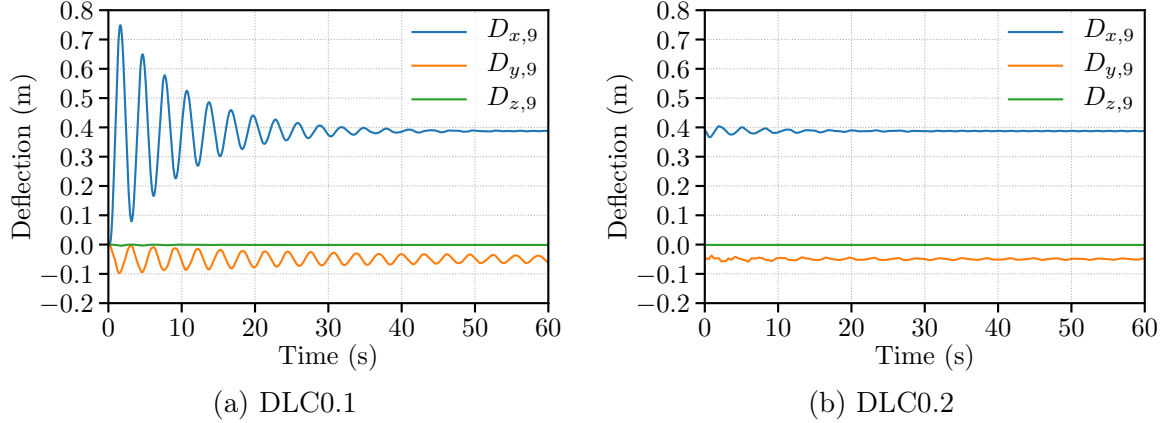


Figure 3.9: Deflections on tower gage 9 during the first minute in (a) DLC0.1 and (b) DLC0.2

As explained in Section 3.2.1.2, the responses in the initialization stage are totally useless and meaningless in physics. The signal of response is too fluctuant and must be ignored in the post-processing. But this stage is indispensable to initialize the simulation and stabilize the structure before any special event takes place. So an appropriate technique to reduce the necessary time for initialization stage can reduce significantly the total simulation time as well.

This technique is hence used in all the following simulations in this dissertation. All the numerical models will be initialized by the final state of wind turbine achieved at the last second in DLC0.1. For all the following simulations, an additional period of 60s is added in the beginning. All types of result calculated during this initializing period are ignored in the post-processing.

Shutdown sequences

The PTF shutdowns the turbine at 300s followed by the HSS brake. Jonkman et al. [Jon09] have defined a default value of $8^\circ/\text{s}$ for the rotation speed of pitch angle at which the control system turns all the blades from their working position (i.e., 0°) to the feathered position (i.e., 90°). So the HSS brake will be initiated at 311.25s (i.e., $300\text{s} + 90^\circ / (8^\circ/\text{s}) = 311.25\text{s}$). According to the definition of NREL 5MW turbine, the HSS brake takes 0.6s to be fully deployed to its maximum torque (i.e., $28.116\text{ MN}\cdot\text{m}$).

To sum up, the PTF operation occurs from 300s to 311.25s at a constant rotation speed of $8^\circ/\text{s}$ for all blades. The HSS brake torque ramps linearly from $0\text{ MN}\cdot\text{m}$ at 311.25s to $28.116\text{ MN}\cdot\text{m}$ at 311.85s. Table 3.4 summarizes some key notes for DLC0.2.

Table 3.4: Summary of uniform steady wind with operational maneuvers (DLC0.2)

DLC0.2	HSS brake after normal PTF shutdown under steady wind flow
Description	Simulation of normal pitch-to-feather shutdown followed by high-speed shaft brake shutdown of rotor
Simulation set-up	Mean wind speed: V_{rate} Turbulence: (not concerned) Gust: (not concerned) Initializing period: 60 s Simulated time: 600 s (10 min)
Special event	PTF shutdown starts at 300 s HSS brake shutdown starts at 311.25 s
Comment	The deployment of HSS brake is initiated when PTF shutdown is completely terminated

Figure 3.10 gathers numerical responses resulted from the emergency shutdown. The hatched region during the first 60 s in all charts indicates the initialization stage of simulation. Once the PTF shutdown is triggered at 300 s, all wind blades change their pitch angle simultaneously to the feathered position (90°) as expected. Thereupon the rotor speed is reduced from the rated speed (12.1 rpm) to zero. Meanwhile, the electrical generator decreases its power production and takes offline when the HSS brake reaches its maximum torque. The rotor thrust drops expeditiously from 800 kN to -250 kN during PTF maneuver and bounces back to 97 kN till the end. As for the rotor torque, it changes slightly between 4300 kN·m and 3300 kN·m while the control system is feathering the blades. Then it oscillates between 2500 kN·m and -2500 kN·m. After the HSS brake is initiated, the magnitude is significantly reduced to ± 425 kN·m. Finally, the rotor torque reaches -82 kN·m at the end of simulation.

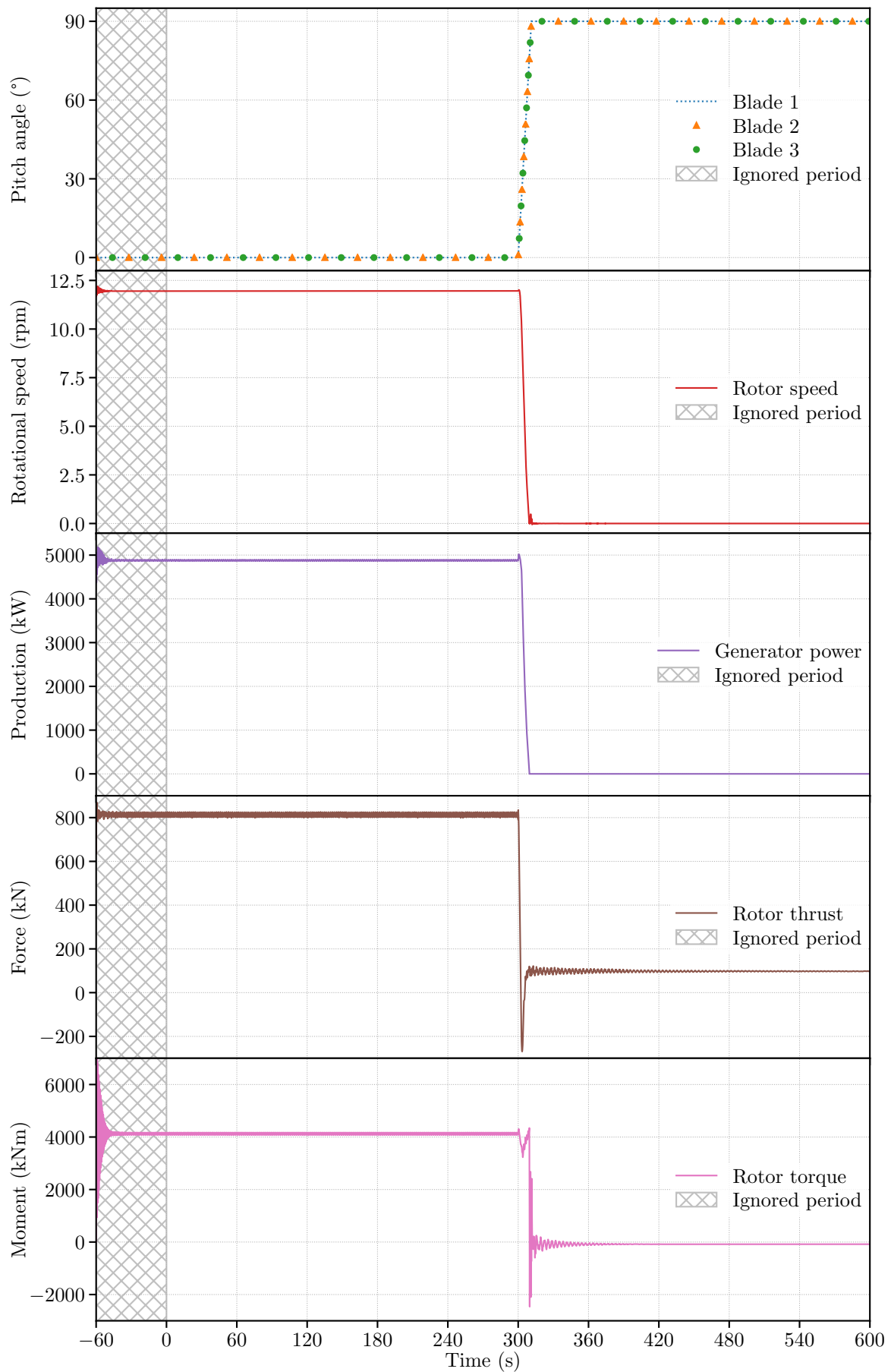


Figure 3.10: DLC0.2 rotor reactions

As for the tower reactions (Figure 3.11), the deflection, local force and moment have the same pattern for fluctuation. When PTF starts, they all fall down from their stabilized level (see Figure 3.6) to a negative value which implies that the movement follows the opposite direction of wind. Then they rebound upon zero level and continue as in free vibration till the end.

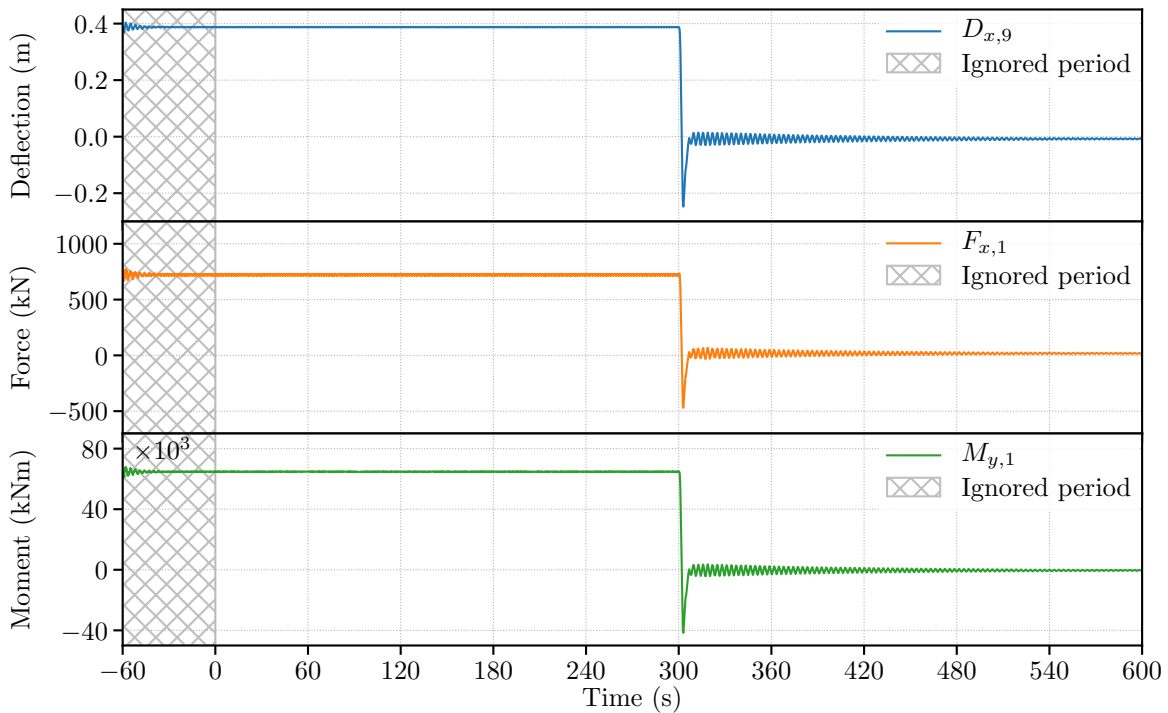


Figure 3.11: DLC0.2 tower reactions

Summary

In conclusion, the PTF shutdown can reduce undoubtedly the power output to zero through lowering the aerodynamic torque on rotor. The HSS brake can disengage the electrical generator when the rotor speed is slow enough and prevent motion of the shaft. However, these maneuvers bring remarkable changes on wind tower's load level. If these changes meet other occasional conditions (e.g., extreme wind speed, system failure, etc.), their magnitude may be amplified and lead to damages on the structure or even a crash. To advance the research on such troublesome situation, a new DLC combining the extreme wind and a technical fault is modeled in the next section.

For the convenience of reading, the initialization stage (plotted as the hatched region in the above figures) will be omitted in all figures hereinafter.

3.3. Scenario U: ultimate loads analysis

3.3.1. Design load case of power production with grid loss (DLC2.3)

A combination of technical failures in wind turbine and extreme wind environment may take place simultaneously in some situations. An unfortunate coincidence of such events may lead to an accident on wind turbine or, more disastrously, a collapse of the whole system [MMVB18]. Chou et al. [COL19] revealed that almost one third of wind turbine collapses are resulted from structural failure or blade failure due to strong wind. Comparing to other components (such as gear box, blades and the power converter), the wind turbine tower has the highest integrated risk value [DS13; SD14]. Accordingly, the load analysis on wind turbine tower subjected both extreme wind speed and system failure should be managed in the first place.

3.3.2. Design situation

The DLC2.3 is a design situation required by the IEC 61400-1 standard. This DLC involves a transient incident caused by a technical fault or loss of electrical network, also called “grid loss”, during the power production. Any significant fault or failure in control system, protection system or internal electrical system shall be considered in this situation. Moreover, the coincidence between such transient event and the extreme wind event (e.g., wind gust) shall also be managed. To achieve the above objective, the IEC 61400-1 suggests an occurrence of external, or internal, electrical fault combined with an extreme wind condition EOG at mean wind speed of V_{rate} , $V_{rate} \pm 2$ m/s and V_{out} . The key requirements for this DLC are listed in Table 3.5.

The extreme operating gust (EOG) has been introduced in Section 2.2.3.2 and the numerical implementation of this extreme wind condition will be detailed in the next section. A special incident, i.e., grid loss, occurs at the same time of wind gust. The coincidence of these two events are analyzed in Section 3.3.3 in order to figure out the moment that induces the worst loading over the wind turbine. The protection system that was developed in DLC0.2 (see Section 3.2.2) will be activated after the presence of grid loss in order to maintain the wind turbine in a safe condition. An analysis of ultimate loads is required by the IEC 61400-1 standard for this DLC and will be carried out in Section 3.3.4.

Table 3.5: Summary of extreme operating gust with electrical fault (DLC2.3)

DLC2.3	Power production plus loss of electrical network
Description	Simulation of power production in wind gust condition with occurrence of grid loss incident
Simulation set-up	Mean wind speed: $V_{rate}-2$ m/s, V_{rate} , $V_{rate}+2$ m/s and V_{out} Turbulence: (not concerned) Gust: Extreme operating gust (EOG) Initializing period: 60 s Simulated time: 130.5 s
Special event	Wind gust presents at 10 s and lasts $T_{gust} = 10.5$ s. The maximum wind speed occurs at $t_{gust} = 15.25$ s. Grid loss occurs at a moment between 0 s and 30.5 s (precised in Table 3.6 for each considered mean wind speed). PTF shutdown starts after a delay of 0.2 s. HSS brake shutdown starts after the PTF is finished.
Comment	The occurrence of grid loss is chosen in the way that the worst loading on turbine is achieved The deployment of HSS brake is initiated when PTF shutdown is completely terminated

3.3.3. Extreme wind and grid loss

In Section 2.2.3.2, the magnitude of wind gust V_{gust} and the wind speed of gust $V(z, t)$ has been given in Equation 2.6 and Equation 2.9, respectively. The duration of gust T_{gust} is fixed at 10.5 s by IEC 61400-1 specifications [Int05]. An additional time of 10 s is added before and after the wind gust event giving a shape of “Mexican hat” for the wind speed of gust (Figure 3.12).

In Figure 3.12, the hatched region in gray illustrates the initialization stage of simulation. It is followed by a pink hatched region which shows the potential occurrence of grid loss. The technical fault (i.e., grid loss) must be introduced after the impact of initial conditions has become negligible. Finally, a supplementary period of 100 s is joined consecutively to the Mexican-hat-like wind in order to perform an analysis of ultimate loads.

As for the grid loss, it is an incident which assumes that the connection to the power network is broken due to an internal or external reason. The electrical generator should be shut down immediately by the protection system. Otherwise, the subsequent loading may lead to a resonance between the natural frequency of tower and 1P, or 3P, frequency as explained in Section 2.1.3.2. Here, the term “immediately” is numerically

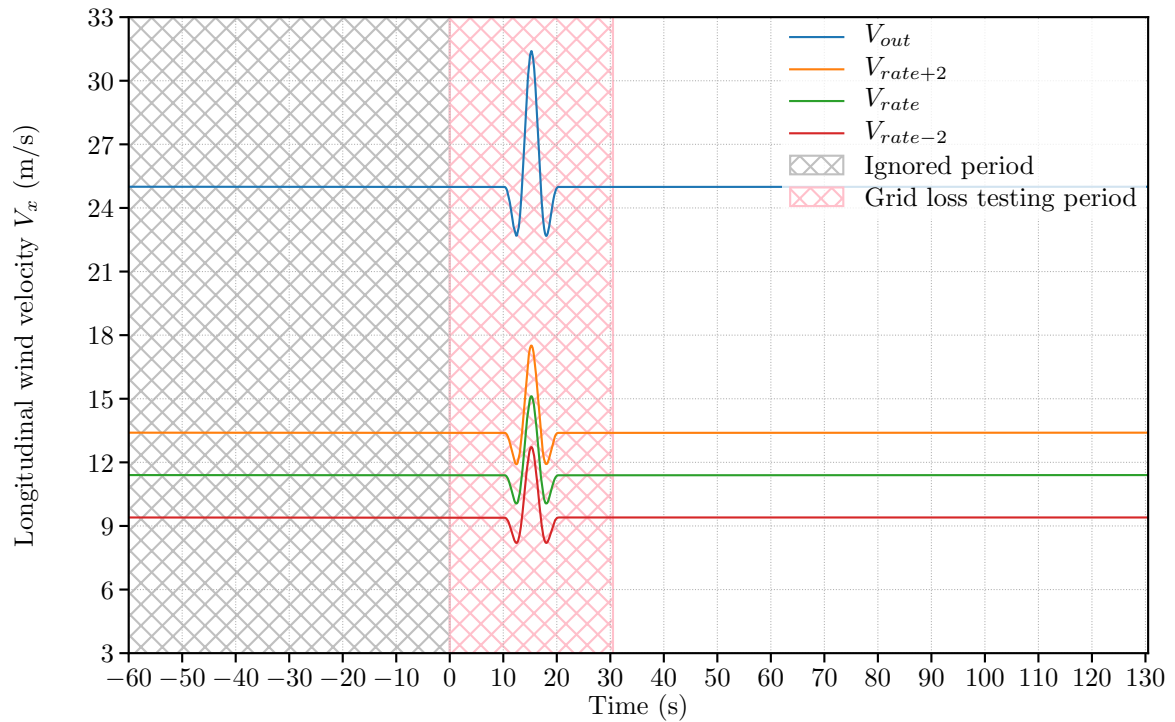


Figure 3.12: Longitudinal wind velocity of EOG at hub height

implemented by a author-defined short time of 0.2 s representing reaction time of the protection system. To achieve the worst loading on wind turbine, the timing of grid loss was tested between 10 s and 30.5 s with a time-step of 0.1 s (i.e., the pink hatched zone in Figure 3.12).

Although only four mean wind speed (i.e., V_{rate-2} , V_{rate} , V_{rate+2} and V_{out}) are required by the IEC standard for seeking the worst loading, an extended research is proposed by the author to cover the whole operating range of wind speed, i.e., $V_{mean} \in [3, 25]$. This full range study for grid loss timing allows to understand the behavior of wind turbine when producing electrical power, and subsequently, design an appropriate damper covering all operating wind speed.

3.3.4. Results and discussions

3.3.4.1. Grid loss timing

Grid loss for V_{rate-2} , V_{rate} , V_{rate+2} and V_{out}

To quantify the worst loading on wind turbine, the fore-aft tower deflection D_x on gage 9 and the fore-aft force F_x and pitching moment M_y on gage 1 is considered, just as usual. For each response simulation, the maximum magnitude $D_x(t)_{\max}$, $F_x(t)_{\max}$ and $M_y(t)_{\max}$ are exported. The timing of grid loss t_{loss} is chosen when the magnitude

of response reaches its maximal value across all simulations, i.e.,

$$t_{loss} = \tau \text{ s.t. } U(t)_{\max}^{\text{grid loss}=t_{loss}} = \max \{U(t)_{\max}^{\text{grid loss}=\tau}\} \text{ where } \tau \in [10.0, 10.1, \dots, 30.5] \quad (3.2)$$

where, U stands for a type of mechanic response like deflection D , force F or moment M . The results for the considered mean wind speed of extreme operating gust (EOG) are listed in Table 3.6

Table 3.6: Grid loss timing to achieve the worst loading on wind turbine

Mean wind speed (value)	Grid loss time t_{loss} (s)		
	$\max\{D_{x,9}\}$	$\max\{F_{x,1}\}$	$\max\{M_{y,1}\}$
V_{out} (25.0 m/s)	14.9	14.9	14.9
V_{rate+2} (13.4 m/s)	14.8	14.8	14.8
V_{rate} (11.4 m/s)	14.6	14.6	14.6
V_{rate-2} (9.4 m/s)	14.7	14.7	14.7

As mentioned in Table 3.5, the time when the wind speed reaches its maximum is 15.25 s. Table 3.6 shows that when grid loss occurs just before the peak of longitudinal wind velocity, the response of tower is maximized, in other words, the loading on turbine reaches its highest value.

Grid loss for all operating wind speed

To better understand the grid loss timing and the consequent loading, the considered mean wind speed V_{mean} is extended to the range of [3, 25] at a step of 0.1 m/s. Figure 3.13 illustrates the correlation between the grid loss, the mean wind speed and the subsequent loading. To clearly discuss the grid loss timing, an example of wind gust at V_{out} is given in the upper line-chart while a contour-chart is plotted in the lower part to demonstrate the peak-to-peak amplitude of fore-aft deflection $D_{x,9}$. The ordinate axis of upper chart is longitudinal component of the instantaneous wind speed V_x , whereas the ordinate axis of lower chart is the mean wind speed V_{mean} . Both the abscissae axes correspond to the duration of wind gust. In the lower chart, the isopleths represent the peak-to-peak amplitude of deflection $D_{x,9}$ subjected to the grid loss at different time and different mean wind speed. The color-bar next to the lower chart clarifies the level-set for these peak-to-peak amplitudes.

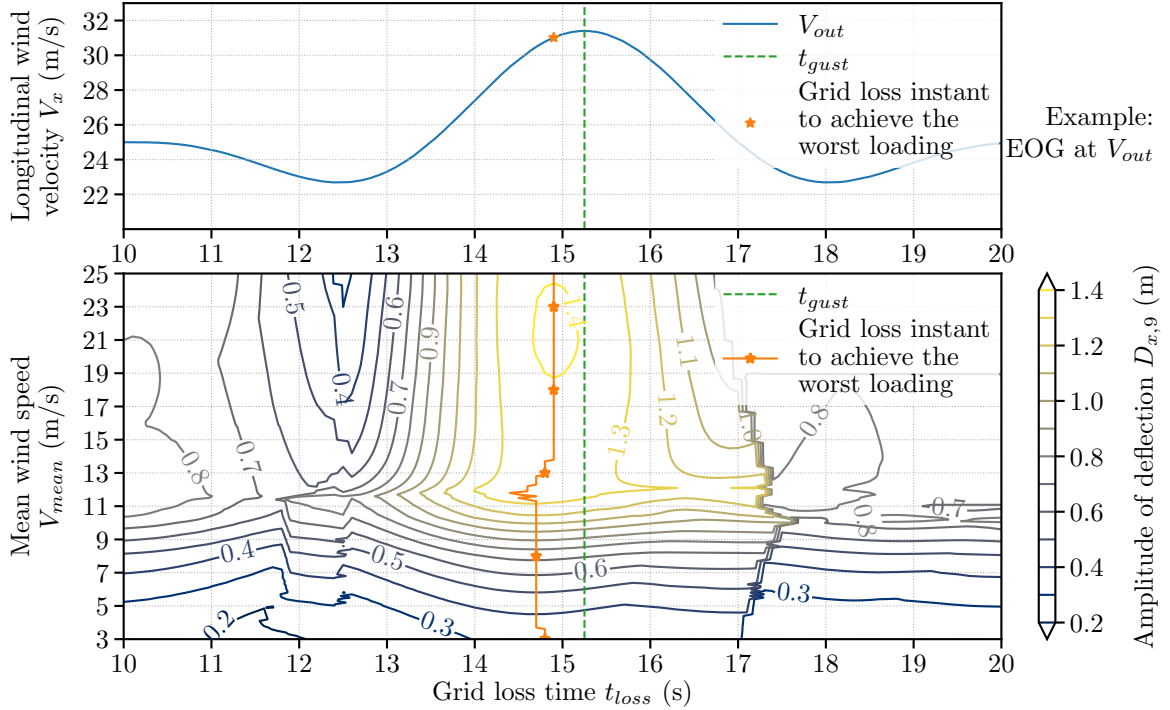


Figure 3.13: Grid loss timing in the range of operating wind speed with reference to tower deflection. The upper line plot gives an example of wind speed of gust at mean wind speed $V_{mean} = V_{out} = 25$ m/s. The lower contour plot shows the peak-to-peak amplitude in relation to the mean wind speed V_{mean} and the grid loss time t_{loss}

For mean wind speed below V_{rate-2} (9.4 m/s), the effect of grid loss before or after the maximum wind gust speed, which occurs at $t_{gust} = 15.25$ s, is not significant. The subsequent deflection $D_{x,9}$ has a peak-to-peak amplitude less than 0.7 m, knowing that the peak-to-peak amplitude due to PTF and HSS operations is around 6.5 m (see Figure 3.11). The grid loss impacts tower's loading much less than that from the maneuvers of protection system. For V_{mean} between V_{rate-2} (9.4 m/s) and V_{rate+2} (13.4 m/s), the peak-to-peak amplitude of $D_{x,9}$ increases progressively and depends mainly on the grid loss instant t_{loss} . When t_{loss} approaches the time of maximum wind gust speed t_{gust} (green dashed line in Figure 3.13), the amplitude becomes higher and higher. Lastly, for V_{mean} greater than V_{rate+2} (13.4 m/s), the peak-to-peak amplitude of fore-aft deflection has a similar fluctuation to that of wind velocity, that is, a trough area of amplitude in 12 s to 13 s and 17.5 s to 18.5 s along with a peak area in 14.5 s to 15.5 s.

The timing of grid loss to achieve the worst loading (orange line in Figure 3.13) lies always before the occurrence of maximum wind speed. It is within the range of $[t_{loss} - 1, t_{loss}]$ in general. When mean wind speed V_{mean} goes higher, the peak-to-peak amplitude gets higher.

Summary

The above research extends the DLC2.3 from four specified wind speed to the full range of operating wind speed. It indicates the timing for grid loss in order to achieve the worst loading at any mean wind speed in EOG condition. The same conclusion can be stated in regard to the local tower force and the local tower moment on gage 1 (see Figure I.1 and Figure I.2 in appendix). In the following section, the grid loss is set to appear at the time at which the peak-to-peak amplitude reaches the maximum for all mean wind speed between V_{in} and V_{out} .

3.3.4.2. Ultimate loads

The superposition of extreme wind and loss of power network lead to the high transient load and intense vibration on wind turbine tower. The tower response after grid loss in EOG condition at mean wind speed of V_{rate} is represented graphically in Figure 3.14. During the transient phase (i.e., period between the initiation of grid loss t_{loss} and the initiation of HSS brake t_{HSS}), the (maximal) peak-to-peak amplitude of deflection, force and moment reaches 1.34 m, 2456 kN and 221 100 kN·m, respectively. Comparing to that due to the protection system maneuvers shown in Figure 3.11 (i.e., 0.63 m for deflection, 1200 kN for force and 106 610 kN·m for moment), the peak-to-peak amplitude due to grid loss in DLC2.3 is at least two times higher.

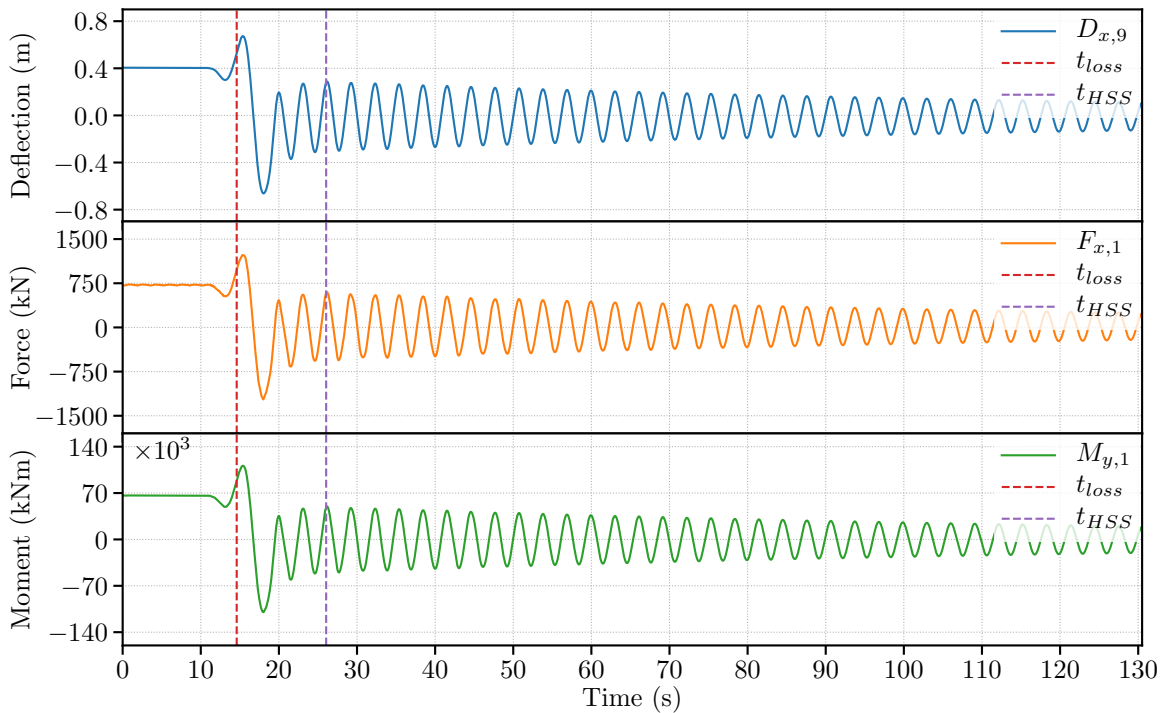


Figure 3.14: DLC2.3 tower reactions at V_{rate} with grid loss at 14.6 s

After the electrical generator is offline, the wind turbine acts in free vibration. Because the lack of structural damping, the wind turbine tower stays in free vibration till the end of response simulation. Although, the fatigue load analysis is not the purpose of DLC2.3, the free vibration in such high magnitude and long duration can accumulate high fatigue damage on tower and induce potential cracks on structure.

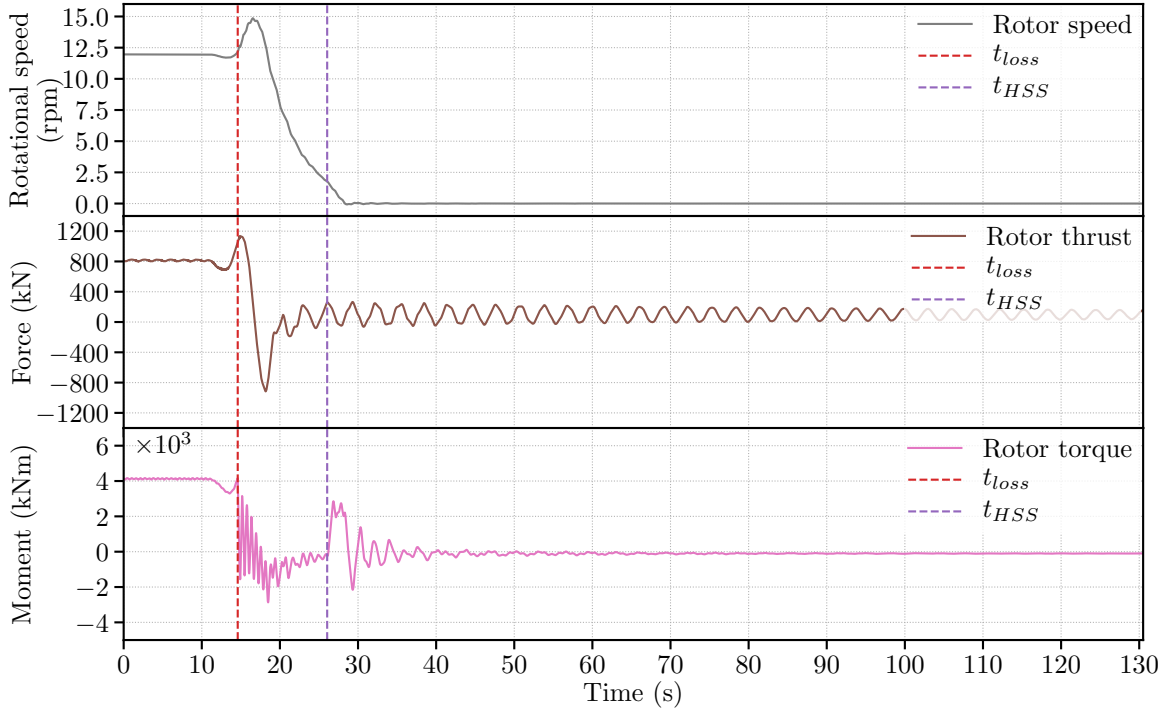


Figure 3.15: DLC2.3 rotor reactions at V_{rate} with grid loss at 14.6s

As for rotor, the rotor speed is reduced gradually as expected (Figure 3.15). It is overspeed just after the sudden loss of electrical network. This is caused by the delay of protection system and full deployment of PTF. At the beginning of PTF operation, the pitch angle of blades remains still in the working range that amplifies the aerodynamic force on wind blades and, consequently, speeds up the rotor. When pitch angle gets more and more close to its feathered position (90°), the aerodynamic force declines and slows down the rotor speed. During the transient period, the rotor thrust drops from 1133 kN to -916 kN, that is, a peak-to-peak amplitude of 2049 kN comparing to that of 1104 kN under PTF and HSS operations in Figure 3.10. Like tower reactions, free vibration occurs in rotor thrust response after the transient phase and lasts till the end of simulation. The rotor torque, on the other hand, vibrates more violently during the transient phase and bounces back to 2855 kN·m when HSS brake initiates at t_{HSS} (purple dashed line in Figure 3.15).

To sum up, the loss of power network connection at mean wind speed of V_{rate} in EOG condition can lead to an amplification on magnitude of extreme loading. This

amplification is at least two times higher than that in normal control operations and can even get worse when mean wind speed V_{mean} gets higher. Due to the lack of structural damping, the wind vibrates freely after the shutdown of power generator. More figures given in Appendix I show the response at mean wind speed of V_{rate-2} , V_{rate+2} and V_{out} confirming the same conclusion (see Figure I.3, Figure I.4 and Figure I.5, respectively).

3.4. Conclusions

In this chapter, the NREL 5MW reference wind turbine is introduced and implemented in FAST simulator. The numerical validation of such baseline wind turbine is taken on condition of steady wind flow, namely DLC0.1 and DLC0.2. (The former DLC figures out the initial conditions that will be applied for all response simulations in this dissertation to stabilize the turbine and save the simulated time.) The latter DLC validates the author-developed protection system with regard to the proper control system defined by NREL. The protection system is constituted by PTF operations and HSS brake offering a manner to shutdown urgently the wind turbine in case of technical faults, internal or external failure or extreme climatic condition.

An analysis of ultimate loads on DLC2.3, a design situation proposed by the IEC 61400-1 standard, is carried out with the protection system described above. Moreover, the analysis is extended to the full operating wind speed (i.e., V_{in} to V_{out}) instead of four specified wind speed (i.e., V_{rate-2} , V_{rate} , V_{rate+2} and V_{out}) suggested by the IEC specifications. Such extended research points out the timing of grid loss to produce the worst loading on wind turbine for any mean wind speed V_{mean} lying in the range of [3, 25]. The load analysis reveals that the peak-to-peak amplitude of wind turbine tower response after the grid loss can be two times higher, or even higher, than that in normal control operations.

All data obtained from simulations and experience gained in this chapter contribute to develop an appropriate damping system in Chapter 5. The DLC0.1 prepares the initial conditions for numerical simulation and discloses the response of NREL 5MW reference wind turbine in stable state at each V_{mean} between V_{in} and V_{out} . The DLC0.2 explains the workflow of the control system as well as the protection system that shows the possibility to integrate an active damping system into the control system of baseline wind turbine. Finally, the DLC2.3 records the response of wind turbine facing the coincidence of extreme wind condition (i.e., EOG) and technical fault (i.e., grid loss). It will be served as the basis for evaluating the performance of active damper developed in Chapter 5.

Chapter 4

Probabilistic fatigue life prediction using deep neural network

This chapter presents a probabilistic study of fatigue damage for the NREL 5MW reference wind turbine based on time domain simulations in FAST. A brief survey on fundamental fatigue analysis methods is given in the first section. The probabilistic framework of fatigue analysis proposed by the author is detailed in the second section and applied to carry out an analysis of fatigue loads (Scenario F) in the following section. Then the numerical results are analyzed in the fourth section seeking the empirical distributions of cumulative fatigue damage on wind turbine tower.

Due to the extreme time consumption in the proposed probabilistic approach of fatigue analysis, a surrogate model based on deep neural network is proposed in the fifth section. Then a demonstration of using the proposed framework to predict the wind turbine's fatigue life is given in the sixth section. What's more, a comparison between the proposed framework and the surrogate model is discussed in this section.

The chapter ends in the seventh section with a brief conclusion and perspective work.

4.1. Deterministic fatigue analysis

Since the discovery of fatigue, many approaches have been considered in order to quantify this phenomenon. From the literature [Alm85; Lee05; Ben12], three different approaches can be defined in the way of assessing the lifetime of a material: the stress-life (S-N) method, the strain-life (ε -N) method and the crack growth method.

The first is a stress-based approach, stress-life (S-N) method. It is one of the most widely used methods in particular to assess the service life of elastic structures with large numbers of cycles. This method is based on the S-N (i.e., Stress - Number of cycles to failure) curves which, for a given material, link applied stress cycles of constant amplitude to lifetime expressed in terms of number of cycles. These approaches remain the most appropriate for assessing the lifetime of most existing structures. From a physical point of view, these are very consistent approaches since it is recognized that cracks generally appear at the locations where stress levels are the highest [PS95].

Secondly, the strain-based approach, strain-life (ε -N) method, is based on the use of ε -N (i.e., Strain - Number of cycles to failure) curves. For a given material, the deformation cycles of constant amplitude is incited to give an estimation of lifetime expressed in terms of number of cycles. This approach is often used when studying fatigue damage in small numbers of cycles. Furthermore, the approaches can be based on deformation energy or deformation energy density [FL89]. These approaches have the particularity of being able to evaluate the damage to a structure imposed simultaneously by loads of different natures (thermal cycle, creep...). It can be adapted to a fatigue analysis with large numbers of cycles as well as small numbers of cycles [Van01]. This method focus mainly on the crack initiation.

Lastly, the crack growth methods predict the propagation of pre-existing defect until it reaches a critical state. Typically, the growth rate used in crack growth methods is calculated by applying thousands of constant amplitude cycles to the specimen and measuring the width of each increment of crack growth. Unlike other methods mentioned above, the crack growth methods have advantages in predicting the intermediate state of cracks. It is commonly used in nuclear power industry or aerospace industry in the way that the periodic inspections are scheduled to avoid the critical state is reached by pre-existing crack [ONM02; JJS03].

The main process for estimating lifetime of structure builds upon two relationships as shown in Figure 4.1. The first relationship establishes the correlation between loading environment and stress state (or strain state). This load-stress, or load-strain, relation is usually deduced from FEM analysis or experiments. More details about this relation is given in Section 4.1.1. The second relationship is that of the stress state (or the strain state) to the fatigue life of the structure. This stress-life, or strain-life,

relation is carried out by using damage modeling with a specified method to assess the cumulative damage which will be detailed in Section 4.1.2.

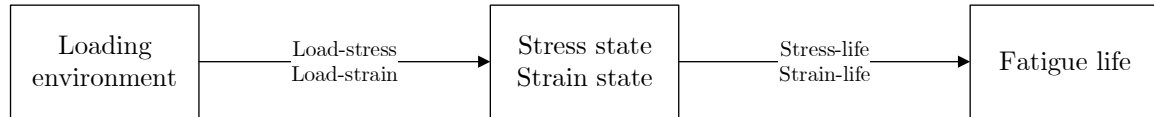


Figure 4.1: Fatigue life estimation process

No matter which approach described above is applied, a cycle counting algorithm is indispensable to extract a series of fatigue cycles from the complex loading sequences. The most widely applied technique is rainflow counting algorithm proposed by Masanori Matsuishi and Tatsuo Endo [ME68]. This technique will be detailed later in Section 4.1.3.

4.1.1. Load-stress relation

4.1.1.1. Axial stress

Under uni-axial assumption, the fatigue damage should be calculated for both axial stress and shear stress. But, for tubular tower, the fatigue damage resulted from shear stress is significantly lower than that from axial stress [KM15]. Thus, the nominal stress is the only component to be considered in fatigue damage analysis, i.e., $\sigma_{nominal} = \sigma_{normal}$. In this dissertation, the wind turbine tower is simplified as a thin-walled cylinder structure. Neither the effects of weld and bolt nor the connection components between tower segments are considered. As the result, the stress concentration factor (SCF), i.e., a ratio of the highest stress to a nominal stress, is fixed to 1.0 in the following equation:

$$\sigma_{local} = SCF \sigma_{nominal} \quad (4.1)$$

To sum up, the local stress σ_{local} for fatigue design would be the normal stress σ_{normal} . The normal stress σ_{normal} across the section of tower is estimated at every local spot along its circumference (Figure 4.2). Ignoring the cross section deformation after the loads are exerted, the nominal stress can be computed by Equation 4.2:

$$\sigma_{normal} = \frac{F_z}{A} - \frac{M_x}{I_{Gx}}y + \frac{M_y}{I_{Gy}}x \quad (4.2)$$

where, F_z is axial force, A is nominal cross section area, M_x and M_y are side-to-side bending moment and fore-aft bending moment of tower, respectively, I_{Gx} and I_{Gy} are second moment of area, z is the vertical distance along \vec{z}_t -axis. In this study,

because the cross section is an annulus centered along \vec{z}_t -axis, the area moment of inertia is determined by:

$$I_{Gx} = I_{Gy} = \frac{\pi}{64}(D^4 - d^4) \quad (4.3)$$

where, D and d are outer diameter and inner diameter of cross section, respectively. By converting the tower-base coordinate system from Cartesian coordinate system to cylindrical coordinate system, the normal stress given in Equation 4.2 can be expressed as following

$$\sigma_{normal}(\alpha) = \frac{F_z}{A} - \frac{M_x}{I_{Gx}}R \sin \alpha + \frac{M_y}{I_{Gy}}R \cos \alpha \quad (4.4)$$

where, R is outer radius of cross section, α is azimuth angle on the plane defined in Section E.2 measuring from spot 1 (located on the positive side of \vec{x}_t -axis) to the target spot in counterclockwise direction (Figure 4.2).

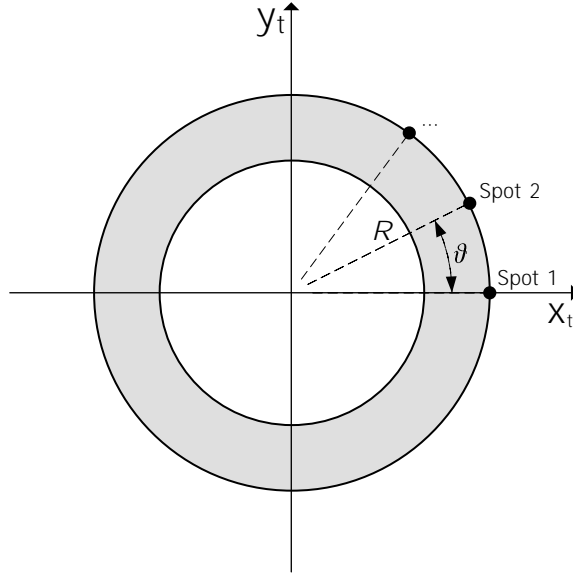


Figure 4.2: Top view of cross section (gray area) and illustration of spot point

Equation 4.4 gives the method to calculate the normal stress on each local spot at angle of α in the plane of tower gage. It should be noted that the tower responses (deflection D , force F and moment M) obtained from numerical simulation are functions in time domain and expressed on each tower gage at the height of z . To assess the fatigue damage over the entire wind turbine tower, Equation 4.4 must be evaluated at different height of tower. In conclusion, the local stress for fatigue design is actually a function of angle α , time t and height z :

$$\sigma_{local}(z, t, \alpha) = \frac{F_z(z, t)}{A(z)} - \frac{M_x(z, t)}{I_{Gx}(z)}R(z) \sin \alpha + \frac{M_y(z, t)}{I_{Gy}(z)}R(z) \cos \alpha \quad (4.5)$$

By evaluating the Equation 4.5 through all tower gages from $z = 0$ to hub height

(HH) and all local spots from $\alpha = 0$ to 2π , the stress-time history of the whole wind turbine tower is achieved.

4.1.2. Stress-life relation

Fatigue or fatigue damage means the modification of the mechanical properties of materials following repeated application of stress cycles, such applications may lead to the failure of parts.

Two fields of study can then be distinguished. The first is so-called low-cycle fatigue which corresponds to the greatest efforts, greater than the material's yield strength, and where the fracture occurs approximately between 10^4 and 10^5 cycles. A rapid plastic deformation takes place in this area followed by a rupture.

The second field is high-cycle fatigue and it is the case that will be studied in this dissertation. There are two sub-fields: the limited endurance, where the finite lifetime regime is discussed, and the unlimited endurance, where the structure can withstand a theoretically infinite number of cycles without breaking. When limited endurance is treated, it is fatigue damage in large numbers of cycles that is counted. The rupture occurs between 10^5 and 10^7 cycles. Under a lower stress than Low-Cycle Fatigue and without the appearance of a measurable plastic deformation, an adaptation phenomenon is observed. Life estimation models for this domain are very often based on the history of stress. Since the appearance of a crack statistically represents more than 90% of the lifetime of a structure, the initiation of a crack within the structure is considered as the major determinant of its lifetime in this work. Finally, the field of unlimited endurance is that of fatigue at very large numbers of cycles where the break does not occur before 10^8 cycles ([Nad99]).

4.1.2.1. S-N curve method

S-N curve method, also known as Wöhler curve, is commonly used in high-cycle fatigue to characterize the materials performance. It is firstly proposed by the German scientist August Wöhler while investigating a train crash in France [Wöh60]. It describes the magnitude of a cyclic stress (S) against the logarithmic scale of cycles to failure (N). Nowadays a S-N curve is often developed by metal coupon testing. A small metal coupon is placed in the machine and subjected to a cyclic stress time history until a crack or failure occurs in the metal coupon. In order to develop a S-N curve, several coupons need to be checked at different stress levels. Figure 4.3 illustrates a standard S-N curve.

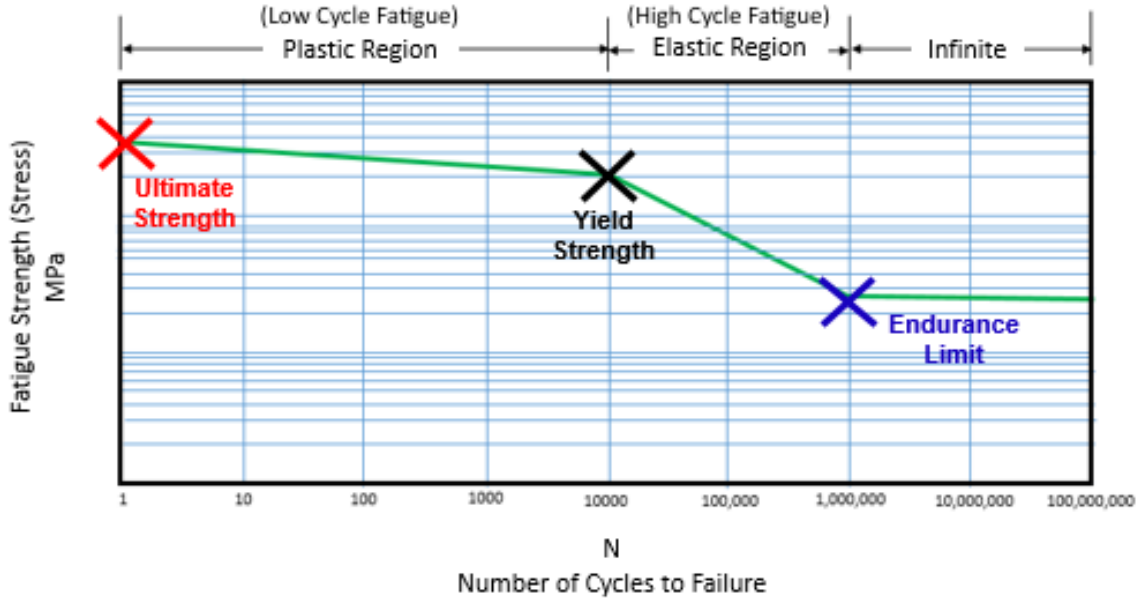


Figure 4.3: An example of S-N curve [Hia19c]

Basically, the S-N curve can be interpreted as:

$$\log_{10} N = \log_{10} \bar{a} - m \log_{10} \Delta\sigma \quad (4.6)$$

where, N = number of cycles to failure for stress range $\Delta\sigma$
 $\Delta\sigma$ = stress range exported from stress-time history
 m = negative inverse slope of S-N curve

$\log_{10} \bar{a}$ = intercept of $\log_{10} N$ -axis by S-N curve

The numerical value of m and $\log_{10} \bar{a}$ for common used materials are often given in many handbooks or industrial standards [DNV16]. Thus, once the stress range $\Delta\sigma$ is exported, the corresponding number of cycles to failure N can be easily found by the above equation.

4.1.2.2. Mean stress effect

S-N curves characterize the fatigue strength of materials under zero mean stress loads, i.e., $\sigma_{mean} = 0$. However, there are enriched findings in literature that highlight the effect of mean stress σ_{mean} on fatigue behavior of materials [RT69; Gur77]. In fact, when a tension stress is superimposed on the alternating stress σ_a , the fatigue life of structure decreases. Oppositely, when a compression stress is present, the fatigue life of structure increases. σ_a refers to the alternating stress which is also known as alternating cycle amplitude given in Equation 4.7.

$$\sigma_a = \frac{\sigma_{max} - \sigma_{min}}{2} \quad (4.7)$$

where, σ_a = alternating stress
 σ_{max} = maximum stress in cycles
 σ_{min} = minimum stress in cycles

When the mean stress is small in front of the stress amplitude, the two models are in agreement. However they are no longer in agreement when the mean stress is close to the amplitude. In this case, it is recommended to adopt the most conservative modeling. Thus it can be considered that the Goodman correction is more suitable to model the influence of a mean stress in compression (Equation 4.8):

$$\frac{\sigma_a}{\sigma_e} + \frac{\sigma_{mean}}{\sigma_{ult}} = 1 \text{ with } |\sigma_{mean}| \leq \sigma_{ult} \quad (4.8)$$

This model, by using the ultimate strength of material σ_{ult} and the endurance limit σ_e (also known as *fatigue limit*), makes it possible to transform each cycle of non-zero mean stress σ_{mean} into an equivalent stress cycle of zero mean with the amplitude σ_a . The Goodman correction model is explicated in Algorithm G.1 with more details as well as other models for considering mean stress effect.

All the corrections made to the data provided by the S-N curves allow these data to be used by the conventional methods in uni-axial fatigue analysis. It is thus possible, for a given amplitude and mean stress cycle, to determine the number of cycles at the end of which the failure will occur. However, for loads composed of different cycles, it becomes necessary to use accumulation laws of fatigue damage.

4.1.2.3. Palmgren-Miner's rule

For stress cycles with amplitude greater than the endurance limit, the damage is irreversible to the structure. The fatigue damage D_m , produced by n_m cycles with amplitude of σ_a , is related to N_m , the total number of cycles producing fatigue failure under a stress of constant amplitude σ_a . If M groups of stress cycles with different amplitudes and zero mean stress are considered, then the damage produced by each group is given by Miner's law [Min45]. Finally, the cumulative fatigue damage D suffered by the structure under all groups of stress cycles is given by the Palmgren formula [Pal24]. To sum up, the Palmgren-Miner linear damage hypothesis is given by:

$$D = \sum_{i=1}^M \frac{n_m}{N_m} \quad (4.9)$$

When the cumulative damage is greater than 1, failure of structure occurs. More information can be found in Algorithm G.2.

By using the S-N curve and Palmgren-Miner's rule, it is simple to calculate the fatigue damage for a structure subjected to a cyclical load of constant amplitude.

When the amplitude of the stress becomes random, it is necessary to have methods capable of extracting the load time history into cycles. These methods are called cycle counting methods.

4.1.3. Rainflow counting

In order to assess the fatigue life of a structure subject to complex loading, a cycle counting method is needed. It filter the essential information for studying fatigue damage by breaking the original stress time history into stress cycles.

There are a numerous methods to perform this counting [AST85]. For all these methods, it is necessary to know how to get rid of small variations (also named *noise*). By doing this correction, a long-duration signals is transformed into signals that can be easily treated. The choice of a method depends on how stress cycles are defined. Each method evaluates the number of cycles with their range ΔS on the basis of a definition of cycle for a duration t in the load time history.

Among the most well-known methods like Level-Crossing counting, Peak counting, Simple-Range counting and Rainflow counting, the last one is by far the most widely used in the field of fatigue analysis under random vibration. It is firstly proposed by Tatsuo Endo, a Japanese engineer, during his visiting at the University of Illinois along with Masanori Matsuishi [ME68]. It extracts individual fatigue cycles from any complex load time history.

It defines the stress cycle as a closed hysteresis loop in a stress-strain diagram. Since this method is commonly recognized to be a good cyclic counting method. Many researchers have proposed improvements to this method like making it useful for long stress histories [GK87], keeping the load sequence [Ant97], counting cycles in real-time application [MJ12] and an equivalent and more convenient definition of the Rainflow cycle counting method [Ryc87]. More details about the Rainflow counting process can be found in Algorithm G.3.

4.1.4. Summary

The fatigue life assessment for wind turbine tower subjected to uni-axial stress involves several steps. The implementation of which in simulation codes is summarized in Figure 4.4 and described algorithmically in Algorithm 4.1.

As indicated in Figure 4.1, the first step in estimating fatigue life is to get loading information on structure or model. Here in this dissertation, this step is achieved by executing numerical simulations on the NREL 5MW reference wind turbine under a specified DLC at mean wind speed of V_{mean} no matter what type of wind condition is. Then, based on these response simulations, the time history of local stress σ_{local} for a given tower gage i at height of z_i can be exported by using Equation 4.5. The stress

state is evaluated on each local spot j at angle of θ_j in the plane of tower gage i . Once the stress-time history is computed, the load-stress relation can be established. Next, by applying techniques mentioned in Section 4.1.2 and Section 4.1.3, the stress-life relation can also be established and, therefore, the cumulative fatigue damage $D^{(i,j)}$ on each tower gage i and local spot j is carried out.

Algorithm 4.1: Deterministic fatigue assessment on wind turbine tower

```

1 Run a numerical simulation in FAST
2 foreach tower gage  $i$  do
3   Get the gage's height  $z_i$ 
4   Export the time history of local force  $F_x(z_i, t)$  and local moment  $M_x(z_i, t)$ 
   and  $M_y(z_i, t)$  on this gage
5   foreach local spot  $j$  do
6     Get the spot's angle  $\theta_j$ 
7     Calculate the time history of local stress  $\sigma_{local}^{(i,j)}(z_i, t, \theta_j)$  on this spot
8     Extract a series of  $M$  stress blocks from stress-time history
9     foreach stress block  $m$  do
10      Count number of cycles  $n^{(i,j)}$  // Rainflow counting
11      Export mean stress  $\sigma_{mean}^{(i,j)}$  and stress range  $\Delta\sigma^{(i,j)}$ 
12      Get alternating stress  $\sigma_a^{(i,j)}$  // Mean stress effect
13      Get number of cycles to failure  $N^{(i,j)}$  // S-N curve method
14    end foreach
15    Calculate the cumulative fatigue damage on tower gage  $i$  and local
    spot  $j$ , i.e.,  $D^{(i,j)}$  // Miner's rule
16  end foreach
17 end foreach
18 Create a set including all fatigue damage over the wind turbine tower, i.e.,
     $\mathbf{D} = \{D^{(i,j)} \in \mathbb{R} : (i, j) \in \mathbb{N}^2\}$ 

```

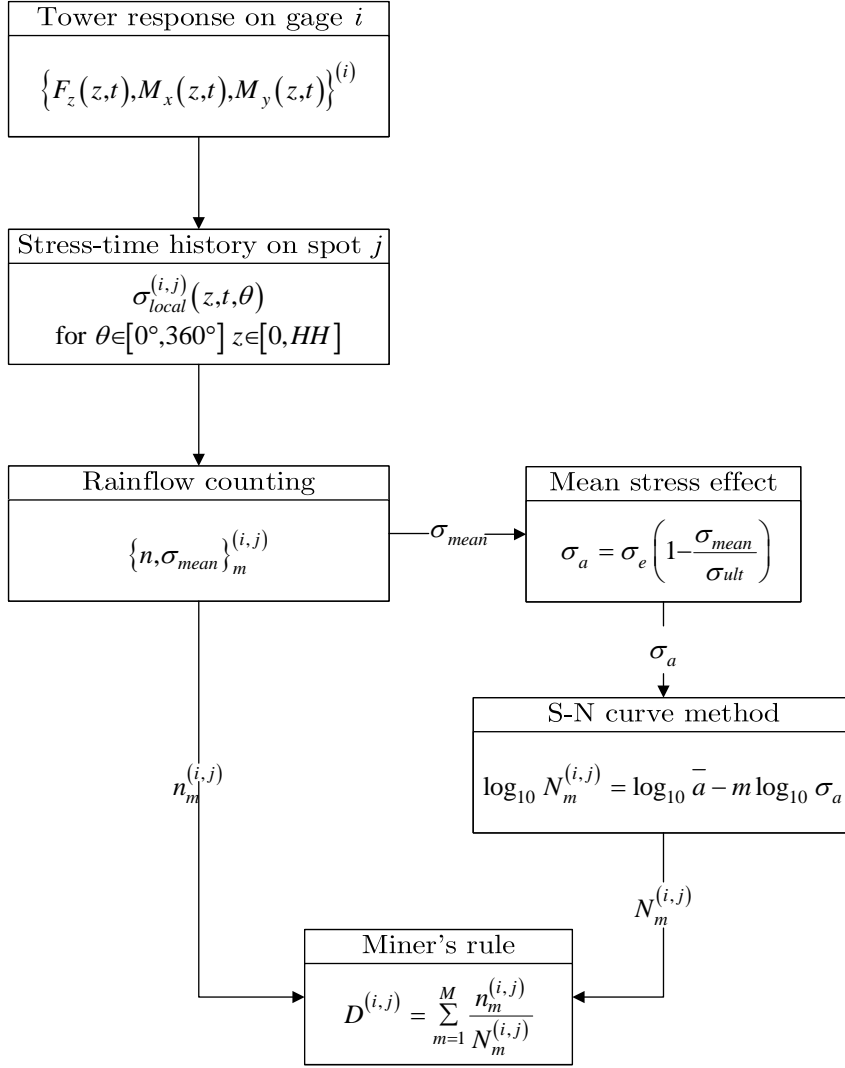


Figure 4.4: Workflow for assessing cumulative fatigue damage D on tower gage i and local spot j

To conclude, the final set of fatigue damage \mathbf{D} describes naturally the spatial distribution of fatigue loading over the entire wind turbine tower at a given mean wind speed V_{mean} . Since the tower gage i and local spot j are numerically discrete, it is capable to assess the fatigue life at any height from tower-base to tower-top subject to the wind flow coming from any direction between 0° and 360° . However, this process is deterministic which means that it cannot tell the probability of occurrence of cumulative fatigue damage. This requires the need to assess the fatigue damage in a probabilistic way and hence will be discussed in the next section.

4.2. Probabilistic fatigue analysis

4.2.1. Monte Carlo simulation

Due to the random nature of wind, the fatigue life estimation process presented in the previous section must be carried out stochastically. Taking turbulent wind condition for example (Section 2.2.3.1), the IEC standards require at least six 10-min stochastic simulations, or a continuous 60-min simulation, for each considered mean wind speed [Int05]. The main idea behinds this approach is that the true response of wind turbine are based on repeated random sampling and statistical analysis.

This estimation procedure is called Monte Carlo simulation which has been widely applied in many disciplinarians for decades [MBV18]. The principal of Monte Carlo method founds on the law of large numbers which says that the average of the results obtained from a large number of samples should be close to the true value.

An application of this approach in the context of wind turbine is given in Section 4.3.1 in which the NTM wind condition is sampled independently and randomly for 10 000 times for each mean wind speed V_{mean} .

4.2.2. Statistical analysis

After generating sufficient samples, the process described in Algorithm 4.1 can predict the cumulative fatigue damage in each sample. In order to conclude a probabilistic distribution of fatigue damage from these samples, a statistical analysis is indispensable including probability distribution fitting and statistical testing.

4.2.2.1. Distribution fitting

The distribution fitting is a technique to fit a theoretical probability distribution to a series of empirical data (namely, *observations*). One of the most dominant methods in distribution fitting is MLE introduced by R.A. Fisher in 1912 [Ald97]. This method determines values for the parameters of probability distribution by maximizing the likelihood function. The likelihood function measures statistically how well a probability distribution fits a set of observations. In other words, it can be considered as a manner to quantify the quality of fitting (also named after *goodness of fit*) of a distribution on observed values. The definition of likelihood function is detailed in Appendix F.1. An example of applying the MLE to fit a sample of 10 000 observations is illustrated in Figure 4.5.

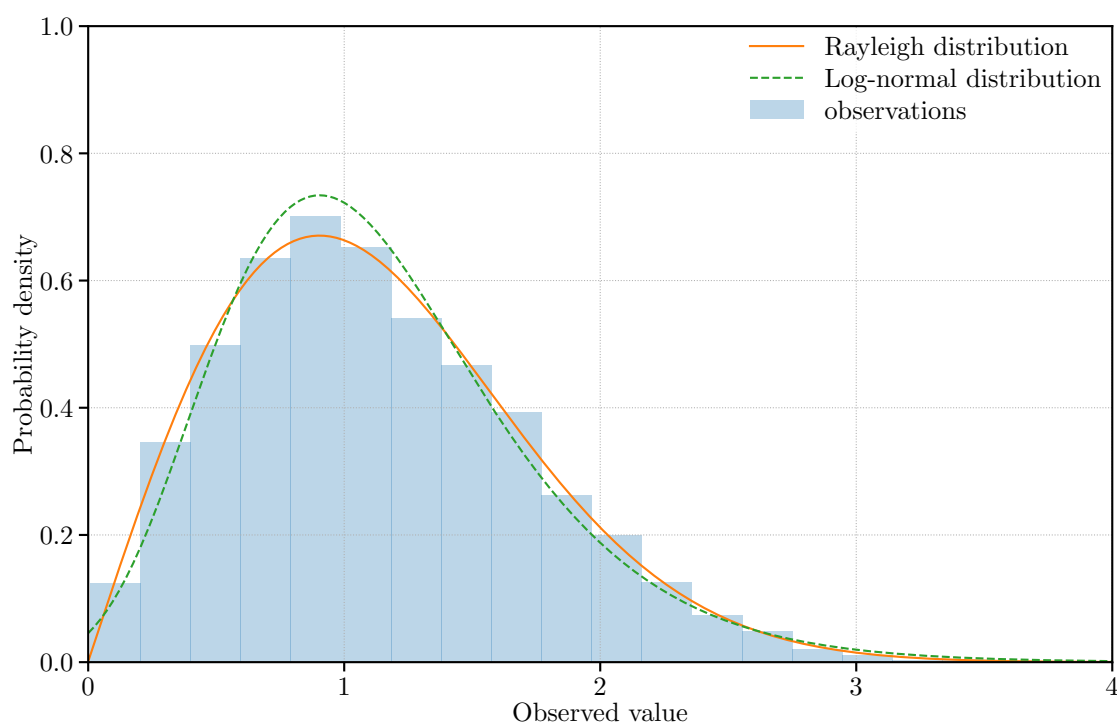


Figure 4.5: An example of distribution fitting using the MLE

In Figure 4.5, the histogram represents the samples that are fitted by two different probability distributions: the Rayleigh distribution (orange line) and the Log-normal distribution (green dashed line). By applying the MLE, the values of parameters of both distributions are optimized to give its best fitting on the samples. However, it is hard to tell which distribution describes the observed data better than the other. Since there is no doubt that a close fit distribution leads to good predictions, it is impossible to confidently predict values if the best fit distribution is not reached. In order to choose a closer fit of distribution on the observed data and to ensure more confident predictions, a comparison between the observed data and the fitted probability distribution must be performed. The ideas to realize this comparison will be discussed in the next section.

4.2.2.2. Statistical testing

One difficulty in distribution fitting is that there may exist more than one probability distributions which can suit the observations well such as that shown in Figure 4.5. To address this problem, one needs to dispose a method to measure the goodness of fit of all reference distributions and select the one that gives the closest fit to the observations. The Kolmogorov-Smirnov test (K-S test) proposed by Andrey Nikolaevich Kolmogorov [Kol33] and Nikolai Vasilyevich Smirnov [Smi48] is a good manner to find out the suitable probability distribution.

The K-S test is a nonparametric test of the equality for one-dimensional probability

distributions. The tested distribution can be either continuous or discontinuous. It can be used to compare a sample to a probability distribution, or to another sample. In principle, the K-S test uses a statistic measuring the distance between the empirical distribution function (ECDF) of the sample and the cumulative distribution function (CDF) of the reference distribution. Like other statistical tests, a null hypothesis \mathbf{H}_0 is required. In the case of comparing a sample to a reference probability distribution (i.e., one-sample K-S test), the null hypothesis assumes that the observed data is sampled from the reference distribution. More details can be found in Appendix F.2.

Taking the sample in Figure 4.5 as an example, the K-S statistic between the sample and the Log-normal distribution is illustrated in Figure 4.6. The green dashed line represents the CDF of the reference distribution fitted by the MLE, the blue dotted line represents the empirical CDF of the sample, the orange line represents distances between the ECDF of the sample and the CDF of the distribution, and lastly, the red line highlights the K-S statistic.

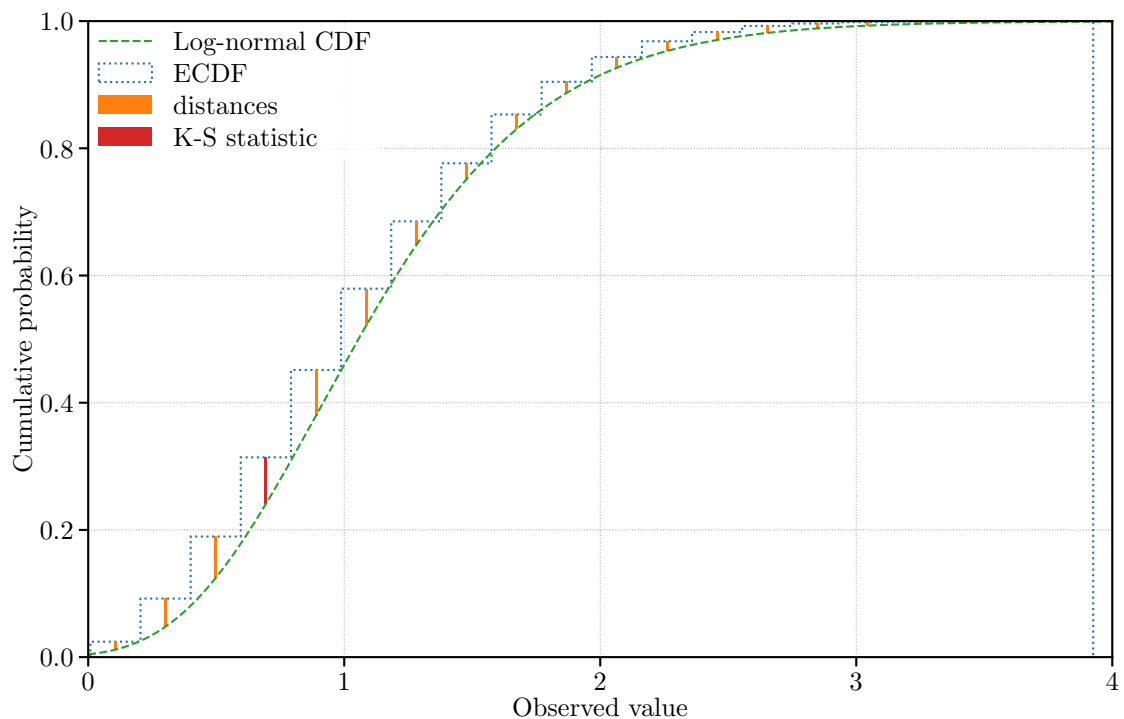


Figure 4.6: An example of the K-S statistic

It should be noted that there are many other methods that can also be used to measure the goodness of fit, for instance, Anderson-Darling test [AD52].

4.2.3. Novel framework for assessing fatigue life of wind turbine tower

A novel approach to assess fatigue damage on wind turbine tower in probabilistic manner is proposed in this section by combining the techniques discussed above. Firstly, the cumulative fatigue damage given by the deterministic process in Section 4.1 is reorganized in probabilistic fashion. Secondly, the wind speed distribution is taken into consideration to offer a lifetime estimation on fatigue damage over the tower.

4.2.3.1. Probabilistic fatigue assessment

From the deterministic approach for fatigue assessment in Section 4.1, the information about cumulative fatigue damage $D^{(i,j)}$ on any tower gage i and local spot j can be accessed by Algorithm 4.1. Considering a sample of N independent and identically distributed (i.i.d.) stochastic simulations generated by Monte Carlo method, each simulation requires a numerical modeling in FAST with arbitrary wind condition. Performing the deterministic fatigue analysis on each simulation results in a set of fatigue damage, i.e.,

$$D_k = \{D^{(i,j)} \in \mathbb{R} : (i,j) \in \mathbb{N}^2\} \text{ for } k = 1, \dots, N \quad (4.10)$$

Next, a pool of reference distributions \mathcal{P} need to be defined by the end-user. It should contain a number of possible distributions to represent the distribution of fatigue damage. For a given position located by tower gage i and local spot j , a subset $\mathbf{D}^{(i,j)}$ can be extracted from the sample in which all available data of fatigue damage on this specified position are included, i.e.,

$$\mathbf{D}^{(i,j)} = \{D_1^{(i,j)}, \dots, D_N^{(i,j)}\} \text{ where } \mathbf{D}^{(i,j)} \subset \{D_k \text{ for } k = 1, \dots, N\} \quad (4.11)$$

According to the distribution fitting process introduced above (i.e., MLE in Section 4.2.2.1), each distribution in the pool \mathcal{P} will be fitted to the subsample $\mathbf{D}^{(i,j)}$ to get the estimated value $\hat{\theta}$ for its parameters. Subsequently, the K-S test takes place to compare this fitted distribution $\mathbf{P}(x | \hat{\theta})$ with the same subsample $\mathbf{D}^{(i,j)}$. The K-S statistic $D_n^{(i,j)}$ resulted from this comparison is used to represent the goodness of fit for this estimated distribution, i.e.,

$$\mathbf{P}(x | \hat{\theta}) \mapsto D_n^{(i,j)} \quad (4.12)$$

Finally, the distribution that returns the minimum K-S statistic is considered consequently as the distribution of cumulative fatigue damage on tower gage i and

local spot j , i.e.,

$$\widehat{\mathbf{P}}^{(i,j)} = \arg \min D_n^{(i,j)} \quad (4.13)$$

To give an example, Figure 4.7 shows an illustration of the distribution of fatigue damage on tower gage 1 and local spot 1 (which means specifically the point on the positive side of \vec{x}_t -axis at the height of 2.19m). The sample is composed by 10 000 observations of cumulative fatigue damage on this specified position. Each of them is calculated by computer codes for a simulated time of 10 min. A pool \mathcal{P} of two reference distributions, Student's t-distribution [Raj05] and Gumbel distribution [Gum35; Gum41], is used to fit the sample and carry out the K-S test. The K-S statistic D_n of Student's t-distribution is 0.053 while that of Gumbel distribution is 0.032. This indicates that the Gumbel distribution is more suitable than the other one to describe the distribution of fatigue damage on this position.

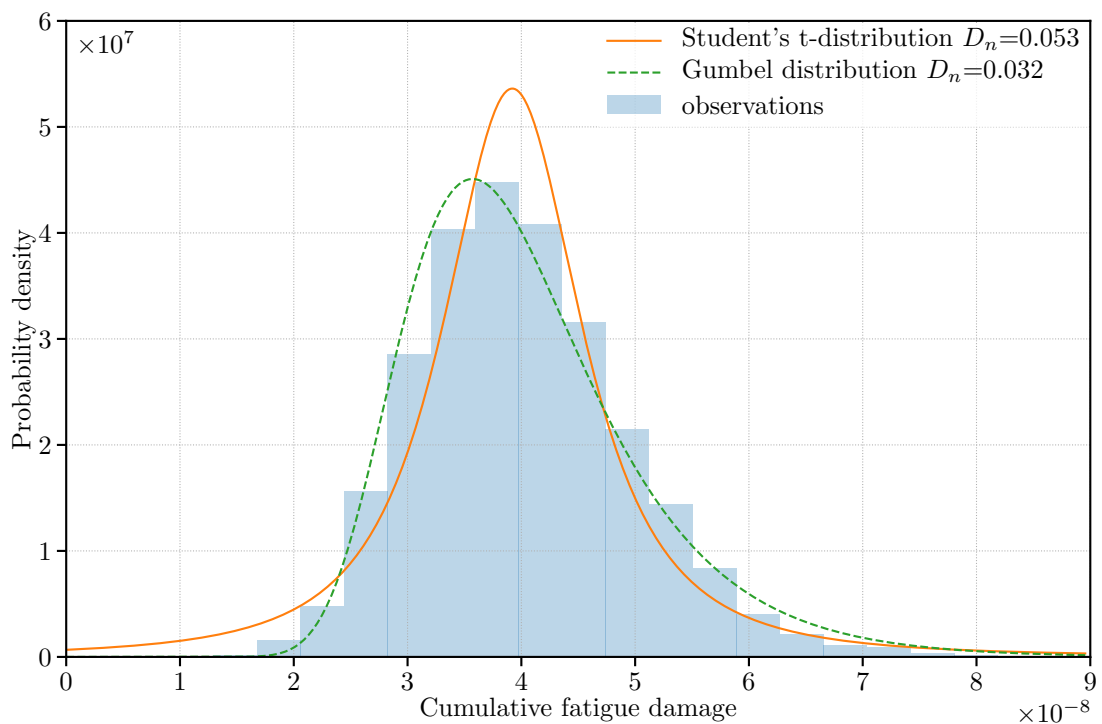


Figure 4.7: An example of probabilistic fatigue analysis on tower gage 1 local spot 1 during a period of 10 min

It should be noted that the process described above concerns only a specified position on the tower (i.e., tower gage i and local spot j). Repeating such process for all positions outlines a probability profile for fatigue damage over the entire wind tower (Equation 4.14). An algorithmic description of the overall process is detailed in Algorithm 4.2.

$$\widehat{\mathcal{P}} = \left\{ \widehat{\mathbf{P}}^{(i,j)} \in \mathcal{P} : (i,j) \in \mathbb{N}^2 \right\} \quad (4.14)$$

Algorithm 4.2: Probabilistic fatigue assessment on wind turbine tower

```

1 Generate a sample  $\mathcal{D}$  of  $N$  i.i.d. observations using Monte Carlo simulation
2 foreach observation  $k$  in  $\mathcal{D}$  do
3   Run a numerical simulation in FAST under an arbitrary wind condition
4   Execute the deterministic fatigue analysis on this simulation and return
   the cumulative fatigue damage on all positions of wind turbine tower,
   i.e.,  $D_k = \{D^{(i,j)} \in \mathbb{R} : (i,j) \in \mathbb{N}^2\}$  // see Algorithm 4.1
5 end foreach
6 Define a pool of reference distributions  $\mathcal{P}$ 
7 foreach tower gage  $i$  do
8   foreach local spot  $j$  do
9     Extract a subset  $\mathbf{D}^{(i,j)}$  from the sample  $\mathcal{D}$  of  $N$  observations
     concerning only the fatigue damage on tower gage  $i$  and local spot  $j$ ,
     i.e.,  $\mathbf{D}^{(i,j)} \subset \mathcal{D}$  such that  $\mathbf{D}^{(i,j)} = \{D_1^{(i,j)}, \dots, D_N^{(i,j)}\}$ 
10    foreach distribution  $\mathbf{P}(x | \theta)$  in  $\mathcal{P}$  do
11      Fit the distribution  $\mathbf{P}(x | \theta)$  on subsample  $\mathbf{D}^{(i,j)}$  to estimate the
      value of its parameters  $\hat{\theta}$  // Maximum likelihood estimation
12      Perform the K-S test between this fitted distribution  $\mathbf{P}(x | \hat{\theta})$  and
      the subsample  $\mathbf{D}^{(i,j)}$ , then record the corresponding K-S statistic
       $D_n^{(i,j)}$ , i.e.,  $\mathbf{P}(x | \hat{\theta}) \mapsto D_n^{(i,j)}$ 
13    end foreach
14    Select the distribution that has the minimum K-S statistic among all
    fitted distributions, i.e.,  $\hat{\mathbf{P}} = \arg \min D_n^{(i,j)}$ 
15    Add this distribution to the set  $\hat{\mathcal{P}} = \{\hat{\mathbf{P}}^{(i,j)} \in \mathcal{P} : \hat{\mathbf{P}}^{(i,j)} = \hat{\mathbf{P}}\}$ 
16  end foreach
17 end foreach

```

In summary, the proposed framework offers a novel way to estimate the fatigue life of the wind turbine tower. It extends the fatigue damage assessment from deterministic process to probabilistic process. The probability profile of fatigue strength of the tower given in Equation 4.14 contributes substantially to many statistical analysis, for example, Reliability-Based Design Optimization (RBDO), in relation to the wind turbine tower.

4.2.3.2. Fatigue life estimation

To give an example about the usage of the probabilistic profile developed previously in Equation 4.14, an estimation to the fatigue life of the wind turbine tower is proposed in this section combining the wind speed distribution.

The wind speed distribution is a continuous probability distribution which determines the occurrence of mean wind speed as well as the occurrence of individual load condition over wind turbine. In practice, it is either assumed by a probability distribution from experience like in Section 2.2.3.1, or by statistical measures in site like in Section 4.6.

Assuming that a wind speed distribution $P_{wind}(v | \theta)$ is pre-acquired covering the operating range of wind turbine, i.e., $[V_{in}, V_{out}]$. For a given mean wind speed V_{mean} , the probabilistic profile $\widehat{\mathcal{P}}_{V_{mean}}$ of fatigue damage in this wind condition is given by the Equation 4.14. Hence, the integrated probability profile of cumulative fatigue damage is:

$$P^{(i,j)}(x | \theta) = \left\{ P_{wind}(v = V_{mean} | \theta) \cdot \widehat{P}_{V_{mean}}^{(i,j)}(x | \widehat{\theta}) : \widehat{P}_{V_{mean}}^{(i,j)} \in \widehat{\mathcal{P}}_{V_{mean}}, (i, j) \in \mathbb{N}^2 \right\} \quad (4.15)$$

Applying the Equation 4.15 to all operating wind speed leads to an overall probability profile of fatigue strength of the wind turbine tower:

$$\mathcal{P}(x) = \left\{ \int_{V_{in}}^{V_{out}} P_{wind}(v | \theta) \widehat{P}_v^{(i,j)}(x | \widehat{\theta}) dv : (i, j) \in \mathbb{N}^2 \right\} \quad (4.16)$$

This overall profile $\mathcal{P}(x)$ interprets spatially the probabilistic distribution of fatigue damage over the entire wind tower. By truncating the wind speed distribution between V_{in} and V_{out} and using the fatigue damage accumulated during the power production, this profile can be used to estimate the cumulative fatigue damage during the design life of wind turbine. By this means, it gives the spatial distribution of fatigue damage during its lifetime and points out the positions on the tower that have intensely cumulative fatigue damage. The above steps are listed in Algorithm 4.3 with an example given in Figure 4.8.

Imaging a wind turbine produces electrical power in the range of [5, 20] for wind speed (i.e., $V_{in}=5$ m/s and $V_{out}=20$ m/s), the distribution of mean wind speed follows the Weillbull distribution [PP02] with a probability density function (PDF) given by:

$$f(x) = \frac{k}{\lambda} \left(\frac{x}{\lambda} \right)^{k-1} \exp \left(- \left(\frac{x}{\lambda} \right)^k \right) \quad (4.17)$$

where, shape parameter $k = 2$
 scale parameter $\lambda = 10$

Algorithm 4.3: Probabilistic fatigue life estimation of wind turbine tower

- 1 Define a wind speed distribution $P_{wind}(v | \theta)$
 - 2 **for** $V_{mean} \leftarrow V_{in}$ **to** V_{out} **do**
 - 3 Take place the probabilistic fatigue assessment to get the probability profile of fatigue damage $\hat{\mathcal{P}}_{V_{mean}} = \{\hat{P}^{(i,j)}(x | \hat{\theta}) : (i, j) \in \mathbb{N}^2\}$ // see Algorithm 4.2
 - 4 Get the probability of occurrence of the current wind speed, i.e., $P_{wind}(v = V_{mean} | \theta)$
 - 5 Calculate the integrated probability profile $P_{wind}(v = V_{mean} | \theta) \times \hat{\mathcal{P}}_{V_{mean}}$
 - 6 **end for**
 - 7 Sum up all integrated probability profiles to form an overall set $\mathcal{P}(x) = \left\{ \sum_{v=V_{in}}^{V_{out}} P_{wind}(v | \theta) \hat{P}_v^{(i,j)}(x | \hat{\theta}) : (i, j) \in \mathbb{N}^2 \right\}$ // discrete version of Equation 4.16
-

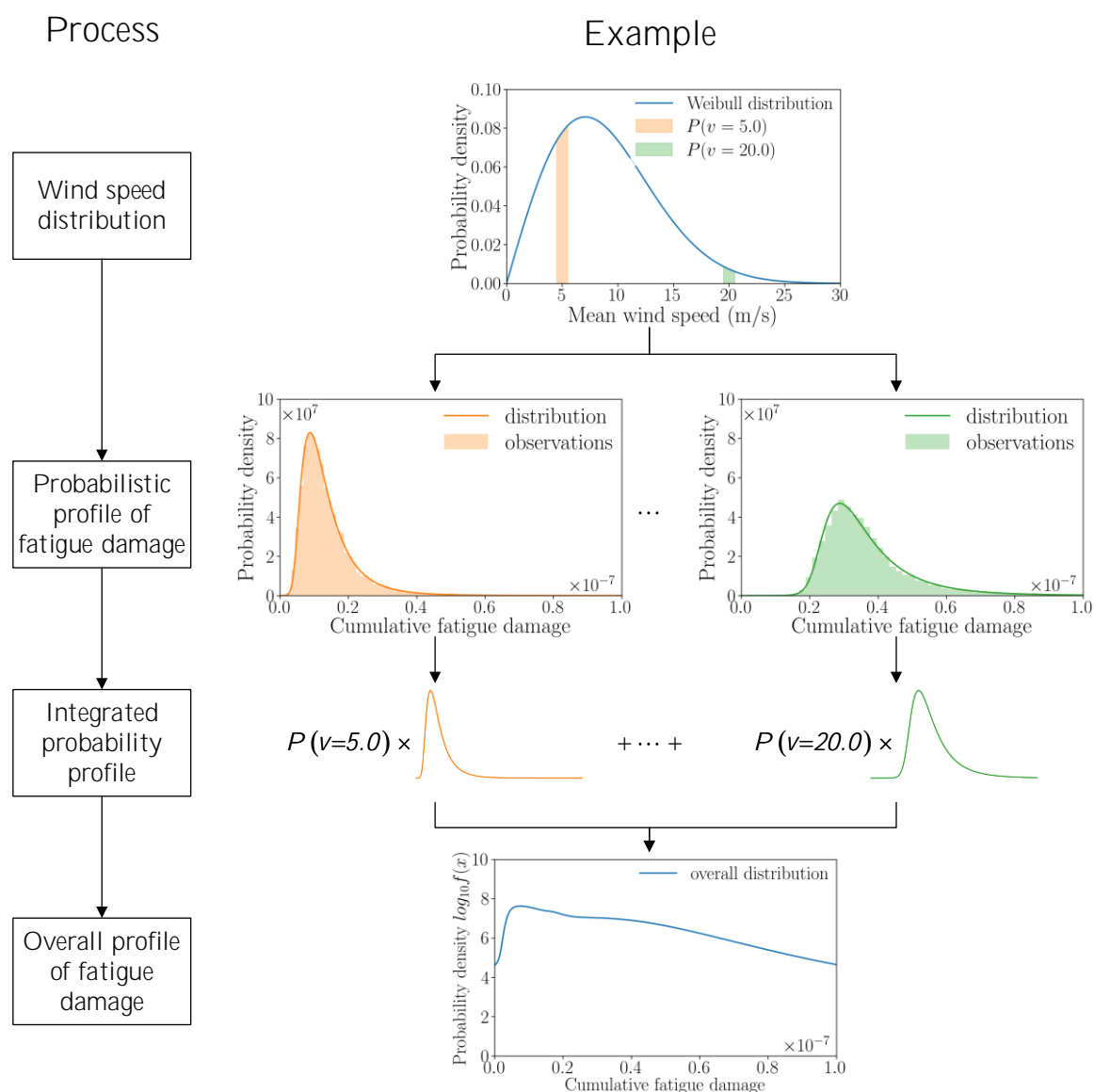


Figure 4.8: An example of probabilistic profile of fatigue life on tower gage 1 and local spot 1 during a period of 10 min

An example of Equation 4.17 is illustrated at the top of Figure 4.8 where the orange area represents the probability of V_{in} and the green area represents the probability of V_{out} . The two followed charts show the probabilistic profile of fatigue damage determined by Algorithm 4.2 for $V_{mean}=V_{in}$ and $V_{mean}=V_{out}$. For the wind speed between V_{in} and V_{out} at step-size of 1 m/s, the probabilistic profile of fatigue damage is generated in the same way. By calculating the integrated probability profile (Equation 4.15) and adding together all profiles, the overall probability profile of cumulative fatigue damage on tower gage 1 local spot 1 is carried out in the last line of Figure 4.8.

Please be aware that the PDF of the overall profile in Figure 4.8 has been plotted in logarithm base 10 for convenience of illustration.

4.2.4. Summary

In this section, the fatigue analysis is extended from the deterministic domain to the probabilistic domain. The novel framework, proposed originally by the author, makes it possible to estimate the fatigue life of the wind turbine tower subjected to the arbitrary wind condition. A demonstration of the proposed method is illustrated in Figure 4.8. However, it should point out that this demonstration shows how to estimate the fatigue life on only one position of the tower, i.e., tower gage 1 local spot 1. To obtain the distribution at a specified height, it needs to expand the process Algorithm 4.3 for all local spots on the same cross-section (Figure 4.9). Furthermore, to obtain the distribution of the entire wind turbine tower, it needs to expand the process for all tower gages locating from $z = 0$ m to $z = HH$.

In Figure 4.9, the overall probability distributions of 10-min cumulative fatigue damage are plotted on tower gage 1. The same Weibull distribution of wind speeds shown in Figure 4.8 is reused here to estimate the overall fatigue damage. As for the probabilistic profile of fatigue damage at each V_{mean} , it is carried out by practicing Algorithm 4.2 for every 1 m/s from $V_{in} = 5$ m/s to $V_{out} = 21$ m/s. The figure is drawn in Cartesian coordinate system where the axes in the plane represent cumulative fatigue damage, and the vertical axis as well as the color legend represents the logarithmic probability density based on 10.

Since the distribution of wind speeds is usually site-specified, it is more valuable and useful to establish a set of probabilistic profiles of fatigue damage covering all mean wind speeds in the operating range (i.e., between V_{in} and V_{out}). Therefore, to investigate the fatigue life of the wind turbine tower in probabilistic fashion, the proposed framework is applied in the next section with turbulent wind conditions.

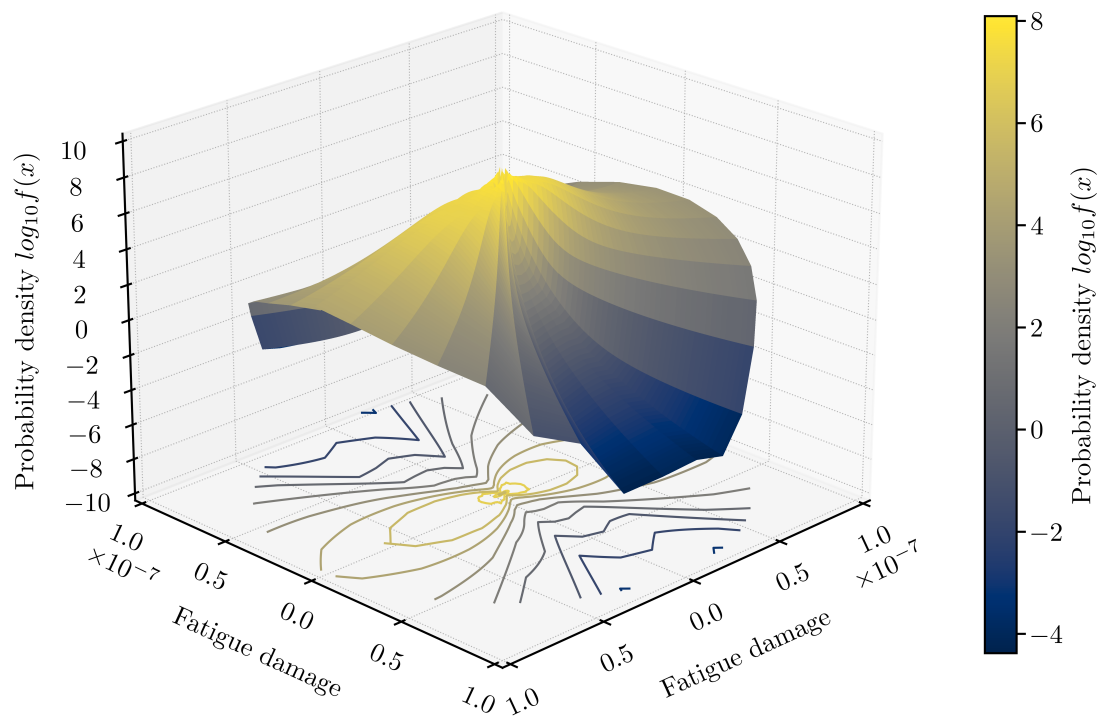


Figure 4.9: An example of overall probability profile of fatigue life on tower gage 1

4.3. Scenario F: fatigue loads analysis

4.3.1. Design load case of power production with normal turbulence model (DLC1.2)

In addition to the ultimate loads analysis (Scenario U) that has already been discussed in Section 3.3.1, the fatigue loads are an other imperative issue in wind turbine design. For this reason, the IEC 61400-1 standard suggests a design load case DLC1.2 to investigate the behavior of wind turbine in terms of fatigue damage.

4.3.2. Design situation

The DLC1.2 issued from the IEC 61400-1 standard specifies a scenario for generating electrical power in the face of wind considering normal turbulence model (NTM). The state of wind turbine is considered as in normal production without technical fault or undesired incident. The wind velocities in three directions (\vec{x}_t , \vec{y}_t and \vec{z}_t) are unsteady and randomly changed during a period of time. The IEC specifications suggest either a period of 10 min with at least six numerical simulations or a full simulation of 60 min. For convenience of running, the 10-min period is chosen by the author as the simulated time in each run. The number of runs depends on the number of observations in the sample. To ensure enough data for probabilistic fatigue analysis, a number of 10 000 observations is planned for each case of mean wind speed. Each observation implies a unique random seed number that will be used to generate a unique NTM wind condition in FAST codes.

By definition, the mean wind speed V_{mean} at hub height (HH) in NTM varies from $V_{in}=3$ m/s to $V_{out}=25$ m/s at step of 1 m/s, that is, a total of 23 cases of mean wind speed. The standard deviation of turbulence in longitudinal direction \vec{x}_t can be deduced from Equation 2.3. Figure 4.10 gives an example of NTM in which the time dependent wind speed is decomposed into its longitudinal velocity V_x (blue line), lateral velocity V_y (orange line) and vertical velocity V_z (green line). A 60-s period will be neglected as usual in post-processing. On the right side of Figure 4.10, the distribution of component wind velocity from 0 s to 600 s is illustrated too. Table 4.1 summarizes all the characteristics of DLC1.2.

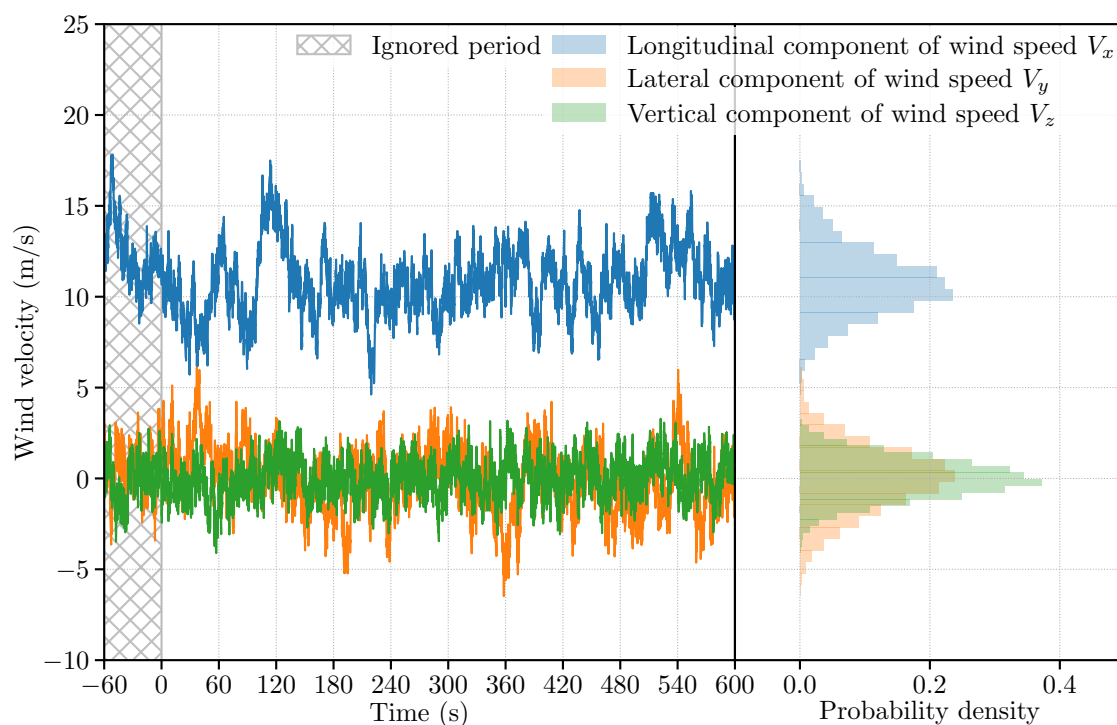


Figure 4.10: An example of NTM at mean wind speed of 11 m/s

Table 4.1: Summary of DLC1.2

DLC1.2	Power production
Description	Simulation of power production in turbulent wind condition
Simulation set-up	Mean wind speed: $[V_{in}, V_{in} + 1, \dots, V_{out}]$, 23 cases in total
	Turbulence: Normal turbulence model (NTM)
	Gust: (not concerned)
	Initializing period: 60 s
	Simulated time: 600 s
Special event	(not concerned)
Comment	A number of 10 000 simulations is planned for each case of mean wind speed. This leads to a sum of 230 000 runs in FAST simulation codes
	As for the post-processing, each run performs the probabilistic fatigue analysis on 11 tower gages, each of them contains 36 equally separated local spots, that is, a total of $11 \times 36 = 396$ local spots.
	The deterministic fatigue assessment follows the guidelines given in the DNVGL-RP-C203 standard [DNV19].

During post-processing of each simulation, mechanic responses for all tower gages listed in Table 3.2 are exported. Each tower gage is equally divided into 36 local spots. Thus, a total of $11 \times 36 = 396$ local spots will be used to take place the probabilistic fatigue analysis for the wind tower. Each of them will have 23 individual probability distributions of 10-min cumulative fatigue damage corresponding respectively to the 23 cases of mean wind speed from V_{in} to V_{out} . That is, to sum up, a total of $396 \times 23 = 9108$ probability functions.

In order to carry out fatigue analysis in numerical environment, the engineering guidance from the recommended practice DNVGL-RP-C203 [DNV19] is applied. The carbon manganese steel material (C-Mn) is considered in the simulation. The S-N curve of class B1 in air environment is assumed true which has an endurance limit of $\sigma_e = 106.97$ MPa at 10^7 cycles.

4.3.3. Process of analysis

The outline of the probabilistic fatigue analysis on DLC1.2 is illustrated in Figure 4.11. The process begins with selecting a case of mean wind speed V_{mean} in the range of $[V_{in}, \dots, V_{out}]$ with step-size of 1 m/s. Then a sample of N seed numbers is randomly initiated, $U(-2^{31}, 2^{31} - 1)$ stands for the uniform random integer between -2^{31} and $2^{31} - 1$. Each random seed is subsequently used to generate a turbulent wind condition with NTM in FAST codes.

After this, the numerical simulation under each wind condition is carried out to export mechanic responses in time domain. The time histories of deflection $D(t)$, force $F(t)$ and moment $M(t)$ are expressed on tower gages from gage 1 to gage 11 (including tower-base and tower-top) listed in Table 3.2. For each tower gage i , the time histories of stress σ_{normal} are estimated by Equation 4.4 on local spots from spot 1 to spot 36.

Next stage is to realize probabilistic fatigue assessment (Algorithm 4.2) on each tower gage i and each local spot j using all cumulative fatigue damage calculated under N wind conditions. All continuous distributions [Scia; Scib] in SciPy [JOP01] are used to accomplish data fitting and K-S test. The distributions estimated by this process construct together the probabilistic profile of cumulative fatigue damage $\hat{\mathbf{P}}_{V_{mean}}$ at this mean wind speed V_{mean} .

Lastly, all the above stages are repeated till all mean wind speed between V_{in} and V_{out} have a corresponding probabilistic profile of cumulative fatigue damage, i.e.,

$$\mathcal{P}_{tower} = \left\{ \hat{\mathbf{P}}_v : v = V_{in}, \dots, V_{out} \right\} \quad (4.18)$$

where, $\hat{\mathbf{P}}_v = \left\{ \hat{P}_v^{(i,j)}(x | \hat{\theta}) : i = 1, \dots, 11; j = 1, \dots, 36 \right\}$

The set \mathcal{P}_{tower} contains a distribution of 10-min cumulative fatigue damage for all tower gages, all local spots and all mean wind speed, that is, a total of $11 \times 36 \times 23 = 9108$ probability distributions. It describes the cumulative fatigue damage in probabilistic fashion considering both spatial characteristics (through tower gage and local spot) and environmental characteristics (through mean wind speed).

The use of \mathcal{P}_{tower} is essential. For example, it can be used to assess spatially the cumulative fatigue damage over the entire wind turbine tower by integrating the distributions from $z = 0$ m to $z = HH$. Furthermore, it can also be combined with a distribution of wind speed to provide an assessment of the fatigue life during the normal power production and predict the fatigue damage in its design lifetime. An application is given in Section 4.6 with consideration of wind source measured in site.

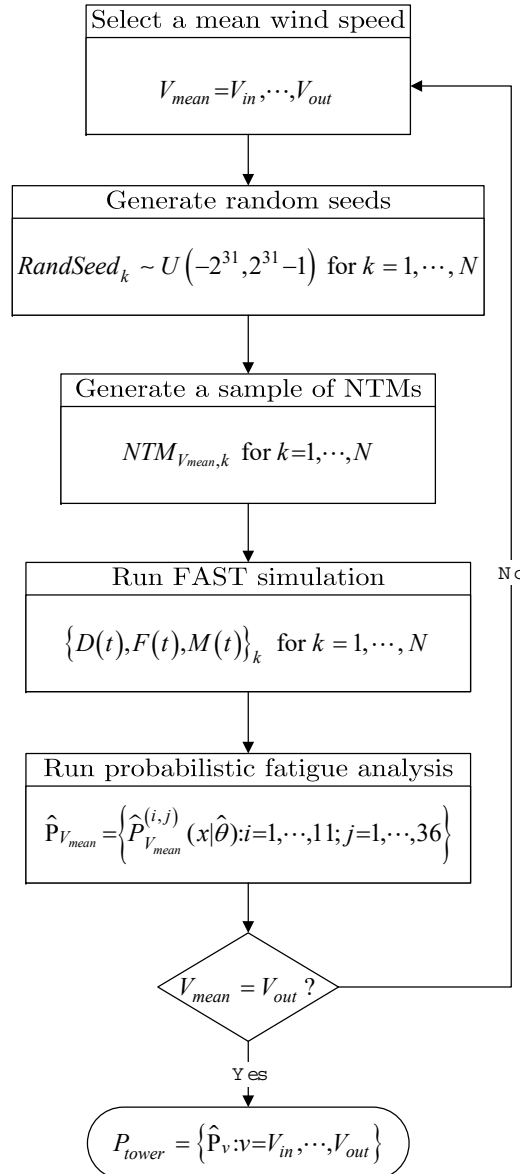


Figure 4.11: Workflow for probabilistic fatigue analysis on DLC1.2

4.3.4. Results and discussions

The fatigue damage considered in this dissertation only depends on the normal stress (Equation 4.1) which is related to three time-dependent variables: local force F_z , local moment M_x and M_y (Equation 4.5). An illustration of normal stress-history on tower gage 1 local spot 1 in a NTM condition at mean wind speed of 11 m/s is given in Figure 4.12. The wind speed in longitudinal direction (i.e., positive direction of \vec{x}_t -axis) is plotted in blue line; the resultant axial force $F_{x,1}$ is plotted in orange dashed line; the resultant roll moment $M_{x,1}$ and pitching moment $M_{y,1}$ are plotted in green dotted line with triangles and red dotted line with circles, respectively; finally, the normal stress $\sigma_{normal}^{(1,1)}$ is shown in purple dotted line.

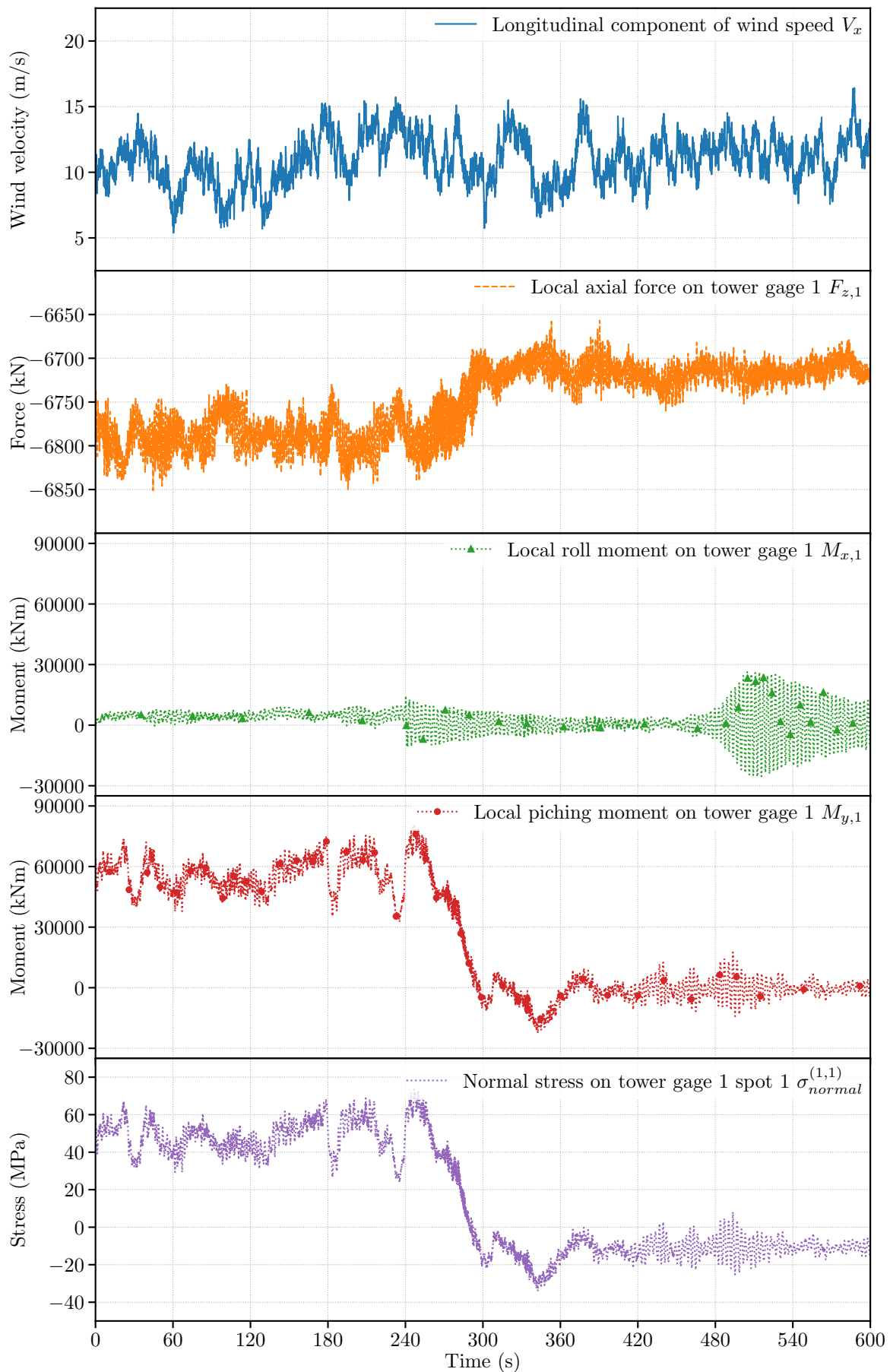


Figure 4.12: DLC1.2 wind speed, tower reactions and tower stress state on tower gage 1 local spot 1 during 10-min simulated time

Once the stress-history on tower gage 1 local spot 1 is available, the 10-min cumulative damage on the same gage can be computed by classical deterministic fatigue analysis (Algorithm 4.1). Iterate the same analysis through all N samples and carry out the probabilistic fatigue analysis (Algorithm 4.2) lead to the probabilistic profile of 10-min cumulative fatigue damage on this position (Figure 4.13a). Extend the same process to other positions, i.e., other local spots, bring about the distributions of 10-min cumulative fatigue damage in all directions on the tower gage 1 (e.g., Figure 4.13b, Figure 4.13c and Figure 4.13d).

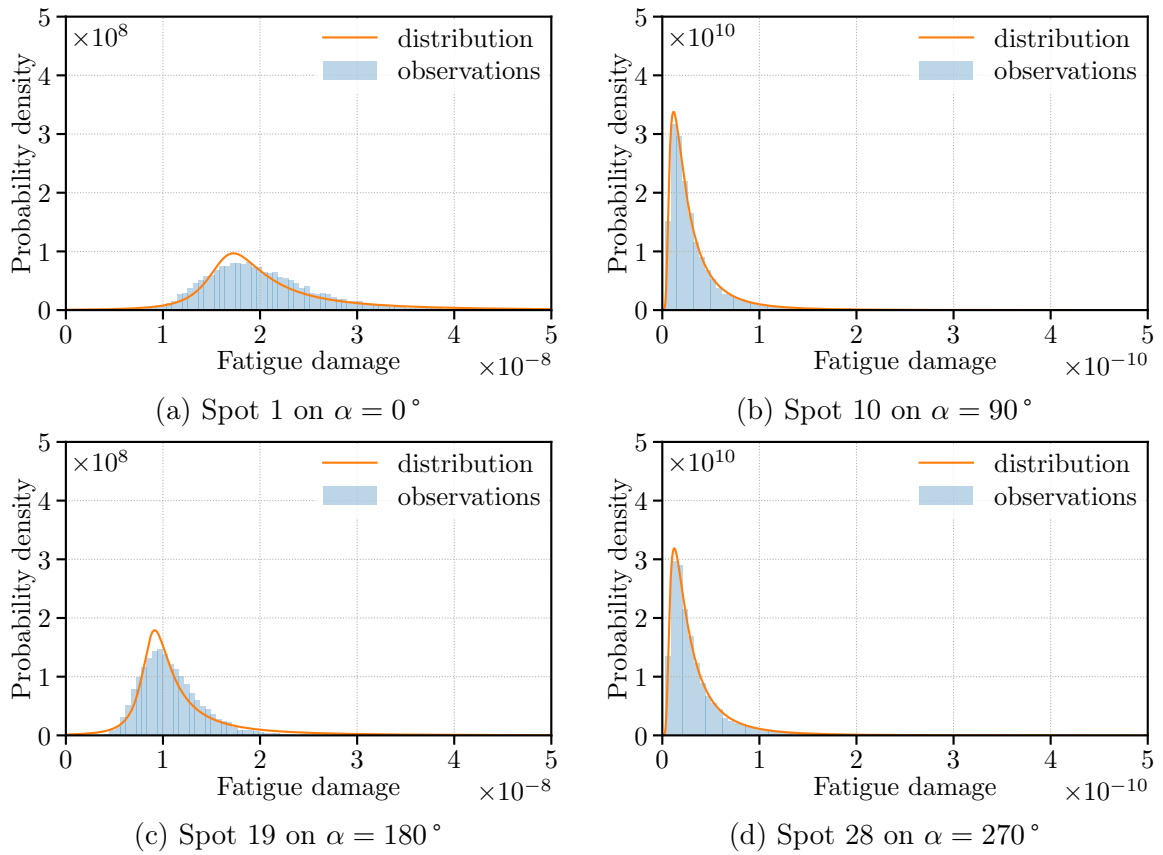


Figure 4.13: DLC1.2 distribution of 10-min cumulative fatigue damage on tower gage 1 (a) local spot 1, (b) local spot 10, (c) local spot 19 and (d) local spot 28

By convention (Section E.2), every local spot is defined by its azimuth angle α measuring counterclockwise between itself and the local spot 1 where $\alpha = 0^\circ$ (see Figure 4.2). Be aware that the value of damage on spot 1 (Figure 4.13a), spot 10 (Figure 4.13b), spot 19 (Figure 4.13c), and spot 28 (Figure 4.13d) are not in the same scale. The abscissae in Figure 4.13b and Figure 4.13d are 100 times larger than that in other two figures. This indicates that the cumulative fatigue damage does not distribute homogeneously on the cross section, yet nonetheless, it distributes quasi-symmetrically in the opposite directions. This phenomenon can be discovered more obviously if the fatigue damage on all spots are plotted (see Figure 4.14).

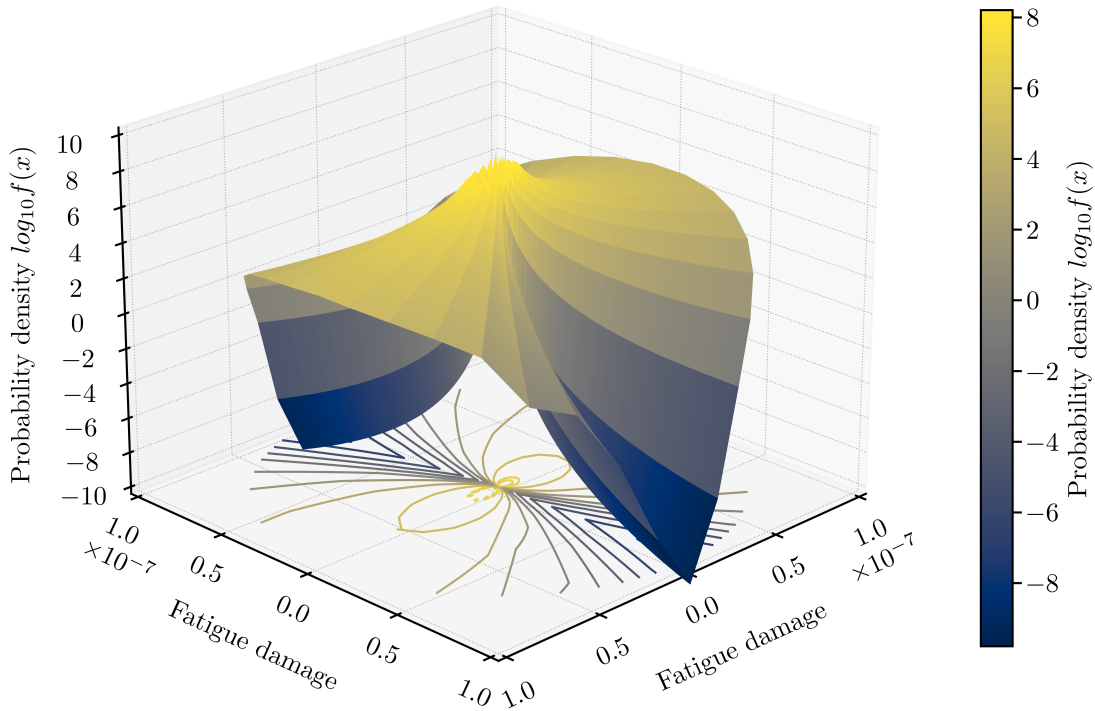


Figure 4.14: DLC1.2 distribution of 10-min cumulative fatigue damage on tower gage 1 (3D map combined with contour map)

Figure 4.14 is composed by a 3D map and a contour map. The latter represents the projection of 3D map on the horizontal plane. Graphically speaking, Figure 4.14 is a collection of all similar subfigures (as shown in Figure 4.13) covering the entire 36 local spots from $\alpha = 0^\circ$ to 360° . The saddle-like surface in Figure 4.14 delineates the probability density function (PDF) at any azimuth angle α on tower gage 1. It should be emphasized that, on 3D map, the axial axis (as well as the colorbar) stands for the probability density scaled to logarithm base 10, i.e., $z = \log_{10} f(x)$. The contour map shows isolines (a.k.a. isarithm) along which the PDF have constant values (Figure 4.15a). From a statistical point of view, these isolines imply the same percentiles from all the probability distributions of fatigue damage on tower gage 1 (Figure 4.15b).

Figure 4.15a extracts the contour map from Figure 4.14 to 2D map where both abscissa and ordinate represent the 10-min cumulative fatigue damage. The isolines depict graphically how the fatigue damage is distributed over the cross section on tower gage 1 (at the height of 2.19 m). All isolines are colored to illustrate the different levels of PDF in logarithm base 10.

Figure 4.15b replots the same data from Figure 4.15a in radar chart (a.k.a. Kiviati diagram [KK73]). The radial axis, or polar axis, represents the 10-min cumulative fatigue damage on which the zero point, i.e., zero damage, is centered in the chart. The interior perimeters indicate the increment on fatigue damage from zero (center)

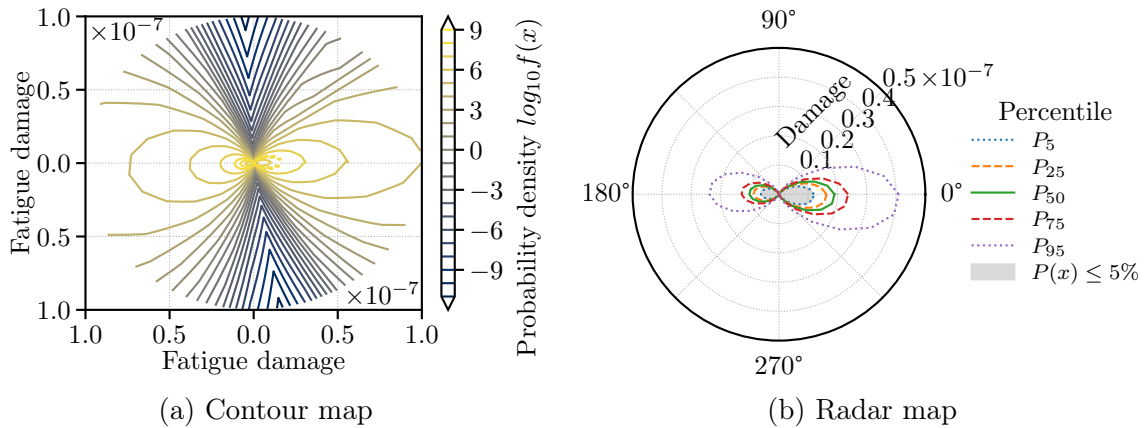


Figure 4.15: DLC1.2 distribution of 10-min cumulative fatigue damage on tower gage 1 regraphed in (a) contour map (Cartesian coordinate system) and (b) radar map (cylindrical coordinate system)

to its maximum (exterior perimeter). On the outside of the exterior perimeter locates the azimuth angle α of local spots in degrees. By convention, the local spot 1 places on the right side of the cross section and has an azimuth angle $\alpha = 0^\circ$ (Figure 4.2). The colored lines inside the radar graph stand for the different percentiles denoted as P_i where i means i -th percentile. For example, P_5 (the blue dotted line) is the 5th percentile below which 5% of the observations may be found (the gray surface in Figure 4.15b). In other words, the wind turbine tower has likely a chance of 5% to subject a fatigue damage value inside the gray surface. More percentiles such as P_{25} , P_{50} , P_{75} and P_{95} are highlighted by orange dashed line, green line, red dashed line and purple dotted line respectively in Figure 4.15b. P_{25} is also known as the first quartile, P_{50} as the second quartile (or median), and P_{75} as the third quartile.

4.3.5. Summary

This section gives an application to the novel probability framework for assessing fatigue damage Section 4.2. The application takes account of turbulent wind condition NTM designed by the IEC standards for normal power production. The cumulative fatigue damage is assessed under all mean wind speed in the operating range of $[V_{in}, V_{out}]$ through all tower gages and local spots. By means of this analysis, a survey of the fatigue damage accumulated over the wind turbine tower is acquired. Since the final profile of fatigue damage is based on statistics and probability, it opens the gate to carry out many statistical analysis and probability based analysis such as RBDO. Based on the results obtained in this section, an empirical analysis is proposed in the next section to investigate:

1. dominant probability distribution for cumulative fatigue damage over the wind

- turbine tower (Section 4.4.1)
- 2. major formation for the distribution of damage on the cross section (Section 4.4.2)
- 3. spatial distribution of the cumulative fatigue damage from tower-base to tower-top (Section 4.4.3)

4.4. Empirical study

4.4.1. Dominant probability distribution of fatigue damage

From one hundred candidate distributions [Scia; Scib], the probabilistic framework (Algorithm 4.2) has succeeded in identifying about ten distributions for the 10-min cumulative fatigue damage on tower gage 1. Figure 4.16 graphs the estimated distributions in parallel coordinates [Oca85] where the mean wind speed are marked on the left ordinate while the azimuth angle of local spots θ_j are located on the right. The central ordinate classifies the lines under different groups with the same color. Each color represents a type of distribution listed in the legend. If a distribution has been identified as the most probable one on a local spot by the K-S test, a curve is plotted from the azimuth of spot on the right axis to the central axis. Meanwhile, if the same distribution has been found in a case of mean wind speed, the same curve will be connected to the value of mean wind speed on the left axis with the same color.

For example, the power log-normal distribution is marked by the black line in Figure 4.16. It is only connected to the local spot on 240° from the right ordinate and the mean wind speed of 25 m/s from the left axis. This involves that the power log-normal distribution is suitable to represent the distribution of fatigue damage only on the local spot on 240° at $V_{mean}=25$ m/s.

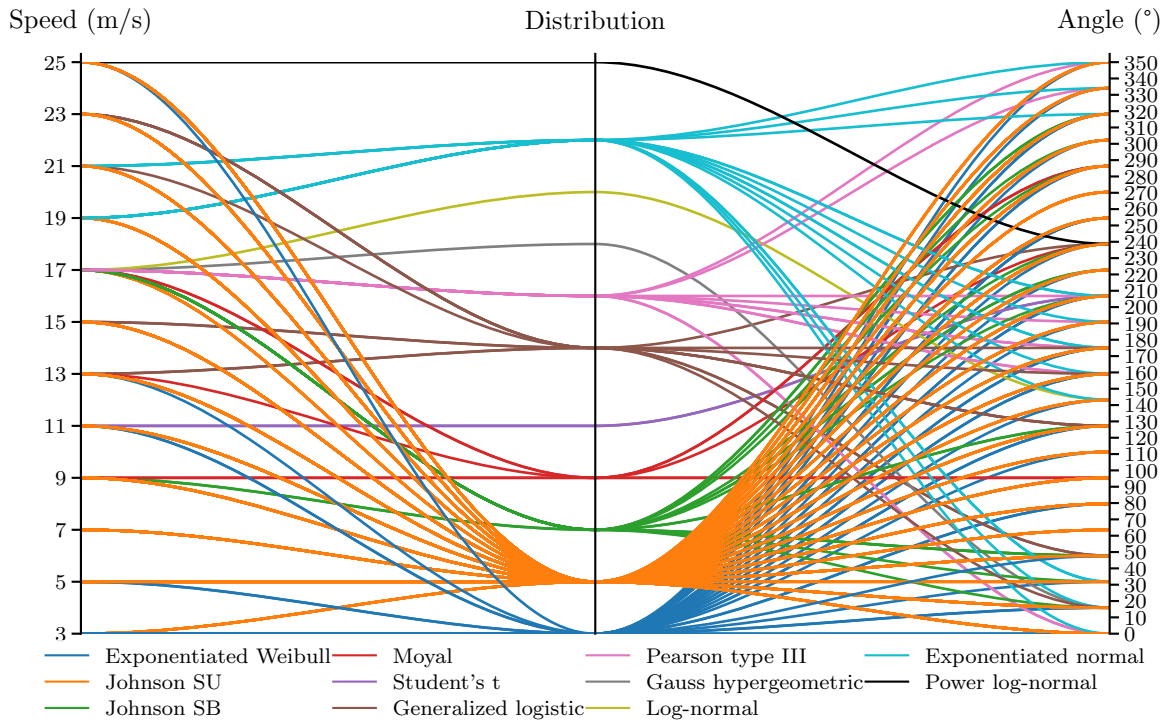


Figure 4.16: Estimated distributions on tower gage 1 with reference to all mean wind speed and all local spots

From the Figure 4.16, it is obviously that the Johnson SU distribution [Joh49] (orange line) may be the most probable distribution to describe statistically the fatigue damage since it has connected to all local spots spanning from 0° to 360° and to all cases of mean wind speed. The PDF of this distribution is firstly proposed by N. L. Johnson in 1949 [JOH49]:

$$f(x | a, b) = \frac{b}{\sqrt{x^2 + 1}} \frac{\exp(-x^2/2)}{\sqrt{2\pi}} \left(a + b \log \left(x + \sqrt{x^2 + 1} \right) \right) \quad (4.19)$$

where, $a \in \mathbb{R}$ and $b > 0$ are shape parameters for $x \in \mathbb{R}$. There is also a variant of the Johnson SU distribution:

$$f(x | a, b) = \frac{b}{x(1-x)} \frac{\exp(-x^2/2)}{\sqrt{2\pi}} \left(a + b \log \frac{x}{1-x} \right) \quad (4.20)$$

where, a and b are the same shape parameters as that in the Johnson SU distribution. This variant, called the Johnson SB distribution, is specially designed for variables in the range $0 \leq x \leq 1$ and has been plotted by green line in Figure 4.16.

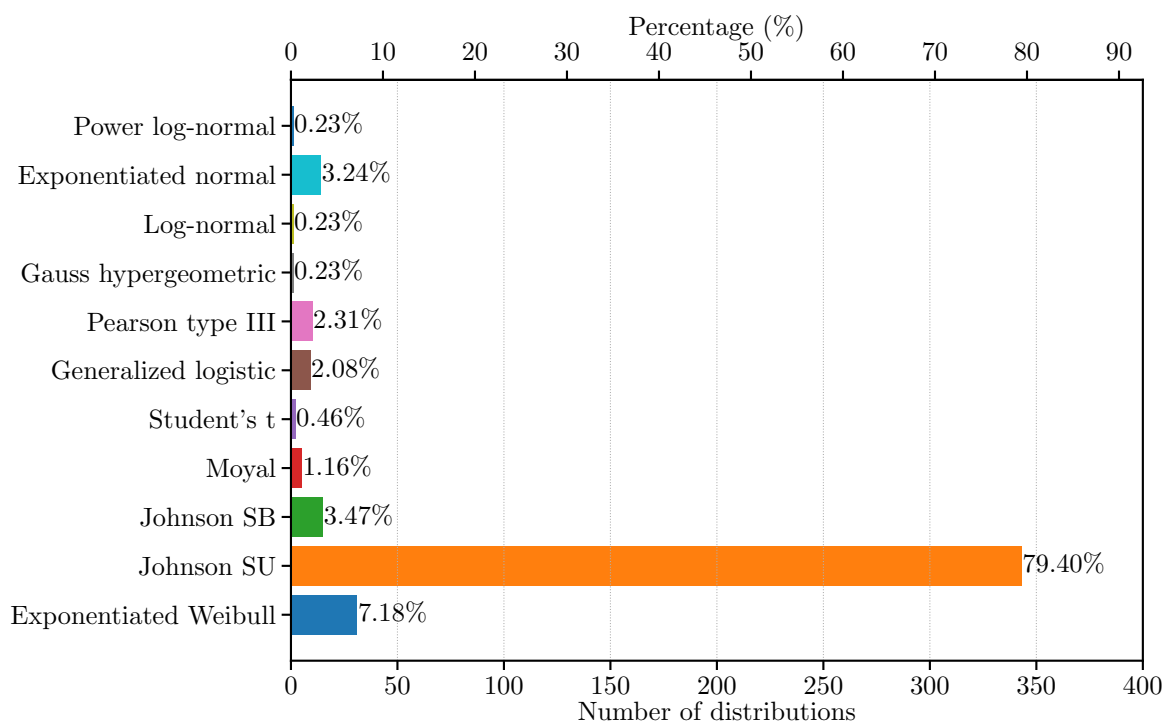


Figure 4.17: Number of estimated distributions on tower gage 1 grouped by types

Although the Johnson SU distribution, and its family distribution the Johnson SB, are clearly the most appropriate types of probability distribution to stand for the 10-min cumulative fatigue damage on tower gage 1, there are also some other possible distributions like the exponentiated Weibull distribution [MS93; MSF95], the exponentiated normal distribution [COC13], the Pearson type III distribution [Pea94] and the generalized logistic distribution [JKB95; GK10]. These distributions help to explain how fatigue damage are distributed on several local spots or under some mean wind speed (see blue line in Figure 4.16 for the exponentiated Weibull distribution, cyan line for the exponentiated normal distribution, pink line for the the Pearson type III distribution, and lastly, brown line for the generalized logistic distribution). Figure 4.17 summarizes statistically the occurrence of every type of distribution on the tower gage 1 from which the Johnson SU and SB distribution have reached a probability of more than 80%.

4.4.2. Silhouette of the distribution of fatigue damage

In this section, the result that has been shown in Figure 4.15 will be extended to all cases of mean wind speed in order to investigate the formation of the distribution in the polar coordinate system (Section E.2). It should be pointed out that the percentiles used in this part are empirical which means the values of percentile come from the

sample of observations not from the fitted distributions.

4.4.2.1. Distributions in polar coordinate system

The empirical distributions of 10-min cumulative fatigue damage on tower gage 1 is given in Figure 4.18. The wind turbine tower is centered in the middle of each radar chart. Every closed curve in the figure represents the damage value at a fixed percentile such as the 25th percentile (1st quartile) P_{25} , 50th percentile (median) P_{50} and 75th percentile (3rd quartile) P_{75} . All the data are visualized in radar chart where the exterior perimeter shows the azimuth of local spots in degrees and the radial axis shows the fatigue damage normalized to a specific value given in the caption. The caption of each radar chart indicates the value of mean wind speed V_{mean} used in the numerical simulation and the normalization value of fatigue damage in parentheses. Be attention that the charts in the same row share the same value of normalization.

Recalling that the wind blows always from the left side to the right side in the polar coordinate system, that is, straightly from the azimuth of 180° to the local spot on 0° in Figure 4.18. So the upwind side of the wind turbine covers the left half-circle in every radar chart, i.e., the semi-circle from 90° to 270° in counterclockwise direction. On the contrary, the downwind side envelops the right half-circle ranging from 270° to 90° counterclockwise.

For mean wind speed at 3 m/s and 5 m/s, the NREL 5MW reference wind turbine stays in the control Region 1^{1/2}, a startup region between Region 1 and Region 2 (Figure D.2). This region is designed to impose a lower limit on the electrical generator speed to limit the turbine's operational speed range. The distribution of the cumulative fatigue damage in this region have a quasi-symmetric form as in Figure 4.18a and Figure 4.18b. It, one is aligned with the nominal wind direction, i.e., the horizontal line from 180° to 0° in the radar chart, and the other is aligned with the perpendicular direction to the wind direction, i.e., the vertical line from 90° to 270° .

When wind turbine enters Region 2 but has not yet reached the rated wind speed ($V_{rate}=11.4\text{m/s}$), the cumulative fatigue damage increases proportionally with the mean wind speed (see Figure 4.18c, Figure 4.18d and Figure 4.18e). In the meantime, the damage is more accumulated on the downwind side, i.e., the fan-like area ranging from the azimuth of 330° to 30° in counterclockwise direction.

From the rated speed V_{rate} till the cut-out speed V_{out} (Figure 4.18f, Figure 4.18g, Figure 4.18h, Figure 4.18i, Figure 4.18j and Figure 4.18k), the contour lines continue to enlarge especially on the downwind side (right part) than the upwind side (left part). The symmetric axis of the contour rotates slightly from the horizontal line 180° - 0° to the line 150° - 330° . The cumulative fatigue damage reaches its maximum at V_{out} , i.e., the inner area closed by the contours in Figure 4.18l is the largest comparing to that in other radar charts.

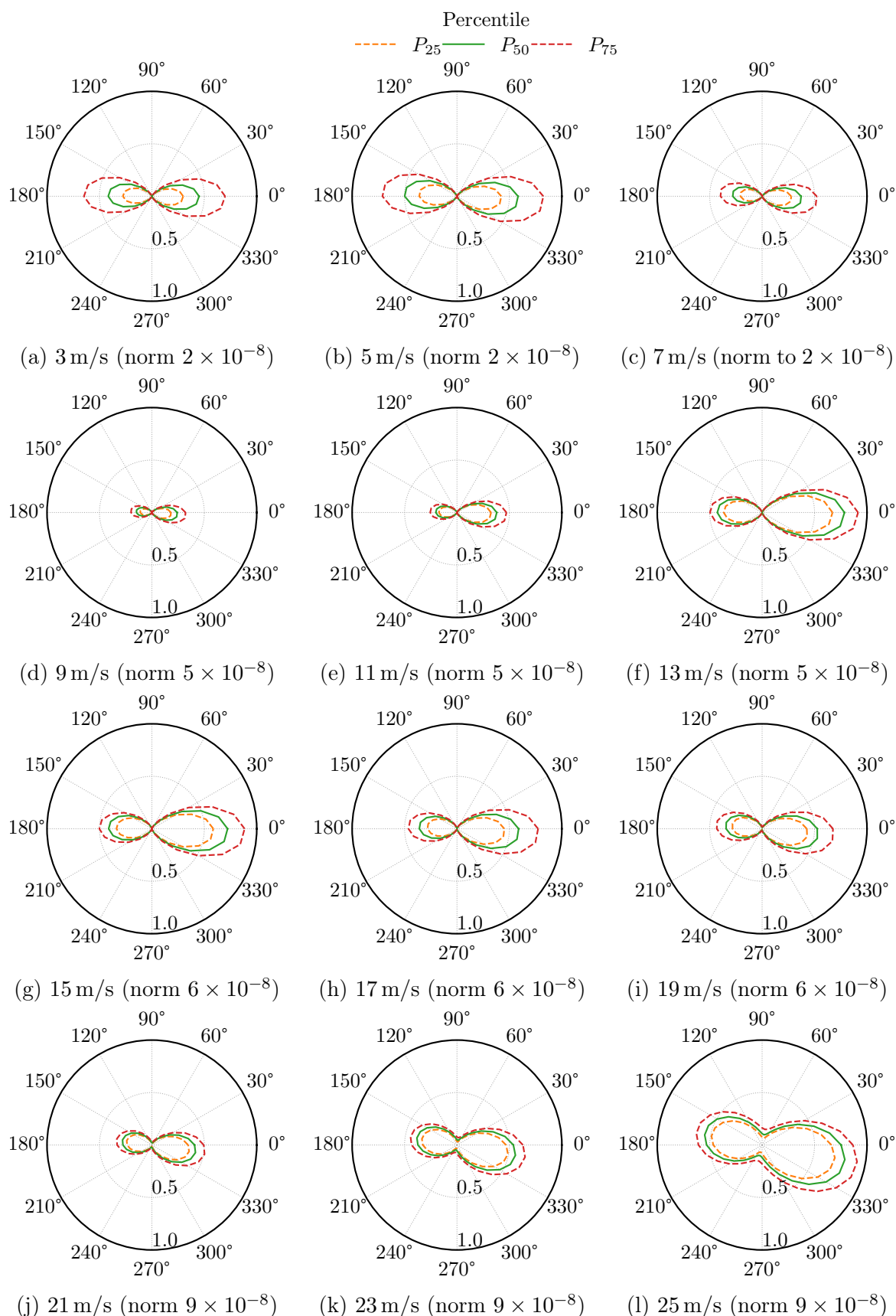


Figure 4.18: Distribution of 10-min cumulative fatigue damage on tower gage 1 under different mean wind speed

4.4.2.2. Peanut law

From the empirical study in the previous section, several features about the distribution of the cumulative fatigue damage can be concluded:

1. The Johnson SU distribution can be used to assess and predict the cumulative fatigue damage over the cross section of wind turbine tower.
2. The cumulative fatigue damage is not always proportional to the mean wind speed (e.g., compare Figure 4.18b to Figure 4.18c). It is highly related to the control system especially for wind turbines equipped with the variable-speed controller.
3. The distribution of the fatigue damage on cross section of the wind tower is more likely symmetric when V_{mean} is small and enlarge on the downwind side when V_{mean} goes up (e.g., compare Figure 4.18a to Figure 4.18g).
4. The longitudinal axis of the contour of the distribution is not always parallel to the wind direction, but can be changed when wind loads increase (e.g., Figure 4.18l).

To better memorize these relationships and to facilitate the citation in the ensuing sections, the above relations are named as ‘‘Peanut law’’ by the author since the form of the distribution is resembling to a peanut in Figure 4.18.

It is necessary to state that the Peanut law is an empirical law based on the experiences in numerical study. It hasn’t been verified by any analytical demonstration and it is far from a mathematical theorem. However, with the help of the expression of the Johnson SU distribution (Equation 4.19), it is feasible to figure out a mathematical expression for the Peanut law through analytical study. More figures about the studied distributions are given in Figure I.6, Figure I.7 and Figure I.8.

4.4.3. Spatial distribution of fatigue damage along the tower

The last empirical analysis concerns about how the cumulative fatigue damage is distributed along the wind turbine tower from tower-base ($z = 0$ m) to tower-top ($z = 87.6$ m). Figure 4.19 illustrates the distributions over the cross section of the tower from gage 1 ($z = 2.19$ m) to gage 9 ($z = 85.41$ m) under NTM wind condition at mean wind speed $V_{mean} = 12.0$ m/s. Like in Figure 4.18, all distributions are plotted in radar chart where the orange dashed line represents the 1st quartile, the green line stands for the median and the red dashed line for the 3rd quartile. The gray surface surrounded by the orange line reveals the possible values for fatigue damage and identifies the most vulnerable spots at a certainty of 25%. The height of each tower gage is marked in the caption below each chart. All fatigue damage are normalized to

the same value 3×10^{-8} .

As expected, the fatigue damage drops significantly when the tower gage's height increases. The area of gray surface in Figure 4.19a is undoubtedly larger than that in Figure 4.19i. It should be pointed out that the area of surfaces in Figure 4.19 represent physically the value of fatigue damage.

The distributions keep the same peanut-like contour through all the tower gages. An eventual application of such study is to assess the total fatigue damage applied to the tower structure by alternating the tower gage by its height z and the local spot by its azimuth α . By this means, the probabilistic profile of fatigue damage given in Equation 4.14 switches from the discrete variable to the continuous variable.

$$\widehat{\mathbf{P}}(x, z, \alpha) = \mathbf{P}(x \mid \widehat{\theta}(z, \alpha)) \quad (4.21)$$

where, x = cumulative fatigue damage value $x \in \mathbb{R}^+$

z = height in cylindrical coordinate system $z \in \mathbb{R}$

α = azimuth angle in cylindrical coordinate system $\alpha \in [0, 2\pi]$

Calculating the integral of this probabilistic profile in cylindrical coordinate system with respect to the height z , from tower-base to tower-top, results in:

$$\widehat{\mathbf{P}}_{tower}(x, \alpha) = \int_0^{z_{tt}} \widehat{\mathbf{P}}(x, z, \alpha) dz \quad (4.22)$$

where, z_{tt} is the height (or elevation) at the tower-top.

Equation 4.22 describes the cumulative fatigue damage applied to the wind turbine tower with regard to the azimuth angle α . It indicates from which direction the tower is more probably damaged. The integral of Equation 4.22 with respect to the azimuth angle, from 0 to 2π will result in a probability distribution of the totally cumulative fatigue damage:

$$\widehat{\mathbf{P}}_{tower}(x) = \int_0^{2\pi} \int_0^{z_{tt}} \widehat{\mathbf{P}}(x, z, \alpha) dz d\alpha \quad (4.23)$$

Unlike the deterministic fatigue analysis which concludes the damage accumulated on the whole structure in a single value, Equation 4.23 gives a probability distribution for the overall fatigue damage applied on the wind turbine tower. The advantage of this probabilistic profile is evident, it allows to investigate the probabilistic features of the cumulative fatigue damage such as uncertainty, reliability, etc. on one side and on the other, it offers a way to avoid the oversizing design in engineering application and consequently reduce the cost of the wind turbine and improve its LCOE. More figures are attached in appendix for the distribution of fatigue damage at the different height of tower at cut-in speed (Figure I.9) and cut-out speed (Figure I.10).

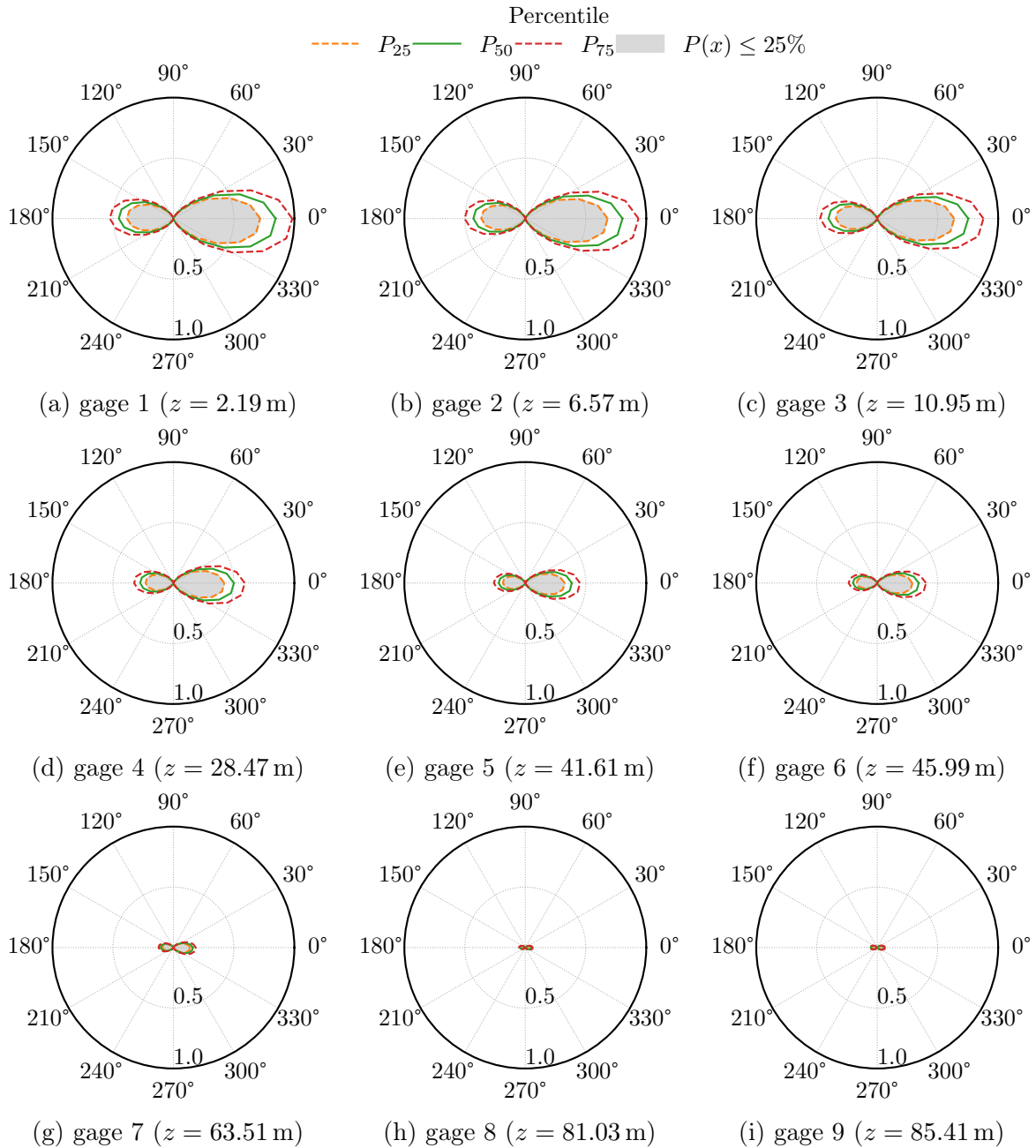


Figure 4.19: Distribution of 10-min cumulative fatigue damage at the different height of tower at mean wind speed of 12.0 m/s (damage value normalized to 3×10^{-8} in all charts)

4.4.4. Summary

This section has accomplished an empirical study on the numerical results obtained in Section 4.3.1. It discloses many implicit relations about the cumulative fatigue damage on the wind turbine tower facing to a turbulent wind condition in normal power production.

Based on the statistical experience in Section 4.4.1, the Johnson SU/SB distribution family seems to be the most appropriate probability function to describe the changes in fatigue damage with respect to the mean wind speed V_{mean} and the azimuth angle α .

Then, the analysis of the distribution of fatigue damage with respect to the mean wind speed V_{mean} in Section 4.4.2 results in an empirical theorem, Peanut law, to describe how the fatigue damage is spatially distributed in regard to the wind speed in probabilistic way.

Finally, the analysis of the distribution of fatigue damage with respect to the tower height z and the azimuth angle α in Section 4.4.3 results in a probability profile of the overall cumulative fatigue damage (Equation 4.23) which allows to assess the total damage in probabilistic fashion.

To sum up, the current section has demonstrated how to investigate the cumulative fatigue damage on wind turbine tower by applying the probabilistic framework proposed in the preceding section (Section 4.2). It offers the fundamentals to carry out an analytical study planned for the future work. An engineering application of this empirical analysis will be discussed in the next section.

4.5. Machine learning for probabilistic fatigue estimation

The novel framework proposed in above sections is extraordinarily time-consuming to have confident outputs for all wind speeds in the operating range between V_{in} and V_{out} . To evade this inconvenience, a surrogate model using the deep neural network (DNN) (a method based on artificial neural network (ANN) with multiple layers between the input and output layers) is designed in this section.

4.5.1. Machine learning and deep neural network

With the breakthrough in computer science in last decades, the machine learning (ML) algorithms have been broadly practiced in many fields including computer vision, natural language processing, computational engineering etc. As for wind energy industry, it has been proved efficient in wind speed forecasting, wind turbine structure optimization, wind blade optimization design and other scientific researches or engineering applications. Taking the fatigue assessment for wind turbine as an example, Slot et al. [Slo20] compared two surrogate models using Kriging and polynomial chaos expansion (PCE) and issued some recommendations to train surrogate models for fatigue estimation. Dervilis [Der13] proposed an auto-associative neural network (AANN) based approach for structural health monitoring (SHM) about wind turbine's blade. Sergio et al. [SL16] used deep learning (DL) techniques (a family of ML methods based on ANN with feature learning) to forecast hourly mean wind speed in Northeastern of Brazil. Similarly, Khodayar et al. [KT16] used a DNN to predict wind speed in short-term and ultra-short-term.

The high extensibility of DNN is an advantageous character to investigate many aere-elasto-strctural problems in wind turbine. For instance, Liu et al. [LZ17] coupled the DNN with the support vector machine (SVM) to anticipate the power productions of seven wind farms in Canada. Xiaosheng et al. [Xia16] used a derivative of DNN named multilayer restricted Boltzmann machine (MRBM) to achieve the same objective, wind power prediction, with better accuracy in prediction. Wang et al. [Wan17] engaged another type of DNN, convolutional neural network (CNN), for probabilistic wind power forecasting. Srivastava et al. [SDK19] applied recurrent neural network (RNN) as a surrogate model to investigate the effects of sloshing on the aeroelastic motion of the aero-structural system. A special kind of RNN, long short-term memory network (LSTM), is utilized by [LKZ19] to simulate numerically the aerodynamic and aeroelastic characteristics for an airfoil of a wind turbine blade pitching and plunging in the transonic flow across multiple Mach numbers.

In summary, many ML techniques, especially the deep neural network-related approaches, have proven their capability and efficiency in solving wind engineering problems. These circumstances inspire the author to develop a DNN based surrogate model to improve the proposed probabilistic framework of fatigue assessment in terms of computational efficiency and fidelity of predictions. To reach this goal, a multilayer perceptron (also called deep feedforward network) (MLP) of DNN is invoked in the following sections starting by a brief introduction to the neural networks.

4.5.2. Introduction to neural network

Multilayer perceptron (also called deep feedforward network) (MLP) [IL67] is a subclass of DNN that is founded on the several layers of artificial neurons [MP43]. It is composed of at least three layers, that is, an input layer, a hidden layer and an output layer. In the first-ever working for MLP from Ivakhnenko [Iva71], a DNN of eight layers has been introduced. Each layer consists of a different number of neurons and is fully connected to the adjacent layer. Each neuron involves a nonlinear activation function, except for those in input layer, to map the weighted inputs to the output. As a supervised learning method, the MLP adopts a backpropagation algorithm [RHW86] to train its feedforward neural networks. The MLP has been universally applied diverse files nowadays such as speech recognition, image recognition, regression analysis etc.

4.5.2.1. Topology of neural network

As mentioned, the architecture of MLP is a classical feedforward network which means that the information (or signal) flows through the functions being calculated from input dataset and finally to the outputs. The outputs of the neural network are not fed back into the network itself. The neural network is essentially built upon the artificial neurons and layers.

Perceptron

As for MLP, a special type of neuron, known as *perceptron* [Ros58], is introduced. Given a vector $\mathbf{x} = [x_1, \dots, x_j]^T, j \in \mathbb{N}$ representing a set of j numerical inputs, the perceptron associates the input vector \mathbf{x} with a weight vector $\mathbf{w} = [w_1, \dots, w_j]^T$ and then calculates the weighted sum as follows:

$$z = \mathbf{w}^T \cdot \mathbf{x} + b \quad (4.24)$$

where, \cdot is the inner product of matrices, b is a scalar value added to the input \mathbf{x} called *bias*. If the signal strength of \mathbf{x} is really trivial, the bias b ensures that at least a few perceptrons are activated to perform actions in case of low signal. The weighted sum z is subsequently fed to an activation function ϕ to output the result, i.e.:

$$h_{w,b}(\mathbf{x}) = \phi(z) = \phi(\mathbf{w}^T \cdot \mathbf{x} + b) \quad (4.25)$$

where, $h_{w,b}(\mathbf{x})$ denotes the output of the perceptron (namely *prediction function*). Figure 4.20 gives an graphic representation of the perceptron described above.

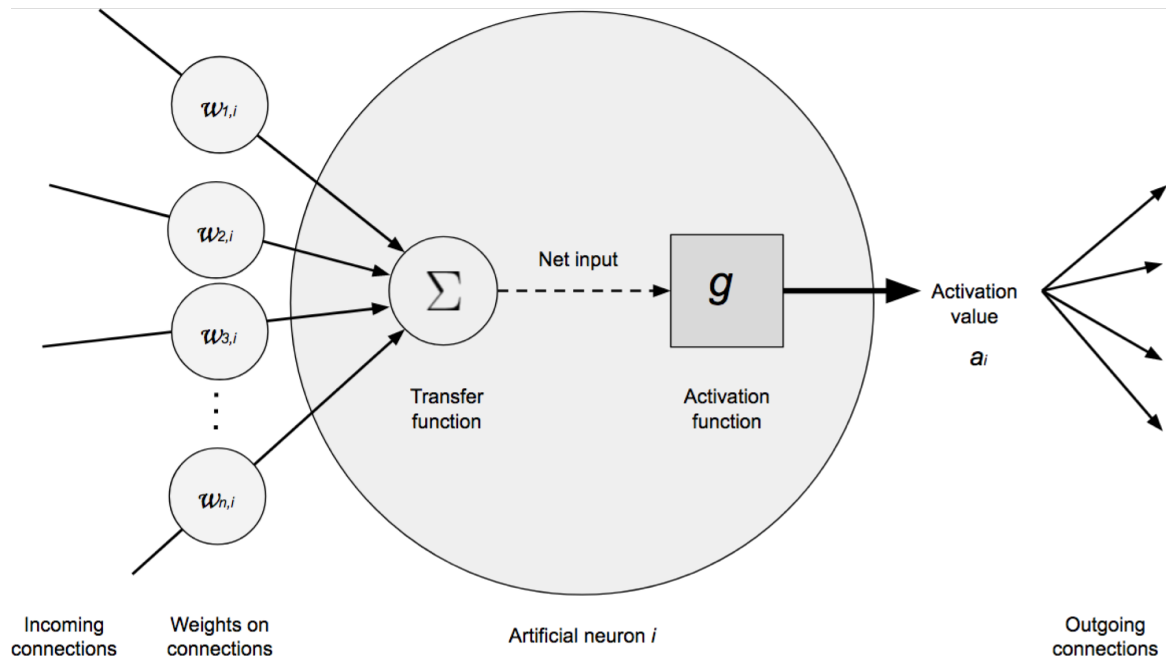


Figure 4.20: Illustration of a perceptron [PG17]

Activation functions

The activation function is crucial for neural networks since it determines the output of every perceptron and, by this means, governs the behavior of neural networks. In a MLP, the outputs from the activation function in any layer are also the inputs for the perceptrons in the next layer. In this manner, since the transmission in activation functions flows from the input to the output, it is therefore named as *forward propagation*. Some popular activation functions are listed below:

Heaviside step function (also known as *unit step function* [AS70]) is a discontinuous function that outputs 0 for negative inputs and 1 for non-negative inputs, i.e.:

$$\phi(z) = \begin{cases} 0 & \text{if } z < 0 \\ 1 & \text{otherwise} \end{cases} \quad (4.26)$$

Linear function describes a proportional relationship between the inputs and the outputs. This function is basically used in the input layer that passes the inputs through unchanged, i.e., $a = 1$.

$$\phi(z) = az \quad (4.27)$$

Hyperbolic tangent function is a continuous and differentiable function that outputs values between -1 and 1 . Empirical studies have shown that this function benefits a good accuracy in estimation for vast majority of MLP applications

[KO11].

$$\phi(z) = \frac{e^{2z} - 1}{e^{2z} + 1} \quad (4.28)$$

Sigmoid function is analogous to hyperbolic tangent function. It maps the independent inputs from infinite range into a normalized range between 0 and 1.

$$\phi(z) = \frac{1}{1 + e^{-z}} \quad (4.29)$$

Rectified linear unit (ReLU) function outputs 0 for all negative inputs but returns a linear relationship for non-negative inputs. Many researches have proven that ReLU function is really effective in practice [LM17; Aga19; ESH19] since its gradient is either zero or a constant which avoids the vanishing gradient issues.

$$\phi(z) = \max(0, z) \quad (4.30)$$

Architecture of network

The neural network architecture signifies how the neurons (perceptrons) are unified together to form a network. As for MLP, this is achieved by connecting multiple layers of perceptrons including:

Input layer is the first layer in the whole network that accepts the input values.

Typically, the number of neurons in this layer equals to the number of features in input dataset, i.e., dimension of input vector \mathbf{x} . In classical feedforward neural network, like MLP, the input layer is fully connected to all the neurons in the adjacent layer.

Hidden layer is the intermediate structure inside the model. A neural network can have only one hidden layer or hundreds, even more than thousands, layers. In fact, the overall number of layers inside a model defines the depth of the neural network and that's where the name "deep neural network (DNN)" comes from. In MLP, each hidden layer encloses a different number of perceptrons described above.

Output layer is the last layer in the model which, as indicated by its name, yields the outputs from the neural network. For regression problems, the output of the model will be a set of real values while for classification problems it will be a set of probabilities.

Figure 4.21 depicts a typical architecture of MLP. The values (both input and output) are shown by squares. The perceptrons defined above are plotted by circles in the figure and stacked vertically to constitute a layer. The arrows between two adjacent layers describe the direction of signal starting from the input layer (the most

left circles) and ending in the output layer (the most right circles). The dashed arrows on both sides illustrate the assignment between values and input/output layer.

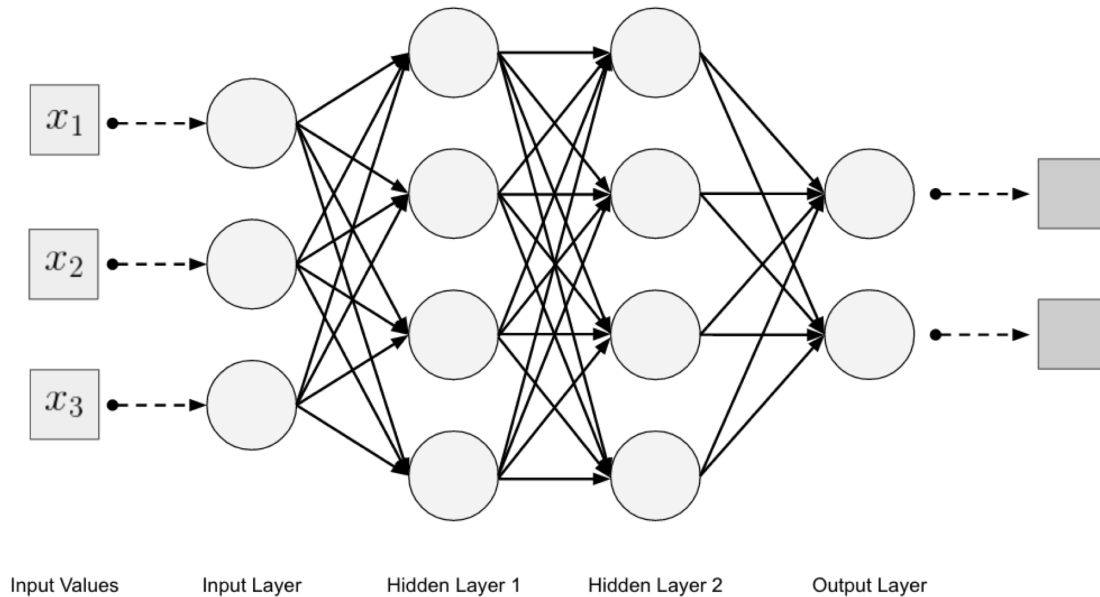


Figure 4.21: Illustration of a fully connected multilayer perceptron [PG17]

Connections

The neural network shown in Figure 4.21 is a classical setup of MLP named *full connected* since the connections between layers are the outgoing connections of all neurons in the previous layer to all neurons in the next layer. It should be pointed out that the layers are not always fully connected in all types of neural networks, for instance, convolutional neural network (CNN) [Goo16].

What's more, the connections between layers can also be established between non-adjacent layers. Take the residual network (ResNet) as an example, He et al. [He15] proposed this specially designed CNN using residual learning technique to improve the accuracy of the prediction. They bring skip connections (a.k.a. shortcut connections) into the neural network which allow the input of a layer to participate directly in the output of a layer located deeper in the neural network Figure 4.22.

He et al. [He15] have shown that the residual learning technique has seeded up remarkably the training process of an extremely deep CNN composed of 152 layers since the signal can flow faster through skip connections than that in a fully-connected neural network. Furthermore, a neural network with skip connections can be considered as a stack of certain small neural networks connected by skip connections.

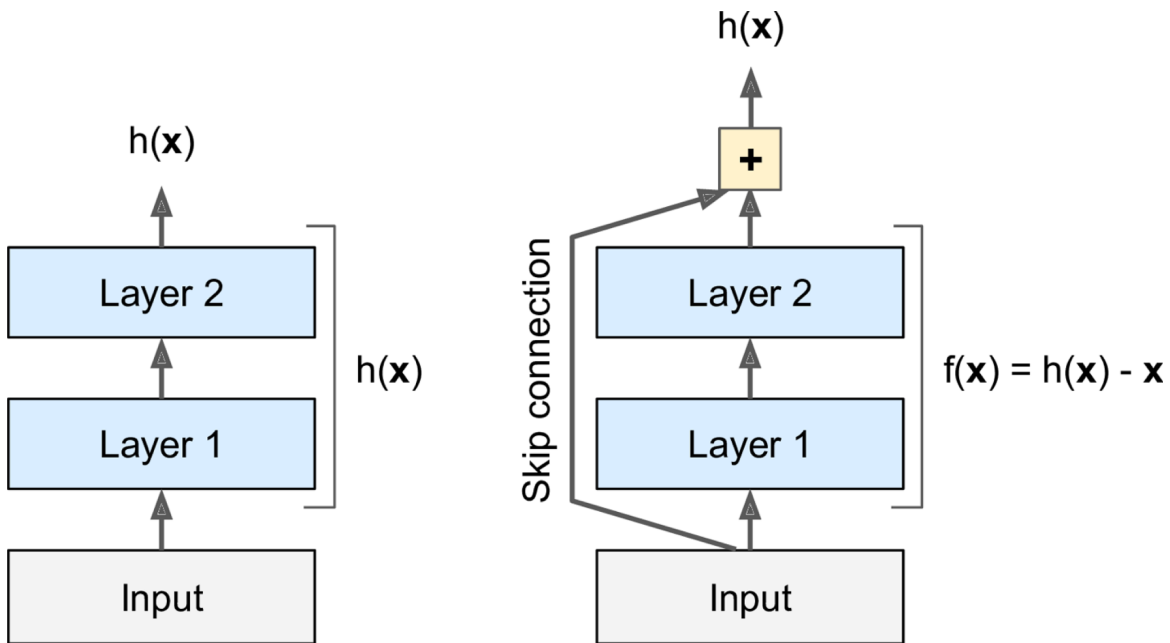


Figure 4.22: Illustration of residual network (ResNet) [Gér17]

Loss functions

A loss function (a.k.a. cost function or error function) is a function that measures the difference between the predictions of the neural network and the real output values. It quantifies how well a neural network is trained to give an accurate prediction. The function maps all the errors observed on the training dataset onto a single real number representing how close the neural network is to its ideal state.

With the help of this function, the problem of training an accurate neural network transforms into an optimization problem of minimizing the loss function through adjusting the weights and the biases of the entire neural network. Depending on the purpose of neural network (i.e., regression, classification or reconstruction), many loss functions have been developed to quantify the agreement between the predictions and the real outputs. Only the loss functions for regression model will be discussed in the following paragraph. Other loss functions can be easily found in many textbooks in deep learning [Goo16; Gér17].

Considering a dataset that has a number of M output features and each feature has a true value (a.k.a. labeled value) y_i for $i = 1, \dots, M$, the loss function of the neural network takes the weights \mathbf{w} and the biases \mathbf{b} of the entire model as the variables and returns intuitively an error estimated in the following ways:

Mean squared error (MSE) is the most commonly used loss function that estimates the average squared difference between the predictions and the true values. It penalizes outliers (i.e., extreme values) much more than other loss

functions.

$$\text{MSE}(\mathbf{w}, \mathbf{b}) = \frac{1}{M} \sum_{i=1}^M (h_{w,b}(\mathbf{x}_i) - y_i)^2 \quad (4.31)$$

Mean squared logarithmic error (MSLE) calculates the error in logarithmic space.

This is truly useful especially when the real value of output features is relatively small. It introduces an asymmetry in the error value and penalizes underfitting more than overfitting.

$$\text{MSLE}(\mathbf{w}, \mathbf{b}) = \frac{1}{M} \sum_{i=1}^M (\log h_{w,b}(\mathbf{x}_i) - \log y_i)^2 \quad (4.32)$$

Mean absolute error (MAE) is very close to mean squared error (MSE) except that it use the absolute value instead of the squared value for errors. Compared to MSE, MAE is not sensitive towards outliers and the optimal prediction will be the median value.

$$\text{MAE}(\mathbf{w}, \mathbf{b}) = \frac{1}{M} \sum_{i=1}^M |h_{w,b}(\mathbf{x}_i) - y_i| \quad (4.33)$$

Mean absolute percentage error (MAPE) enhances the MAE by normalizing the error in percentage.

$$\text{MAPE}(\mathbf{w}, \mathbf{b}) = \frac{1}{M} \sum_{i=1}^M \frac{100 \times |h_{w,b}(\mathbf{x}_i) - y_i|}{y_i} \quad (4.34)$$

Root mean square error (RMSE) measures the standard deviation of the errors that the neural network makes in prediction.

$$\text{RMSE}(\mathbf{w}, \mathbf{b}) = \sqrt{\frac{1}{M} \sum_{i=1}^M (h_{w,b}(\mathbf{x}_i) - y_i)^2} \quad (4.35)$$

4.5.2.2. Training mechanism

Before a neural network can be used in prediction, it must be trained first. When making predictions, the input values (a.k.a. *observations*) are fed to the model through the input layer. Then the model calculates the outputs of each successive layer and gives the predictions in the output layer. This information flow, as discussed in the last section, is the forward propagation, and the dataset used to train the neural network is called *training dataset*.

To train a neural network, Rumelhart et al. [RHW86] proposed a *backpropagation* algorithm that begins with measuring the error between the prediction and the true

value (a.k.a. *labeled data* or, more directly, *labels*) using a loss function defined in the preceding section. Then the algorithm computes the error contribution from each neuron in the last hidden layer to each neuron in the output layer. Next, it continues to measure how much of these error contributions came from each neuron in the previous hidden layer, and so on until the algorithm reaches the input layer. By such manipulation, the algorithm works out the error gradient across all the connections inside the neural network through propagating the error gradient backward in the network. That's where the algorithm gets its name from.

Finally, the backpropagation algorithm adjusts the connections (by changing their weights and biases) to make the predictions fit better the labels. In other words, the backpropagation algorithm tries to minimize the error of loss function by tuning the weighted matrix and biases matrix. From mathematical point of view, this procedure is actually doing gradient descent in parameter space of neural network where the gradient is on the error surface that defines the error between predictions and labels as a function of the parameters of the neural network. A detailed interpretation of backpropagation algorithm and the mathematical clarification on this algorithm can be found in [PG17].

At the end of each epoch (i.e., iteration) during training procedure, the fitted neural network is used to predict outputs for the observations in another dataset named *validation dataset*. In addition to the training dataset, the validation dataset is chiefly used to regulate the architecture of neural network, in other words, tune the hyperparameters, as discussed in the next subsection.

4.5.2.3. Regularization of neural network

Due to the flexibility of neural network, the architecture of network is highly problem-dependent. Take the MLP as an example, despite it is a fully-connected neural network, there are still many parameters that need to be defined by the end-user like the number of layers, the number of neurons per hidden layer and the activation function. These parameters are named as *hyperparameters* in machine learning as they control the outline of the model and tune the configurations of optimization algorithm used in training procedure.

In practice, the value of hyperparameters is mostly determined by following some recommendations from handbooks [Goo16] or from other relevant works using the similar model. Another approach is to implement a hyper-loop of optimization that consider the hyperparameters as design variables and the performance of the model as the objective function. The goal of this hyper-loop optimization problem is to seek an optimized combination of hyperparameters that maximize the performance of the machine learning model in terms of faster training, higher accuracy in prediction and better balance between overfitting and underfitting. To achieve this goal, three

principal algorithms are frequently used: grid search, random search and Bayesian optimization approach [Moc12]. The discussion about these approaches is beyond the scope of this manuscript. More details can be found in [Gér17].

4.5.3. Building a deep neural network for probabilistic fatigue analysis

In Section 4.2, a probabilistic framework of fatigue analysis is introduced. The framework is capable of estimating the cumulative fatigue damage in probabilistic fashion and presenting the damage distribution on the cross-section plane of wind turbine tower. However, since the method founds on the Monte Carlo approach, it requires a large number of samples (i.e., numerical simulations) to give a reliable approximation on real fatigue damage.

In Section 4.3.1, a total number of 230 000 runs (or simulations) have taken place to perform a complete fatigue assessment over the designed wind turbine, NREL 5MW reference wind turbine, whereas it has taken almost half a year to finish all the numerical simulations on a modern server¹. This computationally expensive experience impedes the application of the proposed framework in industry in which a rapid design process is usually required since the design of the product iterates fast.

To address the extreme time-consumption of the proposed framework of probability fatigue assessment, a surrogate model is needed. Attracted by the advantages of DNN and its large applications in wind energy presented in the last section, a MLP coupled with residual learning is proposed.

4.5.3.1. Preprocessing of data

Objective

As stated in the last paragraph, the goal of developing a surrogate model is to propose a reliable approximated model for the probabilistic framework of fatigue analysis. The surrogate model is expected to:

- be less time-consumption
- predict the distributions of cumulative fatigue damage as shown in Section 4.4
- predict the fatigue damage at mean wind speeds that have never been simulated

The fatigue damage discussed in this section is always the 10-min cumulative fatigue damage that have been already studied in the previous sections.

1. Intel(R) Xeon(R) CPU E5-2660 v4 @ 2.00GHz, 28 cores 56 threads, 256 GB memory, 2.5 TB hard disk

Preparing datasets

In order to build a neural network, the training dataset should be firstly prepared. The dataset should contain the input data and the true output data (labels). In the current work, the input is set to be the wind characterized by the mean speeds and the standard deviations in three directions in tower-base coordinate system (Section E.1), i.e.:

$$\mathbf{x} = \begin{bmatrix} \text{Mean}(V_x) \\ \text{Mean}(V_y) \\ \text{Mean}(V_z) \\ \text{Std.}(V_x) \\ \text{Std.}(V_y) \\ \text{Std.}(V_z) \end{bmatrix} \quad (4.36)$$

where, $\text{Mean}(\cdot)$ = arithmetic mean of wind speed during 10 min simulated time

$\text{Std.}(\cdot)$ = standard deviation of wind speed during 10 min simulated time

V_x = wind speeds in longitudinal direction (\vec{x}_t -axis)

V_y = wind speeds in lateral direction (\vec{y}_t -axis)

V_z = wind speeds in vertical direction (\vec{z}_t -axis)

As listed in Table 4.1, 23 cases of mean wind speed between V_{in} and V_{out} have been studied and each case has been evaluated 10 000 times with arbitrary wind conditions. A random selection of 1000 simulations at each case of mean wind speed is performed to compose an input matrix, i.e.:

$$\mathbf{X} = [\mathbf{x}_1, \dots, \mathbf{x}_{N_{train}}] \quad (4.37)$$

where, $N_{train} = 1000 \times 23 = 23000$ is the size of training dataset. The 10-min cumulative fatigue damage on tower gage 1 local spot 0 is defined as the labels for training the present neural network, i.e.:

$$\mathbf{Y} = [D_1^{(1,0)}, \dots, D_{N_{train}}^{(1,0)}] \quad (4.38)$$

Figure 4.23 reveals pairwise relationship between input data and labels. The inner correlations of input data are shown in blue dots, meanwhile, the correlation between input data and labels are colored in orange. The diagonal of the scatter plot matrix shows the histogram of each variable labeled in abscissa.

As suggested by Guyon [Guy97], the ratio between the training set size and the validation set size is close to 4:1 in this work, that is to say $1000 \times 25\% = 250$ simulations per mean wind speed resulting in a total of $250 \times 23 = 5750$ validation set size.

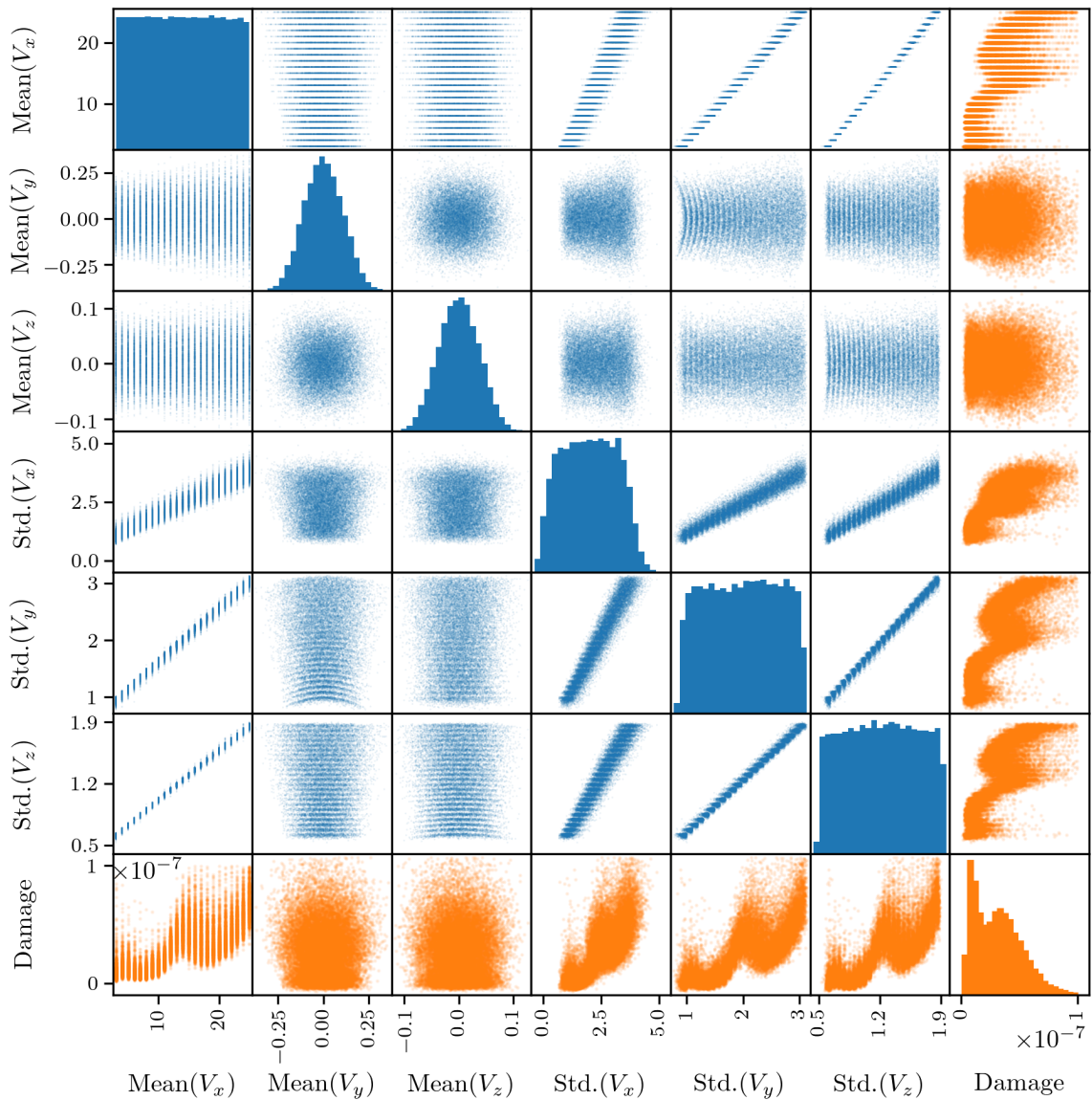


Figure 4.23: Scatter plot matrix of input data and labels

4.5.3.2. Design of residual multilayer perceptrons

In order to develop a deep neural network with residual learning for probabilistic fatigue assessment, the skip connections are introduced to an ordinary MLP. Figure 4.24 illustrates the overall architecture of the proposed neural network.

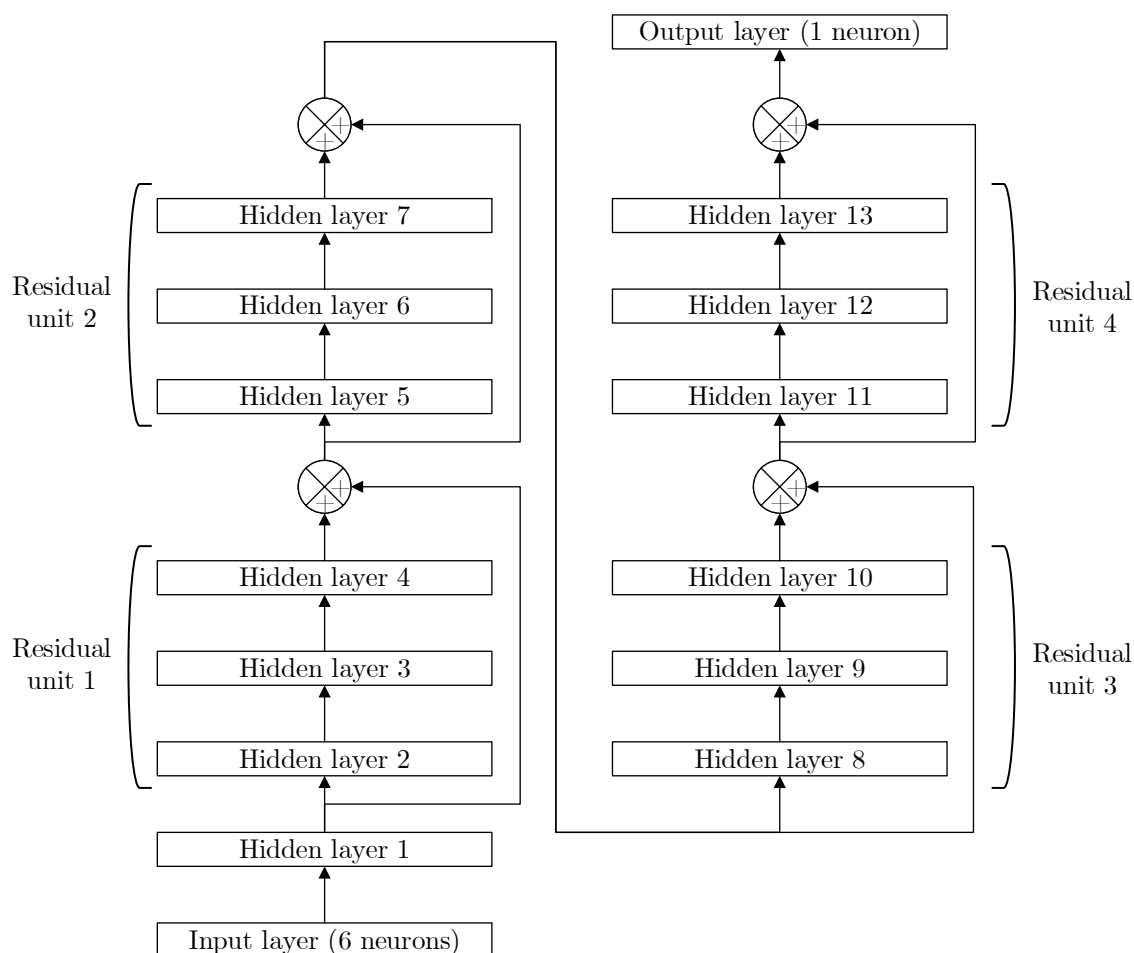


Figure 4.24: Architecture of the residual multilayer perceptrons (ResMLP)

In summary, four clusters of residual unit are implemented. Each cluster contains a three-layer perceptrons model and each layer consists of 300 perceptrons. The ReLU function (Equation 4.30) is used as the activation function for artificial neurons. Because the values of fatigue damage range from 0 to 1×10^{-7} (see Section 4.4), the difference between values are too small and insignificant. This may lead to an insensitive model and inaccurate predictions. In consequence, mean squared logarithmic error (MSLE) (Equation 4.32) is used to define the loss function of the proposed neural network since it expresses all values in logarithmic space and enlarges accordingly the tiny value of error between two damage values. All the hyperparameters of the proposed residual multilayer perceptron (ResMLP) are listed in Table 4.2.

Table 4.2: Hyperparameters for multilayer perceptrons using residual learning

Hyperparameter	Value
Number of residual units	4
Number of hidden layers	13
Number of perceptrons per input layer	6
Number of perceptrons per hidden layer	300
Number of perceptrons per output layer	1
Activation function	ReLU (Equation 4.30)
Loss function	MSLE (Equation 4.32)
Learning rate	0.001
Maximum number of epochs	1000

4.5.4. Results and discussions

As illustrated in Figure 4.25, the designed neural network returns a remarkably small MSLE between the predicted value and the true value for both the training dataset (blue line) and the validation dataset (orange dashed line). The training dataset error drops significantly after the first 100 epochs and retains below 0.2×10^{-3} till the end. To put it another way, the difference between the predicted fatigue damage and the real damage and is intuitively less than 0.02%. However, the error in validation dataset fluctuates during the entire training procedure. To determine at which epoch the neural network reaches its optimal performance, i.e., neither underfitting nor overfitting, the loss history is regraphed in Figure 4.26 where the ordinates are scaled to logarithm base 10.

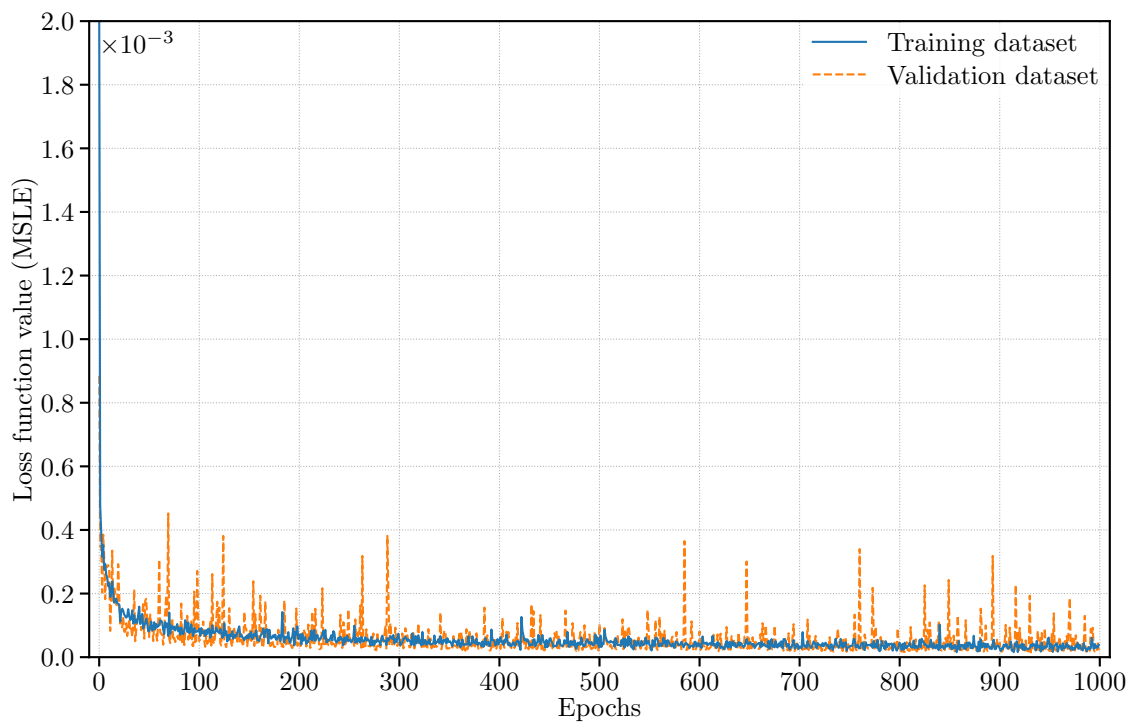


Figure 4.25: Loss history of the proposed neural network

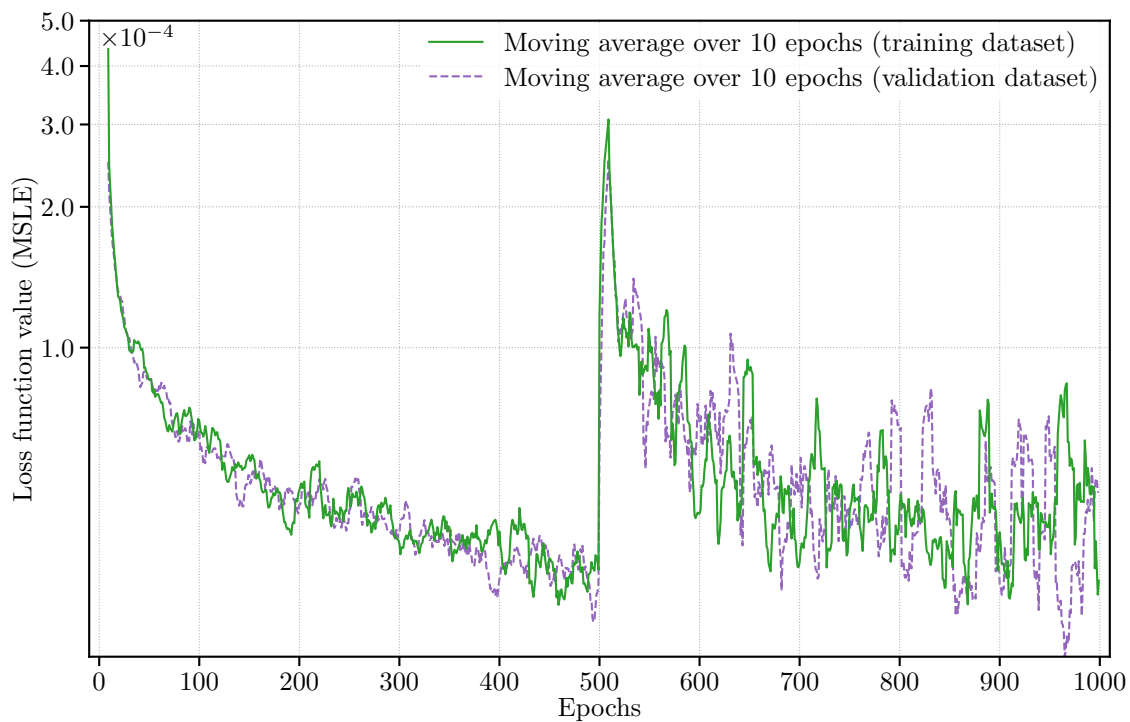


Figure 4.26: Semi-log plot of moving average of loss history

To better observe the trend of changes in loss history, the simple moving average value of loss function is calculated over a period of 10 epochs for the training dataset

(green line) and the validation dataset (purple dashed line) in Figure 4.26. It is clear that the MSLE is reduced successively between 0 and 500 epochs in training procedure. The error bounce up after 500 epochs and fluctuate till the maximum number of epochs. This refers to an overfitting in the trained model [Die95]. Just before the leap in moving average of MSLE, at the 493th epoch, the error value is relatively small in validation dataset along with training dataset. This indicates that the fitted model is optimized and shall be used in the following tests.

The trained network is expected to address two majors problems:

1. predict the probability distribution of 10-min cumulative fatigue damage at mean wind speeds that have never been shown in training process of the proposed neural network.
2. predict the overall distribution of 10-min cumulative fatigue damage for stochastic mean wind speeds between V_{in} and V_{out} .

The effectiveness of the predictions from ResMLP are then assessed by comparing with the results from the high-fidelity simulations in FAST.

4.5.4.1. Predicting cumulative fatigue damage at given mean wind speeds

Firstly, the trained model is used to predict the fatigue response of NREL 5MW reference wind turbine under the same wind condition DLC1.2 presented in Section 4.3.1 but at different mean wind speeds. A new dataset is generated to evaluate the accuracy of the prediction using the proposed probabilistic framework for fatigue analysis (Section 4.2) and the same numerical settings (Table 4.1) except that the mean wind speeds are drawn from [3.5, 4.5, \dots , 24.5]. These cases of mean wind speed have never appeared in the training dataset nor in the validation dataset. Likewise, the number of simulations per mean wind speed is also fixed to 10 000 runs which implies a total of 220 000 simulations in FAST codes. The 10-min cumulative fatigue damages acquired in these numerical simulations are compared to that obtained from the trained neural network in Figure 4.27. To keep this dissertation to be brief, only the comparison at $V_{mean} = 3.5$ m/s (close to V_{in}), 11.5 m/s (close to V_{rate}) and 24.5 m/s (close to V_{out}) are graphed in Figure 4.27. The full comparisons for all tested mean wind speeds can be found in Appendix I including Figure I.11, Figure I.12, Figure I.13, Figure I.14, Figure I.15 and Figure I.16.

The correlation between the predicted damages and the simulated damages are shown in Figure 4.27a, Figure 4.27c and Figure 4.27e along with the histograms compared in Figure 4.27b, Figure 4.27d and Figure 4.27f, respectively. The correlation plots prove that the predicted values are mostly conformed to the simulated values of the fatigue damage. Among 10 000 points at each mean wind speed, only tens

of points are away from the linearly correlated line (red line). The histograms also confirm this high correlation by comparing the probability density of the simulated values (blue bars) to the predicted values (orange bars).

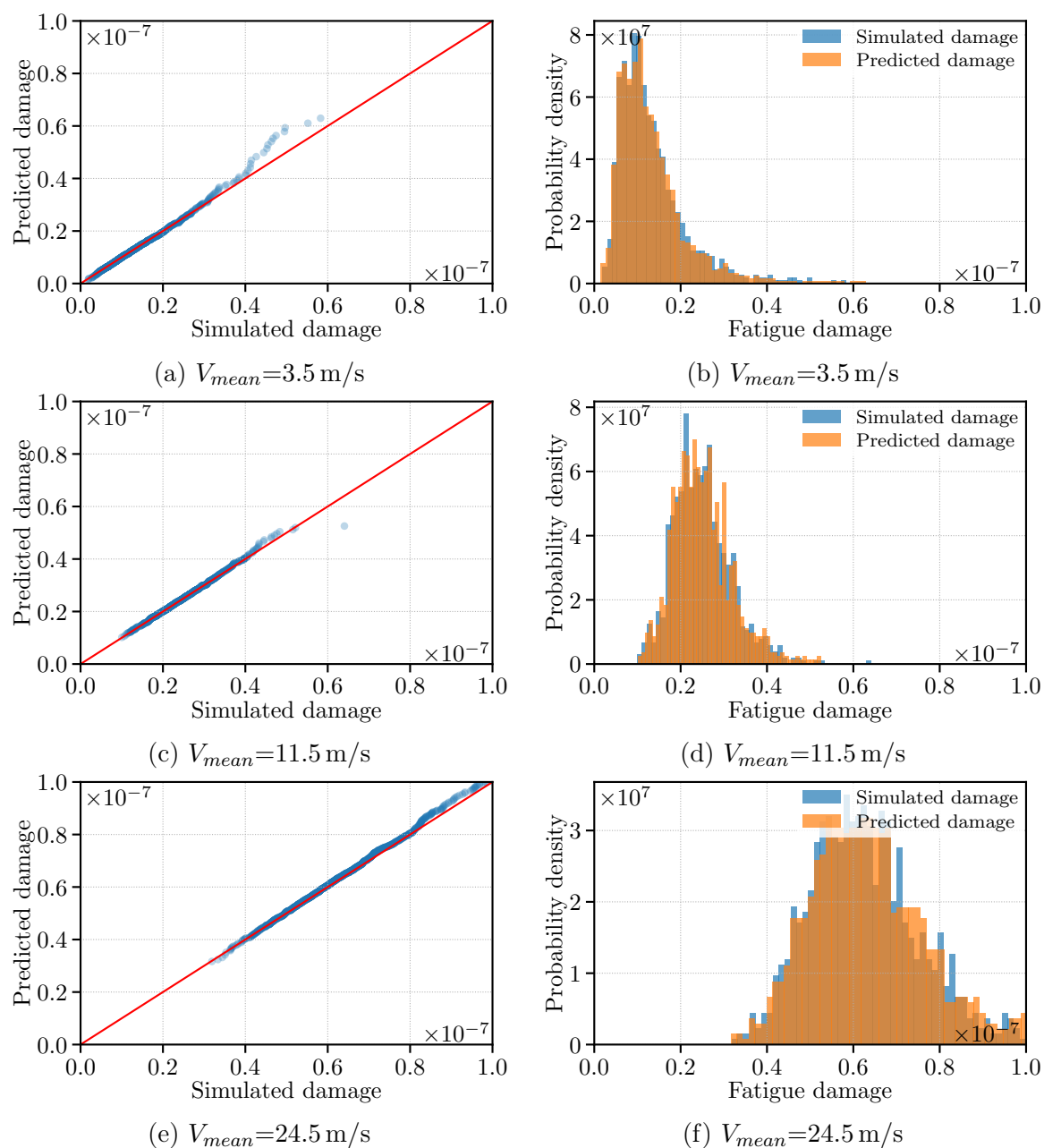


Figure 4.27: Comparison between the predicted values and the simulated values for 10-min cumulative fatigue damage at mean wind speed of 3.5 m/s, 11.5 m/s and 24.5 m/s in: (a, c, e) correlation plot and (b, d, f) histogram

The good accuracy of the trained neural network in predicting 10-min cumulative fatigue damage for untested mean wind speeds encourages the author to use it in predicting the fatigue response of the wind turbine tower under stochastic mean wind speeds.

4.5.4.2. Predicting cumulative fatigue damage under stochastic mean wind speeds

Following to the success in predicting the 10-min cumulative fatigue damage at some mean wind speeds presented in the previous section, another ambition about the application of the trained neural network is to predict the fatigue damages at any mean wind speed between V_{in} and V_{out} . To achieve this goal, a new dataset is generated with a size of 10 000 mean wind speeds. The V_{mean} values are randomized uniformly from the range $[3.0, 25.0]$.

The cumulative fatigue damages computed by using FAST codes and the proposed probabilistic framework for fatigue assessment are used as the reference data for comparison. The predictions made by the trained neural network are then compared to the reference data to evaluate the predicting accuracy. Like in Section 4.5.4.1, the difference between the simulated value and the predicted value is quantified by Pearson correlation coefficient and the p -value of K-S test in Figure 4.28.

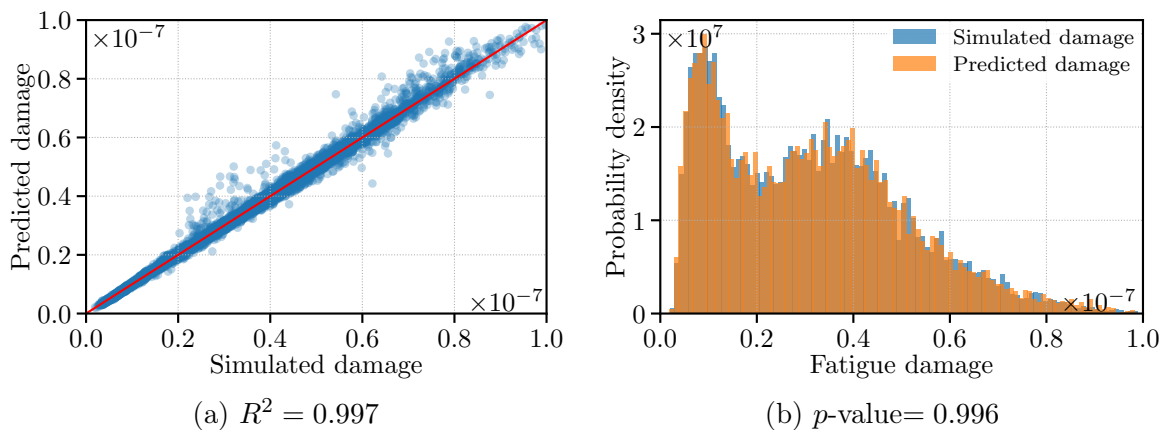


Figure 4.28: Comparison between the predicted values and the simulated values for 10-min cumulative fatigue damage in 10 000 cases of stochastic mean wind speed between V_{in} (3.0 m/s) and V_{out} (25.0 m/s) in (a) correlation plot and (b) histogram

The trained neural network shows again a high accuracy in predicting cumulative fatigue damage on the wind turbine tower. The correlation coefficient R reaches 0.997 indicates that the majority of predicted damages correspond to the damage calculated from the numerical simulation. The p -value of K-S test between the sample of predictions and the sample of simulations is 0.996 which implies that the null hypothesis, i.e., the two samples are drawn from the same distribution, cannot be rejected statistically. The distribution of the 10-min cumulative fatigue damage over the mean wind speed range is shown in Figure 4.29 where the simulated values are plotted in blue squares and the predicted values are plotted in orange circles.

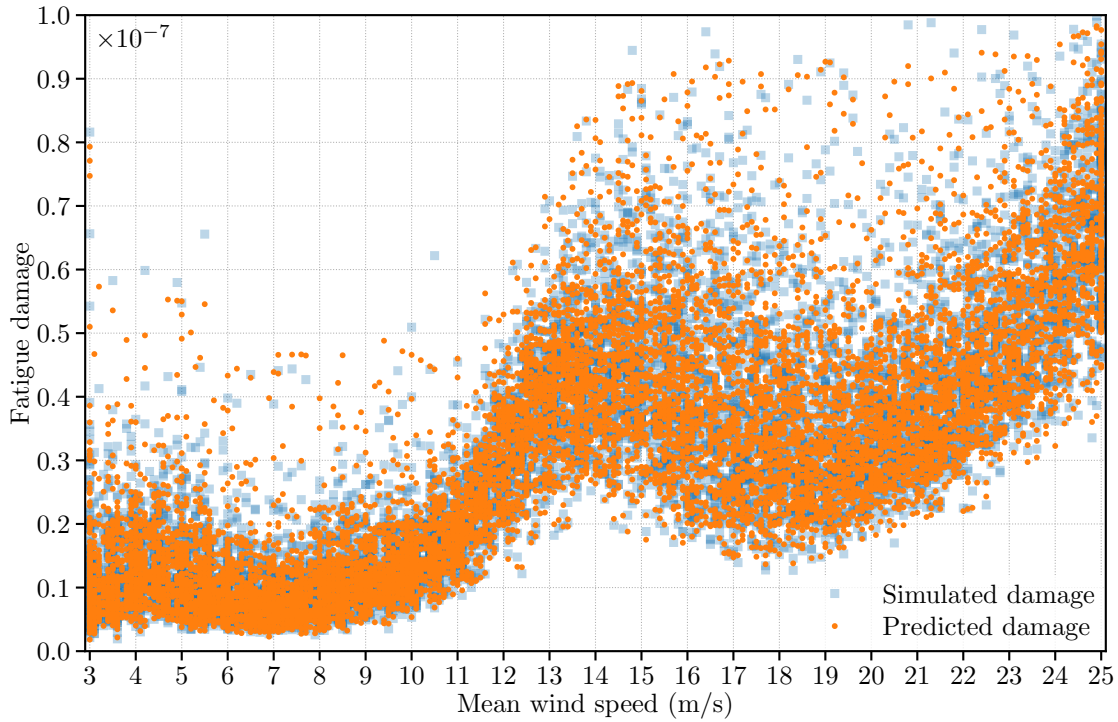


Figure 4.29: Illustration of the predicted values and the simulated values for 10-min cumulative fatigue damage in 10 000 cases of stochastic mean wind speed between V_{in} (3.0 m/s) and V_{out} (25.0 m/s)

4.5.5. Summary

In this section, a surrogate model using the a deep neural network with residual learning (ResMLP) is developed for the probabilistic framework of fatigue analysis described in Section 4.2. The model implements a 13-hidden-layers neural network with 300 perceptrons on each layer to predict the 10-min cumulative fatigue damage of the NREL 5MW reference wind turbine under wind with turbulence. The reference wind turbine is assumed to generate the electrical power normally during a fixed simulated time of 10 minutes.

A sample including 23 000 observations for training dataset and 5750 observations for validation dataset is used to train the ResMLP. The accuracy of the predictions from the trained model are assessed by comparing with the numerical results computed from FAST simulator. It is demonstrated that the surrogate models can accurately and economically predict the distribution of 10-min cumulative fatigue damage for any mean wind speed in the operating range, i.e., $[V_{in}, V_{out}]$. This advantage opens the opportunity to implement the proposed probabilistic framework for fatigue assessment in wind energy industry in which a quick-response design process is usually required. An example of applying ResMLP to design a wind turbine is interpreted in the next section.

Despite the proposed ResMLP has shown an excellent performance in predicting fatigue damage in probabilistic fashion, some improvements for ResMLP or another kind of model are planned for the future:

1. optimize the performance of ResMLP by calibrating its hyperparameters such as number of layers, number of perceptrons per layer, etc.;
2. integrate more new features (e.g., height of tower gage z_i and angle of local spot θ_j) into the decision variables;
3. predict directly the probability distribution of 10-min fatigue damage by using other machine learning models such as mixture density network (MDN) [Bis94].

4.6. Application: long-term fatigue life estimation of wind turbine tower in Caen

To give an example about how the novel framework of fatigue assessment from Section 4.2 and the Peanut law from Section 4.4.1 can help us in design of wind turbine, a probability based design of wind turbine tower is demonstrated in this section considering the real-world environment. The wind data involved in this application issues from the Project M2NUM (Mathematical Modeling and NUMerical simulation) [LMI14b]. Moreover, the neural network based surrogate model described in Section 4.5 is applied to accelerate the design process.

Project M2NUM, supported by the European Regional Development Fund (ERDF) and France, is a project focusing on the mathematical modeling of problems stemming from different applications. One of its sub-themes, named Project E@lin (EOlien LMI INSA) [LMI14a], had developed cutting-edge technologies for rigorous wind velocity field approximation from sparse datasets. The datasets used in their work [Roy13] had been measured in several cities in Normandy, France, such as Rouen, Caen, Le Touquet, Octeville etc. With these real-world datasets, a yearly wind profile can be established statistically, for example, Figure 4.30 shows the wind resource in Caen measured in a whole year.

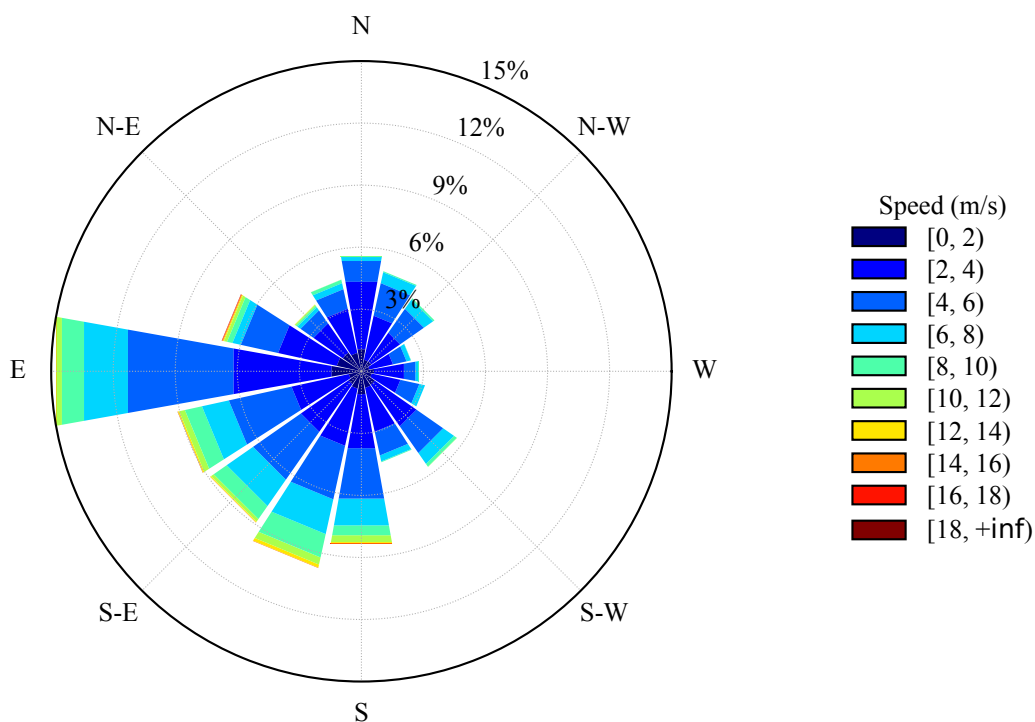


Figure 4.30: Wind rose plot of wind conditions in Caen (France) during 1 year

Figure 4.30 illustrates a succinct view of how wind direction together with speed are typically distributed in Caen, Normandy, France by using wind rose plot, a graphical tool based on polar coordinate system (Section E.2). The radial axis shows the frequency of winds over a period of one year, and the exterior circle shows the direction of wind. The wind speed ranges are colored by the band given in the legend and stacked each other according to the same direction. The direction of the longest spoke betokens the wind direction with the highest frequency, that is, from West.

4.6.1. Prediction of fatigue life using numerical simulations

Suppose that a wind turbine with the same characteristics of NREL 5MW reference wind turbine would be planted near Caen and expected to produce nonstop electrical power for 20 years, that is to say, a 20-years NTM wind condition along with the normal power production. From the Peanut law stated in Section 4.4.2.2, it is reliable to assume that the wind turbine tower is suffered to fatigue loads following the Johnson SU distribution. By this means, the distribution of the 10-min cumulative fatigue damage over the entire tower can be deduced (like that in Figure 4.19).

Calculating the integral of Equation 4.23 will bring out a probability function of the fatigue damage for every design mean wind speed. This stage corresponds to the line 3 in Algorithm 4.3. Next, from the wind rose in Caen (Figure 4.30), the probability

of wind speed in each direction can be provided (line 4 in Algorithm 4.3). Finally, an overall profile of fatigue damage on a NREL 5MW-like wind turbine built in Caen is established and interpreted graphically in Figure 4.31.

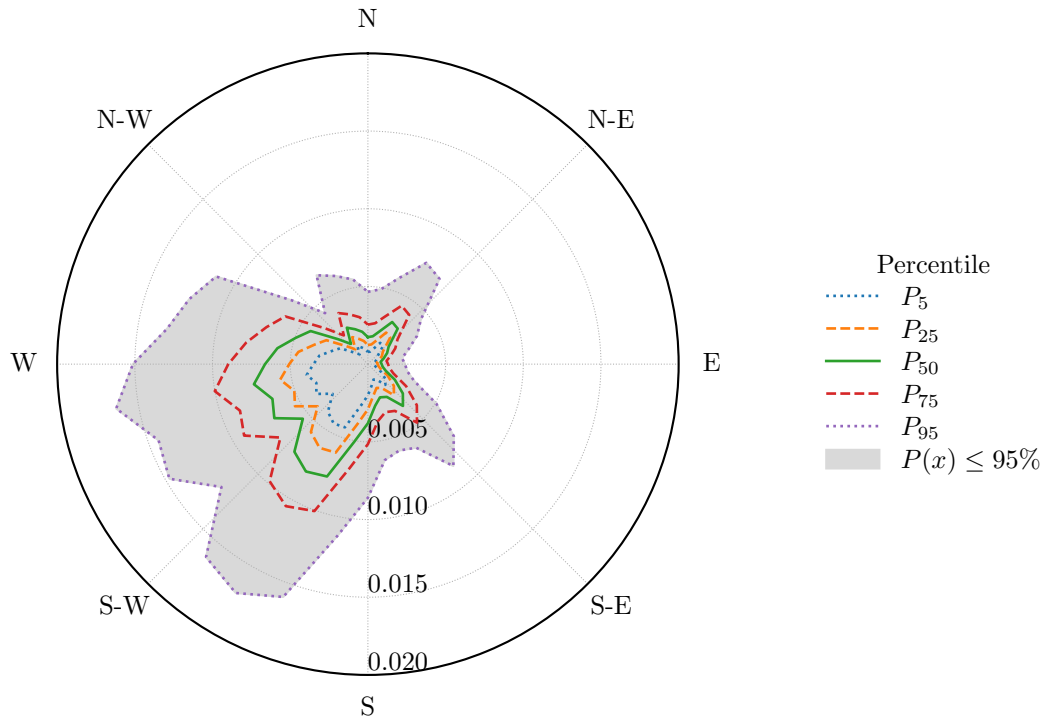


Figure 4.31: Prediction of cumulative fatigue damage for all directions at the end of 20 years

Like the wind rose plot (Figure 4.30), the exterior perimeter in Figure 4.31 represents the direction of wind whereas the radial axis represents the fatigue damage accumulated during 20 years. The estimated fatigue damage on five percentiles have been plotted, that is, 5th, 25th (1st quartile), 50th (median), 75th (3rd quartile) and 95th percentile highlighted by blue dotted line, orange dashed line, green line, red dashed line, purple dotted line, respectively. For the last percentile P_{95} , the surface enclosed by its purple dotted line is colored in gray. The surface area of the gray zone corresponds to the overall fatigue damage applied to the entire wind turbine tower at a probability of 95%.

Although the major wind direction in Caen is West, i.e., 15% of a year has the wind coming from this direction as shown in Figure 4.30, the fatigue damage is most presumably accumulated between the West and South part of the tower as shown in Figure 4.31. This result implies that the cumulative fatigue damage over the wind tower depends on not only the major direction of wind, but also the distribution of wind speed.

An outcome from the spatial probability distribution of damage shown in Fig-

ure 4.31 is that it predicts the high potential damaged location on the cross-section of the tower and offers a way to choose the location of openings (for instance, the door on the lowest segment of tower) in a reliability manner.

Another application for the presented result is to predict the overall fatigue damage in a probability fashion. Considering a certainty of 95% (i.e., the gray zone in Figure 4.31), the overall fatigue damage (i.e. the area of gray surface) equals to 0.31. In another word, the prediction of cumulative fatigue damage to wind tower in Caen at the end of 20 years is 0.31. Physically, it means that 31% of its design fatigue life is consumed during 20 years in condition of nonstop power production under NTM wind, and furthermore, there is 95% of chance to have a consumption equal or lower than this percentage.

4.6.2. Prediction of fatigue life using neural network

In the last section, the design process involves the numerical results obtained in Section 4.3.1 to assess the fatigue damage accumulated during the design lifetime of wind tower. This process leads to a high-fidelity assessment on cumulative fatigue damage but has two main drawbacks:

1. as stated previously in Section 4.5.3, the numerical simulation based design process is computationally expensive. This impedes the design optimization of the wind tower in which a quick fatigue assessment is usually required.
2. since it is impossible to simulate the response of wind turbine under all mean wind speeds, a trade-off between the precision of fatigue assessment and the increment of mean wind speed has to be chosen. In Section 4.6.1, the step-size of mean wind speed is fixed to 1.0 m/s.

The ResMLP introduced in Section 4.5 can handle the above shortcomings as it can predict accurately and economically the 10-min cumulative fatigue damage for any mean wind speed between V_{in} and V_{out} .

However, since the angle of local spot θ_j has not included in ResMLP yet, it is necessary to train more ResMLPs for predicting fatigue damage accumulated in all directions on the cross-section of the wind tower. The effectiveness of prediction made by ResMLPs is evaluated by comparing with that from FAST simulations (Figure 4.31) at percentiles P_{25} , P_{50} , P_{75} and P_{95} . As shown in Figure 4.32, if the value predicted by ResMLP is greater than that from FAST simulation, the fatigue damage is overestimated and colored by green, otherwise, it is underestimated and colored by red.

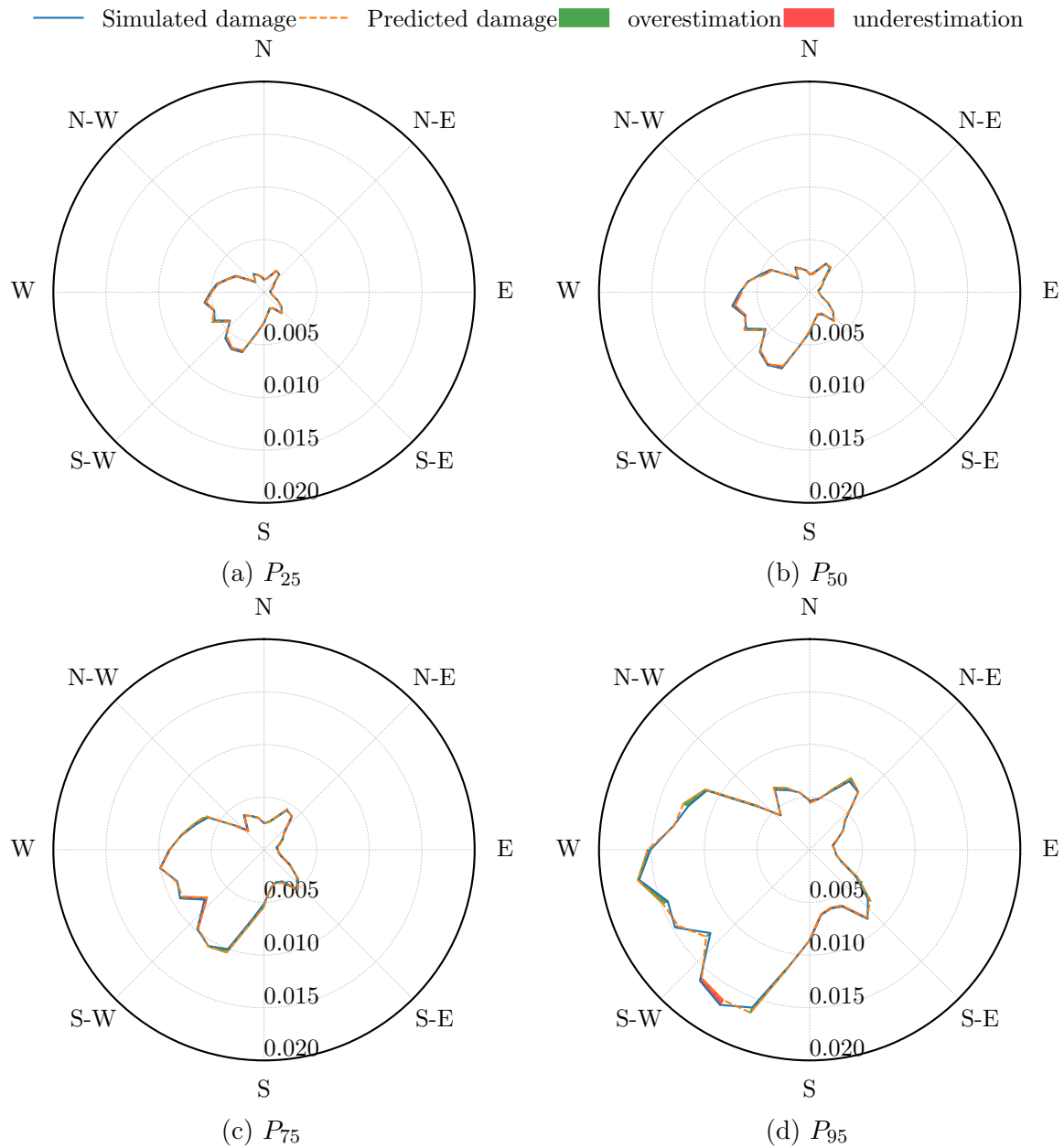


Figure 4.32: Prediction of cumulative fatigue damage for all directions at the end of 20 years using FAST numerical simulator and ResMLP surrogate model

It is hard to tell the difference between the predictions made by these two models. A slight difference can be observed for fatigue assessed at percentile P_{95} (Figure 4.32d), but the magnitude of difference is too small and hence negligible. The surrogate model ResMLP shows again its high effectiveness in offering an accurate prediction for long-term fatigue assessment.

4.6.3. Summary

In conclusion, the assessment of tower's fatigue life in this part gives a full example about how to predict the fatigue life in a probability background using the algorithm proposed in Section 4.2.3.2. It also shows how to apply the results issued from the probability studies (Section 4.4) and the neural network model ResMLP to solve real-world problems in engineering design of wind turbine tower.

4.7. Conclusions

Based on the deterministic fatigue analysis, a novel probability framework of fatigue assessment is proposed in this chapter. Although the framework is applied to the wind turbine tower in this context, it is also applicable to deal with other fatigue problems. For instance, a tubular structure that can be also considered as a cantilevered beam model such as chord in jacket foundation, wind turbine blades, chimney etc.

Under stochastic wind conditions during the normal production phase of wind turbine, the proposed approach offers a way to get the probability distribution of cumulative fatigue damage on the cross-section at different heights of the wind tower. Coupling the current approach with a distribution of wind speed, a probability based design of wind turbine tower can take place.

The deep neural network involved in this part, ResMLP, makes the proposed framework to be easily practiced in industry. The network offers a perfect accuracy in prediction and an outstanding efficiency in computational cost. A typical drawback of such surrogate model is how to tune its hyperparameters to be neither overfitted nor underfitted. This leads to a Bayesian optimization searching for the optimal hyperparameters of DNN. Among all available algorithms for solving hyperparameter optimization [Ber11], the evolutionary algorithms (EAs) are proved to be a suitable and efficient solution in recent years [AD19; BSS18; LH16]. Hence, a variant of EA is proposed in Chapter 6 and expected to optimize the hyperparameters of ResMLP network.

Lastly, it should be noted that the analysis of fatigue loads on DLC1.2 given in this chapter is denoted as the scenario F which, as planned, will be used in the next chapter to evaluate the performance of the active damper in regard to fatigue loads.



Part III



Chapter 5

Design of an active damping system for wind turbine

To address the overloading problem due to wind gust and technical fault elucidated in Chapter 3 and the fatigue loading due to turbulent wind interpreted in Chapter 4, an active damping system for wind turbine is proposed in this chapter. The system is based on an active damping device named TRD that uses the centrifugal forces of eccentrically rotating masses to damp the structural vibrations.

The basic layout of TRD is firstly reviewed and the control algorithm is also summarized. Then an integration of such device into the wind turbine tower is proposed including a structural design in engineering, an integration to the control system and an implementation in computer codes. The effectiveness and the weakness of the proposal is evaluated in the last section. The chapter ends in a conclusion with perspective work.

5.1. Twin rotor damper (TRD)

Twin rotor damper (TRD) is a type of active damper invented by U. Starossek [Sta15] and patented by Soletanche Freyssinet [Sta13]. Unlike all kinds of dampers reviewed in Section 1.3.2, TRD founds on the centrifugal forces produced by two eccentric control masses that rotate about two parallel axes (Figure 5.1). Moreover, this kind of damping device has never been studied in the context of wind turbine. In the following sections, a feasibility study for the such damper regarding the active vibration control for the wind turbine tower is to take place.

5.1.1. Design of TRD

Figure 5.1 sketches the fundamental layout of TRD in which two control masses of $\frac{m_c}{2}$ are hinged eccentrically to two actuators. The mass of two rods that connect the control masses to the axes of rotation is considered as ignorable. The length of these rods, denoted as r , is named as the *radius of TRD*. The angular position $\phi(t)$ determines the motion of two rotors, i.e., the control mass with mass-less rod.

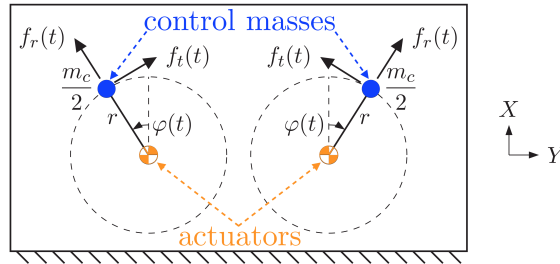


Figure 5.1: Layout of twin rotor damper (TRD) [BS16]

When the rotors are stabilized, i.e., the position of rotors is fixed $\dot{\phi}(t) = 0$, there is not generated force but a total mass of m_c corresponding to the sum of two control masses.

When the rotors are in motion, i.e., the angular velocity of rotors is not null $\dot{\phi}(t) \neq 0$, the centrifugal forces, or radial forces, $f_r(t)$ are generated in the direction away from the axes of rotation (Figure 5.1).

$$f_r(t) = \frac{1}{2} m_c r \dot{\phi}(t)^2 \quad (5.1)$$

When the rotors are accelerated, or decelerated, additional forces are generated in the tangential direction, marked as $f_t(t)$ in Figure 5.1.

$$f_t(t) = \frac{1}{2} m_c r \ddot{\phi}(t) \quad (5.2)$$

If the angular positions of two rotors are the same, the components of the centrifugal forces $f_r(t)$ and the tangential forces $f_t(t)$ in the direction of Y are canceled each other, while the components in the direction of X are superimposed. The resultant force, produced by the TRD, can be described as:

$$f_{TRD}(t) = m_c r [\dot{\phi}(t)^2 \cos \phi(t) + \ddot{\phi}(t) \sin \phi(t)] \quad (5.3)$$

If the angular positions of two rotors are uneven, the resultant force consists of a moment, perhaps and a force, is detailed in this thesis [Sch14].

5.1.2. Operating modes

5.1.2.1. Mode 1: continuous rotation mode

Assuming that both rotors are driven with a constant angular speed $\dot{\phi}$, i.e., $\ddot{\phi}(t) = 0$, Equation 5.3 can be simplified into:

$$f_c(t) = m_c r \dot{\phi}^2 \cos \phi(t) \quad (5.4)$$

where, $\phi(t)$ is the angular position that changes proportional to time:

$$\phi(t) = \dot{\phi}t + \phi_0 \quad (5.5)$$

where, $\phi_0 =$ the initial angular position of control mass

$\dot{\phi} =$ the constant angular speed

From mechanic point of view, $f_c(t)$ in Equation 5.4 is a harmonic force with the constant amplitude $m_c r \dot{\phi}^2$ and the initial direction of ϕ_0 .

5.1.2.2. Mode 2: swinging mode

Assuming that both rotors are driven with an inconstant angular speed $\dot{\phi}(t)$, i.e., $\ddot{\phi}(t) \neq 0$, the term of tangential force in Equation 5.3 is nonzero. In fact, in this mode, it is the tangential force that is chiefly used to damp the vibrations. Therefore, the TRD must keep accelerating and decelerating in order to create the desired resultant force. In this way, the TRD can be considered as a conventional active mass damper [Gaw04] that produces damping action by continuously accelerating and decelerating control masses. However, this mode will not be handled in this dissertation, further information about this mode and the associated control algorithm is discussed in [Bäu14].

5.1.3. TRD in single degree of freedom oscillator

Considering a single degree of freedom (SDOF) oscillator combined with a TRD described in Figure 5.2, the entire oscillating system is characterized by the stiffness k , the damping coefficient c and the total mass $m + m_c$, where m stands for the mass of oscillator and m_c for the mass of TRD.

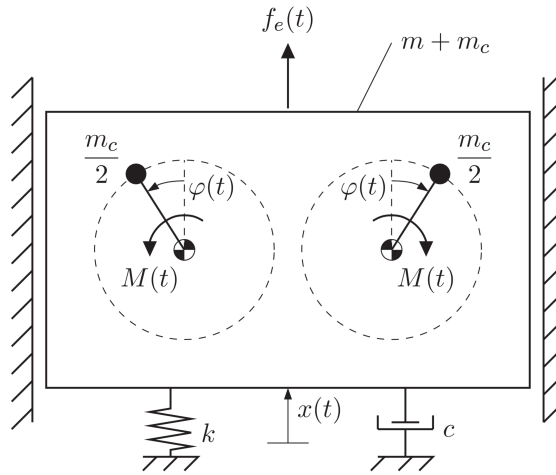


Figure 5.2: TRD for single degree of freedom (SDOF) [BS16]

5.1.3.1. TRD for free damped vibration

If a free vibration (Section 1.3.1.2) takes place, i.e., the angular velocity of rotors is zero $\dot{\phi}(t) = 0$, the TRD doesn't generate the forces in this case. The equation of motion for SDOF oscillator is:

$$(m + m_c)\ddot{x}(t) + c\dot{x}(t) + kx(t) = 0 \quad (5.6)$$

Dividing Equation 5.6 by the total mass $(m + m_c)$ on both sides results in:

$$\ddot{x}(t) + 2\xi\omega_n\dot{x}(t) + \omega_n^2x(t) = 0 \quad (5.7)$$

where, ω_n is the natural angular frequency given in Equation 1.3 and ξ is the damping ratio given in Equation 1.9.

5.1.3.2. TRD for forced damping vibration

If the SDOF oscillator is excited by an external force $f_e(t)$, the TRD will turn on, that is, the angular velocity of rotors is nonzero $\dot{\phi}(t) \neq 0$. The equation of motion in

this case matches the forced damping vibration (Section 1.3.1.3):

$$(m + m_c)\ddot{x}(t) + c\dot{x}(t) + kx(t) = f_{TRD}(t) + f_e(t) \quad (5.8)$$

Taking Equation 5.3 into consideration, the above equation yields:

$$(m + m_c)\ddot{x}(t) + c\dot{x}(t) + kx(t) = m_c r [\dot{\phi}(t)^2 \cos \phi(t) + \ddot{\phi}(t) \sin \phi(t)] + f_e(t) \quad (5.9)$$

Then, as in Section 5.1.3.1, dividing Equation 5.9 by $(m + m_c)$ brings out:

$$\ddot{x}(t) + 2\xi\omega_n\dot{x}(t) + \omega_n^2x(t) = \mu_c r [\dot{\phi}(t)^2 \cos \phi(t) + \ddot{\phi}(t) \sin \phi(t)] + F_e(t) \quad (5.10)$$

where, $\mu_c = \frac{m_c}{m+m_c}$ ratio between the control mass m_c and the total mass $m + m_c$

$F_e(t) = \frac{f_e(t)}{m+m_c}$ excitation force normalized by the total mass $m + m_c$

The first term on the right side of Equation 5.10 is actually the normalized control force, that is generated by the TRD, i.e.:

$$F_{TRD}(t) = \mu_c r [\dot{\phi}(t)^2 \cos \phi(t) + \ddot{\phi}(t) \sin \phi(t)] \quad (5.11)$$

So, Equation 5.10 can also be expressed as follows:

$$\ddot{x}(t) + 2\xi\omega_n\dot{x}(t) + \omega_n^2x(t) = F_{TRD}(t) + F_e(t) \quad (5.12)$$

5.1.3.3. Control algorithm for SDOF oscillator

In control engineering, state-space equations are conventionally used to describe the state of a dynamic system [DK12]. To achieve a state-space representation of Equation 5.12, a state vector must be firstly defined. It should contain all variables that are needed to describe the dynamic behavior of a system such that:

$$\mathbf{x}_s(t) = \begin{bmatrix} x(t) \\ \dot{x}(t) \end{bmatrix} \quad (5.13)$$

where, $\mathbf{x}_s(t)$ is the state vector and $x(t)$ and $\dot{x}(t)$ are the state variables representing the displacement and the velocity of SDOF oscillator, respectively. Inserting the state vector (Equation 5.13) into the equation of motion (Equation 5.12) and solving in a linear time-invariant (LTI) system [Oga10] yield the state-space equations for TRD in SDOF oscillator:

$$\dot{\mathbf{x}}_s(t) = \mathbf{A}\mathbf{x}_s(t) + \mathbf{B}[F_{TRD}(t) + F_e(t)] \quad (5.14)$$

$$x(t) = \mathbf{C}\mathbf{x}_s(t) \quad (5.15)$$

where, Equation 5.14 is called *state equation* for the system, Equation 5.15 is called *output equation* for the system, $\mathbf{x}_s(t)$ is the state vector given in Equation 5.13, $[F_{TRD}(t) + F_e(t)]$ is the control signal, $x(t)$ is the output signal, \mathbf{A} is the state matrix (or system matrix):

$$\mathbf{A} = \begin{bmatrix} 0 & 1 \\ -\omega_n^2 & -2\xi\omega_n \end{bmatrix} \quad (5.16)$$

\mathbf{B} is the input vector (or control vector):

$$\mathbf{B} = \begin{bmatrix} 0 \\ 1 \end{bmatrix} \quad (5.17)$$

\mathbf{C} is the output vector:

$$\mathbf{C} = \begin{bmatrix} 1 & 0 \end{bmatrix} \quad (5.18)$$

In the real-world application, the output of a system usually includes disturbances which is a signal tending to adversely affect the value of the output [Oga10]. If a disturbance is created inside the system, it can be often compensated by adjusting internally the control algorithm. Contrarily, if a disturbance comes from the environment (outside the system), it should be regarded as an input to the system. To reduce the difference between the output of system and the reference input, the feedback control is commonly applied in control engineering [FPEN19]. The feedback control is an operation that measures the difference between the output of a system and the reference input and uses the difference as a manner of control to reduce the impact from disturbance.¹ To do so, a state observer is usually placed at the output of system in order to provide an estimate on state variables.

In context of SDOF oscillator, supposing that an estimate of the state vector $\mathbf{x}_s(t)$ is observed and denoted as $\hat{\mathbf{x}}_s(t)$, thus the state-space equations for this estimate are:

$$\dot{\hat{\mathbf{x}}}_s(t) = \mathbf{A}\hat{\mathbf{x}}_s(t) + \mathbf{B}[F_{TRD}(t) + F_e(t)] \quad (5.19)$$

$$\hat{x}(t) = \mathbf{C}\hat{\mathbf{x}}_s(t) \quad (5.20)$$

Subtracting Equation 5.20 from Equation 5.15 shows up the error of the displacement:

$$x(t) - \hat{x}(t) = \mathbf{C}[\mathbf{x}_s(t) - \hat{\mathbf{x}}_s(t)] \quad (5.21)$$

Based on the principle of feedback control [FPEN19], the estimated model (Equation 5.19) can be corrected continuously in time domain using the error of displace-

1. Such feedback control system is also named as *closed-loop control system*.

ment (Equation 5.21) as feedback, i.e.,

$$\dot{\hat{\mathbf{x}}}_s(t) = \mathbf{A}\hat{\mathbf{x}}_s(t) + \mathbf{B}[F_{TRD}(t) + F_e(t)] + \mathbf{LC}[\mathbf{x}_s(t) - \hat{\mathbf{x}}_s(t)] \quad (5.22)$$

where, \mathbf{L} is a feedback gain vector defined by:

$$\mathbf{L} = \begin{bmatrix} l_1 \\ l_2 \end{bmatrix} \quad (5.23)$$

Deducting Equation 5.22 from Equation 5.14 results in:

$$\dot{\mathbf{x}}_s(t) - \dot{\hat{\mathbf{x}}}_s(t) = \mathbf{A}[\mathbf{x}_s(t) - \hat{\mathbf{x}}_s(t)] - \mathbf{LC}[\mathbf{x}_s(t) - \hat{\mathbf{x}}_s(t)] \quad (5.24)$$

where, $\dot{\mathbf{x}}_s(t) - \dot{\hat{\mathbf{x}}}_s(t)$ is the error dynamics given by the characteristic equation:

$$\det[s\mathbf{I} - (\mathbf{A} - \mathbf{LC})] = 0 \quad (5.25)$$

where, s is the desired closed-loop poles.

To solve the Equation 5.25, in control engineering, a design method named *pole-placement* is applied [Oga10]. By choosing an appropriate feedback gain \mathbf{L} , it is possible to force the system (SDOF oscillator) to have closed-loop poles at the desired locations, provided that the original system is completely state controllable.

5.1.4. Summary

In this section, the theory and the key properties of the TRD is reviewed. To sum up, TRD is a newly invented active damping device that use the eccentric forces to reduce the vibrations from the system. An example of the SDOF oscillator system is presented in regard to both free vibration and forced damping vibration. A development of the control algorithm for the latter situation is also examined. To keep the brevity of this dissertation, more details about the TRD such as the swinging mode, the experimental verification and the two degrees of freedom oscillator with TRD can be found in [Bäu17].

In the next section, an attempt at integrating the TRD into the NREL 5MW reference wind turbine takes place with regard to the structural engineering, the control engineering and the computational mechanics.

5.2. Integration of TRD into wind turbine

5.2.1. Structural design

In collaboration with Freyssinet², an engineering design of TRD for wind turbine is carried out (see Figure 5.3). Due to the lack of space inside the wind turbine, the TRD is planned to be installed inside the wind turbine tower. The TRD unit is attached to the inner surface of the tower by six beams in steel, more clearly, three beams on the top and three beams on the bottom. This ensures a rigid connection between the TRD unit and the structure of wind tower. The actuator is placed along the center line of the tower and connected to the beams through an upper bearing and a lower bearing. Two control masses are then hinged to the actuator by rods. Each control mass is likewise connected to the actuator axis by two rods, that is, an upper one and a lower one.

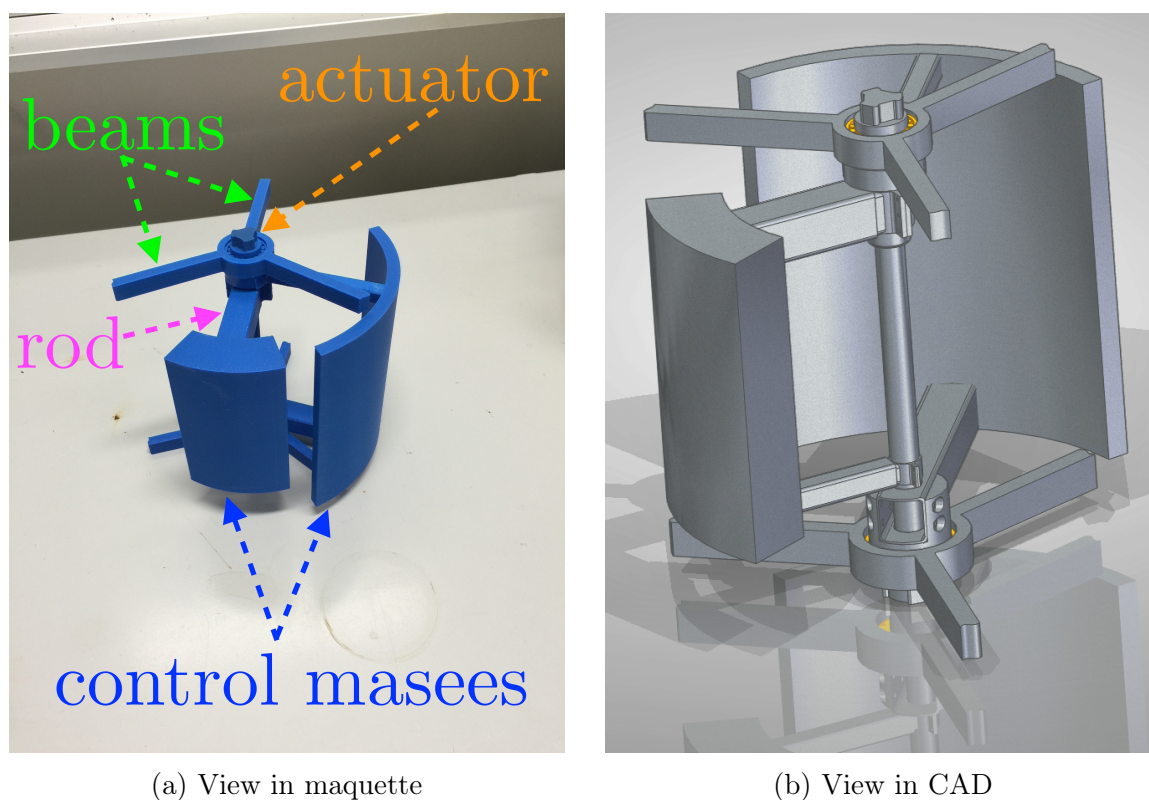


Figure 5.3: Design of TRD for wind turbine³

². Freyssinet is a branch of Soletanche Freyssinet

³. Copyright ©2020 Soletanche Freyssinet. All rights reserved.

When a vibration needs to be damped, the control algorithm of TRD (see Section 5.2.2) will send a signal to the TRD’s actuator to move the rods. Using an electromagnetic coil (or motor-based actuator), the actuator rotates the actuator axis, moving the connected rods, and consequently, rotating the attached control masses. The control masses are made by the same material and have the same mass. But their layouts and radius (the length of rods) are made to be different (Figure 5.3) so that they can be put on the different rings. However, total mass of the rotor on the inner ring, i.e., the control mass and the mass of rod, is kept as same as that on the outer ring.

Recalling the gross properties of NREL 5MW reference wind turbine given in Table 3.1, the following mechanical properties (Table 5.1) are set to the TRD conforming to the related Eurocodes [Eur].

Table 5.1: Mechanical properties of TRD for NREL 5MW reference wind turbine

Property	Value
Total mass of control masses	2.0 t
Radius of TRD	1.0 m
Position of TRD (in tower-base coordinate system)	(0.00, 0.00, 87.60)
Working mode	Mode 1: continuous rotation

The mass ratio between the TRD and the tower is $\frac{2.0}{347.46} \approx 0.58\%$. The TRD is supposed to be positioned on the tower-top (at height of 87.60 m). From Table D.6, the inner radius of tower on the tower-top is 1.910 m, hence, the TRD-to-tower clearance (available space between the radius of TRD and the inner radius of tower) is $1 - \frac{1.0}{1.910} \approx 47.64\%$. The dynamic properties of the TRD will be discussed and set in the next section.

5.2.2. Controller design

In this work, the TRD is supposed to work at mode 1 (Section 5.1.2.1), that is to say, the two control masses of TRD are rotating at the constant angular speed, i.e., $\ddot{\phi}(t) = 0$. To ensure the function of TRD and prevent the re-excitation of the system, Scheller [Sch14] proposed several control methods for TRD. Among all of his propositions, the on-off control (also known as (a.k.a.) *bang-bang control* or *two-step control*) is integrated to the control algorithm of the wind turbine as illustrated in Figure 5.4. It is a closed-loop control based on switching logic and has no intermediate state but only fully ON and fully OFF states. In other words, the damping force from TRD is instantly applied on the structure without any transition phase between ON

state and OFF state.

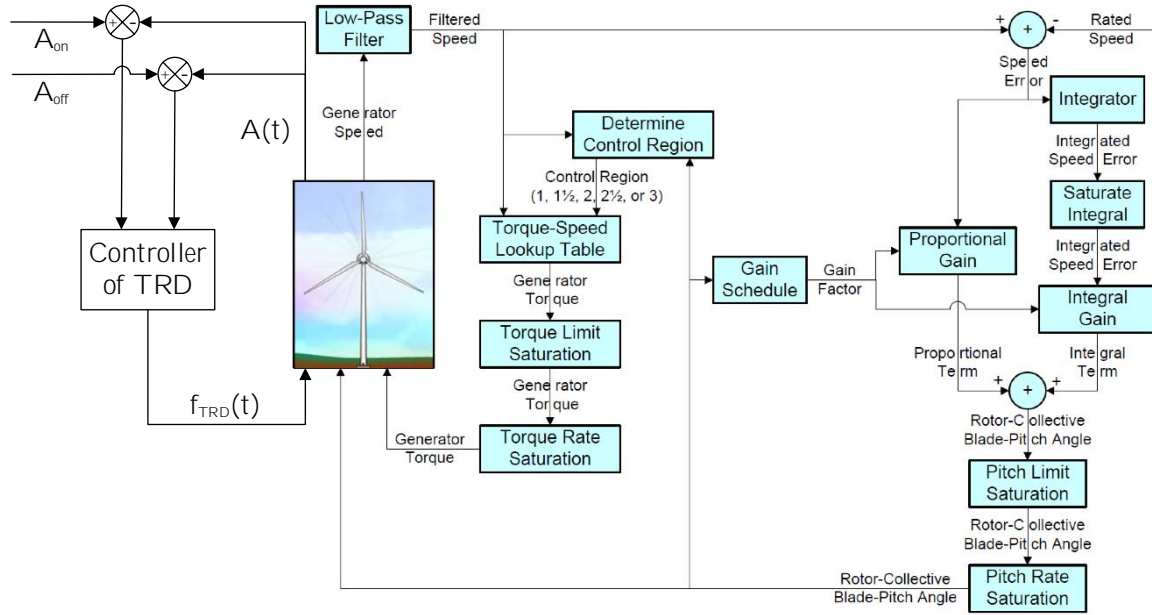


Figure 5.4: Integration of on-off control of TRD to the NREL 5MW reference wind turbine

A time-dependent signal of vibration amplitude $A(t)$ is measured on the tower-top and fed back to the controller of TRD. In the numerical study described later in Section 5.2.3, the external disturbance is not considered. So the measured vibration amplitude of the system (wind turbine tower) is the same as the direct output from the system. Then the measured amplitude $A(t)$ is compared to two thresholds of vibration amplitude, A_{on} and A_{off} , in the way given in Algorithm 5.1.

Algorithm 5.1: On-Off control of TRD for deflection of wind turbine tower

- 1 **if** $A(t) \geq A_{on}$ **then**
 - 2 | Turn on TRD
 - 3 **end if**
 - 4 **if** $A(t) \leq A_{off}$ **then**
 - 5 | Turn off TRD
 - 6 **end if**
-

The value of the threshold A_{off} is set lower than A_{on} . If the measured amplitude $A(t)$ falls below A_{off} , the TRD is turned off to avoid that the wind turbine is re-excited by the forces generated from the TRD. If the measured amplitude $A(t)$ exceeds A_{on} , the TRD is turned back on to eliminate the vibrations on the wind turbine. When TRD is turned on, the forces created by the TRD, $f_{TRD}(t)$ given in Equation 5.3, is applied to the wind turbine at the same position where the vibration amplitude $A(t)$ is

measured, that is, the tower-top. By this means, a closed-loop control algorithm based on the feedback of vibration amplitude is established and used to adjust continuously the behavior of TRD.

It should be recalled that the on-off control method concerns only the mode 1 of TRD, i.e., continuous rotation mode stated in Section 5.1.2.1. As for the other mode, swinging mode, a closed-loop angular position control is involved [Sch14; Bäu14].

In order to make the TRD actively reducing the vibrations on the wind turbine tower, the state feedback gain matrix \mathbf{L} must be deduced from Equation 5.25. To solve this equation, the desired closed-loop poles s is preliminary. It is a complex number given in Cartesian coordinate system [FPEN19]. In this work, the desired positions for poles are set to:

$$\begin{aligned} s_1 &= -\xi_e \omega_{n,e} + \omega_{d,e} j \\ s_2 &= -\xi_e \omega_{n,e} - \omega_{d,e} j \end{aligned} \quad (5.26)$$

with,

$$\omega_{n,e} = \lambda \omega_n \quad (5.27)$$

$$\omega_{d,e} = \omega_{n,e} \sqrt{1 - \xi_e^2} \quad (5.28)$$

where, ω_n = natural angular frequency of the system (rad/s)

λ = desired amplifier of TRD

$\omega_{n,e}$ = natural angular frequency of the closed-loop of TRD (rad/s)

ξ_e = desired damping ratio of TRD

Since the TRD is embedded in the wind turbine tower, the natural angular frequency of the system ω_n is that of the wind tower given in Table D.8. By the definition of the angular frequency given in Equation 1.3, natural angular frequency for the 1st tower fore-after is $\omega_n = 2\pi \times 0.324 \approx 2.036$ rad/s.

Bäumer et al. [BS16] proposed the eigenvalues of the closed-loop $\omega_{n,e}$ to be two to five times faster than that of the system itself ω_n , i.e., $\lambda \in [2, 5]$. Higher the value of λ is, faster the system is stabilized but more energy is consumed by TRD. Additionally, the desired damping ratio ξ_e is suggested to be in the range of [0.80, 0.95]. This ratio describes the efficiency of the TRD unit. In this work, $\lambda = 3$ and $\xi_e = 0.9$ are selected by the author as the suitable and reasonable configurations for the TRD in wind turbine. The dynamic properties of TRD designed for NREL 5MW reference wind turbine are listed in Table 5.2.

Table 5.2: Dynamic properties of TRD for NREL 5MW reference wind turbine

Property	Value
Threshold of vibration-amplitude A_{on}	0.5 m
Threshold of vibration-amplitude A_{off}	0.1 m
Amplifier of TRD λ	3
Damped natural angular frequency $\omega_{n,e}$	6.108 rad/s
Damping ratio ξ_e	0.9

With these dynamic properties of TRD, the poles described in Equation 5.26 can be computed, and subsequently, the state feedback gain vector \mathbf{L} can be found by solving Equation 5.25 through pole-placement method, that is,

$$\mathbf{L} = \begin{bmatrix} -205 \\ -26 \end{bmatrix} \quad (5.29)$$

5.2.3. Digital implementation and numerical simulation

For the purpose of analyzing the effect of integrating TRD into the wind turbine and evaluating the performance of TRD in controlling the vibrations on the wind tower, a numerical study is performed. The simulation codes FAST introduced in Section 2.3.3.1 are modified to implement numerically the theory of TRD shown in Section 5.1 and the engineering design presented in Section 5.2.1 and 5.2.2.

```

32 MODULE TRD_Types
33
34 USE NWTC_Library
35 IMPLICIT NONE
36
37 TRD_InputFile =====
38 TYPE, PUBLIC :: TRD_InputFile
39 CHARACTER(1024) :: TRDFileName !< Name of the input file; re
40 INTEGER(IntKi) :: TRD_CMODE !< control mode {0:none; 1:cont
41 REAL(ReKi), DIMENSION(1:2) :: TRD_K !< TRD K vector [-]
42 REAL(ReKi), DIMENSION(1:2) :: TRD_L !< TRD L vector [-]
43 REAL(ReKi) :: TRD_M !< TRD modal mass of the first mode [kg]
44 REAL(ReKi) :: TRD_F0 !< TRD frequency of the mode to be dam
45 REAL(ReKi) :: TRD_MC !< TRD mass [kg]
46 REAL(ReKi) :: TRD_RC !< TRD radius [m]
47 REAL(ReKi) :: TRD_TIMEON !< Time before activation of TRD [s]
48 REAL(ReKi) :: TRD_AON !< TRD activation threshold [-]
49 REAL(ReKi) :: TRD_AOFF !< TRD deactivation threshold [-]
50 REAL(ReKi), DIMENSION(1:3) :: TRD_P !< position vector of
51 REAL(ReKi), DIMENSION(1:4,1:4) :: TRD_Afilter !< A matrix
52 REAL(ReKi), DIMENSION(1:4) :: TRD_Bfilter !< B matrix for
53 REAL(ReKi), DIMENSION(1:4) :: TRD_Cfilter !< C matrix for
54 REAL(ReKi) :: TRD_Dfilter !< D matrix for filter [-]

```

(a) source code (Fortran)

```

1 ----- TRD V1.03-4 INPUT FILE -----
2 Input file for twin rotor damper
3 ----- TRD GEOMETRICAL CONFIGURATION -----
4 2000.0 TRD_MC - TRD mass (kg)
5 1.0 TRD_RC - TRD radius (m)
6 0.0 TRD_P(1) - x position of the TRD w.r.t. nacelle (m)
7 0.0 TRD_P(2) - y position of the TRD w.r.t. nacelle (m)
8 0.0 TRD_P(3) - z position of the TRD w.r.t. nacelle (m)
9 ----- TRD INITIAL CONDITIONS -----
10 0.0 TRD_PHI_DSP - TRD initial position (radians)
11 ----- TRD CONTROL PARAMETERS - COMMON -----
12 1 TRD_CMODE - control mode {1:continuous rotation mode; 2:
13 60.0 TRD_TIMEON - Time before activation of TRD (s)
14 0.4 TRD_AON - TRD activation threshold [-]
15 0.05 TRD_AOFF - TRD deactivation threshold [-]
16 3.20000E-01 TRD_F0 - TRD frequency of the mode to be damped (Hz)
17 ----- TRD CONTROL PARAMETERS - MODE 1 -----
18 277.8 TRD_K(1) - TRD K vector first coefficient (-)
19 26.7 TRD_K(2) - TRD K vector second coefficient (-)
20 -86.712 TRD_L(1) - TRD L vector first coefficient (-)
21 -17.0222 TRD_L(2) - TRD L vector second coefficient (-)
22 4.78920E+05 TRD_M - TRD modal mass of the mode to be damped (kg)

```

(b) end-user script

Figure 5.5: Example of computer codes for TRD modeling in FAST codes

A snippet of computer codes is shown in Figure 5.5 in which Figure 5.5a demonstrates the source codes of FAST simulator written in Fortran with the digital implementation of TRD's control algorithm, Figure 5.5b gives an example for the end-user

script configuring various properties of TRD. Hereinafter, these codes are used to seek the numerical responses of NREL 5MW reference wind turbine with TRD facing both gusty wind and turbulent wind and, in the next chapter, to find the optimal configurations for TRD.

5.3. Evaluation of TRD performance

Recalling the design process described in Figure 2.5, the TRD is expected to reduce vibrations over the wind turbine tower in two scenarios: (1) Scenario U with DLC2.3 extreme operating gust and technical fault (Section 3.3.1); (2) Scenario F with DLC1.2 normal wind turbulence (Section 4.3.1).

5.3.1. DLC2.3 with TRD

In Chapter 3, the reactions of NREL 5MW reference wind turbine under gusty wind and loss of power network is studied. Through an ultimate load analysis (Section 3.3.4.2), it shows that the intense vibrations with high amplitude have occurred on the tower gage 9, close to tower-top (see Figure 3.14). Likewise, a sensitivity analysis over the grid loss timing (Section 3.3.4.1) shows that the amplitude of fore-after deflection on tower gage 9 is maximized when the mean wind speed V_{mean} approaches the cut-out speed V_{out} (see Figure 3.13). Thereupon, the performance of TRD is evaluated in the wind condition of DLC2.3 at the mean wind speed of V_{out} . The tower response on the tower gage 9 will be examined. The numerical simulation is realized with the same loads used in scenario U (Table 3.5) in consideration of TRD and its associated control method. The effectiveness of TRD in such scenario is evaluated by analyzing the ultimate loads.

5.3.1.1. Results

In Figure 5.6, the numerical results achieved in the scenario U for the case of V_{out} (Section 3.3.4.2) is recalled as the reference. The fore-after deflection on the tower gage 9 from the DLC2.3 is plotted in the blue dotted line, the grid loss time t_{loss} and the initiation time of HSS brake t_{HSS} is shown in the red dashed line and the purple dashed line, respectively. The tower gage 9 fore-after deflection simulated with the TRD is presented in the orange line and has fewer fluctuations than that without the TRD. At the end of simulation ($t = 130$ s), the fore-after deflection from the scenario U (blue dotted line) still oscillates between -0.17 m and 0.20 m whereas, in the case of TRD, the fluctuation (orange line) is stabilized at peak-to-peak amplitude around 0.06 m. That is almost an improvement of $\frac{0.06}{|-0.17-0.20|} \approx 84\%$ in terms of peak-to-peak amplitude.

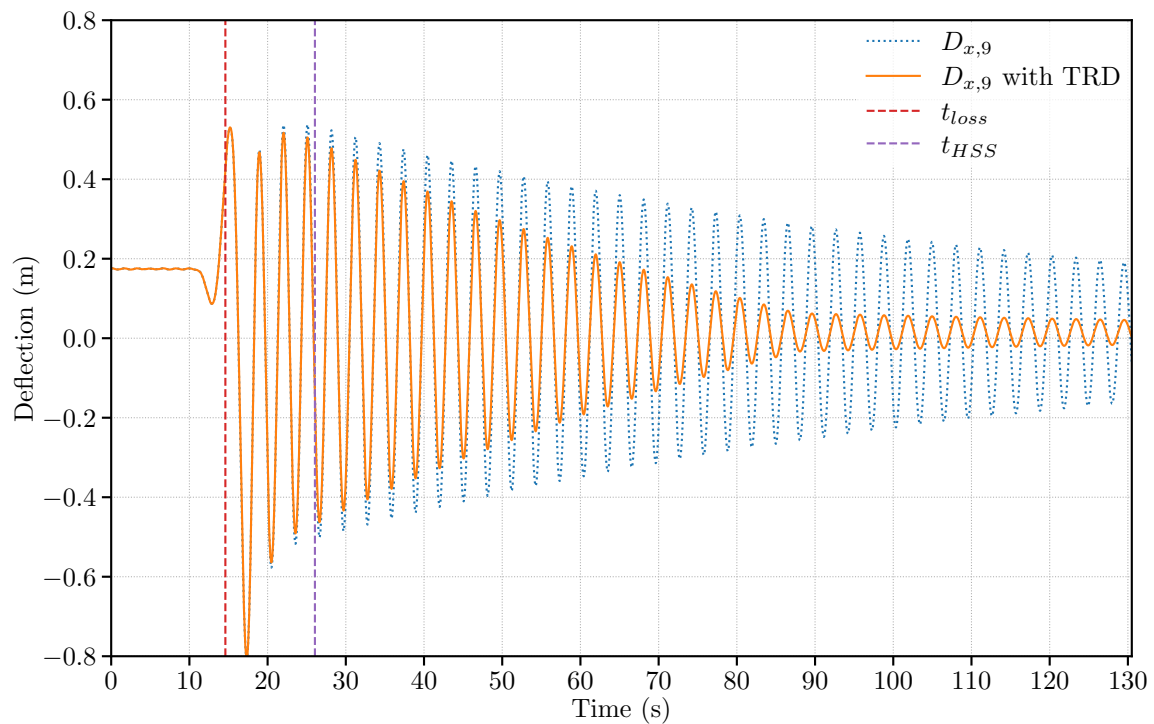


Figure 5.6: Tower gage 9 fore-aft deflection in DLC2.3 at cut-out wind speed ($V_{out}=25.0$ m/s) with TRD

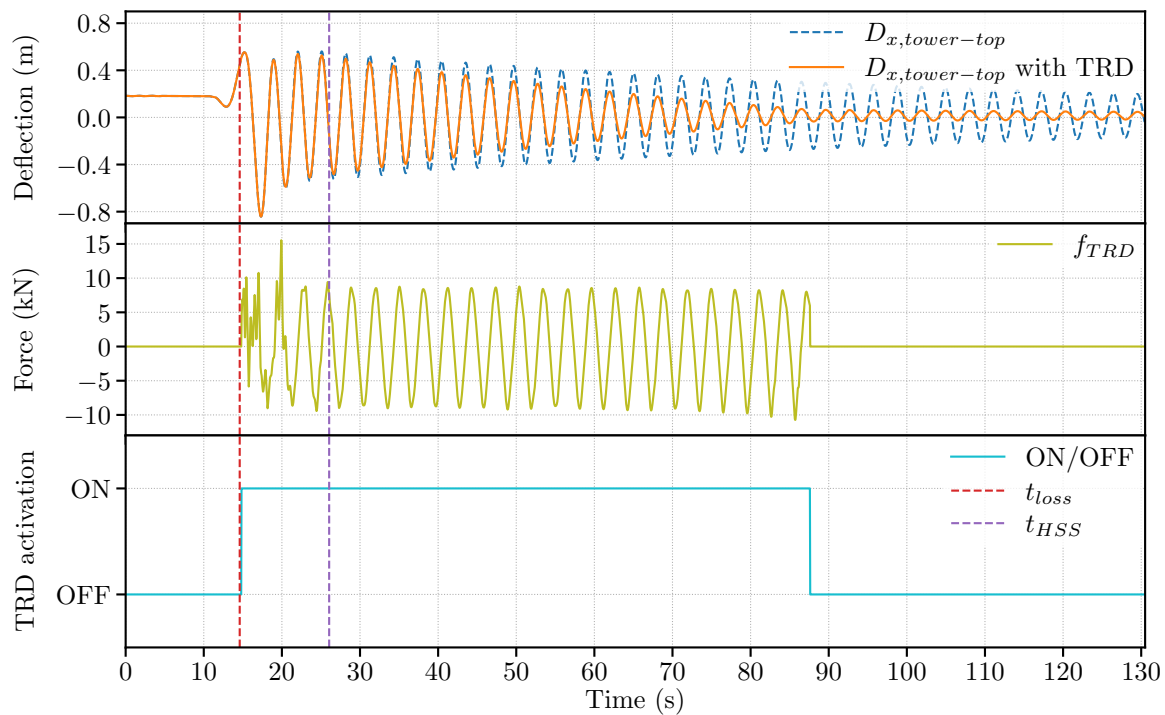


Figure 5.7: Status of TRD in DLC2.3 at V_{out} (the time dependency is omitted in legend)

Figure 5.7 reveals the status of TRD during the gusty wind with grid loss through three charts. The first chart on the top is similar to Figure 5.6 showing the fore-after deflection on tower-top, the second one in the middle draws the forces generated by the TRD while the last chart on the bottom shows the signal sent from the controller of TRD. The TRD is activated since the amplitude of deflection passed the threshold of vibration amplitude $A_{on} = 0.5$ and halted when the amplitude is smaller than $A_{off} = 0.1$ (see cyan line in the bottom chart). The forces created by the TRD (yellow line in the middle chart) vibrate fiercely during the start-up phase, i.e., time-period between the vertical red dashed line and the purple dashed line, and then maintain a sinusoidal form with a phase shift of $\frac{T_{def}}{2}$, where T_{def} is the period of the fore-after deflection on tower-top presented by the orange line in the top chart.

The noise on the generated force $f_{TRD}(t)$ during the start-up phase is mainly caused by two factors. On the one hand, the lack of starting process in the control algorithm results in a “sudden” force applied on the structure once the TRD is turned on. This force strikes the structure on the tower-top in numerical simulation. On the other hand, the TRD is planned to work in the mode 1 (Section 5.1.2.1) which implies that the angular speed of control masses in TRD unit should be constant (see Equation 5.4). However, as the amplitude of fore-after deflection $D_{x,tower-top}$ changes violently during this period, it leads to an inconstant angular speed of TRD, i.e., $\ddot{\phi}(t) \neq 0$, and consequently an unstable force $f_{TRD}(t)$.

5.3.1.2. Discussions

As shown in Figure 5.6, the amplitude of vibration is significantly reduced by TRD comparing to that without the TRD under the same load condition defined in DLC2.3. Although the gain in amplitude reduction is relatively less remarkable between t_{loss} and t_{HSS} , the amplitude decreases more rapidly than the reference amplitude. At the moment when TRD is turned off (around $t = 87$ s), the peak-to-peak amplitude of fore-after deflection with TRD reaches 0.1 m as expected, while the reference peak-to-peak amplitude still remains at 0.6 m. After the shutdown of TRD, the wind tower oscillates like in free damped vibration (Section 1.3.1.2) since the wind speed keeps constantly after the gust (Figure 3.12). More results can be found in Appendix I, where the performance of TRD is evaluated at mean wind speed of V_{rate+2} (Figure I.17), V_{rate} (Figure I.18) and V_{rate-2} (Figure I.19). All these numerical results prove that the TRD is notably effective in reducing vibrations of wind tower under gusty wind.

As for the forces created by TRD, $f_{TRD}(t)$, it depends closely on its control method. A possible solution to eliminate the noise in the signal of $f_{TRD}(t)$ (see the middle chart in Figure 5.7) is to specify a starting and ending process in numerical implementation, for example, a linear ramp-up process or ramp-down process. The linear ramp-up process starts the TRD at $f_{TRD}(t) = 0$ and reaches the target force during a duration

$T_{ramp-up}$. But the linear ramp-down process, by contrast, starts at the target force and turns off the TRD after a period of $T_{ramp-down}$. The $T_{ramp-up}$ and $T_{ramp-down}$ are two design variables for the linear ramp-up process and the linear ramp-down process, respectively. In this way, the forces created by TRD $f_{TRD}(t)$ will not strike the structure at the moment of initiating TRD and result in a smooth signal of $f_{TRD}(t)$ in time series. Another solution is to use the TRD in mode 2 (Section 5.1.2.2) which makes the TRD acting like a conventional active mass damper [Gaw04]. However, this mode requires an advanced control method than on-off control. Since the discussion upon the control algorithm of TRD is beyond the subject of this dissertation, more information can be found in [Bäu14].

5.3.2. DLC1.2 with TRD

In Chapter 4, the performance of NREL 5MW reference wind turbine in terms of fatigue damage is assessed through a novel data-drive probabilistic framework. The probability distributions of cumulative fatigue damage under the wind condition DLC1.2 have been figured out. As shown in Figure 4.18, the overall fatigue damage is maximized when the mean wind speed reaches the cut-out speed (i.e., $V_{mean}=V_{out}$), and another key thing to remind is that the maximum fatigue damage always occurs on the tower gage 1 comparing to the other tower gages (see Figure 4.19). In consequence, it is reasonable to study the TRD in DLC1.2 at V_{out} and appraise its efficiency on tower gage 1.

5.3.2.1. Results and discussions

As shown in Figure 5.8, the local force in \vec{x}_i -axis on tower gage 1 is not significantly reduced by introducing the TRD into the tower. The response of $F_{x,1}$ (orange line) is highly superimposed with the reference result (blue dotted line), and sometimes, even more fluctuant than the reference result.

The malfunction of TRD is also confirmed regarding the normal stress on tower gage 1 local spot 1 in Figure 5.9. The normal stress with TRD (orange line) is completely covered by the reference result (blue dotted line) no matter if the TRD is activated or not.

The reason that the TRD becomes useless in this DLC lies in its operating mode and control algorithm. As stated in Section 5.2.2, only the operating mode 1 of the TRD is engaged in this study. So the TRD is expected to work at a constant rotating speed for its control masses, i.e., $\ddot{\phi} = 0$. However, in DLC1.2, the turbulent wind model NTM is studied. This DLC excites the wind turbine by stochastic loads (see Figure 5.9). To address this kind of loading, the TRD must work at mode 2: swinging mode (Section 5.1.2.2). As the discussion about this operating mode is beyond

the scope of this dissertation, a summary concerning the TRD for the damping of stochastically forced vibrations can be found in [Bäu18].

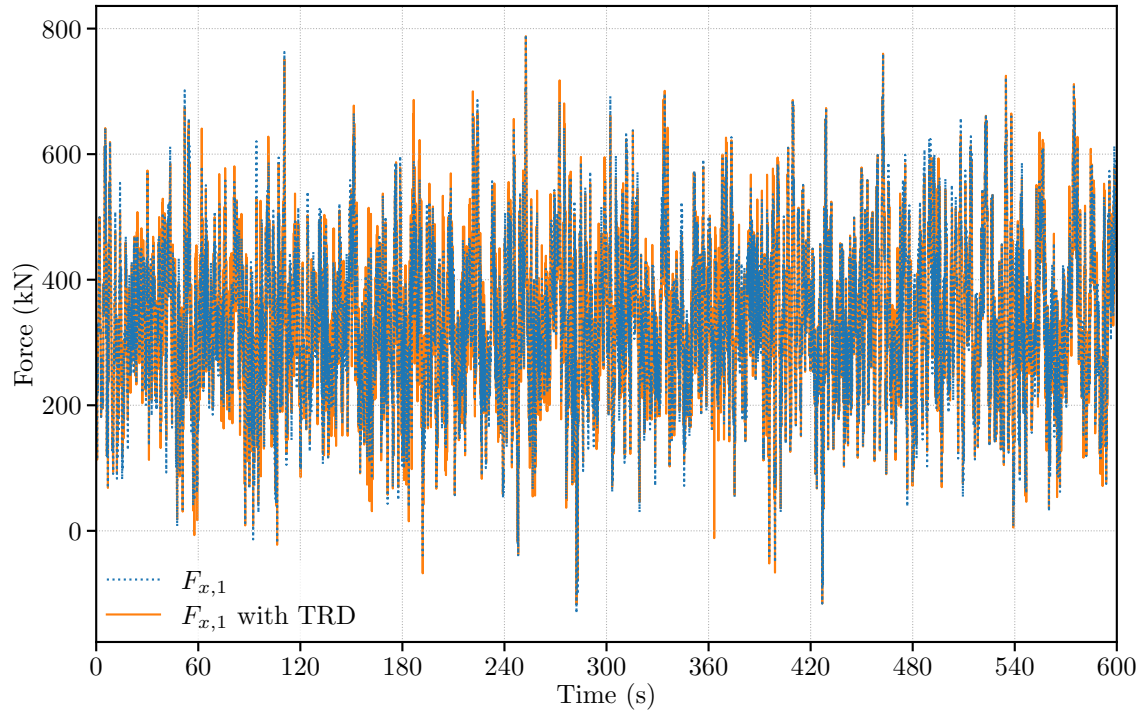


Figure 5.8: Tower gage 1 fore-aft force in DLC1.2 at cut-out wind speed ($V_{mean}=V_{out}$) with TRD

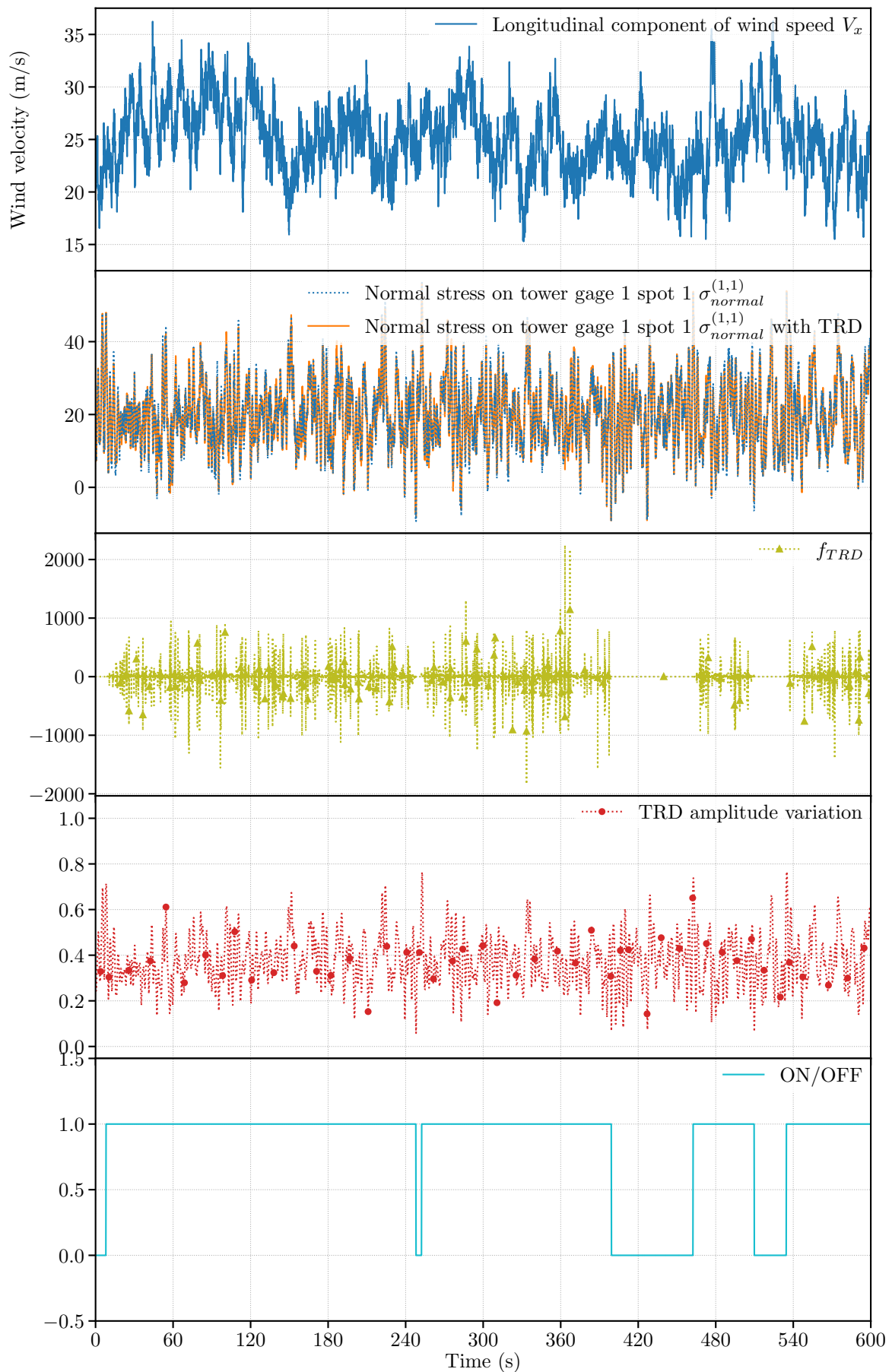


Figure 5.9: Status of TRD in DLC1.2 at V_{out} (the time dependency is omitted in legend)

5.4. Optimization of the design parameters of TRD for wind turbine

5.4.1. Optimization problem set-up

To maximize the performance of TRD in reducing the vibrations on the wind tower facing DLC2.3, an optimization on the design variables of the TRD is studied using a proposed automatic parameter tuning algorithm, named AAC-DE, which will be described later in Chapter 6.

The damping performance of the TRD is estimated by using the logarithmic damping decrement method [LPC00; Han00]. The estimated damping ratio, $\hat{\xi}$, calculated from the logarithmic decrement is therefore used as the objective function for the present optimization problem:

$$\max_{\mathbf{x}} \hat{\xi}(\mathbf{x}) \quad (5.30)$$

where \mathbf{x} is the vector of design variables defined as:

$$\mathbf{x} = \begin{bmatrix} x_1 \\ x_2 \\ x_3 \\ x_4 \end{bmatrix} \quad (5.31)$$

where, $x_1 =$ mass of the TRD within the admissible range $[1, 20]$ (t)

$x_2 =$ radius of the TRD within the admissible range $[1.00, 1.72]$ (m)

$x_3 =$ 1st element of the state feedback gain vector \mathbf{L} within the range $[-220, 0]$

$x_4 =$ 2nd element of the state feedback gain vector \mathbf{L} within the range $[-220, 0]$

The allowable maximum for the mass of TRD ($\max(x_1) = 20$) comes from a design of tuned mass damper for NREL 5MW reference wind turbine [HOK19; HO18], the minimum and maximum for the radius of TRD ($x_2 \in [1.00, 1.72]$) takes an approximate value close to 50% and 90% of the inner radius on the tower-top (1.910 m), the rest values are set according to the experience of the author and the collaborators.

The only constraint considered in this optimization problem is the energy consumed by the TRD during its activation:

$$E_a = \int_{t_{on}}^{t_{off}} P_{TRD}(t) dt \quad (5.32)$$

where, $t_{on}, t_{off} =$ time to turn on/off the TRD

$P_{TRD}(t) =$ power of a TRD unit (including two rotors)

Since the TRD is embedded inside the wind tower, without considering any auxiliary

supply, the energy consumed by the TRD should never pass the energy produced by the generator. In other words, the power of TRD must be always smaller than the maximum power generated by the wind turbine (i.e., 5MW), that is:

$$P_{TRD}(t) = 2M(t)\dot{\phi}(t) \leq P_{max}^{turbine} \quad (5.33)$$

where, $M(t)$ = moment of the rotor
 $\dot{\phi}(t)$ = angular velocity of the rotor
 $P_{max}^{turbine}$ = maximum power generated by the wind turbine

The algorithm involved in this optimization problem, AAC-DE, is a population-based evolutionary algorithm. 100 individuals are used to solve this problem ($NP = 100$) and the maximum number of function evaluations (MaxFES) is set to 10 000. The latter corresponds to the number of numerical simulations carried out by FAST.

As for the stop criteria, a fitness error of 10^{-8} is defined for the improvement between two continuous generations, i.e., $\hat{\xi}(\mathbf{x}^{(g)}) - \hat{\xi}(\mathbf{x}^{(g-1)}) \leq 10^{-8}$, where $\hat{\xi}(\mathbf{x}^{(g)})$ is the best solution found in the generation (g) and $\hat{\xi}(\mathbf{x}^{(g-1)})$ is that in the last generation.

5.4.2. Results and discussions

After a single run of the above optimization problem, the following optimized variables are found:

$$\mathbf{x} = \begin{bmatrix} 1.27 \\ 1.12 \\ -219.93 \\ -76.63 \end{bmatrix} \quad (5.34)$$

Figure 5.10 illustrates the optimized design (green line) compared compared to the initial design (orange dashed line) discussed in Section 5.3.1 and the reference result without the TRD (blue dotted line) given in Section 3.3.4.2.

The improvement of the damping performance of TRD is noteworthy under all mean wind speed required by this DLC (V_{rate-2} , V_{rate} , V_{rate+2} , V_{out}). At V_{out} (Figure 5.10a), the TRD takes a rapid reaction to reduce the vibration of fore-aft deflection during the period between t_{loss} and t_{HSS} . This proves the ability of the TRD to reduce the potential damage due to the extreme loading. As for other mean wind speeds (Figure 5.10b to Figure 5.10d), the optimized TRD always offers a quick and effective reduction on the vibrations amplitude compared to that of the initial design.

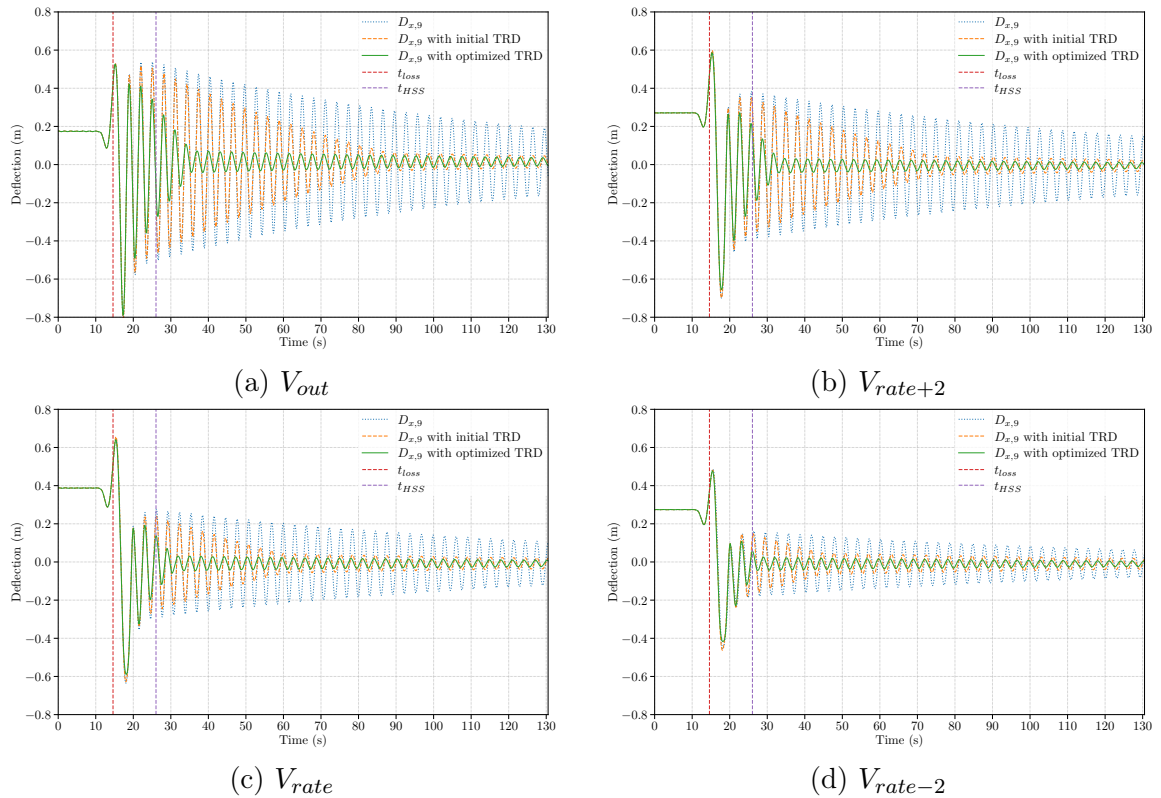


Figure 5.10: Fore-aft deflection on tower gage 9 considering the TRD with optimized configurations for wind turbine tower under DLC2.3

5.5. Conclusions

In this chapter, the idea of damping the vibrations on the wind turbine tower is realized. An active damping device known as twin rotor damper (TRD) is introduced. A SDOF oscillator model with the TRD is then studied to validate the design of TRD in theory followed by a numerical validation in FAST codes. The source code of FAST is accordingly modified to combine the TRD with other existing computational modules. What's more, an on-off control algorithm of TRD is integrated into the control system of NREL 5MW reference wind turbine. Finally, the performance of TRD is evaluated in two different loads cases: DLC2.3 and DLC1.2. The former involves an extreme operating wind gust in coincidence with loss of power network, and the latter describes a wind condition with turbulence.

Based on the numerical results, it proves that the TRD is very effective in controlling the vibrations on the wind tower in DLC2.3 by continuously rotating its control masses at a fixed angular speed ($\ddot{\phi} = 0$). Comparing to the reference result under that same situation studied in Chapter 3, the TRD offers a notable reduction not only the deflection on the tower-top but also the force and moment at the tower-base. By contrast, the performance of TRD in DLC1.2 is less attractive since the wind turbine

is excited by stochastic force in this case. To reduce the vibration in such situation, the mode 2 (swinging mode) is required. But this operating mode requires a more complicated control algorithm and is far beyond the scope of this dissertation.

In summary, the present chapter validate theoretically and numerically the proposal of an active damping system using the TRD for wind turbine. An initial design based on the prior knowledge and the related industrial standard is proposed for integrating the TRD into a wind turbine tower. A new optimization algorithm developed by the author is then used to optimize this initial design. The algorithm is quasi-parameterless which means that it handles its hyperparameters by itself during the execution. The theory and the development behind this algorithm is detailed in the following chapter.

Chapter 6

Automatic parameter tuning optimization algorithm

In Chapter 4, a deep neural network ResMLP is proposed to carry out a probabilistic fatigue analysis on the wind turbine tower. However, the configuration of its hyperparameters (e.g., number of layers, number of perceptrons per layer, learning rate, etc.) remains a tough task for users.

In Chapter 5, an active damping system for wind turbine using the centrifugal forces of eccentrically rotation masses is studied. An initial design for the such active damping system, known as TRD, is proposed. To get an optimized performance of the TRD damping system, an optimization on its design variables is imperative.

Technically speaking, the hyperparameter optimization of ResMLP is a Bayesian optimization problem and the design variable optimization of TRD is a black-box optimization problem. Both problems can be solved by a non-gradient based optimization algorithm, for example, evolutionary algorithms (EAs).

In the first section, a brief survey on EA family and one of its major variant, DE, is presented. Then a novel method named adaptive algorithm configuration for differential evolution (AAC-DE) is proposed based on exploration and exploitation during the search process. An experimental analysis upon the proposed method takes place in the following section compared to other DE variants, and, to give an example, the proposed method is used to optimize the design variables of the TRD.

6.1. Evolutionary algorithm

Evolutionary algorithms (EAs), which are a family of search algorithms inspired by the principles of evolution in nature, are powerful techniques for solving complex optimization problems [Eng07]. However, the performance of an EA usually depends on its algorithm configuration, or parameter setting, including the representation (or encoding scheme), the evolutionary operators (such as mutation, crossover and selection) and the control parameters. Thus, to efficiently solve a problem or to achieve high-quality solutions, the algorithm needs to be properly configured. Algorithm configuration problem [Hoo12] of EAs, that is, to choose suitable evolutionary operator and parameter values, is a routinely encountered and challenging task for both algorithm designers and end-users. Recently, automatic algorithm configuration methods, i.e., automatic approaches to solve algorithm configuration problems, have drawn considerable attention not only in evolutionary computation (EC) community but also in machine learning and other fields of artificial intelligence (AI).

Algorithm configuration problem can be addressed in offline or online manners. In offline algorithm configuration, suitable configuration (or parameter setting) is predefined before applying the algorithm to solve problems at hand. Oppositely, in online algorithm configuration, parameters of the algorithm are adapted dynamically according to some strategies in the time of solving the problem.

Many offline automatic algorithm configuration methods have been proposed in recent decades, such as Bayesian optimization [Sha16; Hua19], ParamILS [Hut09], and Sequential Model-based Algorithm Configuration (SMAC) [HHLB11]. Essentially, offline algorithm configuration approaches work by the “generate and evaluate” principle, that is, generating different configurations and evaluating their performances by running the algorithm with these different configurations [HLY20]. Finding an optimal configuration usually requires a large number of runs of the algorithm with different configurations. Therefore, using offline automatic algorithm configuration approaches to solve algorithm configuration problem is usually computational expensive and time-consuming. This is arguably the most serious disadvantage of offline automatic algorithm configuration. Additionally, in offline algorithm configuration, the obtained configuration keeps unchanged in solving problem, but the proper or optimal configuration may change at different steps or stages of the search process.

To overcome or alleviate the above drawbacks, different online algorithm configuration approaches (a.k.a. *parameter adaptation* or *parameter control*) [EHM99; KHE15] have been presented to handle the algorithm configuration problem of EAs in an online fashion. The online parameter control approaches can be classified into three categories: deterministic, self-adaptive, and adaptive parameter control [KHE15; AM16]. Deterministic parameter control modifies the parameters according to certain

rules without using the feedback from the search process. Self-adaptive parameter control combines the search for optimal parameters with the search for optimal solution by encoding parameters into the individuals and evolving them simultaneously. Adaptive parameter control monitors the search process and uses the feedback as a guide to adjust parameter values.

Differential evolution (DE) algorithm proposed by Storn et al. [SP97] is a simple and efficient EA which performs well on a wide range of optimization problems, especially on continuous optimization. Owing to its simplicity of implementation and high performance, DE has become very popular among researchers and practitioners. Many variants of DE have been introduced by designing different mutation and/or crossover operators. However, the performance of DE is still quite dependent on its configuration, including the population size (N_p), trial vector generation strategy (i.e., the combination of mutation and crossover operator), scale factor (F), and crossover rate (C_r), according to both experimental studies [Gon11] and theoretical analysis [OA18]. Thus, to successfully solve an optimization problem with DE, it is usually required to identify the proper generation strategy and the associated parameter values.

Using offline algorithm configuration methods to find appropriate configuration for DE generally takes high computational costs. Moreover, during the evolution search process, the optimal configuration may be different at different stage. Not to forget that, it is often an exhausting task for the end-user to adjust the algorithm's parameters through trial-and-error process and depends strongly on expertise of the practitioners. Hence, it is desirable to design online algorithm configuration approach for DE as well as other EAs.

In this work, an adaptive algorithm configuration for differential evolution AAC-DE is proposed. The key novelties of this method concern:

1. It originally introduced some machine learning based techniques (e.g., multi-armed bandit algorithm, kernel density estimation) into parameter control of DE.
2. Unlike other algorithm configuration methods [Hut09; Sha16; HHLB11; EHM99; KHE15], AAC-DE allows to adjust adaptively and dynamically both the generation strategy (i.e., the combination of mutation and crossover operators) and the associate control parameters (i.e., F and C_r) during the execution.
3. The proposed method takes place in continuous adaptation based on the exploring and exploiting ability of the strategies and the control parameters instead of directly learning from its historical performance achieved in the previous generations.

6.1.1. Differential evolution algorithm

Assuming an optimization problem $\min_{\vec{x}} f(\vec{x})$ where \vec{x} is a vector of D design variables in a continuous decision space (search domain) $\Omega = \prod_{i=1}^D [L_i, U_i]$, L_i and U_i are lower bounds and upper bounds for design variables, respectively, $f : \Omega \subseteq \mathbb{R}^D \rightarrow \mathbb{R}$ is the objective function that needs to be optimized.

The differential evolution (DE) algorithm [PSL06] is a popular approach to global numerical optimization. It has been widely used in benchmark function sets [Han06] as well as real-world applications [CCW08; LY12]. It is a population based optimization algorithm of which the outline is given in Algorithm 6.1.

Algorithm 6.1: Fundamental framework of differential evolution (DE)

```

1 Set the generation counter  $g \leftarrow 0$ 
2 Initialize a population  $P^{(0)}$  of  $NP$  individuals within the search domain
    $[L_i, U_i]$ , i.e.,  $P^{(0)} = \{\vec{x}_i^{(0)} : i = 1, \dots, NP\}$ 
3 Evaluate the population  $P^{(0)}$ , i.e.,  $\forall \vec{x}_i^{(0)} \in P^{(0)}, f(\vec{x}_i^{(0)})$ 
4 while the stop criterion is not met do
5   foreach  $\vec{x}_i^{(g)}$  in  $P^{(g)}$  do
6     Generate a mutant vector using a mutation operator, i.e.,
        $\vec{v}_i^{(g)} = \text{Mutate}(\vec{x}_i^{(g)})$ 
7     Generate an offspring using a crossover operator, i.e.,
        $\vec{u}_i^{(g)} = \text{Crossover}(\vec{v}_i^{(g)})$ 
8     Evaluate the fitness of offspring, i.e.,  $f(\vec{u}_i^{(g)})$ 
9     if  $f(\vec{u}_i^{(g)}) \leq f(\vec{x}_i^{(g)})$  then
10      Add  $\vec{u}_i^{(g)}$  to the population  $P^{(g+1)}$ 
11    else
12      Add  $\vec{x}_i^{(g)}$  to the population  $P^{(g+1)}$ 
13    end if
14  end foreach
15  Increase the generation counter  $g \leftarrow g + 1$ 
16 end while

```

6.1.1.1. Mutation Operators

In each generation, DE employs the mutation operator to create a mutant vector $\mathbf{v}_i^{(g)}$ for each target vector $\mathbf{x}_i^{(g)}$ in the current population. At present, many different mutation operators are available for DE. Several commonly used mutation strategies [Sto96; QHS09a; PSL06; IL04; ZS09] are listed in Table 6.1.

In above mutation operators, the indices r_1, r_2, r_3, r_4, r_5 are mutually exclusive integers randomly selected from the range $[1, NP]$ and are also different from the index i . F is the control parameter called scale factor, which amplifies the difference vectors.

Table 6.1: Various mutation operators for DE.

Mutation Operator	Formulation
DE/rand/1 [Sto96]	$\mathbf{v}_i^{(g)} = \mathbf{x}_{r_1}^{(g)} + F \cdot (\mathbf{x}_{r_2}^{(g)} - \mathbf{x}_{r_3}^{(g)})$
DE/rand/2 [QHS09a]	$\mathbf{v}_i^{(g)} = \mathbf{x}_{r_1}^{(g)} + F \cdot (\mathbf{x}_{r_2}^{(g)} - \mathbf{x}_{r_3}^{(g)} + \mathbf{x}_{r_4}^{(g)} - \mathbf{x}_{r_5}^{(g)})$
DE/best/1 [Sto96]	$\mathbf{v}_i^{(g)} = \mathbf{x}_{best}^{(g)} + F \cdot (\mathbf{x}_{r_1}^{(g)} - \mathbf{x}_{r_2}^{(g)})$
DE/best/2 [Sto96]	$\mathbf{v}_i^{(g)} = \mathbf{x}_{best}^{(g)} + F \cdot (\mathbf{x}_{r_1}^{(g)} - \mathbf{x}_{r_2}^{(g)} + \mathbf{x}_{r_3}^{(g)} - \mathbf{x}_{r_4}^{(g)})$
DE/current-to-best/1 [PSL06]	$\mathbf{v}_i^{(g)} = \mathbf{x}_i^{(g)} + K \cdot (\mathbf{x}_{best}^{(g)} - \mathbf{x}_i^{(g)})$ $+ F \cdot (\mathbf{x}_{r_1}^{(g)} - \mathbf{x}_{r_2}^{(g)})$
DE/current-to-best/2 [QHS09a]	$\mathbf{v}_i^{(g)} = \mathbf{x}_i^{(g)} + K \cdot (\mathbf{x}_{best}^{(g)} - \mathbf{x}_i^{(g)})$ $+ F \cdot (\mathbf{x}_{r_1}^{(g)} - \mathbf{x}_{r_2}^{(g)} + \mathbf{x}_{r_3}^{(g)} - \mathbf{x}_{r_4}^{(g)})$
DE/current-to-rand/1 [IL04]	$\mathbf{v}_i^{(g)} = \mathbf{x}_i^{(g)} + K \cdot (\mathbf{x}_{r_1}^{(g)} - \mathbf{x}_i^{(g)})$ $+ F \cdot (\mathbf{x}_{r_2}^{(g)} - \mathbf{x}_{r_3}^{(g)})$
DE/current-to- p best/1 [ZS09]	$\mathbf{v}_i^{(g)} = \mathbf{x}_i^{(g)} + K \cdot (\mathbf{x}_{r_p}^{(g)} - \mathbf{x}_i^{(g)})$ $+ F \cdot (\mathbf{x}_{r_1}^{(g)} - \mathbf{x}_{r_2}^{(g)})$

K is a uniform random number within the range of $[0, 1]$. $\mathbf{x}_{best}^{(g)}$ is the best individual in the current population, i.e., the population at generation g . In DE/current-to- p best/1, $\mathbf{x}_{r_p}^{(g)}$ is an individual randomly chosen from the top $100p\%$ individuals in the current population with $p \in (0, 1]$. In fact, DE/current-to- p best/1 [ZS09] is a generalization of DE/current-to-best/1 [PSL06]. Specifically, one of the best $100p\%$ individuals is randomly selected to play the role of the $\mathbf{x}_{best}^{(g)}$ in DE/current-to-best/1.

6.1.1.2. Crossover Operators

Following the mutation operation, the mutant vector is crossed-over with the target vector to yield the trial vector. In DE, the binomial and exponential crossover operators are two common used crossover strategies [OA19].

The binomial crossover operator generates the trial vector $\mathbf{u}_i^{(g)} = [u_{i,1}^{(g)}, \dots, u_{i,D}^{(g)}]$ for the target vector $\mathbf{x}_i^{(g)}$ as follows:

$$u_{i,j}^{(g)} = \begin{cases} v_{i,j}^{(g)}, & \text{if } rand_j[0, 1] \leq C_r \text{ or } j = j_{rand} \\ x_{i,j}^{(g)}, & \text{otherwise} \end{cases} \quad j = 1, 2, \dots, D \quad (6.1)$$

where $rand_j[0, 1]$ is a uniformly distributed random number from the range $[0, 1]$ which is generated for each j , j_{rand} is an integer randomly chosen in the range $[1, D]$, and C_r is the control parameter known as crossover rate, which takes value within the range $[0, 1]$.

The exponential crossover operator produces the trial vector $\mathbf{u}_i^{(g)}$ for the target

vector $\mathbf{x}_i^{(g)}$ as follows:

$$u_{i,j}^{(g)} = \begin{cases} v_{i,j}^{(g)}, & \text{if } j = \langle n \rangle_D, \langle n+1 \rangle_D, \dots, \langle n+L-1 \rangle_D \\ x_{i,j}^{(g)}, & \text{otherwise} \end{cases} \quad (6.2)$$

where $\langle \cdot \rangle_D$ denotes the modulo function with modulus D , n is an integer randomly drawn within $[1, D]$, and L is another integer drawn from the range of $[1, D]$ in the way given in Algorithm 6.2.

Algorithm 6.2: Exponential crossover operator: selection of L integer

```

1 Set  $L \leftarrow 0$ 
2 while  $\text{rand}[0, 1] \leq CR$  and  $L \leq D$  do
3   |  $L = L + 1$ 
4 end while

```

6.1.1.3. Selection

In selection operation, the competition is performed between the offspring (trial vector) and the parent (target vector). Specifically, the objective function value of each trial vector $f(\mathbf{u}_i^{(g)})$ is compared to that of the corresponding target vector $f(\mathbf{x}_i^{(g)})$, and the better one of them (i.e., the one that has the lowest fitness in a minimization problem) will be selected to enter the next generation, i.e.,

$$\mathbf{x}_i^{(g+1)} = \begin{cases} \mathbf{u}_i^{(g)}, & \text{if } f(\mathbf{u}_i^{(g)}) \leq f(\mathbf{x}_i^{(g)}) \\ \mathbf{x}_i^{(g)}, & \text{otherwise} \end{cases} \quad (6.3)$$

where $f(\mathbf{x})$ is the objective function (or fitness function) to be minimized.

6.1.2. Review of adaptive differential evolution algorithms

The search performance of DE is strongly dependent on mutation operator, crossover operator, the scale factor F (related to mutation operator) and the crossover rate CR (related to crossover operator) [DS11]. In order to achieve high performance or high quality solution, the operators and values of the control parameters should be chosen appropriately. Therefore, it is highly desired to develop automatic approaches to select appropriate mutation and crossover operators and/or to select proper values for DE's control parameters (F and/or CR) [NT10; DS11; Der11]. In general, these approaches can be classified into two classes: (1) heuristic rules based techniques; (2) probability distribution based techniques.

6.1.2.1. jDE

jDE is another representative of heuristic rules based parameter adaption technique. Brest et al. [Bre06] J. Brest et al. have firstly proposed this method based on the classic mutation operator “DE/rand/1/bin” in which the F and CR are adapted through a self-adaptive approach. Each individual is assigned to a couple of (F, CR) calculated as follows:

$$F_i^{(g+1)} = \begin{cases} L_F + rand_1 \cdot U_F, & \text{if } rand_2 < \tau_1 \\ F_i^{(g)}, & \text{otherwise} \end{cases} \quad (6.4)$$

$$CR_i^{(g+1)} = \begin{cases} rand_3, & \text{if } rand_4 < \tau_2 \\ CR_i^{(g)}, & \text{otherwise} \end{cases} \quad (6.5)$$

where $F_i^{(g+1)}$ and $CR_i^{(g+1)}$ are the values of F and CR for the i -th individual in generation $(g + 1)$, L_F and U_F are the lower and upper limits of the parameter F set to $L_F = 0.1$ and $U_F = 0.9$ in jDE, respectively. τ_1 and τ_2 are two probabilities used to adjust F and CR with recommended values of $\tau_1 = \tau_2 = 0.1$. And lastly, $rand_j, j = 1, 2, 3, 4$ are uniform random values within the range $[0, 1]$.

The offspring for each parent is generated by the mutation and crossover operators using the newly generated control parameter values (F and CR). The values of control parameter that tend to generate better offspring are more likely to be reused in the next generation. The experimental results have shown that jDE performs better than the classic DE algorithm in benchmark functions [Bre06].

6.1.2.2. EPSDE

EPSDE is another heuristic rules based DE developed by Mallipeddi et al. [Mal11] R. Mallipeddi et al.. In EPSDE, the trial generation strategy (for mutation operator only) is chosen from a strategy pool, and furthermore, the control parameters (F and CR) are chosen from the corresponding sets of discrete candidate values. The generation strategy pool takes three common mutation operators, i.e., $\Omega_{mut} = \{\text{“DE/rand/1/bin”}, \text{“DE/best/2/bin”}, \text{“DE/current-to-rand/1”}\}$. The pool of CR values is taken in the range $[0.1, 0.9]$ at a step of 0.1, i.e., $\Omega_{CR} = \{0.1, 0.2, \dots, 0.9\}$. The pool of F values is taken in the range $[0.4, 0.9]$ with a step-size of 0.1, i.e., $\Omega_F = \{0.4, 0.5, \dots, 0.9\}$.

Initially, each parent $\vec{x}_i^{(0)}$ in the initial population $P^{(0)}$ is randomly associated with a mutation operator from Ω_{mut} and the control parameter values taken from the respective pool, i.e., $rand_F \in \Omega_F$ and $rand_{CR} \in \Omega_{CR}$. Next, for each parent, an offspring is generated using the assigned operator and control parameter values. If the offspring is better than its parent and will enter the next generation, then it keeps the strategy and control parameter values from its parent in the next generation. The

combination of the mutation operator and the parameter values of this offspring is recorded and considered as successful combination. Contrarily, if the parent is better than the offspring, the parent is randomly reinitialized with a new mutation operator associated to new control parameter values either from the respective pool or from the successful combinations stored with equal probability.

6.1.2.3. SaDE

SaDE is a probability distribution based method proposed by Qin et al. [QHS09b]A. K. Qin. This implies that both the offspring generation strategies and their associated control parameter values are adapted by learning from their previous experience of generating promising offspring. The parameter adaptation of SaDE contains two parts: (1) the adaptation of the probability of selecting the generation strategies; (2) the adaptation of two control parameters (F and CR) regarding each generation strategy.

In SaDE, for each parent in the current population $\vec{x}_i^{(g)}$, one offspring generation strategy (mutation operator) is selected from the candidate pool of strategies based on a probability which is learned from its success rate of generating improved solutions in the past LP generations. $LP = 50$ has been suggested by the authors. The candidate pool of strategies includes popular mutation operators such as “DE/rand/1/bin”, “DE/rand-to-best/2/bin”, “DE/rand/2/bin”, and “DE/current-to-rand/1”. Suppose that the probability of selecting the k -th strategy from the candidate pool in the current population is p_k , $k = 1, \dots, K$, where K is the total number of strategies contained in the candidate pool. The probabilities are initialized as $p_k = 1/K$, for $k = 1, \dots, K$. Based on this probability p_k , the Stochastic Universal Selection (SUS) method [Bak87] is performed to apply a generation strategy from the pool to the trail vector $\vec{u}_i^{(g)}$ of each target vector $\vec{x}_i^{(g)}$.

In generation g , the number of trial vectors generated by the k -th strategy that successfully enters the next generation is recorded as $N_{s,k}^{(g)}$ and the number of trial vectors generated by the k -th strategy that are discarded is recorded as $N_{f,k}^{(g)}$. These two numbers along with a fixed number of previous generations (named *learning period* LP) are recorded as the *success and failure memories* during the evolutionary search process. After the initial LP generations, the probabilities of selecting different strategies p_k will be updated at each subsequent generation based on the *success and failure memories*. More specifically, the probability of choosing the k -th ($k = 1, \dots, K$) strategy at the generation g is updated by:

$$p_k^{(g)} = \frac{GS_k^{(g)}}{\sum_{k=1}^K GS_k^{(g)}} \quad (6.6)$$

with

$$GS_k^{(g)} = \frac{\sum_{t=g-LP}^{g-1} N_{s,k}^{(t)}}{\sum_{t=g-LP}^{g-1} N_{s,k}^{(t)} + \sum_{t=g-LP}^{g-1} N_{f,k}^{(t)}} + \epsilon \quad (k = 1, \dots, K; g > LP) \quad (6.7)$$

where $GS_k^{(g)}$ stands for the success rate of the k -th strategy calculated based on the *success and failure memories* within the previous LP generations, the constant $\epsilon = 0.01$ is added to avoid the possible null success rates. Apparently, higher the success rate for the k -th strategy is, higher the probability of this strategy is used to create an offspring at the current generation.

As for the parameter adaption of SaDE, the parameter F for each target vector $\vec{x}_i^{(g)}$ is independently generated by a normal distribution with mean 0.5 and standard deviation 0.3, i.e.,

$$F_i^{(g)} \sim Normal(0.5, 0.3) \quad (6.8)$$

and then truncated to $[0, 2]$.

The parameter CR of the k -th generation strategy in the pool, for each target vector $\vec{x}_i^{(g)}$ is sampled from a normal distribution with mean $m_{CR,k}$ and standard deviation 0.1, i.e.,

$$CR_i^{(g)} \sim Normal(m_{CR,k}, 0.1) \quad (6.9)$$

and then regenerated if $CR_i^{(g)}$ is outside the range $[0, 1]$. The $m_{CR,k}$ is the mean of the k -th generation strategy and initialized to be 0.5. In order to adapt CR in regard to each generation strategy (mutation operator), the memories named $CRMemory_k$ are established to store the successful CR values with reference to the k -th strategy, i.e., those CR values with which the generated offspring successfully entering the next generation, within the past LP generations. Then, at each subsequent generation after LP generations, the median value stored in $CRMemory_k$ is exported to overwrite the mean of normal distribution $m_{CR,k}$. By this means, the mean of CR associated to each generation strategy is updated and, therefore, the adaptation of CR is accomplished.

6.1.2.4. JADE

JADE is another well-known probability distribution based DE developed by Zhang et al. [ZS09]J. Zhang et al.. It adopts an adaptive parameter control mechanism based on Normal and Cauchy distribution. In addition, the authors have also implemented a new mutation operator known as “DE/current-to- p best”. In JADE, at generation g , each individual $\vec{x}_i^{(g)}$ is associated with a scale factor $F_i^{(g)}$ which is generated independently according to a Cauchy distribution with location parameter μ_F (initialized to be 0.5) and scale parameter 0.1, i.e.,

$$F_i^{(g)} = Cauchy(\mu_F, 0.1) \quad (6.10)$$

If $F_i^{(g)} \geq 1$, it will be truncated to 1; if $F_i^{(g)} \leq 0$, it will be regenerated using the same equation above. As for the crossover rate $CR_i^{(g)}$, it is sampled according to a normal distribution with mean μ_{CR} (initialized to be 0.5) and standard deviation 0.1 for each individual $\vec{x}_i^{(g)}$, i.e.,

$$CR_i^{(g)} = Normal(\mu_{CR}, 0.1) \quad (6.11)$$

and then truncated to $[0, 1]$ if the value exceeds the limits.

At the end of each generation g , the values of μ_F and μ_{CR} are updated according to the F and CR values that have generated successful offsprings in that generation, which means the fitness of offspring is smaller than that of the parent in minimization problem, by way of:

$$\mu_F = (1 - c) \cdot \mu_F + c \cdot \text{mean}_L(S_F) \quad (6.12)$$

$$\mu_{CR} = (1 - c) \cdot \mu_{CR} + c \cdot \text{mean}_A(S_{CR}) \quad (6.13)$$

where c is the learning rate (recommended value $c = 0.1$), S_F and S_{CR} are the set of all successful $F_i^{(g)}$ and $CR_i^{(g)}$ at generation g , $\text{mean}_A(\cdot)$ is the usual arithmetic mean, and $\text{mean}_L(\cdot)$ is the Lehmer mean defined by:

$$\text{mean}_L(S_F) = \frac{\sum_{F \in S_F} F^2}{\sum_{F \in S_F} F} \quad (6.14)$$

6.1.2.5. SAKPDE

SAKPDE is a newly developed DE algorithm with strategy adaptation and knowledge-based parameter adaptation proposed by Fan et al. [FWY19]Q. Fan et al.. In SAKPDE, the generation strategies (including mutation operators and crossover operators) are adapted based on the previous experience during the search process which leads itself to be a probability distribution based method. The adaptation of control parameters (F and CR) in SAKPDE are guided by prior knowledge.

During the first G_s generations (suggested $G_s = 0.3 \times G_{max}$, where G_{max} is the maximal number of generations fixed by the end-user), the “DE/rand/1” mutation operator and the binomial crossover operator are used. It has shown that this combination of operators has advantages in global searching from literature [GMK02; Zah07].

In the second stage, for each target vector $\vec{x}_i^{(g)}$, the mutation and crossover operators are selected according to the selection probability of each operator. The selection probability for each mutation and crossover operator is calculated based on the previous performance of the corresponding operator applied in preceding generations. Like JADE, SAKPDE also assumes that F values are produced by a Cauchy distribution and CR values are sampled from a normal distribution, while the parameters of the two distribution are updated differently in SAKPDE. The authors have adopted the

observations from the existing work as the prior knowledge to guide the evolution of F and CR , that is, large F value can provide good exploration capability whereas small F value can accelerate the convergence speed [DS11], and large CR value can provide good local search capability [MC10; Yu14], The implementation of these prior knowledge is carried out by decreasing linearly the value of location parameter of the Cauchy distribution for F when the generation increases. As for CR , the mean of the normal distribution increases gradually during the search process.

6.1.3. Summary

In this section, an optimization algorithm family named evolutionary algorithm (EA) is summarized. One of its branch, differential evolution (DE), is reviewed in details with several representative variants, i.e., jDE, EPSDE, SaDE, JADE and SAKPDE. These five algorithms are compared hereinafter with the proposed method AAC-DE in Table 6.2 and served as the reference methods for assessing the performance of the proposed method in Section 6.3.

6.2. Proposed adaptive DE algorithm

From the literature review of DE variants described in Section 6.1.2, it can be found that every DE variant method has implemented its proper way to adjust the control parameters (F and CR). A widely used idea is to assume that the value of scale factor F follows the Cauchy distribution meanwhile the value of crossover rate CR follows a normal distribution. Then the location parameter of the Cauchy distribution and the mean of the normal distribution will be updated progressively during the search process. Nonetheless, to the best of our knowledge, this assumption, Cauchy distribution for F values and Normal distribution for CR values, has never been demonstrated by neither theoretical results nor experimental results. Accordingly, an approach that can adapt the values of F and CR based on the distribution learned automatically from the previous experience during search process is more encouraging and convincing than the distributions assumed by researchers.

As for the generation strategy adaptation, in the above DE variants, the offspring generation strategies are all selected from a pool either randomly or based on a selection probability. The latter is calculated based on the previous performance of the candidate strategies used in the optimization search process. Most of DE variants adjust dynamically the mutant operator only. As for the crossover operator, it is either kept the same throughout the search process or selected by a predefined pattern. An automatic approach that is able to select dynamically both the mutation operator and the crossover operator based on the preceding performance seems to be more proper

than handling only type of operator.

In addition, to take the dependence and correlation between mutation operators and crossover operators into consideration, each mutation operator is coupled with a crossover operator. To conclude, the key of generation strategy adaptation is to design a proper mechanism to employ the experience of candidate strategies in previous generations as a guide to select strategies for the current generation.

6.2.1. Adaptive algorithm configuration for differential evolution (AAC-DE)

By considering above observations, an adaptive method for generation strategy and control parameter of DE is proposed in this section in which the generation strategy selection and the parameter adaptation are implemented by using machine learning methods, specifically:

- a reinforcement learning technique, that is, the Multi-Armed Bandit (MAB) algorithm, is involved to select properly generation strategy from the pool for each individual in the current population. The selection is dependent on the benefit of each candidate strategy calculated based on the experience from previous generations.
- an unsupervised learning approach, that is, the Kernel Density Estimation (KDE), is adopted to learn the distribution of F and CR pairs that have generated successful trial vectors in previous generations. The following of this section dedicates to describing the proposed AAC-DE.

The use of above two models for each individual depend on its search state (exploration or exploitation) and the progress in search process. To be more clear, in the early stage of search process, the individuals are expected to be more exploring, whereas in the late stage of search process, the individuals will be relatively more exploiting. AAC-DE has implemented these new features and results in an outline given in Algorithm 6.3.

6.2.2. Measurement of exploration and exploitation

The measurement of exploration and exploitation is an key component of AAC-DE, since the strategy selection and parameter adaptation in this work are based on the controlling of exploration and exploitation. The *StateKDE* model plays the role of estimating the state of each generated trial vector $\mathbf{u}_i^{(g)}$. Supposing a dataset \mathcal{D}_{state} , that includes all the individuals generated during the search process, the *StateKDE* model use this data set to measure the density of all the visited points in the search.

Algorithm 6.3: AAC-DE algorithm

Input: Optimizaition problem $\min f(\vec{x})$, candidate strategy pool \mathcal{P}_{str} , and parameter value ranges $[F_{min}, F_{max}]$ and $[C_{r,min}, C_{r,max}]$.

- 1 Set the generation counter $g = 0$, randomly initialize the population $\mathbf{P}^{(0)}$ with N_p individuals within the search domain, set $n_{stagnation} = 0$, initialize the data set of *StateKDE* as $\mathcal{D}_{state} = \mathbf{P}^{(0)}$, initialize the data set of *ExporeKDE* and *ExploitKDE* as $\mathcal{D}_{explore} = \emptyset$ and $\mathcal{D}_{exploit} = \emptyset$.
- 2 Evaluate the population $\mathbf{P}^{(0)}$.
- 3 **while** *the stopping criterion is not true* **do**
- 4 Get N_p strategies and parameter settings $S_i^{(g)}, F_i^{(g)}, C_{r,i}^{(g)}, i = 1, \dots, N_p$ by the AEEC procedure given in Algoritihm 6.4.
- 5 **for** $i = 1$ to N_p **do**
- 6 Create trial vector $\mathbf{u}_i^{(g)}$ for target vector $\mathbf{x}_i^{(g)}$ using the strategy $S_i^{(g)}$ and associated control parameters $(F_i^{(g)}, C_{r,i}^{(g)})$.
- 7 **if** *state*($\mathbf{u}_i^{(g)}$) *is exploration* **then**
- 8 Assign the reward of applying $S_i^{(g)}$ for *ExploreMBA* as 1.
- 9 Assign the reward of applying $S_i^{(g)}$ for *ExploitMBA* as 0.
- 10 $\mathcal{D}_{explore} = \mathcal{D}_{explore} \cup (F_i^{(g)}, C_{r,i}^{(g)})$.
- 11 **else**
- 12 Assign the reward of applying $S_i^{(g)}$ for *ExploreMBA* as 0.
- 13 Assign the reward of applying $S_i^{(g)}$ for *ExploitMBA* as 1.
- 14 $\mathcal{D}_{exploit} = \mathcal{D}_{exploit} \cup (F_i^{(g)}, C_{r,i}^{(g)})$.
- 15 **end if**
- 16 $\mathcal{D}_{state} = \mathcal{D}_{state} \cup \mathbf{u}_i^{(g)}$.
- 17 Evaluate the fitness of trial vector $f(\mathbf{u}_i^{(g)})$.
- 18 **if** $f(\mathbf{u}_i^{(g)}) < f(\mathbf{x}_i^{(g)})$ **then**
- 19 $\mathbf{x}_i^{(g+1)} = \mathbf{u}_i^{(g)}$
- 20 $n_{stagnation} = 0$
- 21 **else**
- 22 $\mathbf{x}_i^{(g+1)} = \mathbf{x}_i^{(g)}$
- 23 $n_{stagnation} = n_{stagnation} + 1$
- 24 **end if**
- 25 **end for**
- 26 Update all the MAB and KDE models, including *ExploreMAB*, *ExploitMAB*, *ExploreKDE*, *ExploitKDE* and *StateKDE*.
- 27 Increment the generation count $g = g + 1$.
- 28 **end while**

Based on the commonly accepted definition [CLM13]: “Exploration is the process of visiting entirely new regions of a search space, whilst exploitation is the process of visiting those regions of a search space within the neighborhood of previously visited points.”, we proposed to determine the state of a newly generated individual (trial vector) $\mathbf{u}_i^{(g)}$ as following:

$$state(\mathbf{u}_i^{(g)}) = \begin{cases} exploration, & \text{if } P_{stateKDE}(\mathbf{u}_i^{(g)}) \leq P_\epsilon \\ exploitation, & \text{otherwise} \end{cases} \quad (6.15)$$

where $P_{stateKDE}$ is the probability density function (PDF) learned by *StateKDE*, $P_{stateKDE}(\mathbf{u}_i^{(g)})$ is the probability density value at $\mathbf{u}_i^{(g)}$ given by the learned PDF $P_{stateKDE}$, P_ϵ is the threshold value that defines the boundary of exploration and exploitation. If $\mathbf{u}_i^{(g)}$ is located at a region where only few individuals have been generated so far, the value of $P_{stateKDE}(\mathbf{u}_i^{(g)})$ will be small. On the contrary, if $\mathbf{u}_i^{(g)}$ is at a region where many trial vector have been generated, the value of $P_{stateKDE}(\mathbf{u}_i^{(g)})$ will be high. Thus, $P_{stateKDE}(\mathbf{u}_i^{(g)})$ can be taken as a measure of exploration and exploitation. In this paper, the threshold value P_ϵ is set as the median of the density values given by $P_{stateKDE}$ for all the individuals in \mathcal{D}_{state} .

6.2.3. Generation Strategy Selection

To maximize the search performance of AAC-DE, a reinforcement machine learning model named multi-armed bandit (MAB) [ACBF02] is applied. The MAB is used to select a pair of mutation operator and crossover operator from a candidate pool of $\mathcal{P}_{GS} = \{(MUT_i, CX_j) : i = 1, \dots, K_{MUT}; j = 1, \dots, K_{CX}\}$, where MUT_i represents a mutation operator, CX_j represents a crossover operator, K_{MUT} and K_{CX} are the numbers of mutation and crossover operators in the candidate pool, respectively. For the convenience of lecture, we use GS_k to alternate the mutation and crossover operator pair (MUT_i, CX_j) in the candidate pool \mathcal{P}_{GS} , i.e.,

$$\mathcal{P}_{GS} = \{GS_k : k = 1, \dots, K_{GS}\} \quad (6.16)$$

where, $K_{GS} = K_{MUT} \cdot K_{CX}$ is the number of arms, in other words, the number of all possible combinations between the mutation operator and the crossover operator.

Each time, if a strategy GS_k generates successfully an offspring $\vec{u}_i^{(g)}$ from its parent $\vec{x}_i^{(g)}$ (i.e., the fitness of offspring $f(\vec{u}_i^{(g)})$ is smaller than that of parent $f(\vec{x}_i^{(g)})$ in an minimization problem), the strategy GS_k will be awarded by 1, otherwise, by 0. This reward stands for the immediate utility of applying the current strategy GS_k .

To select a strategy from the candidate pool \mathcal{P}_{GS} , a MAB model, namely Softmax MAB [KP14], is involved. This specified MAB selects generation strategies using a

Boltzmann distribution, that is to say, the probability of choosing strategy GS_k at the generation (g) is given by the following expression:

$$p_k^{(g)} = \frac{\exp(\mu_k^{(g-1)}/\tau)}{\sum_{i=1}^{K_{GS}} \exp(\mu_i^{(g-1)}/\tau)}, \text{ for } k = 1, \dots, K_{GS} \quad (6.17)$$

where τ is a temperature parameter which controls the randomness of the choice, $\mu_i^{(g-1)}$ is the empirical mean reward of the i -th strategy GS_i during the past ($g-1$) generations, and similarly, $\mu_k^{(g-1)}$ is that of the k -th strategy GS_k . The probability $p_k^{(0)}$ is initialized to $1/K_{GS}$ at ($g=0$), which implies that each strategy GS_k in the candidate pool \mathcal{P}_{GS} can be equally selected, since it is assumed that there is no prior knowledge about the performance of strategy at the beginning.

To eliminate the parameter setting problem of τ in Equation 6.17, we use a simple adaptive strategy to automatically adapt the value of τ as follows:

$$\tau = \min \mu_i^{(g-1)}, \text{ for } i = 1, \dots, K_{GS} \quad (6.18)$$

At the generation (g), a series Ω_{GS} of NP strategies can be sampled from the candidate pool \mathcal{P}_{GS} according to the probability given in Equation 6.17, i.e., $\Omega_{GS} \subseteq \mathcal{P}_{GS}$ such that $\Omega_{GS}^{(g)} = [GS_1^{(g)}, \dots, GS_i^{(g)}, \dots, GS_{NP}^{(g)}]$, where $GS_i^{(g)}$ is the generation strategy assigned to the i -th individual in the population P . At the end of the current generation, a reward value of 0 or 1 will be allocated to each strategy in Ω_{GS} according to the rules described previously. This results in a series of rewards like $\Omega_R^{(g)} = [R_1^{(g)}, \dots, R_i^{(g)}, \dots, R_{NP}^{(g)}]$, $R_i^{(g)} \in \{0, 1\}$, where $R_i^{(g)}$ is the reward corresponding to the i -th generation strategy $GS_i^{(g)}$.

Then, the empirical mean reward of k -th strategy GS_k in the candidate pool \mathcal{P}_{GS} , can be updated in the way that:

$$\mu_k^{(g)} = \frac{1}{N_{GS_k}^{(g)}} \left[\mu_k^{(g-1)} \cdot N_{GS_k}^{(g-1)} + \sum_{i=1}^{NP} R_i^{(g)} \cdot \mathbb{I}_{GS_i^{(g)}=GS_k} \right], \text{ for } k = 1, \dots, K_{GS} \quad (6.19)$$

where $\mathbb{I}_{predicate}$ is the indicator function that takes value of 1 if *predicate* is true and 0 if it is not. $N_{GS_k}^{(g)} = N_{GS_k}^{(g-1)} + \sum_{i=1}^{NP} \mathbb{I}_{S_i^{(g)}=GS_k}$ is the number of times that strategy GS_k has been selected and applied up to the end of generation g ,

Initially, $N_{GS_k}^{(0)} = 0$ and $\mu_k^{(0)} = 0$ for $k = 1, \dots, K_{GS}$. The empirical mean rewards of each generation strategy $\mu_k^{(g)}$ are always updated at the end of each generation by Equation 6.19, and subsequently, the selection probability of each strategy $p_k^{(g)}$ by Equation 6.17. The latter will be used to select generation strategies in the next generation.

6.2.4. Control Parameter (F and CR) Adaptation

After selecting a generation strategy by the mechanism stated in Section 6.2.3, it is indispensable to choose the suitable values for control parameter of the selected generation strategy, that is, the scale factor F for mutation operator and the crossover rate CR for crossover operator. To address the adaptation of these two control parameters, we adopt the kernel density estimation (KDE) [Par62], which is a well-known unsupervised machine learning technique, to learn the distribution of these two control parameters in an online fashion. By the meaning of “unsupervised”, the KDE can learn the probability density function (PDF) from the sample (or data set) and does not require any assumption about the underlying distribution.

In this work, the control parameters are adapted with respect to each generation strategy (i.e., every strategy GS_k in the candidate pool \mathcal{P}_{GS} defined in Equation 6.16) since it is possible that different generation strategies may perform well by using different F and CR values.

Take the scale factor F as an example, let the data set \mathcal{D}_{MUT_k} denote all the F values used in GS_k strategy during the past $(g - 1)$ generations, i.e., $\mathcal{D}_{MUT_k}^{(g-1)} = \Omega_F^{(0)} \cup \dots \cup \Omega_F^{(g-1)}$. The PDF for the distribution of F values learned by KDE model for the generation strategy GS_k at the current generation is:

$$PDF_{MUT_k}(F) = \frac{1}{|\mathcal{D}_{MUT_k}^{(g-1)}| h^2} \sum_{F_i \in \mathcal{D}_{MUT_k}^{(g-1)}} \mathbf{K}\left(\frac{F - F_i}{h}\right), \text{ for } k = 1, \dots, K_{GS} \quad (6.20)$$

where, $|\mathcal{D}_{MUT_k}^{(g-1)}|$ is the number of elements in the data set $\mathcal{D}_{MUT_k}^{(g-1)}$ collected during the past $(g - 1)$ generations, $\mathbf{K} : \mathbb{R}^2 \mapsto \mathbb{R}$ is the non-negative kernel function and $h > 0$ is a smoothing parameter named as *bandwidth* which is kept the same for all KDE models in this work. The Gaussian kernel $\mathbf{K}(p) = \frac{1}{\sqrt{2\pi}} \exp(-\frac{p^2}{2})$, which the one of the most widely applied kernel function [SJ13], is used in this paper.

Similarly, a KDE model can be established for the crossover rate CR of the generation strategy GS_k denoted as $PDF_{CX_k}(CR)$. Therefore, at the generation (g) , a pair of control parameters F and CR can be sampled from their proper distributions:

$$\begin{cases} F_i^{(g)} = \text{SampleBy} \left(PDF_{MUT_i^{(g)}}(F) \right) \\ CR_i^{(g)} = \text{SampleBy} \left(PDF_{CX_i^{(g)}}(CR) \right) \end{cases} \text{ for } i = 1, \dots, NP \quad (6.21)$$

where, $MUT_i^{(g)}$ and $CX_i^{(g)}$ are operators included in the generation strategy $GS_i^{(g)}$ affected to the i -th individual, $F_i^{(g)}$ is the scale factor that will be used by the mutation

operator $MUT_i^{(g)}$ and $CR_i^{(g)}$ is the crossover rate that will be used by the crossover operator $CX_i^{(g)}$.

If the generated parameter pair $[F_i^{(g)}, CR_i^{(g)}]$ is not in the feasible ranges $[F_{min}, F_{max}]$ and $[C_{r,min}, C_{r,max}]$, it is regenerated until satisfying the value ranges. After the mutation operation and crossover operation, if the offspring $\vec{u}_i^{(g)}$ is better than its parent $\vec{x}_i^{(g)}$, i.e., $f(\mathbf{u}_i^{(g)}) \leq f(\mathbf{x}_i^{(g)})$ in minimization problem, the used parameter pair $[F_i^{(g)}, CR_i^{(g)}]$ will be added to the training data set of the corresponding generation strategy $GS_i^{(g)}$, i.e.,

$$\begin{cases} \mathcal{D}_{MUT_i}^{(g)} = \mathcal{D}_{MUT_i}^{(g-1)} \cup F_i^{(g)} \\ \mathcal{D}_{CX_i}^{(g)} = \mathcal{D}_{CX_i}^{(g-1)} \cup CR_i^{(g)} \end{cases} \text{ if } f(\mathbf{u}_i^{(g)}) \leq f(\mathbf{x}_i^{(g)}), \text{ for } i = 1, \dots, NP \quad (6.22)$$

Initially, at the generation ($g = 0$), the $PDF_{MUT_k}(F)$ and $PDF_{MUT_k}(CR)$ are set to follow the uniform distribution. Accordingly, the values for F and CR are randomly selected with the equal probability within their admissible ranges during the first LP generations. LP stands for the learning period which takes 5% of the maximum allowable generations given by the end-user. After LP generations, enough training data have been collected in the data sets and the KDE models will be updated at the end of each generation till the end of run.

6.2.5. Adaptive equilibrium between exploration and exploitation

It is generally believed that EAs should start with exploration and then gradually change into exploitation [CLM13]. This coincides with the commonly accepted idea of encouraging the global search in the early stage of evolutionary optimization process and ensuring the local search in the latter stage [ES98; Urs02]. Based on this belief, an adaptive exploration-exploitation control (AEEC) scheme for strategy and parameter adaptation of DE is proposed.

The proposed AEEC scheme is described in Algorithm 6.4, where $rand$ is a random number drawn within $[0, 1]$, $n_{stagnation}$ is the number of generations over which the best fitness is not improved. As the generation number increasing, the probability of selecting strategy using *ExploreMAB* and generating parameter setting by *ExploreKDE* is linearly increasing.

6.2.6. Discussions

Table 6.2 compares the proposed method AAC-DE to other DE variants that have described in Section 6.1.2. From the perspective of parameters being adapted, jDE and

Algorithm 6.4: Adaptive exploration-exploitation control (AEEC)

```

1 if  $rand \leq g/g_{max}$  or  $n_{stagnation} \geq 10$  then
2   |   Select  $N_p$  strategies  $S_i^{(g)}, i = 1, \dots, N_p$  from  $\mathcal{P}_{str}$  using ExploreMAB.
3   |   Generate associated parameter settings  $(F_i^{(g)}, C_{r,i}^{(g)}), i = 1, \dots, N_p$  within
   |    $[F_{min}, F_{max}]$  and  $[C_{r,min}, C_{r,max}]$  using ExploreKDE.
4 else
5   |   Select  $N_p$  strategies  $S_i^{(g)}, i = 1, \dots, N_p$  from  $\mathcal{P}_{str}$  using ExploitMAB.
6   |   Generate associated parameter settings  $(F_i^{(g)}, C_{r,i}^{(g)}), i = 1, \dots, N_p$  within
   |    $[F_{min}, F_{max}]$  and  $[C_{r,min}, C_{r,max}]$  using ExploitKDE.
7 end if
   Output:  $S_i^{(g)}, F_i^{(g)}, C_{r,i}^{(g)}, i = 1, \dots, N_p$ .

```

JADE only adapt the control parameters (F and CR), SaDE, EPSDE and SAKPDE adapt both generation strategy and control parameters.

As for our proposed method AAC-DE, it handles both the generation strategy adaptation and the control parameter adaptation. Both adaptations are data-driven which means no more assumptions nor prior knowledge is required to conduct the parameter adaptation during the search process.

Table 6.2: Comparison between the proposed method AAC-DE and some DE variants given in Section 6.1.2

Algorithm	Adjusted generation strategies	Adjusted control parameters
CoDE [WCZ11]	mutation only	F and CR (discrete values)
jDE [Bre06]	(not available)	F and CR
EPSDE [Mal11]	mutation operator only	F and CR
SaDE [QHS09b]	mutation operator only	F and CR
JADE [ZS09]	(not available)	F and CR
SAKPDE [FWY19]	both mutation and crossover operator	F and CR
AAC-DE	both mutation and crossover operator	F and CR

6.3. Experimental Study

In order to evaluate the performance of AAC-DE, the CEC2017 [Awa16] benchmark set is involved. Both 30-dimensional ($D = 30$) and 50-dimensional ($D = 50$) design variables are used for every test function in CEC2017. The maximum number of function evaluations (MaxFES) is set to $10000 \times D$ where D is the dimension of the design variable. If the fitness error in a run is less than 10^{-8} , i.e., $f(\mathbf{x}) - f(\mathbf{x}^*) \leq 10^{-8}$

(where \mathbf{x}^* is global optimum of the test function, \mathbf{x} is the best solution found by the algorithm in a run), the run is stopped before the number of function evaluations reaches MaxFES and this run is called a successful run.

The mean and standard deviation of the fitness error $f(\mathbf{x}) - f(\mathbf{x}^*)$ from 25 independent runs in each experiment were recorded for measuring the performance of each algorithm. The effectiveness of AAC-DE was compared with the five well-known adaptive DE algorithms (i.e., jDE, JADE, SaDE, EPSDE and SAKPDE) that have been reviewed in Section 6.1.2 and listed in Table 6.2. For the compared algorithm, the recommended population size NP from their papers are used and, similarly, other parameters for the adaptation procedure are all taken from the papers. The population size for AAC-DE is set to be $NP = 100$. To achieve statistically sound conclusions, Mann–Whitney U test (a.k.a. *Wilcoxon rank-sum test*) [Der11] with 0.05 significance level was conducted on the experimental results. In addition, Friedman test and Nemenyi post-hoc test [Dem06; Der11] were carried out to compare the performance of the compared algorithm in terms of the mean fitness error values on all the tested functions.

6.3.1. Comparison with five state-of-the-art adaptive DE

Table 6.3 and Table 6.4 summarize the experimental results on 30D and 50D test functions of CEC2017, respectively. The mean and standard deviation of the fitness errors for the 25 independent runs for each investigated algorithm on each test function are listed in the tables along with the rank of each algorithm among all compared algorithms in terms of the mean fitness error on each test function is also shown in parentheses.

On each test function, AAC-DE was compared with other five DE variants by Mann–Whitney U test with the significance level of 0.05 over the fitness error from 25 runs. The sign “+”, “–”, and “ \approx ” interpret the Mann–Whitney U test results in last lines of the table, i.e., the number of test functions on which the performance of AAC-DE is significantly better than, worse than, or almost similar to that of the corresponding compared algorithms, respectively. The average of the ranks (R_{avg}) of each algorithm on the tested functions is also given.

Additionally, to analyze the overall performance of each algorithm on both 30D and 50D test problems, Friedman test with Nemenyi post-hoc test [Dem06; Der11] were carried out to assess the overall performance of the five investigated algorithms in terms of the mean fitness errors on all tested functions. The average (R_{avg}) and standard deviation (R_{std}) of the ranks of each algorithm over the 60 test problems

Table 6.3: Experimental Results of seven algorithms on 30D test functions of CEC2017.

F	AAC-DE Mean \pm Std(Rank)	jDE Mean \pm Std(Rank)	JADE Mean \pm Std(Rank)	SaDE Mean \pm Std(Rank)	EPSDE Mean \pm Std(Rank)	SAKPDE Mean \pm Std(Rank)
F_1	0.00E+00 \pm 0.00E+00 (3.5)	0.00E+00 \pm 0.00E+00 (3.5)	0.00E+00 \pm 0.00E+00 (3.5)	0.00E+00 \pm 0.00E+00 (3.5)	0.00E+00 \pm 0.00E+00 (3.5)	3.31E-02 \pm 1.93E-02 (7)
F_2	0.00E+00 \pm 0.00E+00 (3.5)	0.00E+00 \pm 0.00E+00 (3.5)	0.00E+00 \pm 0.00E+00 (3.5)	0.00E+00 \pm 0.00E+00 (3.5)	0.00E+00 \pm 0.00E+00 (3.5)	1.47E-05 \pm 9.86E-06 (7)
F_3	0.00E+00 \pm 0.00E+00 (3)	4.26E-08 \pm 6.75E-08 (6)	0.00E+00 \pm 0.00E+00 (3)	0.00E+00 \pm 0.00E+00 (3)	0.00E+00 \pm 0.00E+00 (3)	1.16E-01 \pm 1.57E-01 (7)
F_4	0.00E+00 \pm 0.00E+00 (3)	6.12E-01 \pm 6.66E-01 (7)	0.00E+00 \pm 0.00E+00 (3)	0.00E+00 \pm 0.00E+00 (3)	0.00E+00 \pm 0.00E+00 (3)	4.09E-03 \pm 1.76E-03 (6)
F_5	3.58E+00 \pm 1.34E+00 (1)	1.04E+01 \pm 2.10E+00 (7)	3.71E+00 \pm 9.04E-01 (2)	3.84E+00 \pm 9.79E-01 (3)	7.85E+00 \pm 1.91E+00 (6)	7.43E+00 \pm 1.39E+00 (5)
F_6	0.00E+00 \pm 0.00E+00 (4)	0.00E+00 \pm 0.00E+00 (4)	0.00E+00 \pm 0.00E+00 (4)	0.00E+00 \pm 0.00E+00 (4)	0.00E+00 \pm 0.00E+00 (4)	0.00E+00 \pm 0.00E+00 (4)
F_7	1.47E+01 \pm 2.07E+00 (2)	2.27E+01 \pm 1.93E+00 (7)	1.36E+01 \pm 8.96E-01 (1)	1.50E+01 \pm 1.54E+00 (3)	2.07E+01 \pm 2.00E+00 (4)	2.18E+01 \pm 2.46E+00 (6)
F_8	4.22E+00 \pm 1.94E+00 (3)	1.17E+01 \pm 2.26E+00 (7)	3.39E+00 \pm 8.36E-01 (1)	3.68E+00 \pm 9.88E-01 (2)	8.99E+00 \pm 1.71E+00 (6)	8.50E+00 \pm 1.64E+00 (4)
F_9	0.00E+00 \pm 0.00E+00 (4)	0.00E+00 \pm 0.00E+00 (4)	0.00E+00 \pm 0.00E+00 (4)	0.00E+00 \pm 0.00E+00 (4)	0.00E+00 \pm 0.00E+00 (4)	0.00E+00 \pm 0.00E+00 (4)
F_{10}	2.07E+02 \pm 8.96E+01 (3)	5.04E+02 \pm 1.14E+02 (7)	9.41E+01 \pm 5.14E+01 (1)	1.96E+02 \pm 8.38E+01 (2)	3.32E+02 \pm 9.69E+01 (5)	2.90E+02 \pm 1.04E+02 (4)
F_{11}	3.09E-01 \pm 5.39E-01 (4)	5.63E-01 \pm 7.66E-01 (5)	2.35E+00 \pm 7.10E-01 (6)	3.04E-01 \pm 6.09E-01 (3)	0.00E+00 \pm 0.00E+00 (1)	4.02E+00 \pm 8.41E-01 (7)
F_{12}	6.64E+00 \pm 2.39E+01 (1)	9.64E+01 \pm 4.09E+01 (5)	7.37E+01 \pm 7.82E+01 (3)	2.99E+02 \pm 1.39E+02 (6)	7.99E+01 \pm 6.88E+01 (4)	1.03E+03 \pm 3.16E+02 (7)
F_{13}	4.79E+00 \pm 3.02E+00 (5)	6.61E+00 \pm 1.74E+00 (6)	3.81E+00 \pm 3.00E+00 (3)	2.74E+00 \pm 2.73E+00 (2)	2.61E+00 \pm 2.89E+00 (1)	9.99E+00 \pm 2.02E+00 (7)
F_{14}	5.85E-01 \pm 6.39E-01 (5)	4.73E-01 \pm 5.47E-01 (4)	6.27E-01 \pm 4.34E-01 (6)	9.81E-02 \pm 2.75E-01 (3)	3.98E-02 \pm 1.99E-01 (2)	4.75E+00 \pm 1.73E+00 (7)
F_{15}	9.15E-02 \pm 1.96E-01 (4)	7.02E-02 \pm 5.68E-02 (3)	5.25E-01 \pm 2.09E-01 (6)	3.13E-01 \pm 4.24E-01 (5)	5.98E-02 \pm 1.47E-01 (2)	1.71E+00 \pm 4.56E-01 (7)
F_{16}	8.63E-01 \pm 3.08E-01 (5)	4.09E-01 \pm 2.11E-01 (2)	1.63E+00 \pm 6.33E-01 (6)	5.34E-01 \pm 2.22E-01 (4)	3.26E-01 \pm 2.41E-01 (1)	2.54E+00 \pm 7.88E-01 (7)
F_{17}	1.99E+00 \pm 8.49E-01 (5)	4.75E+00 \pm 1.62E+00 (6)	4.96E-01 \pm 3.23E-01 (4)	1.47E+00 \pm 2.89E-01 (1)	4.22E-01 \pm 3.06E-01 (3)	1.13E+01 \pm 3.31E+00 (7)
F_{18}	1.84E-01 \pm 2.42E-01 (4)	1.33E-01 \pm 1.47E-01 (2)	5.11E-01 \pm 6.08E-01 (5)	1.47E+00 \pm 4.00E+00 (6)	1.65E-01 \pm 1.98E-01 (3)	6.37E+00 \pm 1.84E+00 (7)
F_{19}	4.41E-02 \pm 4.90E-02 (4)	1.85E-02 \pm 1.92E-02 (2)	4.78E-02 \pm 1.83E-02 (5)	6.27E-02 \pm 3.00E-01 (6)	6.95E-05 \pm 2.77E-04 (1)	8.98E-01 \pm 2.09E-01 (7)
F_{20}	0.00E+00 \pm 0.00E+00 (3)	0.00E+00 \pm 0.00E+00 (3)	0.00E+00 \pm 0.00E+00 (3)	3.75E-02 \pm 1.04E-01 (6)	1.25E-01 \pm 1.56E-01 (7)	0.00E+00 \pm 0.00E+00 (3)
F_{21}	1.13E+02 \pm 4.62E+01 (1)	1.50E+02 \pm 5.81E+01 (4)	1.50E+02 \pm 4.90E+01 (3)	1.71E+02 \pm 4.97E+01 (6)	1.80E+02 \pm 5.10E+01 (7)	1.55E+02 \pm 5.80E+01 (5)
F_{22}	7.68E+01 \pm 4.30E+01 (1)	8.68E+01 \pm 3.19E+01 (3)	9.83E+01 \pm 8.57E+00 (4)	1.00E+02 \pm 1.23E-01 (5)	1.00E+02 \pm 3.85E-01 (6)	1.02E+02 \pm 4.64E-01 (7)
F_{23}	3.05E+02 \pm 2.14E+00 (3)	3.08E+02 \pm 2.38E+00 (5)	3.05E+02 \pm 8.81E-01 (2)	3.03E+02 \pm 2.10E+00 (1)	3.08E+02 \pm 2.06E+00 (6)	3.09E+02 \pm 1.86E+00 (7)
F_{24}	2.67E+02 \pm 1.07E+02 (2)	2.71E+02 \pm 1.09E+02 (3)	2.83E+02 \pm 8.97E+01 (5)	2.81E+02 \pm 1.04E+02 (4)	3.18E+02 \pm 6.56E+01 (7)	2.84E+02 \pm 1.05E+02 (6)
F_{25}	4.09E+02 \pm 2.03E+01 (4)	4.03E+02 \pm 1.51E+01 (3)	4.20E+02 \pm 2.36E+01 (6)	4.18E+02 \pm 2.33E+01 (5)	4.20E+02 \pm 2.33E+01 (7)	4.00E+02 \pm 9.09E+00 (2)
F_{26}	3.00E+02 \pm 0.00E+00 (3.5)	3.00E+02 \pm 0.00E+00 (3.5)	3.00E+02 \pm 0.00E+00 (3.5)	3.00E+02 \pm 0.00E+00 (3.5)	3.00E+02 \pm 0.00E+00 (3.5)	3.00E+02 \pm 0.00E+00 (7)
F_{27}	3.90E+02 \pm 1.93E+00 (4)	3.90E+02 \pm 1.53E+00 (5)	3.89E+02 \pm 1.32E+00 (2)	3.92E+02 \pm 2.45E+00 (7)	3.90E+02 \pm 1.97E+00 (6)	3.89E+02 \pm 5.35E-01 (3)
F_{28}	3.00E+02 \pm 0.00E+00 (2)	3.23E+02 \pm 7.86E+01 (4)	3.39E+02 \pm 1.00E+02 (5)	4.03E+02 \pm 1.41E+02 (7)	3.59E+02 \pm 1.21E+02 (6)	3.11E+02 \pm 5.67E+01 (3)
F_{29}	2.46E+02 \pm 5.43E+00 (2)	2.52E+02 \pm 5.99E+00 (6)	2.45E+02 \pm 6.55E+00 (1)	2.48E+02 \pm 6.38E+00 (4)	2.48E+02 \pm 4.62E+00 (3)	2.61E+02 \pm 6.02E+00 (7)
F_{30}	3.97E+02 \pm 5.29E+00 (2)	4.48E+02 \pm 2.86E+01 (3)	5.13E+02 \pm 2.21E+02 (4)	3.33E+04 \pm 1.63E+05 (6)	5.03E+04 \pm 2.50E+05 (7)	7.55E+02 \pm 1.45E+02 (5)
+		16	8	8	11	25
-		2	5	5	7	0
\approx		12	17	17	12	5
R_{avg}	3.15	4.45	3.62	4.05	4.18	5.73

The "Mean" and "Std" stand for the average and standard deviation of the function error values over 25 runs, respectively. "Rank" represents the ranking of an algorithm among all compared algorithms on the corresponding test function in terms of the "Mean". The "+", "-", and " \approx " signs denote that the performance of AAC-DE is significantly better than, worse than, and almost similar to that of the corresponding compared algorithms in a statistically significant way, respectively. R_{avg} is the average rank of the algorithm on all 30D test functions.

Table 6.4: Experimental Results of seven algorithms on 50D test functions of CEC2017.

F	AAC-DE Mean \pm Std(Rank)	jDE Mean \pm Std(Rank)	JADE Mean \pm Std(Rank)	SaDE Mean \pm Std(Rank)	EPSDE Mean \pm Std(Rank)	SAKPD Mean \pm Std(Rank)
F_1	0.00E+00 \pm 0.00E+00 (2.5)	9.25E-08 \pm 2.26E-07 (5)	0.00E+00 \pm 0.00E+00 (2.5)	0.00E+00 \pm 0.00E+00 (2.5)	0.00E+00 \pm 0.00E+00 (2.5)	3.37E-01 \pm 1.12E+00 (7)
F_2	0.00E+00 \pm 0.00E+00 (1.5)	3.64E+11 \pm 1.29E+12 (6)	0.00E+00 \pm 0.00E+00 (1.5)	8.39E-07 \pm 1.70E-06 (3)	1.37E-06 \pm 2.77E-06 (4)	1.34E+18 \pm 1.95E+18 (7)
F_3	6.74E+00 \pm 9.55E+00 (4)	5.93E+02 \pm 3.39E+02 (5)	3.87E+03 \pm 1.07E+04 (6)	2.39E-08 \pm 6.78E-08 (2)	0.00E+00 \pm 0.00E+00 (1)	3.71E+04 \pm 5.28E+03 (7)
F_4	1.64E+01 \pm 2.57E+01 (1)	8.47E+01 \pm 4.74E+01 (7)	3.39E+01 \pm 2.98E+01 (4)	1.68E+01 \pm 2.56E+01 (2)	3.00E+01 \pm 3.11E+01 (3)	6.21E+01 \pm 5.93E+00 (6)
F_5	3.54E+01 \pm 6.76E+00 (3)	1.09E+02 \pm 8.92E+00 (6)	2.63E+01 \pm 3.88E+00 (1)	2.85E+01 \pm 5.82E+00 (2)	9.65E+01 \pm 8.29E+00 (5)	5.69E+01 \pm 6.78E+00 (4)
F_6	0.00E+00 \pm 0.00E+00 (2.5)	0.00E+00 \pm 0.00E+00 (2.5)	0.00E+00 \pm 0.00E+00 (2.5)	1.44E-08 \pm 2.55E-08 (5)	0.00E+00 \pm 0.00E+00 (2.5)	4.80E-08 \pm 1.68E-08 (6)
F_7	7.00E+01 \pm 6.95E+00 (3)	1.49E+02 \pm 8.01E+00 (6)	5.36E+01 \pm 3.97E+00 (1)	6.90E+01 \pm 8.25E+00 (2)	1.34E+02 \pm 9.54E+00 (5)	9.86E+01 \pm 6.73E+00 (4)
F_8	4.09E+01 \pm 7.58E+00 (3)	1.10E+02 \pm 8.75E+00 (6)	2.59E+01 \pm 4.41E+00 (1)	2.69E+01 \pm 8.04E+00 (2)	9.88E+01 \pm 9.53E+00 (5)	6.07E+01 \pm 5.74E+00 (4)
F_9	1.79E+02 \pm 3.65E+02 (4)	0.00E+00 \pm 0.00E+00 (1)	7.16E-03 \pm 2.48E-02 (3)	8.88E-01 \pm 9.58E-01 (6)	2.21E-01 \pm 3.91E-01 (5)	3.58E-03 \pm 1.79E-02 (2)
F_{10}	2.29E+02 \pm 3.45E+02 (2)	4.84E+03 \pm 2.88E+02 (7)	1.79E+03 \pm 2.72E+02 (1)	3.20E+03 \pm 3.94E+02 (4)	4.48E+03 \pm 2.56E+02 (5)	2.90E+03 \pm 3.16E+02 (3)
F_{11}	2.38E+01 \pm 2.25E+01 (1)	3.38E+01 \pm 2.70E+01 (3)	3.08E+01 \pm 2.56E+01 (2)	6.83E+01 \pm 3.52E+01 (5)	3.55E+01 \pm 2.79E+01 (4)	7.27E+01 \pm 1.73E+01 (7)
F_{12}	1.01E+04 \pm 8.19E+03 (4)	1.59E+04 \pm 7.59E+03 (5)	1.39E+03 \pm 9.79E+02 (1)	6.19E+03 \pm 3.69E+03 (2)	9.74E+03 \pm 1.01E+04 (3)	7.05E+05 \pm 2.83E+05 (7)
F_{13}	2.87E+01 \pm 1.02E+01 (1)	1.34E+02 \pm 1.82E+02 (3)	6.38E+02 \pm 2.99E+03 (5)	3.50E+03 \pm 6.39E+03 (7)	1.30E+03 \pm 4.72E+03 (6)	4.40E+02 \pm 1.24E+02 (4)
F_{14}	1.66E+01 \pm 1.01E+01 (1)	4.71E+01 \pm 6.64E+00 (4)	7.24E+03 \pm 1.27E+04 (7)	1.17E+02 \pm 3.99E+01 (6)	3.71E+01 \pm 1.07E+01 (2)	6.43E+01 \pm 5.98E+00 (5)
F_{15}	1.07E+01 \pm 5.63E+00 (1)	2.61E+01 \pm 5.53E+00 (2)	1.23E+03 \pm 2.43E+03 (7)	2.05E+02 \pm 8.86E+01 (6)	5.51E+01 \pm 3.88E+01 (5)	4.85E+01 \pm 8.01E+00 (4)
F_{16}	3.63E+02 \pm 1.38E+02 (3)	5.11E+02 \pm 1.55E+02 (6)	4.05E+02 \pm 1.29E+02 (4)	2.73E+02 \pm 1.37E+02 (1)	3.00E+02 \pm 1.65E+02 (2)	4.19E+02 \pm 1.33E+02 (5)
F_{17}	6.87E+01 \pm 3.23E+01 (2)	9.02E+01 \pm 2.34E+01 (5)	7.55E+01 \pm 2.04E+01 (3)	6.01E+01 \pm 1.45E+01 (1)	9.83E+01 \pm 1.42E+01 (6)	1.81E+02 \pm 3.32E+01 (7)
F_{18}	2.79E+01 \pm 1.19E+01 (1)	8.20E+01 \pm 3.98E+01 (3)	5.68E+03 \pm 2.79E+04 (6)	3.42E+03 \pm 4.93E+03 (5)	9.75E+02 \pm 1.47E+03 (4)	6.90E+04 \pm 2.46E+04 (7)
F_{19}	9.51E+00 \pm 2.42E+00 (1)	2.08E+01 \pm 2.78E+00 (2)	1.01E+03 \pm 2.86E+03 (7)	1.10E+02 \pm 4.85E+01 (6)	2.53E+01 \pm 2.48E+01 (4)	3.19E+01 \pm 3.53E+00 (5)
F_{20}	9.87E+01 \pm 6.23E+01 (5)	5.71E+01 \pm 2.89E+01 (1)	8.87E+01 \pm 5.02E+01 (4)	7.79E+01 \pm 5.44E+01 (2)	1.06E+02 \pm 5.79E+01 (7)	1.04E+02 \pm 4.16E+01 (6)
F_{21}	2.35E+02 \pm 2.80E+01 (3)	3.10E+02 \pm 7.80E+00 (6)	2.27E+02 \pm 4.16E+00 (2)	2.26E+02 \pm 7.16E+00 (1)	2.94E+02 \pm 9.08E+00 (5)	2.63E+02 \pm 6.30E+00 (4)
F_{22}	1.00E+02 \pm 0.00E+00 (3)	1.00E+02 \pm 0.00E+00 (2)	1.00E+02 \pm 0.00E+00 (1)	1.00E+02 \pm 1.20E+00 (7)	1.00E+02 \pm 6.80E-01 (6)	1.00E+02 \pm 0.00E+00 (4)
F_{23}	3.83E+02 \pm 8.39E+00 (3)	4.54E+02 \pm 1.07E+01 (6)	3.73E+02 \pm 5.73E+00 (2)	3.70E+02 \pm 9.74E+00 (1)	4.41E+02 \pm 8.57E+00 (5)	4.00E+02 \pm 5.22E+00 (4)
F_{24}	4.60E+02 \pm 9.61E+00 (3)	5.15E+02 \pm 2.16E+01 (5)	4.39E+02 \pm 4.84E+00 (1)	4.44E+02 \pm 9.17E+00 (2)	5.18E+02 \pm 1.18E+01 (6)	4.70E+02 \pm 6.59E+00 (4)
F_{25}	3.87E+02 \pm 1.99E-01 (5)	3.87E+02 \pm 1.34E-01 (4)	3.87E+02 \pm 7.32E-01 (2)	3.90E+02 \pm 1.09E+01 (7)	3.87E+02 \pm 2.64E-01 (6)	3.87E+02 \pm 3.28E-02 (1)
F_{26}	1.26E+03 \pm 2.29E+02 (3)	1.91E+03 \pm 1.93E+02 (6)	1.17E+03 \pm 6.67E+01 (2)	1.10E+03 \pm 2.81E+02 (1)	1.80E+03 \pm 9.93E+01 (5)	1.51E+03 \pm 6.88E+01 (4)
F_{27}	5.02E+02 \pm 9.32E+00 (2)	4.99E+02 \pm 5.91E+00 (1)	5.06E+02 \pm 7.54E+00 (5)	5.10E+02 \pm 8.53E+00 (7)	5.05E+02 \pm 8.85E+00 (3)	5.09E+02 \pm 4.69E+00 (6)
F_{28}	3.26E+02 \pm 4.66E+01 (2)	3.44E+02 \pm 5.61E+01 (5)	3.36E+02 \pm 5.41E+01 (3)	3.40E+02 \pm 5.52E+01 (4)	3.47E+02 \pm 6.01E+01 (6)	3.66E+02 \pm 4.06E+01 (7)
F_{29}	4.78E+02 \pm 3.38E+01 (3)	6.00E+02 \pm 4.65E+01 (5)	4.70E+02 \pm 2.90E+01 (1)	4.71E+02 \pm 3.50E+01 (2)	5.17E+02 \pm 5.49E+01 (4)	6.14E+02 \pm 4.67E+01 (6)
F_{30}	2.10E+03 \pm 1.04E+02 (2)	2.59E+03 \pm 5.44E+02 (4)	2.11E+03 \pm 1.15E+02 (3)	2.78E+03 \pm 1.53E+03 (6)	2.76E+03 \pm 8.24E+02 (5)	4.96E+03 \pm 1.05E+03 (7)
+		23	6	14	20	26
-		1	11	8	1	1
\approx		6	13	8	9	3
R_{avg}	2.52	4.32	3.05	3.65	4.40	5.13

The "Mean" and "Std" stand for the average and standard deviation of the function error values over 25 runs, respectively. "Rank" represents the ranking of an algorithm among all compared algorithms on the corresponding test function in terms of the "Mean". The "+", "-", and " \approx " signs denote that the performance of AAC-DE is significantly better than, worse than, and almost similar to that of the corresponding compared algorithms in a statistically significant way, respectively. R_{avg} is the average rank of the algorithm on all 50D test functions.

Table 6.5: The average and standard deviation of ranks of all compared DE algorithms on 30D test functions

Algorithm	AAC-DE	jDE	SaDE	JADE	EPSDE	SAKPDE
R_{avg}	2.27	4.05	3.28	2.73	4.07	4.60
R_{std}	0.98	1.70	1.85	1.72	1.25	1.35
Nemenyi Test	p -value	0.0030	0.2848	0.9000	0.0027	0.0010
Friedman Test	p -value	1.56E-06				

Table 6.6: The average and standard deviation of ranks of all compared DE algorithms on 50D test functions

Algorithm	AAC-DE	jDE	SaDE	JADE	EPSDE	SAKPDE
R_{avg}	2.40	4.07	3.37	2.60	4.57	4.00
R_{std}	1.30	1.66	1.81	1.67	1.07	1.58
Nemenyi Test	p -value	0.0289	0.5923	0.9000	0.0010	0.0436
Friedman Test	p -value	5.33E-06				

are listed in Table 6.5 and Table 6.6 as well as the results of Friedman and Nemenyi tests. The average rank and the standard deviation of ranks for each algorithm are also graphed in Figure 6.1, where the blue bar represents the R_{avg} of the algorithm and the vertical black line on the top of each bar indicates $2R_{std}$ of the corresponding algorithm. From Table 6.5 and Figure 6.1, the average rank of the AAC-DE in 30D is the smallest among all compared algorithms. This indicates that the average performance of AAC-DE is the best among all the investigated DE algorithms. Additionally, the AAC-DE has the smallest standard deviation of ranks among all compared algorithms. It implies that the performance of AAC-DE across different test problems is more robust, or stable, than other algorithms. To conclude, the AAC-DE is expected to perform better than other representative DE variants.

The p -value of Friedman test, that is, p -value = $1.01E - 10$, is largely smaller than the significance level of 0.05, which indicates that the difference of performance from the five compared algorithms is significant. The pair-wise comparison between AAC-DE and other five algorithms are carried out by Nemenyi test. According to the results of Nemenyi test, the overall performance of AAC-DE is significantly better than that of jDE, EPSDE and SAKPDE since the p -value of pair-wise Nemenyi test between AAC-DE and the corresponding algorithm is smaller than 0.05. The p -value of pair-wise Nemenyi test of AAC-DE/SaDE pair and AAC-DE/CoDE pair are also very small, that is, 0.1324 and 0.1140, which also indicates that AAC-DE generally performs better than SaDE and CoDE. Since the p -value of pair-wise Nemenyi test between AAC-DE and JADE reaches 0.8541, it can state that AAC-DE slightly out-

performs JADE considering their average ranks. In summary, the proposed AAC-DE has the best overall performance among the compared algorithm according to the statistical test over the experimental results on CEC2017 benchmark set. The excellent general performance of AAC-DE demonstrates that the proposed OAC (online algorithm configuration) approach is effective and it works well on DE algorithm.

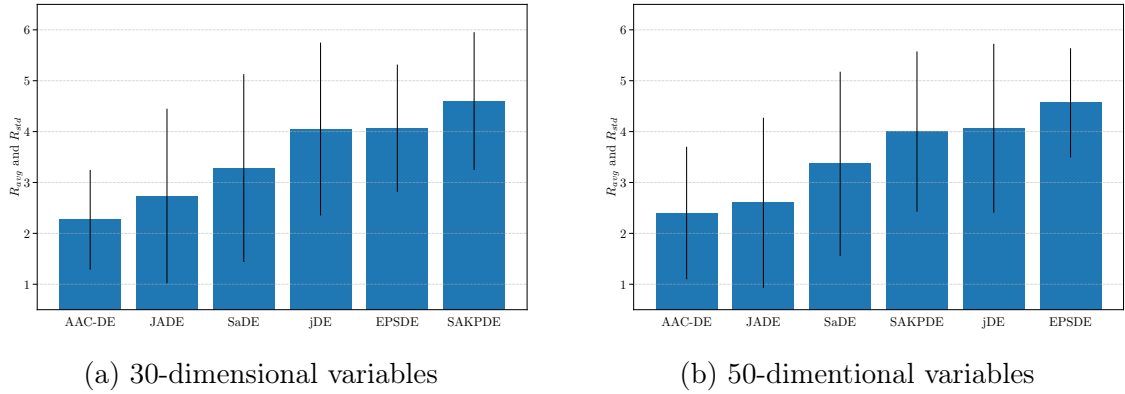


Figure 6.1: The average and standard deviation of the rankings of the compared DE algorithms on the test functions.

Lastly, from the box-plot (Figure 6.2), the AAC-DE is always placed in the top in terms of ranks. Compare to the algorithm in the second place (JADE), the AAC-DE has a narrow variance of ranks for 30D functions and a same ranking for 50D functions. All the five algorithms have the analogous lower whisker, but the AAC-DE has the lowest upper whisker. In fact, AAC-DE is ranked the top 2 among the 6 algorithms on half of all the test problems, the lowest rank is the 5th. While, for other five DE algorithms, they all get the rank of 6th on some test problems. It is apparent that the box-plot of AAC-DE is the shortest among the six algorithms. This suggests that the fluctuation of performance of AAC-DE over different test problems is relatively insignificant. In other words, the performance of AAC-DE is stable on different problems. While the performance of other five algorithms fluctuates significantly on different test functions. This also proves that the proposed AAC-DE has the best average performance and its performance is also the most stable among all of the compared algorithms.

6.3.2. Summary

The performance of DE algorithm is significantly affected by its hyper-parameters such as mutation operator, crossover operator and the associated control parameters. To address the algorithm configuration problem for DE in an online, or adaptive, fashion, this section presented an online algorithm approach AAC-DE which is based on the similarity of individuals. With a technique from reinforcement learning, i.e.,

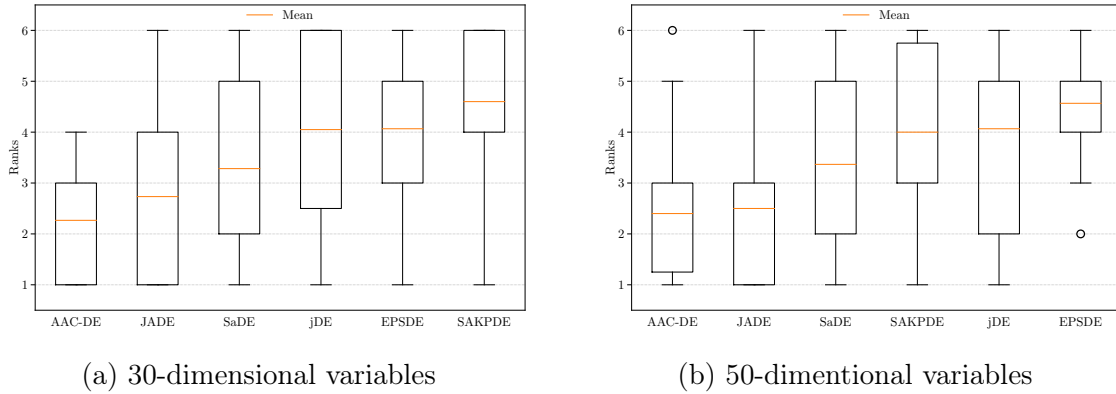


Figure 6.2: Box plots of the ranks of the compared DE algorithms on the test functions.

the multi-armed bandit (MAB) method, and an unsupervised learning approach, i.e., the kernel density estimation (KDE) method, the adaptation of its hyper-parameters is conducted by the experience earned in the history.

To be more clear, at each generation evolved by the AAC-DE, the search state (exploring or exploiting) of each individual is firstly classified. Then, based on the search state of the individual, a MAB and a KDE model is selected to reinforce either the exploring ability of the individuals or the exploiting ability with respect to the progress in the search process. The MAB is adopted to select mutation and crossover operators from the given candidate pools for each individual based on the experience from preceding generations, while the KDE method is used to learn the distribution of the two control parameters (scale factor F and crossover rate CR), and sample the applied parameters in each generation from the learned distribution.

The performance of the AAC-DE is evaluated through the experimental study on a set of benchmark problems, where AAC-DE is compared with five state-of-the-art adaptive DE algorithms regarding parameter control. The experimental results prove that AAC-DE achieves the best average performance on the tested functions and that the performance of AAC-DE is more stable than the compared DE algorithms on different test problems up to 50 dimensions of variables. This validates the effectiveness of the proposed OAC method.

6.4. Conclusions

To address the black-box optimization problem, an adaptive differential evolution algorithm called AAC-DE is proposed in this chapter. The experimental study on the CEC2017 benchmark sets proves that the AAC-DE works stably in terms of average performance compared to other state-of-the-art DE variants.

In the future, AAC-DE is planned to address other optimization problems, such as

multi-objective optimization problems and combinatorial optimization problems. Furthermore, in order to improve the overall performance of AAC-DE, it is also planned to combine the proposed method with the fitness landscape analysis.

As for the design of TRD for wind turbine, an optimized design considering both the damping performance in DLC2.3 and DLC1.2 is also planned. This implies a requirement of a multi-objective optimization algorithm since the objective function (damping performance) is evaluated independently in two different load cases.

Chapter 7

Conclusions and perspective work

The present essay delineates a full design process to develop an active damping system for wind turbine.

From the bibliographic study, the wind turbine design has an ongoing tendency towards higher wind turbine hub height, larger swept areas and higher nameplate capacity. This inevitable movement involves not only a reliably structural design but also an advanced control system to ensure both the structural safety and the stable power production. To achieve this objective, one of the critical challenges that cannot be bypassed is the mechanic vibration over the wind turbine tower as it can bring about potential fatigue damage to the structure due to periodic loading or ultimate loading caused by the extreme vibration-amplitude. Therefore, integrating a damping system into the wind turbine sounds like a reasonable solution to address the vibration problems on the wind tower. What is more, if the damping system can actively control the vibrations at the frequency of the 1st order and the 2nd order, the wind turbine can continue to produce electrical power even in the range close to the natural frequencies of wind turbine tower.

Before the development of damping system, the baseline data must be firstly prepared so that the performance of the damper can be evaluated. An ultimate load analysis under gusty wind with technical fault (DLC2.3) and a fatigue load analysis under turbulent wind (DLC1.2) are accordingly accomplished. In addition, a complementary study about the timing between the technical fault (grid loss) and the wind gust is carried out in DLC2.3. Not to mention that a novel data-driven neural network-assisted probabilistic framework of fatigue analysis is proposed and validated in DLC1.2.

The design of active damping system for wind turbine begins by introducing an active damping device that generates the damping force by eccentrically rotating control masses. This active damper, namely TRD, is then studied with a SDOF oscillator model with more details about its operating modes and the corresponding control methods. An initial design for integrating the TRD into the inherent control system of NREL 5MW reference wind turbine is proposed, and the effectiveness of such integration is assessed by comparing to the baseline data.

In the end, an adaptive algorithm configuration method for differential evolution,

AAC-DE, is proposed to optimize the design of TRD in an online fashion of optimizing process. An experimental verification through CEC2017 benchmark test functions prove that the AAC-DE is very effective and stable in terms of average performance compared to other DE variants. An application of AAC-DE is performed to optimize the design variables of TRD.

The present work depicts completely the design process of integrating a damping device into the wind turbine including the theoretical feasibility analysis, engineering design conformed to the related standards, numerical verification, effectiveness evaluation and design optimization. The suggested design process implies multi-disciplinary studies in wind energy, structural engineering, control engineering, computational mechanic and optimization algorithm.

The original contributions mainly involve:

1. An ultimate load analysis and fatigue analyses are proposed for the wind tower structure. These two analyses are used as the reference results for evaluating the effectiveness of the damping system.
2. A neural network assisted probabilistic framework for fatigue analysis is proposed by using neural network. The proposed method has been numerically tested with the NREL 5MW reference wind turbine.
3. An active damping system using TRD is developed and integrated into the reference wind turbine. The numerical simulation has been carried out to evaluate such integration.
4. A new adaptive algorithm configuration method for differential evolution, AAC-DE, is proposed combining the reinforcement learning (i.e., multi-armed bandit algorithm) and unsupervised learning approaches (i.e., kernel density estimation). The proposed algorithm is applied to seek the optimal design for TRD in the wind turbine.

Several tasks are planned for the future work:

1. integrate the swinging mode of TRD into the current control system and reassess the TRD's performance in DLC1.1 with respect to fatigue loads. This requires a new implementation of the wind turbine's control system.
2. evaluate the performance of TRD in reducing long-term fatigue damage on offshore wind turbine considering both wave loads and wind loads.
3. investigate the possibility of installing multiple TRDs inside the offshore wind turbine in order to improve its safety and productivity, for example, one for wind turbine tower and another for wind turbine foundation.
4. use AAC-DE to optimize the hyperparameters of the deep neural network ResMLP. To obtain this goal, it is indispensable to make AAC-DE eligible for solving Bayesian optimization problems.



Appendix



Appendix A

Basic notions

A.1. Levelized cost of electricity generation

Cost can be calculated in different ways, and each way of accounting for power generation costs brings with its own perspectives. The costs that can be examined include equipment costs (for example wind turbines), financing costs, total installed cost, fixed and variable operating and maintenance costs (O&M), fuel costs (if exist) and the levelized cost of energy (LCOE).

The LCOE is the average price of total cost to build and operate a power-generating plant over its lifetime divided by the total energy produced by the power plant over its lifetime. It gives an economic way to compare different methods of electricity generation. A price higher than this would produce a higher return on capital, while a lower price would yield a lower return on capital or even a loss. It differs by technology, country and project based on the renewable energy resource, capital and operating costs and the efficiency/performance of the technology. Many institutes or organizations have published their own cost metric methodologies considering diverse cost factors in their LCOE model [Uni19; LAZ19; Blo18; Int18]. Many potential trade-offs should be considered while designing a LCOE model.

Considering that the model need to be applied to various technologies and various countries, the model presented here is fairly simplistic Equation A.1. Apparently, a detailed LCOE model results in more accurate values, but also results in a significantly higher overhead in terms of the relevant assumptions and the risks of decreasing transparency. More detailed model can often give the impression of greater accuracy, but if the assumptions are not differentiated based on real-world data or the assumptions cannot be robustly filled, then the supposed accuracy of may be misleading.

$$\text{LCOE} = \frac{\sum_{t=1}^n \frac{I_t + M_t + F_t}{(1+r)^t}}{\sum_{t=1}^n \frac{E_t}{(1+r)^t}} \quad (\text{A.1})$$

where, LCOE = the average lifetime levelized cost of electricity generation

I_t = investment expenditures in the year t

M_t = operating and maintenance expenditures in the year t

F_t = fuel expenditures in the year t

E_t = electricity generation in the year t

r = discount rate

n = expected lifetime of system

The LCOE is normally calculated over the design lifetime of the plant varying from 20 to 30 years in the assumptions from different source of information. Since the LCOE depends highly on the assumptions used in calculation, it should be very prudent to compare the LCOE studies from different research institutes. The assumption of capacity factor, for example, has significant impact on the LCOE assessment and will be discussed in the following section A.2.

However, some researchers indicate that the LCOE is not appropriate for comparing intermittent generating technologies (e.g. wind and solar) with dispatchable generating technologies (e.g. nuclear and coal) because of the ignorance in [Jos11]:

1. the differences in the production profiles of intermittent and dispatchable generating technologies;
2. the variations in the market value of the electricity at the time it is supplied;
3. the expected life-cycle costs associated with different generating technologies.

The LCOE also fails in evaluating the effect of energy efficiency and conservation. In many countries, the energy efficiency and conservation have already stabilized or even reduced the demand of electricity rather than allowing it to grow [Bro14]. Considering only the LCOE will tend to maximize the production and take the risk of overestimating the demand of electricity.

Although different cost metrics are useful in different scenarios, the LCOE of renewable energy is still a commonly used first-order economic metric to compare power generation technologies. The designers of renewable energy project use more detailed methods to determine the feasibility and the profitability in real-world projects taking into account tariffs, subsidies and other incentives. But these are beyond the scope of this dissertation.

A.2. Capacity factor

The capacity factor is a value that describes the actual use of a power plant. It is a ratio between the actual electrical energy produced over a given period and the maximum energy that it would have produced if it had been operated at its installed

capacity during the same period. Typically, the capacity factor is calculated over one year and expressed in percentage, but there is nothing to prevent it from being calculated over different periods.

The higher the capacity factor is achieved, the closer the power plant is to its maximum production capacity. The capacity factor, in theory, can take all values from 0% to 100%. In real-world, it will never be 100% (because of maintenance or intermittence of resource) nor 0% (the plant produce nothing during the calculation period), and will never exceed the availability factor¹.

To give an example of calculation in wind energy, the French onshore wind farm Falfosse & Ramonts in Normandy has an installed capacity of 23.5 MW. It has been commissioned since July 2016 and has an average annual electricity production of 60 GWh produced by 10 wind turbines of 2.35 MW [ENG]. By the definition, the capacity factor of this wind farm is:

$$\text{Capacity factor} = \frac{60000MWh}{(23.5MW) \times (24hours/day) \times (365days)} \approx 29.15\% \quad (\text{A.2})$$

In general, the offshore wind farms have a higher average capacity factor (Table 1.1, Chapter 1). But it is really hard to sentence that the offshore wind farms are "more useful" than the onshore ones. Taking an onshore wind farm in Nicaragua as an example, the Eolo wind farm reached a capacity factor of 61.29% in 2015, while the highest capacity factor for offshore wind farm in the same year was around 50% [INI15; Int18].

A.3. Betz's limit

Based on the two-dimensional momentum theory in fluid mechanics, the disk actuator model provides a simple but usable way to understand and calculate the power efficiency in wind turbine design. Considering a perfect non-compressible fluid flows through a disk actuator in a stream tube Figure A.1. This disk actuator is uniform, in other words, the thrust is uniform over the disk. It represents the area that is swept by the wind turbine rotor and blades and the other components, like wind turbine tower, are ignored. There is a pressure drop in the plane of the disk actuator in where the kinetic energy of the wind is also converted to the mechanical energy, and then, the electric energy.

1. The availability factor of a power plant is the amount of time that it is able to produce electricity over a certain period, divided by the amount of time in the period.

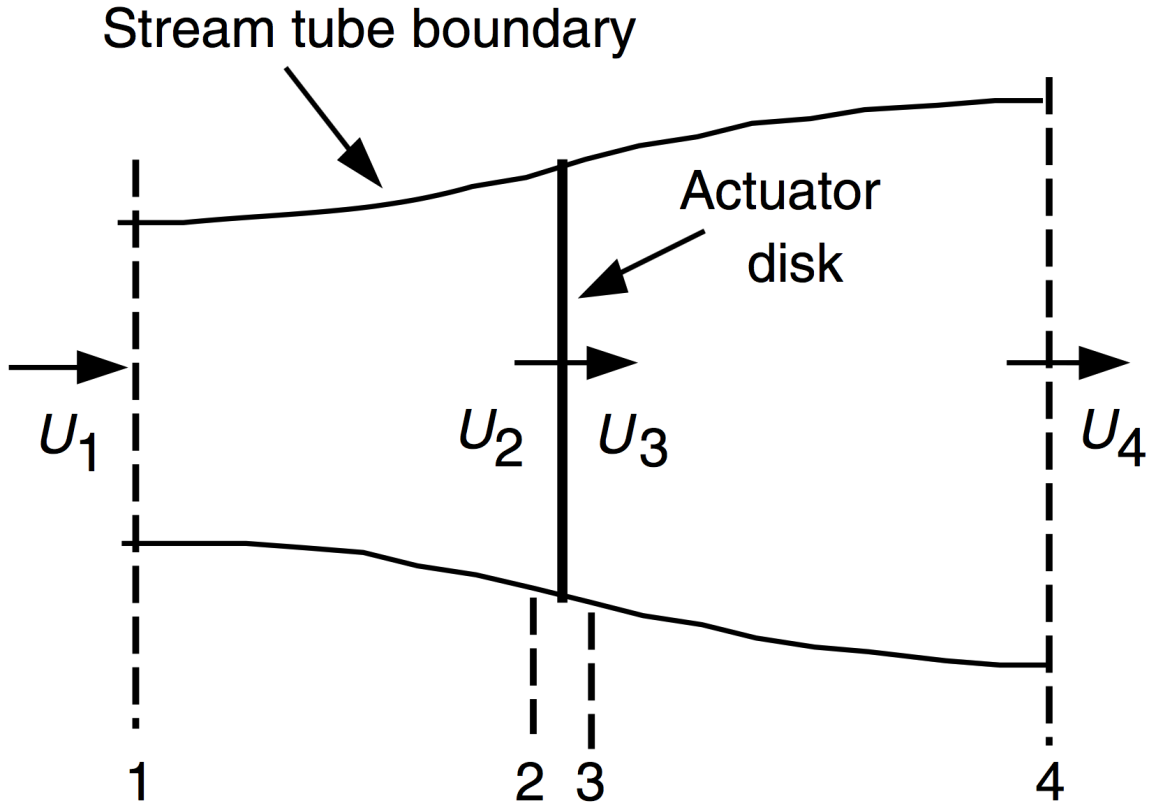


Figure A.1: Disk actuator model

Assuming that the static pressure far upstream and far downstream of the stream tube is equal to the ambient static pressure. The airflow is frictionless (i.e. no frictional drag) and the rotating rotor wake is not considered (i.e. airflow lines deflected only in one plane). Through the elementary physical laws, the total kinetic energy of the fluid is calculated by:

$$P_{total} = \frac{1}{2} \rho A v^3 \quad (\text{A.3})$$

where, ρ = fluid density (usually it's air)

v = free stream speed

A = cross-sectional area of the airflow

Applying the law of conservation of energy, the power that can be extracted from the airflow corresponds to the difference of power in upstream and in downstream:

$$P = P_{upstream} - P_{downstream} = \frac{1}{2} \rho A_u v_u^3 - \frac{1}{2} \rho A_d v_d^3 \quad (\text{A.4})$$

where, v_u = upstream speed

v_d = downstream speed

A_u = area of the fluid before the disk actuator

A_d = area of the fluid after the disk actuator

Applying the law of conservation of mass, the mass flow rate is given by:

$$\dot{m} = \rho A_u v_u = \rho A_a v_a = \rho A_d v_d \quad (\text{A.5})$$

where, v_a = stream speed at the disk actuator

A_a = area of the disk actuator (swept area of the rotor and the blades)

Substituting Equation A.5 into Equation A.4 will yield an expression for the obtainable energy in the airflow:

$$P = \frac{1}{2} \rho A_a v_a (v_u^2 - v_d^2) = \frac{1}{2} \dot{m} (v_u^2 - v_d^2) \quad (\text{A.6})$$

On the other hand, by applying the law of conservation of momentum, the force that the airflow exerts on the disk actuator is:

$$F = \dot{m} (v_u - v_d) \quad (\text{A.7})$$

This force (i.e. thrust) pushes the airflow at the speed of v_a in the plane of the disk actuator. By the basic physical definition, the power required to do this work is:

$$P = Fv = \dot{m}v(v_u - v_d) \quad (\text{A.8})$$

Equating the Equation A.6, which describes the obtainable energy as the difference of power in upstream and downstream, and the Equation A.8, which describes the obtainable energy as the power done by the thrust, yields a relationship for the speed of airflow:

$$\begin{aligned} P &= \frac{1}{2} \dot{m} (v_u^2 - v_d^2) = \dot{m}v(v_u - v_d) \\ v &= \frac{1}{2} (v_u + v_d) \end{aligned} \quad (\text{A.9})$$

So the wind speed at the disk actuator is the average of the upstream speed and downstream speed. By substituting the speed v_a in Equation A.6 by Equation A.9 and differentiating the power P with respect to v_d , it yields:

$$\begin{aligned} P &= \frac{1}{2} \rho A_a v_a (v_u^2 - v_d^2) \\ &= \frac{1}{4} \rho A_a (v_u + v_d) (v_u^2 - v_d^2) \\ &= \frac{1}{4} \rho A_a (-v_d^3 - v_u v_d^2 + v_u^2 v_d + v_u^3) \end{aligned} \quad (\text{A.10})$$

For a given area of disk A and a given speed of the upstream fluid v_u , the maximum

of this power is reached when $v_d = \frac{v_u}{3}$:

$$\begin{aligned} P_{\max} &= \frac{1}{4}\rho A \left(-\left(\frac{v_u}{3}\right)^3 - v_u \left(\frac{v_u}{3}\right)^2 + \frac{v_u^3}{3} + v_u^3 \right) \\ &= \frac{16}{27} \left(\frac{1}{2} \rho A v_u^3 \right) \end{aligned} \quad (\text{A.11})$$

So this is the maximum obtainable energy from the wind.

Therefore, the ratio between the maximum energy extracted from the wind given in Equation A.11 and the total energy of the wind given in Equation A.3 yields a fraction:

$$C_{p,\max} = \frac{P_{\max}}{P_{\text{total}}} = \frac{16}{27} \approx 0.59 \quad (\text{A.12})$$

This value is called Betz's limit which was firstly published by a German physicist, Albert Betz, in 1919 [Bet20]. The Betz's limit is a maximal value that can be theoretically obtained. In real-world, the modern wind turbine usually offers a ratio between 0.4 and 0.5. This ratio, called the power coefficient C_p , will be discussed later (section A.4).

A.4. Power coefficient

To characterize the performance of the entire wind turbine system, the power coefficient is developed to measure the overall turbine system efficiency. It is a non-dimensional coefficient defined as the ratio of the actual produced power over the power in the wind:

$$C_p = \frac{\text{Actual produced power}}{\text{Power in the wind}} = \frac{P_{\text{out}}}{\frac{1}{2}\rho A v^3} \quad (\text{A.13})$$

The Betz's limit calculated in the previous section gives the theoretical maximum of this coefficient by using an ideal model based on disk actuator theory. In real case, the disk actuator theory is incapable to describe the relationship between the wind turbine rotor shape and its aerodynamic properties such as evaluating the influence of the number of wind turbine blades, designing the airfoil of blades etc. In fact, the power coefficient in the real-world is much less than the Betz's limit. The Figure A.2 plots the power coefficient of different wind turbine designs as a function of the tip-speed ratio which is commonly referenced to the tangential velocity of the blade tip:

$$\lambda = \frac{\Omega R}{v} \quad (\text{A.14})$$

where, Ω = angular velocity of the wind turbine rotor
 R = distance from the rotor axis to the tip of blade
 v = speed of wind

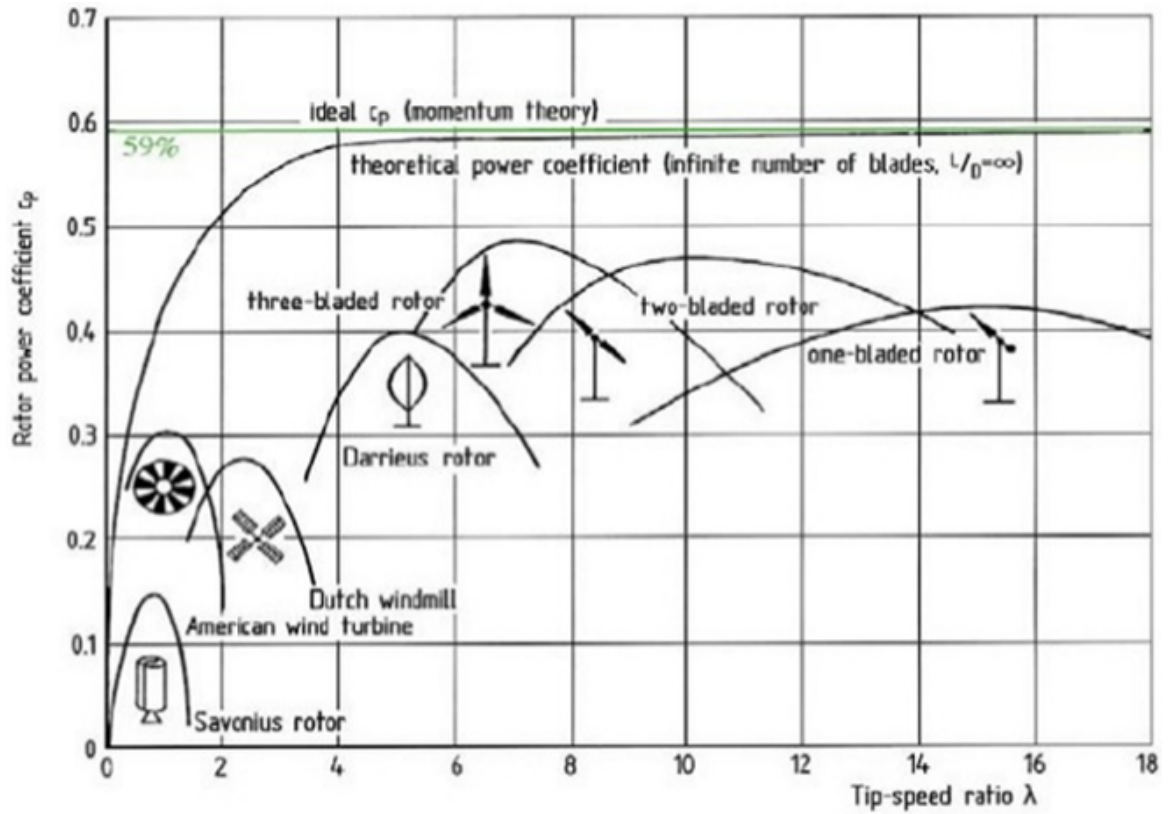


Figure A.2: Power coefficient of wind turbine in different designs [Hau13]

There is a gap between the Betz's limit (the theoretical maximum) and the maximum of power coefficient in the reality. It is more than 10% as shown in Figure A.2. To give a brief explanation, the process that converts wind energy into electricity power goes chiefly through three major conversion steps, namely, aerodynamic conversion, mechanical conversion and electrical conversion. Because of the second law of thermodynamics, a part of energy will be always lost at each conversion. In aerodynamic conversion, the kinetic energy of wind is converted into the mechanical energy that spins the wind turbine shaft. A part of wind energy rotates the blades on the plane of rotation while the others deforms the blades along the rotor axis. Most of the energy is lost in this conversion comparing to the other conversions. In mechanical conversion, the turbine shaft drives a gearbox which adjusts the rotating speed of the blade to a higher speed connecting to the electric generator. Some energy is hence lost here because of friction in gearbox and in bearings supporting the shaft. In electric conversion, the shaft turns the electric generator converting the mechanical energy into electrical energy. Depending on the type of generator, the electricity produced can be

either alternating current or direct current. Nevertheless, the current is alternating (or not), some electronic equipment are still needed to convert the raw electric current into the steady and fixed frequency current that can be integrated to the power grid. So there are loss of energy for both the electric generator and electronic equipment. The accumulation of all these losses in subsystem makes the Betz's limit to be definitely unreachable in the real-world. In general, the modern wind turbines offer a power coefficient that is 70% to 85% of the Betz's limit.

Another conclusion that can be drawn from the power curve above is that the power coefficient increases with the number of blades. But the increment is less and less. While the wind turbines blades increase from one blade to two blades, the power coefficient gains about 10%. When the number of blades increase from two to three, the gain in power coefficient amounts to 3% to 4% which is still considerable. The benefit is only 1% to 2% when adding a fourth blade. However, if there is a large number of the blades (e.g. American wind turbine), the power coefficient actually decreases because of the complicated aerodynamic conditions of airflow (airfoil drag and tip losses).

So the possible gain in power coefficient of a few percent is clearly not enough to cover the cost of an additional blade (i.e. 4-bladed HAWT). On the other hand, the turbines with high tip-speed ratio (i.e. 1-bladed or 2-bladed HAWT) require a higher wind speed to obtain its maximum power coefficient. It also causes some other undesired worries, for instance, the emission of more noise which is unacceptable especially at most onshore sites. The 3-bladed HAWT gives a balance solution. It proposes a high power coefficient at an acceptable low tip-speed ratio than all the others designs. This is one of the major reasons that makes the 3-bladed HAWT to be dominant in today's wind power market and, therefore, chosen as the studied subject in this dissertation.

In conclusion, the power coefficient C_p characterize an overall efficiency of the entire wind turbine system. Although, the maximum energy that can be extracted from the wind energy is about 59%, also known as Betz's limit, but it is hardly to reach this theoretical efficiency due to the loss of energy in the power conversion. The 3-bladed HAWT is an optimum design in balancing the power efficiency, the economical cost, the sustainable design and many other aspects.

One last word, there is a significant difference between the capacity factor (section A.2) and the power coefficient (section A.4). The prior fraction measures the actual electricity production versus the possible production while the posterior fraction indicates the maximum obtainable energy from the energy available in the wind.

A.5. Free damped vibration

In all the following cases, the mass is released with velocity v_0 from position x_0 at time $t = 0$.

Underdamping

If $0 < \xi < 1$, the motion is underdamped (oscillatory). It means that the amount of damping is small enough, the system still vibrates but may stop vibrating over time. In this case, the solution of the equation of motion (Equation 1.7) is:

$$x = e^{-\xi\omega_n t} \left[x_0 \cos(\omega_d t) + \frac{v_0 + \xi\omega_n x_0}{\omega_d} \sin(\omega_d t) \right] \quad (\text{A.15})$$

where, $\omega_d = \omega_n \sqrt{1 - \xi^2}$

ω_d is called the damped angular frequency which is less than the undamped angular frequency ω_n . But the difference is truly negligible in the real world since the damping ratio ξ is relatively small.

Critical damping

If $\xi = 1$, the system is critically damped and the general solution is then:

$$x = e^{-\omega_n t} [x_0 + (v_0 + \omega_n x_0)t] \quad (\text{A.16})$$

Overdamping

If $\xi > 1$, the motion is overdamped (non-oscillatory), the solution to the equation of motion is:

$$x = e^{-\xi\omega_n t} \left[\frac{v_0 + (\xi\omega_n + \omega_d)x_0}{2\omega_d} e^{\omega_d t} - \frac{v_0 + (\xi\omega_n - \omega_d)x_0}{2\omega_d} e^{-\omega_d t} \right] \quad (\text{A.17})$$

where, $\omega_d = \omega_n \sqrt{\xi^2 - 1}$

Appendix B

IEC normal wind conditions

The change of wind speed in time occurs on its velocity magnitude and its direction. The annual variation shows the variation on seasonal or monthly averaged wind speed. Diurnal variation occurs in tropical and temperate latitudes due to the differential heating of the earth's surface during the regular cycle of radiation. Short-term fluctuations over periods of ten minutes or less, which have a stochastic character, reflect turbulence in wind speed. Fatigue damage to wind turbines is most generally seen in short-term variance periods of 10-minute average wind speed [GA11; HCC16; Slo20]. In this work, a 10-minute simulation at a fixed average wind speed is used to measure fatigue damage to the wind turbine tower.

To generate a 10-minutes wind field is based on 10-minutes mean wind speed V_{10} , 10-minutes turbulence intensity I_{10} , and shear exponent *alpha*. The 10-minutes turbulence intensity is the ratio of the wind speed standard deviation to the mean wind speed, determined from the same set of measured data samples of wind speed, and taken over a specified time [Int05] as

$$I_{10} = \frac{\sigma_{10}}{V_{10}} \quad (\text{B.1})$$

where, σ_{10} is the standard deviation of the mean wind speed.

To calculate the 10-minutes standard deviation there is a dependency with the V_{mean} described in standard [Int05]. For normal turbulence model, this dependency is given by the local statistical moments of σ_1 as: $\mathbf{E}(\sigma_1|v) = TI_{ref}(0.75WS + 3.8)$ and $\mathbf{V}(\sigma_1|WS) = (1.4TI_{ref})^2$. The parameters of the σ_1 density probability distribution are given in the following equations as a function of WS and I_{ref} is the expected value of the turbulence intensity at 15m/s depending on wind turbine class [Int05].

$$\sigma_{\sigma_1} = \left[\ln \left(\frac{\mathbf{V}(\sigma_1|WS)}{\mathbf{E}^2(\sigma_1|WS)} + 1 \right) \right]^{1/2} \quad (\text{B.2})$$

$$\mu_{\sigma_1} = \ln[\mathbf{E}(\sigma_1|WS)] - \frac{\sigma_{\sigma_1}^2}{2} \quad (\text{B.3})$$

Taking into account topography and roughness, the shear exponent *alpha* or power-law exponent expresses the presumed difference in wind speed with height

above ground [Int05]. This means that it is important to know the type of wind field that analyzes the wind turbine, which is not always usable, to know the profile at various average wind speeds. A simplified correlation between the mean shear exponent α and V_{mean} based on a common distribution described by [DNK15] as:

$$\mu_\alpha = 0.088(\ln(V_{10}) - 1) \quad (\text{B.4})$$

$$\sigma_\alpha = (1/V_{10}) \quad (\text{B.5})$$

Subsequently, this procedure employs stochastic, full-field, turbulent wind simulations named Turbsim [JK12]. It numerically simulates time series of 3-dimensional wind velocity vectors at points in a regular vertical grid. The theory behind this tool, based on Veer's method [Vee88], generates a 3-dimensional field from a power spectral density (PSD) function and the coherence function. Veer's method uses a general random process simulation method developed by Shinozuka and Jan [SJ72]. To generate the random time-series signal using the following equation:

$$u(t) = \bar{u} + \sum_{j=1}^{M-1} A_j \cos(2\pi n_j t + \phi_j) \quad (\text{B.6})$$

$$A_j = \sqrt{2} l_j \quad (\text{B.7})$$

$$l_j = \sqrt{\left[\frac{S(n_j) + S(n_{j+1})}{2} \right] (n_{j+1} - n_j)} \quad (\text{B.8})$$

A frequency interval has to be selected from the PSD between n_1 to n_M and then discretize in $M - 1$ sub-intervals, each frequency n_j correspond to a value S_j from the spectral density function, \bar{u} is the average wind speed and ϕ_j is a random variable uniformly distributed between 0 and 2π . For each node of the vertical grid and at every time instant observed, it will consider the contribution of every frequency selected between n_1 and n_M .

As mentioned before, a spectral density function is needed to complete the random generation process. The IEC Kaimal Model [Int05] used in this work is given by:

$$\frac{f S_k(f)}{\sigma_k^2} = \frac{\frac{4fL_k}{V_{hub}}}{\left(1 + \frac{6fL_k}{V_{hub}}\right)^{5/3}}, \quad (k = u, v, w \text{ and } f > 0) \quad (\text{B.9})$$

where, f is the frequency in Hertz; k is the index referring to the velocity component direction (i.e u = longitudinal, v = lateral and w = upward); S_k is the single-sided velocity component spectrum; V_{hub} is the mean wind speed at hub height; L_k is the

velocity component integral scale parameter, determined by

$$L_k = \begin{cases} 8.1\Lambda_1, k = u \\ 2.7\Lambda_1, k = v \\ 0.66\Lambda_1, k = w \end{cases} \quad (\text{B.10})$$

where Λ_1 is the longitudinal scale parameter at hub height given by $0.7z$ $z \leq 60m$ or $42m$ $z \geq 60m$. σ_k is the velocity component standard deviation given by

$$\sigma_k = \begin{cases} \sigma_u, k = u \\ 0.8\sigma_u, k = v \\ 0.5\sigma_u, k = w \end{cases} \quad (\text{B.11})$$

where σ_u is calculated used equation B.1.

It is also important to select a coherence function given by the complex magnitude of the cross-spectral density of the u-component (i.e., longitudinal wind velocity component V_x) at two spatially separated points, divided by the autospectrum function. The IEC standard has also stated a widely used root coherence function for V_x [Int05]:

$$\text{Coh}_{j,k} = \exp \left(-b \sqrt{\left(\frac{fr}{V_{hub}} \right)^2 + \left(0.12 \frac{r}{L_c} \right)^2} \right) \quad (\text{B.12})$$

where, f = frequency (Hz)
 r = distance between two points j and k
 $b = 12$, coherence decrement fixed by the standard
 $L_c = 8.1\Lambda_1$ coherence scale parameter

Lastly, the coherence function for the v- and w-components of the IEC spectral models is:

$$\text{Coh}_{j,k} = \begin{cases} 1 & j = k \\ 0 & j \neq k \end{cases} \quad (\text{B.13})$$

Appendix C

IEC extreme wind conditions

The IEC 61400-1 standard stipulates six extreme wind conditions in total. In addition to the conditions explained in Section 2.2.3.2, three other conditions including wind shear events and short-time changes in the wind direction are considered as well.

Extreme direction change (EDC)

The extreme direction change magnitude θ_e is limited to the interval $[-180^\circ, 180^\circ]$ and calculated by using the following equation:

$$\theta_e = \pm 4 \arctan \left(\frac{\sigma_1}{V_{hub} \left(1 + 0.1 \left(\frac{D}{\Lambda_1} \right) \right)} \right) \quad (\text{C.1})$$

where, σ_1 = wind speed longitudinal standard deviation given by Equation 2.3

Λ_1 = turbulence scale parameter given by Equation 2.7

D = diameter of the rotor (m)

Then, the transient of EDC is defined as a function of time t :

$$\theta(t) = \begin{cases} 0^\circ & \text{for } t < 0 \\ \pm 0.5\theta_e \left(1 - \cos\left(\frac{\pi t}{6}\right) \right) & \text{for } 0 \leq t \leq 6 \\ \theta_e & \text{for } t > 6 \end{cases} \quad (\text{C.2})$$

The duration of the EDC is fixed to 6 s. The sign shall be chosen so that the worst transient loading occurs. At the end of the direction change transient, the direction is assumed to remain unchanged. The wind speed shall follow the NWP model in Section 2.2.3.1.

Extreme coherent gust with direction change (ECD)

The magnitude V_{cg} of the ECD is fixed to 15 m/s. The wind speed is then given by:

$$V(z, t) = \begin{cases} V(z) & \text{for } t < 0 \\ V(z) + 0.5V_{cg} \left(1 - \cos\left(\frac{\pi t}{10}\right) \right) & \text{for } 0 \leq t \leq 10 \\ V(z) + V_{cg} & \text{for } t > 10 \end{cases} \quad (\text{C.3})$$

In the similar manner to the EDC, the wind speed $V(z)$ shall follow the NWP model (Section 2.2.3.1) and the rise time of gust is fixed to 10s in Equation C.3. During the rise time, the wind speed is additionally assumed to change its direction from 0° to θ_{cg} , where the magnitude of direction change θ_{cg} is defined as follows:

$$\theta_{cg}(V_{hub}) = \begin{cases} 180^\circ & \text{for } V_{hub} < 4 \\ \frac{720^\circ}{V_{hub}} & \text{for } 4 < V_{hub} < V_{ref} \end{cases} \quad (\text{C.4})$$

Thus, the wind direction changes simultaneously with the wind gust as follows:

$$\theta(t) = \begin{cases} 0^\circ & \text{for } t < 0 \\ \pm 0.5\theta_{cg} \left(1 - \cos\left(\frac{\pi t}{T}\right)\right) & \text{for } 0 \leq t \leq T \\ \pm\theta_{cg} & \text{for } t > T \end{cases} \quad (\text{C.5})$$

The duration of direction change T equals to the rise time of gust 10 s.

Extreme wind shear (EWS)

The extreme wind shear (EWS) is accounted by considering the wind speed transients in the vertical direction as well as the horizontal direction. As such, the transient vertical shear is given by:

$$V(z, t) = \begin{cases} V_{hub} \left(\frac{z}{z_{hub}}\right)^\alpha \pm \left(\frac{z-z_{hub}}{D}\right) \left(2.5 + 0.2\beta\sigma_1 \left(\frac{D}{\Lambda_1}\right)^{0.25}\right) \left(1 - \cos\left(\frac{2\pi t}{T}\right)\right) & \text{for } 0 \leq t \leq T \\ V_{hub} \left(\frac{z}{z_{hub}}\right)^\alpha & \text{otherwise} \end{cases} \quad (\text{C.6})$$

And the transient horizontal shear is:

$$V(y, z, t) = \begin{cases} V_{hub} \left(\frac{z}{z_{hub}}\right)^\alpha \pm \left(\frac{y}{D}\right) \left(2.5 + 0.2\beta\sigma_1 \left(\frac{D}{\Lambda_1}\right)^{0.25}\right) \left(1 - \cos\left(\frac{2\pi t}{T}\right)\right) & \text{for } 0 \leq t \leq T \\ V_{hub} \left(\frac{z}{z_{hub}}\right)^\alpha & \text{otherwise} \end{cases} \quad (\text{C.7})$$

where, $\alpha = 0.2$

$\beta = 6.4$

σ_1 = standard deviation of wind speed given by Equation 2.3 for the NTM

Λ_1 = turbulence scale parameter given by Equation 2.7

D = rotor diameter (m)

$T = 12$ duration of transient (s)

in both Equation C.6 and Equation C.7. The sign for the horizontal wind shear transient shall be chosen so that the worst transient loading occurs. The two extreme wind shears are not applied simultaneously.

Appendix D

NREL 5MW reference wind turbine

NREL (National Renewable Energy Laboratory) decides to make their reference wind turbine to be 5MW because it has much precedence. Based on the publicly available information, they compared 6 different wind turbine models and finally decided to use the specification of the REpower 5M wind turbine as the target specifications for their reference machine.

Because the detailed data was unavailable from turbine manufacturer. But there were many similarities between REpower 5M and DOWEC project¹. So they used huge data from the DOWEC study to design the NREL offshore 5-MW baseline wind turbine.

This wind turbine is a conventional 3-bladed upwind variable-speed and variable blade-pitch-to-feather-controlled turbine. The major properties are listed in Table D.1.

Blade

The actual REpower 5M wind turbine uses blades with built-in prebend as a means of increasing tower clearance without a large rotor overhang. However, this kind of blade is not widely supported by simulation tools. So NREL have chosen a 2.5°-upwind precone in the baseline machine to represent the smaller amount of precone and larger amount of prebend that are built into the actual machine.

The rotor diameter of NREL 5MW wind turbine is 126 m. But this value ignores the effect of blade precone which reduces the actual diameter and swept area. The exact rotor diameter is actually 125.88 m and the actual swept area is 12 445.3 m².

The NREL 5MW baseline wind turbine has three 61.5 m-long blades (Note: the hub radius is 1.5 m). The structural properties of each blade are based on 62.6 m-long LM Glasfiber blade used in DOWEC project. So the LM Glasfiber blade is truncated at 61.5 m span to obtain the structural properties. The structural property of blade tip is obtained by interpolating between the 61.2 m and 61.7 m stations.

NREL have specified a structural damping ratio of 0.477465% critical in all modes of the isolated blade. And they also have increased the blade section mass per unit length by 4.536% in order to scale the overall (integrated) blade mass to 17.74 t, which

1. Dutch Offshore Wind Energy Converter Project (by Energy Research Center of the Netherlands)

Table D.1: Gross properties of NREL 5MW reference wind turbine

Property	Value
Rating power	5 MW
Number of blades	3
Rotor orientation	Upwind
Control system	Variable-speed collective pitch control
Drivetrain	High-speed multiple-stage gearbox
Rotor diameter	125.88 m
Hub diameter	3 m
Hub height (HH)	90 m
Cut-in speed V_{in}	3 m/s
Rated speed V_{rate}	11.4 m/s
Cut-out speed V_{out}	25 m/s
Cut-in rotor speed	6.9 rpm
Rated rotor speed	12.1 rpm
Rated tip speed	80 m/s
Overhang	5 m
Shaft tilt	5°
Precone	2.5°
Rotor mass	110 t
Nacelle mass	240 t
Tower mass	347.46 t

was the nominal mass of the blades in REpower 5M prototype.

Table D.2: Blade structural properties

Property	Value
Length (with respect to root along preconed axis)	61.5 m
Mass scaling factor	4.536%
Overall mass	17.74 t
First mass moment of inertia (w.r.t. blade root)	363 231 kg m
Second mass moment of inertia (w.r.t. blade root)	11 776 047 kg m ²
Center of mass location (w.r.t. root along preconed axis)	20.475 m
Structural damping ratio (for all modes)	0.477465%

The blade aerodynamic properties are based on DOWEC blades, too. NREL set 17 blade elements for integration of the aerodynamic and structural forces.

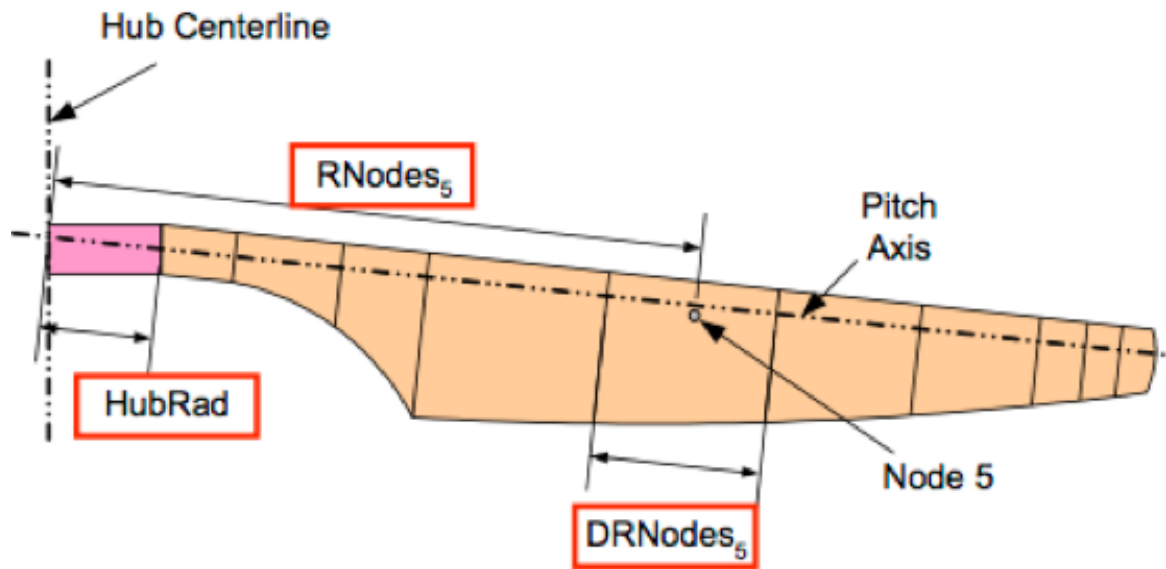


Figure D.1: Blade layout

Table D.3: Distributed blade aerodynamic properties

Node (-)	RNodes (m)	AeroTwst (°)	DRNodes (m)	Chord (m)
1	2.8667	13.308	2.7333	3.542
2	5.6000	13.308	2.7333	3.854
3	8.3333	13.308	2.7333	4.167
4	11.7500	13.308	4.1000	4.557
5	15.8500	11.480	4.1000	4.652
6	19.9500	10.162	4.1000	4.458
7	24.0500	9.011	4.1000	4.249
8	28.1500	7.795	4.1000	4.007
9	32.2500	6.544	4.1000	3.748
10	36.3500	5.361	4.1000	3.502
11	40.4500	4.188	4.1000	3.256
12	44.5500	3.125	4.1000	3.010
13	48.6500	2.319	4.1000	2.764
14	52.7500	1.526	4.1000	2.518
15	56.1667	0.863	2.7333	2.313
16	58.9000	0.370	2.7333	2.086
17	61.6333	0.106	2.7333	1.419

Hub and nacelle

The hub and nacelle properties are given in Table D.4 in which the elevation of yaw bearing above ground, or mean seal level (MSL), is calculated by:

$$\text{MSL} = \text{Hub height (HH)} - \text{Vertical distance from the tower top to the HH}$$

In this case, the HH is 90 m Table D.1 and the vertical distance is taken from DOWEC project — which is 2.4 m.

Table D.4: Nacelle and hub properties

Property	Value
Elevation of yaw bearing above ground (or MSL)	87.6 m
Vertical distance along yaw axis from yaw bearing to shaft	1.962 56 m
Distance along shaft from hub center to yaw axis	5.019 10 m
Distance along shaft from hub center to main bearing	1.912 m
Hub mass	56.78 t
Hub inertia about low-speed shaft	115 926 kg m ²
Nacelle mass	240 t
Nacelle inertia about yaw axis	2 607 890 kg m ²
Nacelle center of mass location downwind of yaw axis	1.9 m
Nacelle center of mass location above yaw bearing	1.75 m
Equivalent nacelle-yaw-actuator linear-spring constant	9 028 320 kN m/rad
Equivalent nacelle-yaw-actuator linear-damping constant	19 160 kN m/(rad s ⁻¹)
Nominal nacelle-yaw rate	0.3 °/s

Drivetrain

The rated rotor speed is as same as the one of REpower 5M wind turbine. The gearbox was assumed to be no frictional losses (i.e., the gearbox efficiency equals to 100%).

Table D.5: Drivetrain properties

Property	Value
Rated rotor speed	12.1 rpm
Rated generator speed	1173.7 rpm
Gearbox ratio	97:1
Electrical generator efficiency	94.4%
Generator inertia about high-speed shaft	534.116 kg m ²
Equivalent drive-shaft torsional-spring constant	867 637 kN m/rad
Equivalent drive-shaft torsional-damping constant	6215 kN m/(rad s ⁻¹)
Fully-deployed high-speed shaft brake torque	28.1162 kN m
High-speed shaft brake time	0.6 s

Tower and material

The tower properties of NREL 5MW baseline onshore wind turbine are based on the DOWEC project. The outer diameter is linearly interpolated between 6.00 m at 0.00 m (tower base) and 3.87 m at 87.60 m (tower top). The thickness is linearly interpolated between 0.0351 m at 0.00 m and 0.0247 m at 87.60 m.

Table D.6: Distributed tower properties

Elevation (m)	Outer diameter (°)	Thickness (m)	Fore-aft stiffness (N m ²)
0.00	6.000	0.0351	6.143×10^{11}
8.76	5.787	0.0341	5.348×10^{11}
17.52	5.574	0.0330	4.633×10^{11}
26.28	5.361	0.0320	3.991×10^{11}
35.04	5.148	0.0309	3.419×10^{11}
43.80	4.935	0.0299	2.910×10^{11}
52.56	4.722	0.0289	2.460×10^{11}
61.32	4.509	0.0278	2.065×10^{11}
70.08	4.296	0.0268	1.719×10^{11}
78.84	4.083	0.0257	1.418×10^{11}
87.60	3.870	0.0247	1.158×10^{11}

The tower fore-aft stiffness in Table D.6 is computed by its definition:

$$k = E \frac{\pi(D_{ext}^4 - D_{int}^4)}{64}$$

where, $E = \text{Young's modulus (GPa)}$
 $D_{ext}, D_{int} = \text{outer diameter and inner diameter of the tower (m)}$

Here is some key properties for tower material:

- Young's modulus 210 GPa
- Shear modulus 80.8 GPa
- Poisson's ratio 0.3
- Density 8500 kg/m³

Be aware that the effective density of tower steel is a little different from steel's typical value (7850 kg/m³), because this value has already taken into consideration the mass from the paint, bolts, welds, and flanges that are not accounted in the tower thickness data.

Generator-torque control

A wind turbine control system is composed of several sensors and actuators, hardware and software work to achieve the better performance possible for which they were designed. In general, hardware are responsible for acquiring the signals from sensors and to drive the actuators as well. The software is in charge of the signal processing, decision making and, by these means, pursues the optimal operational point of the wind turbine like maximizing power, mitigating damaging fatigue loads, detecting faults, and maintaining safe turbine operation.

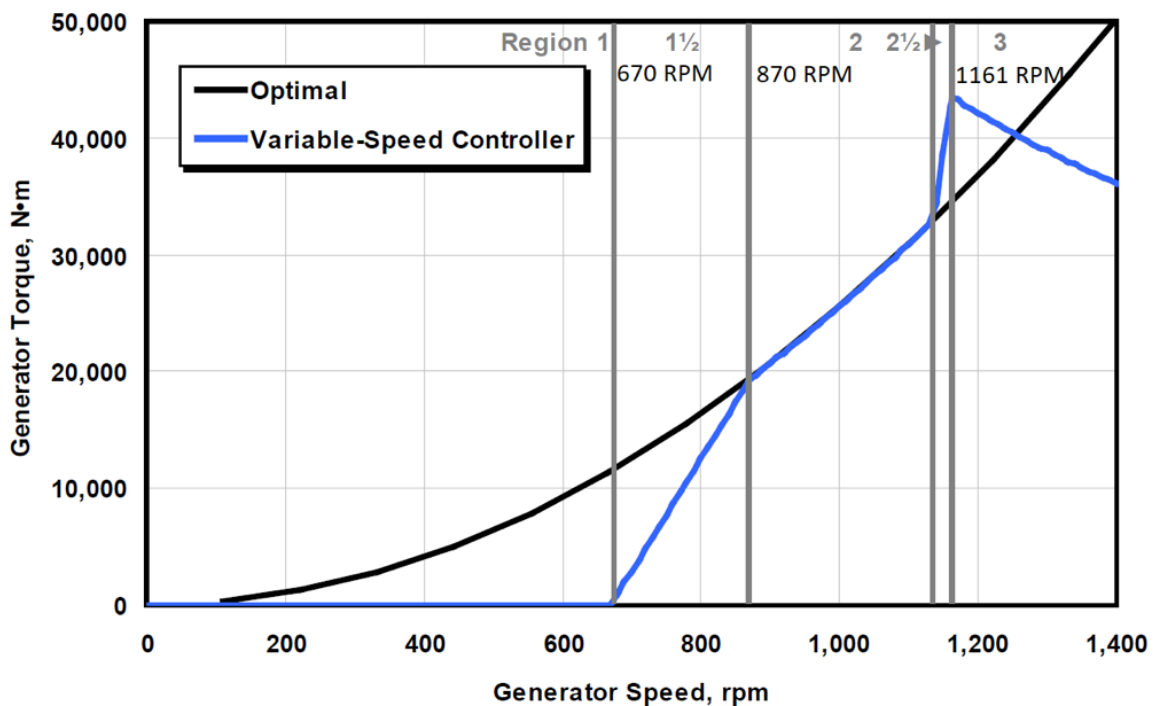


Figure D.2: Torque-versus-speed response of the variable-speed controller

The torque is computed as a tabulated function of the generator speed, i.e., the torque commanded from the controller is dependent of the generator speed. In the NREL 5MW there are five control regions defined: 1, $1^{1/2}$, 2, $2^{1/2}$ and 3. Each of these regions have initial and final generator speed and its respective generator torque. The regions and the optimal and approximated behavior of the generator torque are shown in Figure D.2.

Blade pitch control

When in the region 3, the full range of the blade-pitch-angle is used in a collective manner, i.e. all blades have the same pitch-angle. The controller employed is a gain-scheduled proportional-integral (PI), also based on the generator speed, specifically on the error between the real value and the rated generator speed (1173.7 rpm). To be more clear about the pitch controller, for different wind speeds the controller need to maintain a constant rotor speed and, consequently, power. Table D.7 shows different wind speeds maintaining a constant rotor speed by varying the pitch angle. The last column exhibits the sensitivity of aerodynamic power, P , related to the pitch angle, θ .

Table D.7: Sensitivity of aerodynamic power P to blade pitch angle θ in Region 3

Wind speed (m/s)	Rotor speed (rpm)	Pitch angle θ ($^{\circ}$)	$\frac{\partial P}{\partial \theta}$ (W/rad)
11.4	12.1	0.00	-28.24×10^6
12.0	12.1	3.83	-43.73×10^6
13.0	12.1	6.60	-51.66×10^6
14.0	12.1	8.70	-58.44×10^6
15.0	12.1	10.45	-64.44×10^6
16.0	12.1	12.06	-70.46×10^6
17.0	12.1	13.54	-76.53×10^6
18.0	12.1	14.92	-83.94×10^6
19.0	12.1	16.23	-90.67×10^6
20.0	12.1	17.47	-94.71×10^6
21.0	12.1	18.70	-99.04×10^6
22.0	12.1	19.94	-105.90×10^6
23.0	12.1	21.18	-114.30×10^6
24.0	12.1	22.35	-120.20×10^6
25.0	12.1	23.47	-125.30×10^6

Natural frequencies

Considering the baseline wind turbine in a stationary condition with the high-speed shaft brake engaged, the system wide natural frequencies are computed in FAST. All blades are pitched to their feather position (0°) without considering aerodynamic damping ratio. The first 13th full-system natural frequencies are listed in Table D.8.

Table D.8: Full-System Natural Frequencies

Mode	Description	Natural frequency (Hz)
1	1 st tower fore-aft	0.324
2	1 st tower side-to-side	0.312
3	1 st drivetrain torsion	0.621
4	1 st blade asymmetric flapwise yaw	0.666
5	1 st blade asymmetric flapwise pitch	0.668
6	1 st blade collective flap	0.699
7	1 st blade asymmetric edgewise pitch	1.079
8	1 st blade asymmetric edgewise yaw	1.090
9	2 nd blade asymmetric flapwise yaw	1.934
10	2 nd blade asymmetric flapwise pitch	1.922
11	2 nd blade collective flap	2.021
12	2 nd tower fore-aft	2.900
13	2 nd tower side-to-side	2.936

Appendix E

Coordinate system

Since the major interest of this dissertation concerns about the mechanical behavior of the wind turbine tower regarding the internal and external conditions, tower-base coordinate system is, therefore, advisable to express the tower deflection, local force, moment, etc. Two types of coordinate system are used in this dissertation.

E.1. Cartesian coordinate system

The first is Cartesian coordinate system (Figure 3.1a) which is fixed in the support platform so that it translates and rotates with the platform in such a way that:

Origin intersection point of the tower base connection to the support platform.

\vec{x}_t pointing horizontally in the nominal downwind direction.

\vec{y}_t pointing laterally to the left when looking in the nominal downwind direction.

\vec{z}_t pointing vertically up from the center of the tower.

The tower-base refers to the last flange at the bottom of the tower (Figure 3.1b). It is fixed at the top of the support platform (i.e., foundation, monopile, tripod caisson) by bolts, screws, etc.

For onshore wind turbine, the \vec{x}_t -axis positive direction is aligned with the downwind wind direction and the origin point is defined at the tower base so that the wind velocity can also be expressed in the same coordinate system. This may be changed if the NREL 5MW reference wind turbine is used in sea-based scenario in which the support platform may have pitch or yaw displacement.

E.2. Cylindrical coordinate system

The second coordinate system is cylindrical. Like the Cartesian coordinate system, it is also fixed in the support platform but in another way such that:

Origin intersection point of the tower base connection to the support platform (same as that in Cartesian coordinate system)



Figure E.1: Tower-base coordinate system for upwind turbine: (a) a sketch; (b) an example of land-based wind turbine¹

Reference plane the horizontal plane where locates the **Origin** (same as $\vec{x}_t\text{-}\vec{y}_t$ plane in Cartesian coordinate system)

\vec{r} reference axis, or radial axis, pointing horizontally in the nominal downwind direction (equivalent to \vec{x}_t -axis in Cartesian coordinate system)

\vec{z}_c axial axis, pointing vertically up from the center of the tower (equivalent to \vec{z}_t -axis in Cartesian coordinate system)

In cylindrical coordinate system, a point P is defined by three coordinates (κ, α, z) just as:

κ Euclidean distance from the \vec{z}_c -axis to the point P

α azimuth angle between the reference axis \vec{r} -axis and the line from the **Origin** to the projection of P on the **reference plane**

z signed distance from the **reference plane** to the point P along \vec{z}_c -axis

Equation E.1 lists the equations to convert cylindrical coordinates to Cartesian coordinates, or vice versa.

$$\begin{aligned} x_t &= \kappa \cos \alpha \\ y_t &= \kappa \sin \alpha \\ z_t &= z_c \end{aligned} \tag{E.1}$$

A variant of the cylindrical coordinate system is the polar coordinate system which is a two-dimensional system in the plane through the point P . It is parallel to the reference plane and characterized by two coordinates: the Euclidean distance κ and the azimuth angle α .

¹. “Wind turbine stairs”, by Patrick Finnegan, licensed under CC BY 2.0 / Add lines and texts

In this dissertation, the cylindrical coordinate system is chiefly used in evaluating axial stress on wind turbine tower (Section 4.1.1.1) while the polar coordinate system is mainly used in radar chart (also known as *Kiviat diagram*[\[KK73\]](#)).

Appendix F

Statistical methods

F.1. Maximum likelihood estimation

The distribution fitting is a technique to fit a theoretical probability distribution to a series of empirical data (namely, *observations*). One of the most dominant methods in distribution fitting is MLE introduced by R.A. Fisher in 1912 [Ald97]. This method determines values for the parameters of probability distribution by maximizing the likelihood function. The likelihood function measures statistically how well a probability distribution fits a set of observations. In other words, it can be considered as a manner to quantify the quality of fitting (also named after *goodness of fit*) of a distribution on observed values. The definition of such function is different for discrete and continuous probability distributions. Equation F.1 gives a general definition for a random variable \mathbf{X} that follows a continuous probability distribution with PDF f depending on a parameter θ :

$$\mathcal{L}(\theta | x) = f_{\theta}(x) \text{ for } \theta \in \Theta \quad (\text{F.1})$$

where, \mathcal{L} = likelihood function of θ given the outcome x of \mathbf{X}

Θ = parameter space (a finite-dimensional subset of Euclidean space)

Intuitively, the likelihood function equals the probability density at outcome x when the value of the parameter is θ . So, the MLE aims at finding the values of parameters which maximize the Equation F.1 over the parameter space Θ , i.e.,

$$\hat{\theta} = \arg \max_{\theta \in \Theta} \hat{\mathcal{L}}(\theta | x) \quad (\text{F.2})$$

This implies selecting the parameter values $\hat{\theta}$ that make the observed data to be most probable. This specific value $\hat{\theta}$ is called the maximum likelihood estimate. An example of applying the MLE to fit a sample of 10 000 observations is illustrated below.

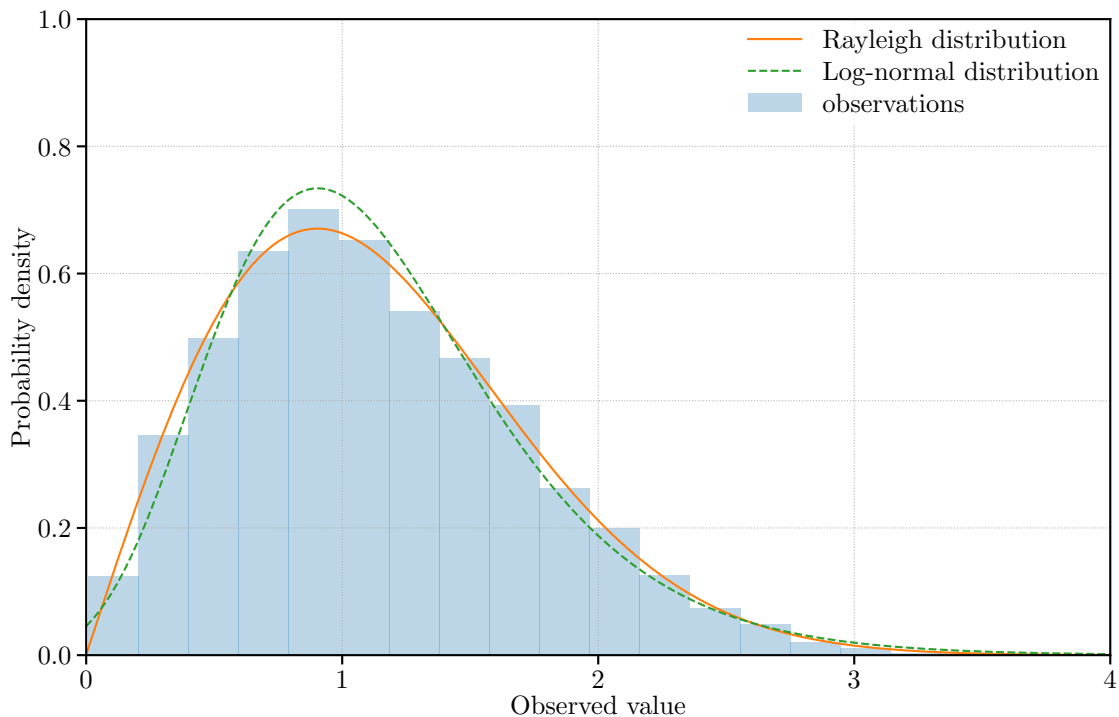


Figure F.1: An example of distribution fitting using the MLE

In Figure 4.5, the histogram represents the samples that are fitted by two different probability distributions: the Rayleigh distribution (orange line) and the Log-normal distribution (green dashed line). By applying the MLE, the values of parameters of both distributions are optimized to give its best fitting on the samples. However, it is hard to tell which distribution describes the observed data better than the other. Since there is no doubt that a close fit distribution leads to good predictions, it is impossible to confidently predict values if the best fit distribution is not reached. In order to choose a closer fit of distribution on the observed data and to ensure more confident predictions, a compare between the observed data and the fitted probability distribution must be performed. The ideas to realize this comparison will be discussed in the next section.

Apart from the MLE, there are many other fitting methods for adapting the parameters of the distribution to observations such as maximum product of spacing estimation (MPS) [CA83], L-moments methods [Hos90] and generalized bootstrap method [KD00].

F.2. Kolmogorov-Smirnov test

One difficulty in distribution fitting is that there may exist more than one probability distributions which can suit the observations well. For example, in Figure 4.5, both Rayleigh distribution and Log-normal distribution have graphically close fit as

their parameters have been adjusted by the MLE to best fit the samples. To address this problem, one needs to dispose a method to measure the goodness of fit of all reference distributions and select the one that gives the closest fit to the observations. The K-S test proposed by Andrey Nikolaevich Kolmogorov [Kol33] and Nikolai Vasilyevich Smirnov [Smi48] is a good manner to find out the suitable probability distribution.

The K-S test is a nonparametric test of the equality for one-dimensional probability distributions. The tested distribution can be either continuous or discontinuous. It can be used to compare a sample to a probability distribution, or to another sample. In principle, the K-S test uses a statistic measuring the distance between the ECDF of the sample and the CDF of the reference distribution. Like other statistical tests, a null hypothesis \mathbf{H}_0 is required. In the case of comparing a sample to a reference probability distribution (i.e., one-sample K-S test), the null hypothesis assumes that the observed data is sampled from the reference distribution. Considering a random variable \mathbf{X} has a sample of N i.i.d. observations X_i , the ECDF is accordingly defined as:

$$F_N(x) = \frac{1}{N} \sum_{i=1}^N I_{[-\infty, x]}(X_i) \quad (\text{F.3})$$

where,

$$I_{[-\infty, x]}(X_i) = \begin{cases} 1, & \text{if } X_i \leq x \\ 0, & \text{otherwise} \end{cases} \quad (\text{F.4})$$

$I_{[-\infty, x]}(X_i)$ is named the indicator function. Supposing that the variable \mathbf{X} follows a reference distribution \mathbf{P} (i.e., $H_0 : \mathbf{X} \sim \mathbf{P}(x | \theta)$) with a known cumulative distribution function $F(x)$, the K-S statistic is then computed by:

$$D_N = \sup_x | F_N(x) - F(x) | \quad (\text{F.5})$$

where \sup_x is the supremum of the set of all distances between the ECDF and the CDF. According to the Glivenko–Cantelli theorem [Tuc59], if the sample X_i comes from distribution $\mathbf{P}(x | \theta)$, then the K-S statistic D_N converges to 0 almost surely in the limit when N goes to infinity. A. N. Kolmogorov has reinforced this conclusion by providing the rate of convergence [Dod08].

Taking the sample in Figure 4.5 as an example, the K-S statistic between the sample and the Log-normal distribution is illustrated in Figure 4.6. The green dashed line represents the CDF of the reference distribution fitted by the MLE, the blue dotted line represents the empirical CDF of the sample, the orange line represents distances between the ECDF of the sample and the CDF of the distribution, and lastly, the red line highlights the K-S statistic. It should be noted that there are many other methods that can also be used to measure the goodness of fit, for instance,

Anderson-Darling test [AD52].

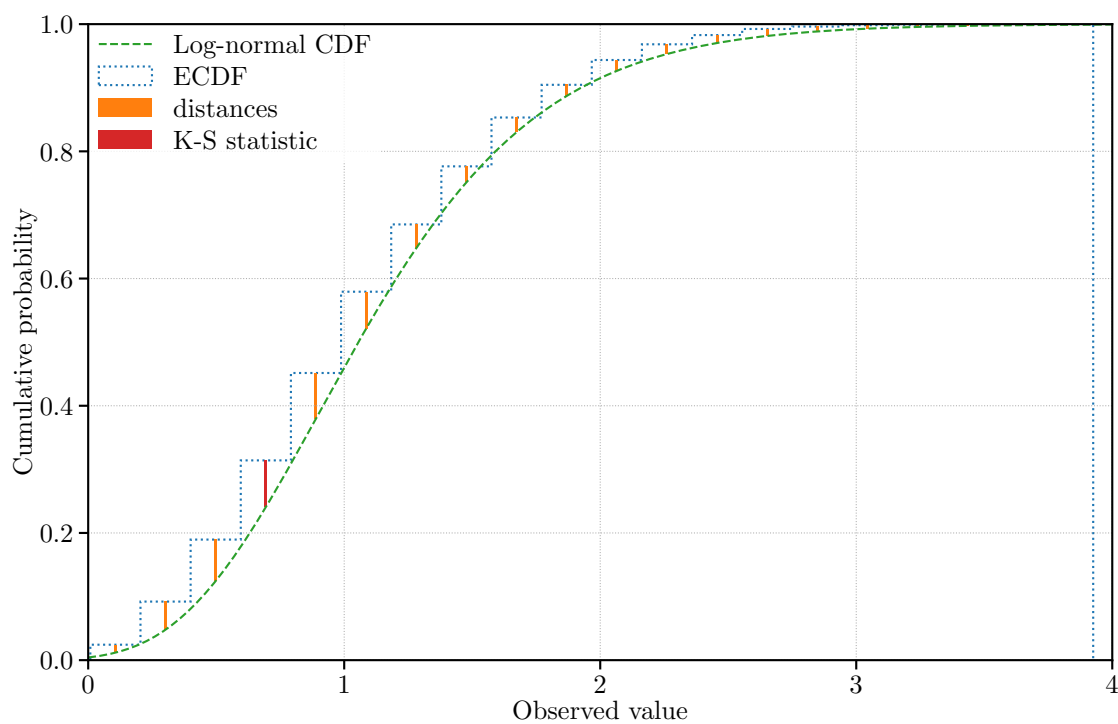


Figure F.2: An example of the K-S statistic

Appendix G

Deterministic fatigue analysis

G.1. Mean stress effect

S-N curves characterize the fatigue strength of materials under zero mean stress loads, i.e., $\sigma_{mean} = 0$. However, there are enriched findings in literature that highlight the effect of mean stress σ_{mean} on fatigue behavior of materials [RT69; Gur77]. In fact, when a tension stress is superimposed on the alternating stress σ_a , the fatigue life of structure decreases. Oppositely, when a compression stress is present, the fatigue life of structure increases. Figure G.1 illustrates S-N curve adjustments due to mean stress σ_{mean} in a diagrammatic way. σ_a refers to the alternating stress which is also known as alternating cycle amplitude given in Equation 4.7.

$$\sigma_a = \frac{\sigma_{max} - \sigma_{min}}{2} \quad (G.1)$$

where, σ_a = alternating stress
 σ_{max} = maximum stress in cycles
 σ_{min} = minimum stress in cycles

Further tests are then required to characterize this effect using a Goodman-Haigh diagram that defines for a fixed lifetime N , the alternating stress σ_a as a function of the mean stress σ_{mean} . The diagram was originally proposed by Goodman in 1899 while Haigh added alternating and mean stress in 1917 [Hai17]. A schema of Goodman-Haigh diagram is shown in Figure G.2 which plots the alternating amplitude of the stress cycle σ_a in Y axis and the mean stress σ_{mean} in X axis. Then, a line that connects the endurance limit σ_e and the ultimate strength σ_{ult} is plotted. Finally, the endurance-ultimate line is projected through the cycle. The intersection between the projected line and the alternating stress axis gives the new cycle amplitude. This intersection defines the new stress time history in which the mean stress is zero.

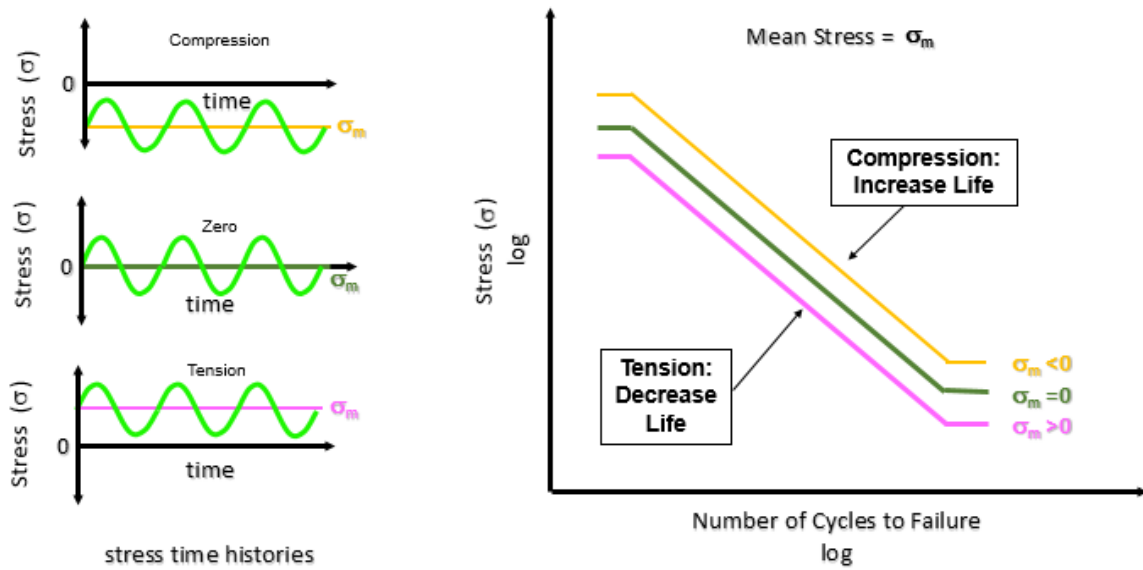


Figure G.1: Mean stress effects on S-N curve [Hia19a]

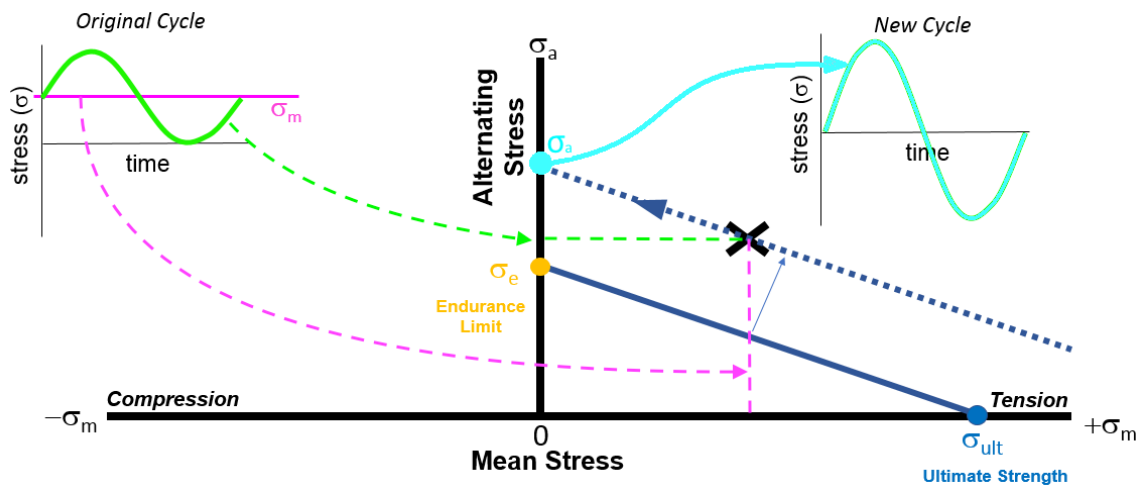


Figure G.2: A demonstration of Goodman-Haigh diagram [Hia19a]

The tests required to generate a Goodman-Haigh diagram are very expensive, several empirical relationships have been consequently developed to link the amplitude of alternating stress to the mean stress. Many tests have yielded results between the models proposed by Goodman and Gerber [Cam08]. When the mean stress is small in front of the stress amplitude, the two models are in agreement. However they are no longer in agreement when the mean stress is close to the amplitude. In this case, it is recommended to adopt the most conservative modeling. Thus it can be considered that the Goodman correction is more suitable to model the influence of a mean stress in compression (Equation 4.8):

$$\frac{\sigma_a}{\sigma_e} + \frac{\sigma_{mean}}{\sigma_{ult}} = 1 \text{ with } |\sigma_{mean}| \leq \sigma_{ult} \quad (G.2)$$

while the parabola of Gerber makes it possible to model the influence of a mean stress in tension (Equation G.3):

$$\frac{\sigma_a}{\sigma_e} + \left(\frac{\sigma_{mean}}{\sigma_{ult}} \right)^2 = 1 \text{ with } |\sigma_{mean}| \leq \sigma_{ult} \quad (\text{G.3})$$

These two models, by using the ultimate strength of material σ_{ult} and the endurance limit σ_e (also known as *fatigue limit*), make it possible to transform each cycle of non-zero mean stress σ_{mean} into an equivalent stress cycle of zero mean with the amplitude σ_a .

All the corrections made to the data provided by the S-N curves allow these data to be used by the conventional methods in uni-axial fatigue analysis. It is thus possible, for a given amplitude and mean stress cycle, to determine the number of cycles at the end of which the failure will occur. However, for loads composed of different cycles, it becomes necessary to use accumulation laws of fatigue damage.

G.2. Palmgren-Miner's rule

For stress cycles with amplitude greater than the endurance limit, the damage is irreversible to the structure. The fatigue damage D_m , produced by n_m cycles with amplitude of σ_a , is related to N_m , the total number of cycles producing fatigue failure under a stress of constant amplitude σ_a . In order to estimate the partial damage D_m produced by n_m cycles, Miner proposed the following relationship [Min45]:

$$D_m = \frac{n_m}{N_m} \quad (\text{G.4})$$

If M groups of stress cycles with different amplitudes and zero mean stress are considered, then the damage produced by each group is given by Miner's law. Finally, the cumulative fatigue damage D suffered by the structure under all groups of stress cycles is given by the Palmgren formula [Pal24]:

$$D = \sum_{m=1}^M D_m \quad (\text{G.5})$$

To sum up, the Palmgren-Miner linear damage hypothesis is given by:

$$D = \sum_{i=m}^M \frac{n_m}{N_m} \quad (\text{G.6})$$

When the cumulative damage is greater than 1, failure of structure occurs. However, Palmgren-Miner's Rule does not consider the order in which the cyclic loads are

applied. For example, if loads are applied in the plastic region, the endurance limit is no longer in effect. Other laws of cumulative damage have been proposed, some of which take into account the order of applied cyclic loads [Sub76; Chr09; Sha10]. Several comparative studies have been issued [Lam76; OSS79; Li01]. It appears that in the case of random loads, method that take into account the order in which stress cycles are applied lose their efficiency. This is why Palmgren-Miner's rule remains one of the most widely used method in fatigue life prediction.

By using the S-N curve and Palmgren-Miner's rule, it is simple to calculate the fatigue damage for a structure subjected to a cyclical load of constant amplitude. When the amplitude of the stress becomes random, it is necessary to have methods capable of extracting the load time history into cycles. These methods are called cycle counting methods.

G.3. Rainflow counting

In order to assess the fatigue life of a structure subject to complex loading, a cycle counting method is needed. It filter the essential information for studying fatigue damage by breaking the original stress time history into stress cycles.

There are a numerous methods to perform this counting [AST85]. For all these methods, it is necessary to know how to get rid of small variations (also named *noise*). By doing this correction, a long-duration signals is transformed into signals that can be easily treated. The choice of a method depends on how stress cycles are defined. Each method evaluates the number of cycles with their range ΔS on the basis of a definition of cycle for a duration t in the load time history.

Among the most well-known methods like Level-Crossing counting, Peak counting, Simple-Range counting and Rainflow counting, the last one is by far the most widely used in the field of fatigue analysis under random vibration. It is firstly proposed by Tatsuo Endo, a Japanese engineer, during his visiting at the University of Illinois along with Masanori Matsuishi [ME68]. It extracts individual fatigue cycles from any complex load time history.

It defines the stress cycle as a closed hysteresis loop in a stress-strain diagram. Since this method is commonly recognized to be a good cyclic counting method. Many researchers have proposed improvements to this method like making it useful for long stress histories [GK87], keeping the load sequence [Ant97], counting cycles in real-time application [MJ12] and an equivalent and more convenient definition of the Rainflow cycle counting method [Ryc87].

Rainflow counting consists four main steps:

Step 1 Hysteresis filtering

Step 2 Peak-Valley filtering

Step 3 Discretization

Step 4 Four-point counting method

G.3.1. Hysteresis filtering

The first step is to delete small cycles in load time history that cause negligible amount of damage. This is done by defining a gate with a specific amplitude. Any cycle with a smaller amplitude than the gate is removed from the load time history. This is done by projecting the gate at each turning point in the time series from left to right. If a turning point is smaller than the gate, it is deleted from the load time history. Usually a percentage of the bin size is used to define the gate size. If a hysteresis gate is zero, this step is skipped.

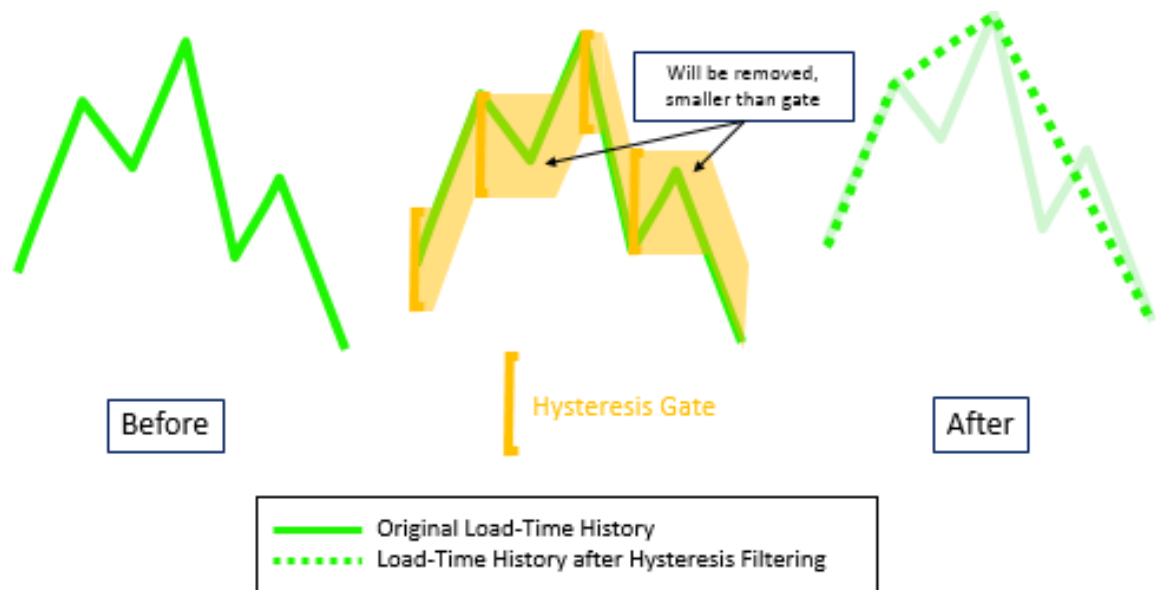


Figure G.3: Hysteresis filtering of signal [Hia19b]

G.3.2. Peak-Valley filtering

The goal of Peak-Valley filtering is to search data points which have reversals in direction.

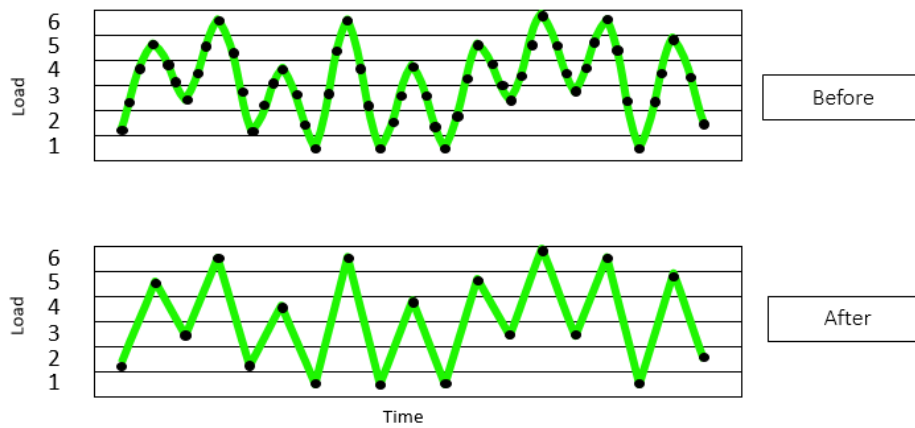


Figure G.4: Peak-Valley filtering of signal [Hia19b]

Within a cycle, only the maximum and minimum value of the cycle are important for assessing fatigue life. Any intermediate data points between the maximum and minimum values of a given cycle can be omitted as they are not relevant for the fatigue calculation.

G.3.3. Discretization

Next, the Y axis is divided into discrete bins. Each bin is a fixed amplitude range that the data is mapped into as shown in Figure G.5. In Figure G.5, there are six discrete bins used to divide the amplitude range. In practice, many more bins are used.

The measured data points are mapped to the centers of their bin, which enables counting procedures.

For instance, if a signal with a range of 128 was divided into 64 bins, each bin would have a range of 2.

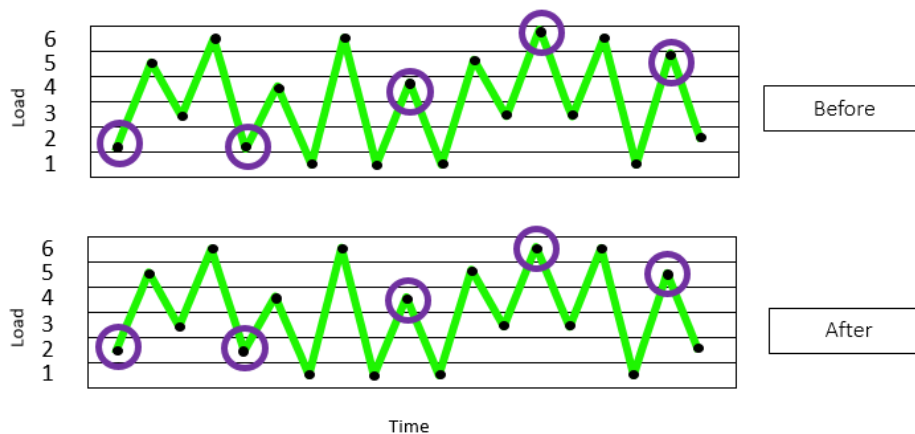


Figure G.5: Discretization [Hia19b]

The amplitude of the data samples are altered slightly by centering them in their respective bins. It is important to use a reasonably sufficient amount of bins for the analysis, so the amplitudes are not altered greatly. Depending on the slope of the S-N Curve, a 15% change in load can result in a factor of two change in fatigue life.

According to the most standards, the Y-axis scale is typically divided into a minimum of 64 bins. In most modern durability software, it is possible to use more bins in the Rainflow count. Increased accuracy is achieved by using more bins, but the file size is larger and computational times are longer.

G.3.4. Principle of extraction

The principle of the extraction of a cycle uses four successive reversals (i.e. two peaks and two valleys). Figure G.6 gives an illustration of the extraction in stress time history. The cycle represents a closed loop in stress-strain space.

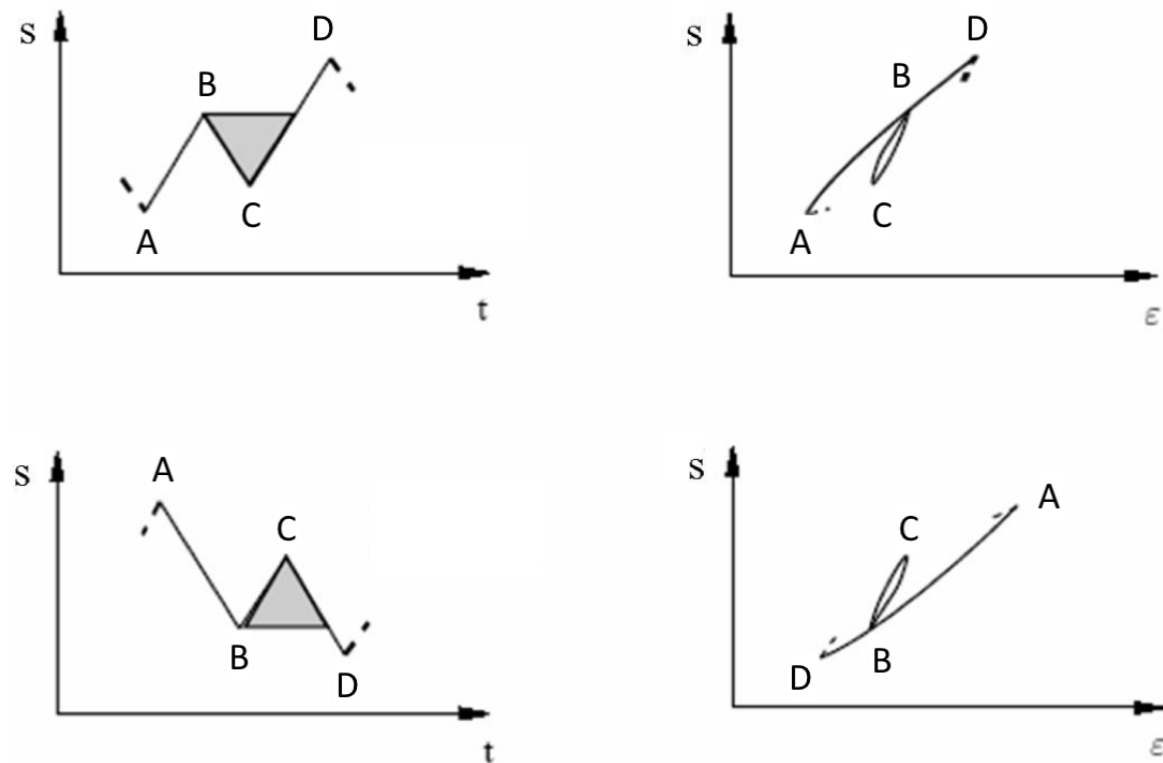


Figure G.6: Extraction of cycle

The major steps to extract cycles from a series of load sequences are:

1. For four sequential points (A, B, C, D), calculate three successive ranges: $\Delta S_{AB} = |B - A|$, $\Delta S_{BC} = |C - B|$ and $\Delta S_{CD} = |D - C|$.
2. If $\Delta S_{AB} \geq \Delta S_{BC}$ and $\Delta S_{BC} \leq \Delta S_{CD}$ then:
 - (a) the cycle closed by the extreme value B and C is extracted

- (b) the point B and C is discarded
 - (c) the two remaining points A and D are connected to each other
3. If not, the following four successive points are considered and the same procedure is applied till the last point in the sequence.
 4. Once the last point is reached, the remaining points give the residue.

The maximum number of reversals in residue can not exceed $2k - 1$, where k is the number of bins used in discretization. The residue is counted by starting at the end of the residue and counting backwards. If a single range remains, it may be counted as a half or full cycle suggested by the standard [AST85].

The result of counting is stored in a three-dimension matrix giving the mean value, the range and the number of cycles. Combining the Rainflow counting approach with Palmgren-Miner's is commonly used in fatigue life prediction. It gives the possibility to predict fatigue life or estimate life consumption of a structure under any complex load history.

Appendix H

Methods for determining tower frequencies

To determine the natural frequencies and mode shapes of wind turbine tower, variant methods may be used according to the different tower type.

H.1. Uniform tower

To be simplified, if the turbine/tower can be represented by a uniform cantilevered beam with a concentrated mass attached on the tower top, the following model can be applied [BM67]:

$$f_n = \frac{1}{2\pi} \sqrt{\frac{3EI}{(0.23m_{Tower} + m_{Top}) L^3}} \quad (\text{H.1})$$

where,

- f_n = 1st order natural frequency of tower
- E = modulus of elasticity
- I = moment of inertia of cross-section
- m_{Tower} = mass of tower
- m_{Top} = mass of tower-top structure
- L = height of tower

H.2. Non-uniform tower

For non-uniform towers, the Rayleigh method gives a good approximation of tower vibration frequencies by calculating the Rayleigh Quotient of the tower [Tho18]:

$$p^2(\psi) = \frac{\int_0^L EI(x)[\psi''(x)]^2 dx}{\int_0^L \rho A(x)[\psi(x)]^2 dx + m_{Top}[\psi(L)]^2} \quad (\text{H.2})$$

where, p = natural frequency of the corresponding mode
 ψ = an exact mode shape of the tower
 E = modulus of elasticity
 I = moment of inertia of cross-section
 ρ = mass density of tower
 A = area of cross-section

m_{Top} = mass of tower-top structure

The term $EI(x)$ and $\rho A(x)$ represents the stiffness distribution of the tower and the mass distribution of the tower, respectively. The Rayleigh Quotient p^2 is stationary with respect to variations in $\psi(x)$ when $\psi(x)$ is an exact mode shape for the tower. This formula can predict accurately the value of natural frequencies on condition that a good approximation to the mode shape is given.

H.3. Guyed tower

For guyed towers, the natural frequencies can be approximated by the Rayleigh-Ritz procedure [Wri81]. This method combines a group of assumed shape functions $\phi_i(x)$ to approach the mode shape of tower $\psi(x)$.

$$\psi(x) = \sum_{i=1}^n c_i \phi_i(x) \tag{H.3}$$

where, c_i = constant to be determined by Rayleigh-Ritz procedure

ϕ_i = a linearly independent function satisfying the boundary conditions

Then, the Rayleigh's Quotient can be expressed as following:

$$p^2(\psi) = \frac{\int_0^L EI(x)[\psi''(x)]^2 dx + K_c[\psi(h)]^2}{\int_0^L \rho A(x)[\psi(x)]^2 dx + m_{Top}[\psi(L)]^2} \tag{H.4}$$

where, p = natural frequency of the corresponding mode
 ψ = an exact mode shape of the tower
 E = modulus of elasticity
 I = moment of inertia of cross-section
 ρ = mass density of tower
 A = area of cross-section
 m_{Top} = mass of tower-top structure
 K_c = stiffness coefficient of the guy wire
 h = height of the attachment point by guy wire

Substitution of the mode shape from in Equation H.3 into Equation H.4 gives:

$$p^2(\psi) = \frac{EI_0 \sum_i \sum_j c_i c_j d_{ij}}{\rho A_0 L^4 \sum_i \sum_j c_i c_j b_{ij}} \quad (\text{H.5})$$

where:

$$\begin{aligned} d_{ij} &= \int_0^1 f(\xi) \phi_i''(\xi) \phi_j''(\xi) d\xi + K'_c \phi_i(\xi_h) \phi_j(\xi_h) \\ b_{ij} &= \int_0^1 g(\xi) \phi_i(\xi) \phi_j(\xi) d\xi + \mu \phi_i(1) \phi_j(1) \\ i, j &= 1, \dots, N \end{aligned} \quad (\text{H.6})$$

where, ξ = dimensionless distance $\frac{x}{L}$
 ξ_h = guy attachment level $\frac{h}{L}$
 $f(\xi)$ = dimensionless stiffness distribution $\frac{EIL(\xi)}{EI_0}$
 $g(\xi)$ = dimensionless mass distribution $\frac{\rho AL(\xi)}{\rho A_0}$
 K'_c = dimensionless guy wire stiffness coefficient $\frac{K_c L^3}{EI_0}$
 μ = mass ratio $\frac{m_{top}}{\rho A_0 L}$

Like non-uniform cantilevered tower, the Rayleigh Quotient p^2 is stationary with respect to variations in $\psi(x)$, this relationship can be expressed in:

$$\det[d_{ij} - W^2 b_{ij}] = 0 \quad (\text{H.7})$$

So the problem is to find the N values of W^2 that make the determinant of Equation H.7 equal to 0. These N values represent the first N frequencies of the tower.

Appendix I

Supplementary figures

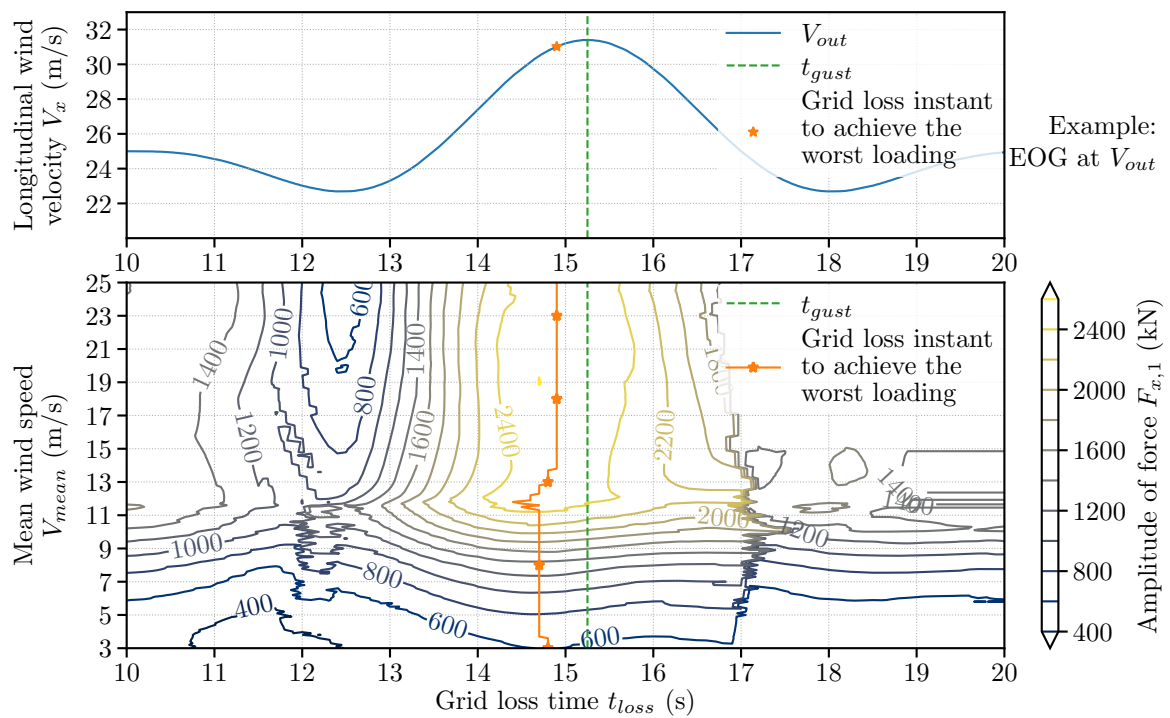


Figure I.1: Grid loss timing in the range of operating wind speed with reference to tower force. The upper line plot gives an example of wind speed of gust at mean wind speed $V_{mean} = V_{out} = 25$ m/s. The lower contour plot shows the peak-to-peak amplitude in relation to the mean wind speed V_{mean} and the grid loss time t_{loss}

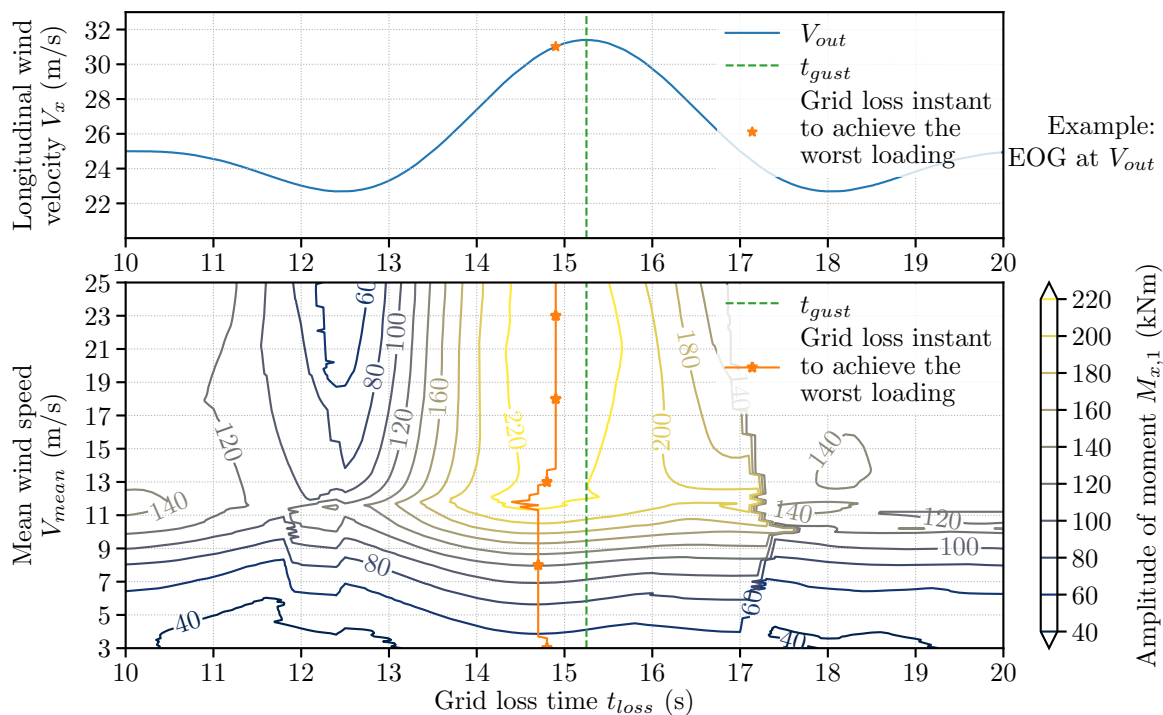


Figure I.2: Grid loss timing in the range of operating wind speed with reference to tower moment. The upper line plot gives an example of wind speed of gust at mean wind speed $V_{mean} = V_{out} = 25$ m/s. The lower contour plot shows the peak-to-peak amplitude in relation to the mean wind speed V_{mean} and the grid loss time t_{loss}

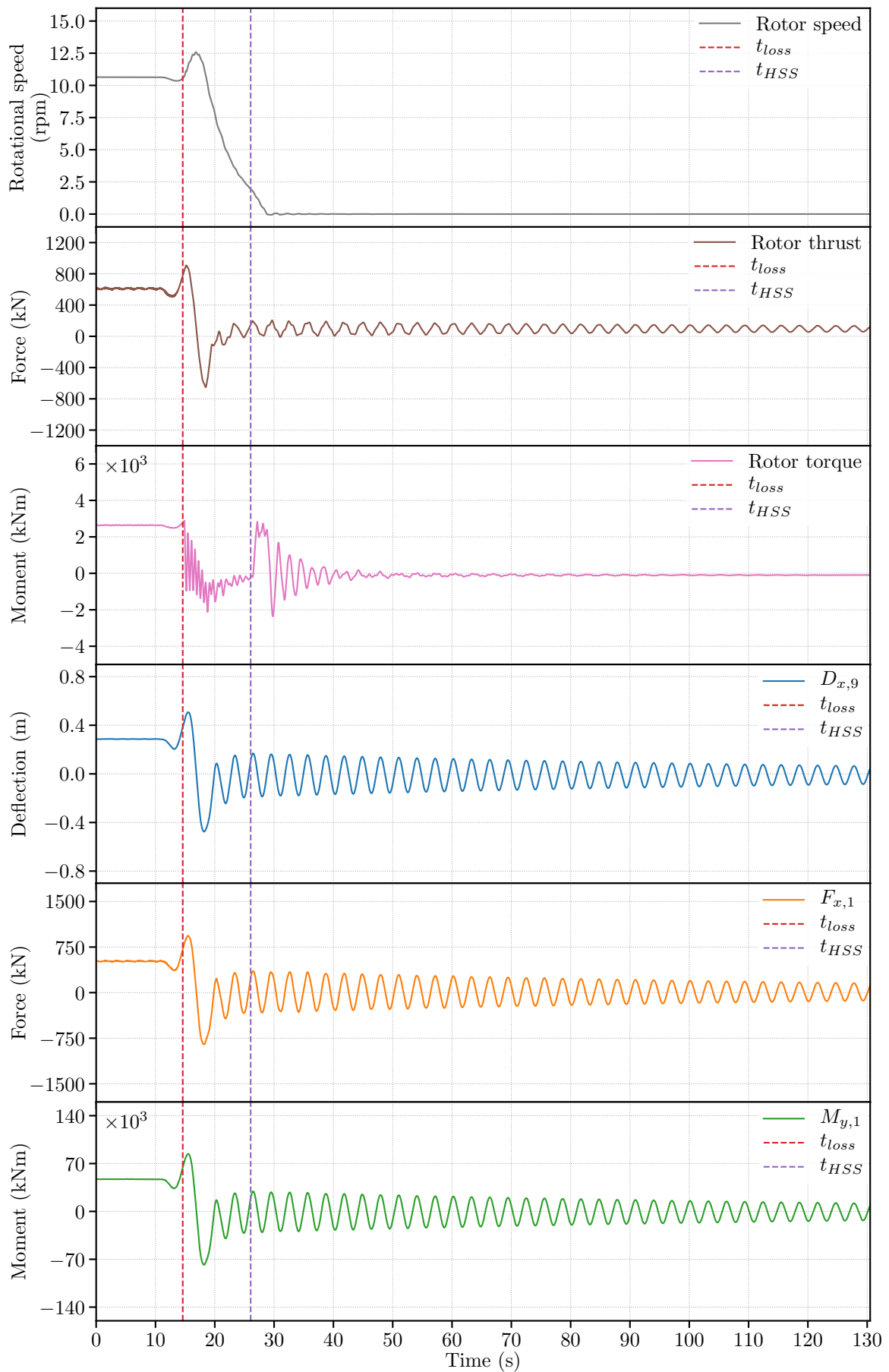


Figure I.3: DLC2.3 rotor and tower reactions at V_{rate-2}

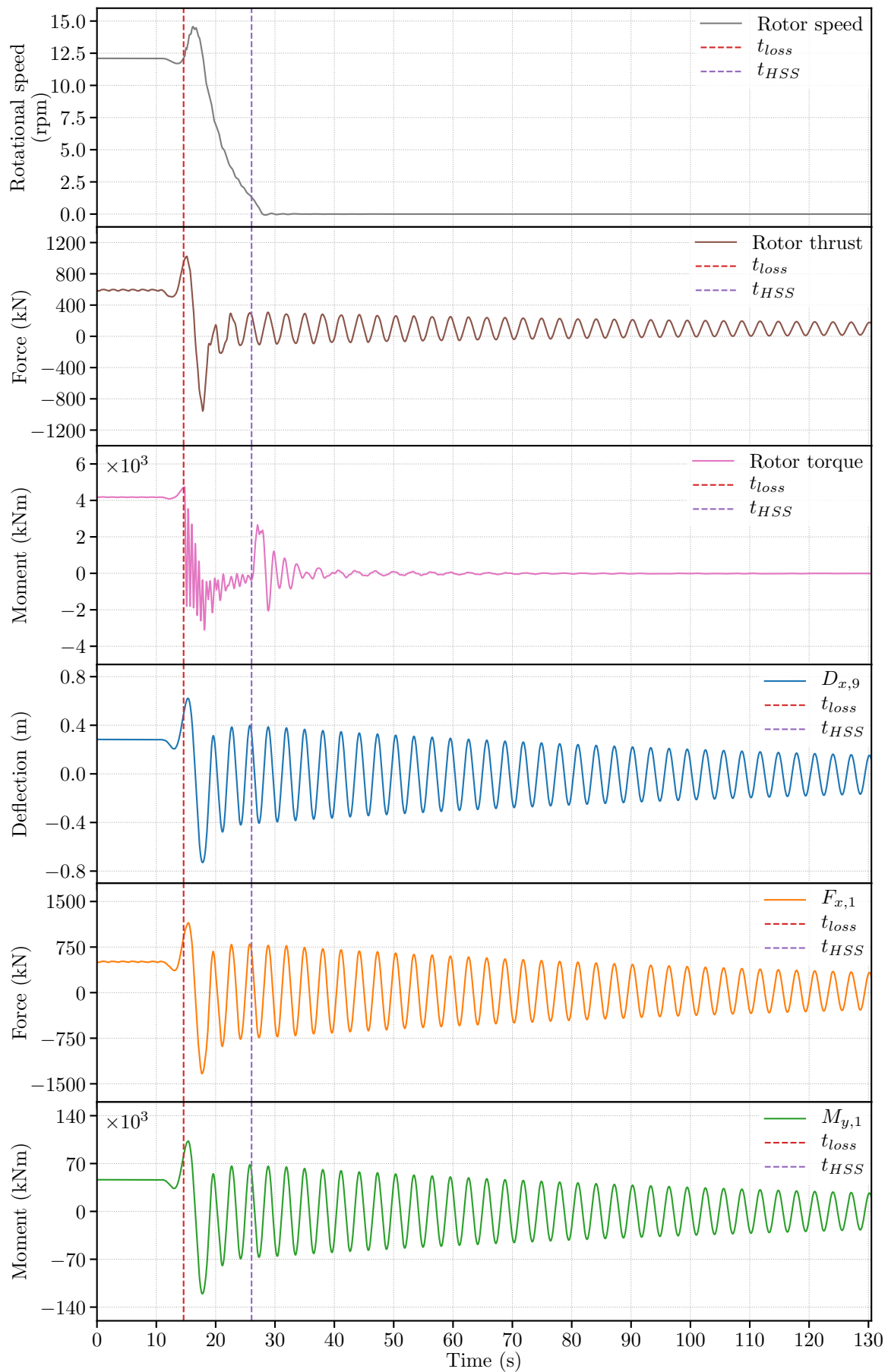


Figure I.4: DLC2.3 rotor and tower reactions at V_{rate+2}

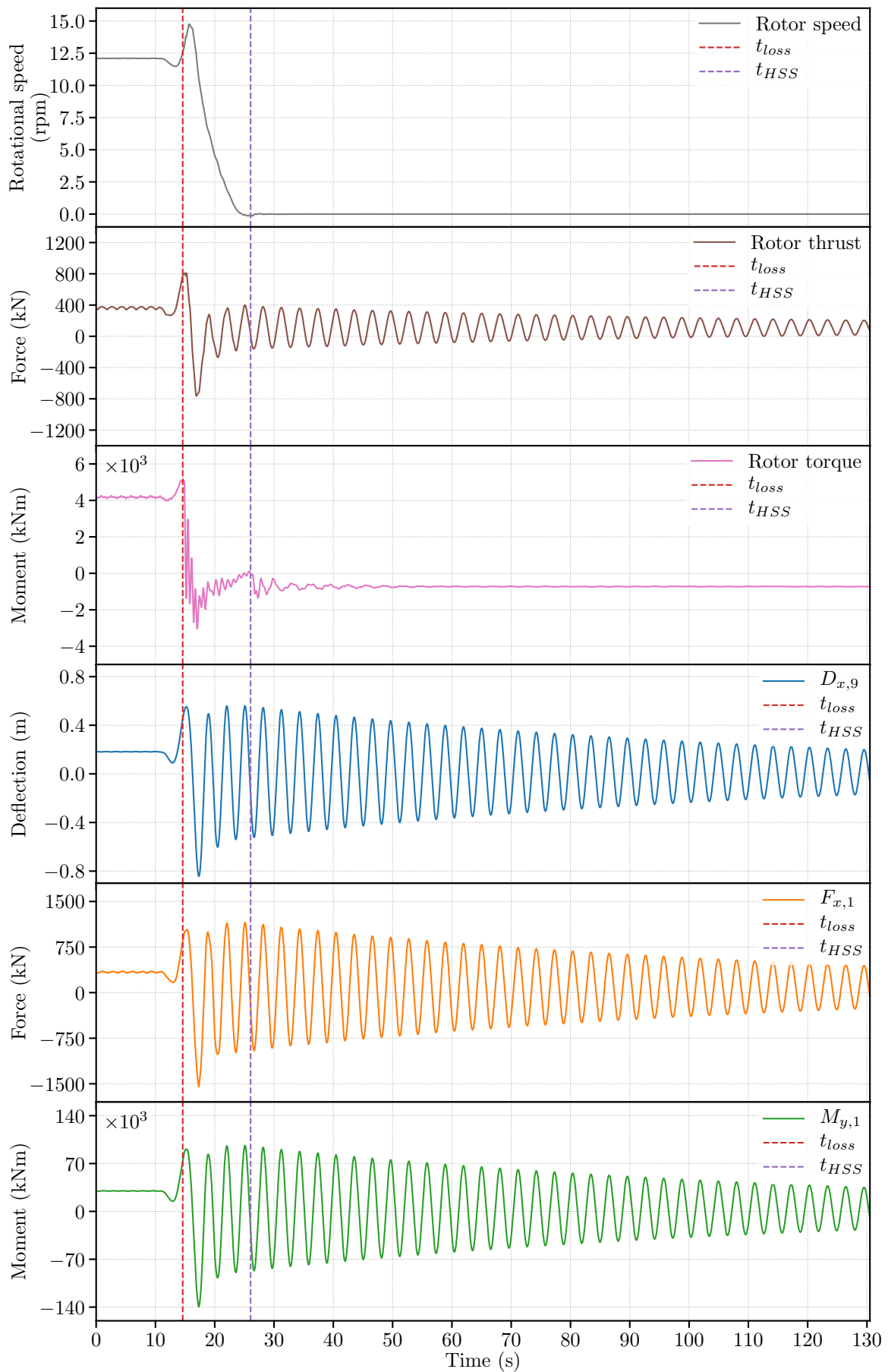


Figure I.5: DLC2.3 rotor and tower reactions at V_{out}

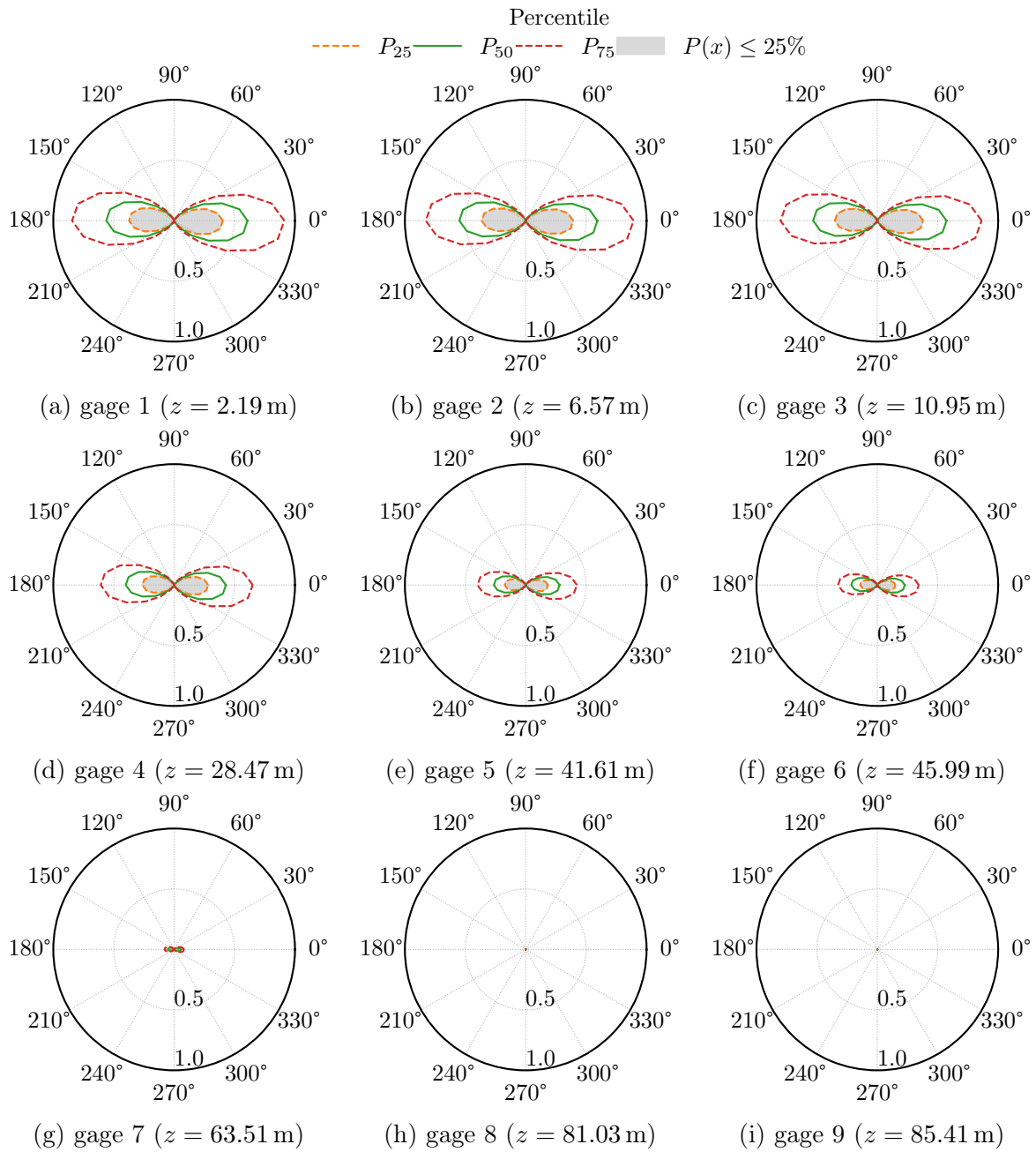


Figure I.9: Distribution of 10-min cumulative fatigue damage at the different height of tower at mean wind speed of 3.0 m/s (damage value normalized to 1.5×10^{-8} in all charts)

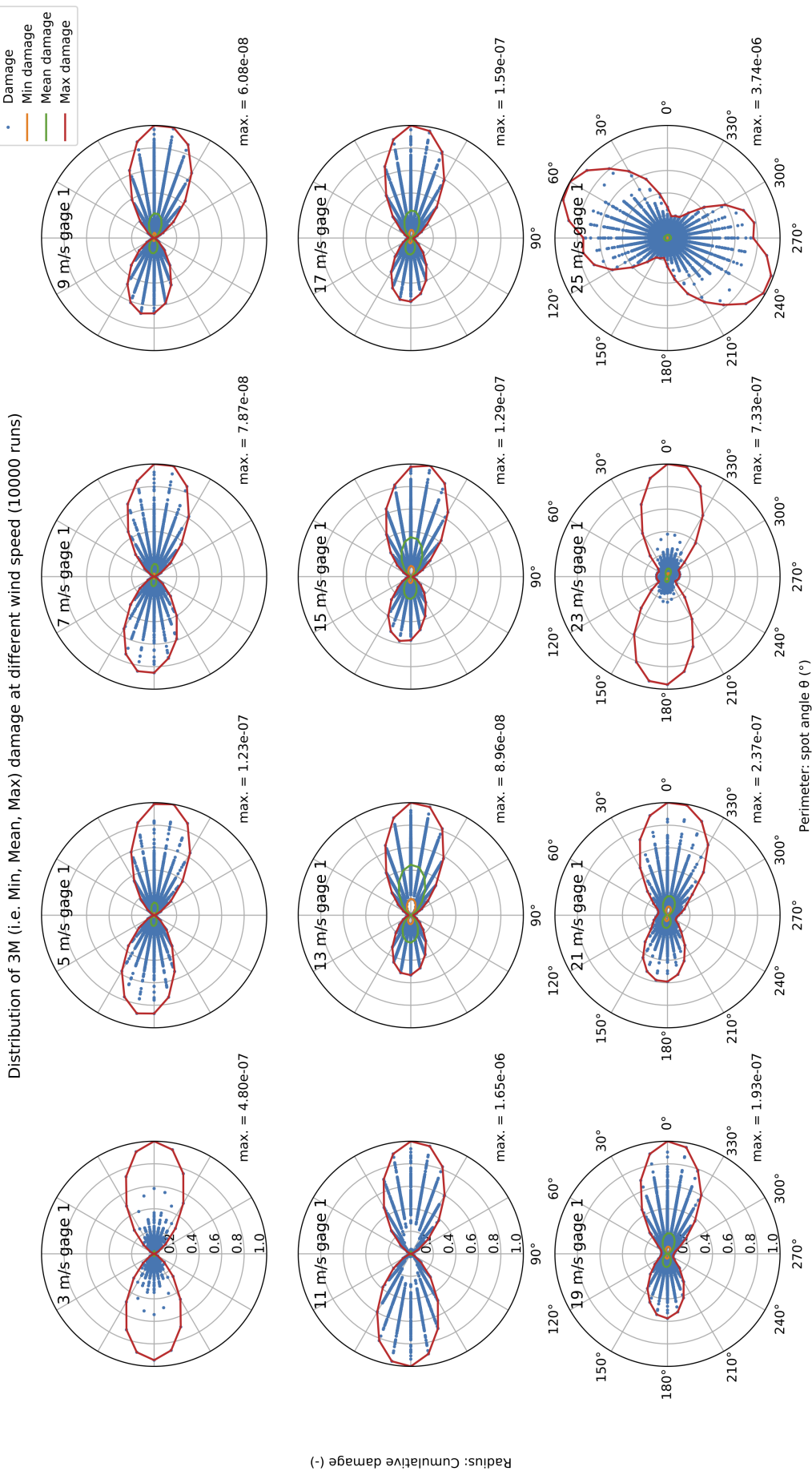


Figure I.6: Visualization of all simulated fatigue damage (blue dots) highlighted by minimal values (orange line), mean values (green line) and maximal values (red line)

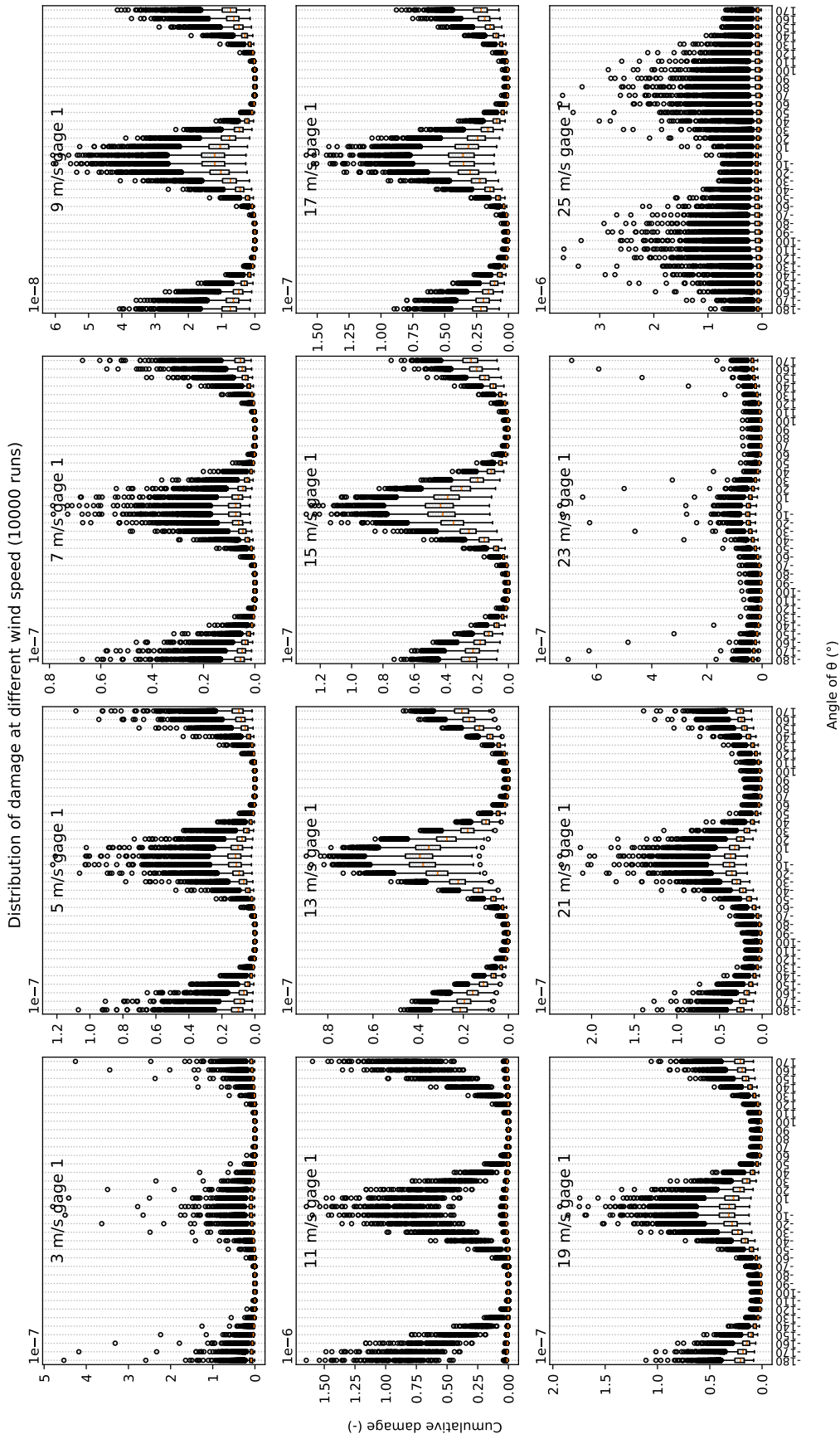


Figure I.7: Distribution of 10-min cumulative fatigue damage on tower gage 1 under different mean wind speed represented by box-and-whisker diagram

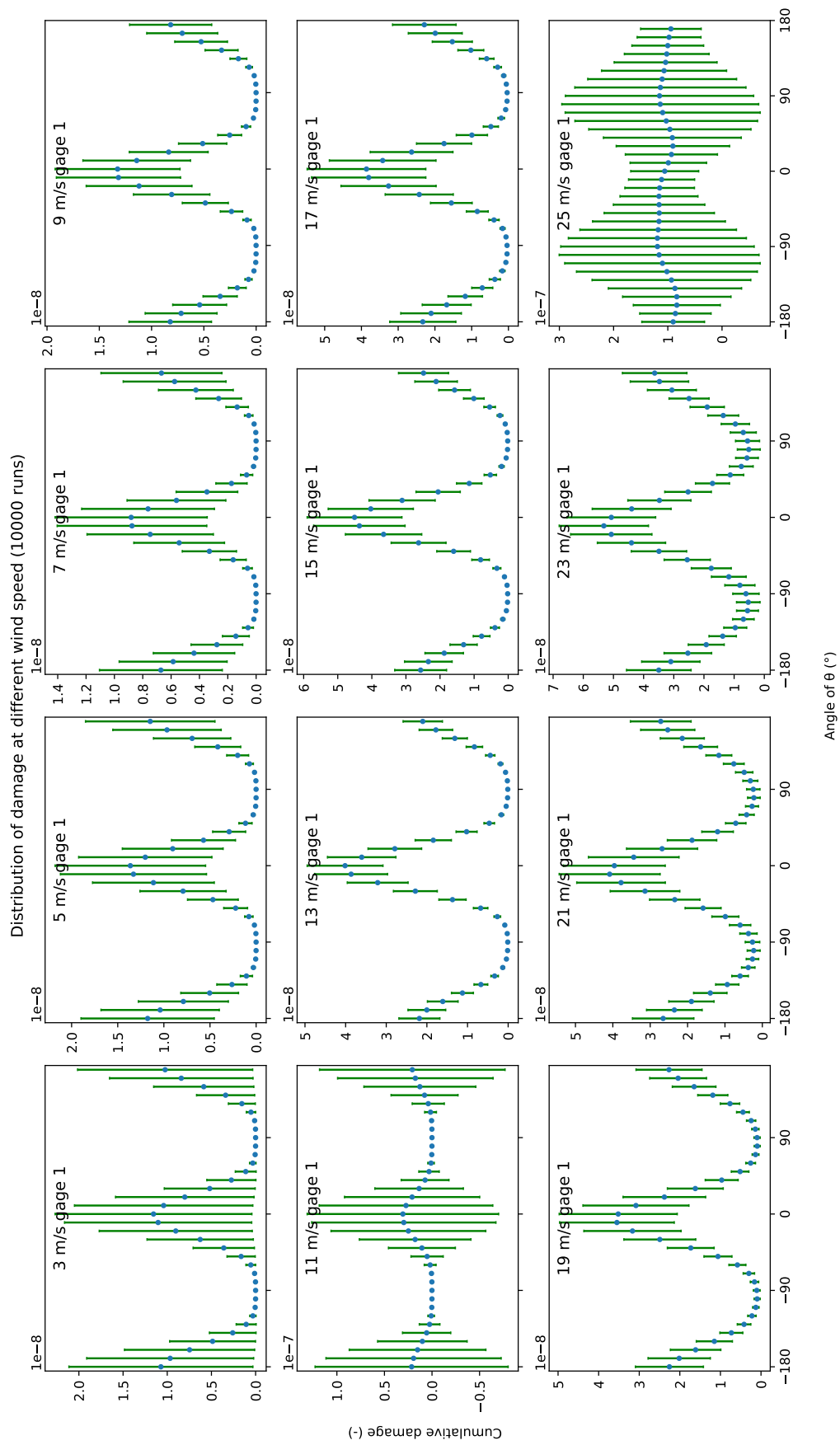


Figure I.8: Distribution of 10-min cumulative fatigue damage on tower gage 1 under different mean wind speed represented by bar chart

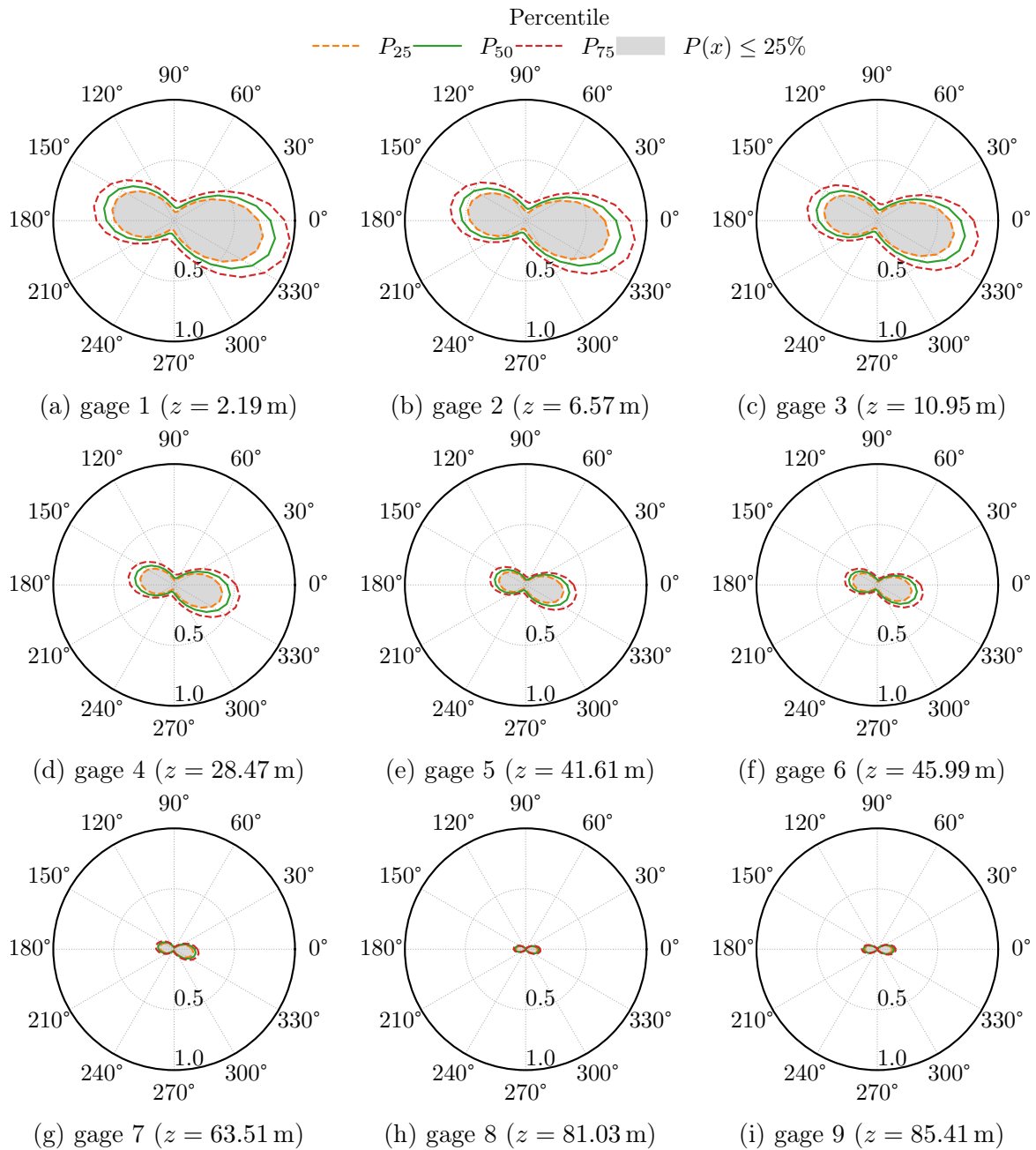


Figure I.10: Distribution of 10-min cumulative fatigue damage at the different height of tower at mean wind speed of 25.0 m/s (damage value normalized to 8.5×10^{-8} in all charts)

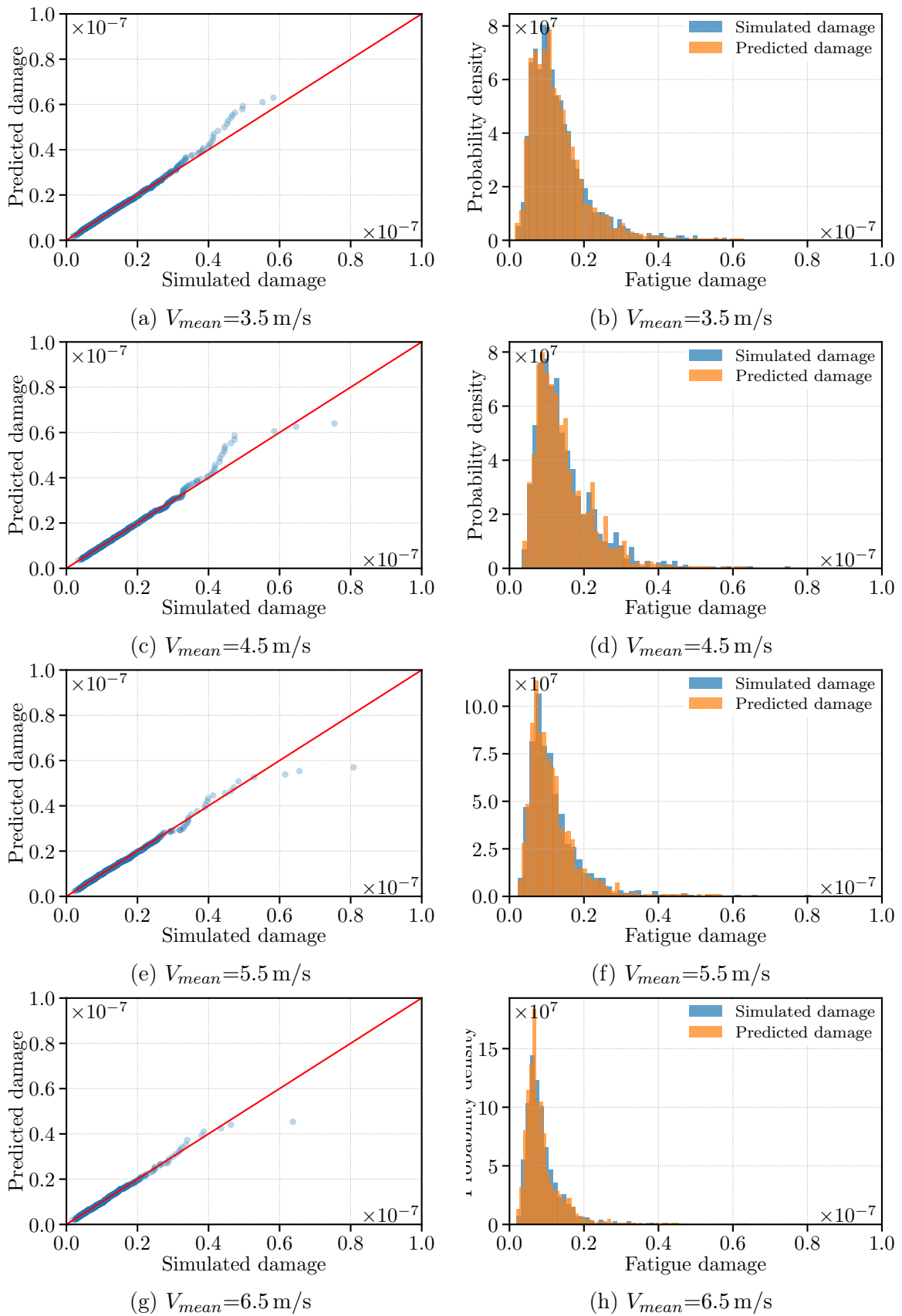


Figure I.11: Comparison between the predicted values and the simulated values for 10-min cumulative fatigue damage at mean wind speed of 3.5 m/s, 4.5 m/s, 5.5 m/s and 6.5 m/s

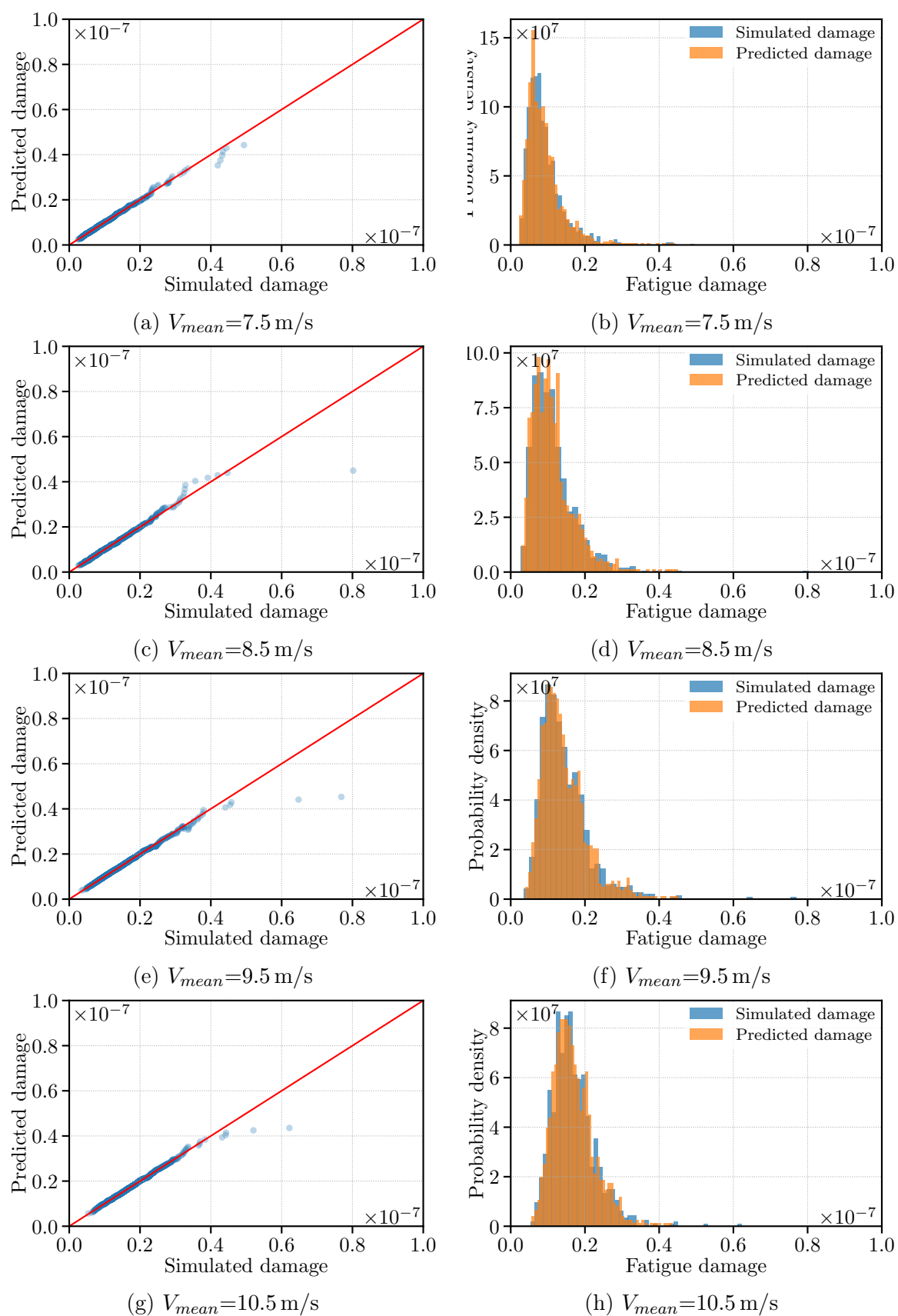


Figure I.12: Comparison between the predicted values and the simulated values for 10-min cumulative fatigue damage at mean wind speed of 7.5 m/s, 8.5 m/s, 9.5 m/s and 10.5 m/s

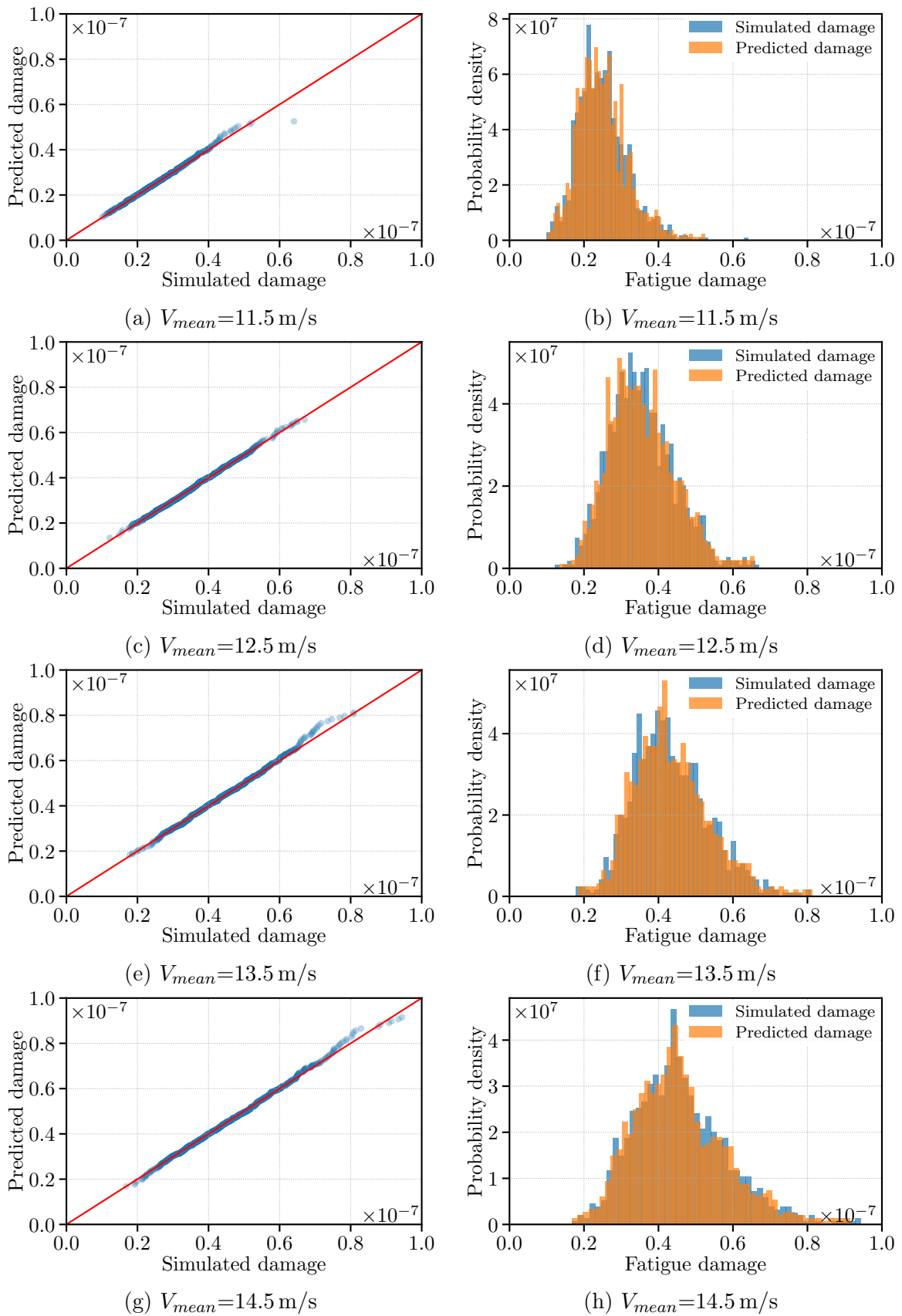


Figure I.13: Comparison between the predicted values and the simulated values for 10-min cumulative fatigue damage at mean wind speed of 11.5 m/s, 12.5 m/s, 13.5 m/s and 14.5 m/s

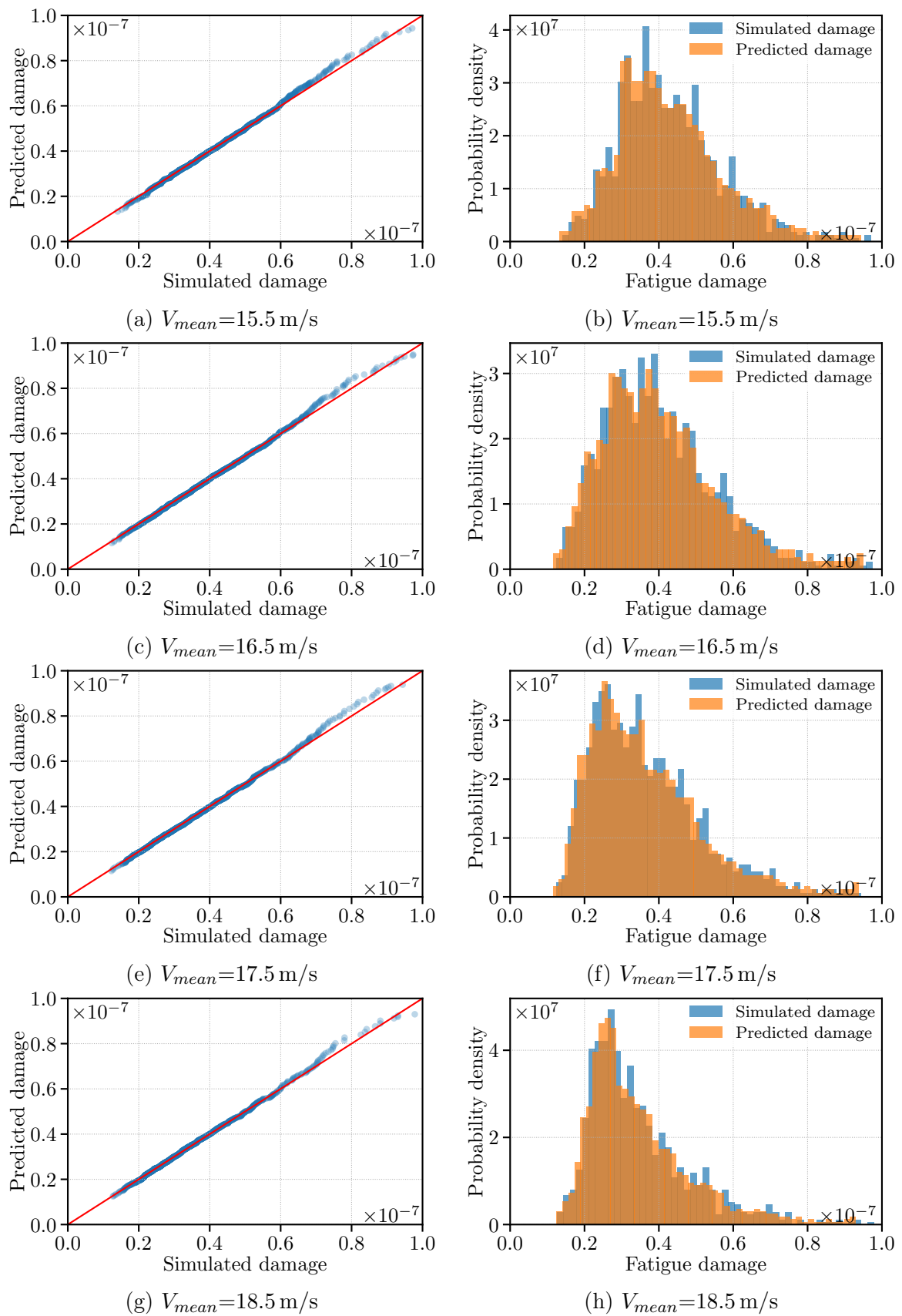


Figure I.14: Comparison between the predicted values and the simulated values for 10-min cumulative fatigue damage at mean wind speed of 15.5 m/s, 16.5 m/s, 17.5 m/s and 18.5 m/s

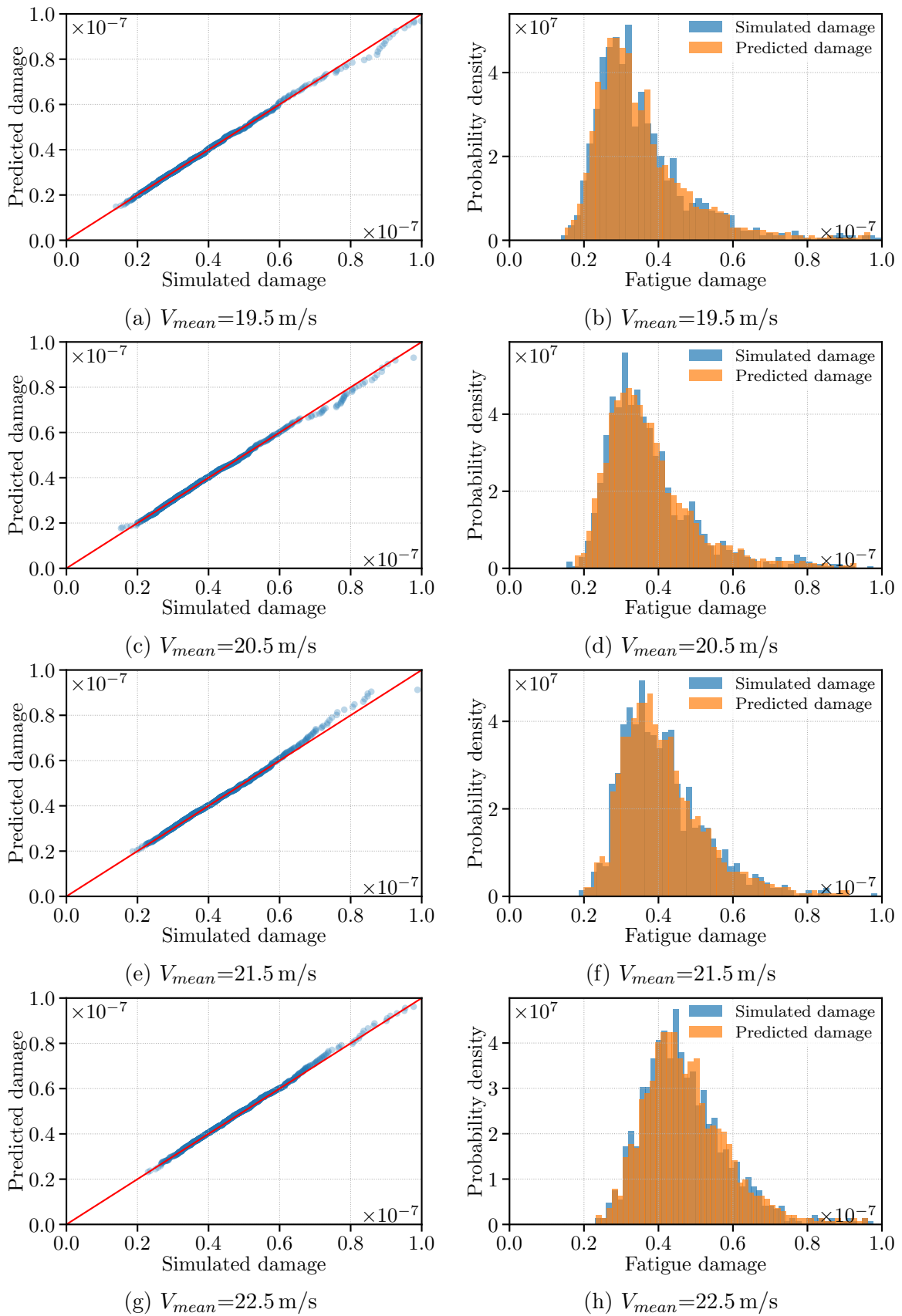


Figure I.15: Comparison between the predicted values and the simulated values for 10-min cumulative fatigue damage at mean wind speed of 19.5 m/s, 20.5 m/s, 21.5 m/s and 22.5 m/s

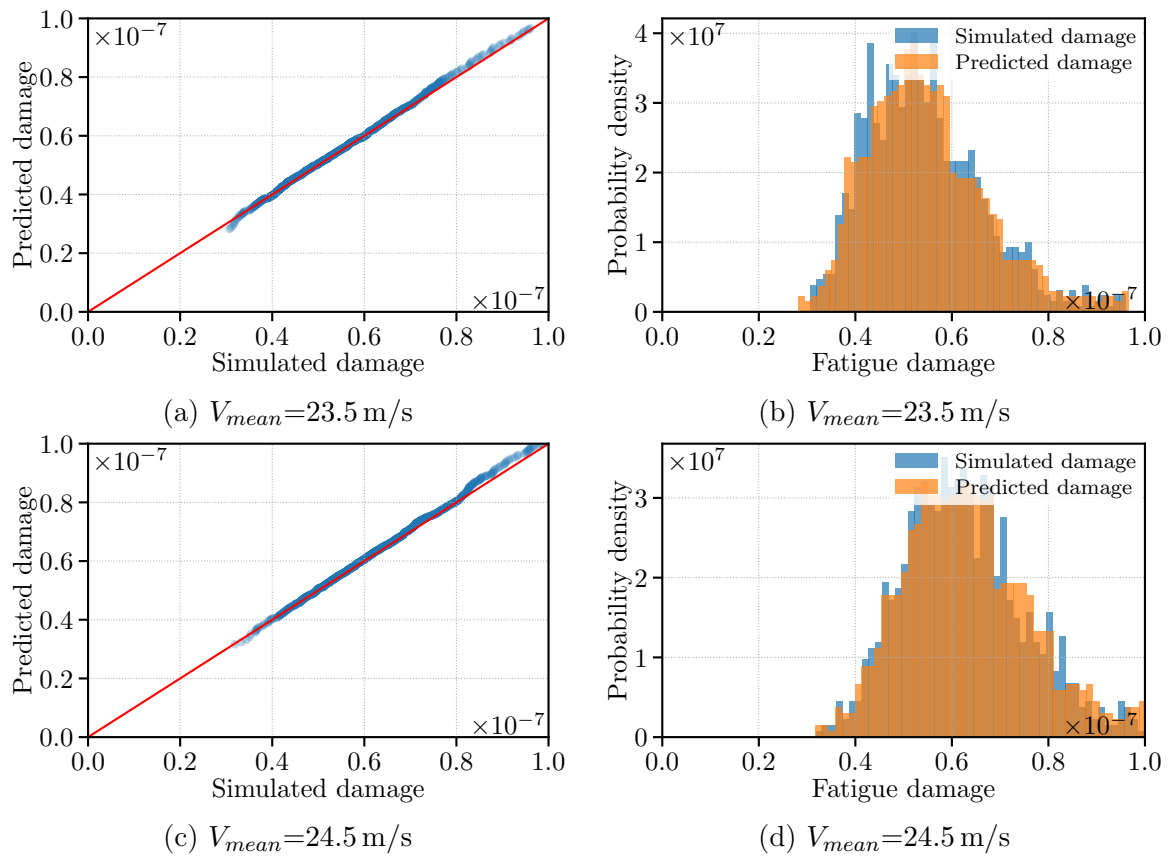


Figure I.16: Comparison between the predicted values and the simulated values for 10-min cumulative fatigue damage at mean wind speed of 23.5 m/s and 24.5 m/s

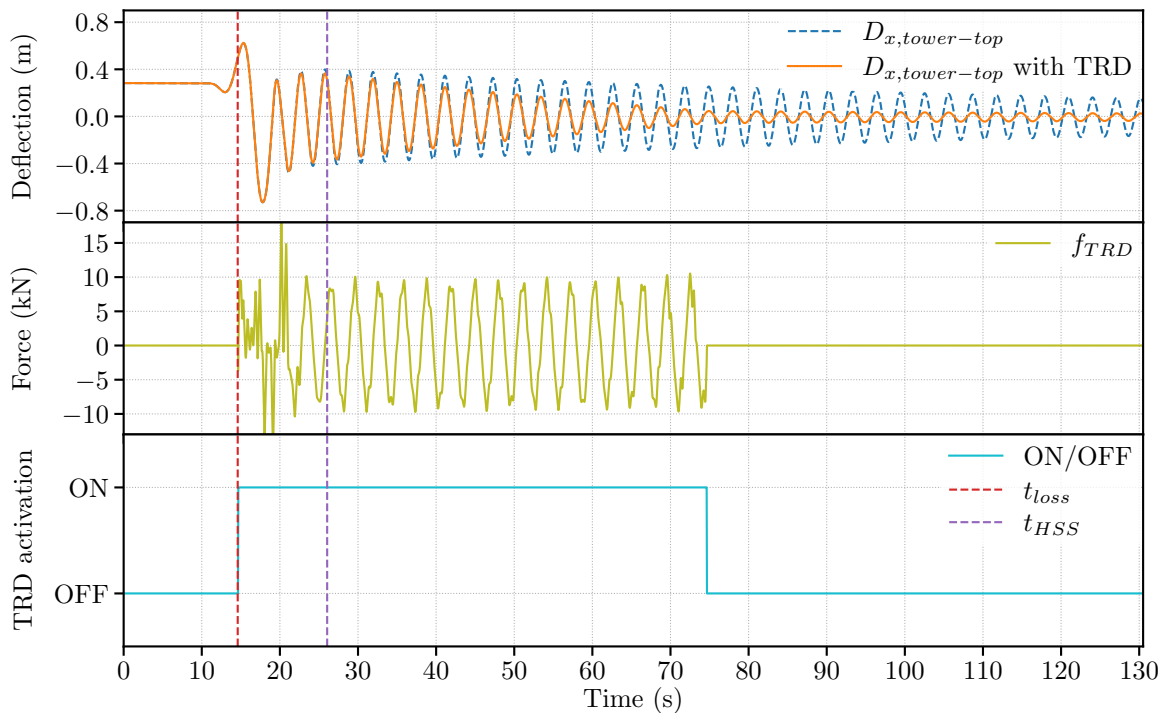


Figure I.17: Tower-top fore-aft deflection and status of TRD in DLC2.3 at V_{rate+2} (the time dependency is omitted in legend)

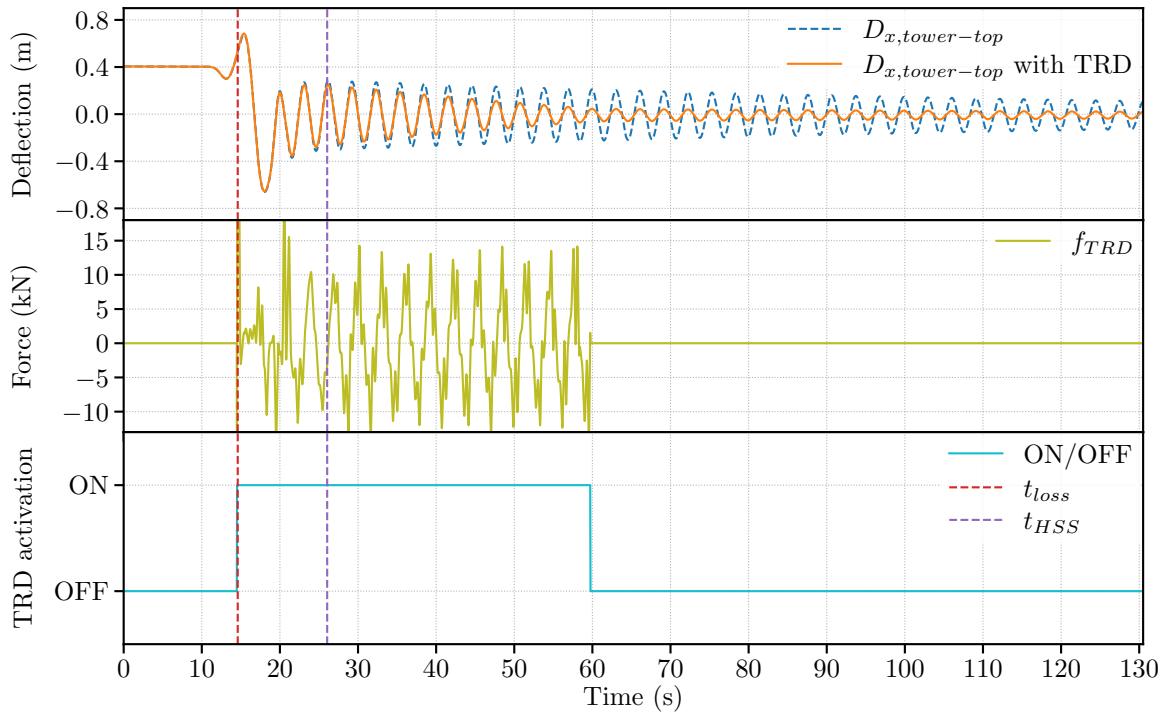


Figure I.18: Tower-top fore-after deflection and status of TRD in DLC2.3 at V_{rate} (the time dependency is omitted in legend)

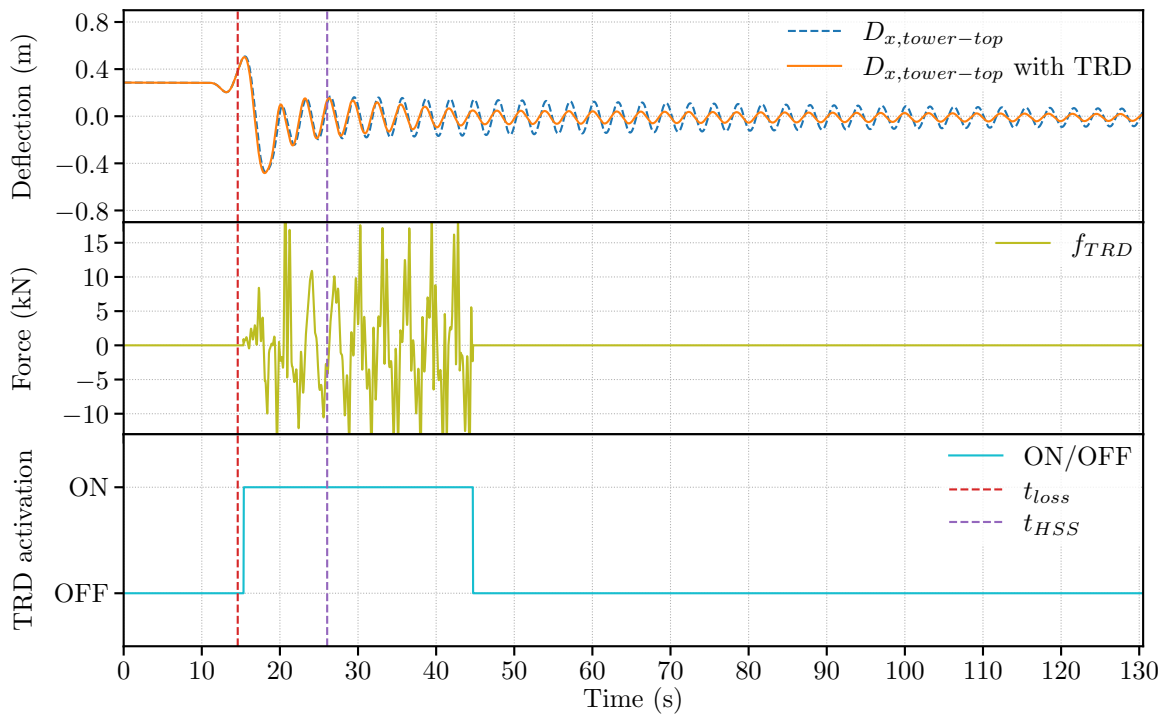


Figure I.19: Tower-top fore-after deflection and status of TRD in DLC2.3 at V_{rate-2} (the time dependency is omitted in legend)

UTILISATION DE
L'APPRENTISSAGE
AUTOMATIQUE POUR
LA PRÉDICTION
PROBABILISTE À
LONG-TERME DU
DOMMAGE PAR
FATIGUE ET LA
RÉDUCTION DES
VIBRATIONS D'UN
MÂT D'ÉOLIENNE PAR
UN CONTRÔLE ACTIF

Hao Bai

*Laboratoire de Mécanique de Normandie
INSA Rouen Normandie, France*



*En mémoire de Hua Hua (2008-2019) :
Merci pour cette belle aventure. Il est temps
pour toi d'en vivre une nouvelle.*



French Abstract



Annexe R

Résumé en français

R.1. Introduction générale

Avec la croissance rapide de l'industrie de l'énergie éolienne, le besoin d'une tour d'éolienne fiable est critique en termes de sécurité de la structure et de la production d'électricité. Un système d'amortissement utilisant un amortisseur actif est développé dans ce mémoire pour contrôler les vibrations sur la tour d'éolienne. Cette thèse détaille le processus de conception couvrant la motivation pour développer un système d'amortissement actif pour les éoliennes, une conception initiale pour intégrer twin rotor damper (TRD) dans la tour d'éolienne, la vérification numérique de la conception, et l'optimisation de la conception de TRD en utilisant l'algorithme modifié de DE. Les contributions de ce travail concernent principalement :

1. Une analyse de charge ultime et une analyse de fatigue sont proposées pour la structure du mât éolienne. Ces deux analyses sont utilisées comme résultats de référence pour évaluer l'efficacité du système d'amortissement.
2. Un cadre probabiliste assisté par réseau de neurones pour l'analyse de la fatigue est proposé en utilisant le réseau de neurones. La méthode proposée a été testée numériquement avec la NREL 5MW reference wind turbine.
3. Un système d'amortissement actif utilisant TRD est développé et intégré dans l'éolienne de référence. La simulation numérique a été réalisée pour évaluer cette intégration.
4. Une nouvelle méthode de configuration d'algorithme adaptative pour DE (AAC-DE) est proposée, combinant l'apprentissage par renforcement (c'est-à-dire l'algorithme du bandit manchot) et les approches d'apprentissage non supervisé (c'est-à-dire l'estimation de la densité du noyau). L'algorithme proposé est appliqué pour rechercher la conception optimale pour TRD dans l'éolienne.

Le plan de cet ouvrage est organisé comme suit :

Section R.2 un bref examen de l'industrie de l'énergie éolienne a lieu démontrant la motivation de développer un système d'amortissement actif pour les éoliennes. (Cette section résume ce qui est décrit au Chapter 1 en anglais)

Section R.3 un processus de conception pour le système d’amortissement actif est proposé, tant du point de vue scientifique que du point de vue technique. (Cette section résume ce qui est décrit au Chapter 2 en anglais)

Section R.4 une éolienne de référence, NREL 5MW, est introduite et simulée sous un vent en rafales avec défaut technique. Le résultat numérique obtenu dans ce chapitre offre une base de référence pour évaluer la performance du système d’amortissement proposé. (Cette section résume ce qui est décrit au Chapter 3 en anglais)

Section R.5 un nouveau cadre probabiliste assisté par réseau neuronal d’analyse de la fatigue est proposé. Le cadre proposé est appliqué à l’éolienne de référence pour étudier les distributions de probabilité des dommages cumulés de fatigue à long terme le long du mât de l’éolienne dans des conditions de vent turbulent. De même, le résultat obtenu par simulation numérique sera utilisé comme référence pour évaluer la performance du système d’amortissement proposé dans une étude future. (Cette section résume ce qui est décrit au Chapter 4 en anglais)

Section R.6 un dispositif d’amortissement actif connu sous le nom de twin rotor damper (TRD) est introduit. Un système d’amortissement pour l’éolienne de référence est ensuite développé en intégrant le TRD dans la tour de l’éolienne. La performance d’amortissement d’un tel système est estimée pour deux DLCs différents et comparée aux données de référence qui ont été étudiées précédemment dans Chapter 3 et Chapter 4. (Cette section résume ce qui est décrit au Chapter 5 en anglais)

Section R.7 , une nouvelle configuration d’algorithme adaptative est proposée pour les algorithmes differential evolution (une branche de la famille EA). L’algorithme proposé, à savoir *Configuration d’Algorithme Adaptative pour l’Evolution Différentielle* (AAC-DE), est comparé à cinq autres algorithmes dérivés de pointe DE et validé en réalisant une étude expérimentale sur les problèmes du test de référence. Une application de l’algorithme proposé est effectuée pour rechercher la conception optimale de TRD pour l’éolienne de référence. (Cette section résume ce qui est décrit au Chapter 6 en anglais)

Cette thèse se termine finalement par une conclusion générale avec une perspective.

Pour permettre une interprétation identique des données visuelles à la fois aux personnes atteintes de daltonisme rouge-vert et aux personnes sans déficience de la vision des couleurs (CVD), une carte des couleurs optimisée pour les CVD nommée *cividis* [NAR18] est pratiquée dans ce travail.

R.2. Chapitre 1 : Objectives

Il ne fait aucun doute que les énergies renouvelables deviennent de plus en plus importantes sur le marché de l'énergie actuel. En 2017, toutes les énergies renouvelables représentaient une part de 13,8% de l'approvisionnement mondial total en énergie primaire et de 18,1% de la consommation mondiale totale d'énergie finale [Int19a]. La présence des énergies renouvelables a rejoint tous les secteurs de notre vie quotidienne, en particulier le chauffage & le refroidissement, les transports et la production d'électricité.

Dans la tendance actuelle à la production d'électricité à un coût inférieur à celui de la production d'électricité à partir de combustibles fossiles la moins chère, l'éolien terrestre et le photovoltaïque solaire se distinguent. L'énergie éolienne est aujourd'hui l'une des technologies les plus importantes dans le développement des énergies renouvelables et joue un rôle croissant dans la part de marché de l'énergie électrique. L'un des principaux facteurs qui explique la baisse du LCOE du vent terrestre est le progrès continu de la conception des éoliennes, notamment la hauteur de l'éolienne, les surfaces balayées plus grandes et la capacité nominale plus élevée. Avec l'augmentation de la hauteur des moyeux, la vibration mécanique au-dessus du mât de l'éolienne est par conséquent augmentée par les forces d'excitation induites par le vent, les vagues et le séisme potentiel. Les vibrations provoquent principalement des dommages de fatigue sur la tour et réduisent la durée de vie de l'installation. Pour contrebalancer cet inconvénient des vibrations, diverses méthodes peuvent être utilisées pour minimiser les vibrations dans la tour et améliorer la dynamique structurelle de l'éolienne. Un système d'amortissement intégré dans la tour de l'éolienne est l'une des solutions intéressantes. Deux systèmes de contrôle majeurs sont mis en œuvre dans l'industrie éolienne : le système de contrôle de décrochage et le système de contrôle de tangage. Tous deux présentent des inconvénients, soit sur le plan mécanique, soit sur le plan aérodynamique, qui limitent l'application de ces méthodes dans les grandes éoliennes modernes.

Dans cette thèse, un amortisseur actif innovant appelé Twin Rotor Damper (TRD) est présenté et devrait permettre de surmonter les difficultés liées aux vibrations des tours d'éoliennes terrestres. Avant d'étudier le système d'amortissement, une nouvelle approche d'évaluation des dommages de fatigue est proposée pour mieux comprendre les dommages de fatigue induits par la vibration de manière probabiliste.

R.3. Chapitre 2 : Méthodologie de dimensionnement du mât d'éolienne

Pour concevoir une éolienne, trois exigences fondamentales doivent être prises en considération : l'efficacité de la production d'électricité, la sécurité structurelle de l'éolienne et la rentabilité des investissements du financement. Cela implique que l'éolienne doit non seulement résister aux charges pendant sa durée de vie, mais aussi produire suffisamment d'énergie pour compenser son coût.

La norme CEI 61400-1 est utilisée dans cette thèse. Elle définit les exigences minimales de conception des éoliennes et n'est pas destinée à une évaluation détaillée ou à une spécification de conception complète. En tant que telle, elle ne comprend pas tous les détails nécessaires à la fabrication d'une éolienne, il y a donc des éléments qui doivent être abordés au-delà du champ d'application de cette norme.

Selon les spécifications de la CEI 61400-1, le processus d'évaluation des charges comprend les étapes suivantes :

1. définir la classe d'éolienne qui répond à l'objectif de conception
2. déterminer les cas de charge de conception d'intérêt qui consiste à la fois en des conditions de fonctionnement normales et des conditions de vent extrêmes
3. évaluer le niveau de charge sur la turbine dans les cas de charge choisis
4. vérifier que les contraintes dues aux charges sont acceptables

Afin de développer un système d'amortissement actif qui est capable de réduire les vibrations dans la plupart des éoliennes, une éolienne de classe IA est préférable. Un cas de charge dans des conditions normales, DLC2.3, et un cas de charge dans des conditions extrêmes, DLC1.1, sont sélectionnés pour réaliser respectivement une analyse des charges ultimes et une analyse des charges de fatigue.

Les deux types d'analyse sont d'abord effectués sur une éolienne de référence nommé, l'éolienne NREL 5MW, afin de quantifier la demande en système d'amortissement actif. Un scénario U, indiquant l'analyse des charges ultimes sur l'éolienne de référence, et un scénario F, indiquant l'analyse de la fatigue sur l'éolienne de référence, sont élaborés afin d'initialiser une conception primaire pour l'amortisseur actif. De plus, ces scénarios servent de référence pour l'optimisation des paramètres de contrôle de l'amortisseur actif.

Un logiciel à code source ouvert nommé FAST, ou OpenFAST, est impliqué dans cette thèse. Il s'agit d'un simulateur dynamique et multif-physique pour les HAWTs à deux et trois pales. Le nom vient des acronymes de *Fatigue, Aérodynamique, Structure et Turbulence* [JB05]. Il s'agit d'un outil de simulation aéro-hydro-servo-élastique basé sur plusieurs corps, composé de divers sous-modules (confer (cf.) Figure R.1). Ces

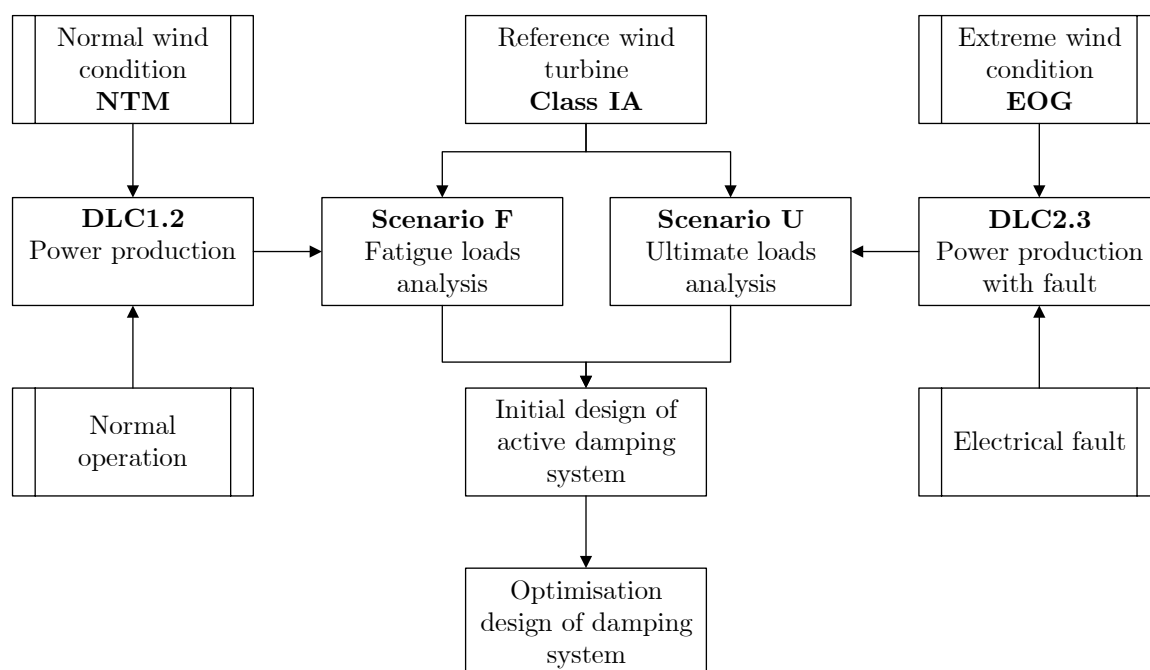


FIGURE R.1 : Dimensionnement d'un système d'amortissement actif pour les éoliennes

codes modélisent l'ensemble de l'éolienne comme une combinaison de corps flexibles et rigides. Il est développé et supporté par NREL.

R.4. Chapitre 3 : Analyse dynamique du mât d'éolienne en cas de perte du réseau

Cette section fournit un résumé d'une éolienne de référence, l'éolienne NREL 5MW, et de la manière dont elle est appliquée dans le cadre du processus de conception. La première section fournit quelques détails sur les principales caractéristiques des éoliennes de référence. La deuxième section fournit une validation de cette turbine en régime permanent. Elle est suivie d'une autre section qui étudie la réponse de l'éolienne dans des conditions de vent extrêmes et en cas de défaut technique. La dernière section met en évidence les améliorations ou les nouvelles propositions mentionnées dans le présent chapitre.

Les résultats obtenus dans ce chapitre sont une condition préalable à la conception d'un amortisseur structurel et serviront ensuite de scénario pour évaluer les performances du système d'amortissement.

R.4.1. Cas de charge DLC2.3 : production normale avec la perte du réseau

R.4.1.1. Situation conceptuelle

L'histoire a montré qu'une combinaison de défaillances technologiques et de vitesses de vent extrêmes s'est produite dans certaines situations. Une coïncidence malheureuse de certains événements peut conduire à un accident sur une éolienne ou, plus désastreux encore, à un effondrement de l'ensemble du système [MMVB18]. CHOU et al. [COL19] a révélé que près d'un tiers des effondrements d'éoliennes sont dus à une défaillance structurelle ou à une rupture de pale due à un vent fort. En comparaison avec d'autres composants (tels que la boîte de vitesses, les pales et le convertisseur de puissance), la tour de l'éolienne a la plus haute valeur de risque intégré [DS13; SD14]. En conséquence, l'analyse de la charge sur la tour d'éolienne soumise à la fois à des vitesses de vent extrêmes et à une défaillance du système doit être gérée en premier lieu.

Le DLC2.3 est une situation conceptuelle requise par la norme CEI 61400-1. Cette DLC implique un incident transitoire causé par une défaillance technique ou une perte de réseau électrique, également appelée "perte de réseau", pendant la production d'électricité. Tout défaut ou toute défaillance significative du système de contrôle, du système de protection ou du système électrique interne doit être pris en compte dans cette situation. En outre, la coïncidence entre un tel événement transitoire et l'événement de vent extrême (par exemple, une rafale de vent) doit également être gérée. Pour atteindre l'objectif ci-dessus, la CEI 61400-1 suggère une occurrence de défaut électrique externe, ou interne, combinée à une condition de vent extrême EOG à une vitesse moyenne de vent de V_{rate} , $V_{rate} \pm 2$ m/s et V_{out} .

Le extreme operating gust (EOG) a été introduit dans Section 2.2.3.2 et l'implémentation numérique de cette condition de vent extrême sera détaillée dans la section suivante. Un incident particulier, c'est-à-dire la perte du réseau, se produit en même temps que la rafale de vent. La coïncidence de ces deux événements est analysée dans Section 3.3.3 afin de déterminer le moment qui induit la plus mauvaise charge sur l'éolienne. Le système de protection qui a été développé dans DLC0.2 (voir Section 3.2.2) sera activé après la présence d'une perte de réseau afin de maintenir l'éolienne dans une condition de sécurité. Une analyse des charges ultimes est requise par la norme CEI 61400-1 pour ce DLC et sera effectuée dans Section 3.3.4.

R.4.1.2. Rafale extrême de fonctionnement (EOG)

Dans Section 2.2.3.2, l'ampleur de la rafale de vent V_{gust} et la vitesse de la rafale $V(z, t)$ ont été données dans Equation 2.6 et Equation 2.9, respectivement. La durée

de la rafale T_{gust} est fixée à 10.5 s par les spécifications de la CEI 61400-1 [Int05]. Un temps supplémentaire de 10 s est ajouté avant et après l'événement de rafale de vent, donnant une forme de "chapeau mexicain" pour la vitesse de la rafale (Figure R.2).

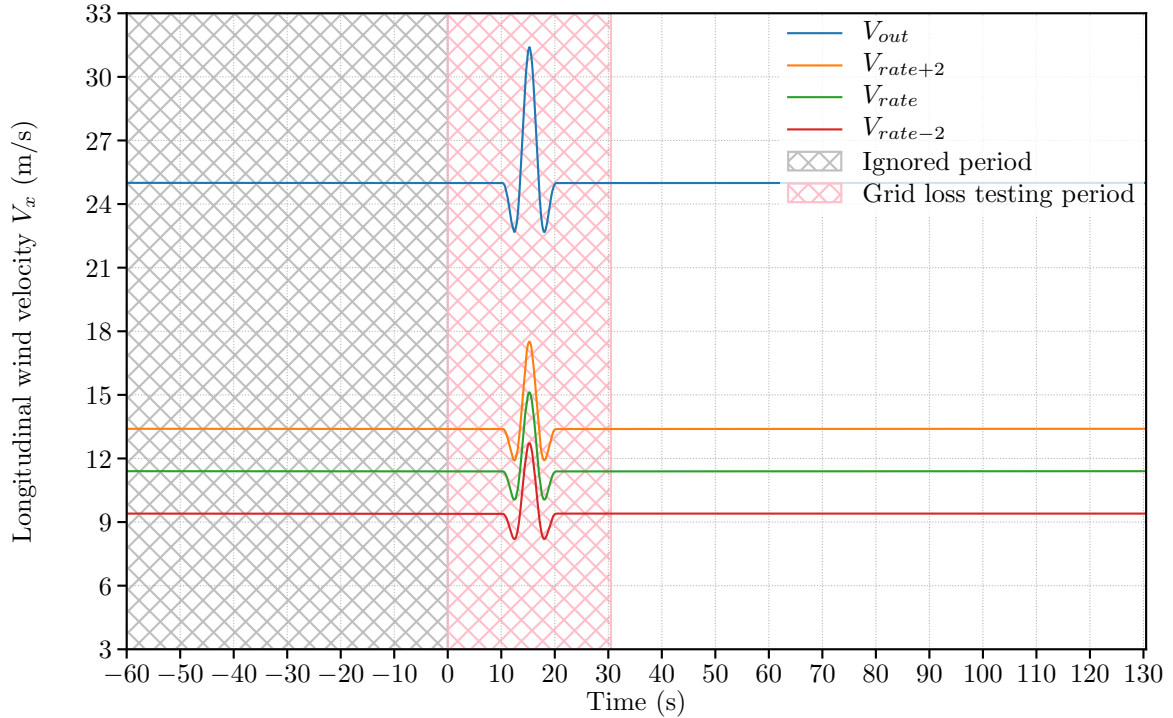


FIGURE R.2 : Vitesse longitudinale du vent de EOG à la hauteur du moyeu

Dans Figure R.2, la zone hachurée en gris illustre l'étape d'initialisation de la simulation. Elle est suivie d'une région hachurée en rose qui montre l'occurrence potentielle d'une perte de réseau. Le défaut technique (c'est-à-dire la perte de réseau) doit être introduit après que l'impact des conditions initiales soit devenu négligeable. Enfin, une période supplémentaire de 100 s est jointe consécutivement au vent de type chapeau mexicain afin d'effectuer une analyse des charges ultimes.

Quant à la perte de réseau, il s'agit d'un incident qui suppose que la connexion au réseau électrique est rompue pour une raison interne ou externe. Le générateur électrique doit être immédiatement arrêté par le système de protection. Dans le cas contraire, la charge ultérieure peut provoquer des dommages de fatigue sur la structure. Ici, le terme "immédiatement" est implémenté numériquement par un temps court défini par l'auteur de 0.2s représentant le temps de réaction du système de protection. Pour obtenir la charge la plus importante sur une éolienne, le moment de la perte du réseau a été testé entre 10s et 30.5s avec un pas de temps de 0.1s (c'est-à-dire la zone hachurée rose en Figure R.2).

Bien que seulement quatre vitesses moyennes du vent (c'est-à-dire, V_{rate-2} , V_{rate} , V_{rate+2} et V_{out}) soient requises par la norme CEI pour rechercher la charge la plus

mauvaise, une recherche étendue est proposée par l’auteur pour couvrir toute la plage de fonctionnement de la vitesse du vent, c’est-à-dire, $V_{moyen} \in [3, 25]$. Cette étude de la gamme complète pour la synchronisation de la perte de réseau permet de comprendre le comportement de l’éolienne lors de la production d’énergie électrique, et par la suite, de concevoir un amortisseur approprié couvrant toute la vitesse du vent en fonctionnement.

R.4.2. Résultats et discussions

Pour mieux comprendre le moment de la perte du réseau et la charge qui en résulte, la vitesse moyenne du vent considérée V_{mean} est étendue à la fourchette de $[3, 25]$ à un pas de 0.1 m/s. Figure R.3 illustre la corrélation entre la perte de réseau, la vitesse moyenne du vent et le chargement ultérieur. Pour interpréter clairement le moment de la perte de réseau, un exemple de rafale de vent à V_{out} est donné dans le graphique en haut tandis qu’un graphique de contour est tracé dans la partie inférieure pour démontrer le peak-to-peak amplitude de la déflexion avant-après $D_{x,9}$. L’axe des ordonnées du graphique supérieur est la composante longitudinale de la vitesse instantanée du vent V_x , tandis que l’axe des ordonnées du graphique inférieur est la vitesse moyenne du vent V_{mean} . Les deux axes des abscisses correspondent à la durée de la rafale de vent. Dans le graphique du bas, les isoplèthes représentent les peak-to-peak amplitude de déviation $D_{x,9}$ soumis à la perte de réseau à différents moments et à différentes vitesses moyennes du vent. La barre de couleur à côté du graphique du bas clarifie le niveau de ces peak-to-peak amplitudes.

Pour une vitesse moyenne du vent inférieure à V_{rate-2} (9.4 m/s), l’effet de la perte de réseau avant ou après la vitesse maximale de la rafale de vent, qui se produit à $t_{gust} = 15.25$ s, n’est pas significatif. La déviation subséquente $D_{x,9}$ a un peak-to-peak amplitude inférieur à 0.7 m, sachant que le peak-to-peak amplitude dû aux opérations PTF et HSS est d’environ 6.5 m (voir Figure 3.11). La perte de réseau a un impact sur la charge du mât beaucoup moins important que celui des manœuvres du système de protection. Pour V_{mean} entre V_{rate-2} (9.4 m/s) et V_{rate+2} (13.4 m/s), le peak-to-peak amplitude de $D_{x,9}$ augmente progressivement et dépend principalement de l’instant de perte du réseau t_{loss} . Lorsque t_{loss} s’approche du moment de la vitesse maximale de la rafale de vent t_{gust} (ligne pointillée verte dans Figure R.3), l’amplitude devient de plus en plus élevée. Enfin, pour les V_{mean} supérieurs à V_{rate+2} (13.4 m/s), le peak-to-peak amplitude de la déviation avant-après a une fluctuation similaire à celle de la vitesse du vent, c’est-à-dire une zone de creux d’amplitude en 12 s à 13 s et 17.5 s à 18.5 s ainsi qu’une zone de crête en 14.5 s à 15.5 s.

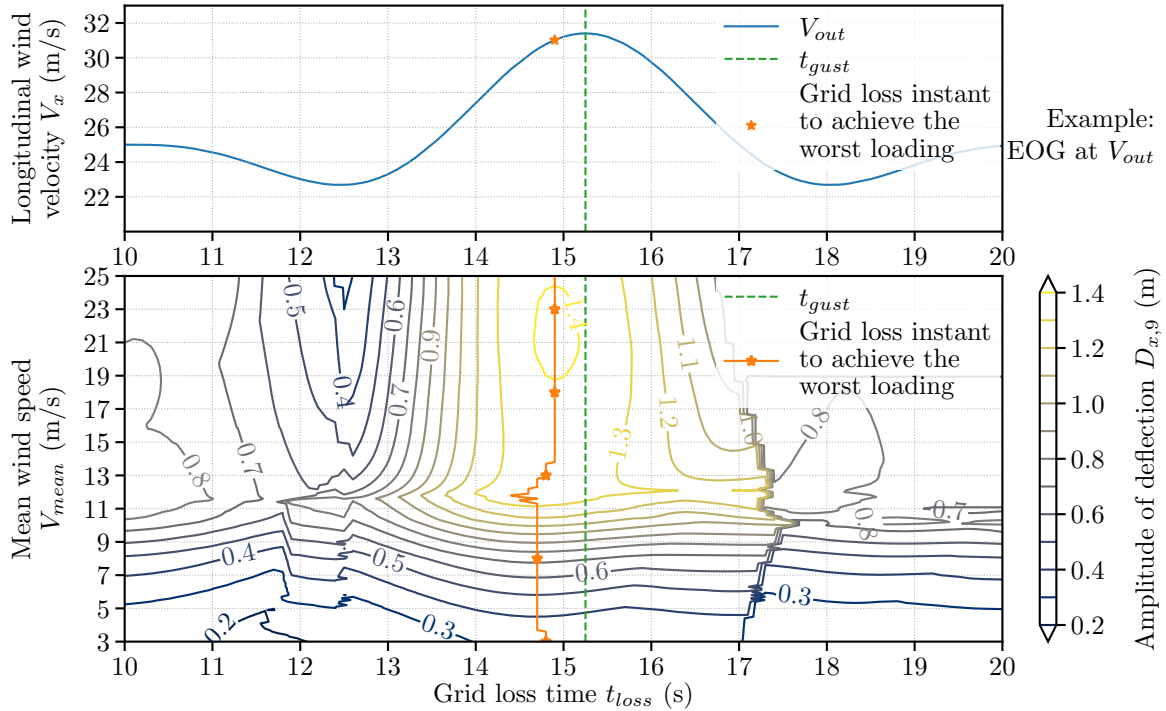


FIGURE R.3 : Moment de la perte de réseau dans la plage de la vitesse du vent de fonctionnement en ce qui concerne la déviation du mât. Le tracé de la ligne supérieure donne un exemple de vitesse de rafale à la vitesse moyenne du vent $V_{moyen} = V_{out} = 25$ m/s. Le tracé de contour inférieur montre l'amplitude crête à crête par rapport à la vitesse moyenne du vent V_{mean} et le temps de perte du réseau t_{perte}

Le moment de la perte de réseau pour atteindre la charge la plus mauvaise (ligne orange dans Figure R.3) se situe toujours avant l'apparition de la vitesse maximale du vent. Il se situe dans la plage de $[t_{loss} - 1, t_{loss}]$ en général. Lorsque la vitesse moyenne du vent V_{mean} augmente, le peak-to-peak amplitude augmente.

La recherche ci-dessus étend la DLC2.3 de quatre vitesses de vent spécifiées à toute la gamme des vitesses de vent de fonctionnement. Elle indique le moment de la perte du réseau afin d'atteindre la charge la plus mauvaise à n'importe quelle vitesse moyenne du vent dans des conditions de EOG. La même conclusion peut être formulée en ce qui concerne la force du mât locale et le moment du mât locale sur les gage 1 (voir Figure I.1 et Figure I.2 en annexe). Dans la section suivante, la perte de réseau est réglée pour apparaître au moment où le peak-to-peak amplitude atteint le maximum pour toutes les vitesses moyennes du vent entre V_{in} et V_{out} .

R.4.3. Conclusions

Dans ce chapitre, l'éolienne NREL 5MW est présentée et implémentée dans le simulateur FAST. La validation numérique de cette éolienne de base est prise en condition de vent stable, à savoir DLC0.1 et DLC0.2. Le premier DLC détermine les

conditions initiales qui seront appliquées pour toutes les simulations de réponse dans cette thèse afin de stabiliser l'éolienne et de gagner le temps simulé. Le second DLC valide le système de protection développé par l'auteur en ce qui concerne le système de contrôle adéquat défini par NREL. Le système de protection est constitué par les opérations PTF et le frein HSS offrant une manière d'arrêter d'urgence l'éolienne en cas de défauts techniques, de défaillance interne ou externe ou de conditions climatiques extrêmes.

Une analyse des charges ultimes sur DLC2.3, une situation de conception proposée par la norme CEI 61400-1, est réalisée avec le système de protection décrit ci-dessus. De plus, l'analyse est étendue à la vitesse du vent en fonctionnement complet (c'est-à-dire de V_{in} à V_{out}) au lieu des quatre vitesses du vent spécifiées (c'est-à-dire V_{rate-2} , V_{rate} , V_{rate+2} et V_{out}) suggérées par les spécifications de la CEI. Ces recherches approfondies mettent en évidence le moment où la perte de réseau produit la pire charge sur l'éolienne pour toute vitesse moyenne du vent V_{mean} se situant dans la fourchette de [3, 25]. L'analyse de la charge révèle que le peak-to-peak amplitude de la réponse du mât de l'éolienne après la perte de réseau peut être deux fois plus élevé, voire plus élevé, que celui des opérations de contrôle normales.

Toutes les données et l'expérience acquises dans ce chapitre contribuent à développer un système d'amortissement approprié en Chapter 5. Le DLC0.1 prépare les conditions initiales pour la simulation numérique et révèle la réponse de l'éolienne NREL 5MW dans un état stable à chaque V_{mean} entre V_{in} et V_{out} . Le DLC0.2 explique le déroulement du système de contrôle ainsi que le système de protection qui montre la possibilité d'intégrer un système d'amortissement actif dans le système de contrôle de l'éolienne de base. Enfin, le DLC2.3 enregistre la réponse de l'éolienne face à la coïncidence d'une condition de vent extrême (c'est-à-dire EOG) et d'un défaut technique (c'est-à-dire la perte du réseau). Il servira de base pour évaluer la performance de l'amortisseur actif développé dans Chapter 5.

R.5. Chapitre 4 : Prédiction probabiliste de la durée de vie en fatigue à l'aide d'un réseau neuronal profond

Ce chapitre présente une étude probabiliste sur les dommages causés par la fatigue de l'éolienne NREL 5MW, basée sur des simulations dans le domaine temporel dans

FAST. Un bref aperçu des méthodes fondamentales d'analyse de la fatigue est donné dans la première section. Le cadre probabiliste de l'analyse de la fatigue proposée par l'auteur est détaillé dans la deuxième section et appliqué numériquement dans la section suivante. La quatrième section propose un modèle de substitution pour ce nouveau cadre. Le chapitre se termine dans la cinquième section par une brève conclusion et un travail de perspective.

R.5.1. Analyse déterministe de la fatigue

L'évaluation de la résistance à la fatigue d'une tour d'éolienne soumise à une contrainte uni-axiale comporte plusieurs étapes. Dont la mise en œuvre dans les codes de simulation est résumée dans Figure R.4 et décrite de manière algorithmique dans Algorithme R.1.

Algorithm R.1: Évaluation déterministe de la fatigue sur une tour d'éolienne

```

1 Effectuer une simulation numérique en FAST
2 foreach tower gage i do
3   Obtenez la hauteur du gage  $z_i$ 
4   Exporter l'historique de la force locale  $F_x(z_i, t)$  et du moment local
    $M_x(z_i, t)$  et  $M_y(z_i, t)$  sur ce gage
5   foreach locale spot j do
6     Obtenez l'angle du spot  $\theta_j$ 
7     Calculer l'historique de la contrainte locale  $\sigma_{local}^{(i,j)}(z_i, t, \theta_j)$  sur ce spot
8     Extraire une série de blocs de contrainte  $M$  de l'historique de la
     contrainte
9     foreach bloc de contrainte m do
10      Comptage du nombre de cycles  $n^{(i,j)}$  // Comptage rainflow
11      Exporter la contrainte moyenne  $\sigma_{moyenne}^{(i,j)}$  et la plage de contrainte
       $\Delta\sigma^{(i,j)}$ 
12      Obtenir une contrainte alterné  $\sigma_a^{(i,j)}$  // Effet de contrainte
      moyenne
13      Obtenir le nombre de cycles jusqu'à l'échec  $N^{(i,j)}$  // Méthode de
      la courbe S-N
14    end foreach
15    Calculer les dommages cumulés dus à la fatigue sur le gage du mât i et
    le spot local j, soit  $D^{(i,j)}$  // Règle de Miner
16  end foreach
17 end foreach
18 Créer un ensemble comprenant tous les dommages de fatigue sur la tour de
    l'éolienne, c'est-à-dire  $\mathbf{D} = \{D^{(i,j)} \in \mathbb{R} : (i, j) \in \mathbb{N}^2\}$ 

```

Comme indiqué dans Figure 4.1, la première étape de l'estimation de la durée de

vie en fatigue consiste à obtenir des informations sur la charge de la structure ou du modèle. Ici, dans cette thèse, cette étape est réalisée en exécutant des simulations numériques sur la turbine sous une vitesse de vent moyenne de DLC spécifiée, quel que soit le type de condition de vent. Ensuite, sur la base de ces simulations de réponse, l'historique des contraintes locales σ_{local} pour une tour donnée gage i à la hauteur de z_i peut être exporté en utilisant Equation 4.5. L'état de contrainte est évalué sur chaque point local j à un angle de θ_j dans le plan du gage du mât i . Une fois que l'historique des contraintes est calculé, la relation charge-contrainte peut être établie. Ensuite, en appliquant les techniques mentionnées dans Section 4.1.2 et 4.1.3, la relation contrainte-durée de vie peut également être établie et, par conséquent, les dommages cumulés dus à la fatigue $D^{(i,j)}$ sur chaque jauge de tour i et chaque point local j sont effectués.

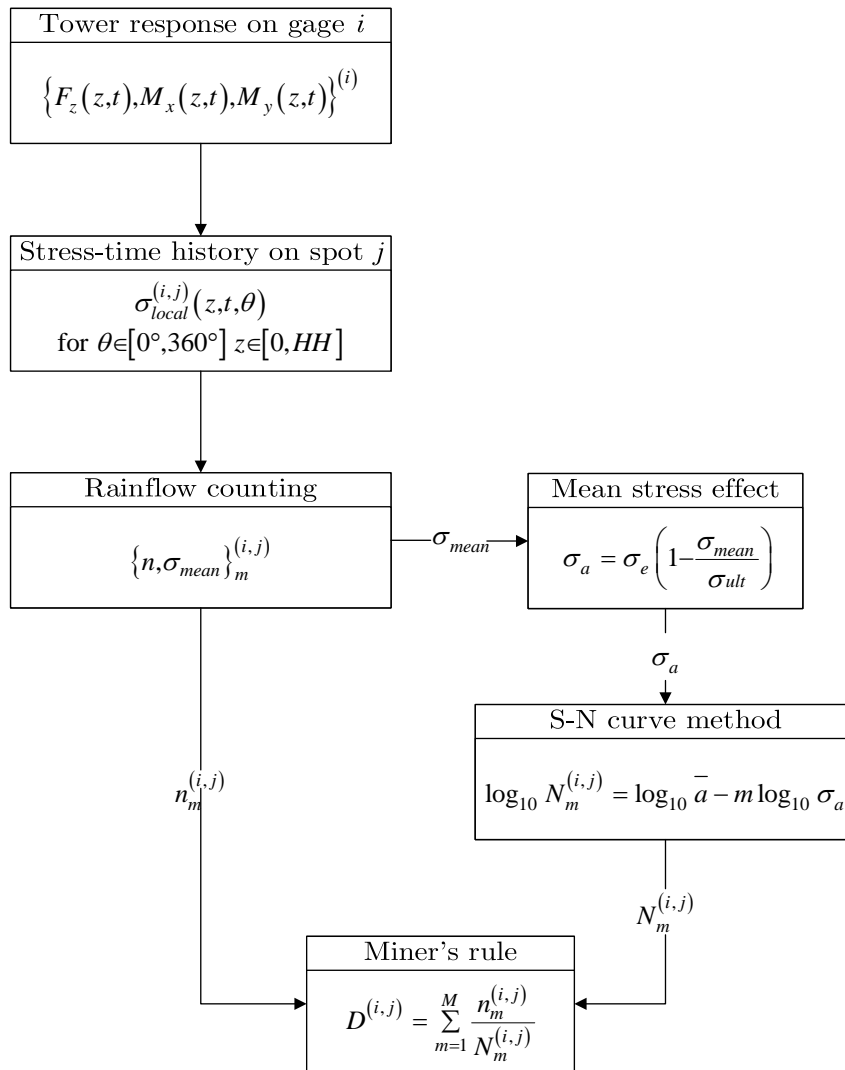


FIGURE R.4 : Fonctionnement pour l'évaluation des dommages cumulés dus à la fatigue D sur le gage du mât i et le spot local j

Pour conclure, l'ensemble final des dommages dus à la fatigue \mathbf{D} décrit naturellement la distribution spatiale de la charge de fatigue sur l'ensemble du mât d'éoliennes à une vitesse de vent moyenne donnée V_{mean} . Comme le gage du mât i et le spot local j sont numériquement discrets, il est possible d'évaluer la durée de vie en fatigue à n'importe quelle hauteur entre la base et le sommet du mât, sous réserve que le vent souffle de n'importe quelle direction entre 0° et 360° . Toutefois, ce processus est déterministe, ce qui signifie qu'il ne peut pas indiquer la probabilité d'apparition de dommages cumulés dus à la fatigue. Il est donc nécessaire d'évaluer les dommages dus à la fatigue de manière probabiliste, ce qui sera examiné dans la section suivante.

R.5.2. Analyse probabiliste de la fatigue

Pour donner un exemple de l'utilisation du profil probabiliste développé précédemment dans Equation 4.14, une estimation de la durée de vie en fatigue du mât d'une éolienne est proposée dans cette section en combinant la distribution de la vitesse du vent.

La distribution de la vitesse du vent est une distribution de probabilité continue qui détermine l'occurrence de la vitesse moyenne du vent ainsi que l'occurrence de la condition de charge individuelle sur l'éolienne. En pratique, elle est soit supposée par une distribution de probabilité issue de l'expérience comme dans Section 2.2.3.1, soit par des mesures statistiques sur site comme dans Section 4.6.

En supposant qu'une distribution de la vitesse du vent $P_{wind}(v | \theta)$ est pré-acquise couvrant la plage de fonctionnement de l'éolienne, c'est-à-dire $[V_{in}, V_{out}]$. Pour une vitesse de vent moyenne donnée V_{mean} , le profil probabiliste $\widehat{\mathcal{P}}_{V_{mean}}$ des dommages de fatigue dans cette condition de vent est donné par le Equation 4.14. Ainsi, le profil de probabilité intégré des dommages cumulés dus à la fatigue est :

$$P^{(i,j)}(x | \theta) = \left\{ P_{wind}(v = V_{mean} | \theta) \cdot \widehat{P}_{V_{mean}}^{(i,j)}(x | \widehat{\theta}) : \widehat{P}_{V_{mean}}^{(i,j)} \in \widehat{\mathcal{P}}_{V_{mean}}, (i, j) \in \mathbb{N}^2 \right\} \quad (\text{R.1})$$

L'application de l'Equation R.1 à toutes les vitesses de vent en fonctionnement permet d'obtenir un profil de probabilité global de la résistance à la fatigue du mât d'éolienne :

$$\mathcal{P}(x) = \left\{ \int_{V_{in}}^{V_{out}} P_{wind}(v | \theta) \widehat{P}_v^{(i,j)}(x | \widehat{\theta}) dv : (i, j) \in \mathbb{N}^2 \right\} \quad (\text{R.2})$$

Ce profil global $\mathcal{P}(x)$ interprète spatialement la distribution probabiliste des dommages dus à la fatigue sur l'ensemble du mât éolienne. En tronquant la distribution de la vitesse du vent entre V_{in} et V_{out} et en utilisant les dommages de fatigue accumulés pendant la production d'électricité, ce profil peut être utilisé pour estimer les dommages de fatigue cumulés pendant la durée de vie nominale de l'éolienne. Il donne

ainsi la distribution spatiale des dommages de fatigue au cours de sa durée de vie et indique les positions du mât qui présentent des dommages de fatigue intensément cumulés. Les étapes ci-dessus sont énumérées dans Algorithme R.2 avec un exemple donné dans Figure R.5.

L'imagerie d'une éolienne produit une puissance électrique de l'ordre de [5, 20] pour la vitesse du vent (c'est-à-dire, $V_{in}=5$ m/s et $V_{out}=20$ m/s), la distribution de la vitesse moyenne du vent suit la distribution de Weibull [PP02] avec un PDF donné par :

$$f(x) = \frac{k}{\lambda} \left(\frac{x}{\lambda}\right)^{k-1} \exp\left(-\left(\frac{x}{\lambda}\right)^k\right) \quad (\text{R.3})$$

where, $k = 2$, Paramètre de forme
 $\lambda = 10$, paramètre d'échelle

Un exemple de cette PDF est illustré en haut de Figure R.5 où la zone orange représente la probabilité de V_{in} et la zone verte représente la probabilité de V_{out} . Les deux sous-graphiques suivants montrent le profil probabiliste des dommages dus à la fatigue, déterminé par l'algorithme 4.2 pour $V_{mean}=V_{in}$ et $V_{mean}=V_{out}$. Pour la vitesse du vent entre V_{in} et V_{out} à une taille de pas de 1 m/s, le profil probabiliste des dommages dus à la fatigue est généré de la même manière. En calculant le profil de probabilité intégré (Equation R.1) et en additionnant tous les profils, le profil de probabilité global des dommages cumulés dus à la fatigue sur le gage 1 et spot local spot 1 du mât d'éolienne est réalisé à la dernière ligne de Figure R.5.

Veillez noter que la PDF du profil global dans Figure R.5 a été tracé en base logarithmique 10 pour faciliter l'illustration.

Algorithm R.2: Evaluation probabiliste de la durée de vie en fatigue d'une tour d'éolienne

- 1 Définir une distribution de la vitesse du vent $P_{wind}(v | \theta)$
 - 2 **for** $V_{mean} \leftarrow V_{in}$ **to** V_{out} **do**
 - 3 Effectuer l'évaluation probabiliste de la fatigue pour obtenir le profil de probabilité des dommages dus à la fatigue
 $\hat{\mathcal{P}}_{V_{mean}} = \{\hat{P}^{(i,j)}(x | \hat{\theta}) : (i, j) \in \mathbb{N}^2\}$ Obtenir la probabilité d'occurrence de la vitesse actuelle du vent, c'est-à-dire $P_{wind}(v = V_{mean} | \theta)$
 - 4 Calculer le profil de probabilité intégré $P_{wind}(v = V_{mean} | \theta) \times \hat{\mathcal{P}}_{V_{mean}}$
 - 5 **end for**
 - 6 Calculer la somme de tous les profils de probabilité intégrés pour former un ensemble global $\mathcal{P}(x) = \left\{ \sum_{v=V_{in}}^{V_{out}} P_{wind}(v | \theta) \hat{P}_v^{(i,j)}(x | \hat{\theta}) : (i, j) \in \mathbb{N}^2 \right\}$
// Version discrète de Equation R.2
-

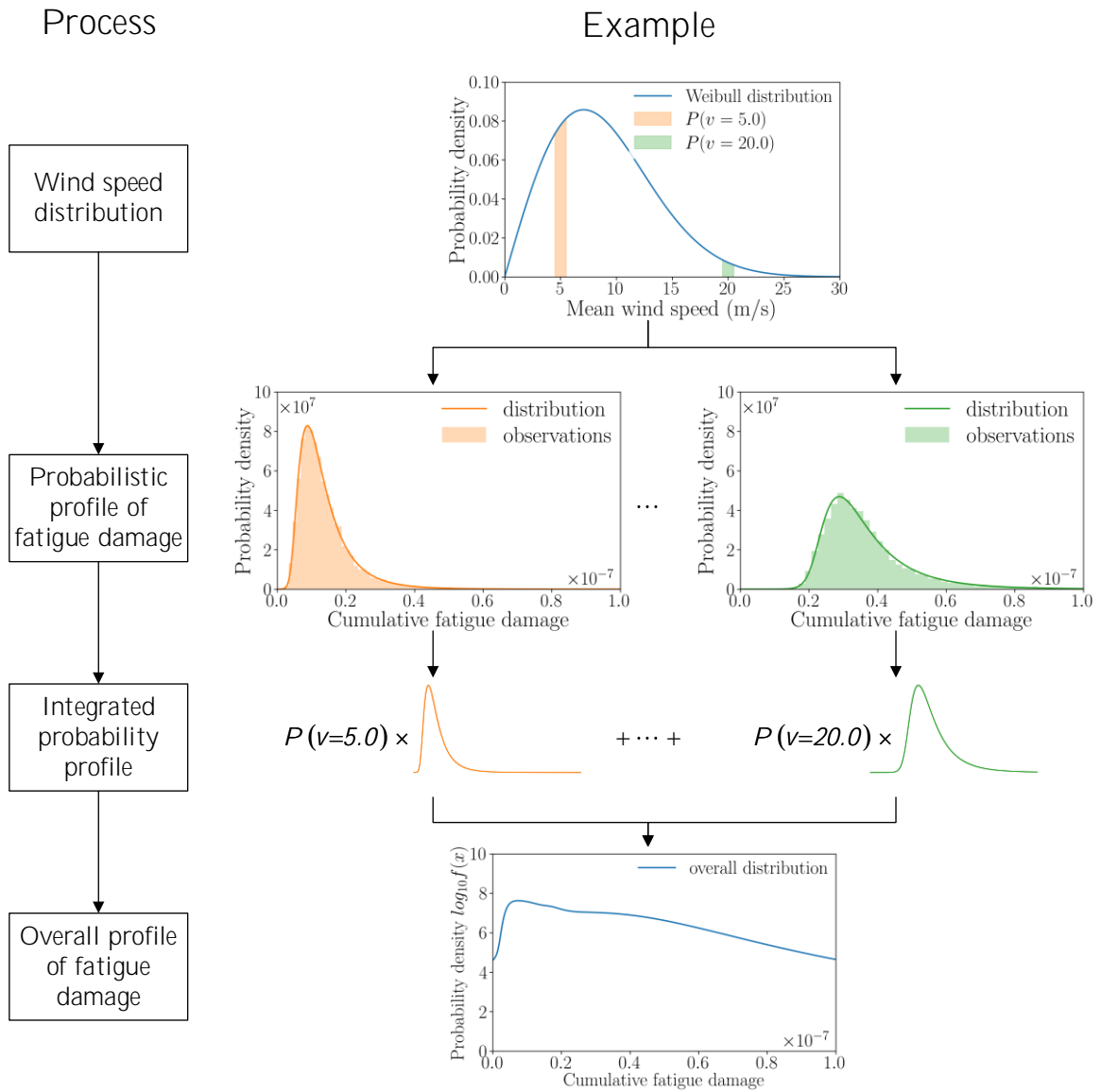


FIGURE R.5 : Exemple de profil probabiliste de la durée de vie en fatigue sur la jauge 1 du mât et le spot local 1 pendant une période de 10 min

R.5.3. Cas de charge DLC1.2 : production normale avec la perte du réseau

La DLC1.2 issue de la norme CEI 61400-1 spécifie un scénario de production d'énergie électrique face au vent en considérant normal turbulence model (NTM). L'état de l'éolienne est considéré comme une production normale sans défaut technique ni incident indésirable. Les vitesses du vent dans trois directions (\vec{x}_t , \vec{y}_t et \vec{z}_t) sont instables et varient de manière aléatoire pendant un certain temps. Les spécifications de la CEI suggèrent soit une période de 10 min avec au moins six simulations numériques, soit une simulation complète de 60 min.

Pour faciliter l'exécution, la période de 10 minutes est choisie par l'auteur comme temps simulé dans chaque exécution. Le nombre d'exécutions dépend du nombre d'observations dans l'échantillon. Pour garantir suffisamment de données pour l'analyse probabiliste de la fatigue, un nombre de 10 000 observations est prévu pour chaque cas de vitesse moyenne du vent. Chaque observation implique un numéro de semence aléatoire unique qui sera utilisé pour générer une condition de vent unique NTM dans les codes FAST.

Par définition, la vitesse moyenne du vent V_{mean} à hub height (HH) en NTM varie de $V_{in}=3$ m/s à $V_{out}=25$ m/s au pas de 1 m/s, soit un total de 23 cas de vitesse moyenne du vent. L'écart-type de la turbulence dans la direction longitudinale \vec{x}_t peut être déduit de Equation 2.3. Figure R.6 donne un exemple de NTM dans lequel la vitesse du vent en fonction du temps est décomposée en sa vitesse longitudinale V_x (ligne bleue), sa vitesse latérale V_y (ligne orange) et sa vitesse verticale V_z (ligne verte). Une période de 60 s sera négligée comme d'habitude dans le post-traitement. Sur le côté droit de Figure R.6, la distribution des composantes de la vitesse du vent à partir de 0 s à 600 s est également illustrée. Table 4.1 résume toutes les caractéristiques de DLC1.2.

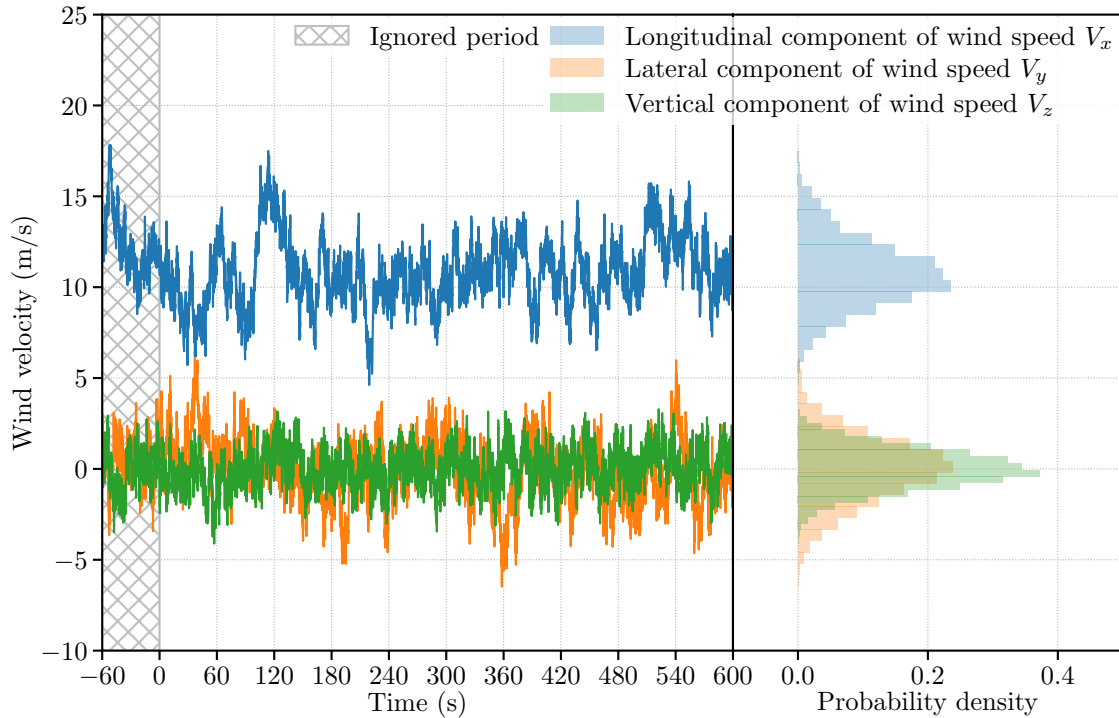


FIGURE R.6 : Un exemple de NTM à la vitesse moyenne du vent de 11 m/s

Lors du post-traitement de chaque simulation, les réponses mécaniques pour tous les gages de tour énumérés dans Table 3.2 sont exportées. Chaque jauge de tour est divisée en parts égales en spots locaux de 36. Ainsi, un total de $11 \times 36 = 396$ de spots locaux sera utilisé pour effectuer l'analyse probabiliste de fatigue du mât éolienne. Chacun d'entre eux aura une distribution de probabilité individuelle de 23 de dommages de fatigue cumulés sur 10 minutes correspondant respectivement aux cas de 23 de vitesse moyenne du vent de V_{in} à V_{out} . Cela représente, en résumé, un total de $396 \times 23 = 9108$ de fonctions de probabilité.

Pour effectuer l'analyse de la fatigue en environnement numérique, on applique les directives techniques de la pratique recommandée DNVGL-RP-C203 [DNV19]. Le matériau acier au carbone et au manganèse (C-Mn) est pris en compte dans la simulation. La courbe S-N de la classe B1 dans l'environnement atmosphérique est supposée vraie, ce qui a une limite d'endurance de $\sigma_e = 106.97$ MPa à 10^7 cycles.

R.5.4. Résultats et discussions

Figure 4.14 est composé d'une carte 3D et d'une carte de contour représentant la projection de la carte 3D sur le plan horizontal. Il convient de souligner que, sur la carte 3D, l'axe axial, ainsi que la barre de couleur, représentent la densité de probabilité mise à l'échelle en base logarithmique 10, c'est-à-dire $\vec{z} = \log_{10} f(x)$. La carte de contour montre les isolignes (également connues sous le nom de *isarithme*)

le long desquelles les probability density function (PDF) ont des valeurs constantes. D'un point de vue statistique, ces isolignes impliquent les mêmes centiles de toutes les distributions de probabilité de dommages dus à la fatigue sur le gage 1 du mât (Figure R.7b).

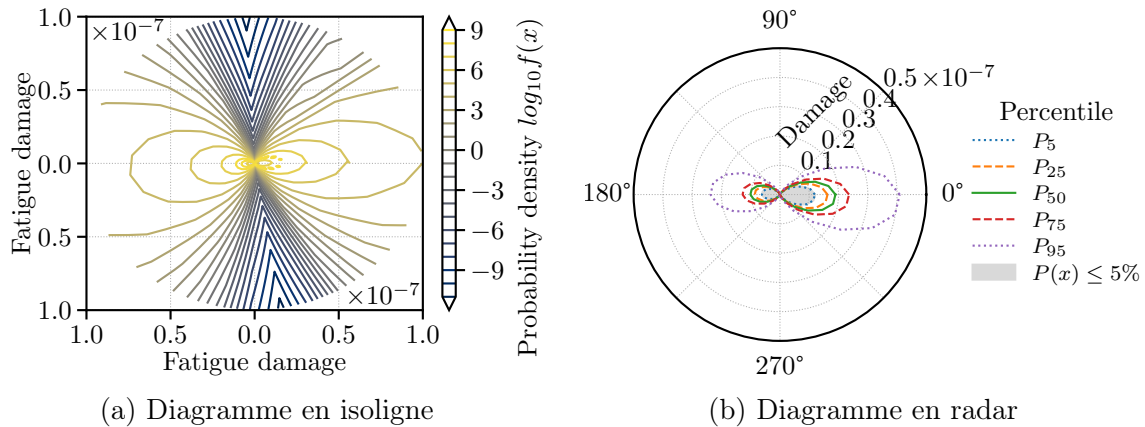


FIGURE R.7 : DLC1.2 distribution des dommages de fatigue cumulés sur 10 minutes sur le gage 1 du mât montrée dans (a) diagramme en isoligne (système de coordonnées cartésiennes) et (b) diagramme en radar (système de coordonnées cylindriques)

Figure 4.15a extrait la carte de contour de Figure 4.14 à la carte 2D où l'abscisse et l'ordonnée représentent les dommages de fatigue cumulés sur 10 minutes. Les isolignes représentent graphiquement comment les dommages de fatigue sont distribués sur la section transversale du mât gage 1. (à la hauteur de 2.19 m). Toutes les isolignes sont colorées pour illustrer les différents niveaux de PDF en base logarithmique 10.

Figure R.7b reprend les mêmes données de Figure R.7a dans la carte radar (également connue sous le nom de *diagramme de Kiviat*[KK73]). L'axe radial, ou axe polaire, représente les dommages de fatigue cumulés sur 10 minutes sur lesquels le point zéro, c'est-à-dire les dommages zéro, est centré dans la carte. Les périmètres intérieurs indiquent l'augmentation des dommages de fatigue de zéro (centre) à son maximum (périmètre extérieur). Le périmètre extérieur indique l'angle d'azimut α des points locaux en degrés. Par convention, le spot 1 local se situe sur le côté droit de la section transversale et a un angle d'azimut $\alpha = 0^\circ$ (Figure 4.2). Les lignes colorées à l'intérieur du graphique radar représentent les différents centiles désignés par P_i , où i signifie i -ième centile. Par exemple, P_5 (la ligne bleue en pointillés) est le 5ème centile en dessous duquel on peut trouver 5% des observations (la surface grise dans Figure R.7b). En d'autres termes, la tour de l'éolienne a probablement une chance de 5% de subir une valeur de dommage par fatigue à l'intérieur de la surface grise. D'autres centiles tels que P_{25} , P_{50} , P_{75} et P_{95} sont mis en évidence respectivement par une ligne pointillée orange, une ligne verte, une ligne pointillée rouge et une ligne pointillée violette dans Figure R.7b. P_{25} est également connu comme le premier quartile,

P_{50} comme le deuxième quartile (ou médiane), et P_{75} comme le troisième quartile.

R.5.4.1. Distribution de probabilité dominante des dommages dus à la fatigue

Parmi une centaine de distributions candidates [Scia ; Scib], le cadre probabiliste (Algorithme 4.2) a réussi à identifier environ dix distributions pour les dommages cumulés de fatigue de 10 minutes sur la tour

des bagages1. Figure 4.17 résume statistiquement l'occurrence de chaque type de distribution sur la tour gage 1 à partir de laquelle les distributions Johnson SU et SB ont atteint une probabilité de plus de 80%. Il en ressort que la distribution Johnson SU, et sa famille de distribution Johnson SB, sont clairement les types de distribution de probabilité les plus appropriés pour représenter les dommages de fatigue cumulés sur 10 minutes sur la tour gage 1, il existe également d'autres distributions possibles comme la distribution exponentielle de Weibull [MS93 ; MSF95], la distribution normale exponentielle [COC13], la distribution de Pearson de type III [Pea94] et la distribution logistique généralisée [JKB95 ; GK10]. Ces distributions aident à expliquer comment les dommages dus à la fatigue sont répartis sur plusieurs points locaux ou sous une certaine vitesse moyenne du vent (voir la ligne bleue dans Figure 4.16 pour la distribution exponentielle de Weibull, la ligne cyan pour la distribution normale exponentielle, la ligne rose pour la distribution de Pearson type III, et enfin la ligne marron pour la distribution logistique généralisée).

R.5.4.2. Loi de Peanut

L'étude empirique des sections précédentes permet de tirer plusieurs conclusions sur la répartition des dommages cumulés dus à la fatigue :

1. La distribution des SU de Johnson peut être utilisée pour évaluer et prévoir les dommages cumulés de fatigue sur la section transversale du mât d'éolienne.
2. Les dommages de fatigue cumulés ne sont pas toujours proportionnels à la vitesse moyenne du vent (par exemple, comparer Figure 4.18b à Figure 4.18c). Il est fortement lié au système de contrôle, en particulier pour les éoliennes équipées du régulateur de vitesse variable.
3. La répartition des dommages dus à la fatigue sur la section transversale du mât éolienne est probablement plus symétrique lorsque le g_{smoyen} est petit et s'agrandit du côté sous le vent lorsque le V_{mean} monte (par exemple, comparer Figure 4.18a à Figure 4.18g).
4. L'axe longitudinal du contour de la distribution n'est pas toujours parallèle à la direction du vent, mais peut être modifié lorsque les charges de vent augmentent (par exemple, Figure 4.18l).

Pour mieux mémoriser ces relations et faciliter la citation dans les sections suivantes, les relations ci-dessus sont nommées "loi d'arachide" par l'auteur puisque la forme de la distribution ressemble à une arachide dans Figure 4.18.

Il est nécessaire de préciser que la loi de l'arachide est une loi empirique basée sur les expériences en matière d'étude numérique. Elle n'a été vérifiée par aucune démonstration analytique et elle est loin d'être un théorème mathématique. Cependant, à l'aide de l'expression de la distribution de Johnson SU (Equation 4.19), il est possible de trouver une expression mathématique pour la loi de Peanut par une étude analytique. D'autres chiffres concernant les distributions étudiées sont donnés dans Figure I.6, Figure I.7 et Figure I.8.

R.5.5. Réseau du neurones résiduels

Afin de développer un deep neural network avec apprentissage résiduel pour l'évaluation probabiliste de la fatigue, les connexions de saut sont introduites dans un MLP ordinaire. Figure R.8 illustre l'architecture globale du neural network proposé.

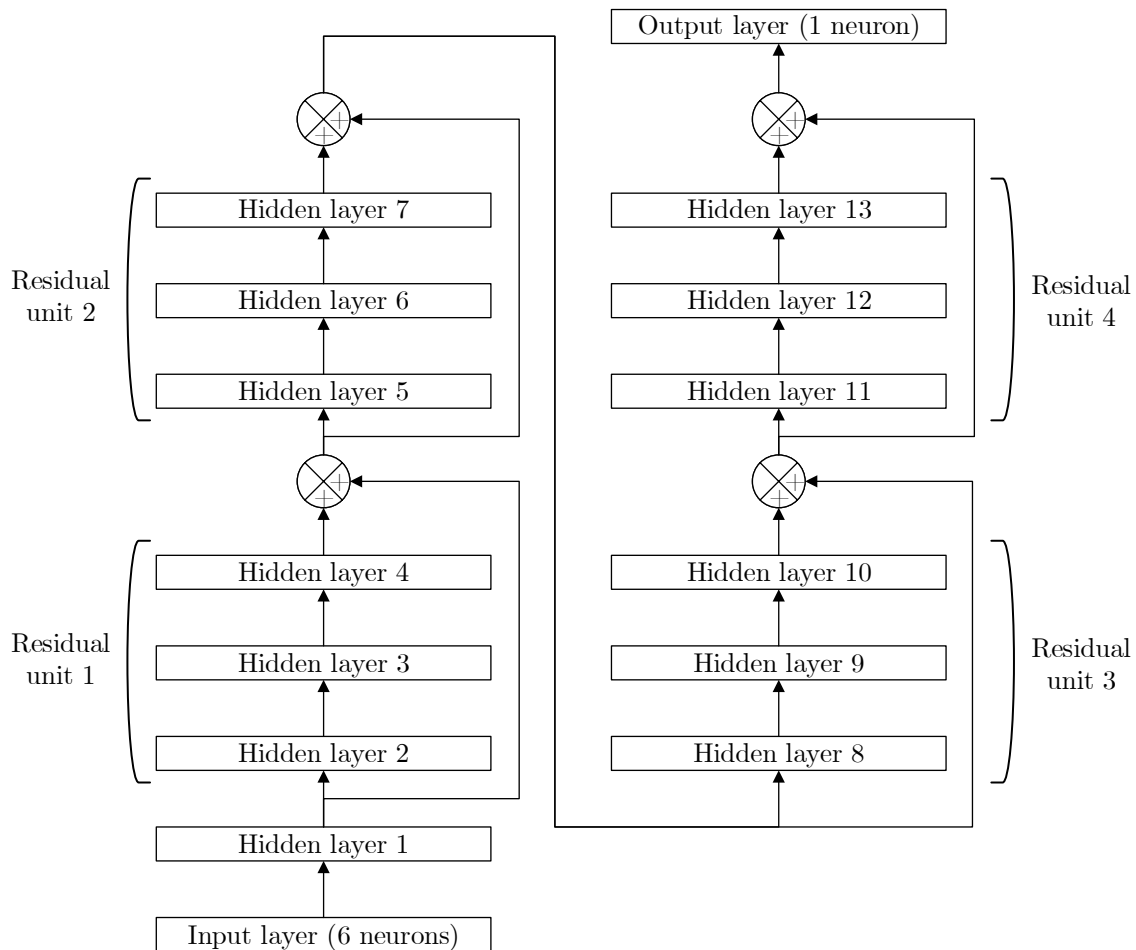


FIGURE R.8 : Architecture des perceptrons multicouches résiduels (ResMLP)

En résumé, quatre groupes d'unités résiduelles sont mis en œuvre. Chaque grappe contient un modèle de perceptrons à trois couches et chaque couche est constituée de 300 perceptrons. La fonction ReLU (Equation 4.30) est utilisée comme fonction d'activation des neurones artificiels. Comme les valeurs des dommages dus à la fatigue vont de 0 à 1×10^{-7} (voir Section 4.4), la différence entre les valeurs est trop faible et insignifiante. Cela peut conduire à un modèle insensible et à des prévisions inexactes. En conséquence, mean squared logarithmic error (MSLE) (Equation 4.32) est utilisé pour définir la fonction de perte du neural network proposé puisqu'il exprime toutes les valeurs dans un espace logarithmique et agrandit en conséquence la minuscule valeur d'erreur entre deux valeurs de dommages. Tous les hyperparamètres du ResMLP proposé sont répertoriés dans Table 4.2.

R.5.6. Résultats et discussions

Après avoir réussi à prédire les dommages de fatigue cumulés sur 10 minutes à certaines vitesses de vent moyennes, comme indiqué dans la section précédente, une autre ambition concernant l'application de l'outil d'entraînement est de prédire les dommages de fatigue à toute vitesse de vent moyenne comprise entre V_{in} et V_{out} . Pour atteindre cet objectif, un nouvel ensemble de données est généré avec une taille de 10 000 vitesses moyennes du vent. Les valeurs V_{mean} sont randomisées uniformément à partir de la plage [3.0, 25.0]. Le site

Les dommages cumulés dus à la fatigue calculés à l'aide des codes FAST et le cadre probabiliste proposé pour l'évaluation de la fatigue sont utilisés comme données de référence, comme d'habitude. Les prédictions faites par les personnes formées sont ensuite comparées aux données de référence pour évaluer la précision des prédictions. Comme dans Section 4.5.4.1, la différence entre la valeur simulée et la valeur prédite est quantifiée par le coefficient de corrélation de Pearson et la p -value de K-S test dans Figure R.9.

Le réseau entraîné montre à nouveau une grande précision dans la prévision des dommages cumulés dus à la fatigue sur la tour d'éolienne. Le coefficient de corrélation R atteint 0,997, ce qui indique que la majorité des dommages prédits correspondent aux dommages calculés à partir de la simulation numérique. La p -value de K-S test entre l'échantillon de prédictions et l'échantillon de simulations est de 0,996 ce qui implique que l'hypothèse nulle, c'est-à-dire que les deux échantillons sont tirés de la même distribution, ne peut être rejetée statistiquement.

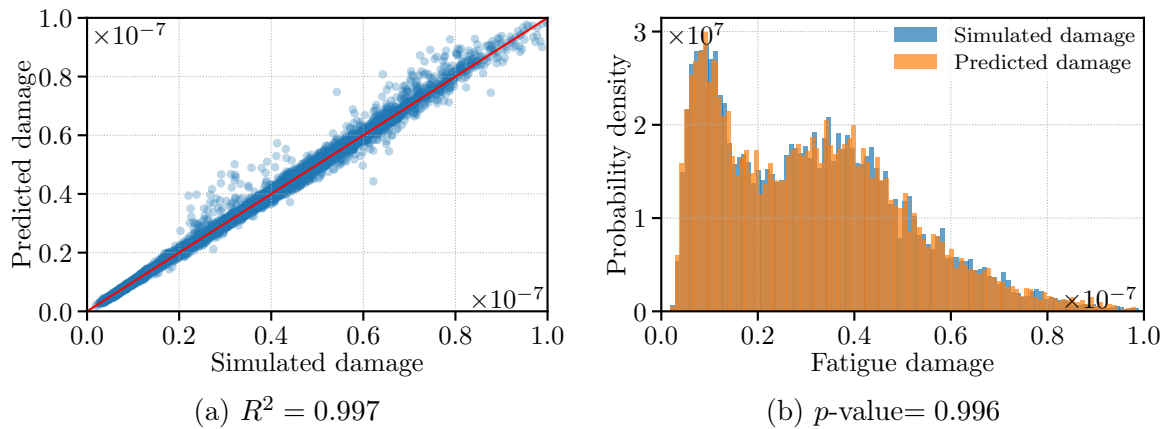


FIGURE R.9 : Comparison between the predicted values and the simulated values for 10-min cumulative fatigue damage in 10 000 cases of stochastic mean wind speed between V_{in} (3.0 m/s) et V_{out} (25.0 m/s) in (a) correlation plot and (b) histogram

R.5.7. Application : estimation de la vie de fatigue d'une éolienne à Caen

Pour donner un exemple de la manière dont le nouveau cadre d'évaluation de la fatigue de Section 4.2 et la loi de Peanut de Section 4.4.1 peuvent nous aider dans la conception d'une éolienne, une conception basée sur les probabilités du mât d'une éolienne est démontrée dans cette section en considérant l'environnement réel. Les données éoliennes utilisées dans cette application proviennent du projet M2NUM (Modélisation mathématique et simulation numérique) [LMI14b]. En outre, le modèle de substitution basé sur le réseau de neurones décrit dans Section 4.5 est appliqué pour accélérer le processus de conception. Avec ces ensembles de données du monde réel, un profil annuel des vents peut être établi statistiquement, par exemple, Figure R.10 montre la ressource éolienne à Caen mesurée sur une année entière.

Figure R.10 illustre une vue succincte de la façon dont la direction du vent ainsi que la vitesse sont typiquement distribuées à Caen, en Normandie, France, en utilisant le tracé de la rose des vents, un outil graphique basé sur le système de coordonnées polaires (Appendix E.2). L'axe radial montre la fréquence des vents sur une période d'un an, et le cercle extérieur indique la direction du vent. Les plages de vitesse du vent sont colorées par la bande indiquée dans la légende et empilées les unes sur les autres selon la même direction. La direction du rayon le plus long indique la direction du vent avec la fréquence la plus élevée, c'est-à-dire en provenance de l'ouest.

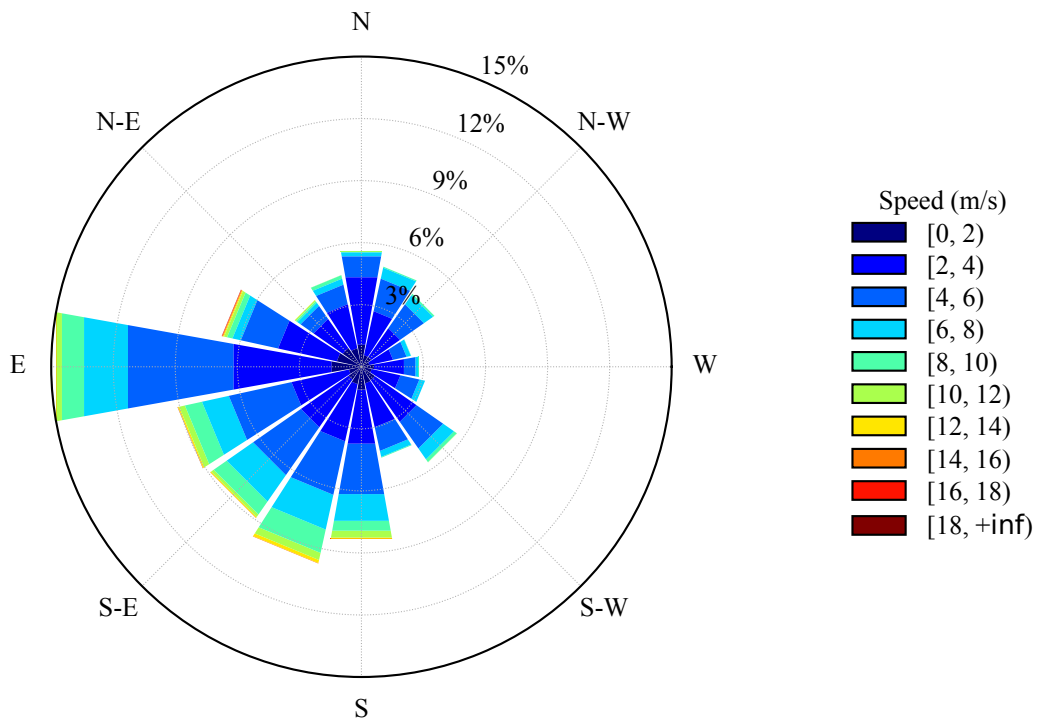


FIGURE R.10 : Graphique des conditions de vent à Caen (France) pendant 1 an

R.5.7.1. Prédiction de la durée de vie en fatigue par simulations numériques

Un profil général des dommages causés par la fatigue sur une éolienne de 5 MW de type NREL construite à Caen est établi et interprété graphiquement en Figure R.11. Le périmètre extérieur en Figure R.11 représente la direction du vent alors que l'axe radial représente les dommages de fatigue accumulés pendant 20 ans. Les dommages de fatigue estimés sur cinq centiles, soit 5^e, 25th (1^{er} quartile), 50^e (médiane), 75^e (3^e quartile) et 95^e centile, ont été tracés mis respectivement par une ligne bleue en pointillés, une ligne orange en tirets, une ligne verte, une ligne rouge en tirets et une ligne violette en pointillés. Pour le dernier centile P_{95} , la surface délimitée par sa ligne pointillée violette est colorée en gris. La surface de la zone grise correspond à l'ensemble des dommages de fatigue appliqués à l'ensemble du mât de l'éolienne avec une probabilité de 95%.

Bien que la principale direction du vent à Caen soit l'ouest, c'est-à-dire que le vent souffle de cette direction pendant 15% de l'année comme montré dans la Figure 4.30, les dommages dus à la fatigue sont probablement plus importants entre la partie ouest et la partie sud du mât. Ce résultat implique que les dommages de fatigue cumulés sur la tour à vent dépendent non seulement de la direction principale du vent, mais aussi de la distribution de la vitesse du vent.

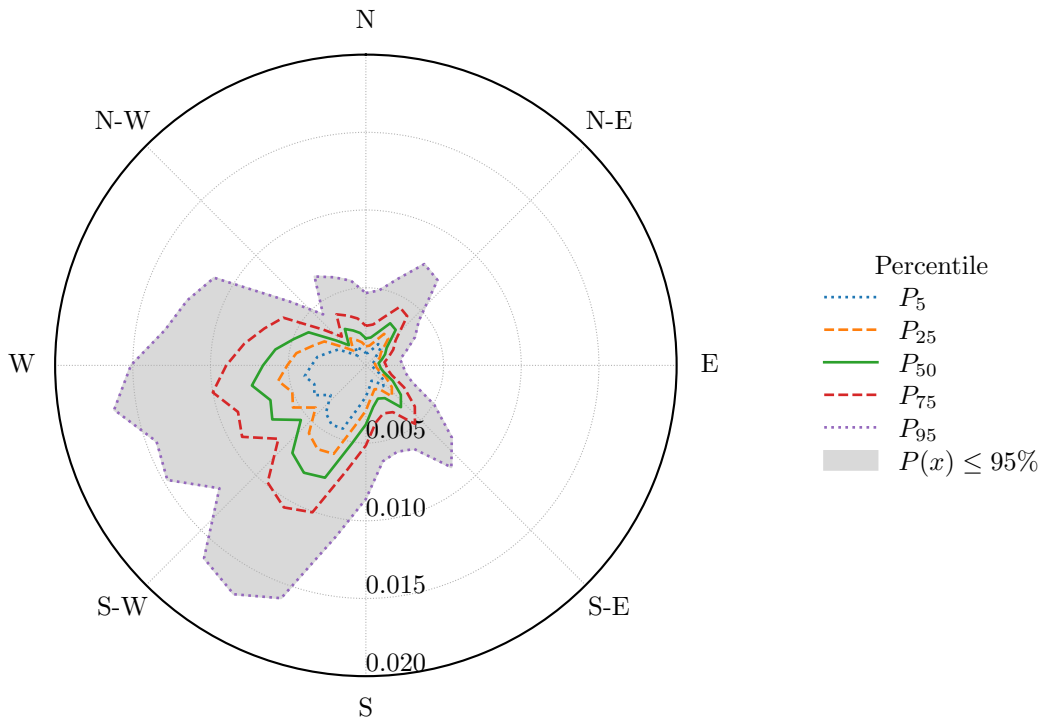


FIGURE R.11 : Prévision des dommages de fatigue cumulés pour toutes les directions au bout de 20 ans

La distribution spatiale de probabilité des dommages présentée dans Figure R.11 permet de prédire l'emplacement des dommages potentiels élevés sur la section transversale du mât et offre un moyen de choisir l'emplacement des ouvertures (par exemple, la porte sur le segment le plus bas du mât) de manière fiable.

Une autre application du résultat présenté consiste à prédire les dommages globaux dus à la fatigue de manière probabiliste. En considérant une certitude de 95% (c'est-à-dire la zone grise dans Figure R.11), le dommage de fatigue global (c'est-à-dire la zone de surface grise) est égal à 0,31. En d'autres termes, la prédiction des dommages cumulés de fatigue sur la tour éolienne de Caen au bout de 20 ans est de 0,31. Physiquement, cela signifie que 31% de sa durée de vie en fatigue est consommée pendant 20 ans en condition de production d'électricité non-stop sous un vent de NTM, et de plus, il y a 95% de chance d'avoir une consommation égale ou inférieure à ce pourcentage.

R.5.7.2. Prévision de la durée de vie en fatigue par réseau de neurons

Le ResMLP introduit dans Section 4.5 peut traiter les défauts ci-dessus car il peut prédire avec précision et de manière économique les dommages cumulés de fatigue de 10 minutes pour toute vitesse moyenne du vent entre V_{in} et V_{out} . Comme le montre Figure R.12, si la valeur prédite par ResMLP est supérieure à celle de la simulation

FAST, les dommages dus à la fatigue sont surestimés et colorés en vert, sinon, ils sont sous-estimés et colorés en rouge.

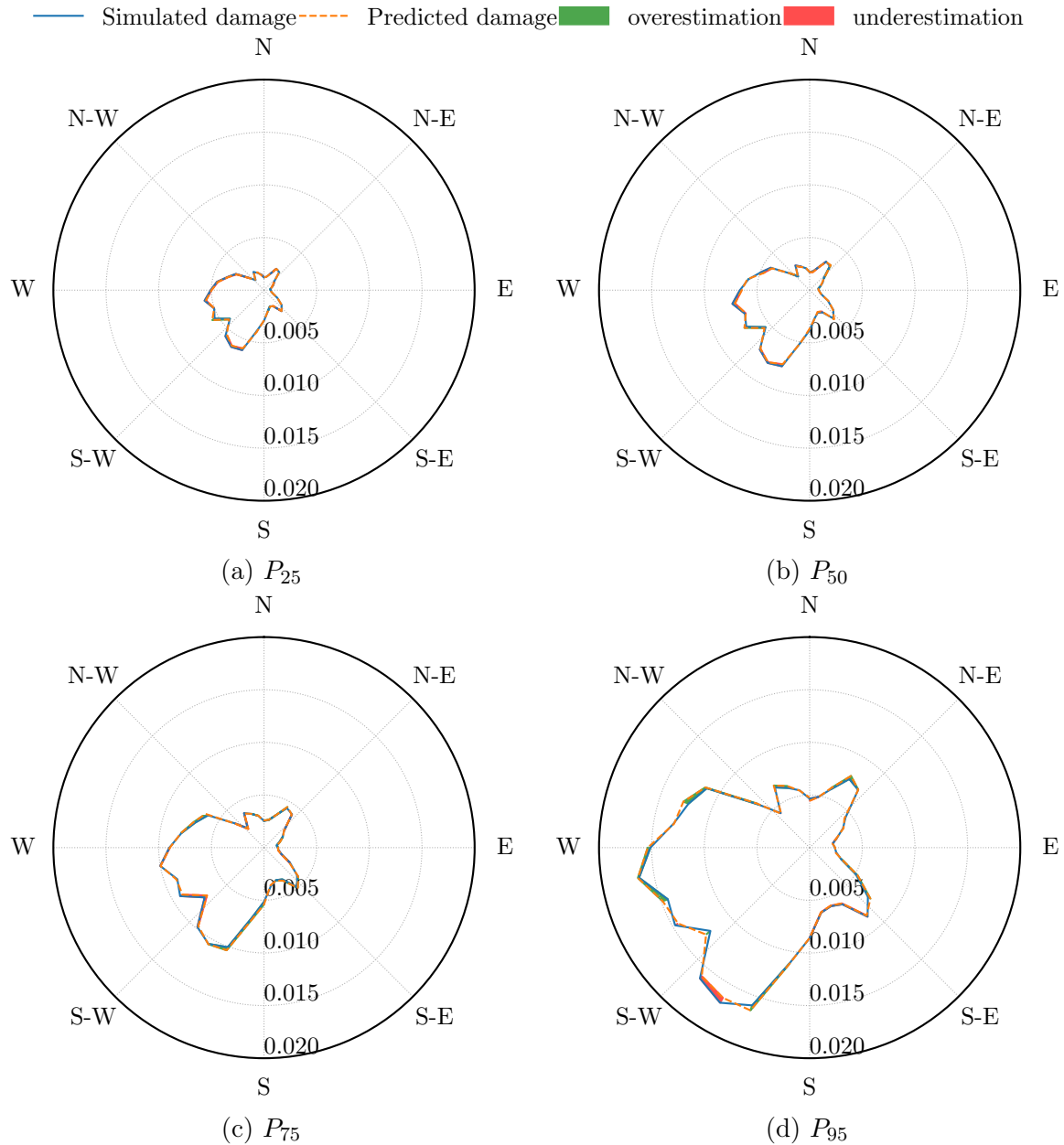


FIGURE R.12 : Prédiction des dommages cumulés dus à la fatigue dans toutes les directions au bout de 20 ans à l'aide du simulateur numérique FAST et du modèle de substitution ResMLP

Il est difficile de faire la différence entre les prédictions faites par ces deux modèles. Une légère différence peut être observée pour la fatigue évaluée au centile P_{95} (Figure R.12d), mais l'ampleur de la différence est trop faible et donc négligeable. Le modèle de substitution ResMLP montre à nouveau sa grande efficacité en offrant une prédiction précise pour l'évaluation de la fatigue à long terme.

R.5.8. Conclusions

Sur la base de l'analyse déterministe de la fatigue, un nouveau cadre de probabilité pour l'évaluation de la fatigue est proposé dans ce chapitre. Bien que le cadre soit appliqué à la tour d'éolienne dans ce contexte, il est également applicable à d'autres structures tubulaires qui peuvent être considérées comme un modèle de poutre en porte-à-faux, par exemple, les pales de l'éolienne, la cheminée, etc.

Dans des conditions de vent stochastiques pendant la phase de production normale de l'éolienne, l'approche proposée offre un moyen d'obtenir la distribution de probabilité des dommages cumulés par fatigue sur la section transversale à différentes hauteurs du mât. En couplant l'approche actuelle avec une distribution de la vitesse du vent, une conception du mât d'éolienne basée sur la probabilité peut avoir lieu.

Enfin, il convient de noter que l'analyse des charges de fatigue sur DLC1.2 donnée dans ce chapitre est désignée comme le scénario F qui, comme prévu, sera utilisé dans le prochain chapitre pour évaluer la performance de l'amortisseur actif en ce qui concerne les charges de fatigue.

R.6. Chapitre 5 : Développement d'un système d'amortissement actif pour les éoliennes

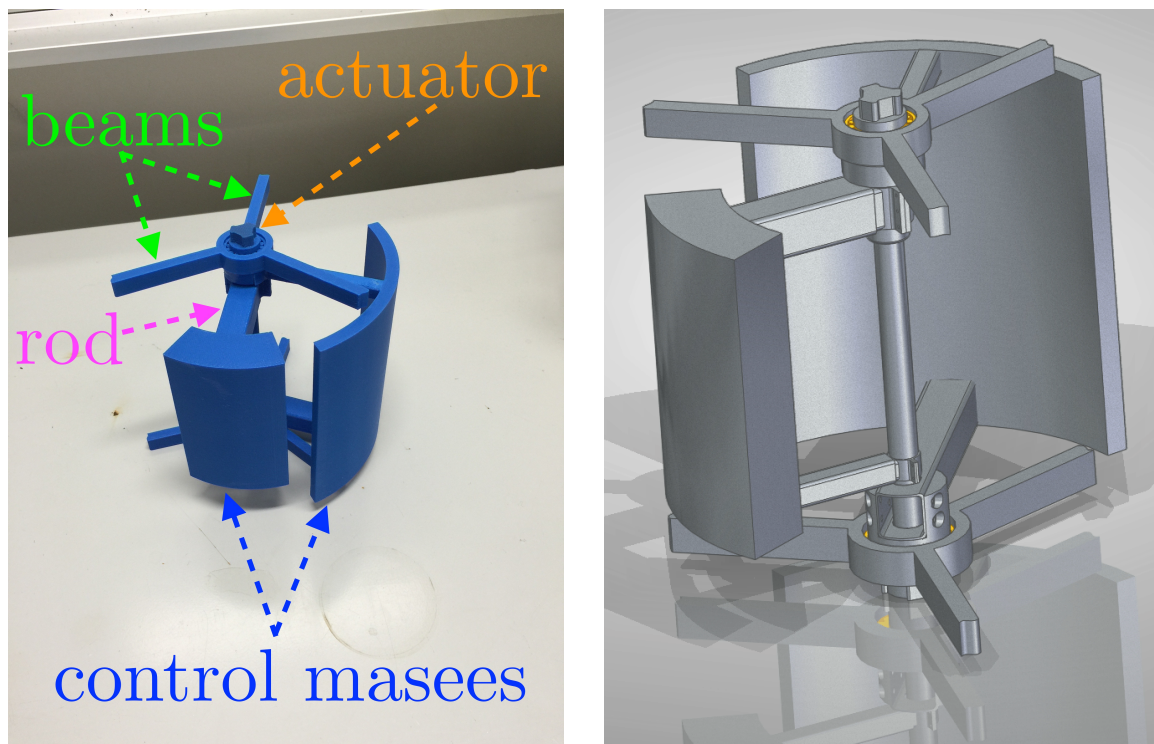
Pour résoudre le problème de surcharge due aux rafales de vent et aux défauts techniques élucidés dans Chapter 3 et la charge de fatigue due au vent turbulent interprété dans Chapter 4, un système d'amortissement actif pour éolienne est proposé dans ce chapitre. Le système est basé sur un dispositif d'amortissement actif appelé *twin rotor damper (TRD)* qui utilise les forces centrifuges de masses en rotation excentrique pour amortir les vibrations structurelles.

Le schéma de TRD est tout d'abord passé en revue et l'algorithme de contrôle est également résumé. Ensuite, une intégration de ce dispositif dans la tour de l'éolienne est proposée, comprenant une conception structurelle en ingénierie, une intégration au système de contrôle et une implémentation dans les codes informatiques. L'efficacité et la faiblesse de la proposition sont évaluées dans la dernière section. Le chapitre se termine par une conclusion avec un travail de perspective.

R.6.1. Intégration du TRD dans l'éolienne

R.6.1.1. Conception structurelle

En collaboration avec Freyssinet¹, une conception technique de TRD pour éolienne est réalisée (voir Figure 5.3). En raison du manque de place à l'intérieur de l'éolienne, il est prévu que le TRD soit installé à l'intérieur de la tour de l'éolienne. L'unité TRD est fixée à la surface intérieure de la tour par six poutres en acier, plus clairement, trois poutres en haut et trois poutres en bas. Cela assure une connexion rigide entre l'unité TRD et la structure de la tour d'éoliennes. L'actionneur est placé le long de la ligne centrale de la tour et relié aux poutres par un palier supérieur et un palier inférieur. Deux masses de contrôle sont ensuite articulées à l'actionneur par des tiges. Chaque masse de commande est également reliée à l'axe de l'actionneur par deux tiges, une supérieure et une inférieure.



(a) Vue en maquette

(b) Vue en CAO

FIGURE R.13 : Conception de TRD pour l'éolienne³

Lorsqu'une vibration doit être amortie, l'algorithme de contrôle de TRD (voir Section 5.2.2) enverra un signal à l'actionneur des TRD pour déplacer les tiges. En

1. Freyssinet est une branche de Soletanche Freyssinet

2. Copyright ©2020 Soletanche Freyssinet. Tous droits réservés.

utilisant une bobine électromagnétique (ou un actionneur à base de moteur), l'actionneur fait tourner l'axe de l'actionneur, ce qui déplace les tiges connectées et, par conséquent, fait tourner les masses de contrôle attachées. Les masses de contrôle sont fabriquées dans le même matériau et ont la même masse. Mais leur disposition et leur rayon (la longueur des tiges) sont différents (Figure R.13) afin qu'elles puissent être placées sur les différents anneaux. Cependant, la masse totale du rotor sur l'anneau intérieur, c'est-à-dire la masse de contrôle et la masse de la tige, est maintenue identique à celle de l'anneau extérieur.

En rappelant les propriétés principales de la NREL 5MW reference wind turbine données dans Table 3.1, les propriétés mécaniques suivantes (Table R.1) sont fixées à la TRD conformément aux Eurocodes correspondants [Eur].

TABLE R.1 : Propriétés mécaniques de TRD pour l'éolienne NREL 5MW

Propriété	Valeur
Masse totale des contrôleurs	2.0 t
Rayon de TRD	1.0 m
Position de TRD (en coordonnées cartésiennes basées au pied du mât)	(0.00, 0.00, 87.60)
Mode de fonctionnement	Mode 1 : rotation continue

Le rapport de masse entre le TRD et la tour est de $\frac{2.0}{347.46} \approx 0.58\%$. Le TRD est censé être positionné sur le tower-top (à une hauteur de 87.60 m). A partir de Table D.6, le rayon intérieur de la tour sur le tower-top est de 1.910 m, donc, la distance TRD à la tour (espace disponible entre le rayon de TRD et le rayon intérieur de la tour) est de $1 - \frac{1.0}{1.910} \approx 47.64\%$. Les propriétés dynamiques du TRD seront discutées et définies dans la section suivante.

R.6.1.2. Conception du contrôleur

Dans ce travail, le TRD est censé fonctionner en mode 1 (Section 5.1.2.1), c'est-à-dire que les deux masses de contrôle du TRD tournent à la vitesse angulaire constante, c'est-à-dire $\ddot{\phi}(t) = 0$. Pour assurer le fonctionnement de TRD et empêcher la ré-excitation du système, Scheller [Sch14] a proposé plusieurs méthodes de contrôle pour TRD. Parmi toutes ses propositions, la commande on-off (alias *bang-bang control* ou *two-step control*) est intégrée à l'algorithme de commande de l'éolienne comme illustré dans Figure R.14. Il s'agit d'une commande en boucle fermée basée sur une logique de commutation et n'a pas d'état intermédiaire mais seulement des états entièrement ON et entièrement OFF.

Un signal d'amplitude de vibration $A(t)$ dépendant du temps est mesuré sur le

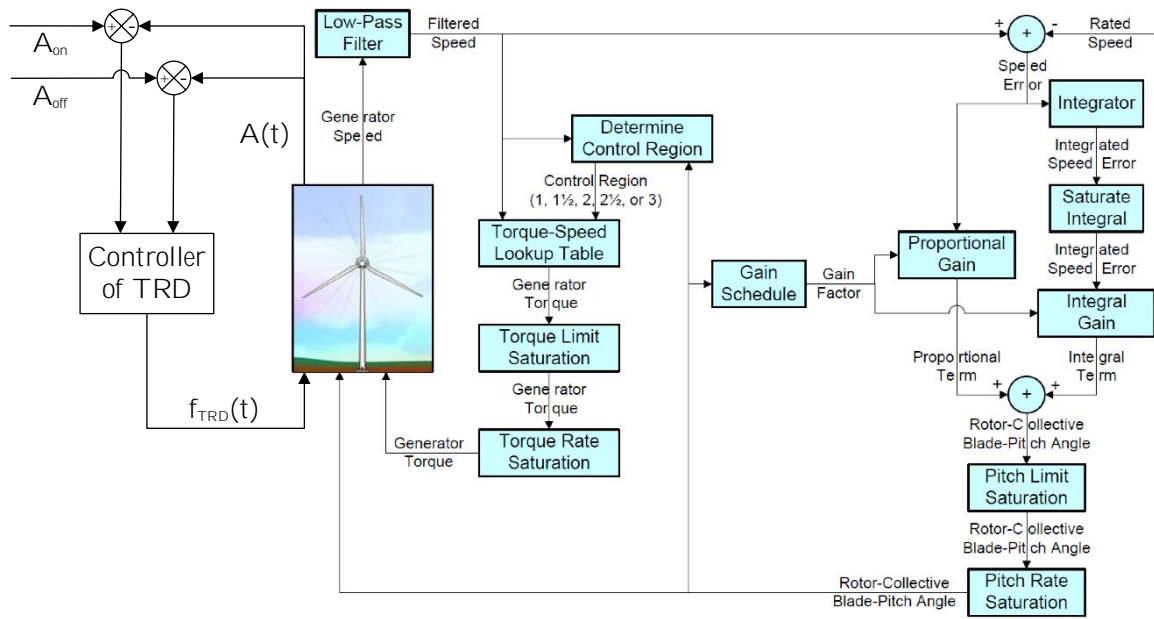


FIGURE R.14 : Intégration de la commande ON-OFF de TRD à la NREL 5MW reference wind turbine

tower-top et renvoyé au contrôleur de TRD. Dans l'étude numérique décrite plus loin dans Section 5.2.3, la perturbation externe n'est pas prise en compte. Ainsi, l'amplitude de vibration mesurée du système (tour d'éolienne) est la même que la sortie directe du système. Ensuite, l'amplitude mesurée $A(t)$ est comparée à deux seuils d'amplitude de vibration, A_{on} et A_{off} . La valeur du seuil A_{off} est fixée à une valeur inférieure à A_{on} . Si l'amplitude mesurée $A(t)$ est inférieure à A_{off} , le TRD est désactivé pour éviter que l'éolienne ne soit ré-excitée par les forces générées par le TRD. Si l'amplitude mesurée $A(t)$ dépasse A_{on} , le TRD est remis en marche pour éliminer les vibrations sur l'éolienne. Lorsque le TRD est allumé, les forces créées par le TRD $f_{TRD}(t)$ donné dans Equation 5.3 est appliqué à l'éolienne à la même position où l'amplitude de vibration $A(t)$ est mesurée, c'est-à-dire le tower-top dans ce travail. Par ce moyen, un algorithme de contrôle en boucle fermée basé sur la rétroaction de l'amplitude de vibration est établi et utilisé pour ajuster en continu le comportement de TRD.

Il faut rappeler que la méthode de commande marche-arrêt ne concerne que le mode 1 de TRD, c'est-à-dire le mode de rotation continue indiqué dans Section 5.1.2.1. Quant à l'autre mode, le mode oscillant, il s'agit d'un contrôle de position angulaire en boucle fermée [Sch14; Bäü14].

Pour que le TRD réduise activement les vibrations sur la tour de l'éolienne, la matrice de gain de rétroaction d'état L doit être déduite de Equation 5.25. Pour résoudre cette équation, les pôles en boucle fermée souhaités s sont préliminaires. C'est un nombre complexe donné dans le système de coordonnées cartésiennes [FPEN19].

Dans ce travail, les positions souhaitées pour les pôles sont fixées à :

$$\begin{aligned} s_1 &= -\xi_e \omega_{n,e} + \omega_{d,e} j \\ s_2 &= -\xi_e \omega_{n,e} - \omega_{d,e} j \end{aligned} \tag{R.4}$$

avec,

$$\omega_{n,e} = \lambda \omega_n \tag{R.5}$$

$$\omega_{d,e} = \omega_{n,e} \sqrt{1 - \xi_e^2} \tag{R.6}$$

where, ω_n = fréquence angulaire naturelle du système (rad/s)

λ = amplificateur souhaité de TRD

$\omega_{n,e}$ = fréquence angulaire naturelle de la boucle fermée de TRD (rad/s)

ξ_e = taux d'amortissement souhaité de TRD

Comme le TRD est intégré dans la tour de l'éolienne, la fréquence angulaire naturelle du système ω_n est celle de la tour de l'éolienne donnée dans Table D.8. Selon la définition de la fréquence angulaire donnée dans Equation 1.3, la fréquence angulaire naturelle de la tour 1st avant est $\omega_n = 2\pi \times 0.324 \approx 2.036$ rad/s.

BÄUMER et al. [BS16] a proposé que les valeurs propres de la boucle fermée $\omega_{n,e}$ soient deux à cinq fois plus rapides que celles du système lui-même ω_n , soit $\lambda \in [2, 5]$. Plus la valeur de λ est élevée, plus vite le système se stabilise mais plus d'énergie est consommée par TRD. En outre, le rapport d'amortissement souhaité ξ_e est suggéré pour être dans la fourchette de $[0, 80, 0, 95]$. Ce rapport décrit l'efficacité de l'unité TRD. Dans ce travail, $\lambda = 3$ et $\xi_e = 0.9$ sont sélectionnés par l'auteur comme étant les configurations appropriées et raisonnables pour l'unité TRD dans l'éolienne. Les propriétés dynamiques du TRD conçu pour NREL 5MW reference wind turbine sont énumérées dans Table 5.2.

Avec ces propriétés dynamiques de TRD, les pôles décrits dans Equation 5.26 peuvent être calculés, et par la suite, le vecteur de gain de rétroaction d'état \mathbf{L} peut être trouvé en résolvant Equation 5.25 par la méthode de placement des pôles, c'est-à-dire,

$$\mathbf{L} = \begin{bmatrix} -205 \\ -26 \end{bmatrix} \tag{R.7}$$

R.6.2. Résultats et discussions

R.6.2.1. DLC2.3 avec TRD

Dans Figure R.15, les résultats numériques obtenus dans le scénario U pour le cas de V_{out} (Section 3.3.4.2) est rappelé comme référence. La déviation avant-après

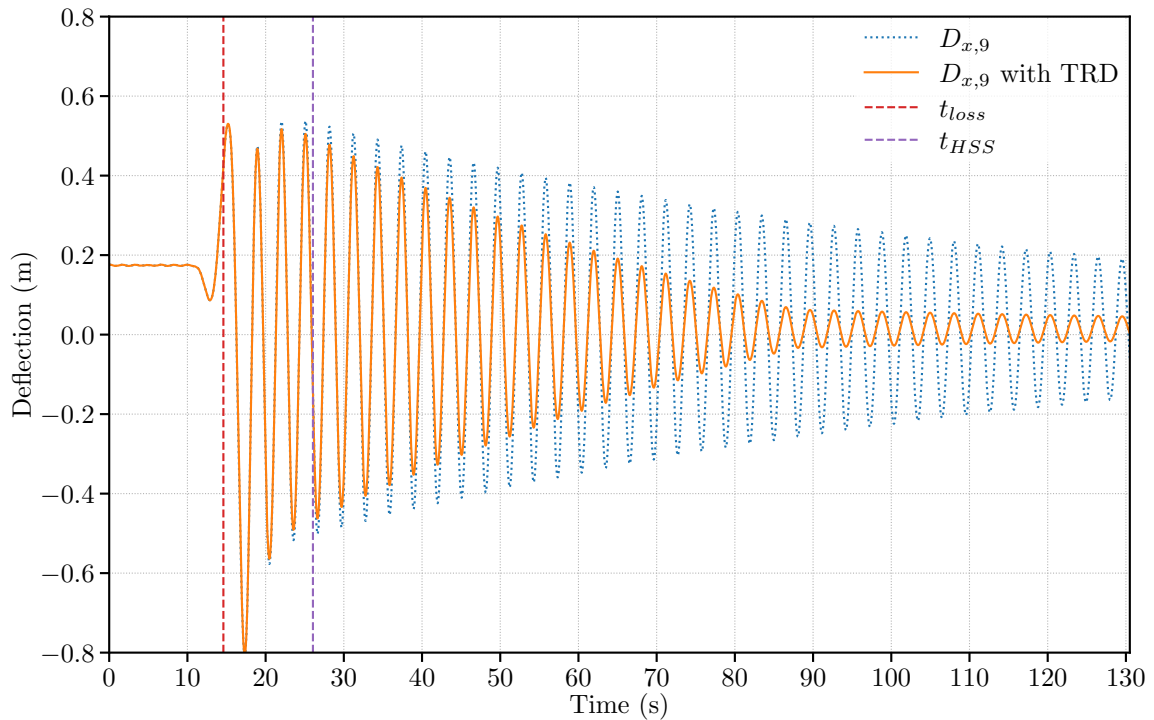


FIGURE R.15 : Déflexion avant-après au gage 9 sous DLC2.3 à la vitesse du vent $V_{out}(25.0\text{ m/s})$ avec TRD activé

sur la tour gage 9 de la DLC2.3 est tracée dans la ligne pointillée bleue, le temps de perte de la grille t_{loss} et le temps de déclenchement du frein HSS est indiqué dans la ligne pointillée rouge et la ligne pointillée violette, respectivement. La déviation avant-après de la tour gage 9 simulée avec le TRD est présentée dans la ligne orange et a moins de fluctuations que celle sans le TRD. A la fin de la simulation ($t = 130\text{ s}$), la déviation avant-après du scénario U (ligne bleue en pointillés) oscille toujours entre -0.17 m et 0.20 m alors que, dans le cas du TRD, la fluctuation (ligne orange) est stabilisée à peak-to-peak amplitude autour de 0.06 m . C'est presque une amélioration de $\frac{0.06}{|-0.17-0.20|} \approx 84\%$ en termes de peak-to-peak amplitude.

Figure R.16 révèle l'état de TRD pendant les rafales de vent avec perte de réseau à travers trois graphiques. Le premier graphique du haut est similaire à Figure R.15 montrant la déviation avant-après sur le tower-top, le second au milieu dessine les forces générées par le TRD tandis que le dernier graphique du bas montre le signal envoyé par le contrôleur du TRD. Le TRD est activé depuis que l'amplitude de la déflexion a dépassé le seuil de l'amplitude de vibration $A_{on} = 0.5$ et s'arrête lorsque l'amplitude est inférieure à $A_{off} = 0.1$ (voir la ligne cyan dans le graphique du bas). Les forces créées par le TRD (ligne jaune dans le graphique du milieu) vibrent fortement pendant la phase de démarrage, c'est-à-dire la période de temps entre la ligne verticale pointillée rouge et la ligne pointillée violette, puis maintiennent une forme sinusoïdale avec un déphasage de $\frac{T_{def}}{2}$, où T_{def} est la période de la déviation avant-après

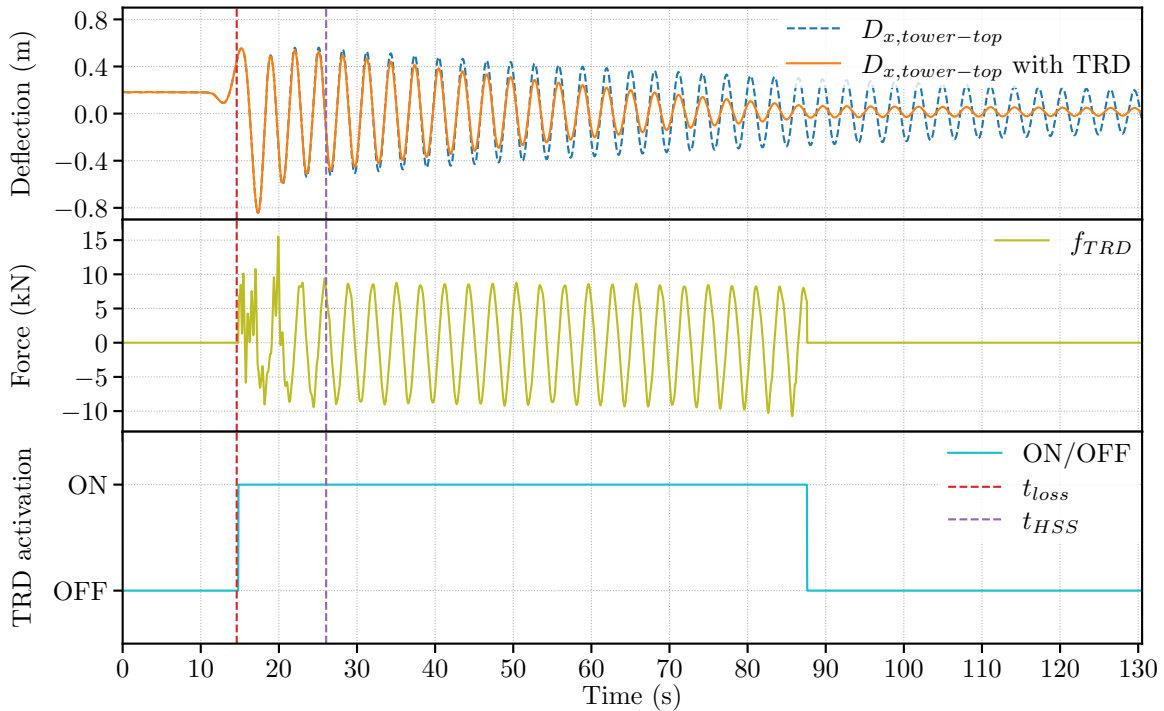


FIGURE R.16 : Etat de TRD dans DLC2.3 à V_{out} (la dépendance temporelle est omise dans la légende)

sur tower-top présentée par la ligne orange dans le graphique du haut.

Le bruit sur la force générée $f_{TRD}(t)$ pendant la phase de démarrage est principalement causé par deux facteurs. D'une part, l'absence de processus de démarrage dans l'algorithme de contrôle entraîne une force "soudaine" appliquée sur la structure une fois que le TRD est allumé. Cette force frappe la structure sur le tower-top en simulation numérique. D'autre part, le TRD est prévu pour fonctionner en mode 1 (Section 5.1.2.1) ce qui implique que la vitesse angulaire des masses de contrôle en unité TRD doit être constante (voir Equation 5.4). Cependant, comme l'amplitude de la déviation avant-après $D_{x,tower-top}$ change violemment pendant cette période, elle conduit à une vitesse angulaire inconstante de TRD, c'est-à-dire $\ddot{\phi}(t) \neq 0$, et par conséquent à une force instable $f_{TRD}(t)$.

Comme indiqué dans Figure R.15, l'amplitude de vibration est significativement réduite avec TRD par rapport à celle sans le TRD dans la même condition de charge définie dans DLC2.3. Bien que le gain en réduction d'amplitude soit relativement moins remarquable entre t_{loss} et t_{HSS} , l'amplitude diminue plus rapidement que l'amplitude de référence. Au moment où TRD est éteint (autour de $t = 87$ s), l'amplificateur peak-to-peak amplitude de la déviation avant-après avec TRD atteint 0.1 m comme prévu, alors que l'amplitude de référence peak-to-peak amplitude reste toujours à 0.6 m. Après l'arrêt de TRD, la tour à vent oscille comme en vibration libre amortie (Section 1.3.1.2) puisque la vitesse du vent se maintient constamment après

la rafale (Figure 3.12). D'autres résultats peuvent être trouvés dans Appendix I, où la performance de TRD est évaluée à une vitesse moyenne du vent de V_{rate+2} . (Figure I.17), V_{rate} (Figure I.18) et V_{rate-2} (Figure I.19). Tous ces résultats numériques prouvent que le TRD est notamment efficace pour réduire les vibrations de la tour éolienne sous les rafales de vent.

Quant aux forces créées par le TRD, $f_{TRD}(t)$, elles dépendent étroitement de sa méthode de contrôle. Une solution possible pour éliminer le bruit dans le signal de $f_{TRD}(t)$ (voir le graphique du milieu dans Figure R.16) est de spécifier un processus de début et de fin dans une implémentation numérique, par exemple, un processus de montée linéaire ou de descente. Le processus de montée en puissance linéaire démarre le TRD à $f_{TRD}(t) = 0$ et atteint la force cible pendant une durée $T_{ramp-up}$, mais le processus de descente linéaire, en revanche, démarre à la force cible et désactive le TRD après une période de $T_{ramp-down}$. Les variables $T_{ramp-up}$ et $T_{ramp-down}$ sont deux variables de conception pour le processus linéaire de montée en puissance et le processus linéaire de descente, respectivement. De cette façon, les forces créées par TRD $f_{TRD}(t)$ ne frapperont pas la structure au moment de l'initiation de TRD et se traduiront par un signal lisse de $f_{TRD}(t)$ dans la série temporelle. Une autre solution consiste à utiliser le TRD en mode 2 (Section 5.1.2.2), ce qui fait que le TRD agit comme un amortisseur de masse active classique [Gaw04]. Cependant, ce mode nécessite une méthode de contrôle plus avancée que le contrôle marche-arrêt. Puisque la discussion sur l'algorithme de contrôle de TRD dépasse le sujet de cette thèse, plus d'informations peuvent être trouvées dans [Bäu14].

R.6.2.2. DLC1.2 avec TRD

Comme indiqué dans Figure R.17, la force locale dans l'axe \vec{x}_t sur la tour gage 1 n'est pas réduite de manière significative en introduisant le TRD dans la tour. La réponse de $F_{x,1}$ (ligne orange) est fortement superposée au résultat de référence (ligne pointillée bleue), et parfois, encore plus fluctuante que le résultat de référence.

Le dysfonctionnement de TRD est également confirmé en ce qui concerne la contrainte normale sur les gage 1 locaux de la tour dans Figure 5.9. La contrainte normale avec TRD (ligne orange) est entièrement couverte par le résultat de référence (ligne bleue en pointillés), que le TRD soit activé ou non.

La raison pour laquelle le TRD devient inutile dans ce DLC réside dans son mode de fonctionnement et son algorithme de contrôle. Comme indiqué dans Section 5.2.2, seul le mode de fonctionnement 1 du TRD est engagé dans cette étude. Ainsi, le TRD est censé fonctionner à une vitesse de rotation constante pour ses masses de contrôle, c'est-à-dire $\ddot{\phi} = 0$. Cependant, dans DLC1.2, le modèle de vent turbulent NTM est étudié. Pour répondre à ce type de charge, le TRD doit fonctionner en mode 2 : mode oscillant (Section 5.1.2.2). Comme la discussion sur ce mode de fonctionnement

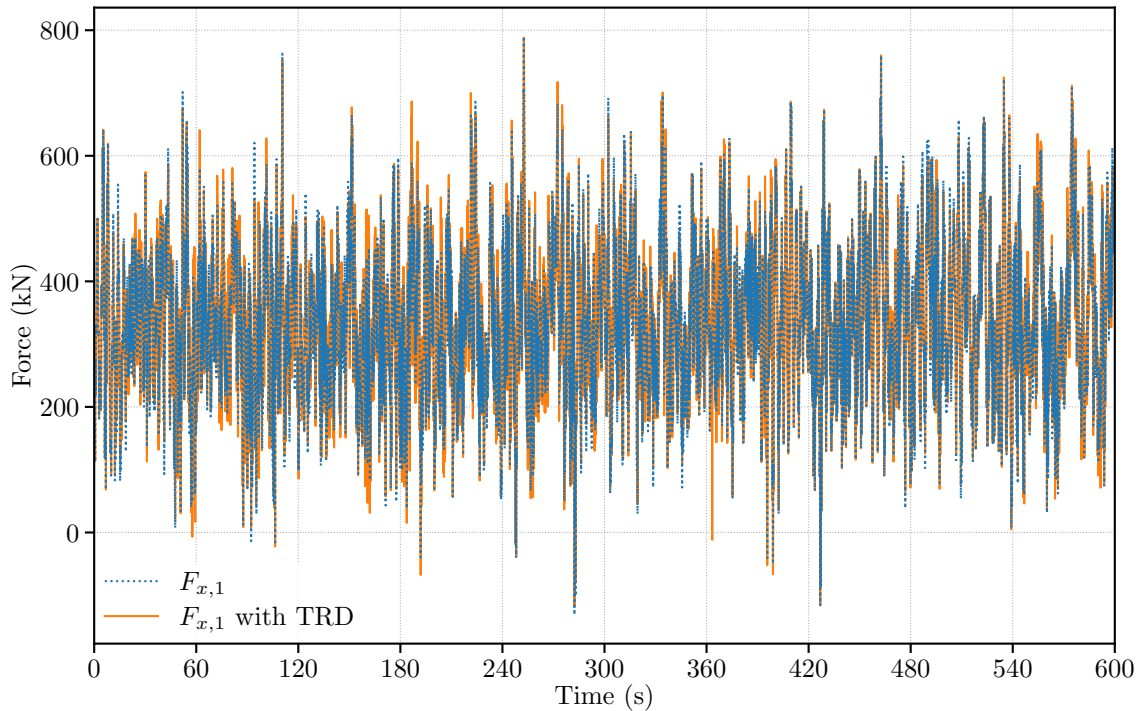


FIGURE R.17 : Tour gage 1 force avant-après dans DLC1.2 à la vitesse du vent cut-out ($V_{mean}=V_{out}$) avec TRD

dépasse le cadre de cette thèse, un résumé concernant le TRD pour l'amortissement des vibrations stochastiques forcées des alliés se trouve dans [Bäu18].

R.6.3. Conclusions

Dans ce chapitre, l'idée d'amortir les vibrations sur la tour de l'éolienne est réalisée. Un dispositif d'amortissement actif connu sous le nom de twin rotor damper (TRD) est présenté. Un modèle d'oscillateur SDOF avec le TRD est ensuite étudié pour valider la conception du TRD en théorie, suivi d'une validation numérique en codes FAST. Le code source de FAST est modifié en conséquence afin de combiner le TRD avec d'autres modules de calcul existants. De plus, un algorithme de contrôle marche-arrêt de la TRD est intégré dans le système de contrôle de l'éolienne NREL 5MW. Enfin, les performances de la turbine sont évaluées dans deux cas de charge différents : DLC2.3 et DLC1.2. Le premier cas implique une rafale de vent extrême en fonctionnement coïncidant avec la perte du réseau électrique, et le second décrit une condition de vent avec des turbulences.

Sur la base des résultats numériques, il s'avère que le TRD est très efficace pour contrôler les vibrations sur la tour éolienne en DLC2.3 en faisant tourner continuellement ses masses de contrôle à une vitesse angulaire fixe ($\dot{\phi} = 0$). Par rapport au résultat de référence dans cette même situation étudié dans Chapter 3, le TRD offre

une réduction notable non seulement de la déflexion sur le tower-top mais aussi de la force et du moment à la tower-base. En revanche, la performance de la TRD en DLC1.2 est moins intéressante puisque l'éolienne est excitée par une force stochastique dans ce cas. Pour réduire les vibrations dans une telle situation, le mode 2 (mode d'oscillation) est nécessaire. Mais ce mode de fonctionnement nécessite un algorithme de contrôle plus compliqué et dépasse largement la portée de cette thèse.

En résumé, le présent chapitre permet de valider théoriquement et numériquement la proposition d'un système d'amortissement actif utilisant le TRD pour éolienne. Une conception initiale basée sur l'expérience de l'auteur et la norme industrielle correspondante est proposée. Selon le processus de conception complet proposé dans Chapter 2, la conception du TRD est sur le point d'être optimisée dans le prochain chapitre.

R.7. Chapitre 6 : Optimisation du TRD à l'aide d'un algorithme évolutif adaptatif

Dans le chapitre précédent, un système d'amortissement actif pour éolienne utilisant les forces centrifuges de masses en rotation excentrique est étudié. Une première conception de ce système d'amortissement actif, connu sous le nom de TRD, est proposée. Pour obtenir une performance optimisée du système d'amortissement TRD, une optimisation de ses variables de conception est réalisée dans ce chapitre.

Puisque l'expression mathématique exacte de la turbine de référence avec TRD est inconnue, il est nécessaire d'utiliser certains algorithmes d'optimisation non basés sur le gradient pour résoudre ce type de problème d'optimisation, par exemple, EAs. Dans la première section, un bref aperçu de la famille EA et de l'une de ses principales variantes, DE, est présenté. Ensuite, une nouvelle méthode appelée configuration d'algorithme adaptative pour differential evolution (AAC-DE) est proposé sur la base de l'exploration et de l'exploitation pendant le processus de recherche. Une analyse expérimentale de la méthode proposée a lieu dans la section suivante par rapport à d'autres variantes de DE, et, pour donner un exemple, la méthode proposée est utilisée pour optimiser les variables de conception du TRD.

R.7.1. Configuration adaptative de l’algorithme pour l’évolution différentielle (AAC-DE)

En considérant les observations ci-dessus, une méthode adaptative pour la stratégie de génération et le paramètre de contrôle de l’évolution différentielle (ED) est proposée dans cette section dans laquelle la sélection de la stratégie de génération et l’adaptation du paramètre sont mises en œuvre en utilisant des méthodes d’apprentissage automatique, en particulier :

- une technique d’apprentissage du renforcement, c’est-à-dire l’algorithme du Bandit Manchot (MAB), est impliqué pour sélectionner correctement la stratégie de génération du pool pour chaque individu de la population actuelle. La sélection dépend de l’avantage de chaque stratégie candidate calculée sur la base de l’expérience des générations précédentes.
- une approche d’apprentissage non supervisée, c’est-à-dire l’Estimation de la Densité du Noyau (KDE), est adoptée pour apprendre la distribution des paires F et CR qui ont généré des vecteurs d’essai réussis dans les générations précédentes. La suite de cette section est consacrée à la description de l’AAC-DE proposée.

L’utilisation des deux modèles ci-dessus pour chaque individu dépend de son état de recherche (exploration ou exploitation) et de la progression du processus de recherche. Pour être plus clair, au début du processus de recherche, on s’attend à ce que les individus soient plus explorateurs, alors qu’à la fin du processus de recherche, les individus seront relativement plus exploitants. AAC-DE a mis en place ces nouvelles fonctionnalités et résultats dans un aperçu donné dans Algorithme R.3.

R.7.2. Résultats et discussions

Pour analyser la performance globale de chaque algorithme sur les fonctions de test 30D et 50D de l’ensemble de référence CEC2017 [Awa16], Friedman test avec Nemenyi post-hoc test [Dem06 ; Der11] ont été réalisés pour évaluer la performance globale des cinq algorithmes étudiés en termes d’erreurs d’aptitude moyennes sur toutes les fonctions testées. La moyenne (R_{avg}) et l’écart-type (R_{std}) des rangs de chaque algorithme sur les 60 problèmes de test sont indiqués dans Table R.2 et Table R.3 ainsi que les résultats des tests de Friedman et Nemenyi. Le rang moyen et l’écart-type des rangs pour chaque algorithme sont également représentés graphiquement dans la Figure 6.1, où la barre bleue représente le R_{avg} de l’algorithme et la ligne noire verticale en haut de chaque barre indique le $2R_{std}$ de l’algorithme correspondant.

De Table R.2 et Figure 6.1, le rang moyen de la AAC-DE dans 30D est le plus petit parmi tous les algorithmes comparés. Cela indique que la performance moyenne de

Algorithm R.3: AAC-DE algorithme

Input: Problème d'optimization $\min f(\vec{x})$, réserve des stratégies \mathcal{P}_{str} , et intervalles admissibles pour $[F_{min}, F_{max}]$ et $[C_{r,min}, C_{r,max}]$.

- 1 Définissez le compteur de génération $g = 0$, initialisez aléatoirement la population $\mathbf{P}^{(0)}$ avec des individus N_p dans le domaine de recherche, définissez $n_{stagnation} = 0$, initialisez l'ensemble des données de *StateKDE* comme $\mathcal{D}_{state} = \mathbf{P}^{(0)}$, initialisez l'ensemble des données de *ExploreKDE* et *ExploitKDE* comme $\mathcal{D}_{explore} = \emptyset$ et $\mathcal{D}_{exploit} = \emptyset$.
- 2 Évaluez la population $\mathbf{P}^{(0)}$.
- 3 **while** le critère d'arrêt n'est pas vrai **do**
 - 4 Obtenez les stratégies N_p et le paramétrage $S_i^{(g)}, F_i^{(g)}, C_{r,i}^{(g)}, i = 1, \dots, N_p$ par la procédure AEEC donnée dans Algorithme 6.4.
 - 5 **for** $i = 1$ to N_p **do**
 - 6 Créer un vecteur d'essai $\mathbf{u}_i^{(g)}$ pour le vecteur cible $\mathbf{x}_i^{(g)}$ en utilisant la stratégie $S_i^{(g)}$ et les paramètres de contrôle associés $(F_i^{(g)}, C_{r,i}^{(g)})$.
 - 7 **if** *state*($\mathbf{u}_i^{(g)}$) est *exploration* **then**
 - 8 Attribuez la récompense de l'application $S_i^{(g)}$ pour *ExploreMBA* comme 1.
 - 9 Attribuez la récompense de l'application de $S_i^{(g)}$ pour *ExploitMBA* à 0.
 - 10 Ajoutez $(F_i^{(g)}, C_{r,i}^{(g)})$ à l'ensemble de données de formation $\mathcal{D}_{explore}$ pour *ExploreKDE*. $\mathcal{D}_{explore} = \mathcal{D}_{explore} \cup (F_i^{(g)}, C_{r,i}^{(g)})$.
 - 11 **else**
 - 12 Attribuez la récompense de l'application $S_i^{(g)}$ pour *ExploreMBA* comme 0.
 - 13 Attribuez la récompense de l'application de $S_i^{(g)}$ pour *ExploitMBA* à 1.
 - 14 Ajoutez $(F_i^{(g)}, C_{r,i}^{(g)})$ à l'ensemble de données de formation $\mathcal{D}_{exploit}$ pour *ExploitKDE*. $\mathcal{D}_{exploit} = \mathcal{D}_{exploit} \cup (F_i^{(g)}, C_{r,i}^{(g)})$.
 - 15 **end if**
 - 16 $\mathcal{D}_{state} = \mathcal{D}_{state} \cup \mathbf{u}_i^{(g)}$.
 - 17 Évaluer l'aptitude du vecteur d'essai $f(\mathbf{u}_i^{(g)})$.
 - 18 **if** $f(\mathbf{u}_i^{(g)}) < f(\mathbf{x}_i^{(g)})$ **then**
 - 19 $\mathbf{x}_i^{(g+1)} = \mathbf{u}_i^{(g)}$
 - 20 $n_{stagnation} = 0$
 - 21 **else**
 - 22 $\mathbf{x}_i^{(g+1)} = \mathbf{x}_i^{(g)}$
 - 23 $n_{stagnation} = n_{stagnation} + 1$
 - 24 **end if**
 - 25 **end for**
 - 26 Mettez à jour tous les modèles MAB et KDE, y compris *ExploreMAB*, *ExploitMAB*, *ExploitKDE*, *ExploitKDE* et *StateKDE*.
 - 27 Augmentez le nombre de générations $g = g + 1$.
 - 28 **end while**

TABLE R.2 : La moyenne et l'écart-type des rangs de tous les algorithmes DE comparés sur les fonctions de test 30D

Algorithme	AAC-DE	jDE	SaDE	JADE	EPSDE	SAKPDE
R_{avg}	2.27	4.05	3.28	2.73	4.07	4.60
R_{std}	0,98	1,70	1,85	1,72	1,25	1,35
Test Nemenyi	p -value	0.0030	0.2848	0.9000	0.0027	0.0010
Test de Friedman	p -value				1.56E-06	

TABLE R.3 : La moyenne et l'écart-type des rangs de tous les algorithmes DE comparés sur les fonctions de test 50D

Algorithme	AAC-DE	jDE	SaDE	JADE	EPSDE	SAKPDE
R_{avg}	2.60	4.07	3.37	2.40	4.57	4.00
R_{std}	1.30	1.66	1.81	1.67	1.07	1.58
Test Nemenyi	p -value	0.0289	0.5923	0.9000	0.0010	0.0436
Test de Friedman	p -value				5.33E-06	

l'AAC-DE est la meilleure parmi tous les algorithmes d'ED étudiés. De plus, l'AAC-DE a le plus petit écart type de rang parmi tous les algorithmes comparés. Cela implique que la performance de l'algorithme AAC-DE dans les différents problèmes de test est plus robuste, ou stable, que les autres algorithmes. En conclusion, l'AAC-DE devrait être plus performante que d'autres variantes représentatives de l'ED.

La p -value du test de Friedman, c'est-à-dire p -value= $1.01E - 10$, est largement inférieure au niveau de signification de 0.05, ce qui indique que la différence de performance des cinq algorithmes comparés est significative. La comparaison par paires entre AAC-DE et les cinq autres algorithmes est effectuée par le test de Nemenyi. Selon les résultats du test Nemenyi, la performance globale de AAC-DE est significativement meilleure que celle de jDE, EPSDE et SAKPDE puisque la valeur en p du test Nemenyi par paires entre AAC-DE et l'algorithme correspondant est inférieure à 0,05. La valeur p du test de Nemenyi par paires entre AAC-DE/SaDE est 0,1324, ce qui indique également que AAC-DE est généralement plus performant que SaDE. Puisque la valeur en p du test de Nemenyi par paire entre AAC-DE et JADE atteint 0,8541, on peut affirmer que AAC-DE surpasse légèrement JADE compte tenu de leur rang moyen. En résumé, la AAC-DE proposée a la meilleure performance globale parmi l'algorithme comparé selon le test statistique sur les résultats expérimentaux sur l'ensemble de référence CEC2017. L'excellente performance générale de l'AAC-DE démontre que l'approche OAC (configuration d'algorithme en ligne) proposée est efficace et qu'elle fonctionne bien sur l'algorithme DE.

Enfin, à partir du box-plot (Figure R.19), la AAC-DE est toujours placée en haut

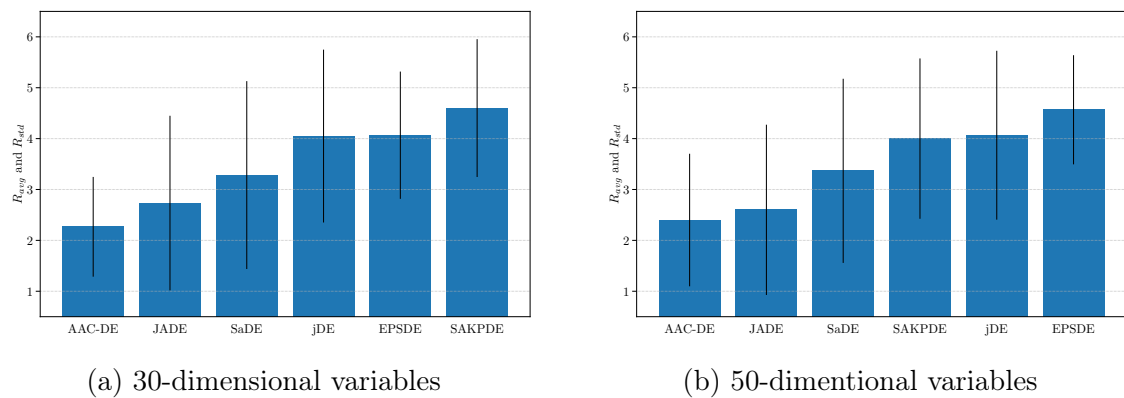


FIGURE R.18 : La moyenne et l'écart-type des classements des algorithmes d'ED comparés sur les fonctions de test.

en termes de rangs. Par rapport à l'algorithme en deuxième position (JADE), la AAC-DE a une faible variance de rangs pour les fonctions 30D et un même classement pour les fonctions 50D. Les cinq algorithmes ont tous la même valeur inférieure, mais la AAC-DE a la valeur supérieure la plus faible. En fait, AAC-DE est classé dans le top 3 des 7 algorithmes sur la moitié de tous les problèmes de test, le rang le plus bas est le 5th. Alors que, pour les cinq autres algorithmes de l'ED, ils obtiennent tous le rang 7th sur certains problèmes de test. Il est évident que le box-plot de AAC-DE est le plus court parmi les six algorithmes. Cela suggère que la fluctuation des performances de AAC-DE sur différents problèmes de test est relativement insignifiante. En d'autres termes, la performance de AAC-DE est stable sur différents problèmes. Alors que la performance des cinq autres algorithmes fluctue de manière significative sur différentes fonctions de test. Cela prouve également que l'AAC-DE proposé a la meilleure performance moyenne et que sa performance est également la plus stable parmi tous les algorithmes comparés.

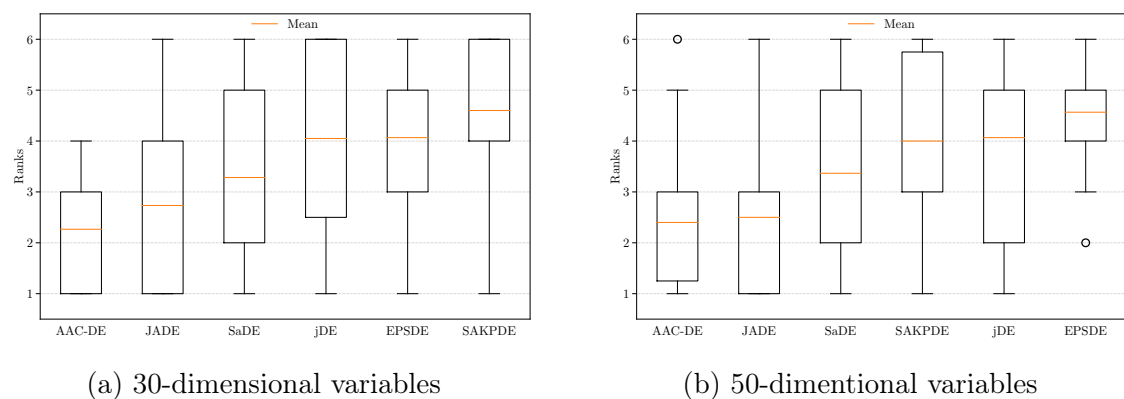


FIGURE R.19 : Box plots of the ranks of the compared DE algorithms on the test functions.

R.7.3. Application : optimisation des paramètres de conception du TRD pour les éoliennes

R.7.3.1. Configuration du problème d'optimisation

Comme l'a prouvé Chapter 5, le TRD est vraiment efficace pour réduire les vibrations sur la tour éolienne en cas de DLC2.3. Pour maximiser ses performances dans cette situation, une optimisation sur les variables conceptuelles de la TRD est étudiée en utilisant la AAC-DE proposée dans cette section.

La performance d'amortissement du TRD est estimée en utilisant la méthode de décrétement d'amortissement logarithmique et définie comme la fonction objective du problème d'optimisation actuel :

$$\max_{\mathbf{x}} \hat{\xi}(\mathbf{x}) \quad (\text{R.8})$$

où \mathbf{x} est le vecteur des variables de conception définies comme :

$$\mathbf{x} = \begin{bmatrix} x_1 \\ x_2 \\ x_3 \\ x_4 \end{bmatrix} \quad (\text{R.9})$$

where, x_1 = masse des TRD dans la fourchette admissible $[1, 20]$ (t)
 x_2 = le rayon des TRD dans la plage admissible $[1.00, 1.72]$ (m)
 x_3 = 1^{er} composant du vecteur de gain \mathbf{L} dans la plage admissible $[-220, 0]$
 x_4 = 2nd composant du vecteur de gain \mathbf{L} dans la plage admissible $[-220, 0]$
 Le maximum autorisé pour la masse de TRD ($\max(x_1) = 20$) provient d'une conception d'amortisseur de masse accordée [HOK19; HO18] pour NREL 5MW reference wind turbine, le minimum et le maximum pour le rayon de TRD ($x_2 \in [1.00, 1.72]$) prend une valeur approximative proche de 50% et 90% du rayon intérieur du tower-top (1.910 m), les autres valeurs sont fixées en fonction de l'expérience de l'auteur et des collaborateurs.

100 individus sont utilisés dans ce problème d'optimisation ($NP = 100$) et le MaxFES est fixé à 10 000. Une erreur de fitness de 10^{-8} est également définie pour l'amélioration entre deux générations continues, soit $\hat{\xi}(\mathbf{x}^{(g)}) - \hat{\xi}(\mathbf{x}^{(g-1)}) \leq 10^{-8}$, où $\hat{\xi}(\mathbf{x}^{(g)})$ est la meilleure solution trouvée dans la génération (g) et $\hat{\xi}(\mathbf{x}^{(g-1)})$ est celle de la dernière génération.

R.7.3.2. Résultats et discussions

Après une seule exécution du problème d'optimisation ci-dessus, les variables optimisées suivantes sont trouvées :

$$\mathbf{x} = \begin{bmatrix} 1.27 \\ 1.12 \\ -219.93 \\ -76.63 \end{bmatrix} \quad (\text{R.10})$$

Figure R.20 illustre la conception optimisée (ligne verte) comparée à la conception initiale (ligne pointillée orange) discutée dans Section R.6.2.1 et le résultat de référence sans les TRD (ligne pointillée bleue) donnée dans Section 3.3.4.2.

L'amélioration de la performance d'amortissement de TRD est remarquable pour toutes les vitesses moyennes du vent requises par ce DLC (V_{rate-2} , V_{rate} , V_{rate+2} , V_{out}). A V_{out} . (Figure R.20a), le TRD prend une réaction rapide pour réduire la vibration de la déviation avant-après pendant la période comprise entre t_{loss} et t_{HSS} . Cela prouve la capacité du TRD à réduire les dommages potentiels dus à la charge extrême. Comme pour les autres vitesses moyennes du vent (Figure R.20b à Figure R.20d), le TRD optimisé offre toujours une réduction rapide et efficace sur l'amplitude des vibrations par rapport à celle de la conception initiale.

R.7.4. Conclusions

Pour résoudre le problème d'optimisation de la boîte noire, un algorithme adaptatif differential evolution appelé AAC-DE est proposé dans ce chapitre. L'étude expérimentale sur les ensembles de référence CEC2017 prouve que l'algorithme AAC-DE fonctionne de manière stable en termes de performances moyennes par rapport à d'autres variantes DE de pointe.

À l'avenir, il est prévu que l'AAC-DE aborde d'autres problèmes d'optimisation, tels que les problèmes d'optimisation multi-objectifs et les problèmes d'optimisation combinatoire. En outre, afin d'améliorer les performances globales de l'AAC-DE, il est également prévu de combiner la méthode proposée avec l'analyse du paysage de la condition physique.

En ce qui concerne la conception de TRD pour les éoliennes, une conception optimisée tenant compte des performances d'amortissement dans DLC2.3 et DLC1.2 est également prévue. Cela implique la nécessité d'un algorithme d'optimisation multi-objectif puisque la fonction objectif (performance d'amortissement) est évaluée indépendamment dans deux cas de charge différents.

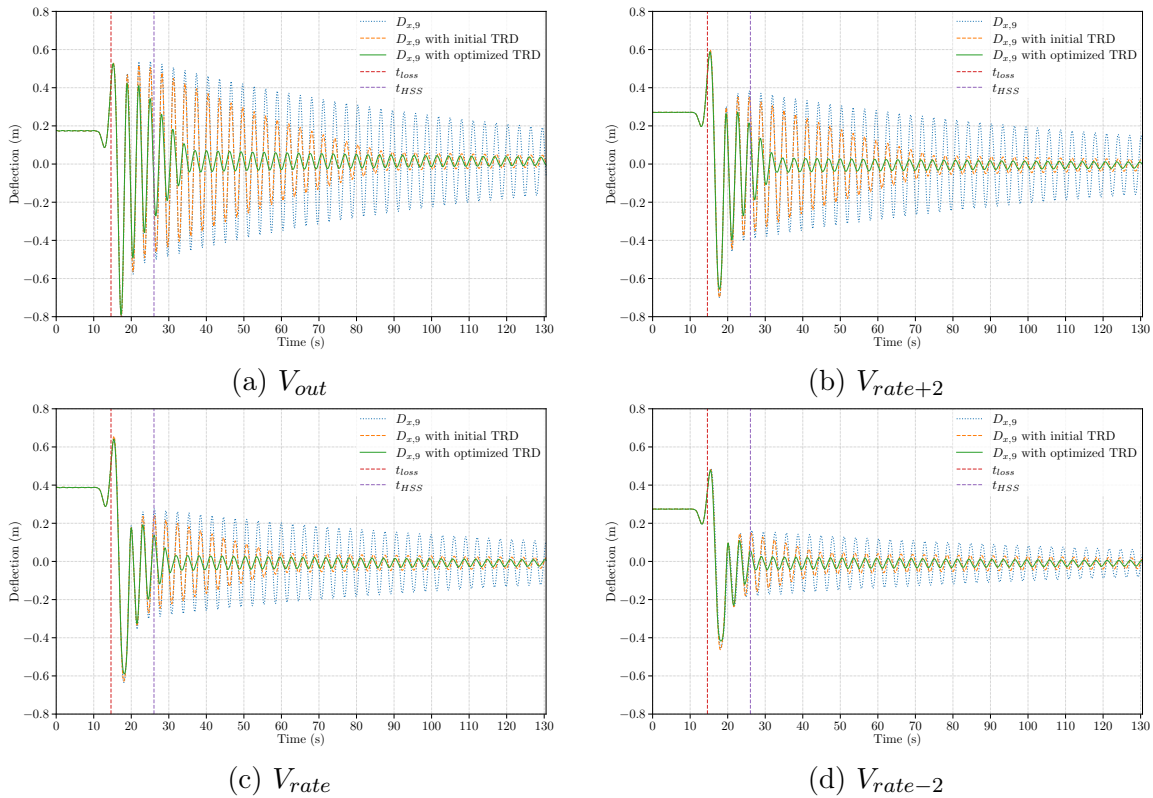


FIGURE R.20 : Déflexion avant-après sur la tour gage 9 en considérant le TRD avec des configurations optimisées pour la tour d'éolienne sous DLC2.3

R.8. Chapitre 7 : Conclusions et perspectives

Le présent essai décrit un processus de conception complet pour développer un système d'amortissement actif pour une éolienne.

D'après l'étude bibliographique, la conception des éoliennes a tendance à s'orienter vers une hauteur de moyeu plus élevée, des surfaces balayées plus grandes et une capacité nominale plus importante. Ce mouvement inévitable implique non seulement une conception structurelle fiable mais aussi un système de contrôle avancé pour assurer à la fois la sécurité structurelle et la stabilité de la production d'énergie. Pour atteindre cet objectif, l'un des défis majeurs à relever est la vibration mécanique de la tour de l'éolienne, car elle peut provoquer des dommages potentiels à la structure en raison de la charge périodique ou de la charge ultime causée par l'amplitude extrême de la vibration. Par conséquent, l'intégration d'un système d'amortissement dans l'éolienne semble être une solution raisonnable pour résoudre les problèmes de vibrations sur la tour de l'éolienne. De plus, si le système d'amortissement peut contrôler activement les vibrations à la fréquence du 1^{er} ordre et du 2^{me} ordre, l'éolienne peut continuer à

produire de l'énergie électrique même dans la gamme proche des fréquences naturelles de la tour de l'éolienne.

Avant de développer un système d'amortissement, il faut d'abord préparer les données de base afin de pouvoir évaluer les performances de l'amortisseur. Une analyse de la charge ultime en cas de rafales de vent avec défaut technique (DLC2.3) et une analyse de la charge de fatigue en cas de vent turbulent (DLC1.2) sont donc réalisées. En outre, une étude complémentaire sur le timing entre le défaut technique (perte de réseau) et la rafale de vent est réalisée dans le paragraphe DLC2.3. Sans oublier qu'un nouveau cadre probabiliste d'analyse de la fatigue assisté par un réseau neuronal basé sur des données est proposé et validé dans le document DLC1.2.

La conception d'un système d'amortissement actif pour éolienne commence par l'introduction d'un dispositif d'amortissement actif qui génère la force d'amortissement par des masses de contrôle en rotation excentrique. Cet amortisseur actif, à savoir TRD, est ensuite étudié avec un modèle d'oscillateur SDOF avec plus de détails sur ses modes de fonctionnement et les méthodes de contrôle correspondantes. Une conception initiale pour l'intégration du TRD dans le système de contrôle inhérent de la NREL 5MW reference wind turbine est proposée, et l'efficacité de cette intégration est évaluée en la comparant aux données de base.

Enfin, une méthode de configuration d'algorithme adaptatif pour differential evolution, AAC-DE, est proposée pour optimiser la conception de TRD dans un mode en ligne du processus d'optimisation. Une vérification expérimentale par le biais de fonctions de test de référence CEC2017 prouve que le AAC-DE est très efficace et stable en termes de performance moyenne par rapport aux autres variantes de DE. Une application de AAC-DE est effectuée pour optimiser les variables de conception de TRD.

Le présent travail décrit complètement le processus de conception de l'intégration d'un dispositif d'amortissement dans l'éolienne, y compris l'analyse de faisabilité théorique, la conception technique conforme aux normes en vigueur, la vérification numérique, l'évaluation de l'efficacité et l'optimisation de la conception. Le processus de conception suggéré implique des études pluridisciplinaires dans les domaines de l'énergie éolienne, de l'ingénierie structurelle, de l'ingénierie du contrôle, de la mécanique computationnelle et des algorithmes d'optimisation.

Les contributions originales de cette thèse concernent principalement :

1. Une analyse de la charge ultime et des analyses de fatigue sont proposées pour la structure de la tour éolienne. Ces deux analyses sont utilisées comme résultats de référence pour évaluer l'efficacité du système d'amortissement.
2. Un cadre probabiliste assisté par un réseau neuronal pour l'analyse de la fatigue est proposé en utilisant un réseau neuronal. La méthode proposée sur méthode

proposée a été testée numériquement avec la NREL 5MW reference wind turbine.

3. Un système d'amortissement actif utilisant TRD est développé et intégré dans l'éolienne de référence. Une simulation numérique a été réalisée pour évaluer cette intégration.
4. Une nouvelle méthode de configuration d'algorithme adaptatif pour differential evolution, AAC-DE, est proposée en combinant l'apprentissage par renforcement (c'est-à-dire l'algorithme du bandit à bras multiples) et les approches d'apprentissage non supervisé (c'est-à-dire l'estimation de la densité du noyau). L'algorithme proposé est appliqué pour rechercher la conception optimale de TRD dans l'éolienne.

Plusieurs tâches sont prévues pour les futurs travaux :

1. intégrer le mode oscillant du TRD dans le système de contrôle actuel et réévaluer les performances du TRD dans le DLC1.1 par rapport aux charges de fatigue. Cela nécessite une nouvelle implémentation du système de contrôle de l'éolienne.
2. évaluer la performance du TRD dans la réduction des dommages de fatigue à long terme sur l'éolienne offshore en considérant à la fois les charges des vagues et du vent.
3. étudier la possibilité d'installer plusieurs TRDs à l'intérieur de l'éolienne offshore afin d'améliorer sa sécurité et sa productivité, par exemple, un pour la tour de l'éolienne et un autre pour la fondation de l'éolienne.
4. utiliser AAC-DE pour optimiser les hyperparamètres du deep neural network ResMLP. Pour atteindre cet objectif, il est indispensable de rendre AAC-DE éligible à résoudre les problèmes d'optimisation bayésienne.



Bibliography



Bibliographie

A

- [AS70] Milton ABRAMOWITZ et Irene A STEGUN. *Handbook of mathematical functions with formulas, graphs, and mathematical tables*. T. 55. US Government printing office, 1970.
- [Aga19] Abien Fred AGARAP. “Deep Learning using Rectified Linear Units (ReLU)”. In : *arXiv preprint arXiv :1803.08375v2* (2019). arXiv : [1803.08375v2](https://arxiv.org/abs/1803.08375v2).
- [Ald97] John ALDRICH. “RA Fisher and the making of maximum likelihood 1912-1922”. In : *Statistical science* 12.3 (1997), p. 162-176.
- [AM16] Aldeida ALETI et Irene MOSER. “A Systematic Literature Review of Adaptive Parameter Control Methods for Evolutionary Algorithms”. In : *ACM Computing Survey* 49.3 (2016).
- [Alm85] Almar ALMARNAESS. “Fatigue handbook : offshore steel structures”. In : (1985).
- [Alt14] Okyay ALTAY et al. “Vibration mitigation of wind turbine towers with tuned mass dampers”. In : *Wind turbine control and monitoring*. Springer, 2014, p. 337-373.
- [AD52] Theodore W ANDERSON et Donald A DARLING. “Asymptotic theory of certain " goodness of fit " criteria based on stochastic processes”. In : *The annals of mathematical statistics* (1952), p. 193-212.
- [Ant97] R J ANTHES. “Modified rainflow counting keeping the load sequence”. In : *International Journal of Fatigue* 19.7 (1997), p. 529-535.
- [Apa04] APACHE SOFTWARE FOUNDATION. *Apache License Version 2.0*. 2004.
- [Arb05] A. ARBELAIZ et al. “Mechanical properties of flax fibre/polypropylene composites. Influence of fibre/matrix modification and glass fibre hybridization”. In : *Composites Part A : Applied Science and Manufacturing* 36.12 (2005), p. 1637-1644. DOI : [10.1016/j.compositesa.2005.03.021](https://doi.org/10.1016/j.compositesa.2005.03.021).
- [Arc21] Francesco ARCIGNI et al. “Analysis of tripod supported offshore wind turbines under conditions of marine growth”. In : *Ocean Engineering* 220 (2021), p. 108441. DOI : [10.1016/j.oceaneng.2020.108441](https://doi.org/10.1016/j.oceaneng.2020.108441).
- [AST85] ASTM. “Standard practices for cycle counting in fatigue analysis”. In : *American Society for Testing and Materials Standards*. 1985, E1049-85.

- [AD19] Nurshazlyn Mohd ASZEMI et P. D.D. DOMINIC. “Hyperparameter optimization in convolutional neural network using genetic algorithms”. In : *International Journal of Advanced Computer Science and Applications* 10.6 (2019), p. 269-278. DOI : [10.14569/ijacsa.2019.0100638](https://doi.org/10.14569/ijacsa.2019.0100638).
- [ACBF02] Peter AUER, Nicolò CESA-BIANCHI et Paul FISCHER. “Finite-time analysis of the multiarmed bandit problem”. In : *Machine Learning* 47.2-3 (2002), p. 235-256. DOI : [10.1023/A:1013689704352](https://doi.org/10.1023/A:1013689704352).
- [Awa16] N H AWAD et al. *Problem Definitions and Evaluation Criteria for the {CEC} 2017 Special Session and Competition on Single Objective Bound Constrained Real-Parameter Numerical Optimization*. Rapp. tech. Nanyang Technological University, Singapore, 2016.

B

- [BCL17] Hao BAI, Jean-Marc CHERFILS et Didier LEMOSSE. “Optimization on high-raise wind tower”. In : *Wind Energy Science Conference 2017*. INSA Rouen Normandie. 2017, p. 1.
- [Bak13] Christian BAK et al. *Description of the DTU 10 MW Reference Wind Turbine*. Rapp. tech. July. Technical University of Denmark, 2013, p. 1-138. DOI : [10.1017/CBO9781107415324.004](https://doi.org/10.1017/CBO9781107415324.004). arXiv : [arXiv:1011.1669v3](https://arxiv.org/abs/1011.1669v3).
- [Bak87] J.E. BAKER. “Reducing bias and inefficiency in the selection algorithm”. In : *Proceedings of the Second International Conference on Genetic Algorithms on Genetic algorithms and their applications*. T. 206. 1987, p. 14-21.
- [Ban07] D J BANG et al. “A new active speed stall control compared to pitch control for a direct-drive wind turbine”. In : *EWEC 2007 Conference proceedings, 2007*. Citeseer, 2007.
- [BM67] Theodore BAUMEISTER et Lionel Simeon MARKS. *Standard handbook for mechanical engineers*. McGraw-Hill, 1967.
- [Bäu17] Richard BÄUMER. “Active vibration control using centrifugal forces created by eccentrically rotating masses”. THES. Hamburg University of Technology, 2017, p. 208.
- [BS16] Richard BÄUMER et Uwe STAROSSEK. “Active vibration control using centrifugal forces created by eccentrically rotating masses”. In : *Journal of Vibration and Acoustics* 138.4 (2016). DOI : [10.1115/1.4033358](https://doi.org/10.1115/1.4033358).
- [Bäu14] Richard BÄUMER et al. “Twin rotor damper applied to the damping of non-harmonic vibrations”. In : *Eurodyn 2014* (2014), p. 1655-1661.

- [Bäu18] Richard BÄUMER et al. “Twin rotor damper for the damping of stochastically forced vibrations using a power-efficient control algorithm”. In : *Journal of Sound and Vibration* 413 (2018), p. 308-331.
- [BC97] M E BECHLY et P D CLAUSEN. “Structural design of a composite wind turbine blade using finite element analysis”. In : *Computers & Structures* 63.3 (1997), p. 639-646.
- [BNH17] Haym BENAROYA, Mark NAGURKA et Seon HAN. *Mechanical vibration : analysis, uncertainties, and control*. CRC Press, 2017.
- [Ben12] Denis BENASCIUTTI. *Fatigue analysis of random loadings. A frequency-domain approach*. LAP Lambert Academic Publishing AG & Co KG, 2012.
- [BT02] Ernesto BENINI et Andrea TOFFOLO. “Optimal design of horizontal-axis wind turbines using blade-element theory and evolutionary computation”. In : *J. Sol. Energy Eng.* 124.4 (2002), p. 357-363.
- [Ber11] James BERGSTRA et al. “Algorithms for hyper-parameter optimization”. In : *Advances in neural information processing systems* 24 (2011), p. 2546-2554.
- [Ber15] Jorgen S BERGSTROM. *Mechanics of solid polymers : theory and computational modeling*. William Andrew, 2015.
- [BS02] P BETSCH et P STEINMANN. “Frame-indifferent beam finite elements based upon the geometrically exact beam theory”. In : *International journal for numerical methods in engineering* 54.12 (2002), p. 1775-1788.
- [Bet20] Albert BETZ. “Das Maximum der theoretisch möglichen Ausnutzung des Windes durch Windmotoren”. In : *Zeitschrift fur das gesamte Turbinenwesen* 20 (1920).
- [BMC04] F D BIANCHI, R J MANTZ et C F CHRISTIANSEN. “Power regulation in pitch-controlled variable-speed WECS above rated wind speed”. In : *Renewable Energy* 29.11 (2004), p. 1911-1922.
- [BDM07] Fernando D BIANCHI, Hernan DE BATTISTA et Ricardo J MANTZ. *Wind turbine control systems : principles, modelling and gain scheduling design*. Springer Science & Business Media, 2007.
- [Bis94] Christopher M. BISHOP. *Mixture density networks*. Rapp. tech. Aston University, 1994, p. 26.
- [Blo18] BLOOMBERG NEW ENERGY FINANCE. *Henbest : Power System Will Dance to Tune of Wind, Solar, Batteries*. 2018.
- [BSS18] Erik BOCHINSKI, Tobias SENST et Thomas SIKORA. “Hyper-parameter optimization for convolutional neural network committees based on evolutionary algorithms”. In : *Proceedings - International Conference on*

- Image Processing, ICIP*. T. 2017-Sept. IEEE, 2018, p. 3924-3928. DOI : [10.1109/ICIP.2017.8297018](https://doi.org/10.1109/ICIP.2017.8297018).
- [BC16] C L BOTTASSO et A CROCE. *Cp-Lambda a Code for Performance, Loads, Aeroelasticity by Multi-Body Dynamics Analysis*. Rapp. tech. 2016.
- [Bot06] Carlo L BOTTASSO et al. “Aero-servo-elastic modeling and control of wind turbines using finite-element multibody procedures”. In : *Multibody System Dynamics* 16.3 (2006), p. 291-308.
- [Bre06] Janez BREST et al. “Self-adapting control parameters in differential evolution : A comparative study on numerical benchmark problems”. In : *IEEE Transactions on Evolutionary Computation* 10.6 (2006), p. 646-657. DOI : [10.1109/TEVC.2006.872133](https://doi.org/10.1109/TEVC.2006.872133).
- [Bre08] Simon-Philippe BRETON. “Study of the stall delay phenomenon and of wind turbine blade dynamics using numerical approaches and NREL’s wind tunnel tests”. Thèse de doct. 2008.
- [BH14] Mark L BRODERSEN et Jan HØGSBERG. “Damping of offshore wind turbine tower vibrations by a stroke amplifying brace”. In : *Energy Procedia* 53 (2014), p. 258-267.
- [Bro14] Peter BRONSKI. *You Down With LCOE? Maybe You, But Not Me*. 2014.
- [BH85] David BROWN et E P HAMILTON. *Electromechanical energy conversion*. MacMillan Press Ltd., London, England, 1985.

C

- [CCW08] H R CAI, C Y CHUNG et K P WONG. “Application of differential evolution algorithm for transient stability constrained optimal power flow”. In : *IEEE Transactions on Power Systems* 23.2 (2008), p. 719-728.
- [Cam08] Flake C CAMPBELL. *Elements of metallurgy and engineering alloys*. ASM International, 2008.
- [Cha06] P K CHAVIAROPOULOS et al. “Enhancing the damping of wind turbine rotor blades, the DAMPBLADE project”. In : *Wind Energy : An International Journal for Progress and Applications in Wind Power Conversion Technology* 9.1-2 (2006), p. 163-177.
- [CHW19] Ping CHENG, Yang HUANG et Decheng WAN. “A numerical model for fully coupled aero-hydrodynamic analysis of floating offshore wind turbine”. In : *Ocean Engineering* 173 (2019), p. 183-196. DOI : [10.1016/j.oceaneng.2018.12.021](https://doi.org/10.1016/j.oceaneng.2018.12.021).

- [CA83] R C H CHENG et N A K AMIN. “Estimating parameters in continuous univariate distributions with a shifted origin”. In : *Journal of the Royal Statistical Society : Series B (Methodological)* 45.3 (1983), p. 394-403.
- [COL19] Jui Sheng CHOU, Yu Chen OU et Kuan Yu LIN. “Collapse mechanism and risk management of wind turbine tower in strong wind”. In : *Journal of Wind Engineering and Industrial Aerodynamics* 193.April 2018 (2019), p. 103962. DOI : [10.1016/j.jweia.2019.103962](https://doi.org/10.1016/j.jweia.2019.103962).
- [CV12] Raymond CHOW et C. P. VAN DAM. “Verification of computational simulations of the NREL 5 MW rotor with a focus on inboard flow separation”. In : *Wind Energy* 15.8 (2012), p. 967-981. DOI : [10.1002/we.529](https://doi.org/10.1002/we.529).
- [Chr09] Richard M. CHRISTENSEN. “A physically based cumulative damage formalism”. In : *Major Accomplishments in Composite Materials and Sandwich Structures*. Springer, 2009, p. 51-65.
- [COC13] Gauss M CORDEIRO, Edwin M M ORTEGA et Daniel C C da CUNHA. “The exponentiated generalized class of distributions”. In : *Journal of Data Science* 11.1 (2013), p. 1-27.
- [CLM13] Matej CREPINSEK, Shih Hsi LIU et Marjan MERNIK. “Exploration and exploitation in evolutionary algorithms : A survey”. In : *ACM Computing Surveys* 45.3 (2013), p. 1-33. DOI : [10.1145/2480741.2480752](https://doi.org/10.1145/2480741.2480752).

D

- [DS11] S DAS et P N SUGANTHAN. “Differential Evolution : A Survey of the State-of-the-Art”. In : *IEEE Transactions on Evolutionary Computation* 15.1 (2011), p. 4-31.
- [DB12] Javier Garcia DE JALON et Eduardo BAYO. *Kinematic and dynamic simulation of multibody systems : the real-time challenge*. Springer Science & Business Media, 2012.
- [Dem06] Janez DEMŠAR. “Statistical Comparisons of Classifiers over Multiple Data Sets”. In : *Journal of Machine Learning Research* 7 (2006), p. 1-30.
- [Der11] Joaquín DERRAC et al. “A practical tutorial on the use of nonparametric statistical tests as a methodology for comparing evolutionary and swarm intelligence algorithms”. In : *Swarm and Evolutionary Computation* 1.1 (2011), p. 3-18. DOI : [10.1016/j.swevo.2011.02.002](https://doi.org/10.1016/j.swevo.2011.02.002).

- [Der13] Nikolaos DERVILIS. “A machine learning approach to Structural Health Monitoring with a view towards wind turbines”. Thèse de doct. University of Sheffield, 2013, p. 176.
- [Dev13] Christof DEVRIENDT et al. “Damping estimation of an offshore wind turbine on a monopile foundation”. In : *IET Renewable Power Generation* 7.4 (2013), p. 401-412.
- [Di 21] Moira DI PAOLO et al. “A friction-based passive control technique to mitigate wind induced structural demand to wind turbines”. In : *Engineering Structures* 232 (2021), p. 111744. DOI : [10.1016/j.engstruct.2020.111744](https://doi.org/10.1016/j.engstruct.2020.111744).
- [Die95] Tom DIETTERICH. “Overfitting and undercomputing in machine learning”. In : *ACM Computing Surveys* 27.3 (1995), p. 326-327. DOI : [10.1145/212094.212114](https://doi.org/10.1145/212094.212114).
- [DNK15] Nikolay DIMITROV, Anand NATARAJAN et Mark KELLY. “Model of wind shear conditional on turbulence and its impact on wind turbine loads”. In : *Wind Energy* 18.11 (2015), p. 1917-1931. DOI : [10.1002/we.1797](https://doi.org/10.1002/we.1797).
- [DS13] Fateme DINMOHAMMADI et Mahmood SHAFIEE. “A fuzzy-FMEA risk assessment approach for offshore wind turbines”. In : *International Journal of Prognostics and Health Management* 4.13 (2013), p. 59-68.
- [DNV16] DNV GL AS. *Recommended Practice - Fatigue Design of Offshore Steel Structures*. 2016.
- [DNV19] DNV GL AS. *Recommended Practice - Fatigue Design of Offshore Steel Structures*. 2019.
- [Dod08] Yadolah DODGE. “Kolmogorov–Smirnov Test BT”. In : *The Concise Encyclopedia of Statistics*. New York, NY : Springer New York, 2008, p. 283-287. DOI : [10.1007/978-0-387-32833-1_214](https://doi.org/10.1007/978-0-387-32833-1_214).
- [DS98] Zhaohui DU et Michael SELIG. “A 3-D stall-delay model for horizontal axis wind turbine performance prediction”. In : *1998 ASME Wind Energy Symposium*. 1998, p. 21.
- [DK12] James DURBIN et Siem Jan KOOPMAN. *Time series analysis by state space methods*. Oxford university press, 2012.

E

- [EM17] Abbas EBRAHIMI et Mohammadreza MOVAHHEDI. “Power improvement of NREL 5-MW wind turbine using multi-DBD plasma actua-

- tors”. In : *Energy Conversion and Management* 146 (2017), p. 96-106. DOI : [10.1016/j.enconman.2017.05.019](https://doi.org/10.1016/j.enconman.2017.05.019).
- [ESH19] Konstantin ECKLE et Johannes SCHMIDT-HIEBER. “A comparison of deep networks with ReLU activation function and linear spline-type methods”. In : *Neural Networks* 110 (2019), p. 232-242. DOI : [10.1016/j.neunet.2018.11.005](https://doi.org/10.1016/j.neunet.2018.11.005). arXiv : [1804.02253](https://arxiv.org/abs/1804.02253).
- [Ede11] Ottmar EDENHOFER et al. *IPCC, 2011 : Summary for Policymakers. In : IPCC Special Report on Renewable Energy Sources and Climate Change Mitigation*. 2011, p. 246. DOI : [10.5860/CHOICE.49-6309](https://doi.org/10.5860/CHOICE.49-6309).
- [EDC03] A J EGGERS JR, R DIGUMARTHI et K CHANEY. “Wind shear and turbulence effects on rotor fatigue and loads control”. In : *J. Sol. Energy Eng.* 125.4 (2003), p. 402-409.
- [EHM99] A E EIBEN, R HINTERDING et Z MICHALEWICZ. “Parameter control in evolutionary algorithms”. In : *IEEE Transactions on Evolutionary Computation* 3.2 (1999), p. 124-141.
- [ES98] A. E. EIBEN et C. A. SCHIPPERS. “On Evolutionary Exploration and Exploitation”. In : *Fundamenta Informaticae* 35.1-4 (1998), p. 35-50. DOI : [10.3233/fi-1998-35123403](https://doi.org/10.3233/fi-1998-35123403).
- [Eke94] Thommy EKELUND. “Speed control of wind turbines in the stall region”. In : *Proceedings of the third IEEE conference on control applications*. T. 1. 1994, p. 227-232.
- [Eng07] Andries P ENGELBRECHT. *Computational intelligence : an introduction*. John Wiley & Sons, 2007.
- [ENG] ENGIE. *Falfose et Ramonts - ENGIE Green*.
- [Eur] EUROPEAN COMMITTEE FOR STANDARDIZATION. *Eurocode 3 : Design of steel structures*.

F

- [FWY19] Qinqin FAN, Weili WANG et Xuefeng YAN. “Differential evolution algorithm with strategy adaptation and knowledge-based control parameters”. In : *Artificial Intelligence Review* 51.2 (2019), p. 219-253. DOI : [10.1007/s10462-017-9562-6](https://doi.org/10.1007/s10462-017-9562-6).
- [FB16] Breiffni FITZGERALD et Biswajit BASU. “Structural control of wind turbines with soil structure interaction included”. In : *Engineering Structures* 111 (2016), p. 131-151. DOI : [10.1016/j.engstruct.2015.12.019](https://doi.org/10.1016/j.engstruct.2015.12.019).
- [For85] E J FORDHAM. “The spatial structure of turbulence in the atmospheric boundary layer”. In : *Wind Engineering* (1985), p. 95-133.

- [FT99] Sten FRANDBSEN et Morten L THØGERSEN. “Integrated fatigue loading for wind turbines in wind farms by combining ambient turbulence and wakes”. In : *Wind Engineering* (1999), p. 327-339.
- [FTP82] Sten FRANDBSEN, Andrew R TRENKA et B Maribo PEDERSEN. *Recommended Practices for Wind Turbine Testing : 1. Power Performance Testing*. International Energy Agency, 1982.
- [FPEN19] Gene F FRANKLIN, J David POWELL et Abbas EMAMI-NAEINI. *Feedback control of dynamic systems*. Sous la dir. de Julian PARTRIDGE. 8^e éd. Pearson, 2019.
- [FSH10] Peter FROHBOESE, Christian SCHMUCK et G L Garrad HASSAN. “Thrust coefficients used for estimation of wake effects for fatigue load calculation”. In : *European Wind Energy Conference*. 2010, p. 1-10.
- [FLT78] Walter FROST, B H LONG et Robert Eugene TURNER. *Engineering handbook on the atmospheric environmental guidelines for use in wind turbine generator development*. 1978.
- [FL89] C. FROUSTEY et S. LASSERRE. “Multiaxial fatigue endurance of 30NCD16 steel”. In : *International Journal of Fatigue* 11.3 (1989), p. 169-175. DOI : [10.1016/0142-1123\(89\)90436-2](https://doi.org/10.1016/0142-1123(89)90436-2).
- [FH01] Zhi-Fang FU et Jimin HE. *Modal analysis*. Elsevier, 2001.

G

- [GN18] Adrian GAMBIER et Yul Yunazwin NAZARUDDIN. “Collective pitch control with active tower damping of a wind turbine by using a nonlinear PID approach”. In : *IFAC-PapersOnLine*. T. 51. 4. Elsevier, 2018, p. 238-243.
- [GMK02] Roger GÄMPELLE, Sibylle D MÜLLER et Petros KOUMOUTSAKOS. “A Parameter Study for Differential Evolution”. In : *Advances in intelligent systems, fuzzy systems, evolutionary computation* 10.10 (2002), p. 293-298.
- [Gaw04] Wodek GAWRONSKI. *Advanced structural dynamics and active control of structures*. Springer Science & Business Media, 2004.
- [Gér17] Aurélien GÉRON. *Hands-On Machine Learning with Scikit-Learn and TensorFlow : Concepts, Tools, and Techniques to build intelligent systems*. O’Reilly Media, 2017, p. 547.
- [GK87] G GLINKA et J C P KAM. “Rainflow counting algorithm for very long stress histories”. In : *International Journal of Fatigue* 9.4 (1987), p. 223-228.

- [Glo20] GLOBAL WIND ENERGY COUNCIL. *GLOBAL OFFSHORE WIND REPORT 2020*. Rapp. tech. 2020, p. 130.
- [Gon11] Wenyin GONG et al. “Adaptive strategy selection in differential evolution for numerical optimization : An empirical study”. In : *Information Sciences* 181.24 (2011), p. 5364-5386. DOI : [10.1016/j.ins.2011.07.049](https://doi.org/10.1016/j.ins.2011.07.049).
- [Goo16] Ian GOODFELLOW et al. *Deep learning*. T. 1. The MIT press, 2016, p. 800.
- [GA11] D Todd GRIFFITH et Thomas D ASHWILL. “The Sandia 100-meter All-glass Baseline Wind Turbine Blade : SNL100-00”. In : *Baseline* June (2011), p. 1-67.
- [Gum35] Emil Julius GUMBEL. “Les valeurs extrêmes des distributions statistiques”. In : *Annales de l’institut Henri Poincaré*. T. 5. 2. 1935, p. 115-158.
- [Gum41] Emil Julius GUMBEL. “The return period of flood flows”. In : *The annals of mathematical statistics* 12.2 (1941), p. 163-190.
- [GK10] Rameshwar D GUPTA et Debasis KUNDU. “Generalized logistic distributions”. In : *Journal of Applied Statistical Science* 18.1 (2010), p. 51.
- [Gur77] Arthur L GURSON. “Continuum theory of ductile rupture by void nucleation and growth : Part I—Yield criteria and flow rules for porous ductile media”. In : *Journal of engineering materials and technology* 99.1 (1977), p. 2-15.
- [Guy97] Isabelle GUYON. “A scaling law for the validation-set training-set size ratio”. In : *AT&T Bell Laboratories* 1.11 (1997), p. 1-11.

H

- [Hai17] B P HAIGH. “Experiments on the fatigue of brasses”. In : *Journal of the Institute of Metals* 18 (1917), p. 55-86.
- [Han00] S. HANS et al. “Damping identification in multi-degree-of-freedom system via a wavelet-logarithmic decrement - Part 2 : study of a civil engineering building”. In : *Journal of Sound and Vibration* 235.3 (2000), p. 375-403. DOI : [10.1006/jsvi.1999.2927](https://doi.org/10.1006/jsvi.1999.2927).
- [Han06] Nikolaus HANSEN. “Compilation of results on the 2005 CEC benchmark function set”. In : *Online, May*. 2006.
- [HPK84] Kermit I HARNER, John P PATRICK et Joseph M KOS. *Predicted motion wind turbine tower damping*. 1984.
- [Has20] Seyed H. HASHEMIZADEH et al. “Calculation of fatigue capacity for a subsea wellhead connector”. In : *Proceedings of the International Conference on Offshore Mechanics and Arctic Engineering - OMAE*. T. 2B-

2020. American Society of Mechanical Engineers, 2020, V02BT02A036. DOI : [10.1115/OMAE2020-19329](https://doi.org/10.1115/OMAE2020-19329).
- [Hau13] Erich HAU. *Wind turbines : Fundamentals, technologies, application, economics*. T. 9783642271. 2013, p. 1-879. DOI : [10.1007/978-3-642-27151-9](https://doi.org/10.1007/978-3-642-27151-9).
- [He15] Kaiming HE et al. “Deep residual learning for image recognition”. In : *Proceedings of the IEEE conference on computer vision and pattern recognition*. 2015, p. 770-778. arXiv : [1512.03385](https://arxiv.org/abs/1512.03385).
- [HO18] Arash HEMMATI et Erkan OTERKUS. “Semi-Active Structural Control of Offshore Wind Turbines Considering Damage Development”. In : *Journal of Marine Science and Engineering* 6 (2018). DOI : [10.3390/jmse6030102](https://doi.org/10.3390/jmse6030102).
- [HOK19] Arash HEMMATI, Erkan OTERKUS et Mahdi KHORASANCHI. “Vibration suppression of offshore wind turbine foundations using tuned liquid column dampers and tuned mass dampers”. In : *Ocean Engineering* 172.May 2018 (2019), p. 286-295. DOI : [10.1016/j.oceaneng.2018.11.055](https://doi.org/10.1016/j.oceaneng.2018.11.055).
- [HLS97] Ward HEYLEN, Stefan LAMMENS et Paul SAS. *Modal analysis theory and testing*. T. 200. 7. Katholieke Universiteit Leuven Leuven, Belgium, 1997.
- [Hia19a] John HIATT. *Mean Stress Corrections and Stress Ratios*. 2019.
- [Hia19b] John HIATT. *Rainflow Counting*. 2019.
- [Hia19c] John HIATT. *What is a SN-Curve ?* 2019.
- [HJB10] Eelco HOOGEDOORN, Gustaaf B JACOBS et Asfaw BEYENE. “Aeroelastic behavior of a flexible blade for wind turbine application : A 2D computational study”. In : *Energy* 35.2 (2010), p. 778-785.
- [Hoo12] Holger H HOOS. “Automated Algorithm Configuration and Parameter Tuning”. In : *Autonomous Search*. Sous la dir. d’Youssef HAMADI, Eric MONFROY et Frédéric SAUBION. Berlin, Heidelberg : Springer Berlin Heidelberg, 2012, p. 37-71.
- [HK01] N HORIUCHI et T KAWAHITO. “Torque and power limitations of variable speed wind turbines using pitch control and generator power control”. In : *2001 Power Engineering Society Summer Meeting. Conference Proceedings (Cat. No. 01CH37262)*. T. 1. IEEE, 2001, p. 638-643.
- [Hos90] Jonathan R M HOSKING. “L-moments : Analysis and estimation of distributions using linear combinations of order statistics”. In : *Journal of the Royal Statistical Society : Series B (Methodological)* 52.1 (1990), p. 105-124.

- [HHD06] Danmei HU, Ouyang HUA et Zhaohui DU. “A study on stall-delay for horizontal axis wind turbine”. In : *Renewable Energy* 31.6 (2006), p. 821-836.
- [Hu14] Wei-Hua HU et al. “Resonance phenomenon in a wind turbine system under operational conditions”. In : *structural health monitoring* 12 (2014), p. 14.
- [HCC16] Weifei HU, K. K. CHOI et Hyunkyoo CHO. “Reliability-based design optimization of wind turbine blades for fatigue life under dynamic wind load uncertainty”. In : *Structural and Multidisciplinary Optimization* 54.4 (2016), p. 953-970. DOI : [10.1007/s00158-016-1462-x](https://doi.org/10.1007/s00158-016-1462-x).
- [HLY20] C HUANG, Y LI et X YAO. “A Survey of Automatic Parameter Tuning Methods for Metaheuristics”. In : *IEEE Transactions on Evolutionary Computation* 24.2 (2020), p. 201-216.
- [Hua19] C HUANG et al. “Automatic Parameter Tuning using Bayesian Optimization Method”. In : *2019 IEEE Congress on Evolutionary Computation (CEC)*. 2019, p. 2090-2097.
- [Hug12] Thomas J R HUGHES. *The finite element method : linear static and dynamic finite element analysis*. Courier Corporation, 2012.
- [HH86] G HUSS et E HAU. *Lastfalldefinition für WKA-60*. Rapp. tech. 1986.
- [HHLB11] Frank HUTTER, Holger H HOOS et Kevin LEYTON-BROWN. “Sequential Model-Based Optimization for General Algorithm Configuration”. In : *Learning and Intelligent Optimization*. Sous la dir. de Carlos A Coello COELLO. Berlin, Heidelberg : Springer Berlin Heidelberg, 2011, p. 507-523.
- [Hut09] Frank HUTTER et al. “{ParamILS} : an automatic algorithm configuration framework”. In : *Journal of Artificial Intelligence Research* 36.1 (2009), p. 267-306.

I

- [Ing11] Grant INGRAM. “Wind turbine blade analysis using the blade element momentum method. Version 1.1”. In : *Durham University, Durham* (2011).
- [INI15] INIDE. *Anuario Estadístico*. Rapp. tech. 2015.
- [Int05] INTERNATIONAL ELECTROTECHNICAL COMMISSION (IEC). *Wind turbines - Part1 : Design requirements*. 2005.
- [Int19a] INTERNATIONAL ENERGY AGENCY. *Key world energy statistics 2019*. Rapp. tech. 2019, p. 81.

- [Int20a] INTERNATIONAL ENERGY AGENCY. *Key World Energy Statistics 2020*. Rapp. tech. August. 2020, p. 81.
- [Int20b] INTERNATIONAL ENERGY AGENCY. *Renewables Information - Overview (2020 Edition)*. Rapp. tech. 2020, p. 31.
- [Int16] INTERNATIONAL RENEWABLE ENERGY AGENCY. *Wind Power Technology Brief*. Rapp. tech. March. 2016.
- [Int18] INTERNATIONAL RENEWABLE ENERGY AGENCY. *RENEWABLE POWER GENERATION COSTS IN 2018*. Rapp. tech. 2018, p. 160.
- [Int19b] INTERNATIONAL RENEWABLE ENERGY AGENCY. *RENEWABLE POWER GENERATION COSTS IN 2019*. Rapp. tech. 2019, p. 160.
- [Int20c] INTERNATIONAL RENEWABLE ENERGY AGENCY. *RENEWABLE CAPACITY STATISTICS 2020*. Rapp. tech. 2020, p. 66.
- [IL04] Antony W IORIO et Xiaodong LI. "Solving rotated multi-objective optimization problems using Differential Evolution". In : *In AI 2004 : Advances in Artificial Intelligence : 17th Australian Joint Conference on Artificial Intelligence*. press, 2004, p. 861-872.
- [Iva71] A. G. IVAKHNENKO. "Polynomial Theory of Complex Systems". In : *IEEE Transactions on Systems, Man and Cybernetics* 1.4 (1971), p. 364-378. DOI : [10.1109/TSMC.1971.4308320](https://doi.org/10.1109/TSMC.1971.4308320).
- [IL67] A.G. IVAKHNENKO et V.G. LAPA. "Cybernetics and forecasting techniques". In : American Elsevier Publishing Company, 1967, p. 168.

J

- [Jam17] Peter JAMIESON. *Innovation in wind turbine design : Second edition*. 2017, p. 1-394. DOI : [10.1002/9781119137924](https://doi.org/10.1002/9781119137924).
- [Jia17] Zhiyu JIANG et al. "Structural reliability analysis of wind turbines : A review". In : *Energies* 10.12 (2017), p. 2099. DOI : [10.3390/en10122099](https://doi.org/10.3390/en10122099).
- [JT99] P K JIMACK et B H V TOPPING. "An overview of parallel dynamic loadbalancing for parallel adaptive computational mechanics codes". In : *Parallel and distributed processing for computational mechanics : Systems and Tools* (1999), p. 350-369.
- [JJS03] R JOHN, K V JATA et K SADANANDA. "Residual stress effects on near-threshold fatigue crack growth in friction stir welds in aerospace alloys". In : *International Journal of fatigue* 25.9-11 (2003), p. 939-948.
- [JOH49] N. L. JOHNSON. "Systems of frequency curves generated by methods of translation." In : *Biometrika* 36.Pt. 1-2 (1949), p. 149-176. DOI : [10.1093/biomet/36.1-2.149](https://doi.org/10.1093/biomet/36.1-2.149).

- [Joh49] Norman L JOHNSON. “Bivariate distributions based on simple translation systems”. In : *Biometrika* 36.3/4 (1949), p. 297-304.
- [JKB95] Norman L JOHNSON, Samuel KOTZ et Narayanaswamy BALAKRISHNAN. *Continuous univariate distributions*. John Wiley & Sons, Ltd, 1995.
- [JBE09] E Russell JOHNSTON, Ferdinand BEER et Elliot EISENBERG. *Vector Mechanics for Engineers : Statics and Dynamics*. McGraw-Hill, 2009.
- [JOP01] Eric JONES, Travis OLIPHANT et Pearu PETERSON. “SciPy : Open source scientific tools for Python”. In : (2001).
- [JK12] Bonnie J. JONKMAN et L. KILCHER. *TurbSim User’s Guide : Version 1.06.00*. Rapp. tech. September. National Renewable Energy Laboratory (NREL), 2012.
- [JB05] Jason M. JONKMAN et Marshall L. BUHL JR. *FAST User’s Guide*. Rapp. tech. National Renewable Energy Laboratory (NREL), 2005, p. 143.
- [Jon09] Jason M. JONKMAN et al. *Definition of a 5-MW Reference Wind Turbine for Offshore System Development*. Rapp. tech. February. National Renewable Energy Laboratory (NREL), 2009. DOI : [10.2172/947422](https://doi.org/10.2172/947422).
- [Jos11] Paul L. JOSKOW. “Comparing the costs of intermittent and dispatchable electricity generating technologies”. In : *American Economic Review*. T. 101. 3. 2011, p. 238-241. DOI : [10.1257/aer.101.3.238](https://doi.org/10.1257/aer.101.3.238).

K

- [KHE15] G KARAFOTIAS, M HOOGENDOORN et A E EIBEN. “Parameter Control in Evolutionary Algorithms : Trends and Challenges”. In : *IEEE Transactions on Evolutionary Computation* 19.2 (2015), p. 167-187.
- [KD00] Zaven A KARIAN et Edward J DUDEWICZ. *Fitting statistical distributions : the generalized lambda distribution and generalized bootstrap methods*. CRC press, 2000.
- [KO11] Bekir KARLIK et A Vehbi OLGAC. “Performance analysis of various activation functions in generalized MLP architectures of neural networks”. In : *International Journal of Artificial Intelligence and Expert Systems* 1.4 (2011), p. 111-122.
- [Kas12] Ahmed M KASSEM. “Robust voltage control of a stand alone wind energy conversion system based on functional model predictive approach”. In : *International Journal of Electrical Power & Energy Systems* 41.1 (2012), p. 124-132.

- [Kel19] Tomas KELLNER. *Extreme Measures : At 107 Meters, The World's Largest Wind Turbine Blade Is Longer Than A Football Field. Here's What It Looks Like*. 2019.
- [Ken18] Ciaran R KENNEDY et al. "Fatigue life of pitch-and stall-regulated composite tidal turbine blades". In : *Renewable energy* 121 (2018), p. 688-699.
- [KT16] Mahdi KHODAYAR et Mohammad TESHNEHLAB. "Robust deep neural network for wind speed prediction". In : *4th Iranian Joint Congress on Fuzzy and Intelligent Systems, CFIS 2015*. IEEE, 2016, p. 1-5. DOI : [10.1109/CFIS.2015.7391664](https://doi.org/10.1109/CFIS.2015.7391664).
- [KFR19] David KNEZEVIC, Emmanuel FAKAS et Hans Jorgen RIBER. "Predictive digital twins for structural integrity management and asset life extension – JIP concept and results". In : *Society of Petroleum Engineers - SPE Offshore Europe Conference and Exhibition 2019, OE 2019*. Society of Petroleum Engineers, 2019. DOI : [10.2118/195762-MS](https://doi.org/10.2118/195762-MS).
- [KK73] Kenneth W KOLENCE et Philip J KIVIAT. "Software unit profiles & Kiviat figures". In : *ACM SIGMETRICS performance evaluation review* 2.3 (1973), p. 2-12.
- [Kol33] Andrey KOLMOGOROV. "Sulla determinazione empirica di una legge di distribuzione". In : *Inst. Ital. Attuari, Giorn.* 4 (1933), p. 83-91.
- [Koo03] H.J.T. KOOLJMAN et al. *DOWEC 6 MW PRE-DESIGN Aero-elastic modelling of the DOWEC 6 MW pre-design in PHATAS*. Rapp. tech. 2003, p. 46.
- [KPH83] Joseph M KOS, John P PATRICK et Kermit I HARNER. *Motion responsive wind turbine tower damping*. 1983.
- [KP14] Volodymyr KULESHOV et Doina PRECUP. "Algorithms for multi-armed bandit problems". In : 1 (2014), p. 1-32. arXiv : [1402.6028](https://arxiv.org/abs/1402.6028).
- [KM15] Marit I KVITTEM et Torgeir MOAN. "Time domain analysis procedures for fatigue assessment of a semi-submersible wind turbine". In : *Marine Structures* 40 (2015), p. 38-59. DOI : [10.1016/j.marstruc.2014.10.009](https://doi.org/10.1016/j.marstruc.2014.10.009).

L

- [LPO13] Lucas I. LAGO, Fernando L. PONTA et Alejandro D. OTERO. "Analysis of alternative adaptive geometrical configurations for the NREL-5MW wind turbine blade". In : *Renewable Energy* 59 (2013), p. 13-22. DOI : [10.1016/j.renene.2013.03.007](https://doi.org/10.1016/j.renene.2013.03.007).

- [LPC00] C. H. LAMARQUE, S. PERNOT et A. CUER. “Damping identification in multi-degree-of-freedom systems via a wavelet-logarithmic decrement - Part 1 : theory”. In : *Journal of Sound and Vibration* 235.3 (2000), p. 361-374. DOI : [10.1006/jsvi.1999.2928](https://doi.org/10.1006/jsvi.1999.2928).
- [Lam76] Ronald G LAMBERT. “Analysis of fatigue under random vibration”. In : *The Shock and Vibration Bulletin*. T. 46. 3. 1976, p. 55-72.
- [LH07] Torben Juul LARSEN et Anders Melchior HANSEN. “How 2 HAWC2, the user’s manual”. In : *December 2007* (2007).
- [LAZ19] LAZARD. *LAZARD’S LEVELIZED COST OF ENERGY ANALYSIS—VERSION 13.0*. Rapp. tech. November. 2019.
- [LK20] Hak Min LEE et Oh Joon KWON. “Performance improvement of horizontal axis wind turbines by aerodynamic shape optimization including aeroelastic deformation”. In : *Renewable Energy* 147 (2020), p. 2128-2140. DOI : [10.1016/j.renene.2019.09.125](https://doi.org/10.1016/j.renene.2019.09.125).
- [Lee05] Yung-Li LEE et al. *Fatigue testing and analysis : theory and practice*. T. 13. Butterworth-Heinemann, 2005.
- [LC00] W E LEITHEAD et Bill CONNOR. “Control of variable speed wind turbines : design task”. In : *International Journal of Control* 73.13 (2000), p. 1189-1212.
- [LLR92] W E LEITHEAD, S A D E LA SALLE et D REARDON. “Classical control of active pitch regulation of constant speed horizontal axis wind turbines”. In : *International Journal of control* 55.4 (1992), p. 845-876.
- [Les19] Grzegorz LESIUK et al. “Fatigue Damage Analysis of Offshore Structures using Hot-Spot Stress and Notch Strain Approaches”. In : *Experimental Mechanics of Solids* 12 (2019), p. 146-154. DOI : [10.21741/9781644900215-21](https://doi.org/10.21741/9781644900215-21).
- [LKZ19] Kai LI, Jiaqing KOU et Weiwei ZHANG. “Deep neural network for unsteady aerodynamic and aeroelastic modeling across multiple Mach numbers”. In : *Nonlinear Dynamics* 96.3 (2019), p. 2157-2177. DOI : [10.1007/s11071-019-04915-9](https://doi.org/10.1007/s11071-019-04915-9).
- [Li01] Ron S. LI. “A methodology for fatigue prediction of electronic components under random vibration load”. In : *Journal of Electronic Packaging, Transactions of the ASME* 123.4 (2001), p. 394-400. DOI : [10.1115/1.1372318](https://doi.org/10.1115/1.1372318).
- [LY12] Xiangtao LI et Minghao YIN. “Application of differential evolution algorithm on self-potential data”. In : *PloS one* 7.12 (2012), e51199.
- [Li20] Zhanwei LI et al. “Aerodynamic and aeroelastic characteristics of flexible wind turbine blades under periodic unsteady inflows”. In : *Journal of Wind Engineering and Industrial Aerodynamics* 197 (2020), p. 104057.

- [Lic89] G N U General Public LICENSE. “GNU General Public License”. In : *Retrieved December 25* (1989), p. 2014.
- [Liu12] De Zheng LIU et al. “The review of computational FE software for creep damage mechanics”. In : *Advanced Materials Research*. T. 510. Trans Tech Publ, 2012, p. 495-499.
- [LZ17] Yiqian LIU et Huajie ZHANG. “An empirical study on machine learning models for wind power predictions”. In : *Proceedings - 2016 15th IEEE International Conference on Machine Learning and Applications, ICMLA 2016*. IEEE, 2017, p. 758-763. DOI : [10.1109/ICMLA.2016.37](https://doi.org/10.1109/ICMLA.2016.37).
- [LMI14a] LMI. *Le projet E@lin*. 2014.
- [LMI14b] LMI. *Mathematical Modeling and NUMerical simulation (M2NUM)*. 2014.
- [LM17] Alessio LOMUSCIO et Lalit MAGANTI. “An approach to reachability analysis for feed-forward ReLU neural networks”. In : *arXiv preprint arXiv :1706.07351* (2017). arXiv : [1706.07351](https://arxiv.org/abs/1706.07351).
- [LH16] Ilya LOSHCHILOV et Frank HUTTER. “CMA-ES for Hyperparameter Optimization of Deep Neural Networks”. In : *arXiv preprint arXiv :1604.07269* (2016). arXiv : [1604.07269](https://arxiv.org/abs/1604.07269).
- [LFR16] Inge LOTSBERG, Arne FJELDSTAD et Knut O. RONOLD. “Background for revision of DNVGL-RP-C203 fatigue design of offshore steel structures in 2016”. In : *Proceedings of the International Conference on Offshore Mechanics and Arctic Engineering - OMAE*. T. 4. American Society of Mechanical Engineers, 2016, V004T03A015. DOI : [10.1115/OMAE2016-54939](https://doi.org/10.1115/OMAE2016-54939).
- [LVA14] Ningsu ; LUO, Yolanda ; VIDAL et Leonardo ACHO. *Wind turbine control and monitoring*. 2014, p. 221. DOI : [10.1007/978-3-319-08413-8](https://doi.org/10.1007/978-3-319-08413-8). arXiv : [arXiv:1011.1669v3](https://arxiv.org/abs/1011.1669v3).
- [Lzy07] LZYVZL. *File :Forced Vibration Response.png - Wikiwand*. 2007.

M

- [MMVB18] Yang MA, Pedro MARTINEZ-VAZQUEZ et Charalampos BANIOPOULOS. “Wind Turbine Tower Collapse Cases : A Historical Overview”. In : *ICE Proceedings Structures and Buildings* (2018). DOI : [10.1680/jstbu.17.00167](https://doi.org/10.1680/jstbu.17.00167).
- [Mal11] Rammohan MALLIPEDDI et al. “Differential evolution algorithm with ensemble of parameters and mutation strategies”. In : *Applied soft computing* 11.2 (2011), p. 1679-1696.

- [MMR09] J.F. MANWELL, J.G. MCGOWAN et A.L. ROGERS. *Wind Energy Explained*. T. 1. 1. John Wiley & Sons, Ltd, 2009, p. 705.
- [ME68] Masanori MATSUSHI et Tatsuo ENDO. “Fatigue of metals subjected to varying stress”. In : *Japan Society of Mechanical Engineers, Fukuoka, Japan 68.2* (1968), p. 37-40.
- [MBV18] Metodi MAZHRAKOV, Dobriyan BENOVA et Nikolai VALKANOV. *The Monte Carlo Method : Engineering Applications*. ACMO Academic Press, 2018.
- [MP43] Warren S MCCULLOCH et Walter PITTS. “A logical calculus of the ideas immanent in nervous activity”. In : *The bulletin of mathematical biophysics* 5.4 (1943), p. 115-133.
- [MB96] A S MERCER et E A BOSSANYI. *Stall regulation of variable speed HAWTS*. Harwell Laboratory, Energy Technology Support Unit, 1996.
- [Mer04] J. L. MERIAM. *Engineering Mechanics : Vol. 1 Statics*. T. 1. 2004.
- [MK12] J. L. MERIAM et L. G. KRAIGE. *Engineering Mechanics : Vol. 2 Dynamics*. T. 2. John Wiley & Sons, 2012.
- [Min45] M A MINER. “Cumulative fatigue damage”. In : *Journal of applied mechanics* 12.3 (1945), A159-A164.
- [Mis17] Leon MISHNAEVSKY et al. “Materials for wind turbine blades : An overview”. In : *Materials* 10.11 (2017), p. 1-24. DOI : [10.3390/ma10111285](https://doi.org/10.3390/ma10111285).
- [Moc12] Jonas MOCKUS. *Bayesian approach to global optimization : theory and applications*. T. 37. Springer Science & Business Media, 2012.
- [MC10] J MONTGOMERY et S CHEN. “An analysis of the operation of differential evolution at high and low crossover rates”. In : *IEEE Congress on Evolutionary Computation*. 2010, p. 1-8.
- [Mor11] Lindsay MORRIS. “Direct drive vs. gearbox : progress on both fronts : will the wind turbine technology showdown leave just one technology standing?” In : *Power Engineering* 115.3 (2011), p. 38-42.
- [Mou20] António MOURÃO et al. “A fatigue damage evaluation using local damage parameters for an offshore structure”. In : *Proceedings of the Institution of Civil Engineers : Maritime Engineering*. T. 173. 2. Thomas Telford Ltd, 2020, p. 43-57. DOI : [10.1680/jmaen.2019.24](https://doi.org/10.1680/jmaen.2019.24).
- [MS93] Govind S MUDHOLKAR et Deo Kumar SRIVASTAVA. “Exponentiated Weibull family for analyzing bathtub failure-rate data”. In : *IEEE transactions on reliability* 42.2 (1993), p. 299-302.
- [MSF95] Govind S MUDHOLKAR, Deo Kumar SRIVASTAVA et Marshall FREIMER. “The exponentiated Weibull family : A reanalysis of the bus-motor-failure data”. In : *Technometrics* 37.4 (1995), p. 436-445.

- [MB01] Eduard MULJADI et Charles P BUTTERFIELD. “Pitch-controlled variable-speed wind turbine generation”. In : *IEEE transactions on Industry Applications* 37.1 (2001), p. 240-246.
- [MPM98] Eduard MULJADI, K PIERCE et P MIGLIORE. “Control strategy for variable-speed, stall-regulated wind turbines”. In : *Proceedings of the 1998 American Control Conference. ACC (IEEE Cat. No. 98CH36207)*. T. 3. IEEE, 1998, p. 1710-1714.
- [Mur08] P. J. MURTAGH et al. “Passive control of wind turbine vibrations including blade/tower interaction and rotationally sampled turbulence”. In : *Wind Energy* 11.4 (2008), p. 305-317. DOI : [10.1002/we.249](https://doi.org/10.1002/we.249).
- [MJ12] Mahera MUSALLAM et C Mark JOHNSON. “An efficient implementation of the rainflow counting algorithm for life consumption estimation”. In : *IEEE Transactions on reliability* 61.4 (2012), p. 978-986.
- [MHJ97] P MUTSCHLER, B HAGENKORT et S JOECKEL. “Control method for variable speed stall controlled wind turbines”. In : *EWEC-CONFERENCE-BOOKSHOP FOR SCIENTIFIC PUBLICATIONS*, 1997, p. 542-545.

N

- [Nad99] Y NADOT et al. “Fatigue life assessment of nodular cast iron containing casting defects”. In : *Fatigue & fracture of engineering materials & structures* 22.4 (1999), p. 289-300.
- [NU83] Syed A NASAR et Lewis Emory UNNEWEHR. *Electromechanics and electric machines*. John Wiley & Sons, 1983.
- [NT10] Ferrante NERI et Ville TIRRONEN. “Recent advances in differential evolution : a survey and experimental analysis”. In : *Artif. Intell. Rev.* 33.1-2 (2010), p. 61-106.
- [Nov95] Peter NOVAK et al. “Modeling and control of variable-speed wind-turbine drive-system dynamics”. In : *IEEE Control Systems Magazine* 15.4 (1995), p. 28-38.
- [NRE] NREL. *OpenFAST*.
- [NAR18] Jamie R. NUÑEZ, Christopher R. ANDERTON et Ryan S. RENSLOW. “Optimizing colormaps with consideration for color vision deficiency to enable accurate interpretation of scientific data”. In : *PLoS ONE* 13.8 (2018), p. 1-14. DOI : [10.1371/journal.pone.0199239](https://doi.org/10.1371/journal.pone.0199239).

O

- [Oca85] Maurice OCAGNE. *Coordonnées parallèles & axiales : méthode de transformation géométrique et procédé nouveau de calcul graphique déduits de la considération des coordonnées parallèles*. Gauthier-Villars, 1885.
- [Oga10] Katsuhiko OGATA. *Modern control engineering*. Sous la dir. de Marcia J. HORTON. 5^e éd. Prentice Hall, 2010.
- [OSS79] H. OKAMURA, S. SAKAI et I. SUSUKI. “Cumulative fatigue damage under random loads”. In : *Fatigue & Fracture of Engineering Materials & Structures* 1.4 (1979), p. 409-419. DOI : [10.1111/j.1460-2695.1979.tb01328.x](https://doi.org/10.1111/j.1460-2695.1979.tb01328.x).
- [OA18] Karol OPARA et Jarosław ARABAS. “Comparison of mutation strategies in Differential Evolution – A probabilistic perspective”. In : *Swarm and Evolutionary Computation* 39 (2018), p. 53-69.
- [OA19] Karol R OPARA et Jarosław ARABAS. “Differential Evolution : A survey of theoretical analyses”. In : *Swarm and Evolutionary Computation* 44 (2019), p. 546-558.
- [OPL11] Harald ORMBERG, Elizabeth PASSANO et Neil LUXCEY. “Global analysis of a floating wind turbine using an aero-hydro-elastic model : Part 1—code development and case study”. In : *International Conference on Offshore Mechanics and Arctic Engineering*. T. 44373. 2011, p. 837-847.
- [ONM02] Pierre OUAGNE, Gareth B NEIGHBOUR et Brian MCENANEY. “Crack growth resistance in nuclear graphites”. In : *Journal of Physics D : Applied Physics* 35.9 (2002), p. 927.

P

- [Pal24] Arvid PALMGREN. “Die lebensdauer von kugellagern”. In : *Zeitschrift des Vereines Duetsher Ingenieure* 68.4 (1924), p. 339.
- [PP02] Athanasios PAPOULIS et S Unnikrishna PILLAI. *Probability, random variables, and stochastic processes*. Tata McGraw-Hill Education, 2002.
- [PS95] Jun-Hyub PARK et Ji-Ho SONG. “Detailed evaluation of methods for estimation of fatigue properties”. In : *International Journal of Fatigue* 17.5 (1995), p. 365-373.
- [Par62] Emanuel PARZEN. “On Estimation of a Probability Density Function and Mode”. In : *The Annals of Mathematical Statistics* 33.3 (1962), p. 1065-1076. DOI : [10.1214/aoms/1177704472](https://doi.org/10.1214/aoms/1177704472).

- [PG17] Josh PATTERSON et Adam GIBSON. *Deep learning : A Practionar Approach*. T. 521. 7553. " O'Reilly Media, Inc.", 2017, p. 436-444. arXiv : [arXiv:1312.6184v5](https://arxiv.org/abs/1312.6184v5).
- [Pea94] Karl PEARSON. "Contributions to the mathematical theory of evolution". In : *Philosophical Transactions of the Royal Society of London. A* 185 (1894), p. 71-110.
- [Pel11] F PELAYO et al. *Operational modal analysis of two wind turbines with foundation problems*. 2011.
- [Per99] M PERALES et al. "Fuzzy logic control of a variable speed, variable pitch wind turbine". In : *IECON'99. Conference Proceedings. 25th Annual Conference of the IEEE Industrial Electronics Society (Cat. No. 99CH37029)*. T. 2. IEEE, 1999, p. 614-618.
- [PDK19] Pasin PLODPRADIT, Van Nguyen DINH et Ki Du KIM. "Coupled analysis of offshore wind turbine jacket structures with pile-soil-structure interaction using FAST v8 and X-SEA". In : *Applied Sciences (Switzerland)* 9.8 (2019), p. 1633. DOI : [10.3390/app9081633](https://doi.org/10.3390/app9081633).
- [Pol07] H POLINDER et al. "10 MW wind turbine direct-drive generator design with pitch or active speed stall control". In : *2007 IEEE International Electric Machines & Drives Conference*. T. 2. IEEE, 2007, p. 1390-1395.
- [Pon16] Fernando L PONTA et al. "Effects of rotor deformation in wind-turbine performance : the dynamic rotor deformation blade element momentum model (DRD-BEM)". In : *Renewable Energy* 92 (2016), p. 157-170.
- [Poz02] Constantine POZRIKIDIS. *A practical guide to boundary element methods with the software library BEMLIB*. CRC Press, 2002.
- [Pra19] A.V. PRADEEP et al. "A comprehensive review on contemporary materials used for blades of wind turbine". In : *Materials Today : Proceedings*. Elsevier BV, 2019. DOI : [10.1016/j.matpr.2019.07.732](https://doi.org/10.1016/j.matpr.2019.07.732).
- [PSL06] Kenneth PRICE, Rainer M STORN et Jouni A LAMPINEN. *Differential evolution : a practical approach to global optimization*. Springer Science & Business Media, 2006.
- [PEL10] Ian PROWELL, Ahmed ELGAMAL et Jinchi LU. "Modeling The Influence Of Soil Structure Interaction On The Seismic Response Of A 5 Mw Wind Turbine". In : *2010 - Fifth International Conference on Recent Advances in Geotechnical Earthquake Engineering and Soil Dynamics* (2010), p. 9.

Q

- [QHS09a] A K QIN, V L HUANG et P N SUGANTHAN. “Differential Evolution Algorithm With Strategy Adaptation for Global Numerical Optimization”. In : *IEEE Transactions on Evolutionary Computation* 13.2 (2009), p. 398-417.
- [QHS09b] A. K. QIN, V. L. HUANG et P. N. SUGANTHAN. “Differential evolution algorithm with strategy adaptation for global numerical optimization”. In : *IEEE Transactions on Evolutionary Computation* 13.2 (2009), p. 398-417. DOI : [10.1109/TEVC.2008.927706](https://doi.org/10.1109/TEVC.2008.927706).

R

- [Raj05] Tonse N K RAJU. “William Sealy Gosset and William A. Silverman : two “students” of science”. In : *Pediatrics* 116.3 (2005), p. 732-735.
- [REN19] REN21. *RENEWABLES 2019 GLOBAL STATUS REPORT*. Rapp. tech. 2019, p. 336.
- [REN20] REN21. *RENEWABLES 2020 GLOBAL STATUS REPORT*. Rapp. tech. 2020, p. 367.
- [RT69] J.R. RICE et Dennis Michael TRACEY. “On the ductile enlargement of voids in triaxial stress fields”. In : *Journal of the Mechanics and Physics of Solids* 17.3 (1969), p. 201-217.
- [RV00] Vasilis A RIZIOTIS et Spyros G VOUTSINAS. “Fatigue loads on wind turbines of different control strategies operating in complex terrain”. In : *Journal of Wind Engineering and Industrial Aerodynamics* 85.3 (2000), p. 211-240.
- [RB99] Janardan ROHATGI et G I L BARBEZIER. “Wind turbulence and atmospheric stability—their effect on wind turbine output”. In : *Renewable energy* 16.1-4 (1999), p. 908-911.
- [Ros58] F. ROSENBLATT. “The perceptron : A probabilistic model for information storage and organization in the brain”. In : *Psychological Review* 65.6 (1958), p. 386-408. DOI : [10.1037/h0042519](https://doi.org/10.1037/h0042519).
- [Roy13] Thibaud ROY et al. “Wind velocity field approximation from sparse data”. In : *2013 IEEE International Geoscience and Remote Sensing Symposium-IGARSS*. IEEE, 2013, p. 1606-1609.
- [RHW86] David E. RUMELHART, Geoffrey E. HINTON et Ronald J. WILLIAMS. “Learning representations by back-propagating errors”. In : *Nature* 323.6088 (1986), p. 533-536. DOI : [10.1038/323533a0](https://doi.org/10.1038/323533a0).

- [Ryc87] Igor RYCHLIK. “A new definition of the rainflow cycle counting method”. In : *International journal of fatigue* 9.2 (1987), p. 119-121.

S

- [Sch14] Jörn SCHELLER. “Power-efficient active structural vibration control by twin rotor dampers”. Thèse de doct. Hamburg University of Technology, 2014.
- [Sch13] Werner SCHIEHLEN. *Advanced multibody system dynamics : Simulation and Software tools*. T. 20. Springer Science & Business Media, 2013.
- [Scia] SCIPY. *Continuous Statistical Distributions*.
- [Scib] SCIPY. *Statistical functions (scipy.stats)*.
- [SL16] Anderson Tenório SERGIO et Teresa B. LUDERMIR. “Deep learning for wind speed forecasting in northeastern region of Brazil”. In : *Proceedings - 2015 Brazilian Conference on Intelligent Systems, BRACIS 2015*. IEEE, 2016, p. 322-327. DOI : [10.1109/BRACIS.2015.40](https://doi.org/10.1109/BRACIS.2015.40).
- [SD14] Mahmood SHAFIEE et Fateme DINMOHAMMADI. “An FMEA-based risk assessment approach for wind turbine systems : a comparative study of onshore and offshore”. In : *Energies* 7.2 (2014), p. 619-642.
- [Sha16] B SHAHRIARI et al. “Taking the Human Out of the Loop : A Review of Bayesian Optimization”. In : *Proceedings of the IEEE* 104.1 (2016), p. 148-175.
- [Sha10] Nima SHAMSAEI et al. “Multiaxial fatigue of titanium including step loading and load path alteration and sequence effects”. In : *International Journal of Fatigue* 32.11 (2010), p. 1862-1874. DOI : [10.1016/j.ijfatigue.2010.05.006](https://doi.org/10.1016/j.ijfatigue.2010.05.006).
- [SJ72] M. SHINOZUKA et C. M. JAN. “Digital simulation of random processes and its applications”. In : *Journal of Sound and Vibration* 25.1 (1972), p. 111-128. DOI : [10.1016/0022-460X\(72\)90600-1](https://doi.org/10.1016/0022-460X(72)90600-1).
- [Shi13] R SHIRZADEH et al. “Experimental and computational damping estimation of an offshore wind turbine on a monopile foundation”. In : *Journal of Wind Engineering and Industrial Aerodynamics* 120 (2013), p. 96-106.
- [Slo20] René M.M. SLOT et al. “Surrogate model uncertainty in wind turbine reliability assessment”. In : *Renewable Energy* 151 (2020), p. 1150-1162. DOI : [10.1016/j.renene.2019.11.101](https://doi.org/10.1016/j.renene.2019.11.101).

- [Smi48] Nickolay SMIRNOV. “Table for estimating the goodness of fit of empirical distributions”. In : *The annals of mathematical statistics* 19.2 (1948), p. 279-281.
- [Sne93] H SNEL et al. “Sectional prediction of 3D effects for stalled flow on rotating blades and comparison with measurements”. In : *Proc. European Community Wind Energy Conference, Lübeck-Travemünde, Germany*. 1993, p. 395-399.
- [SDK19] S SRIVASTAVA, M DAMODARAN et B C KHOO. “Machine Learning Surrogates for Predicting Response of an Aero-Structural-Sloshing System”. In : *arXiv preprint arXiv :1911.10043* (2019), p. 1-29.
- [Sta13] Uwe STAROSSEK. *Dispositif De Contrôle Des Vibrations D'une Construction*. 2013.
- [Sta15] Uwe STAROSSEK. *Device for Vibration Control of a Structure*. 2015.
- [Sto96] R STORN. “On the usage of differential evolution for function optimization”. In : *Proceedings of North American Fuzzy Information Processing*. 1996, p. 519-523.
- [SP97] Rainer STORN et Kenneth PRICE. “Differential evolution—a simple and efficient heuristic for global optimization over continuous spaces”. In : *Journal of global optimization* 11.4 (1997), p. 341-359.
- [Sub76] S SUBRAMANYAN. “A cumulative damage rule based on the knee point of the S-N curve”. In : *Journal of Engineering Materials and Technology* 98.4 (1976), p. 316-321.
- [Sun16] Zhenye SUN et al. “Improved blade element momentum theory for wind turbine aerodynamic computations”. In : *Renewable energy* 96 (2016), p. 824-831.
- [SJ13] Ashish SWAMI et Ritesh JAIN. “Scikit-learn : Machine Learning in Python”. In : *Journal of Machine Learning Research* 12.10 (2013), p. 2825-2830.

T

- [Tho18] William THOMSON. *Theory of vibration with applications*. CrC Press, 2018.
- [Tra13] Anh Tuan TRAN et al. “Resistance of Door Opening in Towers for Wind Turbines”. In : *South-East European Conference on Computational Mechanics : 12/06/2013-14/06/2013*. 2013, p. 312-324.
- [Tuc59] Howard G TUCKER. “A generalization of the Glivenko-Cantelli theorem”. In : *The Annals of Mathematical Statistics* 30.3 (1959), p. 828-830.

U

- [Uni19] UNITED NATIONS ENVIRONMENT PROGRAMME. *GLOBAL TRENDS IN RENEWABLE ENERGY INVESTMENT 2019*. Rapp. tech. 2019, p. 76.
- [Urs02] Rasmus K URSEM. “Diversity-guided evolutionary algorithms”. In : *International Conference on Parallel Problem Solving from Nature*. Springer, 2002, p. 462-471.
- [U.S11] U.S. ENERGY INFORMATION ADMINISTRATION. *Levelized Cost of New Generation Resources in the Annual Energy Outlook 2011*. Rapp. tech. 2011.
- [U.S12] U.S. ENERGY INFORMATION ADMINISTRATION. *Levelized Cost of New Generation Resources in the Annual Energy Outlook 2012*. Rapp. tech. 2012.
- [U.S13] U.S. ENERGY INFORMATION ADMINISTRATION. *Levelized Cost of New Generation Resources in the Annual Energy Outlook 2013*. Rapp. tech. 2013.
- [U.S14] U.S. ENERGY INFORMATION ADMINISTRATION. *Levelized Cost and Levelized Avoided Cost of New Generation Resources in the Annual Energy Outlook 2014*. Rapp. tech. 2014.
- [U.S15] U.S. ENERGY INFORMATION ADMINISTRATION. *Levelized Cost and Levelized Avoided Cost of New Generation Resources in the Annual Energy Outlook 2015*. Rapp. tech. 2015.
- [U.S16] U.S. ENERGY INFORMATION ADMINISTRATION. *Levelized Cost and Levelized Avoided Cost of New Generation Resources in the Annual Energy Outlook 2016*. Rapp. tech. 2016.
- [U.S17] U.S. ENERGY INFORMATION ADMINISTRATION. *Levelized Cost and Levelized Avoided Cost of New Generation Resources in the Annual Energy Outlook 2017*. Rapp. tech. 2017.
- [U.S18] U.S. ENERGY INFORMATION ADMINISTRATION. *Levelized Cost and Levelized Avoided Cost of New Generation Resources in the Annual Energy Outlook 2018*. Rapp. tech. 2018.
- [U.S19] U.S. ENERGY INFORMATION ADMINISTRATION. *Levelized Cost and Levelized Avoided Cost of New Generation Resources in the Annual Energy Outlook 2019*. Rapp. tech. 2019.
- [U.S20] U.S. ENERGY INFORMATION ADMINISTRATION. *Levelized Cost and Levelized Avoided Cost of New Generation Resources in the Annual Energy Outlook 2020*. Rapp. tech. 2020.

- [U.S21] U.S. ENERGY INFORMATION ADMINISTRATION. *Levelized Costs of New Generation Resources in the Annual Energy Outlook 2021*. Rapp. tech. 2021.

V

- [Van01] David VAN AKEN. “Fatigue endurance limit of steel”. In : *Industrial Heating* 68.12 (2001), p. 14.
- [Vee88] Paul S. VEERS. *Three-Dimensional Wind Simulation*. Rapp. tech. 1988.

W

- [Wan17] Huai zhi WANG et al. “Deep learning based ensemble approach for probabilistic wind power forecasting”. In : *Applied Energy* 188 (2017), p. 56-70. DOI : [10.1016/j.apenergy.2016.11.111](https://doi.org/10.1016/j.apenergy.2016.11.111).
- [Wan14] Lin WANG et al. “Nonlinear aeroelastic modelling for wind turbine blades based on blade element momentum theory and geometrically exact beam theory”. In : *Energy* 76 (2014), p. 487-501.
- [WCZ11] Y WANG, Z CAI et Q ZHANG. “Differential Evolution With Composite Trial Vector Generation Strategies and Control Parameters”. In : *IEEE Transactions on Evolutionary Computation* 15.1 (2011), p. 55-66.
- [Wil10] Kitchener Clark WILSON. *Wind turbine damping of tower resonant motion and symmetric blade motion using estimation methods*. 2010.
- [WAWW07] Edmund WITTBRODT, Iwona ADAMIEC-WÓJCIK et Stanislaw WOJCIECH. *Dynamics of flexible multibody systems : rigid finite element method*. Springer Science & Business Media, 2007.
- [Wöh60] August WÖHLER. “Versuche zur Ermittlung der auf die Eisenbahnwagennachsen einwirkenden Kräfte und die Widerstandsfähigkeit der Wagenachsen”. In : *Zeitschrift für Bauwesen* 10.1860 (1860), p. 583-614.
- [Wri81] Alan D WRIGHT et al. “SWECS tower dynamics analysis methods and results”. In : (1981).

X

- [Xia16] Peng XIAOSHENG et al. “A very short term wind power prediction approach based on Multilayer Restricted Boltzmann Machine”. In : *Asia-Pacific Power and Energy Engineering Conference, APPEEC*. T. 2016-

Decem. IEEE, 2016, p. 2409-2413. DOI : [10.1109 / APPEEC . 2016 . 7779917](https://doi.org/10.1109/APPEEC.2016.7779917).

Y

[Yu14] W YU et al. “Differential Evolution With Two-Level Parameter Adaptation”. In : *IEEE Transactions on Cybernetics* 44.7 (2014), p. 1080-1099.

Z

[Zah07] Daniela ZAHARIE. “A comparative analysis of crossover variants in differential evolution”. In : *Proceedings of the IMCSIT*. T. 2007. 2007, p. 183-192.

[ZS09] Jingqiao ZHANG et Arthur C. SANDERSON. “JADE : Adaptive differential evolution with optional external archive”. In : *IEEE Transactions on Evolutionary Computation* 13.5 (2009), p. 945-958. DOI : [10.1109 / TEVC . 2009 . 2014613](https://doi.org/10.1109/TEVC.2009.2014613).

[ZTZ05] Olek C ZIENKIEWICZ, Robert L TAYLOR et Jian Z ZHU. *The finite element method : its basis and fundamentals*. Elsevier, 2005.

[ZM71] Olgierd Cecil ZIENKIEWICZ et P B MORICE. *The finite element method in engineering science*. T. 1977. McGraw-Hill London, 1971.

[ZBH18] Haoran ZUO, Kaiming BI et Hong HAO. “Dynamic analyses of operating offshore wind turbines including soil-structure interaction”. In : *Engineering Structures* 157 (2018), p. 42-62. DOI : [10.1016 / j . engstruct . 2017 . 12 . 001](https://doi.org/10.1016/j.engstruct.2017.12.001).

Index

Symbols

V_{in} xi, xiii, xv, xix, 29, 49, 53, 56, 57, 70,
72, 89–91, 93, 95, 110, 120, 125,
127, 128, 132, 206, 265, 266, 269,
270, 272, 273, 277, 278, 280

V_{mean} . xi, xiv, xix, 53, 56, 68, 69, 72, 80,
82, 83, 89–91, 93, 95, 102, 105,
107, 110, 125–127, 149, 152, 153,
199, 200, 233, 234, 243–248,
264–266, 269, 270, 272, 275, 277,
290

V_{out} .xi–xv, xix, 49, 53, 56, 57, 65–68, 70,
72, 89–91, 93, 95, 105, 110, 120,
125, 127, 128, 132, 149, 150,
152–154, 156, 157, 206, 237,
262–266, 269, 270, 272, 273, 277,
278, 280, 286–288, 290, 297, 298

V_{rate} ix, x, xiii, xv, xix, 29, 49, 53–57, 62,
65–68, 70–72, 105, 125, 151, 156,
157, 206, 249, 262, 263, 266, 289,
297, 298

A

AANNxxi, 111
ANNxxi, 110, 111

C

CDFxxi, 85, 219
CNNxxi, 111, 115

D

DE ...xxi, xxiii, xxiv, 159, 161, 169, 182,
186, 257, 258, 291, 297, 299

DLxxi, 111

DLC0.1 ...53, 57, 58, 60, 61, 72, 265, 266

DLC0.2 . 58, 61, 62, 65, 72, 262, 265, 266

DLC1.1 37, 44, 186, 260, 300

DLC1.2 93–96, 98–101, 125, 134, 149,
152–154, 157, 183, 185, 272, 274,
282, 289–291, 297, 299

DLC2.3 .. 37, 44, 65, 66, 70–72, 149–151,
155, 157, 183, 185, 235–237, 248,
249, 260, 262, 265, 266, 287, 288,
290, 296–299

DNNxxi, 110–112, 114, 119, 134

DOWECxxi, 48

downwind xix

E

EAxxi, 134, 159, 169, 258, 291

ECDFxxi, 85, 219

emergency shutdownxix

EOG . ix, xiii, xxi, 35, 65–68, 70–72, 262,
263, 265, 266

F

FEMxxi, 39, 50, 74

Friedman test xix, 177, 292

G

gage 150, 54–56, 67, 70, 87, 99, 100,
102–107, 109, 120, 152, 153, 238,
242, 270, 274, 275, 289, 290

gage 2 109, 238, 242

gage 3 109, 238, 242

gage 4 109, 238, 242

gage 5 109, 238, 242

gage 6 109, 238, 242

gage 7 109, 238, 242

gage 8 109, 238, 242

gage 9 ... 51, 53, 54, 56, 61, 67, 107, 109,
 149, 150, 157, 238, 242, 287, 298
 grid lossxix, 66, 185
 gustxx
 GWECxxi, 5

H

HAWT ix, xxi, 6, 7, 48
 HH xxi, 48, 49, 77, 91, 93, 96, 272
 HSS ..xxi, 59–62, 64, 66, 69–72, 149, 264,
 266, 287
 hub xx

I

IEAxxi, 3
 IRENAxxi, 4, 5

K

Kolmogorov-Smirnov test xxii, 84–88, 95,
 102, 127, 219, 277

L

LCOE ix, xxii, 5, 6, 23, 108, 259
 LSTMxxii, 111
 LTI xxii, 141

M

MAExxii, 117
 Mann–Whitney U test xx, 177
 MAPE xxii, 117
 MaxFESxxii, 156, 176, 296
 MDN xxii, 129
 MLxxii, 111
 MLEx, xii, xxii, 83–86, 217–219
 MLP ... xxii, 111–115, 118, 119, 121, 276
 MRBMxxii, 111
 MSE xxii, 116, 117
 MSLExxii, 117, 122, 123, 125, 277

N

nacelle xx
 Nemenyi post-hoc test xx, 177, 292

neural network 111–118, 120–123,
 125–128, 276, 277
 NREL xxii, 42, 61, 72, 131, 261, 266, 279
 NTM .. ix, x, xiii, xxii, 34, 36, 83, 93–95,
 97, 101, 107, 130, 132, 152, 272,
 273, 280, 289

P

PCE xxii, 111
 PDF ..xxii, 89, 91, 100, 103, 217, 270, 274
 peak-to-peak amplitude ..xx, 68–72, 149,
 151, 264–266, 287, 288
 power outputxx
 PTF .. xxii, 57, 59–62, 64, 66, 69, 71, 72,
 264, 266

R

rated power xx
 RBDOxxii, 88, 101
 ReLUxxii, 114, 122, 123, 277
 ResMLP xxii, 122, 125, 128, 129, 132–134,
 159, 186, 277, 280, 281, 300
 ResNetxxii, 115
 RMSE xxii, 117
 RNNxxii, 111
 rotor speedxx

S

SDOF ... xi, xxii, 140–143, 157, 185, 290,
 299
 SHMxxii, 111
 spot 0 120
 spot 1 87, 99, 101, 152, 270, 274
 spot 10 99
 spot 19 99
 spot 28 99
 SVMxxii, 111
 swept areaxx

T

tower-base ..50, 51, 82, 95, 102, 107, 108,
 120, 157, 213, 291

tower-top ... 50, 51, 82, 95, 102, 107, 108,
 145–147, 149, 151, 155, 157, 284,
 285, 287, 288, 291, 296

TRD xi, xiii–xvii, xxii–xxiv, 23, 137–141,
 143–159, 183, 185, 186, 248, 249,
 257–259, 282–291, 296–300

U

upwind xx

V


VAWT xxii, 7

W

wind shear xx

Y

yawing xx



Utilisation de l'apprentissage automatique pour la prédiction probabiliste à long-terme du dommage par fatigue et la réduction des vibrations d'un mât d'éolienne par un contrôle actif

Résumé

Cette thèse est consacrée au développement d'un système d'amortissement actif pour la réduction des vibrations du mât d'éoliennes en cas de vent avec rafales et de vent avec turbulence. La présence de vibrations entraîne souvent soit une déflexion ultime au sommet du mât d'éolienne, soit une défaillance due à la fatigue du matériau près du bas du mât d'éolienne. De plus, étant donné la nature aléatoire de l'état du vent, il est indispensable d'examiner ce problème d'un point de vue probabiliste.

Dans ce travail, un cadre probabiliste d'analyse de la fatigue est développé et amélioré en utilisant le réseau de neurones résiduels. Un système d'amortissement utilisant un amortisseur actif, le Twin Rotor Damper, est conçu pour l'éolienne référentielle NREL 5MW. La conception est optimisée par un algorithme évolutionniste avec une méthode de réglage automatique des paramètres basée sur l'exploitation et l'exploration.

Mots-clés Mât d'éolienne, Condition de vent avec rafale, Condition de vent avec turbulence, Analyse probabiliste en fatigue, Contrôle actif, Réseaux de Neurones Profonds, Algorithme évolutionniste, Evolution Différentielle, Optimisation

Machine learning assisted probabilistic prediction of long-term fatigue damage and vibration reduction of wind turbine tower using active damping system

Abstract

This dissertation is devoted to the development of an active damping system for vibration reduction of wind turbine tower under gusty wind and turbulent wind. The presence of vibrations often leads to either an ultimate deflection on the top of wind tower or a failure due to the material's fatigue near the bottom of wind tower. Furthermore, given the random nature of wind conditions, it is indispensable to look at this problem from a probabilistic point of view.

In this work, a probabilistic framework of fatigue analysis is developed and improved by using a residual neural network. A damping system employing an active damper, Twin Rotor Damper, is designed for NREL 5MW reference wind turbine. The design is optimized by an evolutionary algorithm with automatic parameter tuning method based on exploitation and exploration.

Keywords Wind turbine tower, Wind gust condition, Wind turbulence condition, Probabilistic fatigue analysis, Active control, Deep neural network, Evolutionary algorithm, Differential evolution, Optimization